Topics in Current Chemistry Collections

Mario J. Muñoz-Batista
Alexander Navarrete Muñoz
Rafael Luque *Editors*

Heterogeneous Photocatalysis

Recent Advances

Springer

Topics in Current Chemistry Collections

Aims and Scope

The series *Topics in Current Chemistry Collections* presents critical reviews from the journal *Topics in Current Chemistry* organized in topical volumes. The scope of coverage is all areas of chemical science including the interfaces with related disciplines such as biology, medicine and materials science.

The goal of each thematic volume is to give the non-specialist reader, whether in academia or industry, a comprehensive insight into an area where new research is emerging which is of interest to a larger scientific audience.

Each review within the volume critically surveys one aspect of that topic and places it within the context of the volume as a whole. The most significant developments of the last 5 to 10 years are presented using selected examples to illustrate the principles discussed. The coverage is not intended to be an exhaustive summary of the field or include large quantities of data, but should rather be conceptual, concentrating on the methodological thinking that will allow the non-specialist reader to understand the information presented.

Contributions also offer an outlook on potential future developments in the field.

More information about this series at http://www.springer.com/series/14181

Mario J. Muñoz-Batista
Alexander Navarrete Muñoz
Rafael Luque
Editors

Heterogeneous Photocatalysis

Recent Advances

With contributions from

Orlando M. Alfano • María de los Milagros Ballari
Irene Barba-Nieto • Gregory Chatel • Juan Carlos Colmenares
Uriel Caudillo-Flores • Fernando Fresno • Marcos Fernández-García
Dimitrios A. Giannakoudakis • Parag R. Gogate
Patricia Garcia-Muñoz • Giuseppina Iervolino • Nicolas Keller
Anna Kubacka • Yasutaka Kuwahara • Rafael Luque
Mario J. Muñoz-Batista • Kohsuke Mori • Miriam Navlani-Garcia
Víctor A. de la Peña O'Shea • Daily Rodríguez-Padrón • Luigi Rizzo
David Salinas-Torres • María Lucila Satuf • Vincenzo Vaiano
Hiromi Yamashita • Ian Zammit

Springer

Editors
Mario J. Muñoz-Batista
Department of Chemical Engineering
University of Granada
Granada, Spain

Rafael Luque
Departamento de Quimica Organica
Universidad de Cordoba
Córdoba, Spain

Alexander Navarrete Muñoz
Institute for Micro Process Engineering
Karlsruhe Institute of Technology
Karlsruhe, Germany

Partly previously published in Topics in Current Chemistry Volume 377 (2019); Topics in Current Chemistry Volume 378 (2020).

ISSN 2367-4067
Topics in Current Chemistry Collections
ISBN 978-3-030-49491-9

This Springer imprint is published by the registered company Springer Nature Switzerland AG
The registered company address is: Gewerbestrasse 11, 6330 Cham, Switzerland

Contents

Preface

Heterogeneous Photocatalysis has gained great attention from the scientific community during the last decades. Mild operating conditions and the potential utilization of sunlight as a green energy source are two of the main advantages that make this advanced oxidation process an open and very active research line. Applications range from new energy vectors production, to environmental remediation as well as the selective synthesis of chemicals. According to the IUPAC in the "Glossary of terms used in photochemistry, Pure and Applied Chemistry, 79, 2007, 293-465" a photocatalytic reaction is defined as a change in the rate of a chemical reaction or its initiation under the action of ultraviolet, visible or infrared radiation in the presence of a substance, the photocatalyst, that absorbs light and is involved in the chemical transformation of the reaction partners". The definition describes a relatively complex phenomenon where many parameters must be controlled for an efficient control of the photoreactions.

This topical collection provides an updated overview of relevant photocatalytic topics such as novel synthetic protocols of photoactive materials, advanced approaches for its characterization, critical reviews of traditional applications and modelling of the light-matter interaction. The collection starts with relevant contributions associated with novel synthetic protocols in which good control of the chemical, structural, morphologic and optical properties are achieved. Opportunities of waste-derived materials and mechanochemical- and ultrasound-assisted protocols to produce advanced-photocatalytic are presented in contributions 1 to 3. Contribution 4 has focused on ferrite nanomaterials, including magnetically separable materials, and their application for solar fuels processes. Characterization of photocatalysts is shown as a relevant task to understand and optimize the behaviour of the samples. In this regard, contribution 5 covers an analysis of traditional and advanced-characterization approaches. Operando and spectro-kinetic methodologies are reviewed as they would render valuable and trusting results. Two photocatalytic applications have been analyzed in contributions 6 and 7. Photoproduction of H_2 via formic acid decomposition and wastewater treatments respectively, both with a critical

perspective. Finally, contribution 8 provides a photocatalytic engineering approach. Different setup configurations and employed numerical methods to calculate the photon absorption rate are analyzed.

As described throughout the collection, Heterogeneous Catalysis technology has achieved relevant results at laboratory scale. The future will also bring new ways to integrate lab and industry results to scale-up the use of sustainable photocatalytic materials and processes. We hope that the emerging ideas summarized in this collection may inspire the scientific community for the development of more efficient photocatalytic schemes. We finally would like to thank the editorial staff of Topics in Current Chemistry and the editorial board for the support and help assembling this collection.

Mario J. Muñoz-Batista

Mario J. Muñoz-Batista
Department of Chemical Engineering,
University of Granada, Spain

Alexander Navarrete Muñoz
Institute for Micro Process
Engineering, Karlsruhe Institute
of Technology, Germany

Rafael Luque
Departamento de Quımica Organica,
Universidad de Cordoba, Spain

Topics in Current Chemistry (2020) 378:3
https://doi.org/10.1007/s41061-019-0264-1

REVIEW

Waste-derived Materials: Opportunities in Photocatalysis

Daily Rodríguez-Padrón[1] · Rafael Luque[1,2] · Mario J. Muñoz-Batista[1,3]

Received: 3 July 2019 / Accepted: 1 November 2019 / Published online: 28 November 2019

Abstract

Waste-derived materials have been gaining increased attention in recent years due to their great potential and environmentally friendly nature. Several contributions in the literature have covered the advances achieved so far in this area. Nonetheless, to the best of our knowledge, no review has been dedicated specifically to waste-derived or templated photocatalytic materials. Both photocatalysis and (bio)waste-inspired design yield materials of a remarkably green nature. Therefore, the partnership between them may open promising possibilities for both waste valorization and photocatalytic processes, which in turn will lead to sustainable development globally, with the potential for full utilization of renewable energy sources such as biomass and sunlight. Several photocatalytic waste-derived materials, synthetic procedures, and applications will be described throughout this work, including waste-derived/templated TiO_2, ZnO, and metal sulfide materials. Special attention will be given to biomass-inspired carbonaceous materials, including carbon quantum dots and graphitic carbon nitride (g-C_3N_4).

Keywords Photocatalysis · Nanomaterials · Waste · Valorization · Biomass · Green chemistry

Chapter 1 was originally published as Rodríguez-Padrón, D., Luque R. & Muñoz-Batista, M. J. Topics in Current Chemistry (2020) 378: 3. https://doi.org/10.1007/s41061-019-0264-1.

✉ Rafael Luque
rafael.luque@uco.es

✉ Mario J. Muñoz-Batista
mariomunoz@ugr.es

[1] Departamento de Química Orgánica, Universidad de Córdoba, Edificio Marie-Curie (C-3), Ctra Nnal IV-A, Km 396, Córdoba, Spain

[2] Peoples Friendship University of Russia (RUDN University), 6 Miklukho-Maklaya Str, 117198 Moscow, Russia

[3] Department of Chemical Engineering, Faculty of Sciences, University of Granada, Avda. Fuentenueva, s/n, 18071 Granada, Spain

1 Introduction

As defined in *Green Chemistry: Theory and Practice* by Anastas and Warner, catalysis is one of the 12 design principles of green chemistry [1]. Sheldon et al. highlight the paradigm shift in the concept of reaction efficiency, from one that is focused on chemical yield, to one that assigns value to the minimization of waste [2]. In addition, several concepts must be considered in effecting an efficient green catalytic process. The energy consumed in a reaction and the sustainable character of the catalytic materials are both usually analyzed as relevant issues [3].

Heterogeneous photocatalysis is a type of catalysis which refers to chemical processes catalyzed by a solid where the external energy is ultraviolet, visible, or infrared radiation. [4–14] It is a complex phenomenon but is typically schematically represented by the process described in the center of Fig. 1. As can be seen, the photoexcited sample generates electrons and holes. Electrons and holes may initiate a reductive and an oxidative reaction pathway, respectively. In addition, the

Fig. 1 Schematic representation of the potential applications of waste for the design of photocatalytic materials

recombination of electrons and holes and the resulting loss of energy during the process typically reduce the photoactivity of the sample. The electrons and holes generated can initiate a wide range of reactions in both gas and liquid media, which include the production of energy vectors (CO_2 reduction, water splitting, alcohol conversion) [15–22], selective organic synthesis of high-value products [14, 23–29], and elimination/degradation of undesired chemicals [4, 30–37] and microbial pathogens in air and water [38–42]. Obviously, the final efficiency of the process depends on the semiconductor used. In this regard, TiO_2-based materials are the most widely used photocatalysts, as described in numerous reports in the literature [5, 7, 9, 43–45], although ZnO- and g-C_3N_4-based materials and many others have shown outstanding results in a variety of photocatalytic applications [46–52].

This contribution focuses on waste-derived materials which have been employed or can be considered as a potentially attractive option for photocatalytic reactions. Throughout the manuscript, two main concepts are exploited: the reuse of waste as a source of components (e.g. titanium, zinc, sulfur, carbon) for the photocatalyst, and the valorization of waste for use in as catalyst in the synthetic protocol (e.g. sacrificial templates). Figure 1 presents a schematic illustration of all the possibilities that different types of waste, including orange peel, rice husk, spent coffee grounds, and lignocellulosic and electronic residues, to name just a few, can offer for the design of highly sustainable materials. In addition, the optoelectronic, morphological, and textural properties can be tuned by employing these residues using various synthetic strategies, with the ultimate goal of obtaining efficient photocatalytic materials. The concept of waste transformation in photocatalytic applications is itself highly ecofriendly, and the use of green methodologies and alternative sustainable technologies will be considered as well and highlighted in the following sections.

2 TiO_2-based Materials: Ti from Waste

As mentioned above, TiO_2 is by far the most commonly used photocatalyst, showing competitive results in a wide range of photocatalytic applications. Pure TiO_2 and TiO_2-based samples have both been widely studied from a photocatalytic, chemical, morphological, and optical point of view [7, 9, 43, 44]. In fact, some authors highlight TiO_2 as the most extensively studied transition-metal oxide material [44].

Titanium and Ti-related materials have found application in many areas, from aerospace, marine, and automobile industries, to chemical plant materials, medical equipment, buildings, and several consumer products (spectacle frames, golf clubs, etc.) [53]. As is common, during the production of the final product, Ti-containing waste is usually generated. Indeed, there are numerous opportunities for the recovery of Ti and Ti-related compounds in Ti smelting and Kroll processes [53]. One area in which researchers have focused is on the reuse-extraction of Ti or Ti-containing slag [54]. As described by Liu et al., approximately 53% of the Ti is carried through processing into iron-rich concentrations for feeding blast furnaces. The slag generated contains up to 25% of TiO_2. Given that it is produced at a rate of three million tons per year, this is a clear opportunity for the production of a cheap photocatalyst [55]. Extraction, however, has many limitations. From an environmental point of view,

Fig. 2 **a** Schematic representation of titanium recovery from spent SCR materials. **b**, **c** Scanning electron microscopy (SEM) and EDX mapping analysis. **d**, **e** RhB and MB photodegradation results [56]. **f**, **g** XPS and TGA analysis of produced waste anodic electrolyte. **h** Scheme of the extraction of the waste anodic electrolyte. **i**, **j** Photocatalytic degradation of HAs by TiO_2 and UV irradiation. **k**, **l** Photocatalytic degradation of bentazone by N-doped TiO_2 under visible irradiation [58] ▶

the extensive use of acids for the leaching recovery process is still a problem. Nonetheless, acid leaching processes have shown high efficiency during Ti recovery [55].

The extensive use of selective catalytic reduction (SCR) systems has generated large amounts of spent/waste SCR catalysts. The generation of this type of waste will continue and will be vital in the coming years with the implementation of the Euro 6 diesel emission standards. Elemental concentrations in spent SCR catalysts are not a constant variable; however, considerable concentrations of heavy metals such as Ti^{4+}, V^{5+}, Fe^{3+}, W^{6+} and Ca^{2+} have been common [56]. As a representative example, an economical approach for recovering titanium and regenerating TiO_2 photocatalysts from spent SCR catalysts has been reported. Elemental analysis of the SCR catalyst waste carried out by total reflection X-ray fluorescence identified a remarkably high concentration of TiO_2 (68.5 wt%), while other major compounds, namely SiO_2, SO_3, Al_2O_3, and WO_3, showed concentrations of 10.3, 6.45, 5.47, and 4.67 wt%, respectively. Minor components (below 2 wt%) including Fe_2O_3 CaO, V_2O_5, K_2O, Na_2O, MgO, P_2O_5, Nb_2O_5, ZrO_2, As_2O_3, and SrO were also measured. The high TiO_2 concentration in the waste-catalysts makes them especially interesting for recovery of TiO_2 species. In addition, some of the minor entities (Fe_2O_3, V_2O_5, Nb_2O_5, ZrO_2) have shown a beneficial photocatalytic response by modification of the optical and electronic properties of the titania counterpart [5, 6]. The proposed titanium recovery scheme and the further production of TiO_2 is described in Fig. 2a. As can be seen, the protocols followed three general steps: (1) NaOH molten salt decomposition, (2) water leaching to separate Na_2TiO_3 and NaOH recycling, and (3) hydrothermal reaction to regenerate titania. During the leaching process, two treatments (1.0 mol/L HCl or 0.5 mol/L H_2SO_4) were used, and hence two samples A and B were obtained. The morphology of the samples differed considerably, with sample A presenting spherical nanoparticles, while sample B exhibited numerous rod-shaped structures (Fig. 2b, c). Interestingly, both samples presented iron entities in the structure, which was confirmed by energy-dispersive X-ray (EDX) mapping data (Fig. 2b, c) and X-ray photoelectron spectroscopy (XPS) analysis (not shown). Such a small concentration of iron, which according to XPS data was present as Fe_2O_3, would confer enhanced absorption of visible irradiation. Degradation of rhodamine B (RhB) and methylene blue (MB) were used to demonstrate the photocatalytic properties of samples A and B under visible illumination conditions. Sample A showed better photocatalytic performance with both dyes, outperforming the activity of P25 commercial TiO_2 references (Fig. 2d, e) [56].

An important limitation of waste-derived photocatalysts is that in many examples, an uncontrolled structure is obtained [3]. In fact, the poor reproducibility of the synthesis is one of the main drawbacks of waste-derived materials. Such a situation is especially important in photocatalytic materials when minor compositional variations drive very different catalytic results [57]. However, if the waste source

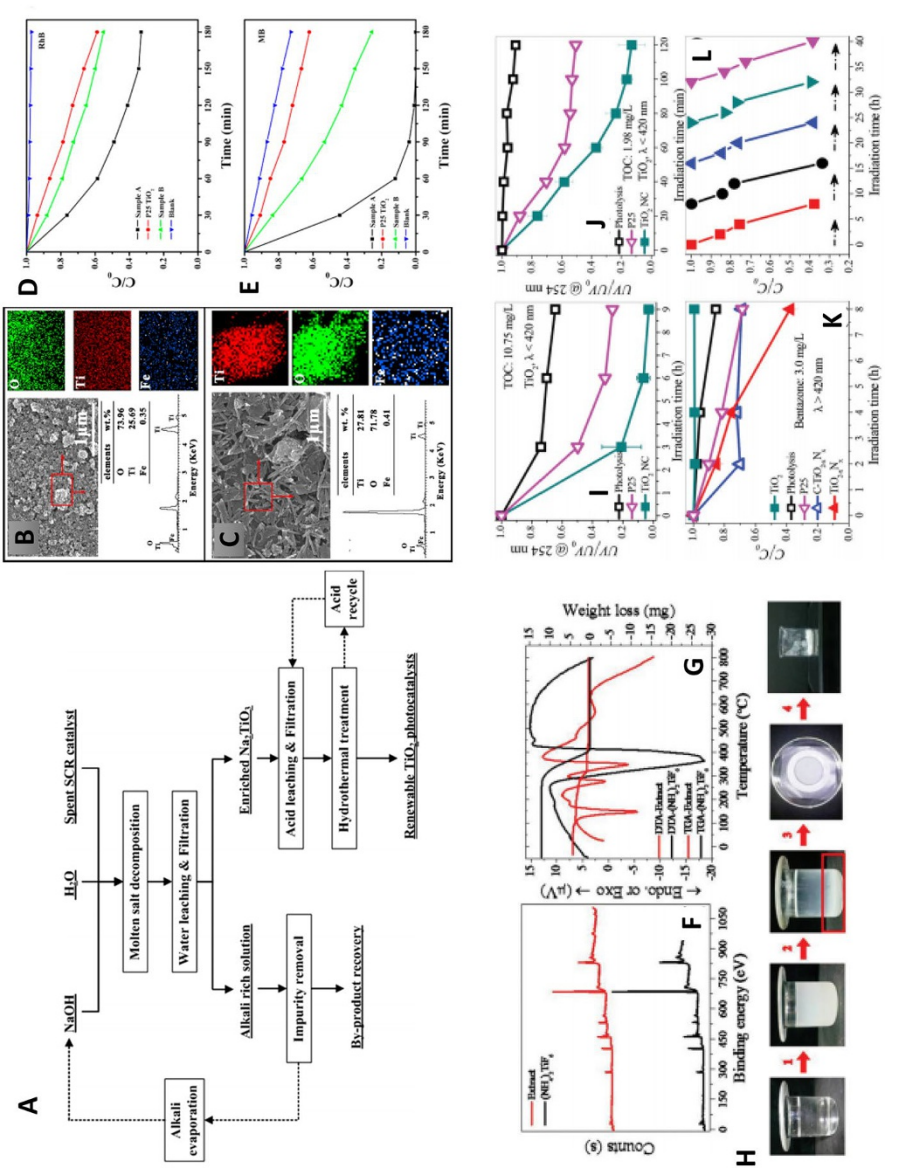
A
NaOH
H2O
Spent SCR catalyst
Molten salt decomposition
Water leaching & Filtration
Alkali evaporation
Alkali rich solution
Impurity removal
By-product recovery
Enriched Na2TiO3
Acid leaching & Filtration
Hydrothermal treatment
Acid recycle
Renewable TiO2 photocatalysts
B
C
D
E
RhB
MB
Time (min)
F
G
Weight loss (mg)
Temperature (°C)
Binding energy (eV)
H
I
J
K
L
Irradiation time (h)
Irradiation time (min)
Photolysis
P25
Benzaone: 3.0 mg/L

is structurally well defined, fine control at a nanometer level can be achieved. This is the case of previously reported work in which TiO_2 anatase nanocrystals with exposed {001} facets were effectively prepared by recycling the waste anodic electrolyte containing ethylene glycol [58]. Figure 2 shows the extraction (h) and analysis (f, g) of the waste anodic electrolyte produced from the anodization process. The electrolyte was later subjected to a calcination process from which the crystal size of the particles and the percentage of exposed {001} facets were relatively easily adjusted over a wide range after cooling to room temperature. The anatase TiO_2 and N-doped TiO_2 (TiO_2–xNx) exhibited higher photocatalytic activity than the P25 TiO_2 commercial sample for humic acid (HA) and bentazone degradation (Fig. 2i–k). Recyclability tests also indicated potential reusability of the obtained photocatalysts [58].

3 ZnO-based Materials: Zn from Waste

ZnO has been proposed as an alternative photocatalyst to TiO_2, as it possesses similar band gap energy but exhibits higher absorption efficiency under sunlight irradiation than TiO_2 [59]. Galvanizing plants produce a significant amount of Zn-containing waste, which constitutes an interesting opportunity to produce cheap ZnO-based materials. In a representative work, ZnO nanoparticles obtained from Zn dust waste from a hot-dip galvanizing plant were used as a photocatalytic material for MB. The study analyzed the influence of precipitation pH level and amount of hydroxypropyl cellulose added during the hydrothermal process on sample morphology and photocatalytic response. ZnO nanorods of different sizes were synthesized, obtaining optimal activity at pH = 12 and 0.10% (w/v) of hydroxypropyl cellulose [60]. As expected, agglomeration of the structure and reduced superficial area were generally found to lead to worse photocatalytic activity. In fact, the real illuminated area, which was associated with the total superficial area, was shown to be one of the most important parameters for obtaining outstanding quantum efficiency results [61]. A Zn dust-derived material with very large surface area was recently reported [62]. The proposed synthetic approach includes the valorization of polyethylene terephthalate (PET) bottle waste to produce a 3D mesoporous carbon (graphite) nanocomposite using a simple thermal decomposition method. As presented in Fig. 3a, b, the carbon structure exhibited a nanosheet appearance, while ZnO particles appeared with relatively good dispersion on the carbonaceous surface. Figure 3c shows the degradation efficiency of MB, with the C/C_0 ratio as a function of irradiation time in the presence of samples PET 700, PETZ 0.1, PETZ 0.5, PETZ 0.75, and PETZ 1.0 (denoting the reference sample obtained in the absence of Zn dust and samples obtained using 10 g of plastic and 0.1, 0.5, 0.75, and 1 g of Zn dust, respectively). The waste-derived nanocomposites exhibited superior photocatalytic activity for the degradation of organic dyes (MB and malachite green) under UV illumination. Composites obtained by upcycling of plastic/metal mixed waste could represent an attractive opportunity in photocatalysis since, as the authors noted, plastic and metal waste exist together in several industries, for example in electronic waste, medical waste, batteries, and accumulators [62]. Another interesting contribution that can be

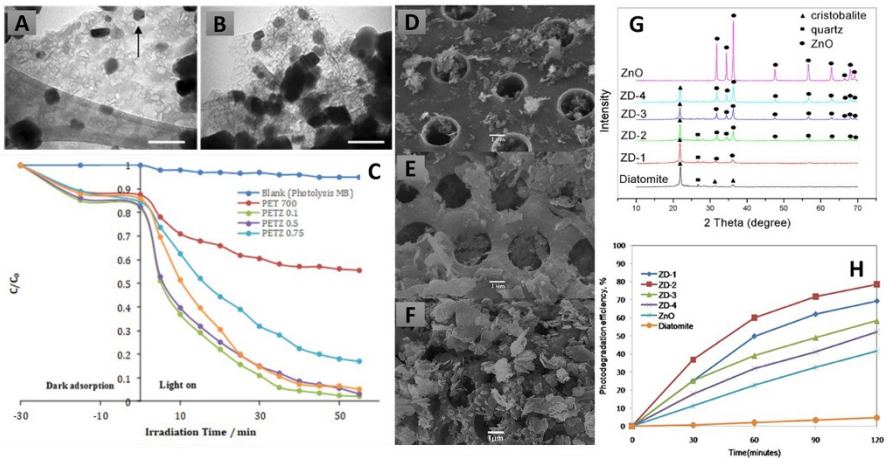

Fig. 3 **a**, **b** Transmission electron microscopy (TEM) images of PETZ 1.0 and photodegradation of MB using the synthesized samples [62]. **d**–**f** Scanning electron microscopy (SEM) images of ZD-1, ZD-3, and ZD-4 samples. X-ray diffraction (XRD) spectra of ZD-X samples and ZnO reference sample. **h** Photodegradation results for samples and references [63]

highlighted involved the preparation of a ZnO/diatomite hybrid photocatalyst. Precursors of the obtained materials came from industrial waste. Zn dust waste from a hot-dip galvanizing process was used as ZnO precursor, while diatomite waste derived from breweries was used as porous substrate (Fig. 3a). In a typical experiment, a Zn salt solution was prepared by dissolving the Zn dust in a nitric acid solution. The final ZnO/diatomite was prepared by a simple impregnation method followed by calcination treatment at 400–700 °C. The sample codes (see XRD in Fig. 3g) were ZD-1, ZD-2, ZD-3, and ZD-4 for diatomite loaded with 10, 20, 30, and 40% of the oxide semiconductor, respectively. A clear decrease in BET surface area was observed with an increase in the amount of ZnO, which was attributed to pore blocking due to the incorporation of ZnO particles in the porous support [63]. The highest efficiency for degradation of the MB solution was obtained using the ZD-2 sample photocatalyst loaded with 20 wt% ZnO (Fig. 3h).

4 Sulfide-based Materials: S from Waste

Sulfides have also been proposed as suitable photocatalysts in several reactions [5]. In particular, transition-metal sulfides such as CdS or ZnS have been documented as photocatalysts. Additionally, Cu_2S, CdS, In_2S_3, WS_2, and MoS_2, as well as more complex structures such as $ZnIn_2S_4$, $CdIn_2S_4$, and $CdLa_2S$ ternary systems, have shown a photocatalytic response [64]. Like those previously described for oxide materials, there are several options for metallic waste valorization during the synthesis of sulfides. However, unlike metallic oxide, in which the final production of the oxide can be easily achieved by calcination in air, a sulfur source is necessary to produce the corresponding sulfides. The extraction of S-containing mining residues

Fig. 4 **a** X-ray diffraction spectra of Cu_2S samples prepared using pig bristles as S and C source [67]. **b** ▶ Photodegradation results of methyl red using synthesized samples and P25 reference. **c** XPS deconvolution analysis of C, Zn, and O elements [68]

may represent an important source of waste-derived sulfur. Physical–mechanical separation by flotation, chemical modification by sulfide addition, and extraction via supercritical H_2O or CO_2 are some of the most common processes for removing this element from the residue [65]. However, further purification steps must be optimized to be able to consider the obtained materials suitable for producing sulfide catalysts. A very interesting case is the use of waste pig bristles as S (and C) source for the production of metallic sulfides, considering that 225,000 tons are produced per year [66, 67]. Figure 4a, b presents some results for microwave-assisted valorization of pig bristles to produce Cu_2S, employed in the photodegradation of methyl red under light-emitting diode (LED) irradiation conditions. Figure 4a shows the X-ray diffraction (XRD) patterns for three samples which were prepared by varying the amount of sodium hydroxide (employed to accelerate the degradation of pig bristles) during microwave-assisted synthesis [67]. The coral-like homogeneous Cu_2O structure obtained showed activity under all experimental conditions tested. The study was performed with an LED lamp (6A) of 465 nm (blue), 515 nm (green), and 630 nm (red), as well as white light (as simultaneous illumination of the three LEDs). As shown in Fig. 4b, a higher degradation of methyl red was obtained using white illumination conditions, which outperformed the photocatalytic response of the P25 titania reference [67]. The authors expanded the idea of using pig bristles as raw materials for the synthesis of two additional compounds, ZnS and Ag/Ag_2S, as recently reported, both with potential photocatalytic applications [66, 68]. As a representative example, Fig. 4c shows the XPS analysis of a series of ZnS materials. The Zn and S XPS regions confirmed the presence of the ZnS structure, while some differences were recorded in the C1s XPS region. XPS deconvolution analysis indicated that a strong interaction could occur between C and Zn which must be considered during the production of this type of material [68].

5 Carbon Quantum Dots: Biomass-derived

Carbon quantum dots (CQDs) have gained increasing attention in recent years as an attractive alternative to other types of multicolor emissive materials such as quantum dots (QDs). QDs possess inherent disadvantages associated mainly with their high toxicity, while CQDs have been well recognized for their low/nontoxic characteristics and biocompatible features, being good candidates for use for in vivo applications including cell imaging, drug delivery, visible light bactericidal activity, and chemical sensing. In addition to biological applications, the use of CQDs as photocatalytic materials for pollutant degradation, solar devices, and in photo/electrochemical water splitting has steadily increased, taking advantage of their high solubility and aqueous affinity, chemical/photo and colloidal stability, notable optical

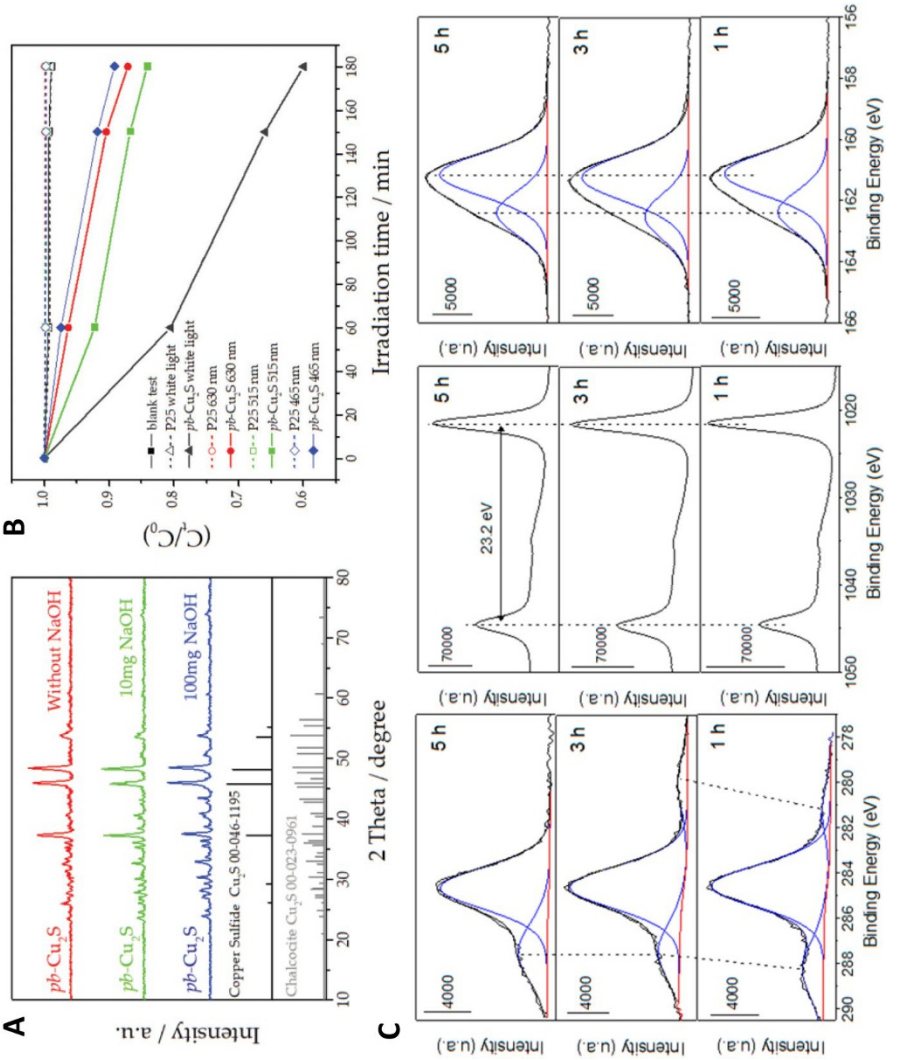
A
pb-Cu2S
Without NaOH
pb-Cu2S
10mg NaOH
pb-Cu2S
100mg NaOH
Copper Sulfide Cu2S 00-046-1195
Chalcocite Cu2S 00-023-0961
Intensity / a.u.
2 Theta / degree
B
blank test
P25 white light
pb-Cu2S white light
P25 630 nm
pb-Cu2S 630 nm
P25 515 nm
pb-Cu2S 515 nm
P25 465 nm
pb-Cu2S 465 nm
(C/C0)
Irradiation time / min
C
5 h
3 h
1 h
4000
70000
5000
23.2 eV
Intensity (u.a.)
Binding Energy (eV)

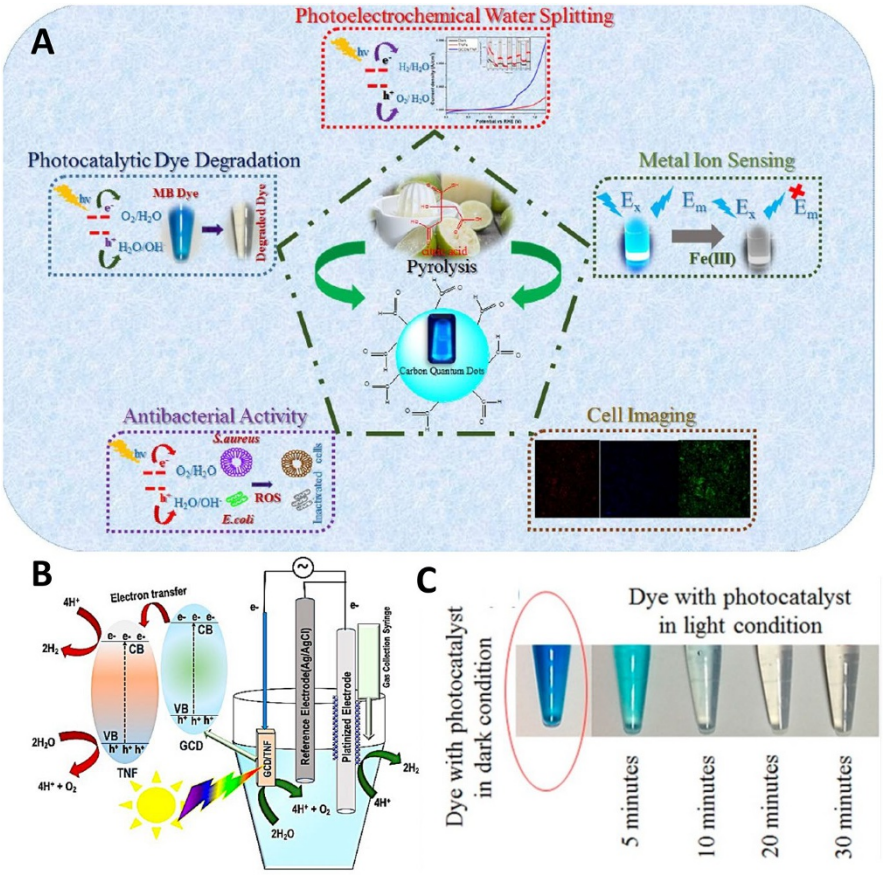

Fig. 5 **a** Schematic representation of citrus limetta organic waste-recycled carbon nanolights for photo/electrocatalytic, sensing, and biomedical applications. **b** Mechanism of photo-electrochemical water splitting with GCD (carbon quantum dots)/TNF (TiO_2 nanofiber) electrodes. **c** Representative images of MB dyes collected at different time intervals [75]

properties, photobleaching resistance, low cost, low toxicity, and good possibilities for functionalization [69].

The cost-effectiveness of CQDs is an additional factor promoting their study and application. CQDs derived from biomass possess a particularly low-cost and outstanding eco-friendly character. Following a top-down strategy, biomass-derived CQDs have been synthesized using several protocols including hydrothermal and electrochemical oxidation, acidic hydrolysis, and microwave-assisted treatments [70]. Several biomass sources have been employed for the preparation of CQDs, including fruit peels, whey from dairy waste, spent coffee grounds, residues from the pulp and paper industry, and cigarette filters, but citric acid is currently the most common starting material used to obtain highly luminescent CDs, usually in

combination with nitrogen-containing dopants. Several examples of the use of biomass residues for the preparation of CQDs will be described in this section [71–74].

For instance, citrus limetta waste pulp was treated using a one-step pyrolysis method to prepare CQDs with interesting optoelectronic features. This carbon-based nanomaterial was demonstrated to be highly versatile, since it was successfully employed for photo-electrochemical water splitting and photocatalytic MB degradation, along with bioimaging, iron ion sensing, and bactericidal activity (Fig. 5a–c) [75]. The photo-electrochemical performance of the prepared CQDs displayed encouraging results, with an efficient current density of ~6 mA/cm^2 for water splitting (Fig. 5b).

Another example of the use of CQDs as photocatalysts was reported by Reisner et al., who highlighted the influence of different amorphous and graphite-like CQDs on photoinduced hydrogen production [76]. The various CQDs were used as photosensitizers to activate a nickel catalytic redox mediator via photoinduced electron transfer. Although improved hydrogen evolution was observed when using graphitic nitrogen-doped CQDs, a complete and precise rationalization of the effects of the CQD morphology and dopant on the photocatalytic performance and light-harvesting properties cannot be drawn, because different carbon sources were used (citric acid for non-doped CQDs and aspartic acid for the N-doped CQDs), and only graphitic CQDs were tested [77].

Prato et al. recently prepared a family of photoredox N-doped CQDs, revealing their potential applicability as photocatalysts due to their tunable oxidation/reduction potential. However, further efforts are still needed in order to expand the knowledge about the proper design of photoredox-active CQDs, considering synthetic methods, carbon sources, and possible dopants [78]. In this regard, the size, degree of carbonization, and morphology of CQDs could be controlled by the synthetic strategy. For instance, hydrothermal approaches generally give rise to incomplete carbonization and therefore to the presence of molecular fluorophores and amorphous CQDs. In turn, pyrolytic conditions lead to CQDs with a predominantly graphitic core structure. However, the optical properties and photoredox activity are still difficult to predict. In particular, the emission type and intensity of CQDs are attributed mainly to the cooperative effects between the molecular fluorophores embedded in both the nanoparticles and the defect states, and the graphitic cores [79].

Of note, Peroza et al. reported the synthesis of CQDs using two different preparation methods, namely hydrothermal and pyrolytic techniques, and using (1) citric acid and (2) citric acid doped with diethylenetriamine [80]. The hydrothermal approach gave rise to amorphous CQDs that were either (1) non-doped (a-CDs) or (2) nitrogen-doped (a-N-CDs). The pyrolytic protocol resulted in the formation of graphitic CQDs, which were (1) non-doped (g-CDs) or (2) nitrogen-doped (g-N-CDs) (Fig. 6a, b). These nanomaterials showed an excitation-dependent emission band, with a maximum between 420 and 500 nm (Fig. 6c–f). The photocatalytic activity of the CQDs was investigated for the photoreduction reaction of methyl viologen (MV) in the absence of redox mediators.

A hydrothermal carbonization method has also been reported as a sustainable and green option for the preparation of carbon particles in an aqueous medium from a readily available biomass residue, namely orange peel (Fig. 7a–c). Remarkably, the

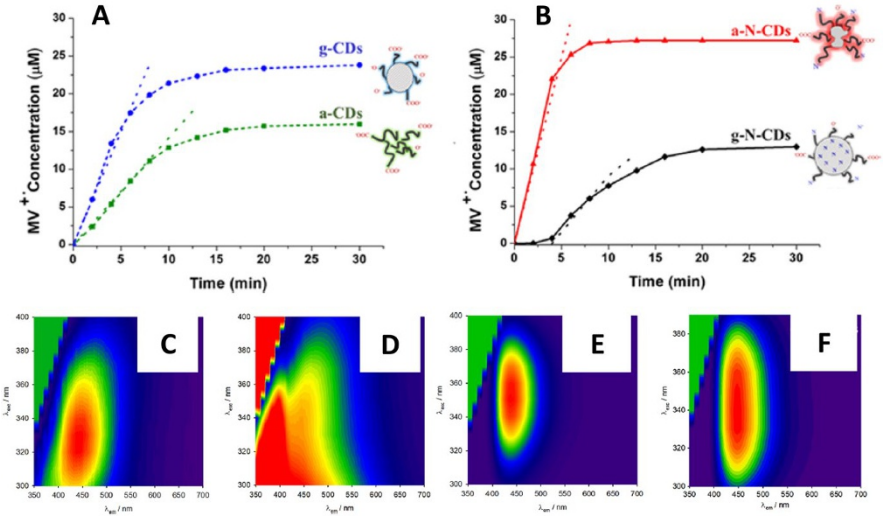

Fig. 6 Reaction kinetics of the formation of $MV^{+\cdot}$ using **a** a,g-CDs and **b** a,g-N-CDs. Contour plot of the emission map at different excitation wavelengths of **c** a-CDs, **d** g-CDs, **e** a-N-CDs, and **f** g-N-CDs. The intensity scale goes from dark violet to red, passing through blue, green, and yellow [80]

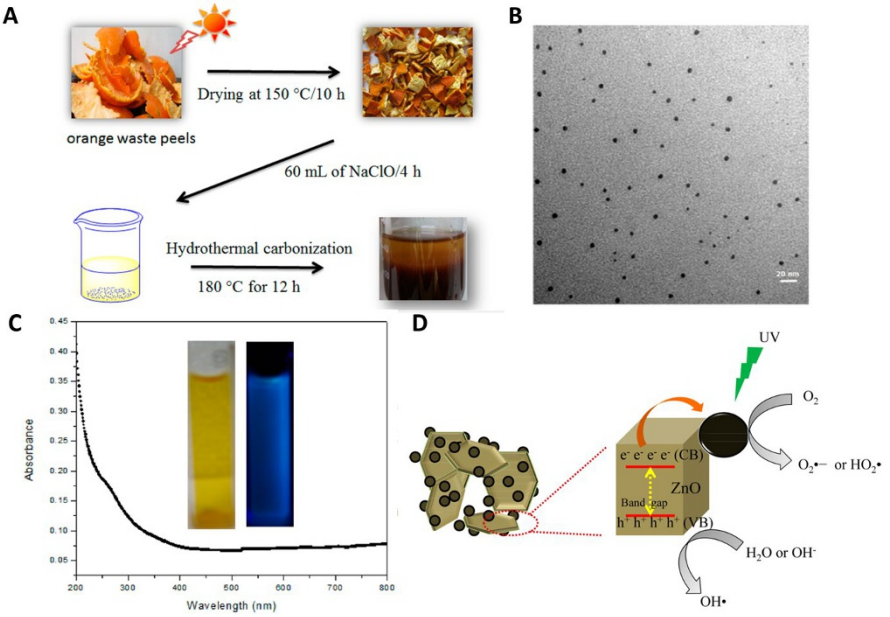

Fig. 7 **a** Formation of carbon dots (C-dots) from the hydrothermal treatment of orange waste peels. **b** Transmission electron microscopy (TEM) image of C-dots from orange waste peels. **c** UV–visible absorption spectrum of C-dots; inset, under daylight. **d** Schematic illustration of the photocatalytic process on C-dots/ZnO [81]

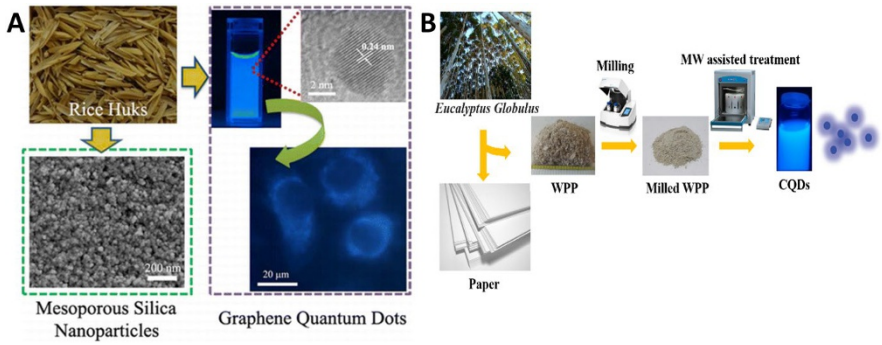

Fig. 8 **a** RH residues used for the synthesis of CQDs and mesoporous silica nanoparticles [82]. **b** Schematic representation of the microwave-assisted conversion of WPP to CQDs [83]

resulting CQDs were soluble in water to form a stable solution for months without precipitation. A composite material based on the prepared CQDs and ZnO was employed as photocatalyst for degradation of naphthol blue-black azo dye under UV irradiation (Fig. 7d), with outstanding results [81].

Other types of biomass waste, such as rice husk (RH) and waste residues from the pulp and paper industry (WPP), have also been reported for the preparation of CQDs, with potential applications in photocatalysis (Fig. 8a). In particular, the employment of RH for preparation of CQDs gave rise to two types of luminescent centers, size/edge-induced intrinsic state and vacancy/functional group-associated defect state. Remarkably, full valorization of RH residues was accomplished during the synthetic process, since the silica content in RHs can be simultaneously employed to synthesize mesoporous silica nanoparticles, thus presenting enormous economic and environmental benefits [82]. Moreover, catalysis represents an innovative option for the synthesis of CQDs. In this sense, a microwave-assisted treatment using a solid acid catalyst has been reported for the valorization of waste from the paper industry toward CQDs with promising fluorescence properties (Fig. 8b) [83].

Another interesting example in this respect was offered by Sun et al., using egg yolk to develop fluorescent nitrogen-doped CQDs (N-CQDs) with relatively high quantum yield. Because of their high protein content, eggs can act as both carbon and nitrogen source. Figure 9a shows the synthetic procedure for the N-CQD preparation, with a relatively high quantum yield of ~35% (Fig. 9b–e). The fluorescence properties of the prepared N-CQDs were investigated in depth, revealing wavelength-dependent emission and a notably long life [84].

Large-scale synthesis of CQDs has also been investigated using several biomass-derived carbons including hydrochar and carbonized biomass via mild oxidation ($NaOH/H_2O_2$ solution). Under these conditions, CQDs were obtained at an outstanding yield of 76.9 wt%, which is much higher than that obtained by traditional hydrothermal and strong acid oxidation processes. The as-synthesized CQDs also presented excellent quantum yield (QY). In this case, the CQDs exhibited a uniform

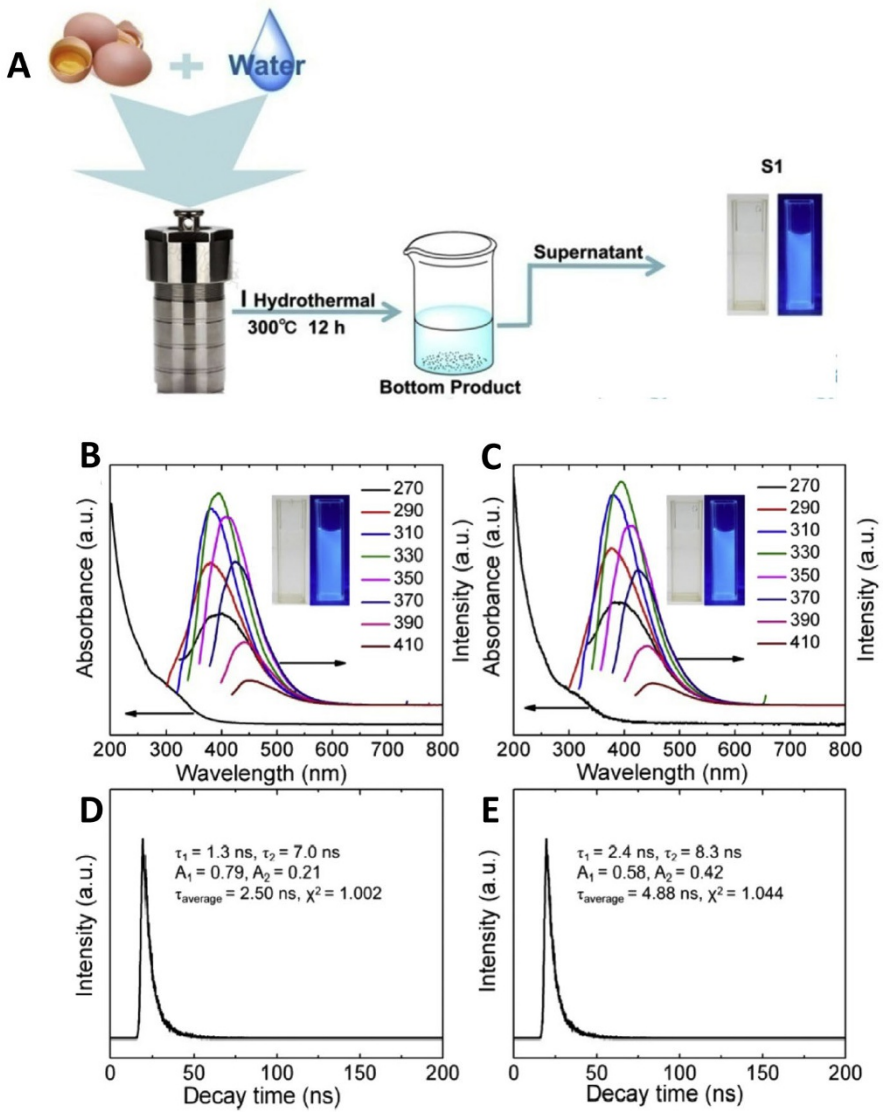

Fig. 9 **a** Sustainable and green one-arrow/two-hawks strategy for the preparation of nitrogen-doped carbon materials from egg yolk. **b**, **c** UV–Vis absorption and PL spectra of fresh CQDs and after 6 months under different excitation wavelengths. **d**, **e** Fluorescence decay profile of as-synthesized CQDs and CQDs after 6 months [84]

size (ca. 2.4 nm), and it was possible to regulate their surface states to significantly improve the QY by adjusting the concentration of oxidants [85].

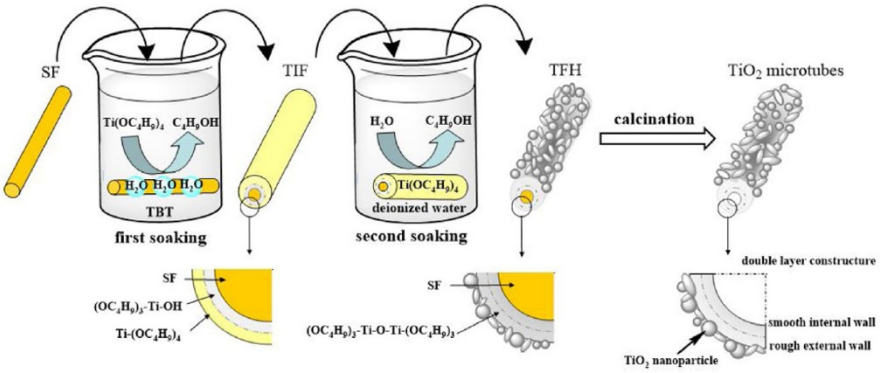

Fig. 10 Schematic representation of the preparation of TiO_2 microtubes through a double-soaking sol–gel route [89]

6 Biomass-templated Materials

The template method is an effective and simple strategy for obtaining nanostructures with different morphologies and large surface areas. Most of the reported approaches in this sense consist of two steps: first, the desired materials or precursors assemble around the surface of a template via chemical or physical adherence to form transitional composites, and then the templates are selectively removed from the composite structures. If the template is fully converted to the desired material, it is called a sacrificial template.

A wide range of composite materials have been synthesized through biomass valorization [3, 86]. Biomass waste can represent an alternative to the typical carbonaceous materials, resulting in both cheaper and more effective catalytic systems with tunable properties. From an environmental point of view, and following the same ideas described in previous sections, it is especially interesting to search for new materials that both enable optimization of photo(catalytic) properties and reuse of waste, and allow the use of environmentally friendly synthetic procedures. These two concepts have been applied to obtain materials that show high efficiency in photocatalytic reactions under solar irradiation or under efficient illumination sources, facilitating the development of industrial applications of photocatalysis as a green technology.

The sacrificial template method has also been used to design photocatalytic materials. In this way, it is possible to synthesize multiple photocatalysts with adequate morphological and desired optical and electronic properties [87]. One study reported that ZnO with a controlled morphology was obtained by solid-state grinding of a zinc precursor [$Zn(NO_3)_2$] with polysaccharides including a biomass-derived agar extracted from macroalgae [88]. The obtained materials showed promising photocatalytic phenol photodegradation activity similar to commercial P25 titania.

In another work, a sacrificial template method was employed in a novel double-soaking sol–gel route for the synthesis of TiO_2 microtubes utilizing seed

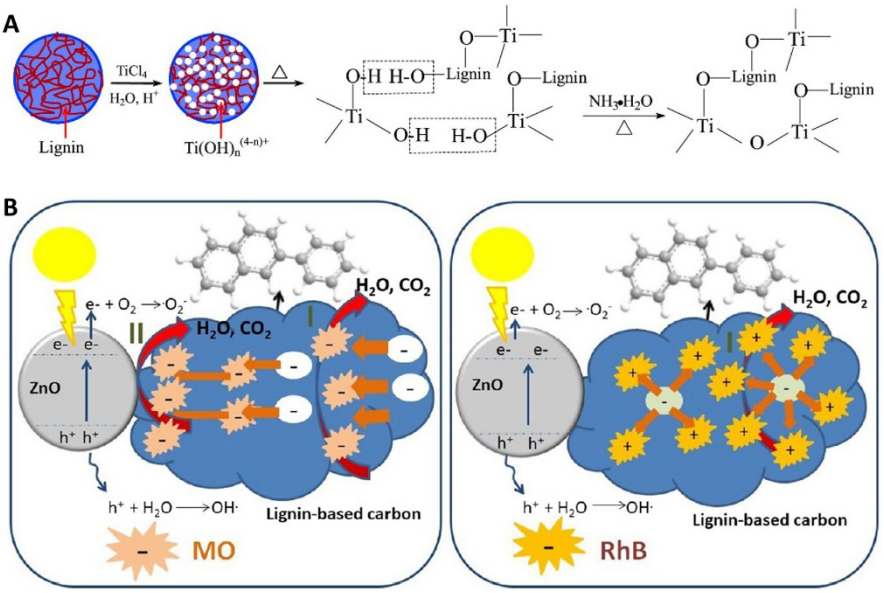

Fig. 11 **a** Formation mechanism of mesoporous TiO_2 with lignin as a template [90]. **b** Photocatalytic mechanism for the degradation of MO (left) and RhB (right) over the LC–ZnO composite [91]

fibers from *Platanus acerifolia* as bio-templates. Seed fibers without any pretreatment were sequentially soaked in tetrabutyl titanate (TBT) and distilled water. The natural moisture in the waste seed fibers played an important role in the two-step hydrolysis of titanium salt. The obtained titanium fiber hybrid (TFH) was dried and calcined to remove the fiber bio-templates to obtain TiO_2 microtubes (Fig. 10). The prepared TiO_2 microtubes displayed outstanding photocatalytic performance in the degradation of tetracycline hydrochloride under visible light irradiation. This result was attributed to their high specific surface area and extension of the absorption spectrum to the visible light region [89].

In addition, mesoporous TiO_2 was synthesized by hydrolysis precipitation followed by a calcination step using a bio-renewable resource of lignin as a template and $TiCl_4$ as a reactant (Fig. 11a). Because of the presence of lignin functionalities and the interactions between its hydroxyl group and the surface hydroxyl groups of the TiO_2 precursor, the calcined samples attained finer crystallite size and mesoporous structure. After calcination at 500 °C, the obtained mesoporous TiO_2 exhibited high activity under UV irradiation for phenol degradation (97.9%) during 120 min of reaction [90].

Similarly, the use of lignin was reported to give rise to a novel lignin-based carbon/ZnO (LC/ZnO) hybrid composite, with excellent photocatalytic performance, via a convenient and environmentally friendly method (Fig. 11b) [91]. The photocatalytic activity of LC/ZnO was much higher than that of pure ZnO. The LC/ZnO hybrid composite showed different photocatalytic mechanisms for degradation of negative methyl orange (MO) and positive rhodamine B (RhB). The lignin-based

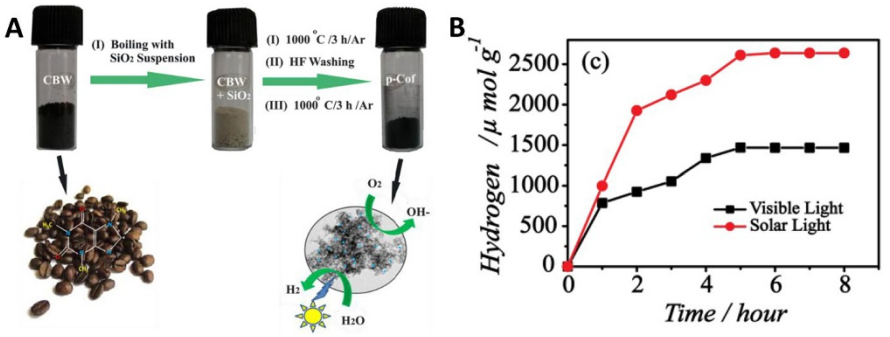

Fig. 12 **a** Schematic representation of the preparation of porous nitrogen-doped carbon from coffee bean waste (CBW) using the silica-templating approach. **b** Comparison of the amount of hydrogen produced on p-Cof under visible light and solar light irradiation [92]

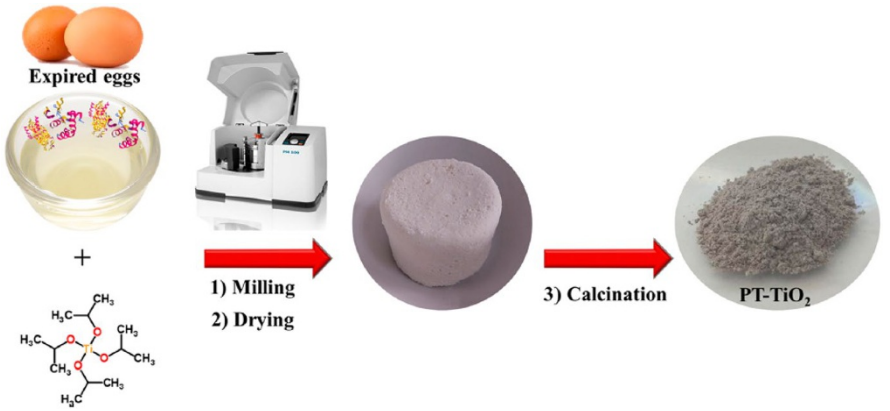

Fig. 13 Schematic representation of the synthetic protocol for Pt-TiO_2 material [93]

carbon modified the surface of ZnO, generating a large number of oxygen vacancies, and hence LC/ZnO was found to be positively charged. RhB, positively charged in water, was consequently firmly adsorbed on the surface of the lignin-based carbon due to the electrostatic adsorption between the positive and negative charges. Such electrostatic interaction hindered the movement of positive RhB toward the surface of ZnO, where it would be degraded. In turn, MO, negatively charged in water, did not interact with the lignin-based carbon, easily passing to the surface of ZnO to be directly degraded. The reported photocatalyst with selective degradation of positive and negative organic dyes may have great application prospects for photoelectric conversion and catalysis [91].

In another instance, Kurungot et al. described an interesting method, employing silica as template, for the valorization of coffee bean waste (CBW) toward the formation of nitrogen-doped porous carbon (p-Cof) with both photocatalytic and electrocatalytic properties (Fig. 12a) [92]. The p-Cof material displayed

outstanding morphological features, with the presence of assemblies of highly porous flat carbon blocks (surface area: 1213 $m^2\ g^{-1}$). In addition, the p-Cof surface exhibited graphitic and pyridone-type nitrogen coordination, resulting in a multifunctional and versatile catalyst for photocatalytic hydrogen production (PHP) and electrocatalytic oxygen reduction reactions. The photocatalytic performance of p-Cof gave rise to 334 μmol $h^{-1}\ g^{-1}$ and 575 μmol $h^{-1}\ g^{-1}$ of hydrogen from water splitting under visible light and solar light irradiation, respectively (Fig. 12b).

In addition to the previously described example of egg valorization toward the formation of CQDs, egg white from expired eggs was employed as a template in the synthesis of titania with enhanced morphological properties (Fig. 13) [93]. The use of egg white as template led to an increase in surface area from 10 to 139 $m^2\ g^{-1}$ as compared with the material prepared in the absence of the residue. Remarkably, the synthetic process was carried out using a solvent-free mechanochemical-assisted strategy. Such composite material could be potentially employed for photocatalysis.

7 Other Examples: Waste-derived Materials

Graphite-like carbon nitride (g-C_3N_4) has recently emerged as one of the most widely studied materials, both as a single phase and as part of a photocatalyst. g-C_3N_4 can be obtained by thermal treatment of nitrogen-rich precursors. Urea, thiourea, melamine, cyanamide, and dicyandiamide are some of the common starting materials. The production of g-C_3N_4 from urea is a good opportunity for waste (e.g. agricultural waste) valorization to move toward a circular economy [94]. Nevertheless, in many examples, the photocatalytic efficiency of the pure g-C_3N_4 is limited by the high recombination rate of its photo-generated electron–hole pairs [49, 51]. Combination with metal-containing materials provides a feasible route toward improving the photocatalytic response of g-C_3N_4. Along these lines, a very recent report describes the valorization of waste toner powder enriched with organic residues and magnetic Fe_3O_4 to produce a g-C_3N_4–Fe_2O_3 photocatalyst through a facile one-step calcination process [95]. The toner powder was first calcinated at 600 °C to produce the Fe_2O_3 structure and then subjected to a second calcination treatment in the presence of thiourea (450 °C in a muffle furnace for 2 h). Figure 14a shows a high-resolution transmission electron microcopy (HR-TEM) image of the pure Fe_2O_3 toner-derived material in which the (110) plane of α-Fe_2O_3 can be identified. A similar result was derived from microscopy analysis of the g-C_3N_4–Fe_2O_3 composite samples, as shown in Fig. 14b, demonstrating the successful formation of a heterojunction and close contact between g-C_3N_4 and Fe_2O_3. As expected, the introduction of iron oxide in the structure led to enhanced visible light absorption as demonstrated by UV–Vis spectroscopy (Fig. 14c). Such enhancement, in addition to a drastic reduction in electron–hole pair recombination as demonstrated by photoluminescence, yielded an outstanding material for MO and textile effluent degradation (Fig. 14d) under sunlight-type illumination conditions. Last but not least, the composite

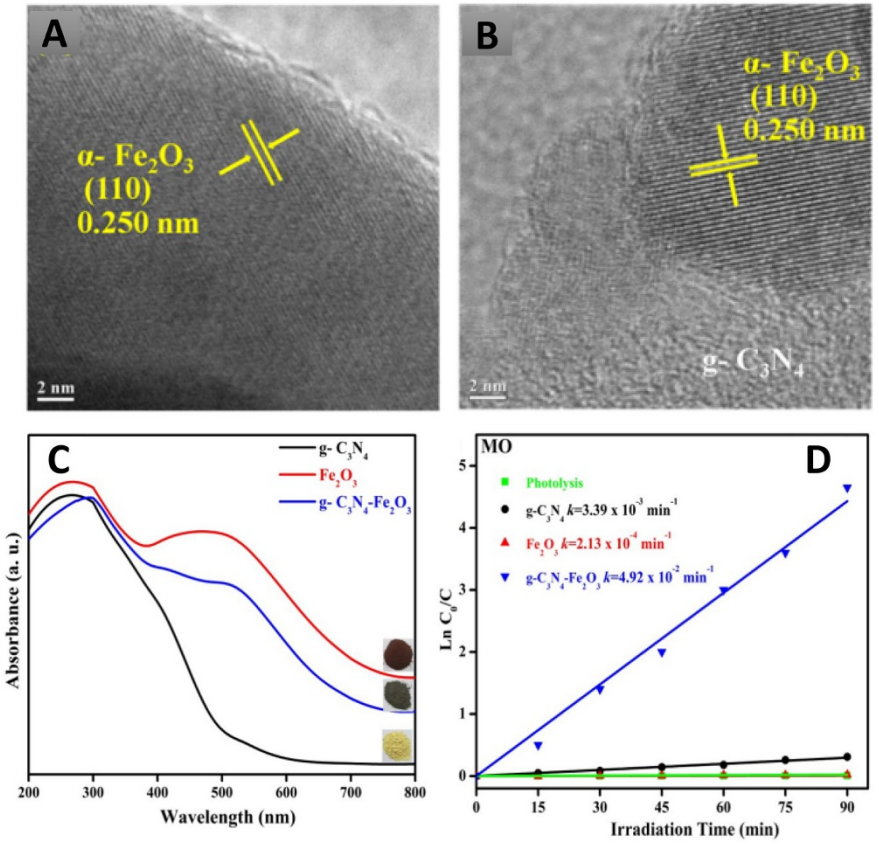

Fig. 14 HR-TEM images of **a** pure Fe_2O_3 and **b** g-C_3N_4-Fe_2O_3 composite samples. **c** UV–Vis spectra of the samples. **d** Kinetic linear simulation of the samples of MO photodegradation [95]

g-C_3N_4–Fe_2O_3 sample showed very good recyclability and sufficient magnetism to allow efficient recovery under an external magnetic field.

Boron-containing materials have recently gained attention in the field of photocatalysis due to their excellent optical properties. In fact, the strong absorption of this material in the UV–Vis/IR range has yielded remarkable local photothermal effects and outstanding results in CO_2 reduction reactions. As in other industrial extraction-purification processes, boron generates a large amount of boron-containing waste. In one study, boron-enriched waste (BEW) was used to produce a photocatalytic material tested during atrazine degradation reaction. The TiO_2-BEW material was obtained using a simple impregnation method followed by calcination at 400 °C, as schematically illustrated in Fig. 15a. Titanium(IV) isopropoxide was used as the Ti source, and the final materials, according to the elemental analysis, presented ca. 13.7 wt% of TiO_2. Characterization of the waste-derived samples was performed using a multi-technique approach. Pseudo-spherical TiO_2 nanoparticles uniformly scattered on BEW were measured by

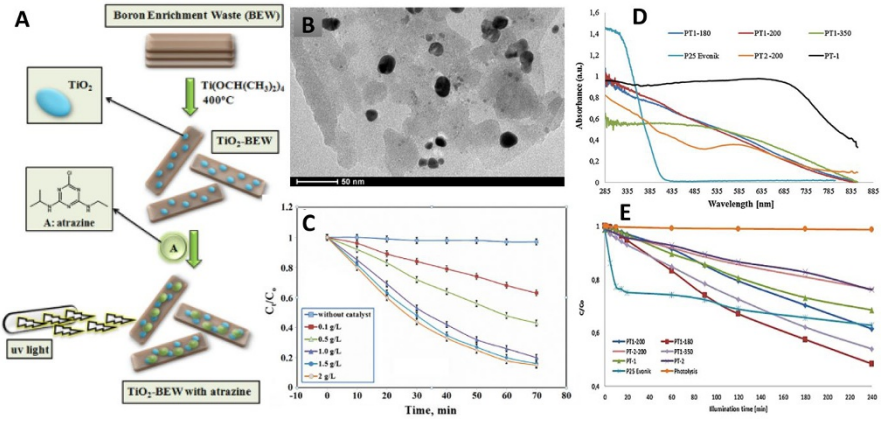

Fig. 15 **a** Schematic representation of the synthesis of TiO_2-BEW samples and their application as photocatalysts. **b** TEM image of prepared sample. **c** Photodegradation results of atrazine from wastewater using several catalyst concentrations. [96]. **d** UV–Vis results for waste-derived samples. **e** Photodegradation of phenol in the samples and P5 reference [97]

microscopy (Fig. 15b), and UV–Vis analysis showed a band gap of 3.08 eV [96], confirming a potential use for sunlight-driven photocatalytic applications. In particular, the samples showed good activity and reusability for the removal of atrazine from wastewater. Unprecedented photocatalytic properties were reported for carbonaceous N-containing materials derived from leather skin residues [97]. The waste-derived material was easily synthesized by carbonization of the rabbit skin residues (provided by Serpelsa S.A. Vic, Spain) at 180–600 °C. In Fig. 15d, e, PT1 and PT2 describe the skin processed using a common chromium salt treatment and that treated with titanium salts, respectively. It can be seen that all samples showed higher absorption of visible light and better photocatalytic response during phenol photooxidation. In fact, the activity data are competitive with respect to previous literature reports and, importantly, in comparison with the well-studied P25-TiO_2 commercial reference [97].

8 Outlook and Conclusions

This review presents waste-derived photocatalytic materials as an attractive option, with tremendous environmental benefits, which has gained popularity in several photocatalysis laboratories around the world. The authors have highlighted the environmental advantages and economic attractiveness of using waste to produce high-value-added materials. It should be noted that the environmental benefits of waste reuse make little sense if the synthetic protocol involves non-efficient consumption of energy or uses large quantities of harmful/toxic chemicals. The same conclusion can be extended to waste valorization using high quantities of expensive commercial additives. As a reference for readers, a qualitative

Table 1 Summary of main harmful reagents and energy-consuming processes during the synthesis of waste-derived photocatalysts

Sample	Waste	Main harmful reagents[a]	Main energy-consuming processes	References
TiO_2-based	Spent catalytic reduction catalyst	NaOH, H_2SO_4 or HCl	Autoclave (180 °C, 1 h)	[56]
N-doped-TiO_2	Waste milk-like electrolyte	–	Furnace (500–600 °C, 3 h)	[58]
ZnO	Zinc-dust	NaOH, HNO_3	Autoclave (170 °C, 8 h)	[60]
ZnO/graphite	Plastic water bottles, zinc-dust	–	Furnace (700 °C, 1 h)	[62]
ZnO/diatomite	Zinc-dust	NaOH, H_2SO_4, HNO_3	Furnace (400–700 °C)	[63]
pb-Cu_2S	Pig bristles	Ethylene glycol, NaOH	Microwave (500 W, 3 min)	[67]
CQDs	Citrus limetta pulp	Acetic acid,	Pyrolysis (190 °C, 20 min)	[75]
CQDs	Orange peel	H_2SO_4, NaClO	Autoclave (180 °C, 12 h)	[81]
Polysaccharide-templated ZnO	Polysaccharides	–	Ball mill (350 rpm, 30 min) Furnace (600 °C, 3 h)	[88]
Natural fiber-templated TiO_2 microtubes	*Platanus acerifolia* seed fibers	–	Furnace (500 °C, 2 h)	[89]
Lignin-templated TiO_2	Lignin	NaOH, HCl, NH_3	Furnace (300–900 °C, 2 h)	[90]
Lignin-based carbon/ZnO	Lignin	NaOH	Furnace (550 °C, 2 h)	[91]
g-C_3N_4–Fe_2O_3	Waste toner powder	–	Furnace (450–600 °C, 2 h)	[95]
TiO_2-BEW	Boron-enriched waste (BEW)	–	Furnace (400 °C, 4 h)	[96]
PT (processed skin)	Leather skin residues	–	Microactivity reactor (180–350 °C, 1 h)	[97]

[a]Metal precursors and washing solutions (e.g. ethanol) are not included

description of the main harmful reagents and energy-consuming processes of materials tested in photocatalytic reactions are summarized in Table 1.

In this regard, it is worth highlighting mechanochemistry as a highly promising methodology, which in addition to its remarkable simplicity, reproducibility, and versatility, reduces or eliminates the need to use additional reagents and solvents, thus rendering it not only economically efficient (including the short reactions times), but also—and more importantly—highly sustainable [86].

There is a long way to go, starting with the problems that are associated with the photocatalytic process itself. The relatively low photonic and quantum efficiency obtained for a wide range of photoreactions, together with the low absorption of the more active pure photocatalysts such as TiO_2 or ZnO (and any advanced material), remain the main drawback of the technology [5]. The development of samples containing minor entities such as iron, copper, cerium oxides, or boron can help in managing the optical properties of the samples in order to improve the final efficiency of the process. However, this is a relatively difficult task considering that in many cases, the wastes used as raw materials have fixed concentrations of relevant elements, which leaves little flexibility in the design of the controlled structures.

The large-scale production of waste-derived catalytic materials must also be further developed. The electronic and automotive industries or galvanizing plants produce enough waste for large-scale catalyst/photocatalyst production [98]. However, most of the reports in the literature provide information only about basic laboratory studies. As photocatalysis is not an established large-scale process, the final structure/properties of the samples is not a defined variable. Activity, selectivity, and stability must be tested using such waste-derived materials under large-scale operating conditions. With regard to the synthetic protocols, it is well known that the formation of precipitates must be avoided, and other processes such as filtration should be as rapid as possible; therefore, some of the aforementioned synthetic methods must be optimized for large-scale material production. It is expected that in the coming years, life-cycle and techno-economic assessment of the most promising photocatalytic processes will provide relevant information about the suitability of waste-derived photocatalysts.

Although these issues are not limited to waste-derived photocatalysts, a comprehensive understanding of the processes occurring in these types of materials is certainly lacking. In situ characterization under real-world operating conditions must be undertaken in order to provide a clear description of entities participating in the photoreaction. In situ X-ray absorption spectroscopy (XAS), XPS, or diffuse reflectance infrared Fourier transform spectroscopy (DRIFTS) studies (under illumination conditions), in combination with modeling and analysis of the optical properties, could prove useful in the interpretation of information related to the mechanistic and photo-handling process [13, 99]. Notwithstanding all the advances in the utilization of waste-derived materials as photocatalysts, the remarkable potential of these materials can lead to even further possibilities. We hope that this contribution can inspire the scientific community involved in the field of photocatalysis to take full advantage of the benefits offered by waste

utilization, enabling the development of more sustainable and efficient photocatalytic processes.

Acknowledgements Rafael Luque gratefully acknowledges MINECO for funding project CTQ2016-78289-P, co-financed with FEDER funds. Daily Rodriguez-Padron also gratefully acknowledges MINECO for providing a research contract under the same project. M. J. Muñoz-Batista thanks the "Plan Propio de Investigación-Proyectos de investigación precompetitivos para Jóvenes Investigadores" from Universidad de Granada and MINECO for a Juan de la Cierva postdoctoral contract (ref. FJCI-2016-29014). This publication was prepared with support from RUDN University, Program 5-100.

References

1. Anastas PT, Warner JC (1998) Green chemistry : theory and practice. Oxford University Press, Oxford
2. Sheldon RA (2012) Fundamentals of green chemistry: efficiency in reaction design. Chem Soc Rev 41:1437–1451. https://doi.org/10.1039/C1CS15219J
3. Rodríguez-Padrón D, Puente-Santiago AR, Balu AM et al (2019) Environmental catalysis: present and future. ChemCatChem 11:18–38. https://doi.org/10.1002/cctc.201801248
4. Spasiano D, Marotta R, Malato S et al (2015) Solar photocatalysis: materials, reactors, some commercial, and pre-industrialized applications. A comprehensive approach. Appl Catal B Environ 171:90–123. https://doi.org/10.1016/j.apcatb.2014.12.050
5. Kubacka A, Fernández-García M, Colón G (2012) Advanced nanoarchitectures for solar photocatalytic applications. Chem Rev 112:1555–1614. https://doi.org/10.1021/cr100454n
6. Colmenares JC, Luque R (2014) Heterogeneous photocatalytic nanomaterials: prospects and challenges in selective transformations of biomass-derived compounds. Chem Soc Rev 43:765–778. https://doi.org/10.1039/C3CS60262A
7. Hoffmann MR, Martin ST, Choi W, Bahnemannt DW (1995) Environmental applications of semiconductor photocatalysis. Chem Rev 95:69–96. https://doi.org/10.1021/cr00033a004
8. Ravelli D, Dondi D, Fagnoni M, Albini A (2009) Photocatalysis. A multi-faceted concept for green chemistry. Chem Soc Rev 38:1999–2011. https://doi.org/10.1039/b714786b
9. Linsebigler AL, Lu G, Yates JT (1995) Photocatalysis on TiO2 surfaces: principles, mechanisms, and selected results. Chem Rev 95:735–758. https://doi.org/10.1021/cr00035a013
10. Granone LI, Sieland F, Zheng N et al (2018) Photocatalytic conversion of biomass into valuable products: a meaningful approach? Green Chem 20:1169–1192. https://doi.org/10.1039/C7GC03522E
11. Chen X, Mao SS (2007) Titanium dioxide nanomaterials: synthesis, properties, modifications, and applications. Chem Rev 107:2891–2959. https://doi.org/10.1021/cr0500535
12. Muñoz-Batista MJ, Ballari MM, Kubacka A et al (2019) Braiding kinetics and spectroscopy in photo-catalysis: the spectro-kinetic approach. Chem Soc Rev 48:637–682. https://doi.org/10.1039/C8CS00108A
13. Caudillo-Flores U, Muñoz-Batista MJ, Kubacka A, Fernández-García M (2018) Operando spectroscopy in photocatalysis. ChemPhotoChem 2:777–785. https://doi.org/10.1002/cptc.201800117
14. Colmenares JC, Varma RS, Nair V (2017) Selective photocatalysis of lignin-inspired chemicals by integrating hybrid nanocatalysis in microfluidic reactors. Chem Soc Rev 46:6675–6686. https://doi.org/10.1039/C7CS00257B
15. Liu J, Liu Y, Liu N et al (2015) Water splitting. Metal-free efficient photocatalyst for stable visible water splitting via a two-electron pathway. Science 347:970–974. https://doi.org/10.1126/science.aaa3145
16. Sasaki Y, Nemoto H, Saito K, Kudo A (2009) Solar water splitting using powdered photocatalysts driven by Z-schematic interparticle electron transfer without an electron mediator. J Phys Chem C 113:17536–17542. https://doi.org/10.1021/jp907128k

17. Chiarello GL, Ferri D, Selli E (2011) Effect of the CH3OH/H2O ratio on the mechanism of the gas-phase photocatalytic reforming of methanol on noble metal-modified TiO2. J Catal 280:168–177. https://doi.org/10.1016/j.jcat.2011.03.013
18. Meng X, Wang T, Liu L et al (2014) Photothermal conversion of CO2 into CH4 with H2 over Group VIII nanocatalysts: an alternative approach for solar fuel production. Angew Chem Int Ed 53:11478–11482. https://doi.org/10.1002/anie.201404953
19. Caudillo-Flores U, Muñoz-Batista MJ, Cortés JA et al (2017) UV and visible light driven H 2 photo-production using Nb-doped TiO2: comparing Pt and Pd co-catalysts. Mol Catal 437:1–10. https://doi.org/10.1016/j.mcat.2017.04.035
20. Ouyang W, Muñoz-Batista MJ, Kubacka A et al (2018) Enhancing photocatalytic performance of TiO2 in H2 evolution via Ru co-catalyst deposition. Appl Catal B Environ 238:434–443. https://doi.org/10.1016/j.apcatb.2018.07.046
21. Sastre F, Versluis C, Meulendijks N et al (2019) Sunlight-fueled, low-temperature ru-catalyzed conversion of CO2 and H2 to CH4 with a high photon-to-methane efficiency. ACS Omega 4:7369–7377. https://doi.org/10.1021/acsomega.9b00581
22. Sastre F, Puga AV, Liu L et al (2014) Complete photocatalytic reduction of CO2 to methane by H2 under solar light irradiation. J Am Chem Soc 136:6798–6801. https://doi.org/10.1021/ja500924t
23. Ouyang W, Kuna E, Yepez A et al (2016) Mechanochemical synthesis of TiO2 nanocomposites as photocatalysts for benzyl alcohol photo-oxidation. Nanomaterials 6:93. https://doi.org/10.3390/nano6050093
24. Verma S, Baig RBN, Nadagouda MN, Varma RS (2016) Sustainable strategy utilizing biomass: visible-light-mediated synthesis of γ-valerolactone. ChemCatChem 8:690–693. https://doi.org/10.1002/cctc.201501352
25. Caudillo-Flores U, Muñoz-Batista MJ, Hungría AB et al (2019) Toluene and styrene photo-oxidation quantum efficiency: comparison between doped and composite tungsten-containing anatase-based catalysts. Appl Catal B Environ 245:49–61. https://doi.org/10.1016/j.apcatb.2018.12.032
26. Li S-H, Liu S, Colmenares JC, Xu Y-J (2016) A sustainable approach for lignin valorization by heterogeneous photocatalysis. Green Chem 18:594–607. https://doi.org/10.1039/C5GC02109J
27. Parrino F, Bellardita M, García-López EI et al (2018) Heterogeneous photocatalysis for selective formation of high-value-added molecules: some chemical and engineering aspects. ACS Catal 8:11191–11225. https://doi.org/10.1021/acscatal.8b03093
28. Krivtsov I, Ilkaeva M, García-López EI et al (2019) Effect of substituents on partial photocatalytic oxidation of aromatic alcohols assisted by polymeric C3N4. ChemCatChem 11:2713–2724. https://doi.org/10.1002/cctc.201900362
29. Kyriakopoulos J, Tzirakis MD, Panagiotou GD et al (2012) Highly active catalysts for the photooxidation of organic compounds by deposition of [60] fullerene onto the MCM-41 surface: a green approach for the synthesis of fine chemicals. Appl Catal B Environ 117–118:36–48. https://doi.org/10.1016/J.APCATB.2011.12.024
30. Nair V, Muñoz-Batista MJ, Fernández-García M et al (2019) Thermo-photocatalysis: environmental and energy applications. Chemsuschem 12:2098–2116. https://doi.org/10.1002/cssc.201900175
31. Caudillo-Flores U, Muñoz-Batista MJ, Kubacka A et al (2018) Measuring and interpreting quantum efficiency of acid blue 9 photodegradation using TiO2-based catalysts. Appl Catal A Gen. https://doi.org/10.1016/j.apcata.2017.10.016
32. Manassero A, Satuf ML, Alfano OM (2013) Evaluation of UV and visible light activity of TiO2 catalysts for water remediation. Chem Eng J 225:378–386. https://doi.org/10.1016/j.cej.2013.03.097
33. Mamaghani AH, Haghighat F, Lee C-S (2017) Photocatalytic oxidation technology for indoor environment air purification: the state-of-the-art. Appl Catal B Environ 203:247–269. https://doi.org/10.1016/j.apcatb.2016.10.037
34. Ballari MM, Brouwers HJH (2013) Full scale demonstration of air-purifying pavement. J Hazard Mater 254–255:406–414. https://doi.org/10.1016/j.jhazmat.2013.02.012
35. Pastrana-Martínez LM, Morales-Torres S, Carabineiro SAC et al (2018) Photocatalytic activity of functionalized nanodiamond-TiO2 composites towards water pollutants degradation under UV/Vis irradiation. Appl Surf Sci 458:839–848. https://doi.org/10.1016/J.APSUSC.2018.07.102
36. Chávez AM, Ribeiro AR, Moreira NFF et al (2019) Removal of organic micropollutants from a municipal wastewater secondary effluent by UVA-LED photocatalytic ozonation. Catalysts 9:472. https://doi.org/10.3390/catal9050472

37. Moreira NFF, Sampaio MJ, Ribeiro AR et al (2019) Metal-free g-C3N4 photocatalysis of organic micropollutants in urban wastewater under visible light. Appl Catal B Environ 248:184–192. https://doi.org/10.1016/J.APCATB.2019.02.001
38. Giannakis S, Rtimi S, Pulgarin C (2017) Light-assisted advanced oxidation processes for the elimination of chemical and microbiological pollution of wastewaters in developed and developing countries. Molecules 22:1070. https://doi.org/10.3390/molecules22071070
39. Rengifo-Herrera JA, Pierzchała K, Sienkiewicz A et al (2009) Abatement of organics and *Escherichia coli* by N, S co-doped TiO2 under UV and visible light. Implications of the formation of singlet oxygen (1O2) under visible light. Appl Catal B Environ 88:398–406. https://doi.org/10.1016/J.APCATB.2008.10.025
40. Rengifo-Herrera JA, Pulgarin C (2010) Photocatalytic activity of N, S co-doped and N-doped commercial anatase TiO2 powders towards phenol oxidation and *E. coli* inactivation under simulated solar light irradiation. Sol Energy 84:37–43. https://doi.org/10.1016/J.SOLENER.2009.09.008
41. Muñoz-Batista MJ, Ferrer M, Fernández-García M, Kubacka A (2014) Abatement of organics and *Escherichia coli* using CeO2-TiO2 composite oxides: ultraviolet and visible light performances. Appl Catal B Environ 154–155:350–359. https://doi.org/10.1016/j.apcatb.2014.02.038
42. Kubacka A, Muñoz-Batista MJ, Ferrer M, Fernández-Garcia M (2018) Er-W codoping of TiO2-anatase: structural and electronic characterization and disinfection capability under UV–vis, and near-IR excitation. Appl Catal B Environ 228:113–129. https://doi.org/10.1016/j.apcatb.2018.01.064
43. Henderson MA (2011) A surface science perspective on TiO2 photocatalysis. Surf Sci Rep 66:185–297. https://doi.org/10.1016/J.SURFREP.2011.01.001
44. Roy P, Berger S, Schmuki P (2011) TiO2 nanotubes: synthesis and applications. Angew Chem Int Ed Engl 50:2904–2939. https://doi.org/10.1002/anie.201001374
45. Fontelles-Carceller O, Muñoz-Batista MJ, Conesa JC et al (2017) UV and visible hydrogen photoproduction using Pt promoted Nb-doped TiO2 photo-catalysts: interpreting quantum efficiency. Appl Catal B Environ 216:133–145. https://doi.org/10.1016/j.apcatb.2017.05.022
46. Lu F, Cai W, Zhang Y (2008) ZnO hierarchical micro/nanoarchitectures: solvothermal synthesis and structurally enhanced photocatalytic performance. Adv Funct Mater 18:1047–1056. https://doi.org/10.1002/adfm.200700973
47. Mclaren A, Valdes-Solis T, Li G, Tsang SC (2009) Shape and size effects of ZnO nanocrystals on photocatalytic activity. J Am Chem Soc 131:12540–12541. https://doi.org/10.1021/ja9052703
48. Sakthivel S, Neppolian B, Shankar MV et al (2003) Solar photocatalytic degradation of azo dye: comparison of photocatalytic efficiency of ZnO and TiO2. Sol Energy Mater Sol Cells 77:65–82. https://doi.org/10.1016/S0927-0248(02)00255-6
49. Ong W-J, Tan L-L, Ng YH et al (2016) Graphitic carbon nitride (g-C3N4)-based photocatalysts for artificial photosynthesis and environmental remediation: are we a step closer to achieving sustainability? Chem Rev 116:7159–7329. https://doi.org/10.1021/acs.chemrev.6b00075
50. Mamba G, Mishra AK (2016) Graphitic carbon nitride (g-C3N4) nanocomposites: a new and exciting generation of visible light driven photocatalysts for environmental pollution remediation. Appl Catal B Environ 198:347–377. https://doi.org/10.1016/j.apcatb.2016.05.052
51. Fontelles-Carceller O, Muñoz-Batista MJMJMJ, Fernández-García M, Kubacka A (2016) Interface effects in sunlight-driven Ag/g-C3N4 composite catalysts: study of the toluene photodegradation quantum efficiency. ACS Appl Mater Interfaces 8:2617–2627. https://doi.org/10.1021/acsami.5b10434
52. Cerdan K, Ouyang W, Colmenares JC et al (2019) Facile mechanochemical modification of g-C3N4 for selective photo-oxidation of benzyl alcohol. Chem Eng Sci 194:78–84. https://doi.org/10.1016/j.ces.2018.04.001
53. Zheng H, Okabe TH (2008) Recovery of titanium metal scrap by utilizing chloride wastes. J Alloys Compd 461:459–466. https://doi.org/10.1016/j.jallcom.2007.07.025
54. Valighazvini F, Rashchi F, Khayyam Nekouei R (2013) Recovery of titanium from blast furnace slag. Ind Eng Chem Res 52:1723–1730. https://doi.org/10.1021/ie301837m
55. Liu XH, Gai GS, Yang YF et al (2008) Kinetics of the leaching of TiO2 from Ti-bearing blast furnace slag. J China Univ Min Technol 18:275–278. https://doi.org/10.1016/S1006-1266(08)60058-9
56. Zhang Q, Wu Y, Zuo T (2018) Green recovery of titanium and effective regeneration of TiO2 photocatalysts from spent selective catalytic reduction catalysts. ACS Sustain Chem Eng 6:3091–3101. https://doi.org/10.1021/acssuschemeng.7b03038

57. Muñoz-Batista MJ, Motta Meira D, Colón G et al (2018) Phase-contact engineering in mono- and bimetallic Cu–Ni Co-catalysts for hydrogen photocatalytic materials. Angew Chem Int Ed 57:1199–1203. https://doi.org/10.1002/anie.201709552
58. Zhang AY, Long LL, Liu C et al (2014) Chemical recycling of the waste anodic electrolyte from the TiO2 nanotube preparation process to synthesize facet-controlled TiO2 single crystals as an efficient photocatalyst. Green Chem 16:2745–2753. https://doi.org/10.1039/c3gc42167h
59. Ong CB, Ng LY, Mohammad AW (2018) A review of ZnO nanoparticles as solar photocatalysts: synthesis, mechanisms and applications. Renew Sustain Energy Rev 81:536–551. https://doi.org/10.1016/j.rser.2017.08.020
60. Sujaridworakun P, Natrchalayuth K (2014) Influence of pH and HPC concentration on the synthesis of zinc oxide photocatalyst particle from zinc-dust waste by hydrothermal treatment. Adv Powder Technol 25:1266–1272. https://doi.org/10.1016/J.APT.2014.03.002
61. Muñoz-Batista MJ, Kubacka A, Hungría AB, Fernández-García M (2015) Heterogeneous photocatalysis: light-matter interaction and chemical effects in quantum efficiency calculations. J Catal 330:154–166. https://doi.org/10.1016/j.jcat.2015.06.021
62. Mohamed HH, Alsanea AA, Alomair NA et al (2019) ZnO@ porous graphite nanocomposite from waste for superior photocatalytic activity. Environ Sci Pollut Res. https://doi.org/10.1007/s11356-019-04684-3
63. Tanniratt P, Wasanapiarnpong T, Mongkolkachit C, Sujaridworakun P (2016) Utilization of industrial wastes for preparation of high performance ZnO/diatomite hybrid photocatalyst. Ceram Int 42:17605–17609. https://doi.org/10.1016/j.ceramint.2016.08.074
64. Hao H, Lang X (2019) Metal sulfide photocatalysis: visible-light-induced organic transformations. ChemCatChem 11:1378–1393. https://doi.org/10.1002/cctc.201801773
65. Halfyard JE, Hawboldt K (2011) Separation of elemental sulfur from hydrometallurgical residue: a review. Hydrometallurgy 109:80–89. https://doi.org/10.1016/j.hydromet.2011.05.012
66. Cova CM, Zuliani A, Puente Santiago AR et al (2018) Microwave-assisted preparation of Ag/Ag2S carbon hybrid structures from pig bristles as efficient HER catalysts. J Mater Chem A 6:21516–21523. https://doi.org/10.1039/C8TA06417B
67. Zuliani A, Muñoz-Batista MJ, Luque R (2018) Microwave-assisted valorization of pig bristles: towards visible light photocatalytic chalcocite composites. Green Chem 20:3001–3007. https://doi.org/10.1039/C8GC00669E
68. Cova CM, Zuliani A, Munoz-Batista MJ, Luque R (2019) A sustainable approach for the synthesis of catalytically active peroxidase-mimic ZnS catalysts. ACS Sustain Chem Eng 7:1300–1307. https://doi.org/10.1021/acssuschemeng.8b04968
69. Lim SY, Shen W, Gao Z (2015) Carbon quantum dots and their applications. Chem Soc Rev 44:362–381. https://doi.org/10.1039/C4CS00269E
70. Abbas A, Mariana LT, Phan AN (2018) Biomass-waste derived graphene quantum dots and their applications. Carbon N Y 140:77–99. https://doi.org/10.1016/j.carbon.2018.08.016
71. Park SY, Lee HU, Park ES et al (2014) Photoluminescent green carbon nanodots from food-waste-derived sources: large-scale synthesis, properties, and biomedical applications. ACS Appl Mater Interfaces 6:3365–3370. https://doi.org/10.1021/am500159p
72. Hsu P-C, Shih Z-Y, Lee C-H, Chang H-T (2012) Synthesis and analytical applications of photoluminescent carbon nanodots. Green Chem 14:917. https://doi.org/10.1039/c2gc16451e
73. Liang Z, Zeng L, Cao X et al (2014) Sustainable carbon quantum dots from forestry and agricultural biomass with amplified photoluminescence by simple NH4OH passivation. J Mater Chem C 2:9760–9766. https://doi.org/10.1039/C4TC01714E
74. Anmei S, Qingmei Z, Yuye C, Yilin W (2018) Preparation of carbon quantum dots from cigarette filters and its application for fluorescence detection of Sudan I. Anal Chim Acta 1023:115–120. https://doi.org/10.1016/J.ACA.2018.03.024
75. Thakur A, Devi P, Saini S et al (2019) Citrus limetta organic waste recycled carbon nanolights: photoelectro catalytic, sensing, and biomedical applications. ACS Sustain Chem Eng 7:502–512. https://doi.org/10.1021/acssuschemeng.8b04025
76. Martindale BCM, Hutton GAM, Caputo CA, Reisner E (2015) Solar hydrogen production using carbon quantum dots and a molecular nickel catalyst. J Am Chem Soc 137:6018–6025. https://doi.org/10.1021/jacs.5b01650
77. Martindale BCM, Hutton GAM, Caputo CA et al (2017) Enhancing light absorption and charge transfer efficiency in carbon dots through graphitization and core nitrogen doping. Angew Chem Int Ed 56:6459–6463. https://doi.org/10.1002/anie.201700949

78. Rigodanza F, Đorđević L, Arcudi F, Prato M (2018) Customizing the electrochemical properties of carbon nanodots by using quinones in bottom-up synthesis. Angew Chem 130:5156–5161. https://doi.org/10.1002/ange.201801707
79. Fang Q, Dong Y, Chen Y et al (2017) Luminescence origin of carbon based dots obtained from citric acid and amino group-containing molecules. Carbon N Y 118:319–326. https://doi.org/10.1016/J.CARBON.2017.03.061
80. Cailotto S, Mazzaro R, Enrichi F et al (2018) Design of carbon dots for metal-free photoredox catalysis. ACS Appl Mater Interfaces 10:40560–40567. https://doi.org/10.1021/acsami.8b14188
81. Prasannan A, Imae T (2013) One-pot synthesis of fluorescent carbon dots from orange waste peels. Ind Eng Chem Res 52:15673–15678. https://doi.org/10.1021/ie402421s
82. Wang Z, Yu J, Zhang X et al (2016) Large-scale and controllable synthesis of graphene quantum dots from rice husk biomass: a comprehensive utilization strategy. ACS Appl Mater Interfaces 8:1434–1439. https://doi.org/10.1021/acsami.5b10660
83. Rodríguez-Padrón D, Algarra M, Tarelho LAC et al (2018) Catalyzed microwave-assisted preparation of carbon quantum dots from lignocellulosic residues. ACS Sustain Chem Eng 6:7200–7205. https://doi.org/10.1021/acssuschemeng.7b03848
84. Wang S, Wang H, Zhang R et al (2018) Egg yolk-derived carbon: achieving excellent fluorescent carbon dots and high performance lithium-ion batteries. J Alloys Compd 746:567–575. https://doi.org/10.1016/j.jallcom.2018.02.293
85. Jing S, Zhao Y, Sun RC et al (2019) Facile and high-yield synthesis of carbon quantum dots from biomass-derived carbons at mild condition. ACS Sustain Chem Eng 7:7833–7843. https://doi.org/10.1021/acssuschemeng.9b00027
86. Muñoz-Batista MJ, Rodriguez-Padron D, Puente-Santiago AR, Luque R (2018) Mechanochemistry: toward sustainable design of advanced nanomaterials for electrochemical energy storage and catalytic applications. ACS Sustain Chem Eng 6:9530–9544. https://doi.org/10.1021/acssuschemeng.8b01716
87. Colmenares JC, Xu Y-J (2016) Heterogeneous photocatalysis from fundamentals to green applications. Springer, Berlin, Heidelberg
88. Francavilla M, Pineda A, Romero AA et al (2014) Efficient and simple reactive milling preparation of photocatalytically active porous ZnO nanostructures using biomass derived polysaccharides. Green Chem 16:2876–2885. https://doi.org/10.1039/C3GC42554A
89. Yang L, Li X, Wang Z et al (2017) Natural fiber templated TiO2 microtubes via a double soaking sol-gel route and their photocatalytic performance. Appl Surf Sci 420:346–354. https://doi.org/10.1016/j.apsusc.2017.05.168
90. Chen X, Kuo D-H, Lu D et al (2016) Synthesis and photocatalytic activity of mesoporous TiO2 nanoparticle using biological renewable resource of un-modified lignin as a template. Microporous Mesoporous Mater 223:145–151. https://doi.org/10.1016/J.MICROMESO.2015.11.005
91. Wang H, Qiu X, Liu W, Yang D (2017) Facile preparation of well-combined lignin-based carbon/ZnO hybrid composite with excellent photocatalytic activity. Appl Surf Sci 426:206–216. https://doi.org/10.1016/J.APSUSC.2017.07.112
92. Unni SM, George L, Bhange SN et al (2016) Valorization of coffee bean waste: a coffee bean waste derived multifunctional catalyst for photocatalytic hydrogen production and electrocatalytic oxygen reduction reactions. RSC Adv 6:82103–82111. https://doi.org/10.1039/c6ra14907c
93. Rodríguez-Padrón D, Puente-Santiago AR, Luna-Lama F et al (2019) Versatile protein-templated TiO2 nanocomposite for energy storage and catalytic applications. ACS Sustain Chem Eng 7:5329–5337. https://doi.org/10.1021/acssuschemeng.8b06349
94. Antonetti E, Iaquaniello G, Salladini A et al (2017) Waste-to-chemicals for a circular economy: the case of urea production (waste-to-urea). Chemsuschem 10:912–920. https://doi.org/10.1002/cssc.201601555
95. Babar S, Gavade N, Shinde H et al (2019) An innovative transformation of waste toner powder into magnetic g-C3N4–Fe2O3 photocatalyst: sustainable e-waste management. J Environ Chem Eng 7:103041. https://doi.org/10.1016/j.jece.2019.103041
96. Yola ML, Eren T, Atar N (2014) A novel efficient photocatalyst based on TiO2 nanoparticles involved boron enrichment waste for photocatalytic degradation of atrazine. Chem Eng J 250:288–294. https://doi.org/10.1016/j.cej.2014.03.116
97. Colmenares JC, Lisowski P, Bermudez JM et al (2014) Unprecedented photocatalytic activity of carbonized leather skin residues containing chromium oxide phases. Appl Catal B Environ 150–151:432–437. https://doi.org/10.1016/j.apcatb.2013.12.038

98. Bennett JA, Wilson K, Lee AF (2016) Catalytic applications of waste derived materials. J Mater Chem A 4:3617–3637. https://doi.org/10.1039/c5ta09613h
99. Puente-Santiago AR, Rodríguez-Padrón D, Quan X et al (2019) Unprecedented wiring efficiency of sulfonated graphitic carbon nitride materials: toward high-performance amperometric recombinant CotA laccase biosensors. ACS Sustain Chem Eng 7:1474–1484. https://doi.org/10.1021/acssuschemeng.8b05107

Topics in Current Chemistry (2020) 378:2
https://doi.org/10.1007/s41061-019-0262-3

REVIEW

Mechanochemical Forces as a Synthetic Tool for Zero- and One-Dimensional Titanium Oxide-Based Nano-photocatalysts

Dimitrios A. Giannakoudakis[1] · Gregory Chatel[2] · Juan Carlos Colmenares[1]

Received: 30 July 2019 / Accepted: 22 October 2019 / Published online: 25 November 2019

Abstract

A new field where the utilization of mechanochemistry can create new opportunities is materials chemistry, and, more interestingly, the synthesis of novel nanomaterials. Ball-milling procedures and ultrasonic techniques can be regarded as the most important mechanochemical synthetic tools, since they can act as attractive alternatives to the conventional methods. It is also feasible for the utilization of mechanochemical forces to act synergistically with the conventional synthesis (as a pre-treatment step, or simultaneously during the synthesis) in order to improve the synthetic process and/or the material's desired features. The usage of ultrasound irradiation or ball-milling treatment is found to play a crucial role in controlling and enhancing the structural, morphological, optical, and surface chemistry features that are important for heterogeneous photocatalytic practices. The focus of this article is to collect all the available examples in which the utilization of sonochemistry or ball milling had unique effects as a synthesis tool towards zero- or one-dimensional nanostructures of a semiconductor which is assumed as a benchmark in photocatalysis, titanium dioxide.

Chapter 2 was originally published as Giannakoudakis, D. A., Chatel, G. & Colmenares, J. C. Topics in Current Chemistry (2020) 378: 2. https://doi.org/10.1007/s41061-019-0262-3.

✉ Dimitrios A. Giannakoudakis
dagchem@gmail.com

✉ Juan Carlos Colmenares
jcarloscolmenares@ichf.edu.pl

[1] Institute of Physical Chemistry, Polish Academy of Sciences, Kasprzaka 44/52, 01-224 Warsaw, Poland

[2] Université Savoie Mont Blanc, LCME, 73000 Chambéry, France

Graphical Abstract

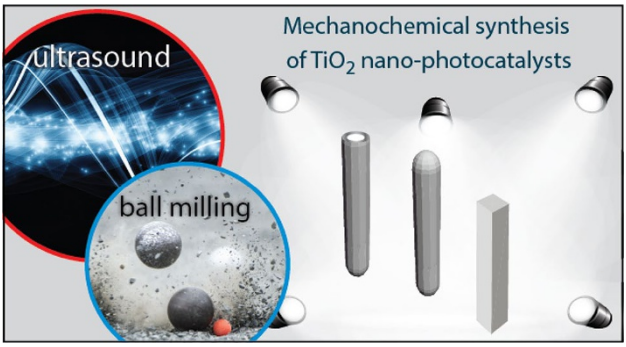

Keywords Mechanochemistry · Sonochemistry · Ultrasound-assisted synthesis · One-dimensional titanium oxide · Photocatalysis · Ball milling

1 Introduction

1.1 Nanotechnology and Photocatalysis

Generally, the impact of nanotechnology has been astonishingly positive in the last decades toward a wide range of environmental, energy, catalysis, as well as synthetic applications and technologies, with a continuous incremental trend of published peer-reviewed articles. Nanostructured and nanoengineered materials garner continuously enhanced research attention and focus due to their unique and novel properties, especially in comparison to bulk materials/counterparts. Application of nanoscaled materials covers a broad range of fields, from electronics and catalytic reactions, to medical and environmental remediation, while novel nanomaterials for new applications are highly desired. The properties of nanomaterials depend on the morphological (shape and size), structural (surface area and porosity), optical (band-gap and light-harvesting capability), and surface chemistry features (nature and availability of the reactive sites). Another important aspect is to obtain well-defined phase composition of high homogeneity. All the above features are directly linked and dependent on the method/protocol of preparation [1]. By tuning specific synthetic parameters, such as temperature, aging, and washing protocol, it is feasible to control the vital features for a targeted use. For instance, the chemical composition and the porosity are crucial features regarding catalytic synthesis and environmental applications. On the other hand, the optical and morphological features are more important for fabricating crystals for photonic devices.

Another important target in laboratory as well as in industrial research is to find novel ways to conduct reactions following "green" approaches. And toward this direction, photocatalysis is a favorable tool, since it is feasible to utilize a natural source of energy, solar light. The harvesting of light from a photocatalyst can

promote specific reactions even without the use of additive chemicals or another source of energy. The most important part in heterogeneous photocatalysis is the development and usage of materials that can function as sufficient photocatalysts, and nanotechnology has been shown capable of providing solutions. Synthesis of nanomaterials and tuning specific features of them like nano-morphological and optical features is an ultimately important and efficient strategy to achieve the above. Even though the synthesis of nanoscaled photocatalysts has been a hot topic during the last decades with many published articles and end-use applications, the use of mechanochemical-based synthetic approaches is not so broadly explored. By gathering the existing knowledge on the effects derived from the mechanochemical forces like ultrasound (US) irradiation and ball milling, it will be realistic to go a step further. The focus of this work is to collect all the reports in which the two above-mentioned techniques were applied during the synthesis of two benchmark semiconductor photocatalysts, titanium dioxide or titanate, in order to obtain various polymorphs with different structural, morphological, and optical features.

1.2 Mechanochemical Synthesis

The exploration and discovery of new synthetic approaches as well as the incorporation of advantageous techniques for the development of new or improved properties of already known nanomaterials as photocatalysts is an ongoing and interesting field of research, with fascinating potential [1, 2]. In recent years, mechanochemical processes were found to hold great promise, since they are effective and can lead to nanomaterials of novel properties. Another important aspect is that various reported active nanocatalysts can be synthesized in a shorter time compared to traditional wet-chemistry synthesis. In many cases, the design of mechanochemical-based methods can have a positive effect on the "green" character and environmental footprint: consumption of less energy, less or even no use of hazardous solvents, need of recycling, purification, etc. According to the International Union of Pure and Applied Chemistry (IUPAC), the definition of a mechanochemical process is: "*a chemical reaction that is induced by the direct absorption of mechanical energy*" [3]. The utilization of mechanochemical forces holds great promise and begets novel approaches in nanocrystalline synthesis (mechanosynthesis), and, more specifically, on how to control the desired features, crucial for different applications [3–7]. Herein, two mechanochemical sources will be introduced: (1) US irradiation (sonochemistry) and (2) ball milling. The rapid growth of the research interest around the utilization of mechanochemistry methods is due to their unique effects. By the correct selection of these effects, it is feasible to obtain novel nanomaterials, and to control desired physical, chemical, and optical properties [5, 8]. Simultaneously, it is possible to eliminate the environmental footprint of the synthesis, avoiding, for instance, the usage of high energy, hazardous and non-recyclable chemicals, or by decreasing the duration and the number of steps of the synthesis [9].

1.3 Sonochemistry

1.3.1 A Brief History

Sound waves not detectable by the human ear with frequencies ranging from 20 kHz to 200 MHz are referred to as ultrasound (US) waves [10]. The effects of sonication are linked to the cavitation phenomena, and they can be chemical, physical, mechanical, or optical. The first reference to the cavitation phenomena by Thornycroft and Barnaby dates from 1895 [11]. By the time Neppiras introduced the term "sonochemistry" in 1980 [12] and Makino et al. showed the formation of radical species during the sonolysis of water in 1982 [13, 14], the research attraction of sonochemistry had increased dramatically. In general, sonochemistry is linked with the understanding and interpretation of the processes and the effects initiated by US irradiation due to the cavitation phenomena. The main derived results are the enhancement of the reaction rate, radical species formation, as well as mass and heat transfer [1, 2, 4, 15–17].

1.3.2 Cavitation Phenomena—Mechanistic Aspects on "How Does Everything Work?"

The formation of cavitation bubbles is due to pressure changes upon the travel of US waves in a liquid. The initially formed microbubbles, consisting of vaporized solvent or/and dissolved gases, grow continuously in size by absorbing energy during the irradiation [18]. After growing to a certain size, they violently collapse, creating a localized "hot spot." The local pressure and temperature can be above 1000 bars and 5000 K, respectively [18–20]. The hot-spot concept and the consequential effects can be described by distinguishing three zones [21, 22]. Zone 1 is inside the bubble (primary sonochemistry), zone 2 is at the gas–liquid interface (secondary sonochemistry), and zone 3 is the bulk liquid phase surrounding zone 2. At the interior of the cavity, cleavage of bonds and formation of radicals occurs due to the harsh energetical environment and to the fact that the gaseous concentration is extended [22–24]. These radical species can also be transported to zone 2, where reaction of free radicals and pyrolysis can take place, or even to the bulk liquid zone 3. In an aqueous environment, the sonolysis of water can lead to the formation of hydroxyl ($HO^{\cdot}$) or hydroperoxyl ($HO_2^{\cdot}$) radicals, and hydrogen peroxide (H_2O_2). These species can initiate secondary reactions that can play a key role in material synthesis or for catalytic reactions [15].

Even if the "hot-spot" theory is the most accepted to explain these phenomenas, several studies lead to the proposition of plasma [25, 26], electrical [27], and supercritical water [28] theories, demonstrating that all the mechanisms involving US are not completely known. In addition to the chemical effect of US, various other mechanisms exist, such as physical, mechanical, or light emission (sonoluminescence). The latter one is also valuable in order to determine the active regions and intensity of the US waves using a hydroxyl radical trapping agent, luminol (through chemiluminescence [29–31]. The physical/mechanical effects can be the formation of microjets, turbulence, microstreaming, shockwaves, and agitations [23]. These effects can

positively promote the reaction rates by affecting the mass (mixing) and heat transfer phenomena or resulting in some structural alterations of the solids, such as erosion, exfoliation, fragmentation, or deformation [6, 8, 22, 32, 33].

The utilization of US irradiation is a complex aspect, since the formation of cavitation in liquids can be affected by numerous parameters [2, 22, 23]. Some of them are described in most of the articles, but some were not reported. The frequency and the power of the irradiated US waves can be considered the most fundamental parameters [16]. Increase of the US frequency leads to shortening of the expansion and compression pressure cycle, and, as a result, to a negative impact on the effectiveness. The formed bubbles/cavitation at higher frequencies have a smaller size and less violent implosion effects, although they have a better size distribution and rate formation. At lower frequency, the cavitation phenomena is more violent and intense with a consequent of higher localized pressure and temperature, as well as higher concentration of free radical formation. However, there are many cases where the high frequencies have desired impact on reaction rates and material synthesis.

Other important parameters that should be taken into consideration for the effective US utilization in synthesis of catalysts and catalytic reactions are the solvent, the presence/concentration of dissolved gases, temperature, and pressure [34]. The physicochemical parameters of the solvent, for example, the solubility of air or oxygen, viscosity, surface tension, or vapor pressure, play key roles in the cavitation threshold. The increment of the latter parameter has a negative impact on the cycle formation, while, on the contrary, increment of the rest has a positive effect. Initiation of cavitation is facilitated by the presence of dissolved gases. However, the extent of the assistance upon cavitation is related to the physical properties of the gas. Contrary to the chemical processes, the increase of the temperature (until a specific range) has a negative impact on the sonochemical reaction due to increase of the vapor pressure and to the decrement of the gaseous solubility. However, there are many circumstances revealing that the temperature increase has positive and desired effects. An increase of the reactor pressure could cause a decrease of the solvent's vapor pressure.

1.4 Ball Milling

1.4.1 A Brief History

The earliest recorded mechanochemical process, according to Takacs [35], dates to the fourth century BC, in which Theophastus of Eresos noted the synthesis of elemental mercury by grinding cinnabar (HgS) with acetic acid in a Cu vessel, the first documented separation of an elemental metal [3, 7, 35]. Since a solvent was needed even in a minimal amount, this process is regarded nowadays as liquid-assisted grinding (LAG). From this point and afterward, mechanochemistry-based approaches were applied widely in metallurgy and mining, and more details can be found elsewhere [35–37]. By the use of a pestle and mortar and without a liquid (dry grinding), it was the great experimental physicist, Michael Faraday (discovered the laws of electrolysis, electromagnetic induction, and the rotation of polarized light by

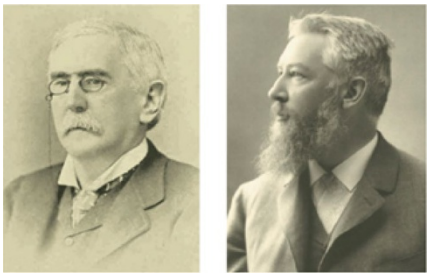

Fig. 1 Mathew Carey Lea (1823–1897) and Friedrich Wilhelm Ostwald (1853–1932) left and right, respectively. Reprinted with permission from [40]. Copyright (2013) Royal Society of Chemistry

magnetism) who conducted displacement reactions between a metal and oxides of less reactive metals [3, 7, 35]. In his first research published in 1820, which can be assumed as the first systematic study of the mechanochemical process, he showed the oxidation of Zn by the reduction of AgCl to Ag by simple mortar grinding [35, 38]. However, there was no specific evidence indicating if the grinding promoted the reaction mechanochemically of just thermodynamically by heat generation through friction.

The American chemist and pioneer of photographic chemistry, Mathew Carey Lea (1823–1897), systematically studied and determined (between 1889 and 1894) that the above kind of redox reactions were initiated/activated by mechanochemical effects rather than thermochemical effects. A clear and loud example was the formation of elemental Ag from grinding of silver halides, while it was just melted without decomposition upon thermal treatment [39] (Fig. 1).

The terminology of mechanochemistry was introduced by L. Crismer in 1912 in a biography of Walthere Spring and his geology-oriented research on the effects derived by high pressure on powdered materials in order to explain the formation of various natural minerals [35, 41]. Although mechanochemistry started to be assumed and accepted as a distinct/separate subdiscipline of chemistry in 1919, a physical chemist and philosopher, the Nobel Laureate Friedrich Wilhelm Ostwald (Nobel prize in Chemistry, 1909, "in recognition of his work on catalysis and for his investigations into the fundamental principles governing chemical equilibria and rates of reaction") introduced it as a separate chemistry sub-discipline alongside electrochemistry, photochemistry, and thermochemistry [42]. Ostwald made this classification due to the fact that different types of energy are required in each sub-discipline.

1.4.2 Mechanistic Aspects on "How Ball Milling Works?"

Even nowadays, there is not a complete and comprehensive mechanistic picture regarding how ball milling and, in general, mechanochemistry works. This is also linked with the diversity of the utilized techniques/equipment (like mortar/pestle, mixer and planetary mills, glass vessel or tube disperser milling, etc. [3]) and the reaction types (dry or wet), conditions (gaseous atmosphere, temperature, etc.), and precursors (minerals, metal oxides, metals, chemicals, etc.). Several processes take place during the ball milling like heat and mass transfer.

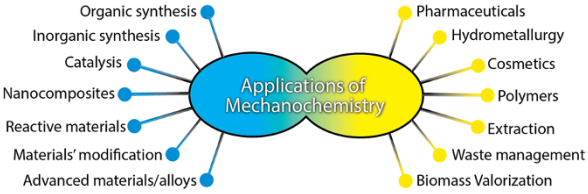

Fig. 2 Applications of mechanochemistry

However, the most crucial driving force is believed to be the generation and relaxation of mechanical stress that have a direct effect on the crystalline lattices [3]. The theory of "hot spots" formation during ball milling is a widely accepted one [7]. Hot spots can be created by the cracking of crystals, resulting in local temperature (up to 5000 K) and pressure, electric fields up to 108 V/m, crack propagation with velocity close to that of sound (105 cm/s), and lifetimes for bond excitation around 100 fs [3, 43, 44]. These effects are analogues of those of US irradiation in a liquid, even though the formation of a hot spot results from the cavitation phenomena. And it is important that the high amount of added energy is localized microscopically, even nanoscopically, without affecting the macroscopic system to a great extent. This localized high amount of energy can lead to a diversity of consequences, such as lattice deformation, cleavage of bonds, or formation of radicals. And these phenomena cannot be achieved by other synthetic approaches in solution. Figure 2 presents the most important fields of mechanochemistry applications based on the report by Elena Boldyreva [43]. More mechanistic aspects and fields of application of mechanochemistry can also be found elsewhere [3, 7, 35, 44]. Even though Boldyreva did not consider US irradiation in her work, the latter can be utilized for the same fields and applications when a liquid phase is required. The rapid growth of the research interest around the application of mechanochemistry is due recent discovery of unique effects. By the correct utilization of these effects, it is feasible to obtain the desired nanostructured materials and enhance their crucial features by simultaneously eliminating the environmental footprint of the synthesis and avoiding the usage of high energy and hazardous and non-recyclable chemicals.

1.5 TiO_2: The Benchmark Semiconductor Photocatalyst

Titanium dioxide (TiO_2) can be regarded as one of the most popular semiconductor photocatalysts, for a wide range of applications; organic pollutant degradation, hydrogen production, solar cells, photocatalysis, etc. It combines high photo-activity for various reactions, high stability, low cost, and low toxicity for humans, animals, and the environment. Use of titanium dioxide started intensively in 1972, when Fujishima and Honda revealed photocatalytic water splitting by titania electrodes [45]. Since then, numerous articles have focused on the use of TiO_2 and its composites for green-oriented heterogeneous catalysis, like valorization of biomass and upgrading of obtained chemicals [1, 46, 47].

Another important property of titanium dioxide is its superhydrophilicity that is crucial for solar fuel production and environmental remediation applications [48]. However, one crucial drawback arises due to the fact that TiO_2 has a wide bandgap

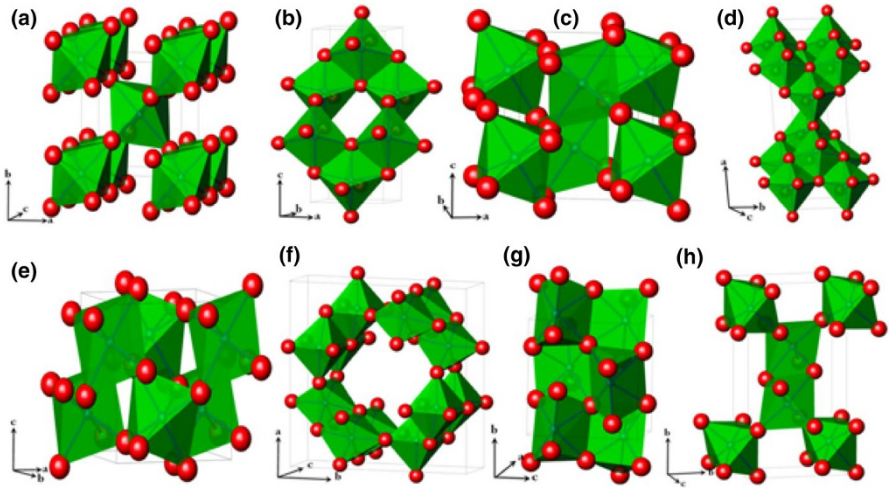

Fig. 3 Crystal structures of rutile (**a**), anatase (**b**), bronze (**c**), brookite (**d**), columbite (**e**), hollandite (**f**), baddeleyite (**g**), and ramsdellite (**h**) phases. Reprinted with permission from [49]. Copyright (2015) Elsevier

ranging from 3.1 to 3.7 eV, and UV light irradiation is required in order to trigger the photoreactivity. Considering that solar light consists predominately of visible and infrared light, with ultraviolet light less than 5% of the total solar light, a persistent research effort is focused on narrowing of the bandgap and, as a result, increase of light absorption and photoreactivity under sunlight. Even though several polymorphs/crystal structures of TiO_2 exist [49], with the most important presented in Fig. 3, only a few of them have been studied and found promising for photocatalytic applications like biomass valorization [33, 50, 51]. The three most studied and stable crystalline phases of titanium oxide are anatase, brookite, and rutile, with the former one possessing the highest photocatalytic activity and the latter the highest stability [52]. Among the various commercially available forms of TiO_2, one of the most active and widely studied is Degussa P25, and, in many cases, it acts as a benchmark (industry standard) [53].

There are many reported methods for the synthesis of nanostructured TiO_2 materials. The sol–gel method is the most often applied method, but, unfortunately, it leads to amorphous nanomaterials, and, so, further treatment is needed to induce crystallization, like annealing. On the other hand, hydrothermal-based methods can promote the crystallinity and shape morphology formation, and can be used for larger scaled synthesis compared to the sol–gel method. Crystallinity in relation with the particle size is found to determine the photo-reactivity not only in the case of Ti-based catalyst [48, 54–57], but also for other materials like ZnO [58–60], MnO_2 [61], graphitic carbon nitride [5, 62–65], or other metal oxides/hydroxides [66–68]. However, the control of the final material's morphological features is related to a wide range of parameters during the synthesis.

Another important aspect in photocatalysis is the rate of the surface reactions. The structural (surface area and porosity) as well as the morphological features

(shape and size) play a key role in the catalysis rates, and, as a result, the engineering of these features is also important [47, 69–80]. Toward the above-mentioned direction, different strategies/approaches were followed for the nano-engineering of the TiO_2 toward key features/properties for application in catalysis. The most important strategies in order to positively trigger the photoreactivity are the following: (1) controlling the crystallographic nature; (2) introducing Ti^{3+} species and lattice disorder; (3) doping with metal or non-metal; (4) decreasing the size of the particles to nanoscale; (5) engineering the shape to 0D, 1D, 2D, 3D, or amorphous; (6) decreasing the size of the particles; (7) chemical modification like hydroxylation/hydrogenation; (8) porosity enhancement; (9) narrowing the bandgap toward the visible range of light; (10) enhancing light absorption; and (11) limitation of e^-/h^+ recombination.

1.6 Our Approach to Organize this Article

The focus of the work herein is based on novel mechanochemical-assisted synthesis/modifications, such as US irradiation and ball milling, in which their utilization has led to beneficial effects in the enhancement of photocatalytic capability. Since the application of mechanochemistry has only lately been assumed and recognized as a useful process-intensification tool, in most works where US or ball milling were applied, the reports have predominately a materials point of view approach without studying a potential photocatalytic reaction. Additionally, the one-dimensional-inspired spatially ordered nanotubular-shaped titanate has gathered intense attention upon its discovery in 1995 [81]. Although the utilization of mechanochemistry in order to improve the synthesis and control specific features has been explored, the photocatalytic capabilities of these titanate nanotubes (TiNTBs) was studied in only a few of these reports. We believe that TiNTBs can display important photocatalyst behavior, and we actively work towards this direction. Based on the above and the available articles, we organized this article into two main parts/sections. In the first part, we collected the reports in which sonication was used in order to obtain nano-engineered materials with enhanced specific features for photocatalytic application, like light absorptivity, decreased bandgap, defects like surface oxygen vacancies, hydroxylation, porosity, etc. The second part is focused on the ball milling-based synthesis/modification approach. Each part is separated in two subsections. The first subsection is focused on zero-dimensional (0-D) photocatalysts, with an emphasis on how to promote the most vital of photochemistry features. In the second subsection, we collect all the research on the synthesis of one-dimensional (1-D) nanostructured titanate, like nanotubes (NTBs) and nanorods.

2 PART A—Sonication-Assisted Approaches

2.1 0-D Particles

2.1.1 Increasing the Porosity

The supramolecular assembly sol–gel method using surfactant molecules as a template/structure-directing agent for the synthesis of mesoporous titania was reported firstly in 1995 by Antonelli and Ying [82]. The main drawback of the obtained hexagonally packed mesostructured TiO_2 was the presence of residual phosphorous from the alkyl phosphate surfactant. From then, different long-chain organic molecules were studied as phosphorus-free surfactants. In 2000, Wang et al. [83] reported a novel synthesis of mesoporous nanostructured titanate of a high porosity, by simultaneous ultrasonication during the synthesis (1.13 cm in diameter Ti horn, 20 kHz, 100 W/cm^2). An ethanolic solution of the organic amine and titanium isopropoxide was added slowly to a doubly distilled water, followed by aging for 6 h. The addition and the aging occurred under high-intensity ultrasonication, with the maximum temperature reaching 80 °C. The removal of the surfactant from the obtained powder by centrifugation was achieved by dilute ethanolic HNO_3 solution and washing with ethanol. The dried powder was also calcinated in a vacuum at 350 °C (8 h) or 450 °C (4 h). Three different long-chain organic amines (decylamine, dodecylamine, and octadecylamine) were studied as the structure-directing agents.

The result was spherical or globular particles between 50 and 200 nm as an aggregation of very small nanoparticles, as can be seen from the high-resolution transmission electron microscopy(HRTEM) image (Fig. 4). The X-ray diffraction (XRD) analysis showed an amorphous nature even after calcination at 350 °C, but the rise of the calcination temperature to 450 °C led to an anatase crystallinity. The surface areas after extraction, and calcination at 350 °C and 450 °C, were 853, 467, and 79 m^2/g, respectively. These values are high for metal oxides and higher than analogous titanate hexagonal mesoporous framework structures synthesized by hydrothermal and then thermal treatment with dodecylamine as a structure-directing agent (710 m^2/g) [83, 84]. The most interesting outcome was the that the obtained nanoparticles had a structure of disordered wormhole framework, rather than a long-ranged hexagonal structure. This kind of channel motif and the high surface area are ultimately important for catalytic application, due to the improved diffusion and the availability of the active reaction sites. Compared to various other reports for the synthesis of mesoporous TiO_2 nanoparticles, the benefits of this sonochemical method is the simplicity and rapid rate of synthesis, that leads also to nanoparticles of a high porosity. The authors linked the role of US irradiation to the accelerated condensation/polymerization of titanium hydroxide at the interface of the gas phase of the hotspots and the bulk solution.

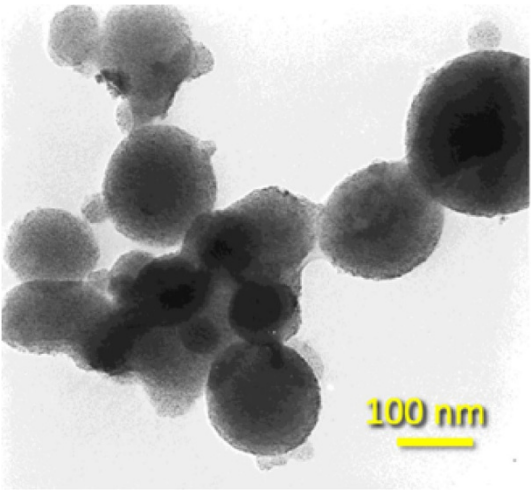

Fig. 4 HRTEM images of the as sono-chemically prepared mesoporous titanium oxide with wormhole-like framework structures. Reprinted with permission from [83]. Copyright (2000) Wiley

2.1.2 Controlling the Crystallinity

In 2000, Huang et al. studied the role of US irradiation in the selective synthesis of anatase or rutile phases from different precursors and conditions [52]. The synthetic protocol was based on the addition of different precursors (TPT: tetraisopropyltitanate, TTC: titanium tetrachloride, or a mixture of TPT and TTC) in water under sonication by a directly immersed horn (20 kHz, 100 W/cm^2). The suspension was ultrasonic-aged for 3 h, with the temperature reaching 80 °C. The precipitates were obtained by centrifugation and subsequently washed with deionized water and ethanol, following by overnight vacuum drying. Compared to the sol–gel-derived materials that were amorphous prior to calcination, the samples obtained via US irradiation showed a high degree of crystallinity. Rutile-phased nanoparticles (crystallographic size based on the application of Scherrer's formula at the XRD: 8.2 nm) were obtained when TTC was used, and anatase phase (3.5 nm) in the case of TPT. The materials synthesized via US were also found to have relatively high surface areas, 103 m^2/g for the rutile phase and 201 m^2/g for the anatase phase. The TPT-derived sample (anatase) had a broad size distribution of mesopores (average of 5 nm), linked by the authors to the aggregation of nanoparticles. The rutile phase TTC-derived sample had a non-mesoporous nature.

When a mixture of TPT and TTC were used in a molar ratio of 63.4:36.6, a mixed anatase/rutile phase was determined. Analysis of the powder X-ray diffraction (PXRD) data revealed a crystallographic ratio of anatase to rutile phases of 47.6:52.4, suggesting that in the case of the mixture, part of the rutile phase formed at the expense of TPT. It should be pointed out that without US irradiation, the material obtained with the same mixture of precursors as above mixture was amorphous. The authors also studied the role of temperature. When the synthesis was conducted at 30 °C instead of 80 °C and TPT as precursor, the result was mixed brookite and anatase phases. On the contrary, when TTC was hydrolyzed under sonication at 10 °C, rutile phase was obtained. The role of pH was also studied, but not

in detail. When TPT was hydrolyzed under sonication at pH 0.7, the obtained sample of limited mass had a mix of rutile and anatase phases. Increasing the pH of the supernatant of the above synthesis to 8.6 and further sonication for 3 h led to a pure anatase phase. Based on all the above, it is obvious that even though US irradiation and temperature play a key role by promoting the crystallization, the pH can determine the finally crystallographic phase. Another outcome derived by the authors was that the hydrolysis of TPT in water is slower compared to TTC, resulting in a more homogeneous and partly condensed gel. The formation of a hotspot due to US waves inside the gel phase promotes the polycondensation of the Ti–OH species and the formation of a large number of seed nuclei, leading to smaller nanoparticles.

In 2001, Yu et al. [85] studied the effect of US irradiation (cleaner bath, 47 kHz, 120 $W_{elec.}$) as well as the role of the ethanol-to-water ratio during the hydrolysis upon precipitation of titanium tetraisopropoxide in pure water or mixed EtOH–H_2O solution at different ratios, followed by in-air calcination at 500 °C for 1 h. The ratio of ethanol to water was found to play a key role in the crystallinity of the final powder, and, as a result, in the photocatalytic reactivity. While in pure aqueous solution, the obtained material had a mix of anatase and brookite phases (in a ratio of around 80:20); the addition of methanol led to the elimination of the brookite phase. The materials obtained without using methanol were found to possess a higher photoactivity against the oxidation of acetone in air compared to P25. On the contrary, the material with a solely anatase phase showed the lowest oxidative performance. The authors linked this to the fact that the presence of two crystallographic phases has a positive impact on the photocatalytic activity, by decreasing the combination of the photogenerated e^-/h^+ pairs. In 2010, Ghows et al. synthesized nanosized TiO_2 by hydrolysis of titanium tetra-isopropoxide in a solution of ethanol/water under low-intensity and high-frequency (500 kHz) sonication [86], although they did not study their photocatalytic properties. The crystalline phase and particle size were dependent on the ethanol-to-water ratio, US irradiation time, and temperature.

2.1.3 Altering the Surface Chemical Features and Bandgap

In 2011, Chen et al. [87] reported that the distortion and doping of the outer surface of TiO_2 nanoparticles by high-pressure and high-temperature hydrogenation led to an enhancement of the visible light absorption. Interestingly, and for the first time, the obtained TiO_2 powder did not have the characteristic white color, but a deep dark one. The reported synthesis of this material was conducted in two phases. In the first phase, titanium dioxide nanocrystals of an ~8-nm diameter were synthesized by a sol–gel method, using an organic template and acid (pluronic F127). The white powder obtained after calcination (500 °C, 6 h) underwent hydrogenation under a high-pressure (20 bars) H_2 atmosphere at ~ 200 °C for 5 days, resulting in a black powder, stable even after 1 year.

The HRTEM analysis revealed no shape alteration upon hydrogenation; however, an outer disordered layer around 1 nm in thickness appeared. The X-ray diffractogram of both white and black samples revealed the characteristic peaks of the anatase structure. The Raman spectrum of the white sample showed the six typical Raman-active modes of the anatase structure. The Raman spectrum of the

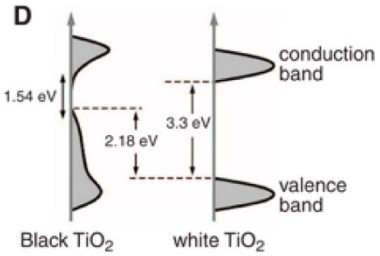

Fig. 5 A schematic illustration of the density of states (DOS) of disorder-engineered black TiO_2 compared to that of the white TiO_2 precursor. Adapted with permission from [87]. Copyright (2011) American Association for the Advancement of Science

black sample revealed a broadening of the six typical Raman-active modes which were appeared in the white powder, and some additional new bands not linked to any of the three classic polymorphs of TiO_2. The X-ray photoelectron spectroscopy (XPS) analysis revealed an almost identical and impurity-free bonding environment for Ti. On the contrary, the hydrogenation also resulted in a new O 1s peak (at 530.9 eV) which was attributed by the authors to the formation of Ti–OH moieties. Since the dangling bonds tends to attract hydrogen, the authors expected that the H doping occurred predominately in the outer disordered layer where more dangling bonds exist compared to the inner crystalline core. The bandgap of the non-hydrogenated materials was determined by diffuse reflectance as 3.3 eV (slightly higher than bulk anatase). The black TiO_2 showed a dramatically narrower bandgap , while the onset of the optical absorption started from ~ 1200 nm (1.0 eV). The authors linked this to the "band tail states" phenomena, where the valence and conduction bands narrow. The density of states (DOS) of the black sample compared to the white one can be seen in Fig. 5. The photocatalytic activity against methylene blue dye was found to be faster by ~ 7.5 folds under solar irradiation, and the photo-activity was found to be stable even after eight cycles. More interestingly, the black titania sample was found capable of photocatalytic hydrogen production from water under sunlight, with a rate two folds higher than the best semiconductor catalysts at that time. The non-hydrogenated sample was not found photoreactive for water splitting, even after loading with Pt. The H production was repeatable for more than 20 cycles. The authors showed that the hydrogenated TiO_2 did not act as an H reservoir, since 40 mg of H_2 were formed after 100 h of irradiation, with the sample having around 0.05 mg of hydrogen.

In 2012, Osorio-Vargas et al. studied the effect of low-frequency US irradiation (20 kHz, 1.2 W/mL) on P25 [88]. Based on electron spin resonance (ESR) measurements, they reported evidence to support the formation of oxygen vacancies for the obtained sample after 6 h of irradiation. These vacancies can be responsible for enhance visible light absorption, and also for the obtained grey-shaded color, although the photoreactivity was not studied. These surface chemistry alterations were assigned to the shock waves from the cavitation phenomena and high-velocity interparticle collisions.

In 2015, Fan et al. utilized ultrasonication in order to synthesize amorphous and porous hydroxylated black TiO_2 [89], avoiding the harsh and expensive synthesis by hydrogenation at high pressure (20 bars) and temperature (200 °C). The pivotal role of US waves during the synthesis was determined by varying the irradiation

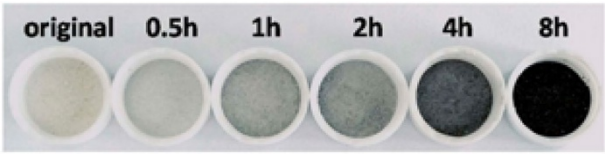

Fig. 6 The powders obtained after different ultrasound irradiation duration. Reprinted with permission from [89]. Copyright (2015) Springer Nature

duration (0.5–8 h), leading to different shades of blackness. At the first step of synthesis, titanium sulfate [$Ti(SO_4)_2$] and ammonia water were inserted in aqueous phase inside an ice-water bath in order to control the reaction rate (2 h, under magnetic stirring). After centrifugation and US washing (25 kHz, 100 W, 20 min) by deionized water, the dispersion was treated with high-power US irradiation (25 kHz, 1500 W/100 mL) using a probe. The synthesis was conducted at 80 °C under different US irradiation durations; 0.5, 1, 2, 4, and 8 h. Afterward, the obtained materials were dried at 80 °C. The degree of the black shade was increased by extending the US irradiation (Fig. 6). After 8 h of US exposure, the obtained powder had a deep black color. It was pointed out that by the application of lower-intensity US irradiation, no powder with a black shade was obtained.

The X-ray diffractograms of all samples were almost identical, revealing no reflections as a result of the amorphous nature. Identical Ti 2*p3/2* and Ti 2*p1/2* peaks were also found in the XPS spectra, and no shifting, widening, or narrowing was observed, linked to the Ti^{4+} of the Ti–O bonds. Since no Ti^{3+} moieties exist in the matrix, all the obtained samples, regardless the color, were assumed as amorphous TiO_2. The XPS analysis also showed the absence of other elements, rather than Ti and O, independent of the US irradiation and duration. The TEM and HRTEM images (Fig. 7) revealed that the obtained materials had an absolute disorder and amorphous structure, with or without US treatment. The same research team reported in a prior work the synthesis of hydroxylated amorphous and disordered TiO_2 nanomaterials of different color shades [90]. The only difference was that instead of US irradiation, the obtained intermediate white powders were thermally treated in a muffle for 3 h (heating rate ~ 20 °C/min) at different temperatures; 200–800 °C. These nanomaterials, as also in the case of those reported by Chen et al. [87], had a specific structure: an anatase nano-core/shell surrounded by a disordered and amorphous hydroxylated phase. Contrarily, the US treatment led to core-free pure amorphous TiO_2 nanocrystals. In order to exclude the possibility of the blackness being associated with N doping, NaOH was used as a base instead of ammonia, and the obtained materials showed similar blackness increment by the extension of US irradiation.

The initially white and all ultrasonictreated samples darker in color showed similarly shaped O1s XPS spectra. The peak was deconvoluted to two symmetric peaks, one assigned to Ti–O bonds (~ 530 eV) and the other to Ti–OH (530.9–532 eV). However,, the Ti–OH/Ti–O ratio of Gauss peaks was increased by increasing the US treatment duration. The amorphous white TiO_2 had a

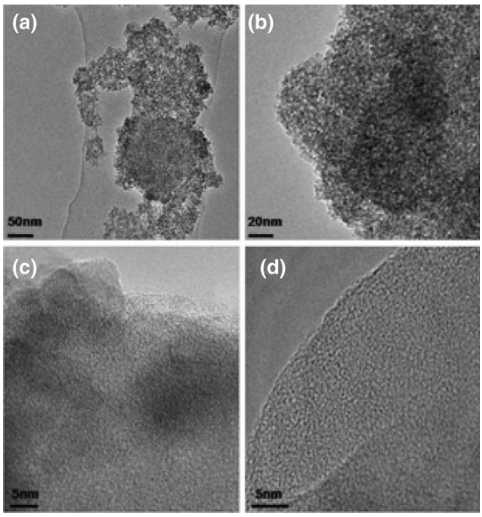

Fig. 7 TEM and HRTEM images of non-ultrasound-treated white TiO_2 (**a**, **c**) and amorphous hydroxylated black TiO_2 obtained after 8 h of ultrasonication (**b**, **d**). Reprinted with permission from [89]. Copyright (2015) Springer Nature

Ti–OH/Ti–O ratio of 0.73, while for the black sample, the ratio was more than double (1.60). The authors determined the hydroxylation degree and assumed a molecular formula of $TiO_{2-x}(OH)_{2x}$, where "x" represents the hydroxylation extension. The reported molecular formulas were $TiO_{1.156}(OH)_{0.844}$ for the white powder and $TiO_{0.768}(OH)_{1.232}$ for the black sample. Calcination of all colored samples at 800 °C until a constant weight led to white powders, as a result of the transformation of Ti–OH to Ti–O. Based on all the above-mentioned results, it was concluded that the high-power US irradiation duration had a direct correlation to the hydroxylation and amorphism.

The increase of the hydroxylation and amorphism as a result of longer ultrasonic irradiation had additional positive impact on the desired, and ultimately key, features in catalysis due to improvement of light harvesting; the structural and optical features. The absorbance intensity through the whole visible and near-infrared regions was improved by the increase of the ultrasonication duration, while the bandgap was decreasing. The white and the black samples had a bandgap of 3.37 and 3.11 eV, respectively. The density of states (DOS) constructed by the optical absorbance and valance band XPS spectra (Fig. 8) showed that the narrowing of the bandgap was assigned to electronic structure alterations due to orbital overlapping, and the blue-shift of the valence band maximum towards the Fermi energy.

The increased porosity is also an important factor for photocatalytic application, since it enhances the reaction rates as a result of improved diffusion of the reactants and the availability of the active sites. For all studied samples, the obtained type IV nitrogen sorption isotherms with type H2 hysteresis loops revealed the existence of meso-pores/voids [91], resulted from the interstitial spaces between the nanoparticles, as was reported in various cases [80]. The lowest porosity values were found for the non-US-treated white powder; a surface area of 166.43 m^2/g and total pore volume of 0.109 cm^3/g. The US irradiation gave rise to the microporosity due to the hydroxylation of TiO_2, as it was reported in other cases [92]. The black sample

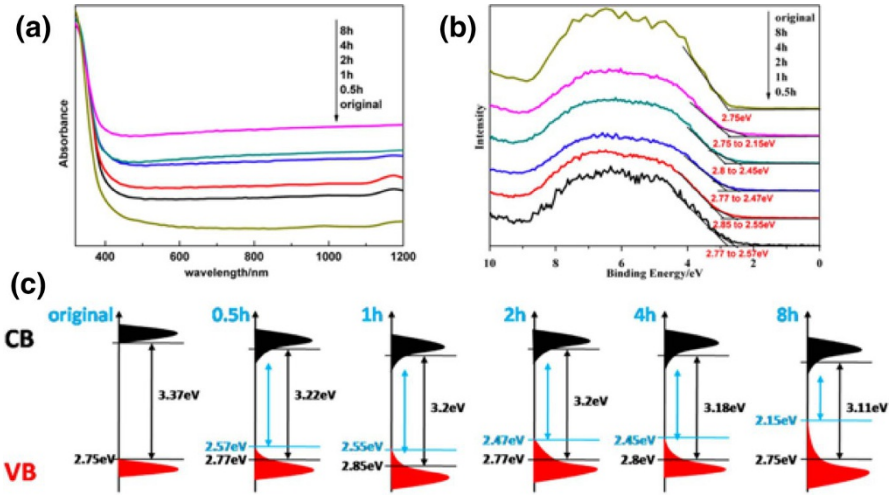

Fig. 8 UV–Vis–IR absorbance spectroscopy (**a**), valance band XPS spectra (**b**), and a schematic illustration of density of states (DOS) of the original samples and amorphous hydroxylated samples ultrasonicated for different durations. The blue and black arrows indicate the bandgaps after and before localized band-bending, respectively. Reprinted with permission from [89]. Copyright (2015) Springer Nature

US-irradiated for 8 h showed the highest structural parameters, which were double compared to the white sample (surface area: 329 m^2/g and total pore volume: 0.251 cm^3/g).

The evaluation of the photocatalytic capability of the samples was performed by monitoring the decomposition/removal of acid fuchsin (AF) in aqueous solution. Since the materials were porous, the removal/reactivity in the dark was evaluated in detail prior the evaluation of photocatalytic performance. It was found that the black nanomaterial had an almost three times higher removal capability in the dark compared than the white one, due to the higher surface area and pore volume. The analysis of the interactions (by eliminating the effect of physical adsorption) showed that the US-assisted synthesis led to samples that possess an improved solar- and the visible-light-driven photocatalytic reactivity. The first-order rate constant obtained by the Langmuir–Hinshelwood model for the black sample was 5.8 and 7.2 times higher under solar and visible light irradiation, respectively, compared to the non-US-treated white sample. The decomposition capability was linked to the formation of hydroxyl radicals. The fact that the photocatalytic reactivity improvement was more pronounced in the case of visible light was linked to the enhanced light utilization/harvesting, photo-response range, and the narrowing of the bandgap. Photoluminescence tests showed that the increase of the ultrasonication duration led to a decrement of the photo-generated electrons and holes pairs, with the latter being trapped at the disordered phase.

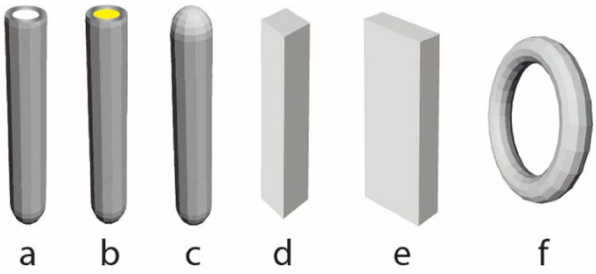

Fig. 9 Schematic illustrations of the most widely synthesized and reported titanium oxide nanoscaled morphologies: open-end nanotube (**a**), core–shell nanotube (**b**), nanorod (**c**), square or rectangular nanorod/belt (**d**, **e**), and nanoring (**f**)

2.2 1-D Particles

2.2.1 1-D Titanium Oxide and Titania

In the literature, various different names/terminologies are used for the characterization of the structure and shape of the 1-D synthesized materials, like fibers, whiskers, nanotubules, fibrils, nanocable, rods, nanowires, belts, since the definition and nomenclature are not well stablished [93]. The geometrical shapes of the titanium oxides that are more widely accepted, reported as a characteristic based on electron microscopy images, and herein used, are collected in Fig. 9. In general, the most important shapes are the open-end NTB (a), the core–shell NTB, the nanorod (c), the square or rectangular nanorod/belt (d, e), and the nanoring (f) [93].

The first report of 1-D TiO_2 NTBs was by Patrick Hoyer in 1995 [81], who used a poly(methyl methacrylate) (PMMA) mold/template for the electrochemical deposition/growth of the titania NTBs. After the dissolution of the polymer, the obtain material consisted of poorly organized arrays of amorphous TiNTBs. The diameter of these NTBs was in the range of 140–180 nm, with an inner hole diameter of 30–50 nm and wall diameter of 30–50 nm. A 45° view of the cross section of the lower part of the amorphous tubes (after the removal of the upper part of the NTBs) is presented in Fig. 10. The electrochemical synthesis is out of the scope of this work. A detailed review article for the electrochemical formation of self-organized TiO_2 NTBs was published by Roy et al. [94].

The fascinating TiNTBs were bulkily and template-free firstly obtained in a powder form via the innovative work of Kasuga et al. in 1998 [95]. TiNTBs with a small diameter (Fig. 11i) were synthesized from the conversion of TiO_2 (mixed rutile and anatase) by a soft chemical method; hydrothermal treatment (110 °C, 20 h) in a strongly basic environment (10 M NaOH). They showed by TEM how the treatment with diluted HCl can lead to nanotubular structures and of high specific surface area, up to 257 m^2/g. Peng's group analyzed in a series of articles in between 2001 and 2003 [96–99] the crystallographic structure of the hydrothermally obtained TiNTBs, and assigned it to trititanate $H_2Ti_3O_7$. They also presented the catalytic role of NaOH and how the NTBs are formed by the rolling of the intermediately formed

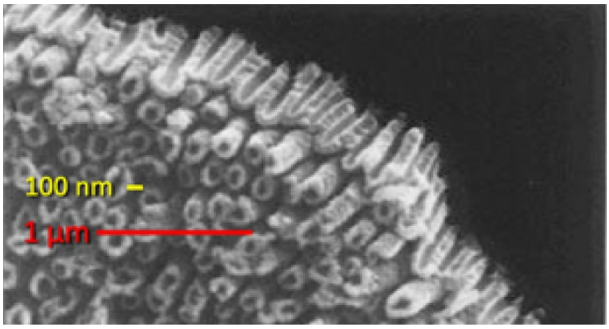

Fig. 10 SEM pictures of the cross section of the as-prepared film of titania (with the upper part of the tubes removed). (Adapted from Fig. 3 of [81]). Reprinted with permission from [81]. Copyright (1996) American Chemical Society

nanosheets (Fig. 11ii). In 2004, Suzuki and Yoshikawa expanded the analysis by proposing that the presence of water molecules is crucial [100], expressing the formula as $H_2Ti_3O_7.nH_2O$, and showed that these moieties of the crystallographic water play a role in the interlayer spacing of titanate layers of the NTB's wall.

In general, this synthetic process involves two main steps, the first being a conventional solid-state reaction between TiO_2 and sodium ions in basic solution, forming layered structures peeled from the initial particles. The second step involves the ion exchange during the acid treatment, HCl in almost all reported cases. Two factors are important regarding the formation of the alkali metal stabilized nanotubes: (1) how the nanosheets are formed from the spherical (in most cases) nanoparticles, and (2) how the nanosheets are converted to NTBs. Regarding the first aspect, Nakahira et al. showed by TEM observation (Fig. 12i) in 2010 that the formation by surface exfoliation of the nanosheets and their rolling/wrapping to NTBs take place on the surface, using as raw material an anatase-type titanium dioxide, and they proposed the entire process by various characterizations [102]. Bavykin et al. presented three different possible mechanisms of the conversion of the nanosheets to open-end multi-wall NTB, resulting in differently structured tubular shapes (Fig. 12ii) [103].

After the first reports of the TiNTBs, an intense research effort was focused on tuning different parameters during synthesis in order to control the structural and morphological features, the homogeneity and purity of the formed TiNTBs, as well as to decrease the synthesis temperature and duration [100, 102–110]. However, some arguments were derived. More details regarding titania NTBs obtained by hydrothermal-based synthesis can be found in the review article reported in 2011 by Wong et al. [111]. In many of the reports regarding the synthesis of the 1-D nanotubular structures, US irradiation was applied at different stages of the process, but without analyzing the possible role. It is feasible to believe that US led to specific effects that were not explored. Sonication can also help the characterization and separation of the TiNTBs. Interestingly, Bavykin et al. showed that US irradiation can be beneficial in order to distinguish the nature of the high observed pore volume by separating the agglomerates into individual NTBs [103].

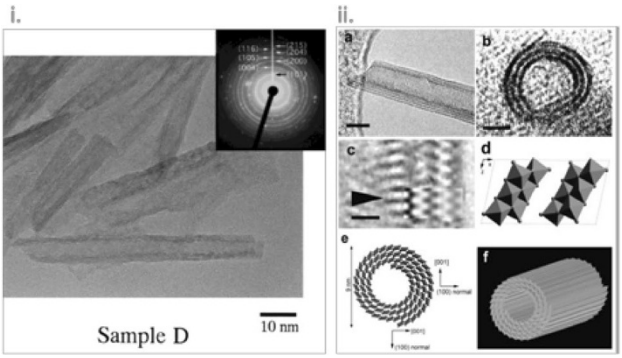

Fig. 11 **i** TEM image and SAED pattern of titanate nanotubes hydrothermally synthesized the for first time by Kasuga et al.; **ii**: **a** HRTEM image showing a nanotube with an open end and three or four layers at the walls (scale bar 6 nm); **b** HRTEM image of the cross section of a three-layered wall nanotube (scale bar: 3 nm); **c** enlarged HRTEM image (scale bar: 1 nm); **d** a structure model of a single unit cell of $H_2Ti_3O_7$ ([010] projection); **e** schematic illustration of the nanotube's structure; **f** 3-D drawing of a titanate nanotube. Adapted with permission from [97, 101], respectively. Copyright (1999) and (2002) Wiley

The focus of the following part is on how the sonication can play a vital role for the manipulation of the TiNTBs' important factors like size, shape, porosity, peeling of the nanosheets, and more, as well as how the process can be achieved faster with a more environmental and energy-friendly manner. The photocatalytic activities and the involved mechanisms, if reported, are also introduced and discussed.

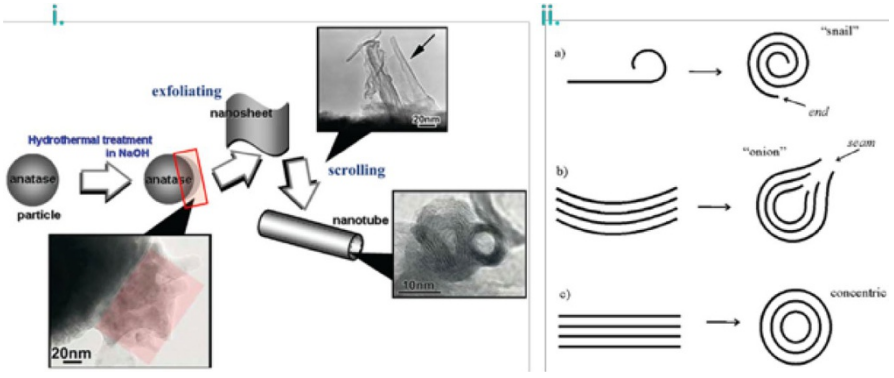

Fig. 12 **i** A schematic collective scheme for the exfoliation and wrapping/scrolling of the formed titanate nano-sheets leading to the nanotubular particles, supported by TEM observations; **ii** a schematic representation showing the possible mechanisms for the formation of the nanotubes. Adapted with permission from [102, 103]. Copyright (2010) American Chemical Society and (2004) RSC, respectively

2.2.2 1D Titania by Ultrasound Irradiation

In 2001, Zhu et al. [112] demonstrated that the utilization of low-frequency US can promote the formation of 1-D titanate nanoparticles. The one-pot synthesis of the

whiskers and nanorods was based on the sonication of synthesized titania nanoparticles in strongly basic solution (NaOH, 10 M), following by washing with dilute HNO_3 (0.1 M) and deionized water and vacuum drying. Compared to other methods used for the synthesis of 1-D structured titania (template synthesis, supra-molecular assembles, hydrothermal synthesis, and inductive synthesis), this synthetic approach taking place in a one-pot synthesis is faster, while avoiding the use and removal step of the templates and the need of calcination for crystallization as the last step.

The used synthesized TiO_2 nanoparticles as precursors were prepared by hydrolysis of titanium butoxide, followed by calcination at 650 °C for 1 h. The average size of them was around 20 nm, while the crystallographic composition was 17% anatase and 83% rutile. For the synthesis of the whiskers, synthesized titanium oxide nanoparticles were dispersed in the basic aqueous solution inside a Teflon vessel. The mixture was ultrasonicated for 80 min (direct immersion of Ti-horn, 560 $W_{elec.}$, frequency not specified but probably in the low-frequency range, 20–80 kHz). The temperature during the synthesis was 80 °C.

Then the mixture after sonication was washed with diluted HNO_3 for 2 h and with deionized water for 6 h. The obtained particles had a slender sheet structure of a 60-nm diameter and a length around 1 μm. The interesting outcome arises from the elemental stoichiometry analysis, which was found to be $H_3Ti_3O_{7.5}$. The bands at ~ 3400 and ~ 1630 cm^{-1} at the IR spectrum were linked to the stretching vibrations of the O–H bond and to bending vibration of H–O–H, revealing the presence of water. Since the XRD pattern matched with that of $H_2Ti_3O_7$ [113], and taking into consideration the thermogravimetric results, the product was assigned from the authors as $H_2Ti_3O_7.0.5H_2O$. Further washing of the product with water for 8 h led to nano-whisker arrays of a 5-nm diameter. The X-ray diffractogram revealed that the crystallographic phase changed to TiO_2 (B) [114] (Fig. 13).

For the preparation of the NTBs, the mixture was treated with half the US power (280 $W_{elec.}$) for 60 min, and afterward, the Teflon vessel was maintained in an oil bath at 110 °C for 4 h. The washing was with HNO_3 (0.1 M, 2 h) and deionized water (14 h). The obtained NTBs had a 5-nm diameter and 200–300-nm length. The XRD analysis revealed that the crystallographic phase was an intermediate between $H_2Ti_3O_7{\cdot}0.5H_2O$ and TiO_2 (B). No Na was detected at the elemental analysis, while the ratio of Ti to O was 1:2.

The proposed mechanism of the whisker formation was based initially on the US-assisted reaction of the base that leads to the cleavage of some Ti–O–Ti bonds. The formed layered titanate lattices have octahedral form with alkali metal ions to occupy the interlayered regions. During the washing with acid and water, ion exchange and dehydration occur, resulting to $H_2Ti_3O_7{\cdot}0.5H_2O$. Extended dehydration by water washing promotes the transformation to titanate bronze. The role of US is vital since it promotes the reaction between the raw nanoparticles and the base, as well as controls the oriented growth. The synthesis is faster by the application of US compared to the reported hydrothermal methods of nanorod formation. It is worth mentioning that without ultrasonication, no whiskers were obtained. A lower US irradiation power and the hydrothermal treatment promotes the formation of bigger titanate sheets and the exfoliation of nanosheets. The latter roll into NTBs during the washing due to the removal of the ions and, as a result, to alterations

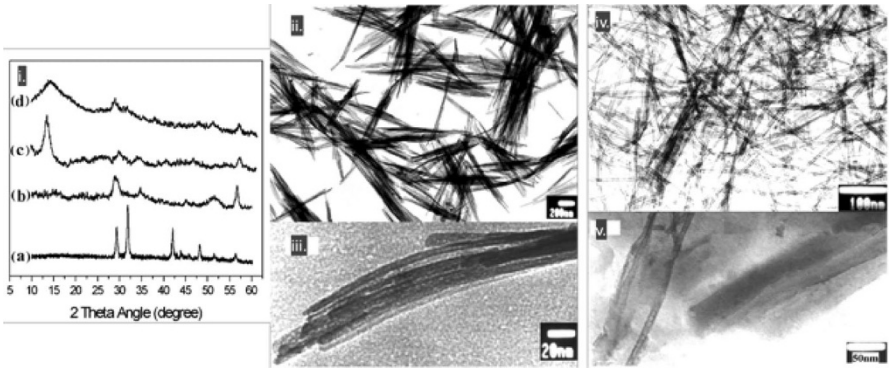

Fig. 13 **i**: XRD patterns of titania particle precursors (a), titania whiskers (b), $H_2Ti_8O_{17}$ whiskers (c), and nanotubes (d); TEM images of titanate (**ii**) and TiO_2 whiskers (**iii**), titania nanotubes (**iv**), and sample obtained by thermal treatment (4 h, 110 °C) of the sonicated products followed by washing with water for 5 min (**v**). Adapted with permission from [115]. Copyright (2005) American Chemical Society

of the electrostatic forces/equilibria. Even though the above US-assisted hydrothermal approach successfully led to the preparation of NTBs significantly faster and easily compared to the hydrothermal synthesis, there is a drawback. The synthesis of the precursor starting with titanium butoxide hydrolysis is time-consuming and complex.

In 2005, Joo et al. [115] reported the synthesis of TiO_2 nanorods of a diameter and length of 3.4 and 38 nm, respectively, by a nonhydrolytic ester elimination reaction between titanium(IV) isopropoxide (TTIP) and oleic acid [OA, $CH_3(CH_2)_7CH{=}CH(CH_2)_7COOH$]. The latter monosaturated fatty acid is among the most common fatty acids in nature, produced both from vegetables and animals, and in this work, it was utilized as surfactant and shape stabilizer during the synthesis. Even though the authors concluded that the obtained crystallographic phase was of anatase, they did not report the region of the XRD for angles lower than 20°. In the following preparation method, TTIP was added to OA, and the suspension was heated gradually until 270 °C within 20 min and was kept at this temperature for 2 h. The initial clear solution of a yellow shade turned progressively to white. The yield was around 70% wt, and the white powder consisted of nanorods and quasi-spherical nanoparticles ~3-nm diameter (Fig. 14a, b). Interestingly, the authors were able to separate the nanorods by conducting a size-selective precipitation from a hexane/ethanol solution (Fig. 14c). They also showed that the nanorods' diameter could be controlled by adding different amounts of 1-hexadexylamine. Sonication for 30 min (experimental conditions not specified) was applied for the removal of the surfactant after the treatment of the powder with superhydride solution (lithium triethylborohydride in THF), but the effect of US was not explored. The finally obtained nanorods presented a specific surface area of 198 m^2/g and they were highly dispersible in water, a fact of a paramount importance for real-life applications. The estimated bandgap of the nanorods was 3.33 eV, a value higher than that of 3.2 eV of the bulk anatase, due to quantum size effect. Compared to commercial TiO_2 P25, the obtained nanorods were found to possess a higher photocatalytic inactivation

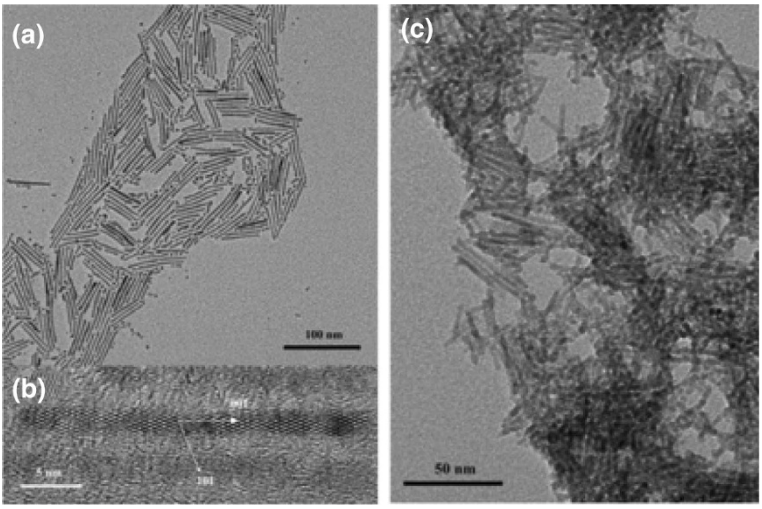

Fig. 14 TEM and HRTEM images of the as-synthesized TiO_2 nanocrystals prior the size-selective separation (**a**, **b**) and TEM image of the final TiO_2 nanorods (**c**). Reprinted with permission from [115]. Copyright (2005) American Chemical Society

capability against *E. coli*, a fact that was assigned by the authors to the increased bandgap, surface area, and amount of surface hydroxyl groups. The improved and faster inactivation performance for the nanorods was linked to the elevated hydroxyl radical formation.

Since the morphological and structural features of TiNTBs (size and porosity) can be controlled, the application of US irradiation towards the increment of these features gained more attention. Ma et al. [116] reported in 2006 the synthesis of longer NTBs with a smaller diameter by a combined sonication-hydrothermal approach and using as precursor the commercial TiO_2 P25. Their approach was based on dispersing the commercial powder in a Teflon vessel filled with NaOH aqueous solution (10 M). Using an immersed titanium horn (probably low-frequency, not specified), the suspension was sonicated at 70 °C under different sonication powers (100, 280, and 380 $W_{elec.}$) and varying also the duration (15, 30, and 60 min). The vessel was placed in a stainless-steel autoclave for hydrothermal treatment for 4 h at 110 °C. The obtained precipitate was washed with HCl (0.1 M) and deionized water until an acidic pH, centrifuged, and dried under vacuum. The role of the precursor on the size of the NTBs was determined by using different commercial TiO_2 precursors.

The hydrothermal treatment of the nanospherically shaped P25 particles of an average size of ~ 30 nm without ultrasonicated pre-treatment led to minimal particle shape alteration. Sonication for 1 h prior the hydrothermal treatment with powers of 100 and 280 $W_{elec.}$ resulted in sheet and fibrous morphologies, respectively. A typical tubular morphology was achieved (diameter: 9–14 nm and length: 100–600 nm) by sonication at a higher power (380 $W_{elec.}$), revealing that the sonication, as well its power, plays a key role in the desired transformation to TiNTBs. TEM images of

the initial TiO_2 P25 and the TiNTBs produced by combining high-energy sonication and hydrothermal treatment can be seen in Fig. 15.

The crystallinity and the chemical composition of the nanorods were investigated by XRD and energy-dispersive spectroscopy (EDS) analysis. It was concluded that the chemical composition was $H_2Ti_4O_9.H_2O$ (JCPDS 36-0655), while traces of rutile fractions were also observed. Considering that the TiO_2 P25 consisted of 70% anatase phase and around 30% rutile phase, the transformation of the latter phase is preferable, while the former type is more stable under the hydrothermal treatment conditions. The EDS elemental analysis showed the absolute absence of Na.

The authors also studied the effect of the higher sonication power (380 W) without the hydrothermal and acid treatment. 15 min of US irradiation did not reveal the ability to alter the shape of the spherical particles. Increase of the irradiation time to 30 min led to swelled nanoparticles with an average diameter of 100 nm, probably as a result of the spherical particles merging. By increasing the duration of irradiation to 60 min, the observed morphology was found to be nanorods like, with lengths in between 100 and 300 nm. By hydrothermal and acidic treatment after the 60 min of US irradiation, the length of the nanorod-like particles increased up to 600 nm. Additionally, the diameter of the tubes was also smaller, but the shape homogeneity was not so perfect. Based on these observations, it can be proposed that the US effects can originate the reaction of the TiO_2 nanoparticles with the base, by promoting the cleavage of the Ti–O–Ti lattice bond and the intercalation of Na^+ at the lattice. The spherical forms are swollen and transformed to nanorods by increasing their length. Calcination at 300 and 450 °C of the sample obtained after the two-step process was not accompanied with notable shape alterations (Fig. 15c, d). On the contrary, calcination at 600 °C led to morphology transformation of the hollow tubular structures to rod-like structured nanoparticles (Fig. 15e).

Interesting outcomes regarding the vital role of the precursor's particle size were derived by using two other commercial TiO_2 powders instead of P25. When the size of the initial particles was around 10 nm (Hombikat UV100, Fig. 16a), the formed NTBs had inner and outer diameters and lengths of 3–6, 7–10, and up to 400 nm, respectively (Fig. 16b). When particles of a bigger average size of 200 nm (BCC100, Fig. 16c) were used as precursor, instead of tubular-shaped particles, sheet-like structures with rolled edges were obtained together with untransformed particles that were slightly changed in size and shape (Fig. 16d). This was linked to the fact that the formed sheet-like structures cannot transform/roll to tubes, perhaps due to a hindrance effect by the larger particles.

Tanthapanichakoon and his colleagues showed and analyzed how the ultrasonication pretreatment can influence controllably the length of the titania NTBs [117, 118]. Interestingly, they used a commercial precursor (KISHIDA) of a low specific surface area (8 m^2/g) and relatively large particles (400 nm) compared to the previous reports. By using a titanium horn (probably low-frequency, not specified in the article), the suspension of TiO_2 in a 10 M NaOH aqueous solution was sonicated prior the hydrothermal treatment for 8 min with different supplied powers, from 0 to 38.1 W. After thermal treatment for 3 days at 150 °C, the obtained suspension was treated/washed with HCl and H_2O. TEM analysis revealed that no US irradiation led to TiNTBs (herein referred to as short) with multilayered walls (2–6 layers

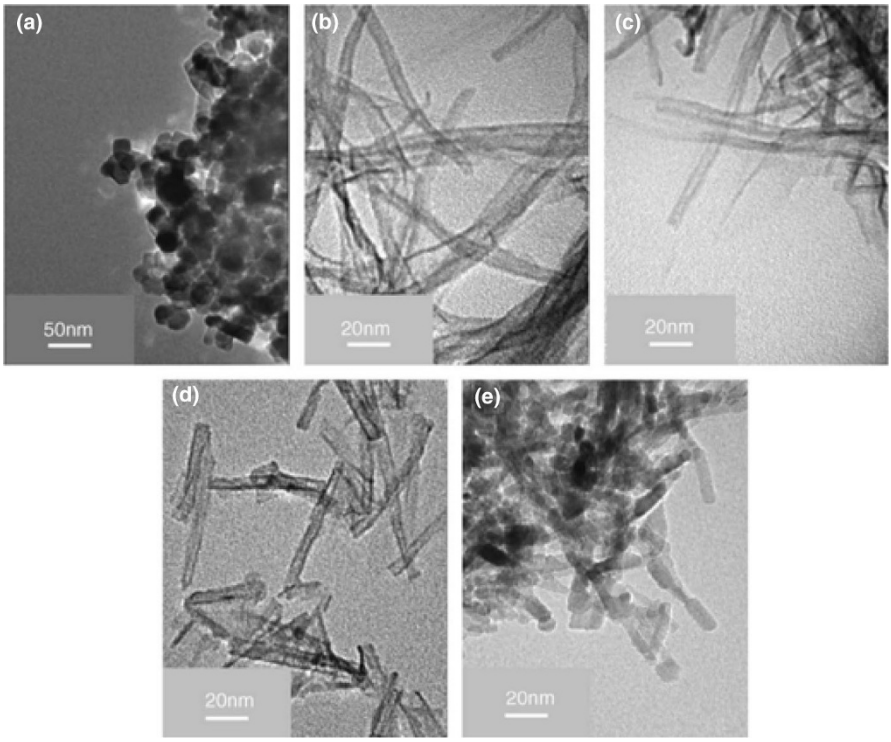

Fig. 15 TEM images of TiO_2 P25 precursors (**a**), titanate nanotubes as received (**b**), after calcination at 300 °C (**c**), at 450 °C (**d**), and 600 °C (**e**). Adapted with permission from [116]. Copyright (2006) Elsevier

and ~ 0.8-nm interlayer spacing), diameters from 4–6 nm, and lengths between 30 and 200 nm. Sonication by two different powers, of 7.6 and 38.1 W, led to increase of the TiNTBs' diameter. The majority of the NTBs had a length above 300 nm, while the diameter was in the same range with that of the short ones. Based on the previous analysis by XRD of the *d*-spacing between the adjacent layers of the tube walls by Suzuki and Yoshikawa, the authors concluded that the US irradiation and the resulted increase of the length was not accompanied with an interlayer spacing change. Additionally, the strong intensity diffractions of the initial TiO_2 (anatase phase) were totally diminish in all synthesized TiNTBs.

The dynamic light scattering (DLS) results showed average sizes of 53, 490, and 1760 nm for the samples prepared under 0, 7.6, and 38.1 W, respectively. Additionally, the size distribution was very narrow in the case without US irradiation, and the distribution was dramatically increased by increment of the applied US power. The formation of NTBs in size many folds higher the pristine particles can be linked to bigger peeled nanosheets prior the rolling, and/or to the connection of the formed tubes. An increasing trend was found between the specific surface area (S_{BET}) and the power of US irradiation. The raw powder had an S_{BET} of 8 m^2/g, and the short

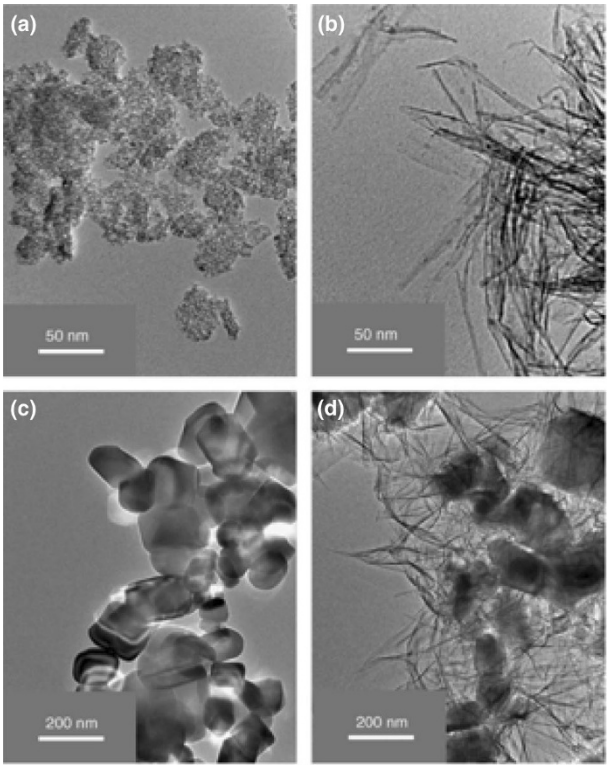

Fig. 16 TEM images of TiO_2 Hombikat UV100 precursor (**a**), titanate nanotubes derived by sonication-hydrothermal treatment of Hombikat UV100 (**b**), TiO_2 BCC100 precursor (**c**), and sample obtained from BCC100 (**d**). Adapted with permission from [116]. Copyright (2006) Elsevier

NTBs 179 m^2/g. The US wave exposure at the pretreatment stage led to S_{BET} of 258 and 245 m^2/g, for US power of 7.6 and 38.1 W, respectively. The positive effect of ultrasonication is via the enhancement of the de-aggregation of the particles, resulting in the peeling thorough swelling of large nanosheets that role to NTBs [118]. Without US waves, the size of the peeled nanosheets and, as a result, the size of the formed NTBs is smaller.

The same research team studied (in 2009) the effect of different preparation variables and combinations like particles size of the raw TiO_2 (400 nm and 1 μm), temperature during the synthesis (90–180 °C), and sonication power, with valuable conclusions on how these variables can adjust the morphological and structural features [117]. The hydrothermal treatment at 150 °C without sonication of the commercial TiO_2 particles of size ~ 400 nm led to NTBs of an average length of 79 nm and a specific surface of 179 m^2/g. The respective values were 143 nm and 118 m^2/g when the largest (1 μm) raw particles were used. This was linked to the formation of bigger but less in number intermediate sheets during the peeling. By studying the effect of different temperatures (90, 120, 150, and 180 °C), it was concluded that the

transformation of titanium dioxide to titanate was complete even at 120 °C. However, increase of the temperature to 180 °C led to a shift of the characteristic diffraction at around 10° 2θ to a higher angler (~ 12°), suggesting a narrow interlayer spacing between the layers of walls. Suzuki and Yoshikawa assigned the characteristic XRD reflection peak at $2\theta = \sim 10°$ of the hydrothermally synthesized $H_2Ti_3O_7.nH_2O$ NTBs to an interlayer distance of 0.92 nm [100]. An interesting parenthetical fact can be added at this point. The high-temperature XRD pattern obtained at 100 °C was almost identical with the one at room temperature, but at 200 °C, the reflection was shifted to 11.2°. This narrowing of the interlayer space to 0.79 nm was linked to the removal of the water moieties between the layers of the wall. It is worth mentioning that thermogravimetric analysis of the NTBs showed that above 200 °C, the weight loss was very limited.

Going a step further, the team of Tanthapanichakoon [117] chose to study the effect of temperature during the synthesis with or without US pre-treatment by using raw particles of an ~ 400-nm diameter, due to the fact that this raw TiO_2 gave higher S_{BET} compared to the raw one with average particle size of 1 μm. The resulted specific surface areas and the morphology of the sample are presented in Fig. 17.

As can be observed, the effect of US pretreatment on the structural and morphological features is loud and clear, and, additionally, it had a key effect on the product purity and shape homogeneity, as confirmed by microscopy analysis. At 90 °C, NTBs, nanosheets, and remaining un-transformed crystals were detected either without or with US pretreatment (Fig. 18). Moreover, the use of sonication did not lead to higher S_{BET}. The effect of US was dramatically more pronounced at a synthesis temperature of 120 °C. The length of the NTBs was much higher and the S_{BET} almost doubled in value. The purity was also enhanced, since no un-transformed crystals were detected after US pre-treatment. Analogous outcomes were derived when the synthesis was performed at 150 °C after US pre-treatment. Further increase to 180 °C had a negative impact on the S_{BET} and the desired morphology, with the US irradiation not leading to a specific effect. The predominant shape of the particles was of nanowires/fibers/rods in both cases, although with a smaller diameter in the case of US irradiation. The shape change was in good agreement with the angle shift of the XRD pattern, as was discussed above. It can be suggested that the thermal effects when the synthesis temperature is higher than 150 °C overcome the effects of the US pre-treatment.

3 PART B

3.1 Ball-Milling-Derived Nanomaterials

The utilization of ball milling (BM) in order to obtain TiO_2 nanoparticles includes different possible pathways with regard to the used raw material. The latter can be either elemental Ti, either TiO_2, or a different source of titanium like a mineral. The duration and the power of the BM plays a crucial role, as does the atmosphere in which the process takes place. The achievement of high temperature is found to be in some

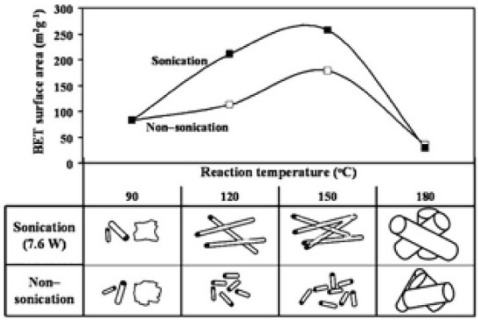

Fig. 17 BET specific surface area and morphology/shape of titanate products synthesized (from raw TiO_2 of an avg. size of 400 nm) at reaction temperature of **a** 90 °C, **b** 120 °C, **c** 150 °C, and **d** 180 °C without or with US irradiation (power of 7.6 W). Reprinted with permission from [117]. Copyright (2009) Elsevier

cases a drawback, and for this reason, the ball milling is performed with breaks or even with the use of a liquid phase. The latter case is referred to as wet ball milling. In most reported cases and especially towards the formation of one dimensional TiO_2 nanostructures, ball milling was utilized as a mechanochemical pretreatment to obtain metastable polymorphs, that can be further tuned in morphology by annealing or wet chemistry. In this part, we collected some reports in which the application of ball milling dramatically affected the final properties of the nanomaterials. Starting with 0-D nanomaterials and ending with 1-D materials, we tried to introduce the reported results following a chronological order. An emphasis was given when the nanomaterials were found to possess an elevated photocatalytic capability.

3.2 0-D Ball-Milling-Derived Nanostructures

In 1994, Begin-Colin et al. studied the polymorphic transformation of TiO_2 from an anatase phase to a rutile phase by ball-milling (BM), based on XRD and Fourier transform infrared (FTIR) spectroscopy techniques [119]. They observed that the phase transformation was not direct, since different transient phases appeared, with the one of type II being predominant. However, no electron microscopy analysis was performed. The importance of this study was the conclusion that the anatase-to-rutile transformation is not a direct process. Based on that, the authors emphasized that the ball-milling technique is feasible to obtain alloys with various non-equilibrium crystallographic phase materials. The intermediate crystallographic phases can further be tuned with various methods, in order to obtain desired photocatalytic properties.

An ultimately serious drawback of the ball-milling technique, especially when the target is a material of a high purity, is the possibility of atmospheric nitrogen incorporation into the structure or metal (predominately iron) from the used ball-milling apparatus. For instance, it was showed by Lu et al. [120] that, depending the atmosphere and the duration of the ball milling, different doping of N or Fe could result, even under air. More interesting, titanium oxynitrile instead of oxide can be obtained within a closed ball-milling system and extension of the mechanochemical process for up to 90 h. In 2007, Pang et al. [121] showed the possibility to synthesize a composite of titanium and hydroxyapatite by a wet ball-milling method. Hydroxyapatite (HP), $Ca_5(PO_4)_3(OH)$, is a natural mineral,

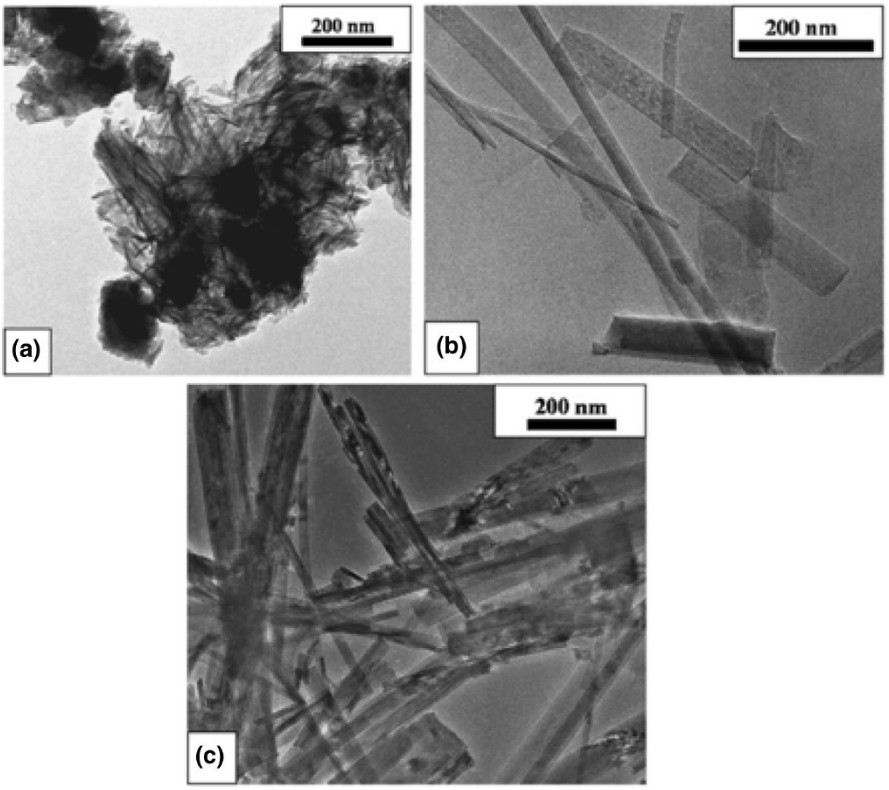

Fig. 18 HRTEM captures of mixed titanate nanostructures obtained from raw TiO_2 (of an average particle size 400 nm) at reaction temperature of 90 °C (**a**) and titanate nanofibers/wires synthesized at 180 °C without sonication (**b**), and with power of 7.6 W (**c**). Adapted with permission from [117]. Copyright (2009) Elsevier

while modified forms of HP are the main compounds of human bones and teeth. The increase of milling duration led to the decrease of the grain size, as well as to an improvement on the homogenously distribution of nano-hydroxyapatite. Analogous composites were synthesized by ball milling the same year by Silva et al. starting with $Ca(H_2PO_4)_2$ and TiO_2 as the raw materials [122].

In 2000, Begin-Colin et al. studied in details the kinetics and mechanisms of phase transformations induced by ball milling in air, starting with a commercial anatase TiO_2 [123]. They concluded that the anatase is transformed by BM to rutile via a TiO_2 II phase. The powder-to-balls ratio of weights (R) influenced the transformation rate. Regarding the nature of ball-milling media, the transformation's kinetics were found faster in the case of alumina compared to steel.

Yadav et al. showed in 2015 the synthesis of titanium oxide nanoparticles from elemental powder of Ti (~0.5 mm) by ball milling for 10 h [124]. The size of the spherically shaped particles was between 10 and 20 nm, while XRD analysis indicated a pure rutile phase. The estimated bandgap was 4.46 eV. They used

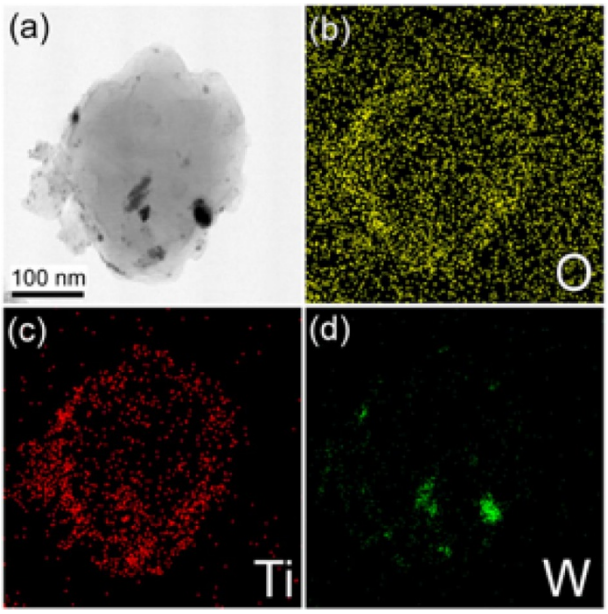

Fig. 19 TEM image (**a**) and EDX maps (**b–d**) of TiO_2-coated boron particles wet-milled for 8 h. Reprinted with permission from [126]. Copyright (2016) MDPI

the obtained material in order to form a solid-state sensor by pelletization and application to an Ag–pellet–Ag electrode configuration. This sensor was found to possess a sensitivity toward liquefied petroleum gas (LPG). The author linked this to the blue-shift of the optical bandgap and to the nanoscaled morphology of the obtained ball-milling-derived nanoparticles.

In 2016, Rejender and Giri [125] presented an anomalous strain-evolution, crystallographic phase alteration, and bandgap narrowing by strain engineering using ball milling and commercially available TiO_2 powder as the precursor (particle size around 80 nm and bandgap 3.14 eV). Except for the decrement in size to 7–18 nm, the finally obtained TiO_2 nanocrystals (NCs) found to obtain a new crystallographic phase of Ti_3O_5, as well as a narrow bandgap of 2.71 eV.

Another interesting application of the wet ball-milling process was reported the same year by Jung et al. [126] for the TiO_2 nano-coating of boron particles. Briefly, a tungsten carbide milling jar was filled with titanium(IV) isopropoxide, boron powder (average particles' size ~ 800 nm), and hexane inside a glove box filled with nitrogen. The as-received suspension was further treated and washed with ethanol inside an US bath. They found that increase of the milling duration can lead to decrease of the final particle size, even up to ~ 150 nm. The particles were coated with an amorphous titania-containing layer (estimated 10 nm). The drawback of the extension of the ball milling was the incorporation of impurities, predominately tungsten, from the jar and balls, as can be seen in energy-dispersive X-ray (EDX) analysis (Fig. 19). The ball-milling-derived TiO_2-coated nanoparticles were promising for hydrogen and oxygen evolution reactions (HERs, OERs) in photoelectrochemical applications.

Another strategy to apply ball milling during the formation of TiO_2 nanoparticles was by mixing and ball milling of different precursors [36]. In 2007, Billik et al. used either $TiCl_4$ with $(NH_4)_2CO_3$ or $TiOSO_4{\cdot}xH_2O$ with Na_2CO_3 [127, 128]. After ball milling, they received amorphous samples, and they linked this to no crystallization having occurred. After annealing, they obtained well-crystalized materials, with higher photoreactivity compared to P25, determined by electron-paramagnetic-resonance (EPR) studies. They reported also that the presence of Fe impurities plays a role in the photoactivity of the final material. In 2008, Salari et al. also used $TiOSO_4{\cdot}xH_2O$ as the Ti source but NaCl as diluent [129].

3.3 1-D Ball-Milling-Derived Nanostructures

An important, abundant, and cheap source used for the industrial production of bulk TiO_2 is the iron–titanium oxide mineral ($FeTiO_3$) mineral, known as ilmenite. A high amount of ilmenite exists in the Earth's crust on all five continents, and on the Moon. The price of the raw material was around 80–107 USD per metric ton in 2004, while a peak was achieved in 2012 reaching even 350 USD per ton. In recent years, the cost has been around 250 USD/ton. The global demand has grown moderately in recent years, since it was estimated at around 6.4 million tons in 2010 with a prediction to reach above 8 million tons in 2025. The industrialized production of bulk TiO_2 from minerals is based on chloride or sulfate processes. In recent decades, there has been increased research effort to expand the use of this mineral in order to prepare nanostructures of TiO_2. The utilization of ball milling in order to promote the formation of nanostructured TiO_2 for a "real-life" application by using ball milling dates from 2008.

Li et al. (2008) [130] reported the formation of meso- and/or micro-porous hydrolysate TiO_2 by an initial mechanical activation of ilmenite using BM, following by a simultaneous dissolution and hydrolysis in a dilute sulfuric acid aqueous solution. The effect of the acid concentration played a key role in the structural parameters, with 10% sulfuric acid leading to a surface area of 258 m^2/g. In order to obtain the rutile-phased final material, calcination was applied. The importance of this work was that the ball-milling pretreatment made feasible the dissolution of the mineral in a dilute acidic solution. For an efficient decomposition in pigment production without mechanochemical utilization, an H_2SO_4 solution of a concentration above 80 wt% is required [130].

In 2011, Tao et al. prepared flower-like $FeTiO_3$ by pretreatment of ilmenite with high-energy BM followed by mild hydrothermal treatment in basic aqueous solution (1 M NaOH) [131]. They stated that the nano-petals comprising the final obtained flower-shaped particles had a thickness of 5–20 nm and sizes 100–200 nm. The hydrothermal treatment at 120 °C, even with 2 M NaOH, did not lead to noticeable changes in morphology. The obtained materials showed attractive capacitance values. Considering the above observations regarding the formation of NTBs, we can derive two possible conclusions/proposals. First, the presence of Fe stabilizes the layered structure of the nano-petals to roll to tubes. Second, the utilization of BM

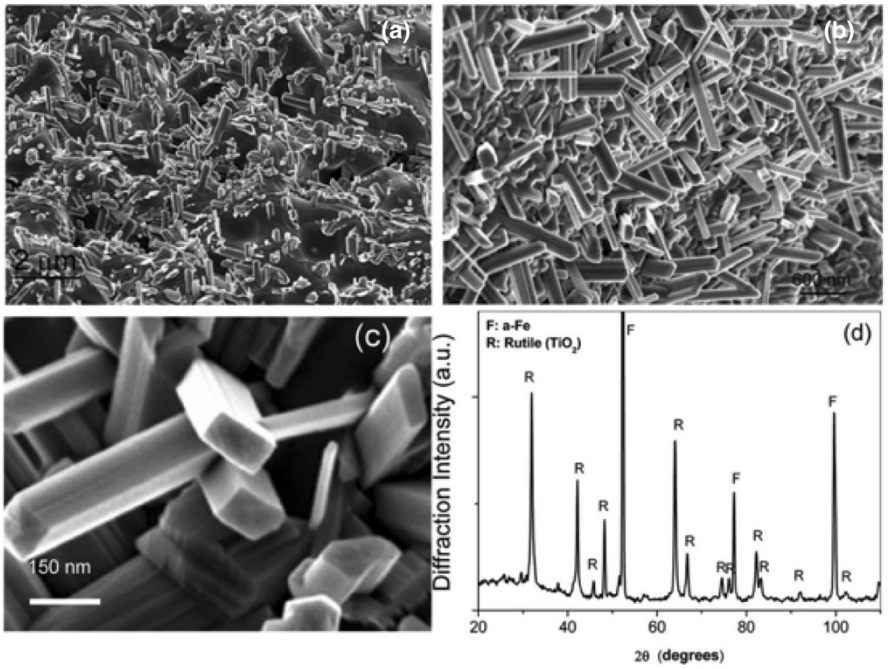

Fig. 20 SEM image after the second annealing step at 700 °C for only 4 h (**a**), SEM image (**b**), a cross section of nanorods (**c**), and the XRD spectra (**d**) after annealing for 8 h at 700 °C. Adapted with permission from [133]. Copyright (2009) American Chemical Society

promotes the peeling of the mineral's particle even at a lower concentration of 10 M, necessary for the hydrothermal peeling of TiO_2 particles.

The formation of the 1-D nanorods obtained from ilmenite sand and the necessity of the metastable polymorphs formation was presented in 2008 and 2010 [132, 133]. It was revealed that for the formation of the nanorods, instead of other particle morphologies, the formation of the metastable phases like Ti_2O_3 to Ti_3O_5 is crucial. The ilmenite mineral was ball-milled with the presence of activated carbon at a ratio 4:1 at room temperature and under vacuum. The role of the latter as mechanical activation agent was to trigger the initial reduction to TiO_2. The obtained ultra-fine powder was annealed first at different high temperatures (900–1200 °C) in order to form the metastable phases. The low and controlled heating rate (5–10 °C) in an argon atmosphere with hydrogen flow was a critical step in order to obtain the desired metastable phases. It was reported that the presence of nitrogen led to an alternative redox reaction and iron nitride was formed. At temperature less than 1100 °C, the formed phase was rutile, which could remain in the same form after the second annealing step. The optimum duration of annealing was 8 h at 1200 °C, since prolonged heat treatment led to the formation of FeTi alloys. The second step of annealing was conducted at 700 °C in a N_2–5%H_2 atmosphere. The result was the gradual formation of TiO_2 nanorods and iron. As can be seen from the SEM images

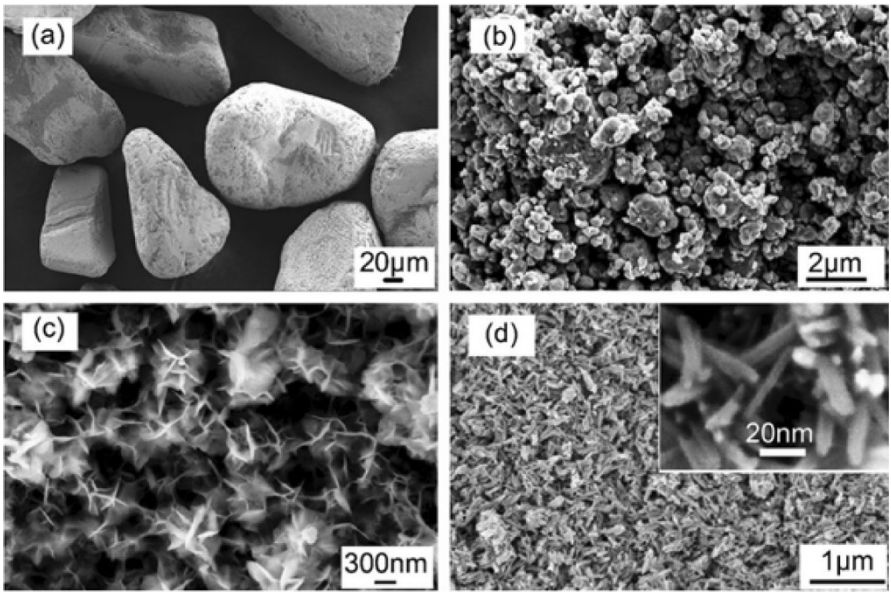

Fig. 21 SEM images of original ilmenite powder (**a**), ball-milled ilmenite powder (**b**), flower-like $FeTiO_3$ nano-structures after treatment with NaOH (**c**), and the obtained nanorods after treatment with HCl for 8 h (**d**); inset: a higher-magnification capture of the nanorods. Reprinted with permission from [134]. Copyright (2013) Wiley

and XRD spectra in Fig. 20, the intermediate phase started to transform to nanorods after 4 h. The length of the nanorods was dependent on the time of annealing, and after 8 h, the intermediate phase was entirely transformed to rutile nanorods of the maximum length. Extension of the thermal treatment led to the sintering of the 1-D structure to coarse nanoparticles.

In 2013, Tao et al. [134] demonstrated a new method for the synthesis of TiO_2 nanorods (single-crystal) from natural ilmenite. The BM pre-treated mineral was further wet-chemistry-treated by mixing in a 2 M NaOH aqueous solution for 2 h at 120 °C, and flower-like $FeTiO_3$ nanoparticles were formed, but the authors concluded that this stage is an optional one. After short and mild drying, treatment with 4 M HCl at 90 °C for 4 h took place. The proposed mechanism was based on dissolution to $TiOCl_2$ and $FeCl_2$, hydrolysis, and precipitation. During the hydrolysis, TiO_2 crystals started to precipitate and grow in a 1-D fashion. The finally obtained rutile TiO_2 tetragonal nanorods (Fig. 21) had a length in the range of 50–100 nm, width of 5–20 nm, and thickness of 2–5 nm. The nanorods have also a moderately high specific area for this kind of nano-structure (up to 97 m^2/g). The most interesting outcome was that they showed excellent photocatalytic capability towards the photodegradation of oxalic acid, analogous with the one of Sigma–Aldrich's Degussa P25.

In 2014, Zhao et al. [135] reported the formation of spindle-like rutile TiO_2 nanorods from the dealloying in acidic conditions of an amorphous $Cu_{50}Ti_{50}$ alloy. The latter was formed by high-energy ball milling of elemental Cu and Ti in an

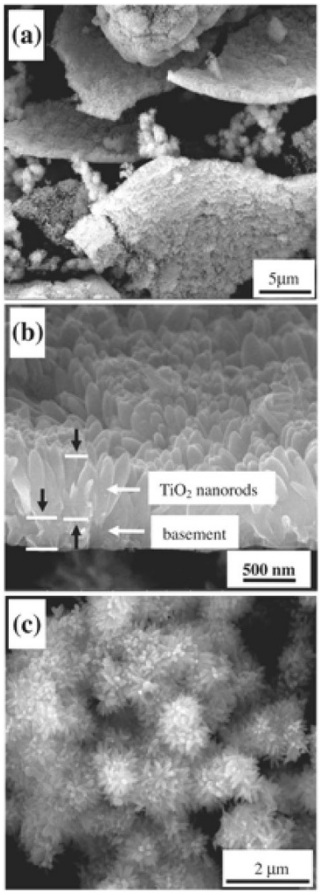

Fig. 22 SEM images of ball-milling-derived amorphous $Cu_{50}Ti_{50}$ after immersing in HNO_3 aqueous solution for 48 h. Reprinted with permission from [135]. Copyright (2014) Elsevier

argon atmosphere. In order to avoid the high temperature as a result of the BM process, after milling for 0.5 h, there was an interruption for also 0.5 h. The as-received material was immersed in a highly concentrated HNO_3 aqueous solution (13.14 M) for dealloying. The obtained nanorods (Fig. 22) revealed a good photocatalytic degradation capability against the dye methyl orange under UV light irradiation, via the formation of radicals.

In the work of Zhao et al. [135], the involved steps/mechanism for the formation of the TiO_2 nanorods from the raw $Cu_{50}Ti_{50}$ alloy were proposed (Fig. 23). Titanium metal cannot react with nitric acid due to the presence of an oxide film. With the mechanical stress that is applied from the ball milling, the dealloying starts by corrosion from the outer surface and the removal of copper atoms and gradually continues to the inner part of the alloy.

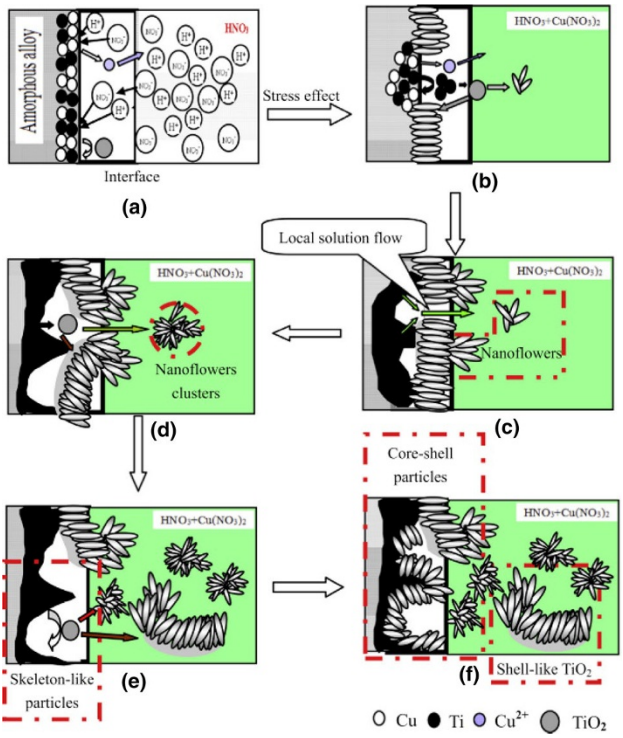

Fig. 23 A schematic illustration of all the involved steps/mechanisms for the dealloying of amorphous $Cu_{50}Ti_{50}$ powders to rutile TiO_2 nanorods. Reprinted with permission from [135]. Copyright (2014) Elsevier

4 Conclusions—Prospectives

Taking into account all the above-mentioned results, it is reasonable to conclude that the formation of the hotspots as well the localized temperature increase during the mechanochemical treatment can antagonize the harsh conditions created inside the autoclave during the hydrothermal treatment, especially when the particle size of the precursor is equal or less than that of P25. It can be suggested that the thermal effects during the synthesis when the temperature is higher than 150 °C overcome the effects of the US pre-treatment. Especially in the case of a basic hydrothermal process, the utilization of sonication (US) as the pre-treatment has a vital role in the formation of 1-D nanostructures. The US effects can be further explored and applied for the synthesis of novel nano-engineered materials by other methods like precipitation, targeting towards the achievement of specific physical, chemical, and optical features.

In general, mechanochemistry can be a useful tool toward the manipulation of the important and desired features for different applications. Ball milling or US waves play a key role in size, shape, bandgap, porosity, light absorption, etc. Considering the above observations regarding the formation of NTBs, we can derive

two possible conclusions/proposals. First, the presence of Fe stabilizes the layered structure of the nano-petals to roll to tubes. Second, the utilization of BM promotes the peeling of the mineral's particle even at a lower concentration of 10 M, necessary for the hydrothermally peeling of TiO_2 particles.

The herein presented results showed that the mechanochemical-derived forces can promote the features of the catalyst, crucial for heterogeneous photocatalytic applications. While the main goal of the research effort towards the formation of 1-D TiO_2 up to nowadays was focused predominately on the explanation of the involved steps and mechanisms, in the cases where the materials were tested as photocatalyst, they revealed elevated photocatalytic capabilities, equal or better compared to the benchmark P25 in most of the cases. The goal of the present work is to highlight the developments in the area mechanochemical approaches when designing new synthetic strategies of nanostructured materials, as well as to call and initiate the attention for the possibilities for future utilization and exploration. We believe that nanoscaled and especially nanotubular-shaped titania can be further studied as photocatalyst, and we actively work towards this direction. Applying mechanochemistry will also be interesting to conduct for the design and synthesis of novel nanostructured electrodes for electrochemical catalytic reactions. Even though it is impossible these two techniques are simultaneously combined, the utilization of both at separate steps of synthesis can beget innovative approaches towards the synthesis of highly photo-active zero- and/or one-dimensional titanium-based catalyst, pure or doped with heteroatoms, like nitrogen or metals. In-depth study of the photocatalytic properties and applications of the TiO_2 NTBs, as, for instance, advanced oxidation processes or biomass valorization, can lead to interesting and important outcomes, as occurred in the case of their application in electrocatalysis and photo-remediation. Additionally, the use of a simple and economic US bath or ball-milling grinder can be utilized as a powerful synthetic tool. It is also important to point out that the use of mechanochemical processes in lab during the synthesis can lead to effects not yet studied, hypothesized, or imagined. Last but not least, we would like to emphasize that it will be absolutely beneficial if more details are provided when mechanochemistry is applied, such as calorimetric evaluation of the setup, luminol mapping, experimental setup details (horn details, photos, or a drawing), and details of the synthesis (yield, purity, size separation techniques, etc.).

Acknowledgements JCC and DAG are very grateful for the support from the National Science Centre in Poland within OPUS-13 project no. 2017/25/B/ST8/01592.

References

1. Colmenares QJC (2013) Ultrasound and photochemical procedures for nanocatalysts preparation: application in photocatalytic biomass valorization. J Nanosci Nanotechnol 13:4787–4798. https://doi.org/10.1166/jnn.2013.7567
2. Chatel G, Valange S, Behling R, Colmenares JC (2017) A combined approach using sonochemistry and photocatalysis: how to apply sonophotocatalysis for biomass conversion? Chem Cat Chem 9:2615–2621. https://doi.org/10.1002/cctc.201700297
3. Rightmire NR, Hanusa TP (2016) Advances in organometallic synthesis with mechanochemical methods. Dalt Trans 45:2352–2362. https://doi.org/10.1039/c5dt03866a
4. Suslick KS (1995) Applications of ultrasound to materials chemistry. MRS Bull 20:29–34. https://doi.org/10.1557/S088376940004464X
5. Cerdan K, Ouyang W, Colmenares JC et al (2018) Facile mechanochemical modification of g-C3N 4 for selective photo-oxidation of benzyl alcohol. Chem Eng Sci. https://doi.org/10.1016/j.ces.2018.04.001
6. Colmenares JC, Lisowski P, Łomot D et al (2015) Sonophotodeposition of bimetallic photocatalysts Pd-Au/TiO_2: application to selective oxidation of methanol to methyl formate. Chemsuschem 8:1676–1685. https://doi.org/10.1002/cssc.201403125
7. James SL, Adams CJ, Bolm C et al (2012) Mechanochemistry: opportunities for new and cleaner synthesis. Chem Soc Rev 41:413–447. https://doi.org/10.1039/C1CS15171A
8. Magdziarz A, Colmenares JC, Chernyayeva O et al (2016) Iron-containing titania photocatalyst prepared by the sonophotodeposition method for the oxidation of benzyl alcohol. ChemCatChem 8:536–539. https://doi.org/10.1002/cctc.201501250
9. Kiss AA, Geertman R, Wierschem M et al (2018) Ultrasound-assisted emerging technologies for chemical processes. J Chem Technol Biotechnol 93:1219–1227. https://doi.org/10.1002/jctb.5555
10. Bhangu SK, Ashokkumar M (2017) Theory of sonochemistry. pp 1–28
11. Thornycroft JI (2009) Torpedo boat destroyers. J Am Soc Nav Eng 7:711–736. https://doi.org/10.1111/j.1559-3584.1895.tb04389.x
12. Neppiras EA (1980) Acoustic cavitation. Phys Rep 61:159–251. https://doi.org/10.1016/0370-1573(80)90115-5
13. Makino K, Mossoba MM, Riesz P (1982) Chemical effects of ultrasound on aqueous solutions. Evidence for hydroxyl and hydrogen free radicals (.cntdot. OH and .cntdot. H) by spin trapping. J Am Chem Soc 104:3537–3539. https://doi.org/10.1021/ja00376a064
14. Makino K, Mossoba MM, Riesz P (1983) Chemical effects of ultrasound on aqueous solutions. Formation of hydroxyl radicals and hydrogen atoms. J Phys Chem 87:1369–1377. https://doi.org/10.1021/j100231a020
15. Behling R, Chatel G, Valange S (2017) Sonochemical oxidation of vanillyl alcohol to vanillin in the presence of a cobalt oxide catalyst under mild conditions. Ultrason Sonochem 36:27–35. https://doi.org/10.1016/j.ultsonch.2016.11.015
16. Al-Juboori RA, Yusaf T, Bowtell L, Aravinthan V (2015) Energy characterisation of ultrasonic systems for industrial processes. Ultrasonics 57:18–30. https://doi.org/10.1016/j.ultras.2014.10.003
17. Toma M, Fukutomi S, Asakura Y, Koda S (2011) A calorimetric study of energy conversion efficiency of a sonochemical reactor at 500 kHz for organic solvents. Ultrason Sonochem 18:197–208. https://doi.org/10.1016/j.ultsonch.2010.05.005
18. Wood RJ, Lee J, Bussemaker MJ (2017) A parametric review of sonochemistry: control and augmentation of sonochemical activity in aqueous solutions. Ultrason Sonochem 38:351–370. https://doi.org/10.1016/j.ultsonch.2017.03.030
19. Suslick KS (1990) Sonochemistry. Science (80-) 247:1439–1445. https://doi.org/10.1126/science.247.4949.1439
20. Flint EB, Suslick KS (1991) The temperature of cavitation. Science 253:1397–1399. https://doi.org/10.1126/science.253.5026.1397
21. Suslick KS, Hammerton DA, Cline RE (1986) The sonochemical hot spot. J Am Chem Soc 108:5641–5642. https://doi.org/10.1021/ja00278a055
22. Pokhrel N, Vabbina PK, Pala N (2016) Sonochemistry: science and engineering. Ultrason Sonochem 29:104–128. https://doi.org/10.1016/j.ultsonch.2015.07.023
23. Cravotto G, Cintas P (2012) Harnessing mechanochemical effects with ultrasound-induced reactions. Chem Sci 3:295–307. https://doi.org/10.1039/c1sc00740h

24. Berlan J, Trabelsi F, Delmas H et al (1994) Oxidative degradation of phenol in aqueous media using ultrasound. Ultrason Sonochem 1:S97–S102. https://doi.org/10.1016/1350-4177(94)90005-1
25. Lepoint-Mullie F, De Pauw D, Lepoint T et al (1996) Nature of the "extreme conditions" in single sonoluminescing bubbles. J Phys Chem 100:12138–12141. https://doi.org/10.1021/jp9615060
26. Nikitenko SI, Pflieger R (2017) Toward a new paradigm for sonochemistry: short review on non-equilibrium plasma observations by means of MBSL spectroscopy in aqueous solutions. Ultrason Sonochem 35:623–630. https://doi.org/10.1016/j.ultsonch.2016.02.003
27. Margulis MA (1985) Sonoluminescence and sonochemical reactions in cavitation fields. A review. Ultrasonics 23:157–169. https://doi.org/10.1016/0041-624X(85)90024-1
28. Hua I, Hoechemer RH, Hoffmann MR (1995) Sonolytic hydrolysis of p-nitrophenyl acetate: the role of supercritical water. J Phys Chem 99:2335–2342. https://doi.org/10.1021/j100008a015
29. Yasuda K, Torii T, Yasui K et al (2007) Enhancement of sonochemical reaction of terephthalate ion by superposition of ultrasonic fields of various frequencies. Ultrason Sonochem 14:699–704. https://doi.org/10.1016/j.ultsonch.2006.12.013
30. Son Y (2017) Simple design strategy for bath-type high-frequency sonoreactors. Chem Eng J 328:654–664. https://doi.org/10.1016/j.cej.2017.07.012
31. Kojima Y, Asakura Y, Sugiyama G, Koda S (2010) The effects of acoustic flow and mechanical flow on the sonochemical efficiency in a rectangular sonochemical reactor. Ultrason Sonochem 17:978–984. https://doi.org/10.1016/j.ultsonch.2009.11.020
32. Guo J, Zhu S, Chen Z et al (2011) Sonochemical synthesis of TiO_2 nanoparticles on graphene for use as photocatalyst. Ultrason Sonochem 18:1082–1090. https://doi.org/10.1016/j.ultsonch.2011.03.021
33. Ouyang W, Kuna E, Yepez A et al (2016) Mechanochemical synthesis of TiO_2 nanocomposites as photocatalysts for benzyl alcohol photo-oxidation. Nanomaterials 6:93. https://doi.org/10.3390/nano6050093
34. Chatel G (2018) How sonochemistry contributes to green chemistry? Ultrason Sonochem 40:117–122. https://doi.org/10.1016/j.ultsonch.2017.03.029
35. Takacs L (2013) The historical development of mechanochemistry. Chem Soc Rev 42:7649–7659. https://doi.org/10.1039/c2cs35442j
36. Balaz P (2008) Mechanochemistry in nanoscience and minerals engineering. Springer, Berlin
37. Kipp S, Šepelák V, Becker KD (2005) Mechanochemie: chemie mit dem hammer. Chemie Unserer Zeit 39:384–392. https://doi.org/10.1002/ciuz.200500355
38. Stodart J, Faraday M (1820) V. Experiments on the alloys of steel, made with a view to its improvement. Philos Mag 56:26–35. https://doi.org/10.1080/14786442008652361
39. Takacs L (2003) M.Carey Lea, the father of mechanochemistry. Bull Hist Chem 28:26–34
40. Šepelák V, Düvel A, Wilkening M et al (2013) Mechanochemical reactions and syntheses of oxides. Chem Soc Rev 42:7507–7520. https://doi.org/10.1039/c2cs35462d
41. Takacs L (2018) Two important periods in the history of mechanochemistry. J Mater Sci 53:13324–13330. https://doi.org/10.1007/s10853-018-2198-3
42. Ostwald W (1919) Die chemische literatur und die organisation der wissenschaft. Akad Verlag, Gesel
43. Boldyreva E (2013) Mechanochemistry of inorganic and organic systems: what is similar, what is different? Chem Soc Rev 42:7719–7738. https://doi.org/10.1039/c3cs60052a
44. Takacs L (2014) What is unique about mechanochemical reactions? Acta Phys Pol A 126:1040–1043. https://doi.org/10.12693/APhysPolA.126.1040
45. Fujishima A, Honda K (1972) Electrochemical photolysis of water at a semiconductor electrode. Nature 238:37–38. https://doi.org/10.1038/238037a0
46. Colmenares JC, Luque R, Campelo JM et al (2009) Nanostructured photocatalysts and their applications in the photocatalytic transformation of lignocellulosic biomass: an overview. Materials (Basel) 2:2228–2258. https://doi.org/10.3390/ma2042228
47. Colmenares JC, Luque R (2014) Heterogeneous photocatalytic nanomaterials: prospects and challenges in selective transformations of biomass-derived compounds. Chem Soc Rev 43:765–778. https://doi.org/10.1039/C3CS60262A
48. Ibhadon A, Fitzpatrick P (2013) Heterogeneous photocatalysis: recent advances and applications. Catalysts 3:189–218. https://doi.org/10.3390/catal3010189
49. Aravindan V, Lee Y-S, Yazami R, Madhavi S (2015) TiO_2 polymorphs in 'rocking-chair' Li-ion batteries. Mater Today 18:345–351. https://doi.org/10.1016/j.mattod.2015.02.015

50. Vuyyuru KR, Strasser P (2012) Oxidation of biomass derived 5-hydroxymethylfurfural using heterogeneous and electrochemical catalysis. Catal Today 195:144–154. https://doi.org/10.1016/j.cattod.2012.05.008
51. Li SH, Liu S, Colmenares JC, Xu YJ (2016) A sustainable approach for lignin valorization by heterogeneous photocatalysis. Green Chem 18:594–607. https://doi.org/10.1039/c5gc02109j
52. Huang W, Tang X, Wang Y et al (2000) Selective synthesis of anatase and rutile via ultrasound irradiation. Chem Commun. https://doi.org/10.1039/b003349i
53. Palmisano G, Yurdakal S, Augugliaro V et al (2007) Photocatalytic selective oxidation of 4-methoxybenzyl alcohol to aldehyde in aqueous suspension of home-prepared titanium dioxide catalyst. Adv Synth Catal 349:964–970. https://doi.org/10.1002/adsc.200600435
54. Chen X, Mao SS (2007) Titanium dioxide nanomaterials: synthesis, properties, modifications and applications. Chem Rev 107:2891–2959. https://doi.org/10.1021/cr0500535
55. Gupta SM, Tripathi M (2011) A review of TiO_2 nanoparticles. Chin Sci Bull 56:1639–1657. https://doi.org/10.1007/s11434-011-4476-1
56. Zatloukalová K, Obalová L, Kočí K et al (2017) Photocatalytic degradation of endocrine disruptor compounds in water over immobilized TiO_2 photocatalysts. Iran J Chem Chem Eng 2017:36
57. Higashimoto S, Kitao N, Yoshida N et al (2009) Selective photocatalytic oxidation of benzyl alcohol and its derivatives into corresponding aldehydes by molecular oxygen on titanium dioxide under visible light irradiation. J Catal 266:279–285. https://doi.org/10.1016/j.jcat.2009.06.018
58. Giannakoudakis DA, Arcibar-Orozco JA, Bandosz TJ (2015) Key role of terminal hydroxyl groups and visible light in the reactive adsorption/catalytic conversion of mustard gas surrogate on zinc (hydr)oxides. Appl Catal B Environ 174:96–104. https://doi.org/10.1016/j.apcatb.2015.02.028
59. Li D, Haneda H (2003) Morphologies of zinc oxide particles and their effects on photocatalysis. Chemosphere 51:129–137. https://doi.org/10.1016/S0045-6535(02)00787-7
60. Szabó T, Németh J, Dékány I (2003) Zinc oxide nanoparticles incorporated in ultrathin layer silicate films and their photocatalytic properties. Colloids Surfaces A Physicochem Eng Asp 230:23–35. https://doi.org/10.1016/j.colsurfa.2003.09.010
61. Giannakoudakis DA, Nair V, Khan A et al (2019) Additive-free photo-assisted selective partial oxidation at ambient conditions of 5-hydroxymethylfurfural by manganese (IV) oxide nanorods. Appl Catal B Environ 256:117803. https://doi.org/10.1016/j.apcatb.2019.117803
62. Jun YS, Hong WH, Antonietti M, Thomas A (2009) Mesoporous, 2D hexagonal carbon nitride and titanium nitride/carbon composites. Adv Mater 21:4270–4274. https://doi.org/10.1002/adma.200803500
63. Chen X, Jun Y-S, Takanabe K et al (2009) Ordered mesoporous SBA-15 type graphitic carbon nitride: a semiconductor host structure for photocatalytic hydrogen evolution with visible light. Chem Mater 21:4093–4095. https://doi.org/10.1021/cm902130z
64. Giannakoudakis DA, Seredych M, Rodríguez-Castellón E, Bandosz TJ (2016) Mesoporous graphitic carbon nitride-based nanospheres as visible-light active chemical warfare agents decontaminant. ChemNanoMat 2:268–272. https://doi.org/10.1002/cnma.201600030
65. Wei H, Zhang Q, Zhang Y et al (2016) Enhancement of the Cr(VI) adsorption and photocatalytic reduction activity of g-C_3N_4 by hydrothermal treatment in HNO_3 aqueous solution. Appl Catal A Gen 521:9–18. https://doi.org/10.1016/j.apcata.2015.11.005
66. Antonakou EV, Kalogiannis KG, Stefanidis SD et al (2014) Catalytic and thermal pyrolysis of polycarbonate in a fixed-bed reactor: the effect of catalysts on products yields and composition. Polym Degrad Stab 110:482–491. https://doi.org/10.1016/j.polymdegradstab.2014.10.007
67. Saroyan HS, Bele S, Giannakoudakis DA et al (2019) Degradation of endocrine disruptor, bisphenol-A, on an mixed oxidation state manganese oxide/modified graphite oxide composite: a role of carbonaceous phase. J Colloid Interface Sci 539:516–524. https://doi.org/10.1016/j.jcis.2018.12.088
68. Stefanidis SD, Karakoulia SA, Kalogiannis KG et al (2016) Natural magnesium oxide (MgO) catalysts: a cost-effective sustainable alternative to acid zeolites for the in situ upgrading of biomass fast pyrolysis oil. Appl Catal B Environ 196:155–173. https://doi.org/10.1016/j.apcatb.2016.05.031
69. Han C, Tang ZR, Liu J et al (2019) Efficient photoredox conversion of alcohol to aldehyde and H_2 by heterointerface engineering of bimetal-semiconductor hybrids. Chem Sci 10:3514–3522. https://doi.org/10.1039/c8sc05813j
70. Giannakoudakis DADA, Hu Y, Florent M, Bandosz TJTJTJ (2017) Smart textiles of MOF/g-C 3N 4 nanospheres for the rapid detection/detoxification of chemical warfare agents. Nanosc Horiz 2:356–364. https://doi.org/10.1039/C7NH00081B

71. Giannakoudakis DA, Bandosz TJ (2018) Detoxification of chemical warfare agents, 1st edn. Springer, Cham
72. Lombardi J, Yang L, Pearsall FA et al (2019) Stoichiometric control over ferroic behavior in Ba(Ti 1–x Fe x)O_3 nanocrystals. Chem Mater 31:1318–1335. https://doi.org/10.1021/acs.chemmater.8b04447
73. Weng B, Liu S, Tang ZR, Xu YJ (2014) One-dimensional nanostructure based materials for versatile photocatalytic applications. RSC Adv 4:12685–12700. https://doi.org/10.1039/c3ra47910b
74. Li JY, Yuan L, Li SH et al (2019) One-dimensional copper-based heterostructures toward photo-driven reduction of CO_2 to sustainable fuels and feedstocks. J Mater Chem A 7:8676–8689. https://doi.org/10.1039/c8ta12427b
75. Tang ZR, Han B, Han C, Xu YJ (2017) One dimensional CdS based materials for artificial photoredox reactions. J Mater Chem A 5:2387–2410. https://doi.org/10.1039/C6TA06373J
76. Liu S, Yang MQ, Tang ZR, Xu YJ (2014) A nanotree-like CdS/ZnO nanocomposite with spatially branched hierarchical structure for photocatalytic fine-chemical synthesis. Nanoscale 6:7193–7198. https://doi.org/10.1039/c4nr01227e
77. Liu S, Tang ZR, Sun Y et al (2015) One-dimension-based spatially ordered architectures for solar energy conversion. Chem Soc Rev 44:5053–5075. https://doi.org/10.1039/c4cs00408f
78. Giannakoudakis DA, Florent M, Wallace R et al (2018) Zinc peroxide nanoparticles: surface, chemical and optical properties and the effect of thermal treatment on the detoxification of mustard gas. Appl Catal B Environ 226:429–440. https://doi.org/10.1016/j.apcatb.2017.12.068
79. Magdziarz A, Colmenares JC, Chernyayeva O et al (2017) Insight into the synthesis procedure of Fe_3+/TiO_2-based photocatalyst applied in the selective photo-oxidation of benzyl alcohol under sun-imitating lamp. Ultrason Sonochem 38:187–196. https://doi.org/10.1016/j.ultsonch.2017.03.012
80. Giannakoudakis DA, Pearsall F, Florent M et al (2018) Barium titanate perovskite nanoparticles as a photoreactive medium for chemical warfare agent detoxification. J Colloid Interface Sci 531:233–244. https://doi.org/10.1016/j.jcis.2018.07.053
81. Hoyer P (1996) Formation of a titanium dioxide nanotube array. Langmuir 12:1411–1413. https://doi.org/10.1021/la9507803
82. Antonelli DM, Ying JY (1995) Synthesis of hexagonally packed mesoporous TiO_2 by a modified sol–gel method. Angew Chemie Int Ed English 34:2014–2017. https://doi.org/10.1002/anie.199520141
83. Wang Y, Tang X, Yin L et al (2000) Sonochemical synthesis of mesoporous titanium oxide with wormhole-like framework structures. Adv Mater 12:1183–1186. https://doi.org/10.1002/1521-4095(200008)12:16%3c1183:AID-ADMA1183%3e3.0.CO;2-X
84. Antonelli DM (1999) Synthesis of phosphorus-free mesoporous titania via templating with amine surfactants. Micropor Mesopor Mater 30:315–319. https://doi.org/10.1016/S1387-1811(99)00042-6
85. Yu JC, Yu J, Ho W, Zhang L (2001) Preparation of highly photocatalytic active nano-sized TiO_2 particles via ultrasonic irradiation. Chem Commun 2001:1942–1943. https://doi.org/10.1039/b105471f
86. Ghows N, Entezari MH (2010) Ultrasound with low intensity assisted the synthesis of nanocrystalline TiO_2 without calcination. Ultrason Sonochem 17:878–883. https://doi.org/10.1016/j.ultsonch.2010.03.010
87. Chen X, Liu L, Yu PY, Mao SS (2011) Increasing solar absorption for photocatalysis with black hydrogenated titanium dioxide nanocrystals. Science (80–) 331:746–750. https://doi.org/10.1126/science.1200448
88. Osorio-Vargas PA, Pulgarin C, Sienkiewicz A et al (2012) Low-frequency ultrasound induces oxygen vacancies formation and visible light absorption in TiO_2 P-25 nanoparticles. Ultrason Sonochem 19:383–386. https://doi.org/10.1016/j.ultsonch.2011.11.013
89. Fan C, Chen C, Wang J et al (2015) Black hydroxylated titanium dioxide prepared via ultrasonication with enhanced photocatalytic activity. Sci Rep 5:11712. https://doi.org/10.1038/srep11712
90. Fan C, Chen C, Wang J et al (2014) Enhanced photocatalytic activity of hydroxylated and N-doped anatase derived from amorphous hydrate. J Mater Chem A 2:16242–16249. https://doi.org/10.1039/c4ta03179b
91. Thommes M, Kaneko K, Neimark AV et al (2015) Physisorption of gases, with special reference to the evaluation of surface area and pore size distribution (IUPAC Technical Report). Pure Appl Chem 87:1051–1069. https://doi.org/10.1515/pac-2014-1117

92. Li W, Liu M, Feng S et al (2014) Template-free synthesis of uniform magnetic mesoporous TiO_2 nanospindles for highly selective enrichment of phosphopeptides. Mater Horizons 1:439–445. https://doi.org/10.1039/c4mh00030g
93. Comini E, Baratto C, Faglia G et al (2009) Quasi-one dimensional metal oxide semiconductors: preparation, characterization and application as chemical sensors. Prog Mater Sci 54:1–67. https://doi.org/10.1016/j.pmatsci.2008.06.003
94. Roy P, Berger S, Schmuki P (2011) TiO_2 nanotubes: synthesis and applications. Angew Chemie Int Ed 50:2904–2939. https://doi.org/10.1002/anie.201001374
95. Kasuga T, Hiramatsu M, Hoson A et al (1998) Formation of titanium oxide nanotube. Langmuir 14:3160–3163. https://doi.org/10.1021/la9713816
96. Du GH, Chen Q, Che RC et al (2001) Preparation and structure analysis of titanium oxide nanotubes. Appl Phys Lett 79:3702–3704. https://doi.org/10.1063/1.1423403
97. Chen Q, Zhou W, Du GH, Peng LM (2002) Trititanate nanotubes made via a single alkali treatment. Adv Mater 14:2000–2003. https://doi.org/10.1002/1521-4095(20020903)14:17%3c1208:AID-ADMA1208%3e3.0.CO;2-0
98. Zhang S, Peng L-M, Chen Q et al (2003) Formation mechanism of $H_2Ti_3O_7$ nanotubes. Phys Rev Lett 91:2–5. https://doi.org/10.1103/physrevlett.91.256103
99. Chen Q, Du GH, Zhang S, Peng L-M (2002) The structure of trititanate nanotubes. Acta Crystallogr Sect B Struct Sci 58:587–593. https://doi.org/10.1107/S0108768102009084
100. Suzuki Y, Yoshikawa S (2004) Synthesis and thermal analyses of TiO_2-derived nanotubes prepared by the hydrothermal method. J Mater Res 19:982–985. https://doi.org/10.1557/JMR.2004.0128
101. Kasuga T, Hiramatsu M, Hoson A et al (1999) Titania nanotubes prepared by chemical processing. Adv Mater 11:1307–1311. https://doi.org/10.1002/(SICI)1521-4095(199910)11:15%3c1307:AID-ADMA1307%3e3.0.CO;2-H
102. Nakahira A, Kubo T, Numako C (2010) Formation mechanism of TiO_2-derived titanate nanotubes prepared by the hydrothermal process. Inorg Chem 49:5845–5852. https://doi.org/10.1021/ic9025816
103. Bavykin DV, Parmon VN, Lapkin AA, Walsh FC (2004) The effect of hydrothermal conditions on the mesoporous structure of TiO_2 nanotubes. J Mater Chem 14:3370–3377. https://doi.org/10.1039/b406378c
104. Seo DS, Lee JK, Kim H (2001) Preparation of nanotube-shaped TiO_2 powder. J Cryst Growth 229:428–432. https://doi.org/10.1016/S0022-0248(01)01196-4
105. Zhang Q, Gao L, Sun J, Zheng S (2002) Preparation of long TiO_2 nanotubes from ultrafine rutile nanocrystals. Chem Lett 31:226–227. https://doi.org/10.1246/cl.2002.226
106. Bai Q, Lavenas M, Vauriot L et al (2019) Hydrothermal transformation of titanate scrolled nanosheets to anatase over a wide pH range and contribution of triethanolamine and oleic acid to control the morphology. Inorg Chem 58:2588–2598. https://doi.org/10.1021/acs.inorgchem.8b03197
107. Bin Liu, Eray S, Aydil (2009) Growth of oriented single-crystalline rutile TiO_2 nanorods on transparent conducting substrates for dye-sensitized solar cells. J Am Chem Soc 113:3985–3990
108. Pavasupree S, Suzuki Y, Yoshikawa S, Kawahata R (2005) Synthesis of titanate, TiO_2 (B), and anatase TiO_2 nanofibers from natural rutile sand. J Solid State Chem 178:3110–3116. https://doi.org/10.1016/j.jssc.2005.07.022
109. Tsai CC, Teng H (2004) Regulation of the physical characteristics of titania nanotube aggregates synthesized from hydrothermal treatment. Chem Mater 16:4352–4358. https://doi.org/10.1021/cm049643u
110. Oskam G, Nellore A, Penn RL, Searson PC (2003) The growth kinetics of TiO_2 nanoparticles from titanium(IV) alkoxide at high water/titanium ratio. J Phys Chem B 107:1734–1738. https://doi.org/10.1021/jp021237f
111. Wong CL, Tan YN, Mohamed AR (2011) A review on the formation of titania nanotube photocatalysts by hydrothermal treatment. J Environ Manage 92:1669–1680. https://doi.org/10.1016/j.jenvman.2011.03.006
112. Zhu Y, Li H, Koltypin Y et al (2001) Sonochemical synthesis of titania whiskers and nanotubes. Chem Commun 24:2616–2617. https://doi.org/10.1039/b108968b
113. Izawa H, Kikkawa S, Koizumi M (1982) Ion exchange and dehydration of layered [sodium and potassium] titanates, $Na_2Ti_3O_7$ and $K_2Ti_4O_9$. J Phys Chem 86:5023–5026. https://doi.org/10.1021/j100222a036

114. Marchand R, Brohan L, Tournoux M (1980) TiO_2(B) a new form of titanium dioxide and the potassium octatitanate $K_2Ti_8O_{17}$. Mater Res Bull 15:1129–1133. https://doi.org/10.1016/0025-5408(80)90076-8
115. Joo J, Kwon SG, Yu T et al (2005) Large-scale synthesis of TiO_2 nanorods via nonhydrolytic sol–gel ester elimination reaction and their application to photocatalytic inactivation of *E. coli*. J Phys Chem B 109:15297–15302. https://doi.org/10.1021/jp052458z
116. Ma Y, Lin Y, Xiao X et al (2006) Sonication–hydrothermal combination technique for the synthesis of titanate nanotubes from commercially available precursors. Mater Res Bull 41:237–243. https://doi.org/10.1016/j.materresbull.2005.08.020
117. Viriya-empikul N, Charinpanitkul T, Sano N et al (2009) Effect of preparation variables on morphology and anatase-brookite phase transition in sonication assisted hydrothermal reaction for synthesis of titanate nanostructures. Mater Chem Phys 118:254–258. https://doi.org/10.1016/j.matchemphys.2009.07.042
118. Viriya-Empikul N, Sano N, Charinpanitkul T et al (2008) A step towards length control of titanate nanotubes using hydrothermal reaction with sonication pretreatment. Nanotechnology. https://doi.org/10.1088/0957-4484/19/03/035601
119. Begin-Colin S, Le Caer G, Mocellin A, Zandona M (1994) Polymorphie transformations of titania induced by ball milling. Philos Mag Lett 69:1–7. https://doi.org/10.1080/09500839408242430
120. Lu CJ, Zhang J, Li ZQ (2004) Structural evolution of titanium powder during ball milling in different atmospheres. J Alloys Compd 381:278–283. https://doi.org/10.1016/j.jallcom.2004.03.130
121. Pang P, Li W, Liu Y (2007) Effect of ball milling process on the microstructure of titanium-nanohydroxyapatite composite powder. Rare Met 26:118–123. https://doi.org/10.1016/S1001-0521(07)60170-3
122. Silva CC, Graça MPF, Valente MA, Sombra ASB (2007) Crystallite size study of nanocrystalline hydroxyapatite and ceramic system with titanium oxide obtained by dry ball milling. J Mater Sci 42:3851–3855. https://doi.org/10.1007/s10853-006-0474-0
123. Bégin-Colin S, Girot T, Le Caër G, Mocellin A (2000) Kinetics and mechanisms of phase transformations induced by ball-milling in anatase TiO_2. J Solid State Chem 149:41–48. https://doi.org/10.1006/jssc.1999.8491
124. Yadav BC, Singh S, Yadav TP (2015) Titania prepared by ball milling: its characterization and application as liquefied petroleum gas sensor. Synth React Inorg Met Nano-Metal Chem 45:487–494. https://doi.org/10.1080/15533174.2012.749892
125. Rajender G, Giri PK (2016) Strain induced phase formation, microstructural evolution and band-gap narrowing in strained TiO_2 nanocrystals grown by ball milling. J Alloys Compd 676:591–600. https://doi.org/10.1016/j.jallcom.2016.03.154
126. Jung HJ, Nam K, Sung HG et al (2016) Preparation of TiO_2-decorated boron particles by wet ball milling and their photoelectrochemical hydrogen and oxygen evolution reactions. Materials (Basel). https://doi.org/10.3390/ma9121012
127. Billik P, Plesch G (2007) Mechanochemical synthesis of nanocrystalline TiO_2 from liquid TiCl4. Scr Mater 56:979–982. https://doi.org/10.1016/j.scriptamat.2007.01.048
128. Billik P, Plesch G, Brezová V et al (2007) Anatase TiO_2 nanocrystals prepared by mechanochemical synthesis and their photochemical activity studied by EPR spectroscopy. J Phys Chem Solids 68:1112–1116. https://doi.org/10.1016/j.jpcs.2007.02.010
129. Salari M, Rezaee M, Marashi SPH, Aboutalebi SH (2009) The role of the diluent phase in the mechanochemical preparation of TiO_2 nanoparticles. Powder Technol 192:54–57. https://doi.org/10.1016/j.powtec.2008.11.011
130. Li C, Liang B, Song H et al (2008) Preparation of porous rutile titania from ilmenite by mechanical activation and subsequent sulfuric acid leaching. Microporous Mesoporous Mater 115:293–300. https://doi.org/10.1016/j.micromeso.2008.01.045
131. Tao T, Glushenkov AM, Liu H et al (2011) Ilmenite $FeTiO_3$ nanoflowers and their pseudocapacitance. J Phys Chem C 115:17297–17302. https://doi.org/10.1021/jp203345s
132. Yu J, Chen Y (2010) One-dimensional growth of TiO_2 nanorods from ilmenite sands. J Alloys Compd 504:S364–S367. https://doi.org/10.1016/j.jallcom.2010.02.145
133. Yu J, Chen Y, Glushenkov AM (2009) Titanium oxide nanorods extracted from ilmenite sands. Cryst Growth Des 9:1240–1244. https://doi.org/10.1021/cg801125w
134. Tao T, Chen Y, Zhou D et al (2013) Expanding the applications of the ilmenite mineral to the preparation of nanostructures: TiO_2 nanorods and their photocatalytic properties in the degradation of oxalic acid. Chem A Eur J 19:1091–1096. https://doi.org/10.1002/chem.201202451

135. Zhao Z, Xu J, Liaw PK et al (2014) One-step formation and photocatalytic performance of spindle-like TiO_2 nanorods synthesized by dealloying amorphous $Cu_{50}Ti_{50}$ alloy. Corros Sci 84:66–73. https://doi.org/10.1016/j.corsci.2014.03.014

Topics in Current Chemistry (2020) 378:29
https://doi.org/10.1007/s41061-020-0293-9

REVIEW

Improvements in Catalyst Synthesis and Photocatalytic Oxidation Processing Based on the Use of Ultrasound

Parag R. Gogate[1]

Received: 8 January 2020 / Accepted: 18 February 2020 / Published online: 3 March 2020

Abstract

The efficacy of photocatalysis strongly depends on the activity of the catalysts and the operational factors, especially factors associated with mass transfer and the possibility of catalyst deactivation. The use of ultrasound has great potential to enhance catalyst activity, during both the synthesis and actual oxidation processes due to the cavitational effects of turbulence and liquid streaming. This article presents an overview of the application aspects of ultrasound, both in the synthesis of the photocatalyst and applications for wastewater treatment. A review of the literature revealed that the use of ultrasound in the synthesis processes can result in a catalyst with a lower mean size and higher surface area as well as uniform size distribution. The application of ultrasound in the actual photocatalytic oxidation facilitates enhancement of the oxidation capacity, leading to higher degradation rates, sometimes synergistic results and definitely lower treatment times. This article also presents guidelines for the selection of the best operating conditions for the use of ultrasound in photocatalytic systems and includes a discussion on the possible reactor configurations suitable for large-scale operations. Overall, a combination of ultrasound with photocatalytic oxidation or the optimized application of ultrasound in catalyst synthesis can yield significant benefits.

Keywords Hybrid methods · Improved catalyst · Particle size distribution · Photocatalytic oxidation · Sonochemical reactors · Synergistic index

Chapter 3 was originally published as Gogate, P. R. Topics in Current Chemistry (2020) 378: 29. https://doi.org/10.1007/s41061-020-0293-9.

✉ Parag R. Gogate
pr.gogate@ictmumbai.edu.in

[1] Chemical Engineering Department, Institute of Chemical Technology, Matunga, Mumbai 40019, India

1 Introduction

The presence of recalcitrant pollutants in wastewater streams has shown an increasing trend in recent years, in particular due to the advent of newer chemicals required by human beings, such as novel pharmaceutical drugs for tackling various ailments. A similar trend has been seen for pesticides due to the aim to achieve higher production from agricultural fields. These newly developed chemical compounds are often biorefractory in nature and have a longer half-life than many of their predecessors and represent a challenge to the efficacy of the conventional wastewater treatment methods. Consequently, focus has been on developing newer oxidation schemes based on, for example, advanced oxidation processes [1, 2].

Among the different advanced oxidation processes proposed in recent years, photocatalytic oxidation based on both ultraviolet (UV) and solar irradiations is considered to be one of the more promising approaches. One target of such treatment is the destruction of complex pollutants, either completely or by converting the pollutant into smaller, easily digestible and non-toxic compounds [3, 4]. The two most important factors contributing to the efficacy of a photocatalytic oxidation system are the catalyst and the operation of the photocatalytic reactor, including the design [5]. The most common problems associated with the photocatalyst are limited activity of the catalyst, uneven particle size distribution, lack of control over the catalyst morphology and possible deactivation during the operation. The actual operation of photocatalytic oxidation is limited by mass transfer resistances based on the heterogeneous nature of the catalyst, oxidants and effluent. In this article, I highlight the important aspects of tackling these commonly observed disadvantages in photocatalytic oxidation operations using ultrasound.

The passage of ultrasound through a liquid medium causes the formation of cavities (either gas filled or vaporous depending on the medium). The generated cavities grow under the driving pressure field, controlled by the amplitude and power of the ultrasound, and ultimately collapse, violently releasing significant energy [6, 7]. The phenomenon is described as cavitation, and the net effects are the generation of local hot spots, liquid circulation currents and turbulence as well as production of free radicals (both of the chemical compounds present and the oxidants). The effects are classified as being either physical or chemical, and these can be tailored based on the operating conditions of the ultrasound system. The physical effects, such as turbulence and micromixing, are expected to be beneficial in terms of improving catalyst synthesis and eliminating mass transfer resistances in the actual photocatalytic oxidation operation [8]. The chemical effects in terms of radical production can be synergistic for photocatalytic oxidation [9]. An in-depth analysis of the application of ultrasound for both catalyst synthesis and the actual operation of photocatalytic oxidation is presented in subsequent sections of this article.

2 Mechanistic Understanding of Cavitation and Its Effects

Cavitation generated by the passage of ultrasound through a liquid has been described as acoustic cavitation. When the ultrasound waves are introduced into the liquid, the rarefaction and compression cycles drive different stages of cavitation.

During the rarefaction cycle, the degree of stretching of the liquid molecules is dependent on the driving pressure amplitude. The stretching gives rise to the formation of cavities which subsequently grow based on the alternate compression/rarefaction cycles of the sound waves. The maximum growth of the cavities depends on the operating conditions, as does the final collapse process in terms of the required time and the type (staged or instantaneous) affecting the final pressure pulse generated. A schematic representation of the process of ultrasound-induced cavitation, including the different stages of the cavitation, is shown in the Fig. 1.

The intensity of cavitational collapse, which can be quantified in terms of the collapse pressure/temperature or the quantum of free radicals generated, is strongly dependent on the operating conditions. Bubble dynamics simulations can be performed to understand the effect of the equipment (number of transducers, ultrasonic power dissipation and ultrasonic frequency) and the system operating conditions (temperature and presence of additives). In general, depending on the specific applications, guidelines for the operating conditions can be established based on the required dominance of the physical or chemical effects with the required intensities [10–12]. For the case of catalyst synthesis, dominant physical effects, such as micro-streaming and intense turbulence, are required and hence lower frequencies of irradiation with lower power dissipation would be useful. For the application of ultrasound in photocatalytic oxidation, dominant physical effects are again required for the elimination of the mass transfer resistances. However, if chemical effects need to be dominant, then pyrolytic reactions and the production of free radicals will be required. This can be achieved typically through the usage of higher frequencies (mostly up to an optimum of about 200–400 kHz) and power dissipations.

The presence of different additives, such as salts, catalyst, gases and radical promoters, can help to intensify the cavitational effects, especially in combination with

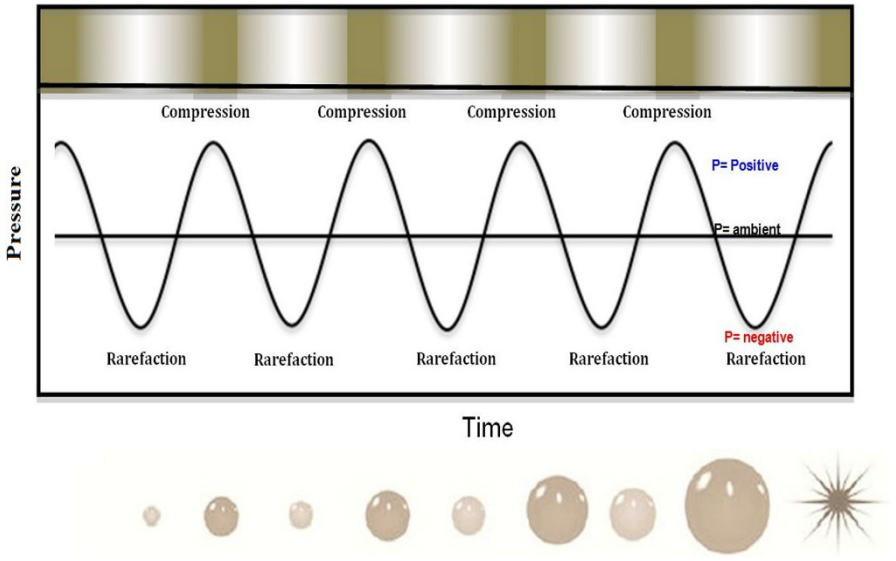

Fig. 1 Schematic representation of different stages in acoustic cavitation

photocatalytic oxidation [11]. Some additives help to enhance the basic cavitational effects, and these same additives will be equally helpful to enhance catalyst synthesis, though the alterations in catalyst purity need to be looked at. The presence of solid particles or gases help to provide additional nuclei due to the introduced surface heterogeneity in the continuous liquid medium, resulting in a higher number of nuclei. It is also important to note that there is an optimum loading as too much presence will lead to scattering effects and hence reduced energy transfer. The use of salts can help in pushing the organic molecules towards the site of cavity collapse, giving higher exposure to cavitating conditions and hence higher extents of degradation in the combined operation of ultrasound and photocatalytic oxidation [13]. Catalysts can provide both the effects of more nuclei and enhanced formation of free radicals based on the intrinsic chemical mechanisms; for example, the presence of TiO_2 or CuO bestows surface activation together with heterogeneous nucleation, often yielding synergistic effects in combination approach. The use of radical promoters, such as hydrogen peroxide or carbon tetrachloride or ozone, enhances the formation of radicals due to the dissociation of the added compounds, which can result in a higher extent of degradation [14, 15] depending on the type of pollutant.

3 Improvements in Catalyst Synthesis Based on the Use of Ultrasound

Various methods have been conventionally developed for the synthesis of metal nanoparticles to be used as photocatalysts. Each method has also been subjected to variations to arrive at best conditions to control the size, shape, structure and properties of the photocatalyst. The choice and composition of the precursor is also a very important factor in determining the characteristics of the synthesized catalyst. Various conventional methods of synthesis include chemical vapour deposition, laser ablation, physical evaporation, solvo-thermal processes, among others [16]. Conventional methods are often associated with several drawbacks, including long synthesis times (up to several days), requirement for various chemicals, including solvents, and energy-intensive conditions. In addition, it is difficult to efficiently remove the solvents and precursors used in conventional synthesis methods, as well as in maintaining the uniformity of the nanoparticles [16]. For example, the conventional method of synthesizing mesoporous titanium photocatalysts involves the use of alkyl phosphate surfactants [17]; however, the phosphorous becomes bound to the particles and there is subsequently great difficulty in removing it. Similarly, the other conventionally used processes, such as calcination and solvent extraction, are also ineffective in terms of giving the best catalyst morphology and required purity. Multiple reports on phosphorus-free mesoporous titanium catalysts have been published [18, 19], but the use of phosphorus-free titania requires very long synthesis times (up to 15 days) [20]. Similarly, the synthesis of CdSe photocatalysts requires thermal treatment as one of the important processing steps; this process process is highly energy intensive and demonstrates difficulty in maintaining uniform crystalline distribution [21].

Ultrasound-assisted synthesis of photocatalysts has been receiving considerable attention in the past few years. The local hotspots during ultrasonic cavitation are

able to reduce the metal to form nanoparticles. The advantages of using ultrasound is its simplicity, application in ambient conditions, energy efficiency, rapid reactions and fast synthesis, uniformity in formation and distribution [22–24]. An analysis of the important reports that have been published on the sonochemical synthesis of semiconductor photocatalysts are presented in the following paragraphs. The first photcatalyst described is TiO_2, which is often the most recommended photocatalyst.

Pinjari et al. [25] studied the synthesis of TiO_2 based on the sol–gel process, focusing on understanding the effect of calcination and sonication time. These authors noted that the use of ultrasound and the sonication time did affect the phase transformation from anatase to rutile, a very important observation considering the possible application of this phase transformation in the photocatalysis. Typically, rutile content and crystallinity increased with calcination time and both were higher for the catalyst obtained using ultrasound-assisted approach (US in Fig. 2) compared with the silent conditions without use of ultrasound (NUS in Fig. 2). They also demonstrated that optimum sonication time was required to obtain the best rutile content in the obtained catalyst and that the use of ultrasound resulted in higher yields, with an actual yield of 95% compared to the 83.22% yield with the conventional approach without ultrasound [25]. In another study [26], the same group reported their elucidation of the effect of ultrasonic amplitude on the phase transformation, reporting that an optimum amplitude does exist for obtaining the best results for the yield, rutile content and the crystallinity. The reported effect of amplitude on rutile content and crystallinity has been reproduced in Fig. 3 to demonstrate a quantitative understanding of the results. The existence of the optimum amplitude was attributed to the fact that the introduced heat energy due to collapse of cavities is not utilized for the phase transformation. Also, the process of acoustic shielding based on too much cavitation around the surface of transducer reduces the effective energy transfer and hence lower cavitational intensity is observed that in turn drives lower phase transformation. The vaporization of 2-propanol due to excess heat energy dissipation at higher power dissipations locally shifts the equilibrium, resulting in lower yields and also lower cavitational intensity, again contributing to lower rutile content.

A mesoporous TiO_2 having a wormhole structure was effectively synthesized using very high-intensity ultrasound [20]. The first step included the formation of bare-TiO_2 using ultrasound-assisted hydrolysis and subsequent controlled condensation, and the second step included tailoring the particle size using high-intensity ultrasound. The reported advantages of this process were rapid synthesis, high activity and thermal stability. Similarly, the synthesis of mesoporous bicrystalline TiO_2 containing anatase and brookite phases showing high photocatalyst activity was reported using a tri-block copolymer [27]. The application of ultrasound resulted in the enhanced content of the brookite phase, which was favourable for higher activity. The other reported benefit of the use of ultrasound was obtaining mesoporous TiO_2 with narrow pore size distribution. In addition, a reduction in the synthesis time was observed based on enhancements in the hydrolysis of the precursor, crystallization and extraction of the surfactants used during the synthesis.

Apart from the application of ultrasound for the synthesis of native TiO_2, there have also been reports of ultrasound being used for the synthesis of composites based on TiO_2. Sonochemical synthesis was used to develop a novel-shaped TiO_2/

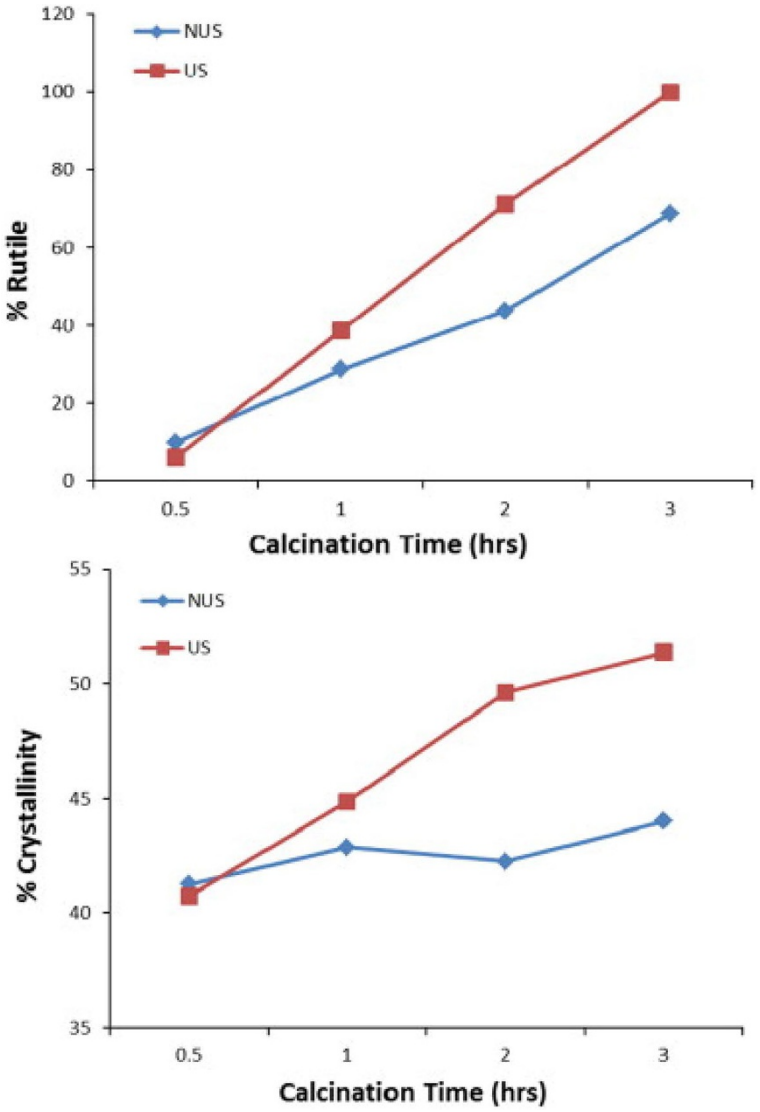

Fig. 2 Effect of calcination time and use of ultrasound on the rutile content and crystallinity of synthesized TiO_2. *NUS* Approach without the use of ultrasound, *US* ultrasound-assisted approach. Reproduced from Pinjari et al. [25]

WO_3 photocatalyst [28]. The source of the ultrasound was an ultrasonic horn operating at a frequency of 20 kHz and a power intensity of 100 W/cm^2. It was reported that nanomaterials having a diameter of 8–12 nm that were square and hexagonal in shape were obtained within a total synthesis time of 9 h, including the steps of calcination and drying. Brunauer–Emmett–Teller (BET) surface area analysis revealed that the obtained surface area of 1.38 m^2/g was higher than that of other nanocomposites reported in the literature. A simple ultrasonic bath synthesis method for the

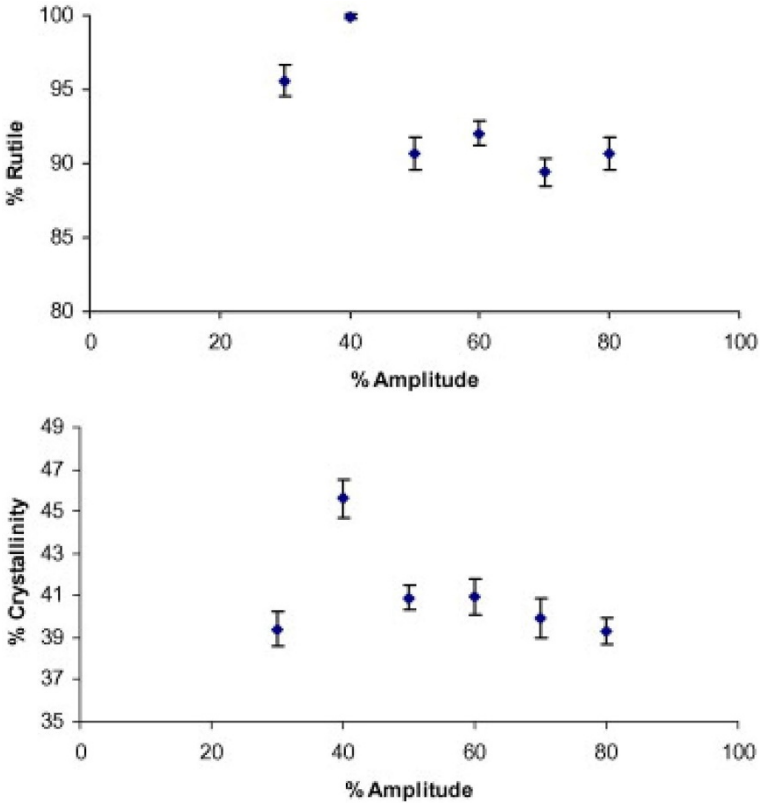

Fig. 3 Effect of ultrasonic amplitude on the rutile content and crystallinity of synthesized TiO_2. Reproduced from Prasad et al. [26]

CdSe-TiO_2 photocatalyst has also been reported [21]. CdSe acts as a photosensitizer and adds the visible light spectrum for TiO_2 application and also prevents recombination, resulting in higher activity. In that study, an ultrasonic bath enhanced the uniformity of the photocatalyst and reduced the synthesis time [21]. In a different study, CdS/TiO_2 nanoparticles were synthesized, with sonoluminescence used to produce nanoparticles of different sizes, morphologies and shapes [29]. The application of ultrasound was based on the horn-type system, and different transducers operating at various frequencies were used to study the effect of frequency. It was clearly established that the effect of ultrasonic intensity was dominant in defining the morphology and shape of the nanoparticles. Figure 4 shows that both nanorod and nanoparticle structures are produced and that the morphological characteristics depends on the ultrasonic frequency. This figure also reveals that with an increase in ultrasound frequency the diameter of the spherical nanoparticles increases slightly and the probability of the occurrence of the rod-like structure is decreased. The observed trend indicates that lower frequency drives the higher crystallinity of CdS, possibly attributable to the dominance of physical effects [29]. In another study, Shende

et al. [30] studied the synthesis of Graphene–Ce–TiO_2 and Graphene–Fe–TiO_2 nanocomposites in the presence of ultrasound (horn-type system with a frequency of 22 kHz and rated power dissipation of 200 W). The proper formation of the composites was confirmed based on the X-ray powder diffraction (XRD) analysis. X-ray fluorescence analysis confirmed the presence of metals (Ce and Fe) in the obtained catalyst. Subsequently, the obtained catalyst was also successfully demonstrated to show excellent activity for degradation of crystal violet dye. Comparison of the different catalysts revealed that the Fe-based composite showed a higher degradation rate constant than both the Ce-based composite and the bare graphene–TiO_2 [30]. The presence of Fe or Ce helped in enhancing the charge transfer, as shown in Fig. 5 which reproduces the schematic representation of the proposed mechanism. Also, the rate of the recombination of the electron–hole pair reduced to drive the higher photocatalytic oxidation activity.

Another modification in the application of TiO_2 as the catalyst is the use of metal doping with the objective of enhancing the interfacial charge transfer in photocatalytic degradation processes. Metal deposition is the most frequently studied modification for TiO_2 in terms of effects on the photochemical properties of its surface. Metal deposition involves the loading of metal nanoparticles at the TiO_2 surface by either photodeposition [31] or impregnation [32]. UV irradiation on metal-modified TiO_2 surfaces induces a Fermi level equilibration between the metal and TiO_2 via

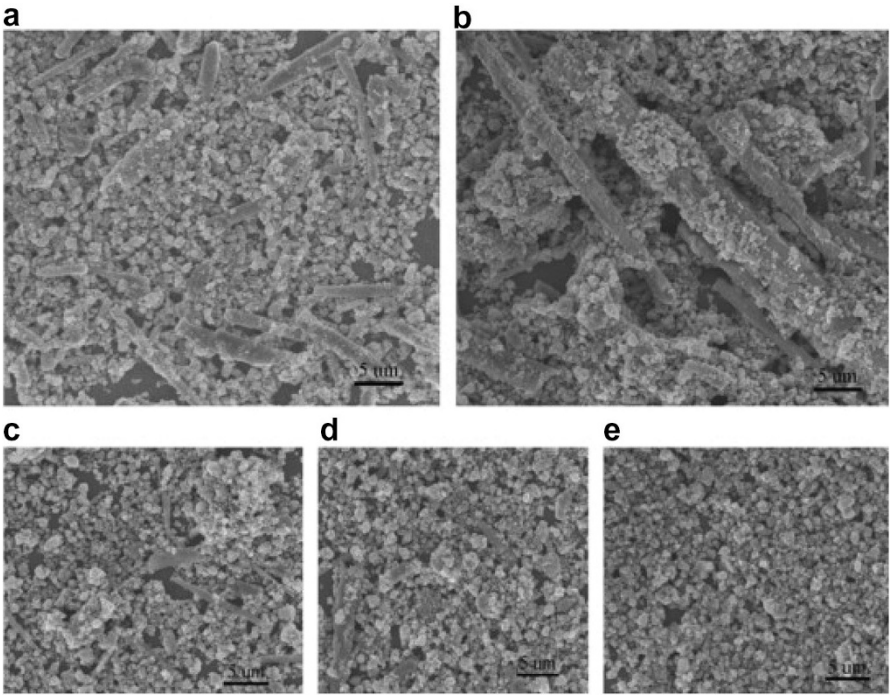

Fig. 4 Understanding the effect of ultrasonic frequency on the morphology of the obtained CdS/TiO_2 nanocomposite. **a** CdS/TiO_2, 20 kHz; **b** CdS/TiO_2, 25 kHz; **c** CdS/TiO_2, 30 kHz; **d** CdS/TiO_2, 35 kHz; **e** CdS/TiO_2, 40 kHz. Reproduced from Li et al. [29]

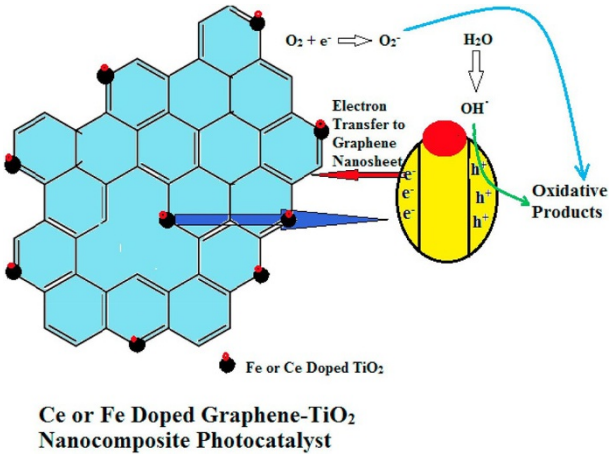

Fig. 5 Proposed mechanism for the charge transfer during the application of nanocomposites for photocatalytic degradation. Reproduced from Shende et al. [30]

charge distribution, thereby shifting the Fermi level, leading to a more efficient electron transfer in the system. The purpose of doping semiconductors is to create defect states in the band gap to enhance the interfacial charge transfer. These defect states trap the VB holes and CB electrons, thereby inhibiting and retarding the recombination of holes and electrons. The type of dopant used is critical in determining the overall activity of the photocatalysts. There have been multiple reports on sonochemical synthesis of metal-doped TiO_2. For example, Ambati and Gogate [33] studied the synthesis of iron-doped TiO_2 catalyst using the ultrasound-based approach and compared the efficacy of the ultrasound-assisted approach with the conventional sol–gel method in terms of the difference in characteristics of the obtained catalyst. Optimum synthesis conditions in terms of the irradiation time, extent of doping, type of solvent and temperature were established. These authors reported that the particle size obtained with the ultrasound-assisted approach was 99 nm and much smaller than that obtained with conventional approach, i.e. 325 nm (see Fig. 6 for the particle size distribution data). The XRD analysis results reported by these authors (see Fig. 7) allowed the doping efficacy to be established on the basis of the diffraction peaks at a specific angle. More importantly, the crystallite size for the catalyst obtained using the ultrasound-based approach (~25.4 nm) was lower than that observed for the conventionally obtained catalyst (~31.2 nm). In addition, the results of the scanning electron microscopy (SEM) analysis established that the surface was more uniform, and the UV–Vis band gap energy estimations demonstrated beneficial results for the ultrasound assisted approach [33]. In another study, Stucchi et al. [34] demonstrated that ultrasound increased the loading of Ag and Au onto the semiconductor surface. These authors reported that the deposition of silver using the conventional method resulted in a narrow distribution of nano-sized particles (typical range 0.5–3 nm) and that while the use of ultrasound did not increase the dispersion, but it did provide a higher quantum of Ag being loaded. The application of ultrasound induced the growth of Ag crystallites over the TiO_2

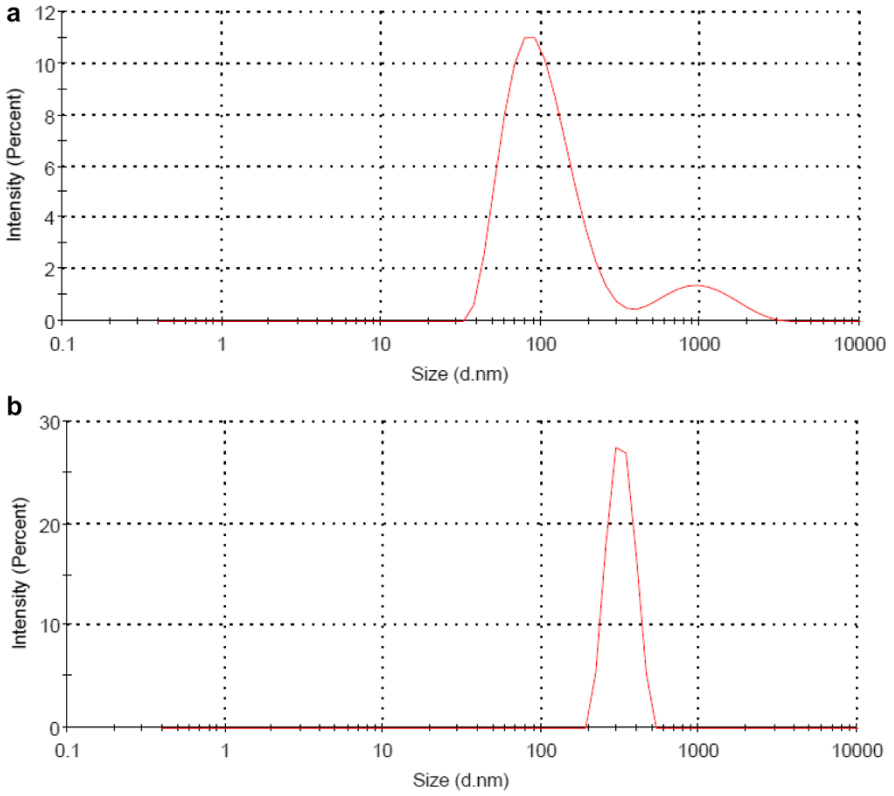

Fig. 6 Particle size analysis for Fe-doped TiO_2 catalysts using dynamic light scattering (DLS) for the ultrasound-assisted approach (**a**) and the conventional approach (**b**). Reproduced from Ambati and Gogate [33]

surface as aggregates, leading to higher material deposition. The increased loading of Ag also enhanced the visible light absorption of the semiconductor, subsequently increasing the photocatalytic degradation of acetone [34]. Uniform coating and distribution of gold on titanium dioxide has been reported to be effectively achieved under sonication in another set of investigations [35, 36]. Ultrasonically loaded gold nanoparticles onto the TiO_2 surface readily accept the electronic charges during photoexcitation due to their highly ordered distribution, thereby preventing electron–hole recombination processes. Similarly, N, Cl-co-doped TiO_2 was synthesized from titanium(IV) butoxide and ammonium chloride using the sonochemical method [37]. The authors reported that sonication shifted the start of absorption toward a lower energy, thereby subsequently improving the crystallinity of the semiconductor. Another advantage reported was the rapid synthesis within 4 h. In a recent study, nanosized (4–5 nm) TiO_2 particles on graphene were reported to be synthesized within a few hours with no surfactant using sonication [38]. In that study, graphene facilitated electron transfer and prevented recombination in UV light spectrum for photodegradation giving enhanced effects. Another novel method of nanoparticle synthesis was based on the pH swing method combined with ultrasound. pH swings

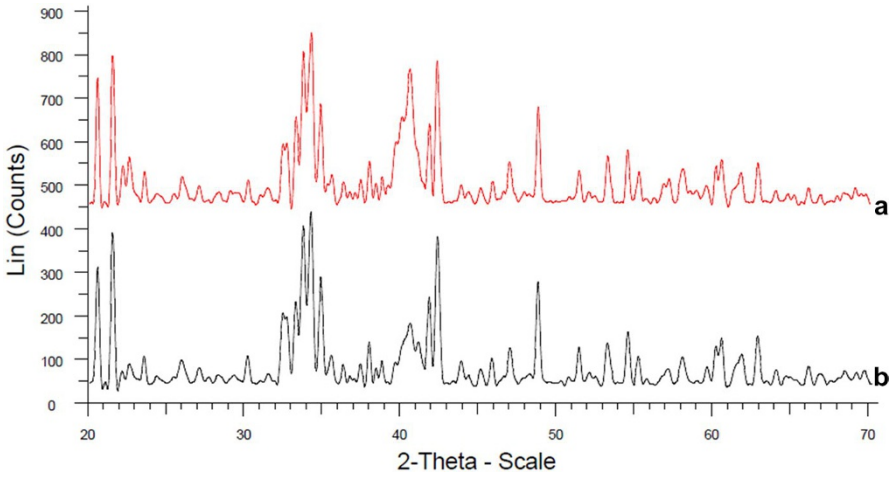

Fig. 7 X-ray diffraction pattern reported for both the ultrasound-assisted approach (**a**) and the conventional assisted approach (**b**) for the synthesis of Fe-doped TiO_2 catalyst. Reproduced from Ambati and Gogate [33]

along with ultrasonic irradiation proved effective in controlling the size of TiO_2 nanoparticles, leading to more effective degradation in the subsequent application [39].

ZnO-based photocatalysts, in addition to TiO_2 photocatalysts, have also received considerable attention for their use in the degradation of organic pollutants. Here I discuss the various reports on ZnO photocatalyst synthesis using ultrasonication. Both undoped and Dy-doped ZnO synthesized by sonication were found to yield good photodegradation results due to the uniformity of the synthesized nanorod-structure morphologies [40]. In that study, an ultrasonic bath operating at 35 kHz was used as the source of ultrasound during the synthesis of the catalyst. In another study, silica coated ZnO was synthesized using ZnO, tetraethoxysilane (TEOS), and ammonia mixed in an ethanol–water medium [41]. The authors of that study reported that the use of sonication could reduce the time of synthesis to 2 h. Similarly, in another study, the application of sonication successfully produced larger lattice volumes in Mg-doped ZnO photocatalyst [42]. In that work, ultrasound was applied using an ultrasonic processor operating at a power intensity of 800 W/cm^2 and a frequency of 25 kHz. The authors reported that the obtained nanoparticles of ZnO doped with Mg(II) had a spherical shape and that all particles were almost similar in size [42].

Other than TiO_2- and ZnO-based photocatalysts, various other semiconductor nanomaterials have also been effectively synthesized using sonication. For example, the Bi_2O_3 photocatalyst was effectively synthesized using a simple sonochemical method in which polyvinylpyrrolidone (PVP) surfactant was used to control grain sizes and morphologies [43]. Bi_2O_3 could be synthesized within 75 min and showed 86% photodegradation of methyl orange in the actual photocatalytic oxidation application. In another study, Ag/AgCl nanocubes using a PVP precursor were rapidly synthesized ultrasonically within 35 min [44]. The ultrasonically synthesized Ag

nanocubes were effectively applied for the visible light photodegradation of methyl orange, rhodamine B and methylene blue. An interesting middle-sagged $CaSn(OH)_6$ microcube morphology, which could not be synthesized by conventional methods, was reported to be uniformly synthesized sonochemically [45]. The obtained catalyst sonochemically demonstrated higher photodegradation activity and stability as compared to the conventionally prepared catalyst with different morphology. Other interesting sonochemically synthesized photocatalysts that have been found to demonstrate superior performance in photocatalysis or easier synthesis process for the catalyst as compared to conventional methods are Nano $BiPO_4$ and silver-doped $BiPO_4$ nanostructures [46], $CdWO_4$ nanoparticles [47] and Ag-$PbMoO_4$ [48].

4 Sonophotocatalytic Degradation

In sonophotocatalytic processes, the photocatalytic degradation of contaminants is supplemented with the physiochemical effect of ultrasonic cavitation. The hydroxyl radicals generated during the collapse of cavities provide a synergistic effect with the electron–hole generation in the photocatalyst for inducing oxidation reactions. Sonophotocatalytic (SPC) degradation has been studied widely to provide synergistic effects of sonolysis and photocatalysis in the combined process. The expected benefit of using ultrasound with photocatalysis is that ultrasound promotes the mechanical disaggregation of catalysts, enhancing the surface area for photocatalytic degradation. Also, it enhances the formation of reactive hydroxyl radicals by sonolysis and thereby abatement of the effect of electron–hole recombination in photodegradation [49]. In addition to these beneficial effects on photocatalysis, the presence of solid catalysts also supports the cavitation phenomena. The heterogeneity due to the presence of solids favours the generation of cavities based on the nucleation events and, consequently, the overall cavitational activity increases, further contributing to the synergy.

4.1 SPC Reactors

Studies on SPC degradation have generally involved batch reactors and three commonly used approaches [50–54]. One approach involves the use of a bath-type sonicator (with ultrasonic transducers at the bottom of the reactor) with a UV/light source at either the top of the vessel or immersed in the solution using quartz tubes, as shown in Fig. 8. A second approach involves the use of a horn-type sonicator in a cylindrical reactor, with UV light provided from the opposite direction, as shown in Fig. 9. The third configuration is based on sequential sonolysis (with horn) and a UV reactor (separate and not combined operation of ultrasound/UV), with a pump to drive the solution through the system, as shown in Fig. 10. It is important to understand that though these options are commonly used, most studies have been at the laboratory scale and these may not be scaled up effectively to large-scale operation. A major factor in deciding the commercial application is the need for continuous reactors. Also, an optimized design needs to be looked at based on the use of

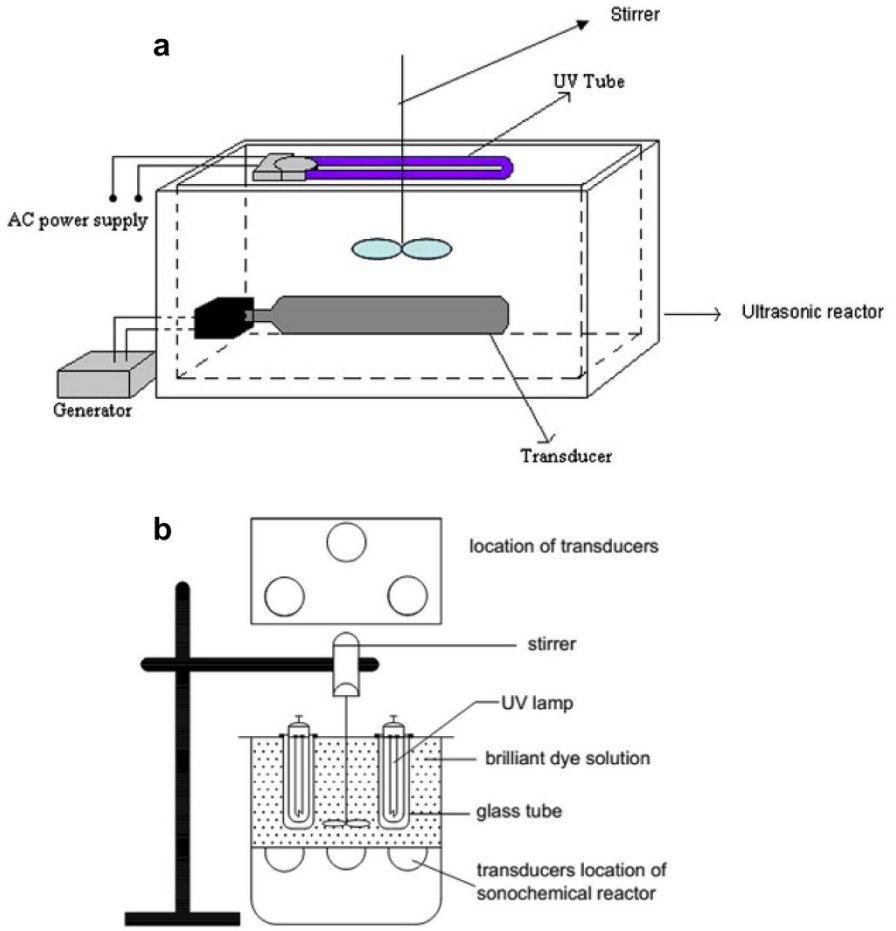

Fig. 8 Various commonly used sonophotocatalytic (SPC) reactors based on bath-type sonicator reactors with transducers and ultraviolet (*UV*) light. **a** With direct contact of ultrasound, **b** with indirect contact of ultrasound. Adopted from Mishra and Gogate [50] and Gole et al. [51]

multiple transducers for ultrasound and multiple UV lights. There are some configurations for continuous flow reactors, although these are not commonly reported for research purposes [55]. The important parameter in the design is the position and number of UV light sources and the transducers. In addition, the power dissipation per unit volume of the reactor also needs to be properly chosen.

Some of the guidelines to be taken into consideration for the optimum design of combination reactors are as follows:

1. Select lower frequencies of irradiation (typically in the range of 20 to 200 kHz) so as to have dominant physical effects that can help in enhancing the mass transfer rates and also in cleaning the catalyst. In addition, there will always be some contribution to the chemical effects of hydroxyl radical formation.

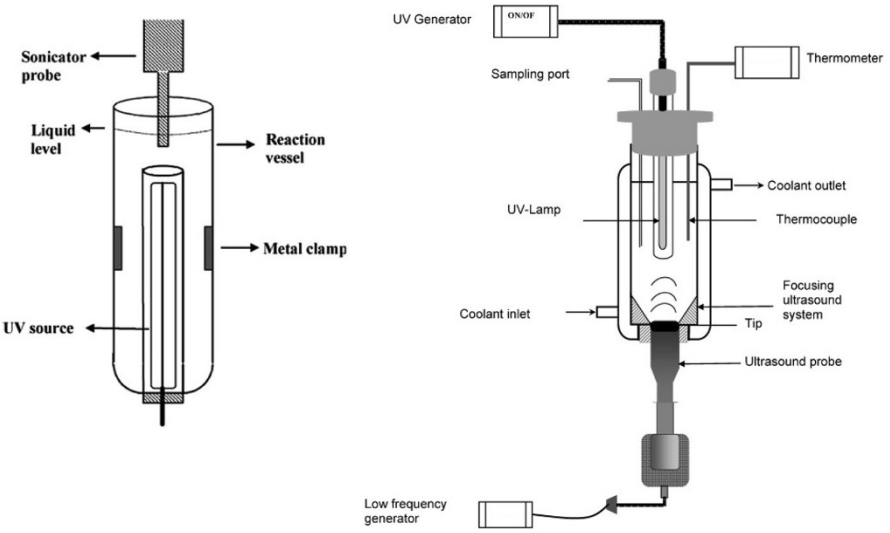

Fig. 9 Various commonly used SPC reactors based on the horn-type ultrasonicator in combination with UV light. Adopted from Taghizadeh and Abddlahi [52] and Ahmedchekkat et al. [53]

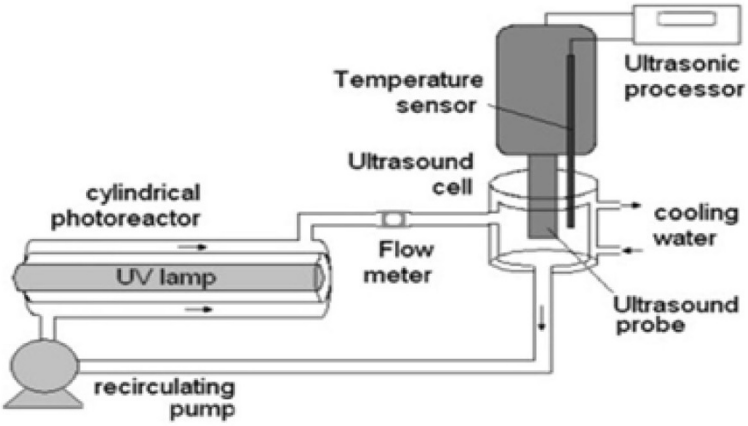

Fig. 10 Configuration of SPC reactors based on sequential sonolysis (horn-type sonicator) and photolysis (UV light) reactor. Adopted from González AS and Martínez [54]

2. It is better to have multiple transducers so that the cavitationally active volume can be on a higher side. This will also allow operating at a lower intensity of irradiation, resulting in a more intense collapse of cavities.
3. It is recommended to select multiple frequencies of irradiation that can give similar contributions of physical and chemical effects (e.g. a combination of 20 kHz with 200 kHz would be ideal). Also, the frequencies can be tuned to give resonant and standing wave effects that drive a maximum intensity of cavitational collapse.

4. It is better to use simultaneous ultrasound and UV or solar irradiations so that synergism can be obtained. This operation will also ensure that the catalyst is kept clean during the entire operation, resulting in higher degradation efficacies.
5. For the UV irradiation, it is better to use designs that yield a uniform distribution of the incident lights. Annular locations of UV and ultrasonic irradiation sources would be a good geometry to look at [55].
6. Large-scale designs can also involve the inclusion of mechanical mixing, especially when a slurry-type operation is looked at. This will also allow the introduction of gases or solid catalysts as radical promoters to provide overall higher oxidation capacity.

A possible model design based on the combination of solar and/or UV irradiations with multiple transducers is shown in Fig. 11. The ultrasound part of the system is based on a large tank-type reactor equipped with transducers at the bottom (typical cleaning tank or ultrasonic bath-type system) and on the sides (parallel plate-type system offering the possibility of creating standing waves). The pitch of the arrangement of the transducers at the bottom of the reactor can be such that a uniform distribution of the incident sound energy is obtained. The photocatalytic part of the system can be mainly based on the concentrating parabolic-type reflectors suitable for application involving direct sunlight. In addition, mercury vapour-based UV lamps can be introduced into the annular space or directly dipped in the effluent, with adequate protection provided by the quartz tube being a necessity. The

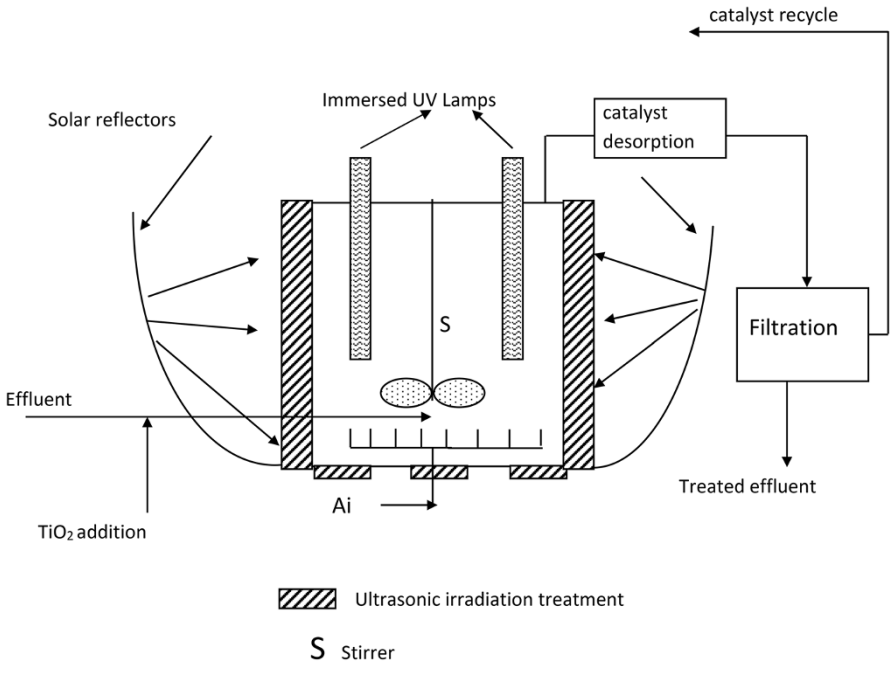

Fig. 11 Schematic representation of the model SPC reactor

immersed tubes should be at a location where there is no interference with the passage of the ultrasound. The system can be tuned to use the appropriate combination of solar and UV irradiations, depending on the operating conditions (incident intensity of solar irradiation, initial loading of the effluent, etc.). The irradiation time for UV irradiations can be adjusted to a minimum based on the composition of the effluent, which should result in savings due to the maximum use of natural resources. Agitation would be required so as to appropriately distribute the solid catalyst in suspension as well as to achieve mixing of any supporting oxidants introduced in the system. The proposed design should offer flexibility in both batch and continuous modes of operation, depending on the application to a specific effluent treatment plant.

4.2 Synergy Index

The synergy index is an important factor governing the efficacy of the hybrid processes, and it has been quantitatively measured in most of the studies conducted to date. The value of this index provides a quantitative estimate of the enhancement of performance by using the combination of sonolysis with photocatalysis. Synergy is measured using the rate constants obtained for US + catalyst, UV + catalyst and the SPC oxidation process; however, there are variations in the calculations based on the individual processes studied [49]. The general representation of the synergy index can be given as:

$$\text{Synergy Index} = \frac{K_{\text{US+UV+Catalyst}}}{K_{\text{US or US+Catalyst}} + K_{\text{UV+Catalyst}}},$$

where K is the rate constant for the specific processes mentioned in the subscript in the equation. For the process to be synergistic, or for a positive enhancement using combinations, the synergy index has to be more than unity. The actual value of the synergy index has been seen to strongly depend on the type of pollutant, mostly on the rate of utilization of the generated hydroxyl radicals by the pollutants depending on the specific reactivity. For example, the kinetic rate constant reported for the combined US + UV + TiO_2 approach applied for the degradation of ofloxacin was 0.1054 min^{-1}, whereas the combined rate constants for the individual approaches were 0.0916 min^{-1}, giving an synergistic index of 1.15 [56]. In another study on the degradation of rhodamine B [57], a synergy index of 2.76 was reported for the combined operation at the optimum ultrasonic operating condition of a power of 210 W. Sunasee et al. [58] reported a synergy index of 2.2 for the degradation of bisphenol A using ultrasound at the optimum power of 50 W and TiO_2 (Degussa P25) as the photocatalyst. Vinoth et al. [59] studied the SPC degradation of methyl orange as the model pollutant using TiO_2–NiO photocatalysts obtained with different NiO loading. These authors reported that under optimum 10 wt% NiO loading, a synergy index of 4.8 was obtained for the combination approach applied using the diffused sunlight [59]. For selecting the possible combination of ultrasound with photocatalysis, the synergy index needs to be established based on feasibility studies

performed at the laboratory scale, before the actual application at the commercial level depending on the cost–benefit analysis.

4.3 Overview of Reported Studies on SPC Degradation and Guidelines for Operating Conditions

A number of recent studies on SPC degradation [60–93] are summarized in Table 1 in terms of the operating conditions applied for sonolysis and photocatalysis, the pollutant studied and the main results obtained in the work. Some of the representative cases for the most commonly applied catalysts, such as TiO_2 and ZnO, are discussed in the following subsections to provide a better insight into the expected intensification and controlling mechanisms.

4.3.1 Use of TiO_2 Catalyst

Neppolian et al. [94] studied both the synthesis of the catalyst and subsequent degradation of 4-chlorophenol using ultrasound combined with photocatalysis. TiO_2, GO (graphene oxide)–TiO_2 and Pt–GO–TiO_2 were sonochemically synthesized and compared for their SPC degradation efficiency. The results clearly established that the frequency of ultrasonic irradiation was an important factor in determining the extent of degradation and that the effect was not synergistic, but additive. Platinum-doped GO–TiO_2 showed the best degradation performance for 4-chlorophenol at acidic pH [94]. A similar additive effect was seen for the SPC degradation of diclofenac using Fe–TiO_2 [95]. The observed effect, i.e. additive or synergistic, depends strongly on the pollutant in question. A synergistic effect was reported for the use of gold-doped TiO_2 in the SPC degradation of simazine, a herbicide, with 1.38- to 1.68-fold enhanced mineralization for the combined approach compared to the sonochemical and photocatalytic processes separately [96]. The reported trends for the kinetic rate constant (K) obtained for different processes as a function of catalyst loading are shown in Fig. 12. This graph shows that the rate constant of degradation reached an optimum with respect to the catalyst loading and also that the rate constant for the combination approach was higher than that for the individual processes separately. The results for the mineralization of simazine reported in the study using the various approaches in the absence and presence of Au–TiO_2 (1.5 g/L as the optimum loading) confirmed the role of the catalyst in enhancing the mineralization and also the better efficacy of the combination approach. Another study on a low-cost Fe–TiO_2 photocatalyst demonstrated a total decolourization of Orange II dye using sonophotocatalysis in the visible light spectrum [84]. The study also confirmed the synergistic effects of the combination of ultrasound and UV irradiations. Studies in which different ultrasonic frequencies (250, 500 and 1000 kHz) were used confirmed that the best results were obtained at 500 kHz. Test results also established that total decolourization is achieved by the combined process based on visible light, without any formation of hazardous byproducts. A recent study reported that along with the increase in the final degradation percentage of oflaxcin, the rate of degradation was also higher in SPC oxidation due to the faster formation

Table 1 Summary of different published studies on the sonophotocatalytic treatment of wastewaters containing hazardous/toxic pollutants

Pollutant	Catalyst	Sonication	Photolysis	Degradation performance	References
1,4-Dichlorobenzene (1,4-DCB)	TiO_2 (0.1 g/L)	Two ultrasonic transducers (20 kHz, 20 W, 40 W)	Two iron halogenide lamps (550 W, 640 W, 340–400 nm)	Three-fold higher degradation as compared to individual sonolysis	[60]
4-Chlorophenol	Bi_2O_3–$TiZrO_4$ catalyst (50–150 mg/60 mL)	Ultrasonic horn (20 kHz)	Xe lamp (300 W, 200–800 nm)	Visible light SPC was the most efficient as compared to individual processes, Good synergy. The solution pH did not affect SPC	[61]
Acid Blue 113 (AB113)	Gd^{3+}, Nd^{3+}, Y^{3+}-TiO_2 (1 mg/L)	Ultrasonic horn (42 kHz)	UV lamp ($\geq$420 nm)	1.4-fold (synergy index) increased rate of degradation as compared to individual process. The degradation rate was dominated by hydroxyl radicals, oxygen vacancies and oxide oxidation states. Y^{3+}-TiO_2 demonstrated the maximum SPC activity	[62]
Acid Yellow 23 dye	Fe/ZnO composite nanocatalyst (1 g/L)	Titanium probe sonicator horn (20 kHz, 60 W)	UV tungsten lamp (4 W)	Highest degradation of 97.6% with Fe-ZnO; very high synergy compared to sonolysis or photolysis. 53% degradation in real textile effluent. H_2O_2 addition provided higher degradation	[63]

Table 1 (continued)

Pollutant	Catalyst	Sonication	Photolysis	Degradation performance	References
Alachlor	TiO_2 (anatase, anatase and rutile mixture) (0.01–0.1 g/L), ZnO (0.05–0.3 g/L)	Ultrasonic horn (20 kHz, 120 W)	Two UV–C lamps (254 nm)	Complete degradation and maximum rate for SPC. TiO_2 (mixture of anatase and rutile) demonstrated better activity than ZnO and TiO_2-anatase	[64]
Aldehydes	TiO_2 (1 g/L)	Sonicator (200 kHz, 200 W)	UV-A (365 nm, 6.3 W)	SPC yielded enhanced degradation at higher catalyst concentrations. Synergistic results	[65]
Basic Violet 1 and Basic Green 4	Cu–ZnO (0.2 g/L)	Ultrasonic bath (40 kHz)	Visible light tungsten filament lamp 200 W	95–100% degradation of dye was observed at pH 10, H_2O_2 addition and 0.2 g of catalyst. Ultrasound was dominating in the synergistic effect	[66]
Bismarck Brown G	TiO_2, Fe doped TiO_2, ZVI doped TiO_2 (0.1–1 g/L)	Transducer sonicator (20 kHz, 100 W)	UV lamp (4 W, 256 nm)	Maximum colour degradation in the presence of Fe (0)-doped TiO_2. Highest degradation rate with argon gas bubbling	[67]
Bisphenol-A (BPA)	TiO_2 (0.05 g/L)	Ultrasonic bath (300 kHz, 80 W)	Solar range lamp (300–800 nm, 830 W/m^2)	The highest synergy observed at low catalyst loading (0.05 g/L) in 4 h. 62% DOC reduction, 6 and 12% of DOC for individual sonolysis and photolysis	[68]

Table 1 (continued)

Pollutant	Catalyst	Sonication	Photolysis	Degradation performance	References
Bisphenol-A (BPA)	Graphitic carbon nitride ($g\text{-}C_3N_4$, GCN) 0.05 g/L	Ultrasonic horn (35 kHz 50 W)	Visible light tungsten halogen lamp 500 W	More than 60% BPA removed at acidic pH. Rate follows Vis-L/US/GCN > US/GCN > Vis-L/US ≈ Vis-L/US/P25 > Vis-L/GCN > US > Vis-L. SPC could overcome discrete problems in individual degradation processes. High synergy	[69]
Carbamazepine	TiO_2 (500–3000 mg/L)	Ultrasonic horn (digital Sonifier 450 Branson model, 20 kHz)	UV A (9 W power) and simulated solar radiation	Solar had lower degradation efficiency than UV A. Less or no effect of addition of H_2O_2. 82% maximum degradation under UV A	[70]
Chitason	TiO_2 nanocatalyst (0.1–0.6 g/L)	Ultrasonic horn (24 kHz, 100 W)	8 W UV lamp 254 nm	Highest rate constant for US + UV at 0.6 g/L catalyst loading. Up to 53% synergy achieved. 80% total degradation at optimum conditions	[53]
Diazinon	Fe-TiO_2 nanocatalyst (0.4 g/L)	Ultrasonic bath (37 kHz, power = 100 W)	Low pressure mercury lamps (45 cm, 15 W)	Synergistic effect as compared to individual processes. Higher degradation than bare TiO_2. Highest removal efficiency of 85%	[71]

Table 1 (continued)

Pollutant	Catalyst	Sonication	Photolysis	Degradation performance	References
Dichlorvos (DDVP)	$Fe_3O_4/SiO_2/TiO_2$ (0.2 g/L)	Transducer sonicator (20 kHz, 200 W)	UV lamp (500 W, 254 nm)	Higher COD removal by SPC than individual processes. Photocatalytic activity remains unchanged even after several uses	[72]
Diclofenac (DFC) and ibuprofen (IBP)	TiO_2 (500 mg/L)	Ultrasonic horn (20 kHz, 3.5–8.4 W/cm^2)	Xenon arc lamp (1 kW, <290 nm) and UV-A lamp (9 W, 350–400 nm)	SPC achieved a higher degradation of 85% (IBP) and 95% (DCF) as compared to the individual sonochemical treatment and photocatalysis	[73]
Diethyl phthalate (DEP)	TiO_2	Ultrasonic bath and ultrasonic horn (35, 283, 450 and 935 kHz, 65–70 W)	Four UV lamps (10.5 W, 254 nm)	Formation of H_2O_2 by sonication and UV was the reason for enhanced degradation rates at 283 kHz. SPC reported the best degradation	[74]
Dinitrotoluenes (DNT) and trinitrotoluene	TiO_2 (1 g/L)	Ultrasonic transducer (20 kHz, 800 W)	Twelve low pressure mercury vapor lamps (8 W, 254 nm)	Complete elimination of DNT observed under the combination approach	[75]
Direct Blue 71	ZnO (0–2 g/L)	Ultrasonic bath (20 kHz, 95 W)	UV-C (254 nm, 4.4 mW/cm^2)	Decolorization improved by SPC in the presence of ZnO catalyst. A synergistic enhancement in the degradation rate for combination than individual processes. Lower pH, higher catalyst concentration and low dye concentration were favourable conditions	[76]

Table 1 (continued)

Pollutant	Catalyst	Sonication	Photolysis	Degradation performance	References
Dodecylbenzenesulfonate (DBS)	Pt-GO-TiO_2 (100 mg/60 mL)	Ultrasonic bath (215 kHz, 55 mW/L)	Xe Arc lamp (300 W, 200–800 nm)	SPC demonstrated threefold enhancement using Pt–GO–TiO_2 photocatalyst	[77]
Eosin B	Cobalt-iron oxide powder (300 mg/250 mL)	Ultrasonic bath (500 W)	Solar light irradiation	Degradation was 78, 82, 83 and 87% under microwave, photocatalysis, sonocatalysis and SPC, respectively. Only minor improvement reported	[78]
Formetanate hydrochloride	TiO_2 (1 g/L), Iron (III) nitrate nonahydrate	Ultrasonic transducer (213 kHz, 55 mW/mL as the power density)	Xenon lamp (450 W)	Negative effect was observed for SPC (synergy index was 0.7). Better synergy of 1.6 was observed with Fe^{3+}-mediated SPC	[79]
Methyl Orange	CuO-TiO_2/rGO (graphene oxide) (1 mg/mL)	Ultrasonic bath (40 kHz)	UV light irradiation	Degradation of 99% in 90 min. Synergy factor of 3.7. 1.5% Cu and 2% GO was optimum loading. Photocatalyst reused more than 5 times	[80]
Naphthol Blue Black dye	1:7 Fe-TiO_2 (2.2 g/L)	Ultrasonic bath (36 kHz, 200 W)	Phillips UV C 256 nm, 4 W	96% degradation achieved with SPC process. Degradation dominant in acidic medium. Synergistic removal as compared to sonolysis and photolysis. Doping enhances SPC extent of degradation	[81]

Table 1 (continued)

Pollutant	Catalyst	Sonication	Photolysis	Degradation performance	References
Nigrosene dye	N-doped ZnO, Bare ZnO (4 g/L)	Ultrasonic bath (40 kHz, 200 W)	Tungsten Lamp (60 mW/cm^2)	92% degradation after 90 min. Optimum condition was a neutral pH. Highest rate of degradation for SPC. Use of solar irradiation was better than UV irradiation	[82]
Norflurazon	TiO_2, ZnO and Au–ZnO (1 g/L)	Ultrasoic bath (42 kHz)	> 420 nm wavelength illuminator	Increased rate for sonophotocatalysis as compared to individual processes with catalyst activity as Au-ZnO > ZnO > TiO_2. 2.5–3.5 fold increase in degradation extent with combined process	[83]
Orange II dye	Fe_2O_3-TiO_2 nanocatalyst (0.3 mg/mL)	Ultrasonic bath (42 kHz, 170 W)	UV LED lamp (5 W), Visible range LED lamp (50 W)	Visible light outperfomed UV irradiation. Synergistic effect observed as compared to individual processes giving complete removal	[84]
Perfluorooctanoic acid (PFOA)	Powdered titanium dioxide (0.66 g/L)	Ultrasonic transducer (40 kHz, 500 W)	Low pressure mercury lamp (16 W, 254 nm)	pH 10 was the best. 60–70% degradation but 7 h of treatment. Sol–gel based TiO_2 performed better	[85]

Table 1 (continued)

Pollutant	Catalyst	Sonication	Photolysis	Degradation performance	References
Phenol	ZnO and TiO_2 (0.1 g/100 mL)	Ultrasonic bath (40 kHz, 100 W)	Mercury vapor quartz lamp (400 W)	A maximum of 85% degradation by using ZnO, higher compared to 65% for TiO_2 after 2 h. A synergy value of 1.25 and 1.22 in case of ZnO and TiO_2, respectively	[86]
P-Nitrophenol	TiO_2 (0.5–4 g/L)	Ultrasonic bath (25 kHz, 1 kW)	UV lamp (11 W, 350–450 nm)	Acidic pH, low initial concentration and an optimum concentration of photocatalyst resulted in a 94.6% degradation	[51]
Reactive Blue 19	S-TiO_2 (0.1–1 mg/mL)	Ultrasonic bath (35 kHz, 300 W)	200 W Fornix Phillips bulp visible light	Synergistic effect as compared to all individual processes. 90% as best degradation in 120 min. Catalytic efficiency $TiO_2 < 1$ (wt%) S-$TiO_2 < 3$% S-$TiO_2 < 5$% S-TiO_2	[87]
Rhodamine 6G	CuO and TiO_2 (1.5–4.5 g/L)	Ultrasonic bath (50 kHz, 170 W)	UV lamp (9 W)	With SPC 63.3% was degraded using 4 g/L catalyst. There was a slight increase in rate of degradation with additives such as methanol at low concentration	[88]

Table 1 (continued)

Pollutant	Catalyst	Sonication	Photolysis	Degradation performance	References
Rhodamine B	TiO_2 (0.5–4 g/L)	Transducer-type sonicator (25 kHz, 1 kW)	UV lamp (11 W)	92.9% degradation of Rhodamine B in 150 min. Much higher than US or UV/TiO_2. Addition of H_2O_2 and CCl_4 resulted in a drastic change in the rate of degradation	[89]
Rhodamine B	ZnO micro- and nano-particles (0.5 mg/mL)	Ultrasonic bath (40 or 57 kHz, 1 W/cm^2)	White Lamp (140 W/m^2)	About 8-fold increase in rate for SPC. Substantial decrease in half-life times. 100% degradation within 10 min as compared to 180 min for sonolytic process	[90]
Salycylic acid	ZnO (0.2 g/500 mL)	Ultrasonic bath (35 kHz, 300 W)	Phillips UV Lamp 40 W	Best result for SPC H_2O_2 oxidation. Effect of H_2O_2 was dominant. High degradation and synergy observed	[91]
Tetracycline	Au/B-TiO_2/rGO (10 mg/40 mL)	Ultrasonic bath (40 kHz, 600 W)	Visible light halogen lamp (300 W)	Synergistic effect seen. 100% degradation with SPC, much higher as compared to individual process. Excellent charge transport by GO	[92]
Trypan Blue (TB) and Vesuvine (VS)	Ag_3PO_4/Bi_2S_3 (0.15–0.35 g/L)	Ultrasonic bath (25 kHz)	Blue LED lamp (14.4 W/m^2, 465–470 nm)	SPC degradation for TB and VS was 98.44 and 99.36%, respectively. Synergy index was 2.53	[93]

DOC Dissolved organic carbon, *GO* graphene oxide, *LED* light-emitting diode, *SPC* Sonophotocatalysis, *US* ultrasound, *UV* ultraviolet

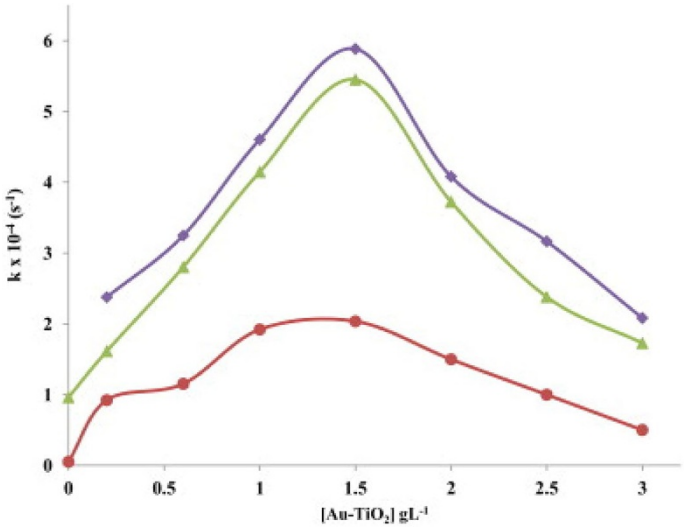

Fig. 12 Data on variation of the kinetic rate constant (*K*) with Au–TiO_2 loading for the SPC (filled diamonds), sonocatalytic (filled triangles) and photocatalytic (filled circles) degradation of the herbicide simazine. Reproduced from Sathishkumar et al. [96]

of oxidizing radicals [56]. The data shown in Fig. 13 in terms of the observed rate constants clearly establish the synergy for the combined operation. The data also confirm the utility of the catalyst in enhancing the rate of degradation, especially in the ultrasound-assisted approach. It was also reported in this study that ofloxacin degradation efficacy could be improved with addition of the H_2O_2 and that the optimum level was 0.14 mM/L for the best results.

The observed effects for the combination can be strongly dependent on the operating conditions, which determine the rate of utilization of the generated

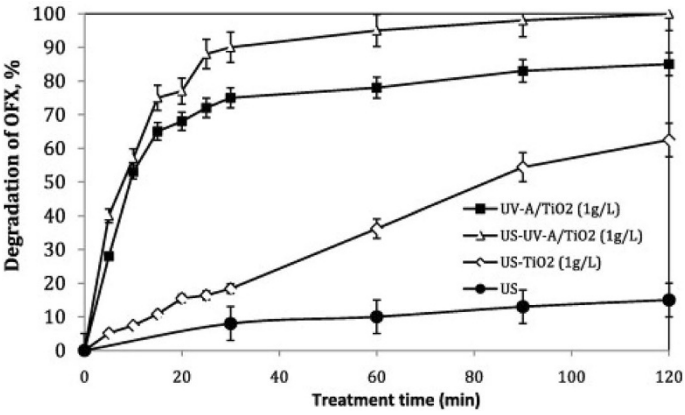

Fig. 13 Data for the effect of the treatment process on the degradation of ofloxacin (*OFX*). Data reproduced from Hapeshi et al. [56]

hydroxyl radicals as well as the form of the pollutant in the medium. A detailed study on the degradation of trichloroacetic acid using a UV/TiO_2/US combined process revealed that the maximum extent of degradation for the combined process largely depended on the pH and the speciation of the parent compound [97]. In all cases, however, SPC degradation was always showing better efficacy than sonolysis or photolysis alone. A study performed by Tabasideh et al. [71] on the degradation of diazinon showed that maximum degradation using the SPC process with iron-doped TiO_2 was obtained under acidic conditions (pH 5.5), while a much lower degradation was observed in strongly alkaline conditions (pH 9.5). These authors also noted that the effect of pH was dominant in the case of photocatalytic oxidation alone and less significant in the case of SPC oxidation (see Fig. 14).

Catalyst loading also plays a major role in determining the efficacy of SPC oxidation. For example, Tabasideh et al. [71] studied the effect of catalyst loading over the range of 0.2–0.6 g/L and reported that optimum catalyst loading did exist at 0.4 g/L. These authors reported that significantly higher loading of the catalyst interfered with both the passage of ultrasonic energy and the transmission of light energy, resulting in detrimental effects. In addition, the negative effect of catalyst loading beyond the optimum was more dominant in the case of only sonocatalytic oxidation as compared to SPC oxidation [71] (see Fig. 15).

Several studies have also focussed on the effect of doping of the catalyst on SPC processes. Reddy et al. [81] studied various iron loadings and reported that 96% degradation of naphthol-blue-black dye was observed at the optimum loading. Multi-walled carbon nanotubes (CNTs) deposited with Fe–TiO_2 under both visible and UV light showed enhanced formation of reactive radicals and prevention of electron–hole recombination, with sonophotocatalysis giving the better results [98]. These results show that the use of doping or composites definitely helps in enhancing catalyst activity as compared to bare forms of the oxide catalyst.

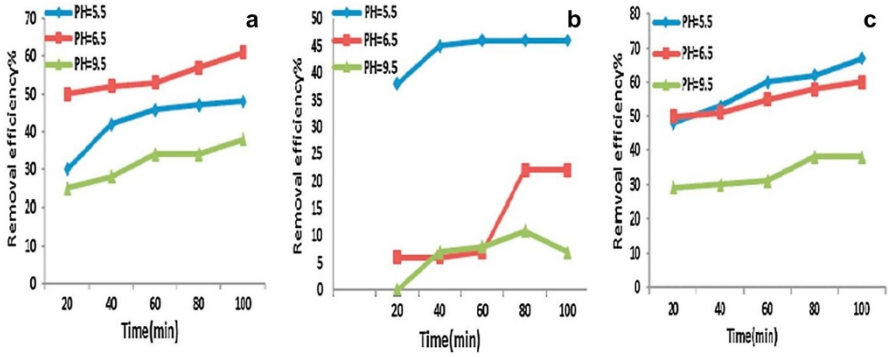

Fig. 14 Data for the effect of pH on the degradation of diazinon in presence of Fe-doped TiO_2 using photocatalytic (**a**), sonocatalytic (**b**) and SPC (**c**) treatment approaches. Data reproduced from Tabasideh et al. [71]

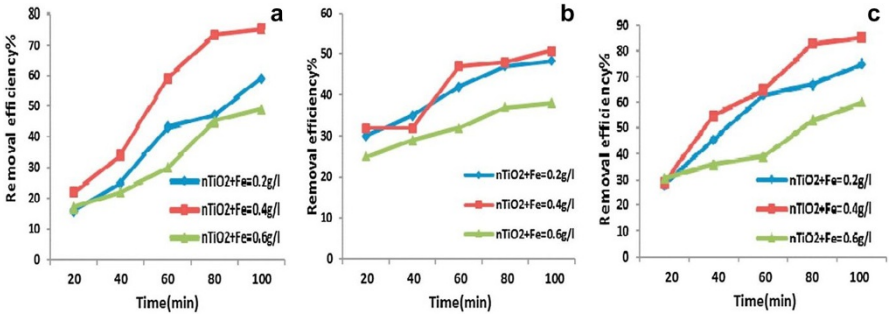

Fig. 15 Data for the effect of catalyst loading on the degradation of diazinon in presence of Fe-doped TiO_2 using photocatalytic (**a**), sonocatalytic (**b**) and SPC (**c**) treatment approaches. Data reproduced from Tabasideh et al. [71]

4.3.2 Use of ZnO Catalyst

Zinc oxide has been reported to be an active catalyst for the SPC (UV + US) degradation of phenol [86]. The synergistic effect was demonstrated, with about 89% degradation achieved, which was higher than that achieved by sonochemical and photocatalytic degradation separately. Comparison of the two catalysts used in the work, ZnO and TiO_2, confirmed better efficacy for the ZnO catalyst (Fig. 16) in all treatment approaches, which the authors attributed to its higher ability to absorb energy in the spectrum. Acidic pH was reported to be preferred for SPC degradation of phenol due to the increased formation of hydroxyl radicals [86]. In two other studies, heterogeneous ZnO-based SPC oxidation was reported to degrade 98% of the

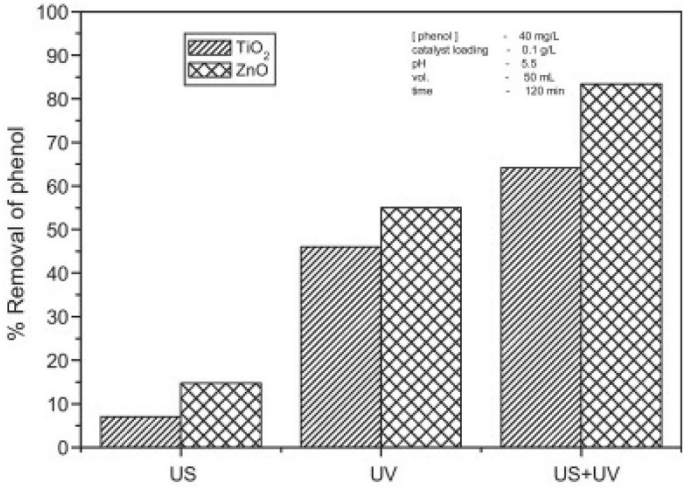

Fig. 16 Effect of type of catalyst and the treatment approach on the degradation of phenol. Data reproduced from Anju et al. [86]

dye using 95 W of ultrasonic power for only 20 min [76], and ZnO-decorated CNTs showed 49% rhodamine B degradation under SPC conditions [99]. The effect in the latter study was reported to be pronounced due to the prevention of electron hole recombination as a result of the presence of CNTs [99]. A synergistic effect was also reported for the use of Pr-doped ZnO catalysis combined with sonochemistry, leading up to 89% degradation for the sonocatalytic degradation of AR17 dye [100].

4.3.3 Guidelines for the Operating Parameters

Based on the critical analysis of the literature and personal expertise in the research field, the following useful guidelines for the selection of the operating parameters can be given so as to maximize the degradation or mineralization efficacy:

1. Operating pH plays a key role in deciding the efficacy of treatment. In general, acidic conditions are favoured although it also depends on the dissociation coefficient of the pollutants present in the system. It is also possible that the effects are less pronounced in the combined approach, and exact intensification should be quantified before deciding on the pH adjustment. This is even more important in the case of commercial effluent treatment schemes as usually the discharge conditions mandate neutral pH conditions.
2. Catalyst loading needs to be properly decided so that all of the catalyst is in proper suspension in the reactor and that it is also not affecting the passage of the incident irradiations in the reactor. An optimum catalyst loading usually exists, which can be established using laboratory studies for the specific applications in question.
3. Use of radical promoters, such as hydrogen peroxide or persulphate, can bestow beneficial results, especially when the free radical attack is the controlling mechanism for oxidation and the rate of reaction between the radicals and pollutant molecules is also substantially high. This is important as the generated hydroxyl radicals must be utilized quickly so as to get any beneficial results. Use of persulphate offers simultaneously acting oxidation mechanism based on the sulphate radicals.
4. The observed synergy for the combined approach as compared to individual approaches is also dependent on the pollutants in question. Specifically, if the sonochemical oxidation is based on the pyrolytic mechanism of oxidation, significantly beneficial results may not be obtained as the combination is typically accelerating the free radical formation. This has also been confirmed based on the reported data for the synergy in Table 1.
5. Use of doping and composites allow the utilization of the solar bandwidth which can result in a cost-effective operation. Consequently, the utilization of such catalyst forms is recommended as compared to the traditionally used single oxide forms. This is also important to obtain a catalyst that can be recycled back into the operation, leading to favourable economics for the treatment system.
6. Use of gases has been reported to enhance the degradation efficacy, especially in terms of enhanced sonochemical activity and also the production of a higher quantum of radicals. Taking the operating costs into consideration, especially

those on the commercial scale, the use of gases such as air is recommended in contrast to argon which has been reported to be quite effective by researchers on the laboratory scale.

7. It will be important to select optimum power dissipation for both the ultrasonic and UV irradiations from the perspective of restricting cavitational effects to the optimum possible extent and in terms of restricting the overall costs of the treatment.

5 Concluding Remarks

The aim of this article was to demonstrate the beneficial effects of using ultrasound during the catalyst synthesis processes as well as the actual application of ultrasound in the photocatalytic oxidation. The key benefits in the catalyst synthesis process include lower particle size, higher surface area and better control over the morphology of the particles. The synthesis conditions in terms of ultrasonic power and time of application play a key role in determining the benefits and economics of the process. The application of ultrasound has been established to be beneficial for all forms of photocatalysts, including bare, composite and doped photocatalysts. Ultrasound often opens alternative synthesis routes for efficiently obtaining nanocatalysts [101] that are also active in the visible light region, making it very attractive proposition for commercial applications in wastewater treatment.

In the case of SPC treatment, it is important to note that the beneficial effects are generally observed when free radical formation and the attack of free radicals on the pollutants are the controlling mechanisms. The extent of intensification (less than the additive effect or the synergistic effect) typically depends on the pollutant in question and mostly on the utilization of the generated free radicals and the problems of catalyst poisoning in the individual operation. It should be noted that ultrasonic power is an important factor in determining the efficiency of the process, and the choice of power presents a trade-off between economic aspects and degradation efficiency. Optimum power dissipation will usually be recommended, using multiple transducers, thus giving lower intensities of irradiation. Also, operation at a lower frequency (e.g. in the range 20–100 kHz) would be more suited for ultrasound. Additional operating parameters, such as pH and temperature, also need to be optimized as these are strongly dependent on the specific pollutant in question. Typically, doped photocatalysts perform better under SPC conditions than do bare catalyst. Similarly, the enhancement of charge transfer and abatement of electron hole recombination based on modifications, such as using GO sheets or CNTs as a support for the catalyst, has an additional synergistic effect on the SPC degradation efficiency. The use of solar irradiation instead of UV light is preferable for the applicability and possibility of a scale-up of the process; using doping to enhance the light adsorption spectrum to include visible light is practical for this purpose. The addition of radical promoters, such as H_2O_2, can also be advantageous although the exact effect needs to be established for specific compounds.

Overall, the application of ultrasound offers a lucrative approach for improving the catalyst synthesis process, and the actual application of ultrasound in the

photocatalytic oxidation and tailored operation can indeed yield synergism, leading to much more effective treatment in a cost-effective manner.

References

1. Wang J, Zhuan R (2020) Degradation of antibiotics by advanced oxidation processes: an overview. Sci Total Environ 701:135023
2. Mohapatra DP, Kirpalani DM (2019) Advancement in treatment of wastewater: fate of emerging contaminants. Can J Chem Eng 97(10):2621–2631
3. Akerdi AG, Bahrami SH (2019) Application of heterogeneous nano-semiconductors for photocatalytic advanced oxidation of organic compounds: a review. J Environ Chem Eng 7(5):103283
4. Aiyer SSC, Ramachandran S, Thiruma Valavan K, Prakash Kumar BG (2015) A review of solar photocatalytic degradation of wastewater using advanced oxidation processes. J Ind Pollut Control 31(2):297–309
5. Ballari MM, Satuf ML, Alfano OM (2019) Photocatalytic reactor modeling: application to advanced oxidation processes for chemical pollution abatement. Top Curr Chem 377(5):22
6. Bhangu SK, Ashokkumar M (2016) Theory of sonochemistry. Top Curr Chem 374(4):56
7. Pokhrel N, Vabbina PK, Pala N (2016) Sonochemistry: science and engineering. Ultrason Sonochem 29:104–128
8. Chatel G (2019) Sonochemistry in nanocatalysis: the use of ultrasound from the catalyst synthesis to the catalytic reaction. Curr Opin Green Sustain Chem 15:1–6
9. Adewuyi YG (2005) Sonochemistry in environmental remediation. 2. Heterogeneous sonophotocatalytic oxidation processes for the treatment of pollutants in water. Environ Sci Technol 39(22):8557–8570
10. Wood RJ, Lee J, Bussemaker MJ (2017) A parametric review of sonochemistry: control and augmentation of sonochemical activity in aqueous solutions. Ultrason Sonochem 38:351–370
11. Gogate PR, Sutkar VS, Pandit AB (2011) Sonochemical reactors: important design and scale up considerations with a special emphasis on heterogeneous systems. Chem Eng J 166(3):1066–1082
12. Sutkar VS, Gogate PR (2009) Design aspects of sonochemical reactors: techniques for understanding cavitational activity distribution and effect of operating parameters. Chem Eng J 155(1–2):26–36
13. Pang YL, Abdullah AZ, Bhatia S (2011) Review on sonochemical methods in the presence of catalysts and chemical additives for treatment of organic pollutants in wastewater. Desalination 277(1–3):1–14
14. Dalodière E, Virot M, Moisy P, Nikitenko SI (2016) Effect of ultrasonic frequency on H_2O_2 sonochemical formation rate in aqueous nitric acid solutions in the presence of oxygen. Ultrason Sonochem 29:198–204
15. Gogate PR, Shaha S, Csoka L (2015) Intensification of cavitational activity using gases in different types of sonochemical reactors. Chem Eng J 262:1033–1042
16. Anandan S, Ashokkumar M (2010) Sonochemical preparation of monometallic, bimetallic and metal-loaded semiconductor nanoparticles. In: Pankaj, Muthupandian A (eds) Theoretical and experimental sonochemistry involving inorganic systems. Springer, Berlin, pp 151–169
17. Bagheri S, Mohd Hir ZA, Yousefi AT, Abdul Hamid SB (2015) Progress on mesoporous titanium dioxide: synthesis, modification and applications. Microporous Mesoporous Mater 218:206–222
18. Antonelli DM (1999) Synthesis of phosphorus-free mesoporous titania via templating with amine surfactants. Microporous Mesoporous Mater 30:315–319
19. Alapi T, Sipos P, Ilisz I, Wittmann G, Ambrus Z, Kiricsi I, Mogyorósi K, Dombi A (2006) Synthesis and characterization of titania photocatalysts: the influence of pretreatment on the activity. Appl Catal A Gen 303:1–8
20. Yu JC, Zhang L, Yu J (2002) Rapid synthesis of mesoporous TiO_2 with high photocatalytic activity by ultrasound-induced agglomeration. New J Chem 26:416–420
21. Ho W, Yu JC (2006) Sonochemical synthesis and visible light photocatalytic behavior of CdSe and CdSe/TiO_2 nanoparticles. J Mol Catal A Chem 247:268–274
22. Colmenares JC, Kuna E, Lisowski P (2016) Synthesis of photoactive materials by sonication: application in photocatalysis and solar cells. Top Curr Chem 374:59

23. Giannakoudakis DA, Chatel G, Colmenares JC (2020) Mechanochemical forces as a synthetic tool for zero- and one-dimensional titanium oxide-based nano-photocatalysts. Top Curr Chem 378:2
24. Magdziarz A, Colmenares JC (2017) In situ coupling of ultrasound to electro- and photo-deposition methods for materials synthesis. Molecules 22(2):216
25. Pinjari DV, Prasad K, Gogate PR, Mhaske ST, Pandit AB (2015) Synthesis of titanium dioxide by ultrasound assisted sol-gel technique: effect of calcination and sonication time. Ultrason Sonochem 23:185–191
26. Prasad K, Pinjari DV, Pandit AB, Mhaske ST (2010) Synthesis of titanium dioxide by ultrasound assisted sol-gel technique: effect of amplitude (power density) variation. Ultrason Sonochem 17:697–703
27. Yu JC, Zhang L, Yu J (2002) Direct sonochemical preparation and characterization of highly active mesoporous TiO_2 with a bicrystalline framework. Chem Mater 14:4647–4653
28. Anandan S, Sivasankar T, Lana-Villarreal T (2014) Synthesis of TiO_2/WO_3 nanoparticles via sonochemical approach for the photocatalytic degradation of methylene blue under visible light illumination. Ultrason Sonochem 21:1964–1968
29. Li D, Wang J, Li X, Liu H (2012) Effect of ultrasonic frequency on the structure and sonophotocatalytic property of CdS/TiO_2 nanocomposite. Mater Sci Semicond Proc 15:152–158
30. Shende TP, Bhanvase BA, Rathod AP, Pinjari DV, Sonawane SH (2018) Sonochemical synthesis of Graphene-Ce-TiO_2 and Graphene-Fe-TiO_2 ternary hybrid photocatalyst nanocomposite and its application in degradation of crystal violet dye. Ultrason Sonochem 41:582–589
31. Yogi C, Kojima K, Takai T, Wada N (2009) Photocatalytic degradation of methylene blue by Au-deposited TiO_2 film under UV irradiation. J Mater Sci 44:821–827
32. Jang JS, Choi SH, Kim HG, Lee JS (2008) Location and state of Pt in platinized CdS/TiO_2 photocatalysts for hydrogen production from water under visible light. J Phys Chem C 112:17200–17205
33. Ambati R, Gogate PR (2018) Ultrasound assisted synthesis of iron doped TiO_2 catalyst. Ultrason Sonochem 40:91–100
34. Stucchi M, Bianchi CL, Argirusis C, Pifferi V, Neppolian B, Cerrato G, Boffito DC (2018) Ultrasound assisted synthesis of Ag-decorated TiO_2 active in visible light. Ultrason Sonochem 40:282–288
35. Pol VG, Wildermuth G, Felsche J, Gedanken A, Calderon-Moreno J (2005) Sonochemical deposition of Au nanoparticles on titania and the significant decrease in the melting point of gold. J Nanosci Nanotechnol 5(6):975–979
36. Anandan S, Ashokkumar M (2009) Sonochemical synthesis of Au–TiO_2 nanoparticles for the sonophotocatalytic degradation of organic pollutants in aqueous environment. Ultrason Sonochem 16:316–320
37. Teh CY, Wu TY, Juan JC (2015) Facile sonochemical synthesis of N, Cl-codoped TiO_2: synthesis effects, mechanism and photocatalytic performance. Catal Today 256:365–374
38. Guo J, Zhu S, Chen Z, Li Y, Yu Z, Liu Q, Li J, Feng C, Zhang D (2011) Sonochemical synthesis of TiO_2 nanoparticles on graphene for use as photocatalyst. Ultrason Sonochem 18:1082–1090
39. Neppolian B, Celik E, Anpo M, Choi H (2008) Ultrasonic-assisted pH swing method for the synthesis of highly efficient TiO_2 nano-size photocatalysts. Catal Lett 125:183–191
40. Yayapao O, Thongtem T, Phuruangrat A, Thongtem S (2013) Sonochemical synthesis of Dy-doped ZnO nanostructures and their photocatalytic properties. J Alloys Compd 576:72–79
41. Siddiquey IA, Furusawa T, Sato M, Bahadur NM, Md. Alam M, Suzuki N (2012) Sonochemical synthesis, photocatalytic activity and optical properties of silica coated ZnO nanoparticles. Ultrason Sonochem 19:750–755
42. Lu X, Liu Z, Zhu Y, Jiang L (2011) Sonochemical synthesis and photocatalytic property of zinc oxide nanoparticles doped with magnesium(II). Mater Res Bull 46:1638–1641
43. Zhang L, Wang W, Yang J, Chen Z, Zhang W, Zhou L, Liu S (2006) Sonochemical synthesis of nanocrystallite Bi_2O_3 as a visible-light-driven photocatalyst. Appl Catal A Gen 308:105–110
44. Chen D, Yoo SH, Huang Q, Ali G, Cho SO (2012) Sonochemical synthesis of Ag/AgCl nanocubes and their efficient visible-light-driven photocatalytic performance. Chemistry 18:5192–5200
45. Meng S, Li D, Sun M, Li W, Wang J, Chen J, Fu X, Xiao G (2011) Sonochemical synthesis, characterization and photocatalytic properties of a novel cube-shaped $CaSn(OH)_6$. Catal Commun 12:972–975
46. Fulekar MH, Singh A, Dutta DP, Roy M, Ballal A, Tyagi AK (2014) Ag incorporated nano BiPO4: sonochemical synthesis, characterization and improved visible light photocatalytic properties. RSC Adv 4:10097–10107

47. Hosseinpour-Mashkani SM, Sobhani-Nasab A (2016) A simple sonochemical synthesis and characterization of $CdWO_4$ nanoparticles and its photocatalytic application. J Mater Sci Mater Electron 27:3240–3244
48. Gyawali G, Adhikari R, Joshi B, Kim TH, Rodríguez-González V, Lee SW (2013) Sonochemical synthesis of solar-light-driven Ag̊-$PbMoO_4$ photocatalyst. J Hazard Mater 263:45–51
49. Panda D, Manickam S (2017) Recent advancements in the sonophotocatalysis (SPC) and doped-sonophotocatalysis (DSPC) for the treatment of recalcitrant hazardous organic water pollutants. Ultrason Sonochem 36:481–496
50. Mishra KP, Gogate PR (2011) Intensification of sonophotocatalytic degradation of p-nitrophenol at pilot scale capacity. Ultrason Sonochem 18:739–744
51. Gole VL, Priya A, Danao SP (2017) Decolorization of brilliant green dye using immersed lamp sonophotocatalytic reactor. Appl Water Sci 7:4237–4245
52. Taghizadeh MT, Abdollahi R (2011) Sonolytic, sonocatalytic and sonophotocatalytic degradation of chitosan in the presence of TiO_2 nanoparticles. Ultrason Sonochem 18:149–157
53. Ahmedchekkat F, Medjram MS, Chiha M, Al-Bsoul AMA (2011) Sonophotocatalytic degradation of Rhodamine B using a novel reactor geometry: effect of operating conditions. Chem Eng J 178:244–251
54. González AS, Martínez SS (2008) Study of the sonophotocatalytic degradation of basic blue 9 industrial textile dye over slurry titanium dioxide and influencing factors. Ultrason Sonochem 15:1038–1042
55. Gogate PR, Pandit AB (2004) Sonophotocatalytic reactors for wastewater treatment: a critical review. AIChE J 50:1051–1079
56. Hapeshi E, Fotiou I, Fatta-Kassinos D (2013) Sonophotocatalytic treatment of ofloxacin in secondary treated effluent and elucidation of its transformation products. Chem Eng J 224:96–105
57. Lu Y, Jing H, Yu H, Zhao Y, Li Y, Huo M, Zhu S, Crittenden JC (2019) Enhanced catalytic performance of $BiVO_4$/Pt under the combination of visible-light illumination and ultrasound waves. J Taiwan Inst Chem Eng 102:133–142
58. Sunasee S, Wong KT, Lee G, Pichiah S, Ibrahim S, Park C, Kim NC, Yoon Y, Jang M (2017) Titanium dioxide-based sonophotocatalytic mineralization of bisphenol A and its intermediates. Environ Sci Pollut Res 24(18):15488–15499
59. Vinoth R, Karthik P, Devan K, Neppolian B, Ashokkumar M (2017) TiO_2–NiO p–n nanocomposite with enhanced sonophotocatalytic activity under diffused sunlight. Ultrason Sonochem 35:655–663
60. Selli E, Bianchi CL, Pirola C, Cappelletti G, Ragaini V (2008) Efficiency of 1,4-dichlorobenzene degradation in water under photolysis, photocatalysis on TiO_2 and sonolysis. J Hazard Mater 153:1136–1141
61. Neppolian B, Ciceri L, Bianchi CL, Grieser F, Ashokkumar M (2011) Sonophotocatalytic degradation of 4-chlorophenol using Bi_2O_3/$TiZrO_4$ as a visible light responsive photocatalyst. Ultrason Sonochem 18:135–139
62. Sathishkumar P, Mangalaraja RV, Rozas O, Mansilla HD, Gracia-Pinilla MA, Anandan S (2014) Low frequency ultrasound (42 kHz) assisted degradation of Acid Blue 113 in the presence of visible light driven rare earth nanoclusters loaded TiO_2 nanophotocatalysts. Ultrason Sonochem 21:1675–1681
63. Dinesh GK, Anandan S, Sivasankar T (2016) Synthesis of Fe/ZnO composite nanocatalyst and its sonophotocatalytic activity on acid yellow 23 dye and real textile effluent, Clean Tech. Environ Policy 18:1889–1903
64. Bagal MV, Gogate PR (2013) Photocatalytic and sonophotocatalytic degradation of alachlor using different photocatalyst. Adv Environ Res 2:261–277
65. Sekiguchi K, Sasaki C, Sakamoto K (2011) Synergistic effects of high-frequency ultrasound on photocatalytic degradation of aldehydes and their intermediates using TiO_2 suspension in water. Ultrason Sonochem 18:158–163
66. Shah J, Jan MR, Khitab F (2018) Sonophotocatalytic degradation of textile dyes over Cu impregnated ZnO catalyst in aqueous solution. Proc Saf Environ Prot 116:149–158
67. Dinesh GK, Anandan S, Sivasankar T (2015) Sonophotocatalytic treatment of Bismarck Brown G dye and real textile effluent using synthesized novel Fe (0)-doped TiO_2 catalyst. RSC Adv 5:10440–10451

68. Torres RA, Nieto JI, Combet E, Pétrier C, Pulgarin C (2008) Influence of TiO_2 concentration on the synergistic effect between photocatalysis and high-frequency ultrasound for organic pollutant mineralization in water. Appl Catal B Environ 80:168–175
69. Sunasee S, Leong KH, Wong KT, Lee G, Pichiah S, Nah I, Jeon B-H, Yoon Y, Jang M (2019) Sonophotocatalytic degradation of bisphenol A and its intermediates with graphitic carbon nitride. Environ Sci Pollut Res 26:1082–1093
70. Jelic A, Michael I, Achilleos A, Hapeshi E, Lambropoulou D, Perez S, Petrovic M, Fatta-Kassinos D, Barcelo D (2013) Transformation products and reaction pathways of carbamazepine during photocatalytic and sonophotocatalytic treatment. J Hazard Mater 263:177–186
71. Tabasideh S, Maleki A, Shahmoradi B, Ghahremani E, McKay G (2017) Sonophotocatalytic degradation of diazinon in aqueous solution using iron-doped TiO_2 nanoparticles. Sep Purif Technol 189:186–192
72. Lirong M, Jianjun S, Ming Z, Jie H (2014) Synthesis of magnetic sonophotocatalyst and its enhanced biodegradability of organophosphate pesticide. Bull Korean Chem Soc 35:3521–3526
73. Michael I, Achilleos A, Lambropoulou D, Torrens VO, Pérez S, Petrović M, Barceló D, Fatta-Kassinos D (2014) Proposed transformation pathway and evolution profile of diclofenac and ibuprofen transformation products during (sono)photocatalysis. Appl Catal B Environ 147:1015–1027
74. Na S, Ahn Y-G, Cui M, Khim J (2012) Significant diethyl phthalate (DEP) degradation by combined advanced oxidation process in aqueous solution. J Environ Manag 101:104–110
75. Chen W-S, Huang S-C (2011) Sonophotocatalytic degradation of dinitrotoluenes and trinitrotoluene in industrial wastewater. Chem Eng J 172:944–951
76. Ertugay N, Acar FN (2014) The degradation of Direct Blue 71 by sono, photo and sonophotocatalytic oxidation in the presence of ZnO nanocatalyst. Appl Surf Sci 318:121–126
77. Neppolian B, Bruno A, Bianchi CL, Ashokkumar M (2012) Graphene oxide based Pt–TiO_2 photocatalyst: ultrasound assisted synthesis, characterization and catalytic efficiency. Ultrason Sonochem 19:9–15
78. Sharfalddin A, Alzahrani E, Alamoudi M (2016) Micro, sono, photocatalytic degradation of eosin B using ferric oxide doped with cobalt. Am Chem Sci J 13:1–13
79. Madhavan J, Grieser F, Ashokkumar M (2010) Degradation of formetanate hydrochloride by combined advanced oxidation processes. Sep Purif Technol 73:409–414
80. Babu SG, Karthik P, John MC, Lakhera SK, Ashokkumar M, Khim J, Neppolian B (2019) Synergistic effect of sono-photocatalytic process for the degradation of organic pollutants using CuO–TiO_2/rGO. Ultrason Sonochem 50:218–223
81. Reddy DR, Dinesh GK, Anandan S, Sivasankar T (2016) Sonophotocatalytic treatment of Naphthol Blue Black dye and real textile wastewater using synthesized Fe doped TiO_2. Chem Eng Proc 99:10–18
82. Kumawat S, Meghwal K, Kumar S, Ameta R, Ameta C (2019) Kinetics of sonophotocatalytic degradation of an anionic dye nigrosine with doped and undoped zinc oxide. Water Sci Technol 80(8):1466–1475
83. Sathishkumar P, Mangalaraja RV, Rozas O, Vergara C, Mansilla HD, Gracia-Pinilla MA, Anandan S (2016) Sonophotocatalytic mineralization of Norflurazon in aqueous environment. Chemosphere 146:216–225
84. May-Lozano M, Mendoza-Escamilla V, Rojas-García E, López-Medina R, Rivadeneyra-Romero G, Martinez-Delgadillo SA (2017) Sonophotocatalytic degradation of Orange II dye using low cost photocatalyst. J Clean Prod 148:836–844
85. Panchangam SC, Lin AY-C, Tsai J-H, Lin C-F (2009) Sonication-assisted photocatalytic decomposition of perfluorooctanoic acid. Chemosphere 75:654–660
86. Anju SG, Yesodharan S, Yesodharan EP (2012) Zinc oxide mediated sonophotocatalytic degradation of phenol in water. Chem Eng J 189–190:84–93
87. Khan MAN, Siddique M, Wahid F, Khan R (2015) Removal of reactive blue 19 dye by sono, photo and sonophotocatalytic oxidation using visible light. Ultrason Sonochem 26:370–377
88. Bokhale NB, Bomble SD, Dalbhanjan RR, Mahale DD, Hinge SP, Banerjee BS, Mohod AV, Gogate PR (2014) Sonocatalytic and sonophotocatalytic degradation of rhodamine 6G containing wastewaters. Ultrason Sonochem 21:1797–1804
89. Mishra KP, Gogate PR (2011) Intensification of degradation of aqueous solutions of rhodamine B using sonochemical reactors at operating capacity of 7 L. J Environ Manag 92:1972–1977

90. Lops C, Ancona A, Di Cesare K, Dumontel B, Garino N, Canavese G, Hérnandez S, Cauda V (2019) Sonophotocatalytic degradation mechanisms of Rhodamine B dye via radicals generation by micro- and nano-particles of ZnO. Appl Catal B Environ 243:629–640
91. Fatimah I, Pradita RY, Nurfalinda A (2017) Study on ZnO catalytic activity in salycilic acid degradation by sonophotocatalysis. Chem Eng Trans 56:1651–1656
92. Vinesh V, Shaheer ARM, Neppolian B (2019) Reduced graphene oxide (rGO) supported electron deficient B-doped TiO_2 (Au/B-TiO_2/rGO) nanocomposite: an efficient visible light sonophotocatalyst for the degradation of Tetracycline (TC). Ultrason Sonochem 50:302–310
93. Mosleh S, Rahimi MR, Ghaedi M, Dashtian K (2016) Sonophotocatalytic degradation of trypan blue and vesuvine dyes in the presence of blue light active photocatalyst of Ag_3PO_4/Bi_2S_3-HKUST-1-MOF: central composite optimization and synergistic effect study. Ultrason Sonochem 32:387–397
94. Neppolian B, Vinoth R, Bianchi C, Ashokkumar M (2015) Degradation of 4-chlorophenol and NO_x using ultrasonically synthesized TiO_2 loaded graphene oxide photocatalysts. Sci Adv Mater 7:1149–1155
95. Madhavan J, Kumar PSS, Anandan S, Zhou M, Grieser F, Ashokkumar M (2010) Ultrasound assisted photocatalytic degradation of diclofenac in an aqueous environment. Chemosphere 80:747–752
96. Sathishkumar P, Mangalaraja RV, Mansilla HD, Gracia-Pinilla MA, Anandan S (2014) Sonophotocatalytic (42 kHz) degradation of simazine in the presence of Au–TiO_2 nanocatalysts. Appl Catal B Environ 160–161:692–700
97. Hu B, Wu C, Zhang Z, Wang L (2014) Sonophotocatalytic degradation of trichloroacetic acid in aqueous solution. Ceram Int 40:7015–7021
98. Zhang K, Oh W-C (2010) Kinetic study of the visible light-induced sonophotocatalytic degradation of MB Solution in the presence of Fe/TiO_2-MWCNT catalyst. Bull Korean Chem Soc 31:1589–1595
99. Ahmad M, Ahmed E, Hong ZL, Ahmed W, Elhissi A, Khalid NR (2014) Photocatalytic, sonocatalytic and sonophotocatalytic degradation of Rhodamine B using ZnO/CNTs composites photocatalysts. Ultrason Sonochem 21:761–773
100. Khataee A, Karimi A, Arefi-Oskoui S, Soltani RDC, Hanifehpour Y, Soltani B, Joo SW (2015) Sonochemical synthesis of Pr-doped ZnO nanoparticles for sonocatalytic degradation of Acid Red 17. Ultrason Sonochem 22:371–381
101. Colmenares JC (2014) Sonication-induced pathways in the synthesis of light-active catalysts for photocatalytic oxidation of organic contaminants. ChemSusChem 7(6):1512–1527

Topics in Current Chemistry (2020) 378:6
https://doi.org/10.1007/s41061-019-0270-3

REVIEW

Ferrite Materials for Photoassisted Environmental and Solar Fuels Applications

Patricia Garcia-Muñoz[1] · Fernando Fresno[2] · Víctor A. de la Peña O'Shea[2] · Nicolas Keller[1]

Received: 7 September 2019 / Accepted: 21 November 2019 / Published online: 16 December 2019

Abstract

Ferrites are a large class of oxides containing Fe^{3+} and at least another metal cation that have been investigated for and applied to a wide variety of fields ranging from mature technologies like circuitry, permanent magnets, magnetic recording and microwave devices to the most recent developments in areas like bioimaging, gas sensing and photocatalysis. In the last respect, although ferrites have been less studied than other types of semiconductors, they present interesting properties such as visible light absorption, tuneable optoelectronic properties and high chemical and photochemical stability. The versatility of their chemical composition and of their crystallographic structure opened a playground for developing new catalysts with enhanced efficiency. This article reviews the recent development of the application of ferrites to photoassisted processes for environmental remediation and for the synthesis of solar fuels. Applications in the photocatalytic degradation of pollutants in water and air, photo-Fenton, and solar fuels production, via photocatalytic and photoelectrochemical water splitting and CO_2 reduction, are reviewed paying special attention to the relationships between the physico-chemical characteristics of the ferrite materials and their photoactivated performance.

Keywords Ferrite · Photocatalyst · Heterojunction · Water treatment · Air detoxification · Solar fuels

Chapter 4 was originally published as Garcia-Muñoz, P., Fresno, F., de la Peña O'Shea, V. A. & Keller, N. Topics in Current Chemistry (2020) 378: 6. https://doi.org/10.1007/s41061-019-0270-3.

✉ Patricia Garcia-Muñoz
garciamunoz@unistra.fr

[1] Institut de Chimie et Procédés pour l'Energie, l'Environnement et la Santé (ICPEES), CNRS/University of Strasbourg, 25 rue Becquerel, Strasbourg, France

[2] Photoactivated Processes Unit, IMDEA Energy Institute, Móstoles, 28935 Madrid, Spain

1 Ferrites: Structure, Synthesis and Properties

1.1 Structure of Ferrites

Ferrites—whose etymology is from the Latin word *ferrum* meaning iron—are a large class of oxides containing Fe^{3+} and at least another metal cation that have been investigated and applied as powder, films or ceramic bodies for the last 50 years. They are classified according to their crystal structure and the way the oxygen anions are arranged around the metal cations, as spinel, garnet, magnetoplumbite and orthoferrite. While spinel and garnet ferrites both crystallize within a cubic structure, magnetoplumbites and orthoferrites crystallize within a hexagonal and orthorhombic structure, respectively.

1.1.1 Spinel Ferrites

Spinel ferrites are compounds with a general chemical formula MFe_2O_4, where M refers to a divalent metal cation, and that crystallize in a crystallographic structure isomorphic with that of the naturally occurring mineral spinel $MgAl_2O_4$ (AB_2O_4 as general composition). They crystallize in a cubic symmetry structure containing eight formula units $A[B]_2O_4$, with a rigid sublattice of 32 closely packed oxygen anions giving rise to 64 tetrahedral (A)-type and 32 octahedral [B]-type interstitial sites partially occupied by 24 M^{2+} and Fe^{3+} metal cations (Fig. 1). Depending on the synthetic conditions, tetragonal unit cells can be obtained as well [1]. In the spinel ferrites, the electrical neutrality is maintained by M^{2+} and Fe^{3+} cations occupying both tetrahedral and octahedral interstitial sites. The interstitial fourfold and sixfold sites have r_t and r_o radii in the $0.055\ \text{nm} < r_t < 0.067\ \text{nm}$ and $0.070\ \text{nm} < r_o < 0.075\ \text{nm}$ range, so that they can be occupied by many transition metal cations with d^0 to d^{10} electronic configurations.

The octahedral vs. tetrahedral site occupation—and therefore the spinel ferrite structure—is reported to be driven by the electrostatic contribution to the lattice energy, the cation radii, the cation charge and the crystal field effect. The reader can refer to the work of Sickafus et al. [2]. According to the M^{2+} and Fe^{3+} metal cation balance between both tetrahedral and octahedral sites, the spinel ferrites are categorized as follows:

- Normal spinels $(M^{2+})^{Td}[Fe^{3+}]_2^{Oh}O_4$, in which the smaller divalent M^{2+} cations occupy only the tetrahedral A-sites and the trivalent Fe^{3+} cations occupy the octahedral B-sites, e.g. $ZnFe_2O_4$ or $CdFe_2O_4$.
- Inverse spinels $(Fe^{3+})^{Td}[M^{2+}Fe^{3+}]^{Oh}O_4$ in which the divalent M^{2+} cations are located in the octahedral B-sites, while the trivalent Fe^{3+} cations are equally distributed between both tetrahedral A-sites and octahedral B-sites, e.g. $MgFe_2O_4$, $CoFe_2O_4$, $CuFe_2O_4$, $NiFe_2O_4$, $NiCoFe_2O_4$, $CuMnFe_2O_4$ or $MgCuFe_2O_4$.
- Mixed spinels $(M_x^{2+}Fe_y^{3+})^{Td}[M_{1-x}^{2+}Fe_{2-y}^{3+}]^{Oh}O_4$, in which both the divalent M^{2+} and trivalent Fe^{3+} cations are distributed between both tetrahedral A-sites and octa-

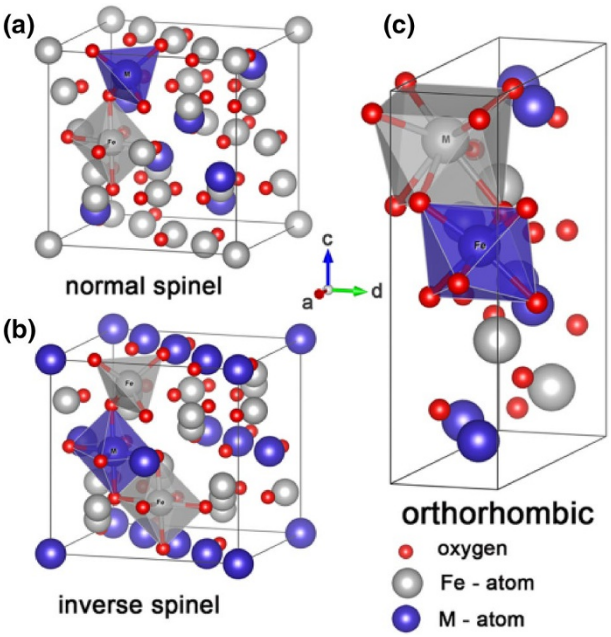

Fig. 1 Crystallographic structure of AB_2O_4 spinel ferrites schematizing the different crystallographic sites: **a** normal spinel, **b** inverse spinel and **c** orthorhombic. Reproduced with permission from Ref. [1]. Copyright SPIE

hedral B-sites, e.g. $NiZnFe_2O_4$, $MgZnFe_2O_4$, $ZnMnFe_2O_4$, $MnNiFe_2O_4$, $CuZnFe_2O_4$ or $NiCuZnFe_2O_4$.

Some spinel ferrites, such as $MgFe_2O_4$, $CaFe_2O_4$ and $BaFe_2O_4$, are also reported to crystallize as orthorhombic phases [3–5] (Fig. 1c).

1.1.2 Garnet Ferrites

Garnets are ferrites with a general chemical formula $M_3Fe_5O_{12}$, where M is a rare-earth cation. They crystallize in the structure of the $X_3Y_2(SiO_4)_3$ silicate mineral garnet, in which the X and Y sites are usually occupied by divalent (Ca^{2+}, Mg^{2+}, Fe^{2+}) and trivalent (Al^{3+}, Fe^{3+}, Cr^{3+}) cations, respectively, while the $(SiO_4)^{4-}$ units provide a tetrahedral framework [6]. They crystallize in the cubic system, within a relatively complex structure based on a unit cell composed of eight formula units. Three kinds of cation sites coexist within this structure, and the cation distribution is usually expressed as $\{M_3\}(Fe_3)[Fe_2]O_{12}$. The M rare-earth cations occupy the largest dodecahedral (eightfold) sites, while the Fe^{3+} cations distribute among both tetrahedral (fourfold) and octahedral (sixfold) sites. By contrast to the spinel structure, the oxygen sublattice is better described as a polyhedral arrangement rather than as a close-packed one.

1.1.3 Magnetoplumbite Ferrites

Magnetoplumbites are synthetic ferrites first prepared at Philips Lab in the 1950s and they mainly share the general chemical formula $M^{2+}Fe_{12}O_{19}$, where M^{2+} can be Ba^{2+}, Pb^{2+}, Sr^{2+} or Ca^{2+}. Although they are labelled also as hexaferrites, they crystallize in a hexagonal or rhombohedral symmetry structure. In addition to the $MFe_{12}O_{19}$ form (labelled as M-type ferrite, Fig. 2), they can be categorized within five other groups, consisting in $M_{1–4}Me_2Fe_{12–36}O_{22–60}$ type ferrites. While M^{2+} is considered as a large divalent cation, Me^{2+} represents usually a smaller divalent first-row transition metal cation such as Co^{2+}, Fe^{2+}, Zn^{2+} or Ni^{2+}. They are consequently categorized as Z-type ($Ba_3Me_2Fe_{24}O_{41}$), Y-type ($Ba_2Me_2Fe_{12}O_{22}$), X-type ($Ba_2Me_2Fe_{28}O_{46}$), W-type ferrites ($BaMe_2Fe_{16}O_{27}$) and U-type ($Ba_4Me_2Fe_{36}O_{60}$) ferrites [7]. The most studied magnetoplumbites are ferrites containing Ba and Co as divalent cations, but a large range of cation-substituted hexaferrites have been investigated, especially M, W, Z and Y ferrites containing Sr, Zn, Ni and Mg. Hexaferrites can also form many solid solutions, and partial substitution with trivalent or tetravalent cations can be performed. The reader can refer to the review by Pullar for in-depth analysis [7].

1.1.4 Orthoferrites

Orthoferrites are ferrites with a general chemical formula $MFeO_3$, where M is very often a rare-earth cation, an alkali metal cation or an alkaline earth metal cation. They crystallize in a distorted perovskite structure with an orthorhombic symmetry and an ABO_3 formula unit, in which FeO_6 as a rotary tilted BO_6 element fills the

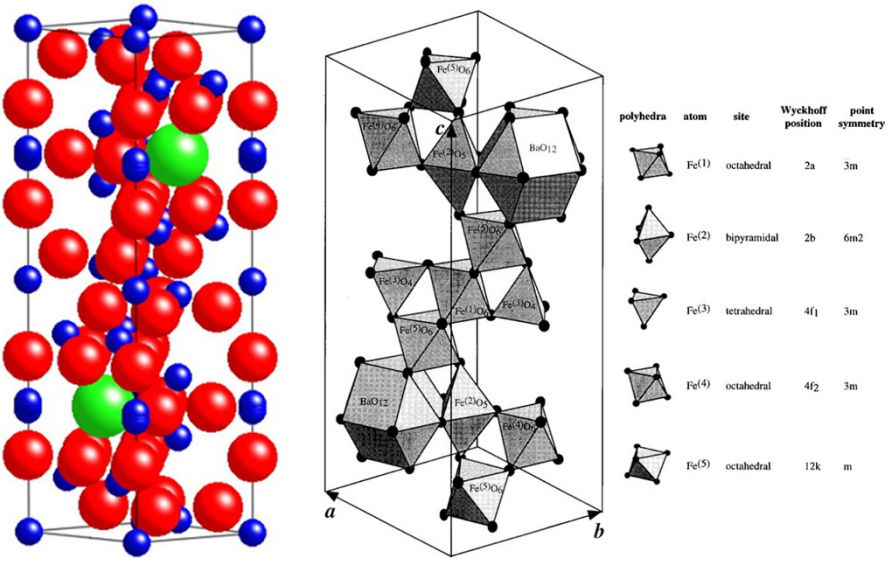

Fig. 2 Perspective view [8] (left) and polyhedra (right) of the unit cell in the case of the M-ferrite structure ($BaFe_{12}O_{19}$) (Fe blue, Ba green, O red). Reproduced with permission from Ref. [7]. Copyright Elsevier and Wiley

empty space left around the A cation (Fig. 3). In this structure, the Fe cations occupy octahedral sites and are sixfold coordinated to oxygen anions, while the larger M cation is 12-fold coordinated to anions [9]. While the ideal perovskite-type structure displays a cubic symmetry with a unit cell composed of four formula units in which the atoms are touching one another, the deviation from the ideal perovskite structure to give pseudo-cubic—mainly orthorhombic—symmetry has been rationalized by Goodenough [10]. He introduced a tolerance factor t applicable at room temperature to the empirical ionic radii and materializing the stability and the distortion of the crystal structure within the following range:

$$0.75 < t = \frac{(r_A + r_O)}{\sqrt{2}(r_B + r_O)} < 1.$$

For instance, lanthanum orthoferrite $LaFeO_3$ shows a high Goldschmidt tolerance factor of 0.954, indicating that the distorted structure maintains a high level of symmetry, while the yttrium orthoferrite $YFeO_3$ structure displays a far lower symmetry with a lower tolerance factor of 0.855 [11].

1.2 Preparation Methods

Progress in the synthesis of orthoferrites and spinel ferrites has been driven in the last decades by the technological interest aroused by the ferrite materials in various interdisciplinary application fields and by that derived from their tunable magnetic properties. Whether they are categorized as bottom-up or top-down approaches, or as chemical or physical methods, a large variety of preparation methods have been investigated for synthesizing ferrite nanoparticles. Among them, co-precipitation, sol–gel methods, thermal methods and solid-state reactions remain the most popular strategies implemented for elaborating catalysts for heterogeneous photo-Fenton or photocatalysis, whereas a large (non-exhaustive) panel of methods such as sonochemical, microemulsion, reverse micelle, electrospinning, polyol, electrochemical,

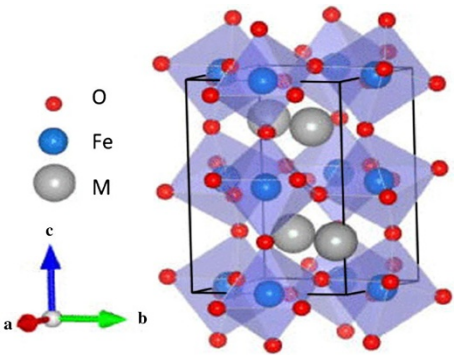

Fig. 3 Crystallographic structure of $MFeO_3$ orthoferrites with distorted perovskite structure (orthorhombic crystal symmetry). Adapted and reproduced with permission from Ref. [12]. Copyright AIP Publishing

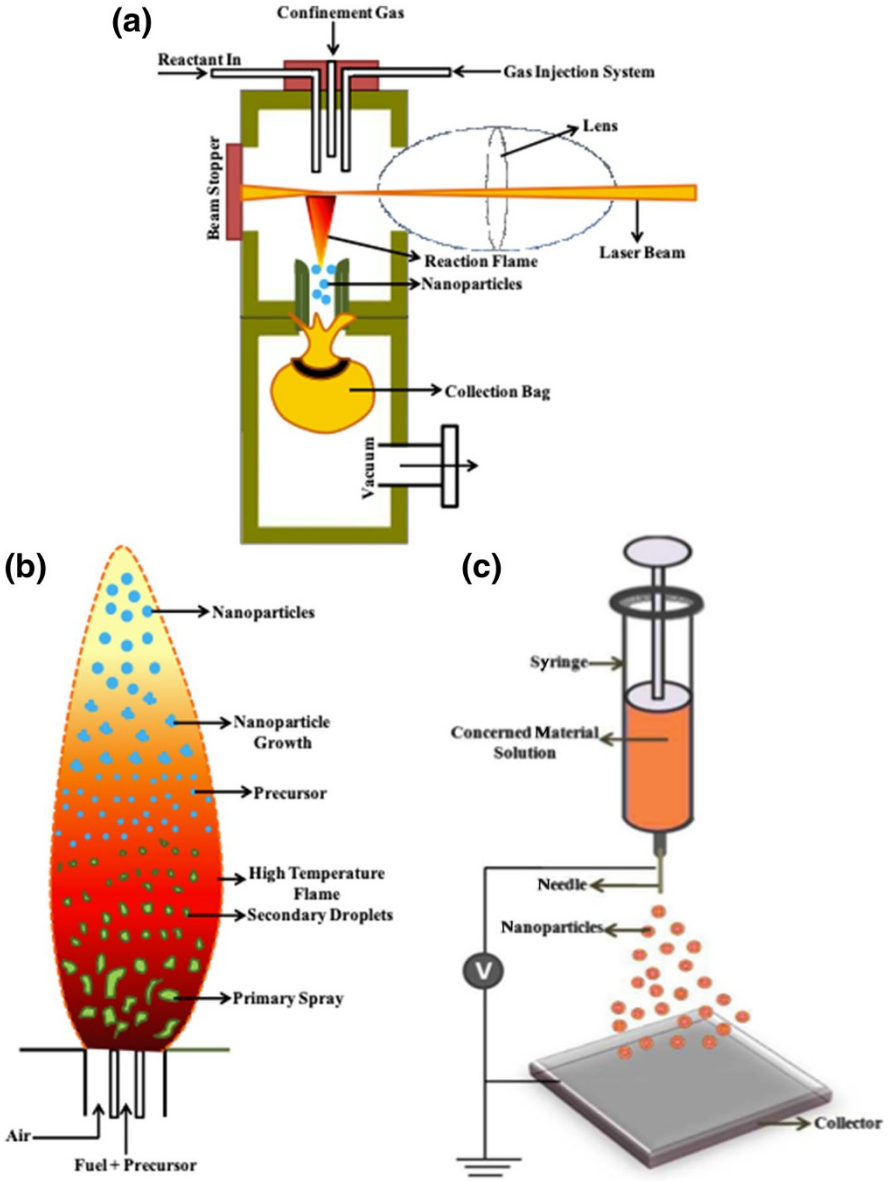

Fig. 4 Schematic diagrams of some selected less conventional synthesis methods. **a** Laser pyrolysis, which uses a laser for the decomposition of materials by heating gas-phase reactants in an oxygen-poor environment. **b** Flame spray pyrolysis, which is the latest of the flame aerosol technologies, and consists in a one-step combustion process with self-sustaining flame where less volatile precursors are in liquid form, with significantly higher combustion enthalpy (> 50% of total energy of combustion), usually in an organic solvent. **c** Electrospraying technique, which is similar to electrospinning with the exception that it forms nanoparticles rather than nanofibres. Reproduced with permission from Ref. [17]. Copyright Royal Society of Chemistry

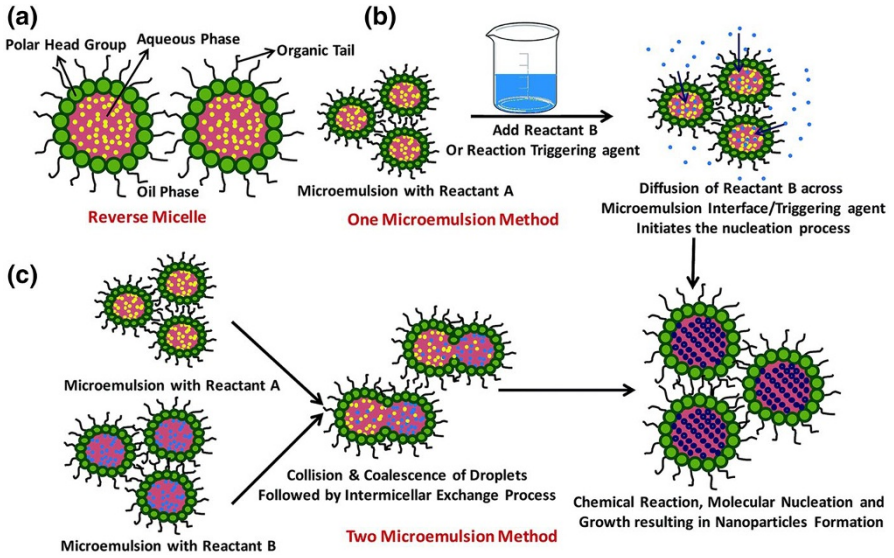

Fig. 5 Schematic diagrams depicting microemulsion-based syntheses. **a** Typical reverse micelle system, which is a water-in-oil microemulsion where the polar head groups of the surfactants creating the aqueous core reside towards the inside, whereas the organic tails of the surfactant molecules are directed towards the outside. **b** One-microemulsion synthesis method. **c** Two-microemulsion synthesis method in which the microemulsions carrying the separate reactants are mixed together in the appropriate ratio. Reproduced with permission from Ref. [17]. Copyright Royal Society of Chemistry

(auto)combustion, vapour deposition, laser ablation or flame spray pyrolysis methods have been also reported (Figs. 4, 5) [13–16].

For applications in photocatalysis or photo-Fenton processes, the specific surface area exposed, the crystallinity as well as the possibility to tune the intrinsic properties of the ferrites (such as the surface redox properties, the bandgap values or the light absorption profile) are the main criteria to be considered for selecting the synthesis method. The cationic or anionic mono- or bisubstitution within the defined structure of the ferrites is an elegant and powerful way to tailor those properties. Further, as far as the catalysts need to operate in a manner consistent with the constraints of industrial implementation, whether it concerns liquid or gas-phase applications, the synthesis method should allow the ferrite catalyst to be immobilized on macroscopic supports. In addition, since most of the methods require a thermal treatment for increasing the crystallinity of the ferrite materials, the methods enabling a lower temperature to be achieved are preferred because they do not impact too strongly on the specific surface area. Therefore, the chemical syntheses in solution remain the preparation methods of choice, among which co-precipitation, sol–gel methods and thermal methods are the most popular ones.

1.2.1 Co-precipitation Method

The co-precipitation is a very common and fast synthesis method consisting in favouring the simultaneous precipitation of insoluble or low solubility products

formed under high supersaturation conditions, from aqueous solutions of metal precursors, through pH adjustment and use of precipitating agents. The overall process in solution consists in nucleation, growth, coarsening and/or agglomeration processes that are highly difficult to uncouple, while a final thermal treatment is needed for decomposing the intermediate precipitate into the usable ferrite as well as for crystallizing the oxide. The co-precipitation method has been successfully used for synthesizing a large variety of spinel ferrites [18–23] or orthoferrites, mono-, bi- or non-substituted.

1.2.2 Sol–Gel Methods

The sol–gel method is a versatile approach in which a metal alkoxide solution undergoes hydrolysis and condensation polymerization reactions, with the formation of a sol and subsequent cross-linking to form a gel. It requires usually a final heat treatment for removing volatile byproducts and crystallizing the ferrite material. It takes advantage of a relatively low annealing temperature compared to solid-state reactions for maintaining a relatively high surface area. It generally benefits from its simplicity, low implementation costs and tunability for preparing a large range of spinel ferrites [24–28] and orthoferrite structures [29–33] with controlled composition, structure and morphology. One can note that the sol–gel method combined with combustion was used for preparing $BaFe_{12}O_{19}$ and $CoFe_{12}O_{19}$ hexaferrites (magnetoplumbite structure) [26, 34].

Pechini developed a modified sol–gel method for materials which do not have favourable hydrolysis equilibria, and in which the metal ions undergo complexation through the addition of bi- or tridentate organic chelating agents [35, 36]. The method builds on the principles of sol–gel chemistry involving small-molecule chelating ligands that in the initial step form a solution of metal–chelate complexes. It takes this further to convert the mixture into a covalent polymer network to entrap the metal ions. The use of chelating agents allows stable complexes to be formed with a large variety of metals and gets rid of the requirement that the metal has to form stable hydroxo species. The underlying strategy of the method lies in the delay of the thermal decomposition of the organic matrix in order to afford more control over the growing ceramic phase. While citric acid is the most popular chelating agent (i.e. citrate method), it can be also replaced by ethylenediaminetetraacetic acid (EDTA), which has the advantage of chelating most metals and, with four carboxylate groups, it is easily cross-linked to form a gel. When ethylene glycol is used in association with citric acid, the key reaction is the esterification between citrate and ethylene glycol (Fig. 6). The metal salt dissolved in water with citric acid and ethylene glycol forms a homogeneous precursor solution containing the metal–citrate chelate complexes, while the heat-induced polyesterification between the citrate and ethylene glycol creates an extended covalent network. The method requires a final calcination step for combusting the organic matrix and forming the oxide. It became very popular for synthesizing ferrite materials, notably owing to its ability to form a polymeric precursor where two or more metals may be dispersed homogeneously throughout the network [37, 38].

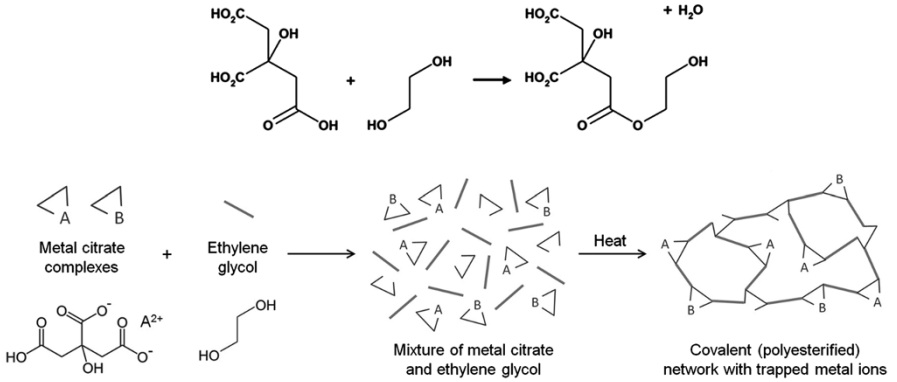

Fig. 6 Esterification reaction occurring between citric acid and ethylene glycol in a typical Pechini process (top). Proposed schematic of the process of making metal/organic gels (bottom). Reproduced with permission from Ref. [36]. Copyright Royal Society of Chemistry

1.2.3 Thermal Methods

The thermal methods are mainly based on thermal decomposition [39], as well as on hydrothermal [40–43], solvothermal and microwave-assisted methods. While the thermal decomposition consists in the simple decomposition of precursors, organic solvents and surfactants during heat treatment to get the ferrite, the other methods are driven by the need to lower the temperature used for crystallization in order for the ferrite to maintain a suitable specific surface area. Hydrothermal and solvothermal usually differ in terms of solvent, aqueous vs. non-aqueous, respectively, in which the soluble metal salts are dissolved. Temperature, pressure, synthesis duration as well as choice of solvent, of precursors and of additional surfactant are the main synthesis parameters impacting on the physico-chemical properties of the ferrites [13, 14, 44, 45]. While the temperature can be as high as 500 °C for the thermal decomposition method, it can be decreased to 100–200 °C for solvothermal, hydrothermal and microwave-assisted methods. However, although the microwave-assisted syntheses allow shorter reaction durations to be achieved, they suffer usually from low synthesis yields.

1.2.4 Solid-State Reaction Methods

Besides the bottom-up chemical syntheses in solution reported above, the solid-state reaction methods are a suitable top-down approach consisting in treating solid precursors at high temperature, usually oxides or carbonates, for inducing solid–solid diffusion, with a further stabilization/crystallization of the ferrite defined structure. $CoFe_2O_4$, $CuFe_2O_4$, $NiFe_2O_4$ and $Ni_{1-x}Mn_xFe_2O_4$ spinel ferrites have notably been synthesized [46–49]. However, the obtained ferrites usually suffer from low specific surface area when compared to chemical synthesis in solution. Therefore, the mechanical milling method has been implemented as a high-energy collision

top-down approach method using planetary ball mill, high-energy shaker or tumbler mill for inducing proper conditions in which solid-state chemical reactions can take place, mostly through mechanical activation or mechanochemistry. However, while the method is low-cost and time-saving with easy up-scaling, it suffers notably from strong contamination problems during prolonged milling, non-stoichiometric structure, non-uniform size distribution and low crystallinity.

Further, many more or less complex and versatile bottom-up or top-down methods have been implemented for preparing ferrite materials, alone or as part of the main popular methods described above. Without being exhaustive, one can list notably microemulsion, flame spray pyrolysis, auto-combustion, vapour deposition, liquid exchange, self-reactive quenching, or electrospinning. The reader can refer to the reviews by Kefeni et al. [13] and Tatarchuk et al. [24], or directly to the original research cited therein.

Finally, it is worth noting that the optimal physico-chemical properties that the ferrite materials need to exhibit are highly dependent on their application fields, so that putting into perspective the advantages vs. disadvantages of the different preparation methods remains in many cases inappropriate.

1.3 Ferrite Properties

Ferrites are generally considered as being thermally and chemically stable in aqueous systems [44], and the Pourbaix diagrams indicate that most of the ferrites are stable in most of the alkaline or near-neutral media used in photoelectrochemical cells [9]. However, ferrites are reported to suffer from corrosion in acidic media [50, 51]. Independently of the crystallographic structure, the mono- or bisubstitution of the cations within the ferrite materials is known to affect many of their physico-chemical properties, including the resistivity (conductivity), the optical properties (reflectivity), the bandgap energy, the energy position of both valence and conduction bands, or the p/n-type behaviour [9]. Therefore, the controlled cationic single- or multisubstitution in the ferrite network, whether A- or B-sites are concerned, became an elegant, versatile and promising way to tune both bulk and surface physico-chemical properties of the ferrite-based photocatalysts used for environmental (water and air depollution) and solar fuel applications.

The specific surface area exposed by the ferrite materials is strongly dependent on the preparation method. However, the ferrite catalysts generally exhibit low to medium specific surface area (< 100 m^2 g^{-1}) in contrast to lab-made or commercially available titania photocatalysts that can reach high surface areas of 200–350 m^2 g^{-1} thanks to the implementation of adequate synthesis approaches. Table 1 reports some selected spinel ferrites and orthoferrites, substituted or not, with their specific surface area, crystallite size and isoelectric point together with their preparation method and final calcination temperature. It highlights to what extent the synthesis method impacts on some properties of the materials. It has to be mentioned that maintaining a relatively low or moderate calcination temperature does not necessarily guarantee ferrites with a high specific surface area; in contrast,

Table 1 Preparation method and final calcination temperature of selected spinel ferrites and orthoferrites with their specific surface area, crystallite size and isoelectric point

Ferrites	Specific surface area ($m^2\ g^{-1}$)	Crystallite size (nm)	Isoelectric point	Preparation method (calcination temperature)	References
$CuFe_2O_4$	48–69	30–110[b]	7.3	Combination of acid leaching, chemical exchange and ferrite process from printed circuit board sludge	Tu et al. [66–68]
$CuFe_2O_4$	70	72[a]	–	Microemulsion (650 °C)	Rehman et al. [69]
$CoFe_2O_4$	149	20–30[c]	8.1	Hydrothermal (100 °C)	Sun et al. [70]
$CoFe_2O_4$	202	10–20[c]	8.0	Hydrothermal (100 °C)	Sun et al. [70]
$Co_{0.6}Fe_{0.4}Fe_2O_4$	97	14[c]	2.9	Thermal decomposition (400 °C)	Duan et al. [71]
$MnFe_2O_4$	48	50–80[c]	6	Hydrothermal (100 °C)	Sun et al. [70]
$ZnFe_2O_4$ hollow fibres	132	50	6.5	Sol–gel using kapok fibres as bio-template (700 °C)	Li et al. [72]
$MgFe_2O_4$	54	25–35[c]	11	Co-precipitation (500 °C)	Srivastava et al. [73]
$MnFe_2O_4$	3–156	200–290[b]	6.6	Co-precipitation (400 °C)	Yang et al. [74]
$MnFe_2O_4$	138	30–50[c]	7.5	Co-precipitation	Zhang et al. [75]
$CaFe_2O_4$	5–42	15–30[c]	4.7	Sol–gel in presence of citric acid (200–800 °C)	An et al. [76]
$Ni_{0.6}Fe_{0.4}Fe_2O_4$	114	15[c]	4.1	Microemulsion (400 °C)	Zeng et al. [77]
$Ni_{0.5}Zn_{0.45}Fe_2O_4$	70	15–18[a]	–	Sol combustion (400 °C)	Liu et al. [78]
$BiFeO_3$	8	80–120	–	Pechini (citric acid) sol–gel (500 °C)	Gao et al. [79]
$LaFeO_3$	21–49	1–22[a]	–	Pechini (citric acid) sol–gel (500–1000 °C)	Li et al. [80]
$LaFeO_3$ dendrites	68	84[a]	–	Hydrothermal (800 °C)	Thirumalairajan et al. [81]
$LaFeO_3$	4–11	27–46[a]	–	Citric acid assisted sol–gel (700–900 °C)	Ismael et al. [82]
$LaFeO_3$	6–25	24–104[a]	–	Sol–gel autocombustion (500–900 °C)	Parida et al. [83]
$LaFe_{0.95}Mn_{0.05}O_3$	20	22	–	Citric sol–gel method (600 °C)	Gong et al. [84]
$LaFe_{0.95}Ni_{0.05}O_3$	21	22	–	Citric sol–gel method (600 °C)	Gong et al. [84]
$La_{1-x}Ti_xFeO_3$ ($0 < x < 0.2$)	8–40	14–23[a]	–	Pechini (citric acid) sol–gel (800 °C)	Garcia-Muñoz et al. [37]

Crystallite sizes derived from [a]X-ray diffraction (XRD), [b]scanning electron microscopy (SEM) and [c]transmission electron microscopy (TEM) analysis

it may result in materials with low crystallinity and therefore with a low photoactivity due to a high recombination rate.

Most of the ferrite materials are semiconductors and take advantage of being able to absorb visible light owing to a bandgap of about 2 eV (corresponding to wavelengths lower than 621 nm). This contrasts with the very popular anatase TiO_2 reference material, whose bandgap of 3.2 eV allows only the absorption of UV light, corresponding to wavelengths lower than 388 nm. Most of ferrites display energy positions of both valence and conduction bands suitable for either the oxidation of water, the reduction of protons and/or the generation of active hydroxyl radicals from water and the reduction of dioxygen into the superoxide radical, as necessary for environmental and water splitting applications. Figure 7 gathers the band positions of the most popular ferrite materials with AB_2O_4 spinel structure. Similarly to their influence on the reactivity in thermal catalysis [52, 53], the chemical nature of the substituted metals and the magnitude of the mono- and bisubstitution ratios are known to influence some of the physicochemical properties directly affecting the reactivity in photocatalysis, such as the optical properties via the bandgap energy and the material reflectivity, the conductivity [54–56] as well as the n/p-type behaviour of the semiconductor [57, 58].

The p or n nature of the spinel ferrite influences the positions of both conduction and valence bands, and consequently the bandgap value as well. This can be evidenced in the case of the $MgFe_2O_4$ spinel ferrite, with a conduction band for the p-ferrite being 1.8 eV more cathodic compared to its n-counterpart, and bandgap being ca. 0.3 eV smaller for the p-ferrite. By contrast, the p- or n-nature of the $ZnFe_2O_4$ ferrite has been reported to only affect the band position, for the p-ferrite being ca. 1.2 eV more cathodic compared to its n-counterpart.

Growing interest has been paid to ABO_3 transition-metal oxide orthoferrites thanks to a small bandgap (2.0–2.7 eV), that allows the catalyst to be activated by visible light, and that results from the relative location of valence and conduction

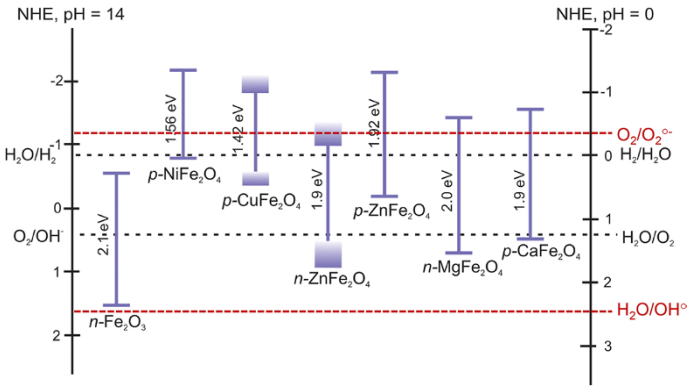

Fig. 7 Band positions of the most popular spinel ferrites in contact with aqueous solution referenced to normal hydrogen electrode (RHE) (right pH 0 and left pH 14) relative to the standard potentials for the oxidation and reduction of water, as well as for the reduction of dioxygen into the superoxide radical and the oxidation of water into the hydroxyl radical. Adapted from Ref. [9]

bands, mainly comprising strongly mixed e_g states of Fe 3*d* and O 2*p* states, and of the t_{2g} states of Fe 3*d*, respectively. For instance, $LaFeO_3$, one of the most common and promising perovskite-like ferrite catalysts, is usually reported with a bandgap between 2.0 and 2.6 eV, depending on the synthesis method and their resulting physico-chemical properties [37, 82]. Ansari et al. used $CoFe_{12}O_{19}$ hexaferrites as photocatalyst with a 3-eV bandgap [34]. By contrast Zielinska-Jurek et al. graphically estimated the bandgap of the $BaFe_{12}O_{19}$ semiconductors material at 1.0 eV [26].

1.4 Towards More Efficient Ferrite-Based Photocatalytic Materials

Ferrite semiconductor-based photocatalysis and photoelectrochemistry have attracted attention because of the ability of the ferrite materials to absorb and consequently use visible light—and therefore to directly convert the solar energy—for performing surface redox reactions allowing environmental remediation to be implemented and solar fuels to be synthesized. During the photocatalytic process, the recombination of the photo-generated electron–hole pairs plays a highly negative role. Thus, similarly to the wide-bandgap semiconductor TiO_2, considered as the most frequently used semiconductor photocatalyst under UVA light, the photocatalytic efficiency of the ferrites is usually defined by the abundance and stability of the photo-generated charges (electron and holes). Therefore, efforts have been devoted to extending the lifetime of such charge carriers, i.e. to slow down their recombination rate. Many approaches have been investigated for that purpose, including the modification of the shape of the nanoparticles or of their chemical compositions through the design and fabrication of semiconductor heterostructures, hybrid nanocomposites, doped-nanostructures or more generally multiphase materials.

The design of semiconductor heterojunctions is a general and very promising strategy for elaborating ferrite-based photocatalysts with improved efficiency, whether the reactions concern environmental applications (water and air depollution) or the solar fuel field for the energy-related applications (CO_2 conversion or H_2 production). Basically, a heterojunction can in general be schematically described as the interface between two different semiconductors with unequal band structure, which can result in band alignments [59, 60]. In recent years, most of the studies were devoted to the creation of controlled heterojunctions with anatase TiO_2 of different morphologies absorbing UVA light, or with the smaller gap graphitic g-C_3N_4 semiconductor absorbing visible light, as well as to the design of visible-light-responsive ferrite/ferrite interface heterojunctions. Whatever the configuration investigated, the heterojunction strategy was mainly implemented for use as photocatalysts and photoelectrodes for energy applications. Details are given in the further corresponding sections.

In some cases like for conventional Z-scheme heterojunctions, there is no physical contact between both systems and the charges migrate through donor/acceptor pairs [61]. Depending on the bandgaps and on the relative position of the valence and conduction bands of both semiconductors, the engineering of ferrite-based heterojunctions aims (1) to separate spatially the photo-generated charges to extend the

charge carrier lifetime thanks to efficient semiconductor/semiconductor interfacial charge transfers and/or (2) to use the ferrite semiconductor as a solid visible light absorption/harvesting system for the photosensitization of wider-bandgap semiconductors (i.e. TiO_2).

The reader can refer to the critical reviews by Low et al. [62] and Jang et al. [63] that extensively depicted and systematically discussed the basic principles of various heterojunction photocatalysts, namely conventional heterojunctions of type I–III depending on the relative positions of both bandgaps, p–n heterojunctions, direct Z-scheme heterojunctions (including solid-state Z-scheme) as well as graphene-based heterojunctions.

The elaboration of metal–ferrite semiconductor junctions is another strategy followed by different research groups reported in the next sections of this review. The supported metals consist usually in nanoscale metal islands on the semiconductor. The junction forms an electric field that facilitates the separation the photo-generated electrons and holes [64, 65], together with the formation of local space–charge separation zones at the interphase. Beside their role in enhancing the lifetime of the charge carries, the supported metallic nanoparticles also act as co-catalyst in different innovative ferrite-based systems used as photocatalysts or photoelectrodes for hydrogen production and CO_2 reduction (see "Ferrite-Based Photocatalysts and Photoelectrodes for EnergyApplications: Hydrogen Production and CO_2 Reduction").

The association of ferrites nanoparticles with adsorbent materials such as montmorillonite or palygorskite clays is also reported in the field of environmental remediation for trying to take advantage of the synergistic effect of adsorption and catalysis (see "Ferrite Photocatalysts for Environmental Applications: WaterDetoxification and Air Depollution").

Finally, the cationic doping of ferrite—usually depicted as partially substituted ferrites—is a very promising approach investigated by many research groups for improving the efficiency of the ferrite photocatalysts and photoelectrodes, and reported in the next sections. Indeed, whatever the crystallographic structures of the catalysts, the compositional versatility of the ferrites—e.g. as $A_{1-x}A'_xB_{1-y}B'_yO_{3\pm\delta}$ or $A_{1-x}A'_xB_{2-y}B'_yO_{4\pm\delta}$ in the case of orthoferrites or spinel ferrites, respectively—is a great advantage for modifying many bulk and surface physico-chemical properties of the ferrites, including their textural, structural or electronic properties, and as a result for tuning the redox and catalytic ability of the ferrites through A- and/or B-site cationic partial substitution.

The objective of improving the efficiency of the ferrite-based photocatalysts and photoelectrodes requires investigating charge trapping and recombination as well as understanding the factors affecting the related processes. Furthermore, deeper understanding of the relationship between the physico-chemical properties of the ferrite-based systems and the catalytic behaviour and efficiency indicators under visible or solar light is absolutely necessary. In particular, understanding the physico-chemical phenomena taking place in the bulk, and at the surface and the interfaces of the multicomponent systems, is of high interest, as well as understanding the catalytic mechanism(s) taking place in such systems, and how the material design can orientate the efficiency indicators.

2 Ferrite Photocatalysts for Environmental Applications: Water Detoxification and Air Depollution

2.1 Introduction

Photocatalysis as an advanced oxidation process has been applied for water treatment and for air depollution. These processes are based on the formation of highly oxidative species that can convert recalcitrant organic pollutants into mineral compounds, i.e. CO_2, H_2O and mineral acids. Ferrites are among the catalysts that can be employed. The main properties of those materials are their high stability and the good mobility of the oxygen in the network and so the ability to form vacancies and to stabilize metals with unusual oxidation states [13, 16]. In this scenario, ferrites have been employed in both fields (water and air treatment), taking advantage of their activation by visible light to generate the species that carry out the photocatalytic process [44]. Applications of ferrites in environmental remediation include not only their use as photocatalysts but also as catalysts in intensified processes by simultaneously applying single processes with the purpose of obtaining a higher efficiency by reducing the inherent drawbacks of each single treatment [31, 37].

2.2 Ferrite Photocatalysts for Water Detoxification

There are several works dealing with the use of ferrite catalysts for the treatment of water by photocatalysis (Table 2). The first ones were reported in 2015 by Zaharieva et al. [85] and Mahto et al. [86]. In the first case, the authors synthesized $Cu_{0.25}Fe_{2.75}O_4$ by a co-precipitation method with a further thermal treatment and applied it for the degradation of malachite green. They obtained better activity than the reference TiO_2-P25. In the second case, Fe_3O_4, $MnFe_2O_4$ and $ZnFe_2O_4$, also obtained by co-precipitation, were employed to degrade azo dyes in aqueous solution. Materials were functionalized with citric acid to improve the photoactivity.

Recently, other methods, as mentioned in "Ferrites: Structure, Synthesis and Properties", have been employed for the synthesis of ferrites such as combustion route, electrospinning and sol–gel [34, 87, 88]. Ansari et al. synthesized a cobalt hexaferrite, $CoFe_{12}O_{19}$, by sol–gel method and using a natural agent as reducing agent: maltose and fructose. In order to increase the activity, the nanoparticles were supported on carbon nanotubes or graphene sheets. The effect of the reducing agent as well as the calcination temperature was evaluated. The bandgap value of 3.0 eV allowed their use in the photocatalytic degradation of methyl orange under visible light. The authors obtained 75% of methyl orange degradation in 50 min of reaction as well as a higher activity when the ferrite was supported owing to an improved charge separation and a lower charge recombination.

$CaFe_2O_4$, with spinel structure, was obtained by electrospinning by El-Rafei's group [87]. The material showed good magnetization, a key parameter for recovery purposes in water treatment, as well as photoactivity under simulated sunlight. The study focused on the effect of heat-treatment temperature and showed the need for treatment above 800 °C to get a well-formed ferrite phase.

Table 2 Summary of ferrite materials used as photocatalyst for water treatment

Catalyst	Method of synthesis	Pollutant	Conversion	Advantages	Disadvantages	References
$ZnSm_xFe_{2-x}O_4$	Co-precipitation	Methyl orange (MO)	92% MO (80 min)			Rashmi et al. [21]
$CuS/BiFeO_3$	Two-step	Alachlor	90% alachlor removed (60 min)			Bhoi and Mishra [92]
$LaFeO_3/SnS_2$	Hydrothermal method	Tetracycline		Better rates with 10% $LaFeO_3$; Z-scheme		Luo et al. [40]
$LaFeO_3/AgBr$	Precipitation	Dye, methyl orange		Better photoactivity	No complete degradation	Song et al. [90]
$LaFeO_3$/montmorillonite	Assembling sol–gel	Rhodamine B	100% rhodamine removed (75 min)			Peng et al. [29]
$ZnFe_2O_4$/PMS (peroxymonosulfate)	Soft chemical process	Orange II	Total removal (90 min)			Zhu et al. [93]
$TiO_2/CoFe_2O_4$	Two-spinneret electrospinning	Phenol	20% phenol removed (210 min)			Li et al. [94]
$Zn_xFe_{3-x}O_4$	Soft chemical route	Dye Acid Blue 113; disinfection		92% of dye removal; synergetic effect with H_2O_2		Mandal et al. [95]
TiO_2@Mn-Zn ferrite	Sol–gel hydrolysis precipitation.	Methylene blue	Complete removal (360 min)			Chen et al. [96]
$BiFeO_3$/ozone	Thermal decomposition	Oxalic acid	80% degradation (60 min)	Improved mineralization by processes combination		Liao et al. [39]
$Cu_{0.25}Fe_{2.75}O_4$	Co-precipitation, mechanochemical and/or thermal treatment	Malachite green		Better activity than P25 TiO_2		Zaharieva et al. [85]
La-doped $BiFeO_3$	Sol–gel method	Phenol removal	Complete phenolic removal with 15% La (180 min)			Meng et al. [97]

Table 2 (continued)

Catalyst	Method of synthesis	Pollutant	Conversion	Advantages	Disadvantages	References
$CaFe_2O_4$	Electrospinning	TPA				El-Rafei et al. [87]
$Ag/AgCl/ZnFe_2O_4$	Hydrothermal method	Bisphenol A; rhodamine B	85% removal bisphenol (120 min); 100% rhodamine (70 min)	Enhanced electron–hole pair separation efficiency		Liu et al. [41]
$ZnO/ZnFe_2O_4$	Zn-Fe mixed metal organic framework	Rhodamine B and methylene blue		Higher photodegradation efficiency		Xu et al. [98]
$ZnFe_2O_4$ nanoparticles	Combustion route	Dyes; antibacterial	Total removal of mixed dyes (150 min)	Good reusability over 4 cycles		Patil et al. [88]
Barium ferrite/activated carbon composite	Sol–gel	Dyes	Complete discoloration (30 min)	Visible light		Roonasi and Mazinani [89]
$Fe_3O_4/SiO_2/TiO_2$; $CoFe_2O_4/SiO_2/TiO_2$; $BaFe_{12}O_{19}/SiO_2/TiO_2$	Sol–gel combustion	Phenol; carbamazepine	No loss of activity when incorporated ferrites; magnetic separation	Reusability during 4 cycles		Zielinska-Jurek et al. [26]
$CuFe_2O_4/g\text{-}C_3N_4$ heterojunctions nanocomposite/PMS	Sol–gel combustion	Propranolol (pharmaceutical compound)	Peroxymonosulfate (PMS) enhances the activity			Li et al. [99]
$BiFeO_3$	Thermolysis	Doxorubicin	79% pollutant removal (180 min)			Dumitru et al. [100]
$Ag_3PO_4\text{-}CoFe_2O_4\text{-}GO$	Hydrothermal	Methylene blue		Stability after 6 cycles of reaction		Liu et al. [42]
$CoFe_{12}O_{19}$	Sol–gel method	Methyl orange	75% of degradation in presence of graphene (50 min)	Higher surface area, charge separation and lower recombination of charges		Ansari et al. [34]

Table 2 (continued)

Catalyst	Method of synthesis	Pollutant	Conversion	Advantages	Disadvantages	References
$Co_{0.5}Zn_{0.25}M_{0.25}Fe_2O_4$–$TiO_2$	Co-precipitation, hydrolysis and thermal treatment	Methyl orange and methylene blue				
$BaFe_{1-x}Cu_xO_{3-\delta}$	Pechini method	Atrazine	90% degradation (120 min)	Best activity at pH 11; higher surface area and more oxygen vacancy		Jamil et al. [38]
MFe_2O_4 (M = Fe, Mn, Co)	Chemical co-precipitation	Azo dyes		Citric acid functionalization improves the photocatalytic activity		Pereira et al. [23]

The last technique employed for the synthesis of ferrite as photocatalysts for water treatment is the autocombustion route as performed by Patil et al. [88]. In this case, the authors got $ZnFe_2O_4$ by using sugar cane as fuel. The resulting material showed a bandgap value of 2.8 eV and was used for two objectives: as photocatalyst for dye removal and for antibacterial purposes. The data indicated that complete removal of mixed dyes after 150 min was achieved as well as good inhibition of *Escherichia coli*, *Staphylococcus aureus* and *Pseudomonas aeruginosa*. $ZnFe_2O_4$ showed good reusability over a minimum of four cycles.

However, the perovskite specific surface areas are usually quite low and, in most cases, the activity can be limited by this parameter. In order to increase the activity, they have been immobilized on different supports like montmorillonite and active carbon. A few works have been developed in this sense. It is worth highlighting the works of Peng et al. [29] and Roonasi and Mazinani [89]. In the former, $LaFeO_3$ was deposited on montmorillonite and employed to oxidize rhodamine B in water [29]. The composite photoactivity was higher than that of pristine $LaFeO_3$, which was associated with adsorption onto the surface. They got complete degradation of rhodamine B in 75 min, but the main drawback was that the total organic carbon (TOC) evolution was not followed during the time course of the photoreactions. Roonasi and Mazinani [89] supported barium ferrite on active carbon for the discoloration of dyes in water. When comparing the unsupported ferrite with the supported one, data showed that the photoactivity improved when adding active carbon owing to a synergetic effect.

Other strategies have been developed to improve the activity, too. Among them, coupling semiconductors in heterojunctions has gained importance. In this context, it is worth highlighting the employment of $LaFeO_3/SnS_2$, $LaFeO_3$/AgBr, $BiFeO_3$/BiOI and Ag_3PO_4-$CoFe_2O_4$-GO, the last one with a double improvement by the addition of an adsorbent. In the first case, $LaFeO_3$ was obtained by a hydrothermal method and was well dispersed in SnS_2 nanosheets [40]. Better activity than pristine $LaFeO_3$ was observed for tetracycline oxidation. In parallel, Song et al. [90] obtained a $LaFeO_3$/AgBr composite, used for rhodamine B removal. They got a faster movement of charges with the 10% $LaFeO_3$/AgBr. In these two cases, the enhancement of the photoactivity could be ascribed to the prevalence of Z-scheme mechanism of charge transfer. The synthesis of a $BiFeO_3$/BiOI composite by wet impregnation was carried out by Malathi et al. [91]. The authors designed a photocatalyst that was quite active and stable after several runs. The 2% $BiFeO_3$/BiOI afforded the maximum activity for complete rhodamine B depletion within the first 60 min of reaction and after three sequential cycles of reaction. The good activity was related to the efficient charge separation of photoinduced hole–electron pairs by transferring the electrons from the BiOI to $BiFeO_3$ surface [91]. Finally, the last work with composites was performed by Zielinska-Jurek et al. [26]. In this case, the role of ferrites was to provide a magnetic core to a TiO_2/SiO_2-coated material for recovery purpose after application. Figure 8 shows the high-angle annular dark-field (HAADF) images of the catalyst for illustration.

The last recently reported strategy deals with the partial substitution of cations in the ferrite structure. A few works have developed this method thus far. Jamil et al. synthesized a $BaFe_{1-x}Cu_xO_{3-\delta}$ material [38], the group of Rashmi et al. prepared

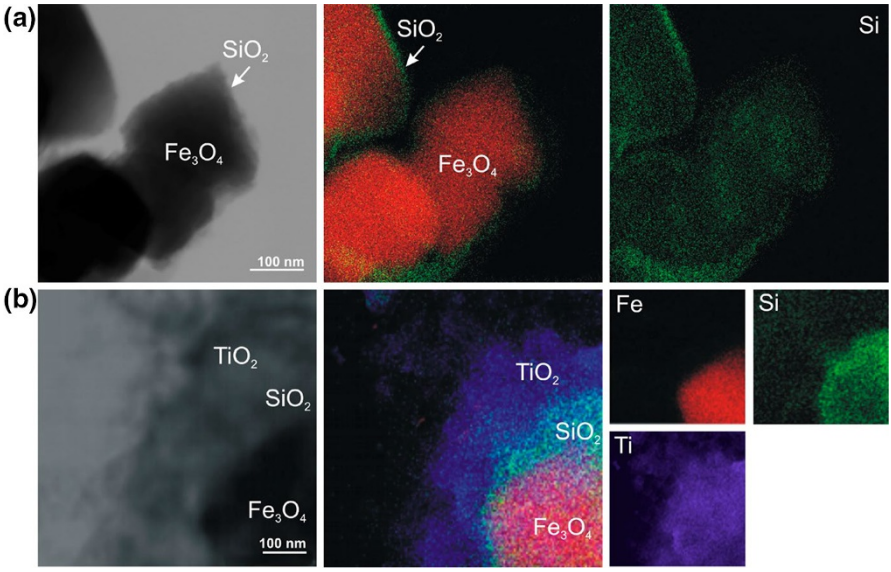

Fig. 8 HAADF images of Fe_3O_4/SiO_2 (**a**) and $Fe_3O_4/SiO_2/TiO_2$ (**b**) combined with mappings of Fe_3O_4, SiO_2 and TiO_2 (blue is Ti, red is Fe and green Si). Reproduced with permission from Ref. [26]. Copyright MDPI

$ZnSm_xFe_{2-x}O_4$ [21] and recently Garcia-Muñoz et al. obtained a $La_{1-x}Ti_xFeO_3$ ferrite by sol–gel method [37].

A Pechini synthesis of $BaFe_{1-x}Cu_xO_{3-\delta}$ catalyst led to a material rich in oxygen vacancies that was successfully employed for the degradation of atrazine in aqueous solution. The best photoactive catalysts comprising $BaFe_{0.95}Cu_{0.05}O_{3-\delta}$ provoked 90% atrazine removal (in 180 min of reaction) that resulted not only from the vacancies created during synthesis but also from the higher surface area [38]. In contrast, $ZnSm_xFe_{2-x}O_4$ nanoparticles were synthesised by co-precipitation method. In this case, the insertion of Sm^{3+} ions in the $ZnFe_2O_4$ spinel matrix increased the lattice parameter and crystallite size leading to an extension of the light absorption spectrum toward the visible range as Sm content increased up to $x=1.5$ with narrow bandgap (1.42 eV). This fact reduced the recombination of electron and holes, thereby improving the degradation of methyl orange [21]. A modified Pechini method was used for the synthesis of Ti-modified $LaFeO_3$ catalysts [37]. The best performance was achieved by adding 10% of nominal TiO_2 to the synthesis. However, low activity was seen for 4-chlorophenol depletion, whether solar light or visible light was used as activation source, which led to the implementation of other strategies that will be discussed below.

2.3 Ferrite Photocatalysts for Air Depollution

In contrast to water treatment, in the scope of air depollution, only a few works have been recently detailed, all of them treating NO_x (Table 3). The requirement for immobilizing ferrites onto supports improves the dispersion (avoiding

Table 3 Summary of ferrite catalysts for air detoxification

Catalyst	Method of synthesis	Pollutant	Conversion (%)	Advantages	Disadvantages	References
$BiFeO_3$	Sol–gel autocombustion	NO_x	36		UV light	Aghdam et al. [101]
$LaFe_{1-x}Ni_xO_3$/palygorskite	Sol–gel	NO_x	> 90	Visible light		Li et al. [32]
CQDs/$PrFeO_3$/palygorskite	Sol–gel impregnation	NO_x				Li et al. [33]

agglomeration of particles) of those kinds of catalysts characterized by relatively small surface areas. Therefore, more complex further studies are needed.

Only two works with pure single ferrite have been published up to now, to the best of our knowledge. Aghdam et al. [101] reported the synthesis of $BiFeO_3$ by a sol–gel procedure. The resultant material showed a bandgap value of 2.1 eV, and it was employed for the removal of NO_x under UV light. The authors got 36% conversion by using a reusable catalyst.

Other strategies have also been applied in air treatment. Li et al. developed the immobilization of several ferritic composites onto a palygorskite support [32, 33]. The first immobilized ferrite was $LaFeO_3$ where Ni was replacing Fe inside the perovskite structure; and the second was a ternary material composed of N-CQDs (nitrogen-doped carbon quantum dots) and of $PrFeO_3$ acting as consistent structure to be further supported. In the first case, the $LaFe_{1-x}Ni_xO_3$ structure was conditioned by the fraction of Ni added to the synthesis. While ratios below 0.4 gave rise to pure $LaFe_{1-x}Ni_xO_3$, when $x > 0.4$ the material contained a heterojunction due to the co-precipitation of some $LaNiO_3$. However, it must be said that 90% conversion was obtained when employing a ferrite with $x = 0.5$ [32]. In the second case, the ternary composite with 5% of CQDs/$PrFeO_3$ afforded 93% conversion with a total selectivity toward N_2 (Fig. 9). The good results obtained are associated with the formed Z-scheme that not only enhanced the separation of charges but also promoted the absorption of visible light [33].

2.4 Combination of Ferrite Photocatalysts and Other Oxidizing Agents

To take advantage of the redox surface properties of ferrite materials and to improve the reactivity, the ferrite catalysts started to be employed simultaneously as Fenton catalysts, with the addition of H_2O_2 as oxidizing agent, under light irradiation [22, 30, 92, 102, 103]. In this approach, materials with different compositions have been used for this purpose, like $LaFeO_3$, $CoFe_2O_4$, mesoporous $CuFe_2O_4$, $NiFeMO_4$ (M = La, Sm, Gd, Dy) and CuS/$BiFeO_3$.

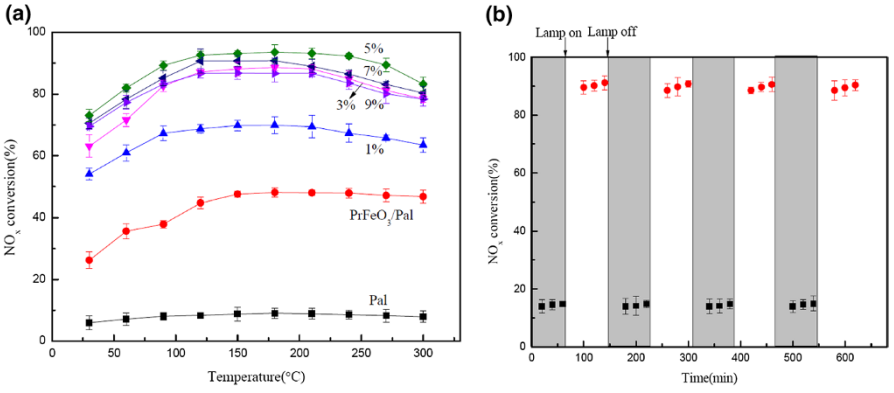

Fig. 9 NO_x conversion by N-CQDs/$PrFeO_3$/palygorskite with various amounts of N-CQDs (**a**) and 5 wt% N-CQDs/$PrFeO_3$/Pal during several lamp-on/off tests (**b**). Reproduced with permission from Ref. [33]. Copyright ACS

By adding H_2O_2, a larger variety of pollutants have been degraded than in the case of pure photocatalysis using ferrites (Table 4). In the first case, Sannino et al. [30] employed $LaFeO_3$ for the removal of acetic acid. Only 60% depletion in 300 min was obtained for the best case. Then $CoFe_2O_4$ ferrite was used to oxidize methylene blue, with almost complete oxidation in 75 min of reaction [22]. Gao et al. [102] employed mesoporous $CuFe_2O_4$ ferrite for the elimination of sulfonamides in water. The antibiotic conversion was 31% within 180 min, but no mineralization data was available. Samoila et al. [103] evidenced differences between pristine $NiFeO_4$ and $NiFeO_4$ substituted with La^{3+}, Sm^{3+}, Gd^{3+} or Dy^{3+} cations. The undoped material afforded 30% of Orange II azo dye decolorization vs. around 90% in 30 min with the La-substituted catalyst. Recently, a mixed strategy has been the employment of a co-catalyst with H_2O_2 [92]. The heterojunction of $CuS/BiFeO_3$ was exploited for alachlor degradation. The combined mechanism in the presence of H_2O_2 led to 90% of pesticide removal in 1 h of reaction.

Several efforts have been made to intensify the reactivity of ferrite materials in water in simultaneous application of advanced oxidation processes (AOPs). In this sense, the addition of H_2O_2 to the reaction media was not enough to improve substantially the activity. Lately, research has moved towards the material modification taking into account the composition of a ferrite and its ability to exchange A or B cation and so to tune its catalytic properties. In this scenario, the latest trend has been the doping of the materials with transition metals [31, 43, 95, 104, 105]. $Zn_xFe_{3-x}O_4$ materials were synthesized by a soft chemical route by Mandal et al. [95]. This magnetic catalyst was employed for the degradation of Acid Blue 113 and also for antimicrobial purposes. The pristine and modified ferrites showed very good photoactivity when H_2O_2 was added in the reaction media. The ferrites were quite stable after eight cycles of reaction and their magnetic properties allowed recovery after each sequential run. Around the same time, Soltani and Lee [31] obtained $BiFeO_3$ substituted by barium via sol–gel method. The ratio of substitution of $Bi_{1-x}Ba_xFeO_3$ was between 0.03 and 0.12. The experimental results indicate that the increase of Ba until 12% affected the redox cycle and provoked oxygen vacancies that significantly enhanced the toluene degradation under pure visible light.

In 2018, Cu-doped $LaFeO_3$ was obtained by Phan et al. [104]. The catalysts were employed for the decoloration of dye, in this case methyl orange. The best reactivity resulted from the catalyst with 15% copper. The authors attributed this improvement to the fact that it generates much more HO· than pristine $LaFeO_3$. This behaviour was associated with an enhancement of the H_2O_2 decomposition by the two metals, Cu and Fe, which provoke additional reactions, as well as an improvement of the availability of Fe(II) at the surface. The greater generation of HO· was corroborated by electron spin resonance (ESR) technique. In the same way, Co-doped $MgFe_2O_4$ was synthesized from saprolite laterite ore [43]. The low addition of Co (ca. 1%) greatly improved the activity; 97% of the dye was degraded and 68% of TOC mineralized after 180 min. The authors pointed out a synergistic effect between photocatalysis and heterogeneous photo-Fenton mechanism with this stable catalyst. The measurement of the iron leached into the solution showed that the activity was associated with the surface iron of the catalyst and not the iron in homogeneous solution. Besides this, the ferrite lost 10% of activity during its reuse.

Table 4 Summary of ferrite catalysts employed in simultaneous application of oxidation systems

Catalyst	Method of synthesis	Pollutant	Conversion	Advantages	Disadvantages	References
Cu-doped $LaFeO_3$	Hydrothermal	Methyl orange	90% MO with 15% Cu (60 min)	Visible light	No TOC data	Phan et al. [104]
$LaFeO_3$	Sol–gel	Acetic acid	60% TOC with Fe substitution (300 min)	Higher effective use of H_2O_2		Sannino et al. [30]
$CoFe_2O_4$	Co-precipitation	Methylene blue	98.6–99.3% MB (75 min)			Vinosha et al. [22]
Co-$MgFe_2O_4$	Hydrothermal	Rhodamine B	95% rhodamine B; TOC > 85% (180 min)	Visible light		Diao et al. [43]
Mesoporous $CuFe_2O_4$	Synthesis including template	Sulfonamide	31% TOC (40 min)	Good reusability	No mineralization	Gao et al. [102]
$NiFeMO_4$ (M = La, Sm, Gd, Dy)	Sol–gel autocombustion	Dyes, Orange II	30% undoped material; 90% La doped (30 min)		No TOC data	Samoila et al. [103]
$(Ba,Bi)FeO_3$	Sol–gel	Toluene	Total degradation; 85% TOC (40 min)	Visible light		Soltani and Lee [31]
$Ni_xZn_{1-x}Fe_2O_4$	Sol–gel autocombustion	4-Cl-phenol	Total degradation; 99% TOC (120 min)	Stable after 5 runs		Kurian and Nair [27]
$CuS/BiFeO_3$	Two-step	Alachlor	90% alachlor removed (60 min)	High stability		Bhoi and Mishra [92]
$Zn_xFe_{3-x}O_4$	Soft chemical route	Dye Acid Blue 113; disinfection		92% of dye removal; synergetic effect with H_2O_2		Mandal et al. [95]
Metal-doped zinc ferrite nanosphere	Two-step method	Congo red	96% removal of dye in 3 h (180 min)	60% TOC depletion	Loss of activity with cycles of use	Li et al. [105]
$La_{1-x}Ti_xFeO_3$	Pechini sol–gel	4-Cl-phenol (4-CP)	100% 4-CP removal under different light spectra	100% TOC removal (120 min)		Garcia-Muñoz et al. [37, 106]

Recently, Li et al. [105] obtained a metal-doped zinc ferrite material by a modified microwave hydrothermal method. The authors compared synthesis using metals in wastewater and also using chemical precursors. The catalytic test showed that the doped material synthesized by using metals contained in wastewater was much more active than the one using chemical precursors. Also, the substituted ferrite exhibited better efficiency than the pristine $ZnFe_2O_4$. The authors postulated that HO· are formed through photo-generated h^+ and H_2O_2 decomposition by Fe^{3+} and Mn^{3+} on the catalyst surface. After the first cycle of reaction, 95% of Congo red was depleted within 3 h which led to 60% of TOC conversion. After the third cycle of reaction, 75% decoloration was reached, indicating a slight loss of activity of the material.

Finally, the $La_{1-x}Ti_xFeO_3$ material synthesized through a modified Pechini sol–gel method by Garcia-Muñoz et al. [37] was employed as a combined photocatalyst and heterogeneous photo-Fenton catalyst without any homogeneous contribution (Fig. 10). The authors demonstrated that the strategy combining both AOPs within

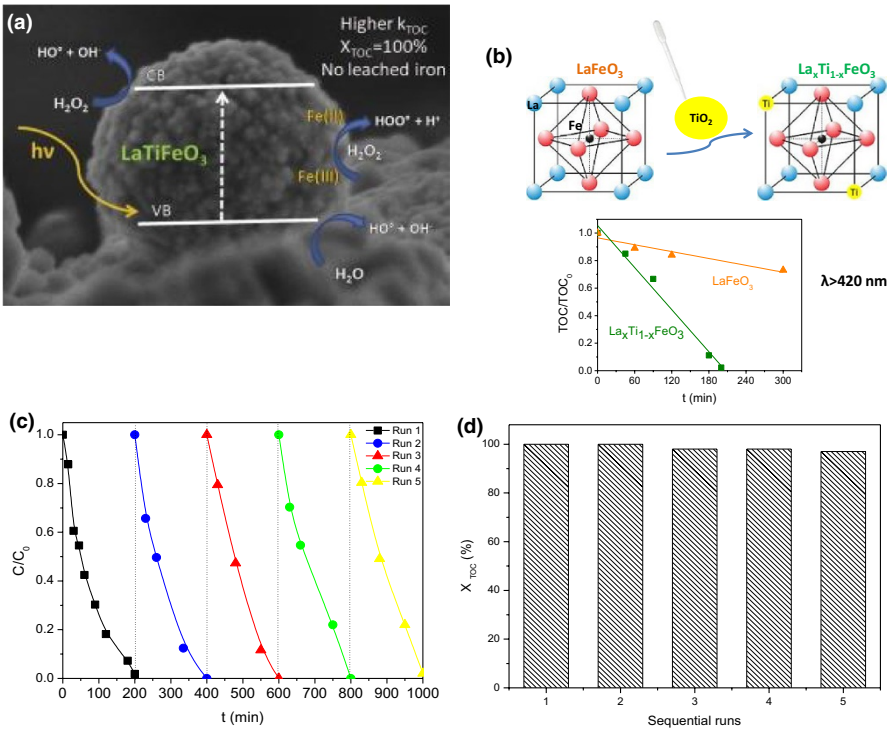

Fig. 10 **a** Scheme of the mechanism of reaction of the combined H_2O_2/photocatalytic process. Reproduced with permission from Ref. [37]. **b** Partial Ti → La cationic substitution in the $LaFeO_3$ network and the resulting strong TOC removal rate improvement under pure visible light ($\lambda > 420$ nm). Reproduced with permission from Ref. [106]. Copyright Elsevier. Reusability tests with five consecutive runs performed on the $La_{1-x}Ti_xFeO_3$ dual catalyst in the system H_2O_2/visible light: **c** evolution of the relative 4-chlorophenol concentration and **d** TOC mineralization degree obtained after 210 min of test. Operating conditions: $[4\text{-Cl-phenol}]_0 = 25$ mg l^{-1}; $[H_2O_2]_0 = 125$ mg l^{-1}; $T = 25$ °C; [cat] = 0.5 g l^{-1}; ($\lambda > 420$ nm). Reproduced with permission Ref. [106]. Copyright Elsevier

a single dual catalyst allowed $La_{1-x}Ti_xFeO_3$ to simultaneously take advantage of the higher reaction rate of the photoassisted heterogeneous Fenton process and of the higher mineralization yield of photocatalysis. This Ti-substituted $LaFeO_3$ dual catalyst was reported to be very active in water treatment, by reaching complete mineralization and total pollutant removal with higher efficiencies than via single AOPs, whether the process operates under UVA light, simulated solar light or pure visible light ($\lambda > 420$ nm). The dual catalyst operates via pure heterogeneous surface reactions with an increase in the catalyst robustness by more than two orders of magnitude compared to the unsubstituted ferrite. This was symbolized by the absence of any Fe release and by the stability of catalytic performance with test cycles with no loss of activity [106].

3 Ferrite-Based Photocatalysts and Photoelectrodes for Energy Applications: Hydrogen Production and CO_2 Reduction

3.1 Introduction

Energy applications of photocatalysis, mainly CO_2 reduction and hydrogen production by water splitting or photoreforming, are technologically less developed than environmental ones (viz. pollutant degradation), although their scientific interest has increasingly grown in the last decades as a result of their appealing possibilities in a hopefully not-so-long-term circular economy based on solar energy [107].

The production of hydrogen from renewable feedstock and energy sources is crucial for its implementation as a clean energy vector in a future non-carbon-based energy system [108]. Photocatalysis and photoelectrochemistry offer the possibility of directly converting sunlight into chemical energy by splitting the water molecule into hydrogen and oxygen, making use at the surface of semiconductor photocatalysts of the reductive and oxidative power of photo-generated electrons and holes, respectively. Alternatively, as a result of the kinetic constraints of water oxidation, hydrogen can be produced using organic sacrificial agents, ideally derived from biomass feedstock, in the process called photoreforming [109, 110]. In the last decades, vast amounts of semiconductors have been tested as photocatalysts for photocatalytic or photoelectrochemical water splitting [107, 111, 112], among which iron-based oxides and particularly ferrites have been less explored than other types of materials. This is generally related to low charge carrier mobilities and hence short exciton lifetimes, which nevertheless can be improved by doping or by other chemical, structural or surface modifications [113, 114]. Some ferrites indeed have the adequate band positions for at least one of the half-reactions (proton reduction and water oxidation) involved in water splitting and, furthermore, these positions can be tuned by means of the inclusion of different metals into the ferrite structure [114]. As described below, some ferrites have been reported active for photocatalytic hydrogen evolution. Selected examples are summarized in Table 5.

Regarding photoelectrochemical hydrogen production, varied chemical composition, multiple valence states and choice of metal cation, narrow bandgaps and both n-type and p-type behaviour convert ferrites into attractive candidates as electrodes

Table 5 Photocatalytic hydrogen production with selected single-phase ferrite photocatalysts

Catalyst	Bandgap (eV)	Co-catalyst	Sacrificial agent	Light source	H_2 evolution rate (mmol h^{-1} g_{cat}^{-1})	Apparent quantum yield (%)	References
Fe_3O_4	2.7	Pt	Ethanol	2×200 W tungsten lamp	8.275	–	Mangrulkar et al. [142]
Fe_3O_4	2.84	–	Methanol	Simulated solar	1.25	–	Gobara et al. [144]
$NiFe_2O_4$	1.7	–	Methanol	250 W Xe lamp $\lambda \geq 420$ nm	0.155	0.52 ($\lambda \geq 420$ nm)	Peng et al. [145]
$NiFe_2O_4$	1.56	–	$S_2O_3^{2-}$	500 W halogen lamp	1.529	0.53 (full spectrum)	Rekhila et al. [127]
$NiFe_2O_4$	1.7	–	Methanol	Xe lamp $\lambda \geq 420$ nm	0.045	7.5×10^{-3} ($\lambda = 450 \pm 10$ nm)	Hong et al. [146]
$NiFe_2O_4$	1.73	Au	Triethanolamine	300 W Xe lamp $\lambda \geq 420$ nm	3.162	–	Zeng et al. [149]
$NiFe_2O_4$	1.62	–	Methanol	Simulated solar	4.95	–	Gobara et al. [144]
$NiFe_2O_4$	1.6	–	Methanol	250 W metal halide lamp	0.040	–	Domínguez-Arvizu et al. [147]
$NiFe_2O_4$	1.79	–	Methanol	250 W metal halide lamp	0.016	–	Rodríguez-Rodríguez et al. [150]
$ZnFe_2O_4$	2.23	–	Methanol	Simulated solar	4.37	–	Gobara et al. [144]
$ZnFe_2O_4$	1.90	–	Methanol	250 W metal halide lamp	0.044	–	Rodríguez-Rodríguez et al. [150]
$ZnFe_2O_4$	1.93	–	Methanol	500 W Hg lamp $\lambda \geq 420$ nm	0.134	0.19 ($\lambda \geq 420$ nm)	Dom et al. [151]
$CoFe_2O_4$	1.39	–	Methanol	250 W metal halide lamp	0.016	–	Rodríguez-Rodríguez et al. [150]
$CoFe_2O_4$	1.15	–	Methanol	250 W Hg lamp	0.436	–	Ortega López et al. [153]
$CuFe_2O_4$	–	–	Oxalic acid	250 W Xe lamp	1.72	–	Yang et al. [154]

Table 5 (continued)

Catalyst	Bandgap (eV)	Co-catalyst	Sacrificial agent	Light source	H_2 evolution rate (mmol h^{-1} g_{cat}^{-1})	Apparent quantum yield (%)	References
$CaFe_2O_4$	1.83	Pt	Methanol	Hg arc lamp $\lambda = 420 \pm 10$ nm	1.09	1.57 ($\lambda = 420 \pm 10$ nm)	Dom et al. [155]
$SrFe_2O_4$	1.77	–	Methanol	250 W Hg lamp	0.730	–	Jiménez-Miramontes et al. [156]
$LaFeO_3$	2.11	–	Methanol	125 W Hg lamp $\lambda \geq 420$ nm	8.6	8.07 ($\lambda \geq 420$ nm)	Parida et al. [83]
$LaFeO_3$	2.07	Pt	Ethanol	2 × 200 W tungsten lamp	3.315	–	Tijare et al. [157]
$LaFeO_3$	2.0	–	Glucose	10 W LED 440 nm	0.292	–	Iervolino et al. [158]
Ru-doped $LaFeO_3$	1.98	–	Waste water from brewing	10 W LED 460 nm	0.532	–	Iervolino et al. [199]
$LaFeO_3$	2.22	Pt	Triethanolamine	300 W Xe lamp $\lambda \geq 420$ nm	0.707	–	Chen et al. [159]
$La_{0.925}Sr_{0.075}Fe_{0.925}Ti_{0.075}O_3$	2.1	Pt	Methanol	300 W Xe lamp $\lambda \geq 420$ nm	0.555	–	Hojamberdiev et al. [160]
$LaSrFeO_4$	2.16	Pt	Na_2SO_3	500 W Hg lamp $\lambda \geq 400$ nm	0.158	0.19 ($\lambda \geq 420$ nm)	Chen et al. [200]

for photoelectrochemical cells (PECs). However, even if they are considered as promising, terrestrially abundant and non-toxic alternative photoactive materials for PECs, only a few works have been published using ferrites as photocathodes and photoanodes [114, 115]. Actually, the measured photocurrents of PECs with ferrite photoelectrodes are still low, which is mainly related to the charge mobility limitations mentioned above. Similarly to the case of photocatalysis, different strategies proved that higher photocurrents can be achieved, including nanostructuring, heterojunctions, co-catalyst loading and control of the defect chemistry [114, 115]. Pioneering work on the fundamental investigation using ferrites as electrodes in (photo)electrochemical reactions dates back to the late 1970s and early 1980s and has continued in the subsequent years, including different compositions; p-type $CaFe_2O_4$ [116–123], $CdFe_2O_4$ [124], p- and n-type $Co_xFe_{3-x}O_4$ and $CoTi_xFe_{2-x}O_4$ [125], p-type $CoFe_2O_4$ [126], p- and n-type $NiFe_2O_4$ [58, 127], $Li_{0.5}Fe_{2.5}O_4$ [128], $MgFe_2O_4$ [129, 130], $Ti_xFe_{3-x}O_4$ [131] and n-type $ZnFe_2O_4$ [128–134] are remarkable examples.

In turn, CO_2 reduction is probably the lowest-TRL (technology readiness level) application of photocatalysis. In spite of its scientific interest, providing a route for CO_2 valorisation coupled to solar energy harnessing [135], it still faces a number of issues mainly related to the inherent difficulty associated with the stability and relative inertness of the CO_2 molecule and to the complex nature of water oxidation. Indeed, the latter is in principle the preferred reaction to complete the electron balance as nature does in photosynthesis [136]. Among the different semiconductors that have been reported as CO_2 reduction photocatalysts [137–139], ferrite-based ones do not play a prominent role, even if some of these oxides have adequate band positions for some of the reactions involved in CO_2 reduction [140]. Nevertheless, a few works have reported photocatalytic and photoelectrochemical CO_2 reduction using ferrite materials, as will be described in the next sections.

3.2 Ferrite Photocatalysts for Water Splitting and CO_2 Reduction

3.2.1 Single-Phase Ferrite Photocatalysts

Magnetite, the chemically simplest ferrite (Fe_3O_4 or $Fe^{II}Fe^{III}_2O_4$), can be employed for water oxidation in the presence of the appropriate co-catalyst, as shown by Neudeck and co-workers, who prepared Fe_3O_4 nanoparticles using xyloglucan as stabilizing agent [141]. This method yields size-controllable nanoparticles with narrow size distributions, which are able to oxidize water into oxygen under irradiation with a blue-light LED, with the participation of the $[Ru(bipy)_3]^{3+}$ complex as sensitizer/co-catalyst and using sodium persulfate as electron scavenger. In the presence of other nanoparticle-stabilizing polymers such as dextran, magnetite also showed oxygen evolution, although lower than that attained with the xyloglucan. This reveals an effect of the latter that, according to the authors, is beyond surface area and might be related to the lifetime of the photo-generated excited Ru complex that would favour charge transfer to water molecules.

Sacrificial hydrogen production over magnetite was reported by Mangrulkar and co-workers in the presence of ethanol as sacrificial reagent, with platinum as co-catalyst, and under UVA–Vis (tungsten filament lamp) irradiation [142]. The material was synthesized in the form of 10–12 nm nanoparticles, and the bandgap was roughly estimated from the UV–Vis spectrum as 2.7 eV, considerably larger than the value of ca. 1.9 eV determined from photoelectrochemical measurements [143]. The Pt/Fe_3O_4 photocatalytic system was active for hydrogen evolution in the presence of different sacrificial reagents, with ethanol giving the best results over methanol and ethanolamine. Experiments carried out in different conditions revealed that hydrogen evolved only above a certain value of irradiation power, and that, in the dark, there was hydrogen evolution when the temperature was raised. This suggests that the reaction has a thermal component, and indeed experiments under photothermal conditions revealed a synergistic effect of the photocatalytic and the thermocatalytic effects, even at temperatures as low as 100 °C. Deactivation of the catalyst was observed in all cases, and photothermal conditions also enhanced this deactivation.

Gobara et al. compared the activity of magnetite for hydrogen production from methanol aqueous solutions under simulated solar radiation with those of different ferrites resulting from the substitution of several divalent cations (Zn^{2+}, Cd^{2+} or Ni^{2+}) for Fe^{2+} [144]. All catalysts were prepared by co-precipitation methods which resulted in nanocrystalline cubic phases except for the cadmium ferrite which was considerably less crystalline and contained a segregated Fe_2O_3 phase. The bandgaps decreased upon metal substitution from 2.8 eV in Fe_3O_4 to 1.62, 1.90 and 2.23 eV in Ni, Cd and Zn ferrites, respectively. All samples gave rise to hydrogen evolution without the use of any co-catalyst and with stable rates along 72 h. All three ferrites led to higher hydrogen evolution rates than magnetite in the order $Zn < Cd < Ni$, although in the case of the cadmium sample this should be viewed cautiously because of the presence of the mentioned iron oxide phase. The superior activity of nickel ferrite was attributed to the affinity of Ni for hydrogen. Nonetheless, the $NiFe_2O_4$ sample displayed the highest metal surface area as determined by hydrogen chemisorption.

Indeed, $NiFe_2O_4$ is probably the most extensively explored ferrite photocatalyst for water splitting reactions. As summarized in Table 5, some works have reported its activity in different experimental conditions, with a quite wide range of hydrogen production rates. An apparent quantum yield of 0.53% was obtained by Rekhila et al. with a sol–gel-prepared nickel ferrite using thiosulfate as sacrificial reagent without any co-catalyst, under the full spectrum of a halogen lamp [127] and under optimum conditions of pH, $S_2O_3^{2-}$ concentration and catalyst mass. An electrochemical impedance spectroscopy analysis revealed the p-type semiconductivity of $NiFe_2O_4$, as well as the drastic increase of the lifetime of electrons under illumination in the presence of the sacrificial reagent, emphasizing its crucial role in improving the charge separation by hole scavenging. Peng and co-workers obtained $NiFe_2O_4$ nanoparticles with homogeneous size distribution and high surface area by means of a surfactant-assisted hydrothermal method [145]. These nanoparticles gave rise, under visible light ($\lambda \geq 420$ nm) and in the absence of any co-catalyst, to hydrogen evolution from an aqueous methanol solution with an apparent quantum yield of 0.52%, after an optimum calcination temperature of 500 °C in which a compromise between

crystallinity and surface area is reached. The effect of particle size and distribution is revealed by the lower efficiency of $NiFe_2O_4$ synthesized without any structure-directing agent, which was formed by inhomogeneous agglomerations of particles. X-ray diffraction (XRD) and X-ray photoelectron spectroscopy (XPS) studies of the solid together with inductively coupled plasma atomic emission spectroscopy (ICP-AES) analyses of the liquid reaction medium and consecutive activity runs confirmed the stability of the ferrite in the reaction conditions. In the absence of any sacrificial reagent, some hydrogen evolution was observed in water spitting experiments, although without any oxygen production, which suggests the possibility of self-oxidation or the possible role of organic matter remaining from the synthesis as hole scavenger. A structure-directing agent, in this case Pluronic F-127, was also used by Hong and co-workers to obtain mesoporous $NiFe_2O_4$ photocatalysts with high crystallinity and large surface area by a self-assembly associated aerosol spray pyrolysis method [146], which were tested for methanol photoreforming under visible light irradiation ($\lambda > 420$ nm). Again, the highest activity of all the catalysts appears as a compromise between crystallinity and surface area, with well-crystallized mesoporous samples resulting in higher H_2 evolution rates than amorphous ones with small pore size and high Brunauer–Emmett–Teller (BET) values, but also higher than a non-mesoporous, highly crystalline ferrite with relatively low surface area. The photocatalytic character of the reaction was demonstrated by an action spectrum study that showed that the dependence of hydrogen evolution on the irradiation wavelength closely matched the absorption spectrum of $NiFe_2O_4$ (Fig. 11). This mesoporous ferrite was shown to be stable up to three photocatalytic runs without any loss of activity and without structural or morphological modifications.

A modification of the Pechini method was employed by Domínguez-Arvizu et al. to obtain single-phase nickel ferrite with average crystal size of 25 nm and 50 $m^2\ g^{-1}$ of BET surface area after calcination temperature of 400 °C, which was determined as the minimum one to remove all the organic matter after the chelation step [147].

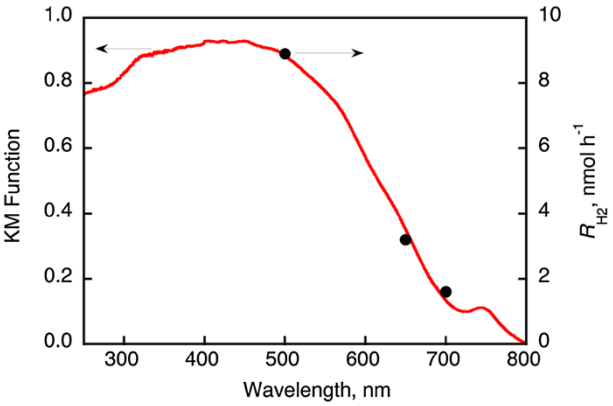

Fig. 11 Dependence of H_2 evolution rates (R_{H2}) on the wavelength of monochromatic light irradiation of a 25 vol.% methanol aqueous solution with a mesoporous $NiFe_2O_4$ photocatalyst. Reproduced with permission from Ref. [146]. Copyright American Chemical Society

The authors studied some optical characteristics such as the absorption spectrum and scattering, absorption and extinction coefficients, as a basis for future designs of photoreactors using this catalyst. Under white light and without any co-catalyst present, $NiFe_2O_4$ produced ca. five times larger amount of hydrogen than TiO_2 P25 after 8 h from an aqueous methanol solution.

In photocatalytic hydrogen evolution reactions, the presence of a co-catalyst, most generally a noble metal, improves the hydrogen yield by boosting charge separation and acting as catalytic sites for H–H bond formation [148]. In addition, in the case of some metals with appropriate particle size, the localized surface plasmon resonance effect may enhance light absorption in the visible range [107]. In recent work, Zeng and co-workers examined the combined effect of plasmonic gold nanoparticles and fluorescein sensitization on the activity of $NiFe_2O_4$ photocatalysts for visible-light-induced hydrogen production from water using triethanolamine as sacrificial reagent [149]. The presence of gold increased the hydrogen yield by a factor of 5 at an optimum metal loading with respect to the pure ferrite, which the authors ascribed to stronger absorption in the visible range and slower recombination on the basis of UV–Vis and photoluminescence spectra, respectively. A synergistic effect of fluorescein sensitizer and plasmonic Au co-catalyst further improved the photoactivity by one order of magnitude, with stable hydrogen production throughout six photocatalytic cycles.

In contrast to the work by Gobara et al. [144] cited above, Rodríguez-Rodríguez and co-workers obtained a higher hydrogen yield with the spinel zinc ferrite $ZnFe_2O_4$ compared to $NiFe_2O_4$ [150]. The authors prepared nanosized Ni, Co and Zn ferrites in oil-in-water microemulsions and tested them without any co-catalyst for photocatalytic hydrogen evolution from methanol aqueous solutions. The photocatalytic activity followed the order $ZnFe_2O_4 > NiFe_2O_4 > CoFe_2O_4$, which is mainly attributed to conduction band energies increasing in the reversed order on the basis of UV–Vis spectra. A higher conduction band energy would thus imply a stronger driving force for the transfer of electrons to protons. Dom and co-workers used a microwave solid-state synthesis method to improve the activity of zinc ferrite by a factor of 4 with respect to the one obtained by a conventional solid-state reaction [151]. Electrochemical measurements together with physicochemical and optical characterizations let the authors conclude that the absence of agglomeration of nanoparticles in the microwave method compared to the conventional one modified the electronic band positions and the electron mobility, resulting in improved photocatalytic behaviour. Doping zinc ferrite may also lead to improved photocatalytic hydrogen production, as shown by Boudjemaa and co-workers, who prepared $M_{0.2}Zn_{0.8}Fe_2O_4$ spinels by a co-precipitation method, wherein M is Co, Ni or Cu [152]. In this work, a considerable improvement of the activity of the zinc ferrite is reported in the case Co doping and Ni doping, with the former giving the best results of the series. In contrast, Cu doping resulted in a decrease of activity with respect to $ZnFe_2O_4$. On the basis of electrochemical, photoelectrochemical and optical characterization, the authors mainly ascribe the effect of the guest cation on activity to its influence on the electronic structure of the ferrites, with the bandgap values of the different samples decreasing in the same order as the obtained hydrogen evolution rates increase.

Ortega López et al. reported significant hydrogen production with the cobalt spinel ferrite $CoFe_2O_4$ [153]. They compared two different synthetic methods, namely co-precipitation, followed by a relatively low temperature crystallization, and ball-milling of a stoichiometric mixture of iron metal and Co_3O_4 previously activated and solid-state reaction at 700 °C. The latter method yielded a final $CoFe_2O_4$ cubic spinel with 5 nm crystal size vs. 20 nm with the former synthesis. This, however, resulted in a lower surface area of the ball-milled sample than the co-precipitated one and, contrary to what may be expected from the quantum-size effect, to a considerably lower bandgap (1.15 vs. 1.38 eV). The authors ascribe both results to the differences in the secondary particle size (100–500 vs. 25 nm), which is more plausible in the case of the surface area than in that of the electronic structure. In any case, the ball-milled sample exhibited a higher adsorption capacity which the authors relate to oxygen vacancies created by the high-energy mechanochemical process and invoke to explain the higher hydrogen production per surface area unit displayed by this catalyst.

Copper ferrite ($CuFe_2O_4$) has also been shown to be active for photocatalytic hydrogen evolution. Yang et al. obtained $CuFe_2O_4$ nanoparticles by sol–gel, solid-state reaction and co-precipitation methods, among which the first one yielded the highest hydrogen formation rate using oxalic acid as sacrificial reagent [154]. The use of citric acid in the sol–gel method resulted in a relatively homogeneous particle size distribution, which according to the authors had a key influence on the higher activity of the obtained photocatalyst, as a result of the shorter path travelled by photo-generated charges to the surface. The $CuFe_2O_4$ photocatalyst was active in four consecutive cycles, although a decline in the hydrogen evolution rate can be observed in each of them.

Regarding ferrites of non-transition metals, some alkali and alkaline earth metal ferrites have been tested for photocatalytic hydrogen evolution. For example, Boudjemaa and co-workers synthesized the $MgFe_2O_4$ spinel ferrite by calcination of a Mg–Fe layered double hydroxide obtained by co-precipitation [130]. This material gave rise to hydrogen evolution under visible light from an aqueous sulfite solution, although production declined after 20 min of reaction. This authors ascribed this deactivation to the saturation of catalytic sites and competitive reduction of the end product $S_2O_6^{2-}$ for conduction band electrons. Dom et al. reported the synthesis of orthorhombic $CaFe_2O_4$ nanoparticles using different preparation methods, namely solid-state reaction, polymer complex, microwave sintering and self-propagating combustion (SPC) [155]. As they already reported for zinc ferrite [151], the microwave-directed method yielded interesting results, outperforming by nearly one order of magnitude the activities obtained with the rest of syntheses, which gave very similar results [155]. The authors ascribed this difference to an optimum combination of high crystallinity with monodispersed morphology together with efficient visible light absorption, suitable band energetics and relatively low charge transfer resistance. Photodeposition of platinum as a hydrogen evolution co-catalyst resulted in further improvement of the activity by a factor of ca. 2.5, resulting in an apparent quantum yield of 1.57% under 420 nm irradiation. Different strontium ferrites, namely the cubic, hexagonal and orthorhombic $SrFe_2O_4$, $SrFe_{12}O_{19}$ and $Sr_7Fe_{10}O_{22}$, respectively, were selectively

obtained by Jiménez-Miramontes et al. by modifying the crystallization conditions in the Pechini synthetic method [156]. Among the three crystalline phases, the activity towards hydrogen production under UV irradiation was maximum for the cubic one, with the hexagonal phase yielding a two orders of magnitude lower amount of hydrogen as a result of unsuitable band positions.

The perovskite-type lanthanum ferrite, $LaFeO_3$, has been studied for photocatalytic hydrogen evolution in a number of articles. It is considered as a promising catalyst for this application by combining adequate band positions, visible light absorption and (photo)chemical stability. Parida and co-workers actually reported that $LaFeO_3$ was active both for hydrogen evolution from water by using an electron-donating (methanol) sacrificial agent and for oxygen evolution with an electron-scavenging (Ag^+) agent. High productions were obtained in both cases (see Table 5 for the case of hydrogen), although no overall water splitting experiments were reported [83]. Using ethanol as sacrificial agent, Tijare and co-workers reported a relatively similar hydrogen evolution rate (even if the usual difficulties to quantitatively compare different works must be considered) that could be further boosted by using platinum as co-catalyst [157]. However, in this case the improvement caused by platinum was considerably low if compared to its effect on other semiconducting catalysts [148]. Indeed, Iervolino and co-workers studied $LaFeO_3$ as a promising noble-metal-free hydrogen evolution photocatalyst [158]. Interestingly, they reported stoichiometric overall water splitting (i.e. without any sacrificial reagent) under UV light over $LaFeO_3$ photocatalysts synthesized using the solution combustion method. The hydrogen yield increased by a factor of 4 when using glucose as sacrificial electron donor. Under purely visible light irradiation (440 nm), the activity of the best-performing catalyst, obtained from an optimized synthetic method, for glucose photoreforming was above 70% of that under UV, revealing the interest of this material as a visible-light-active photocatalyst. Using a similar synthetic procedure, Chen et al. obtained a homogeneously nanocrystalline $LaFeO_3$ that was further modified by encapsulation with a conductive polyaniline (PANI) aerogel (Fig. 12) as a means to control the hydrophilicity of the surface and to improve charge mobility. An improvement of hydrogen evolution activity of about four times with respect to the unmodified ferrite was observed, using in this case platinum as co-catalyst and triethanolamine as electron donor [159]. Doping Ru^{3+} into the Fe^{3+} positions of the $LaFeO_3$ structure improved the hydrogen evolution rate in this reaction by a factor of ca. 4.5 under UV irradiation [158], which was ascribed to the role of the dopant cation as electron scavenger, preventing electron–hole recombination. The optimum doped catalyst was also active in glucose photoreforming under visible light and, in an especially interesting result, in the valorisation of real waste water from a brewing company by using it as sacrificial agent for the production of hydrogen. Partial substitution of Sr^{2+} for La^{3+} and Ti^{4+} for Fe^{3+}, using a flux growth synthetic method, was studied by Domen and co-workers as a way of further improving the photocatalytic activity of $LaFeO_3$ for hydrogen evolution by methanol photoreforming, using Pt as co-catalyst [160]. Simultaneous cation substitution led to improvement in photocatalytic activity attributed to the concurrence of modified structural properties by Sr doping and electronic characteristics due to Ti doping, as well as reduced grain boundaries and lattice defects, which relates to the

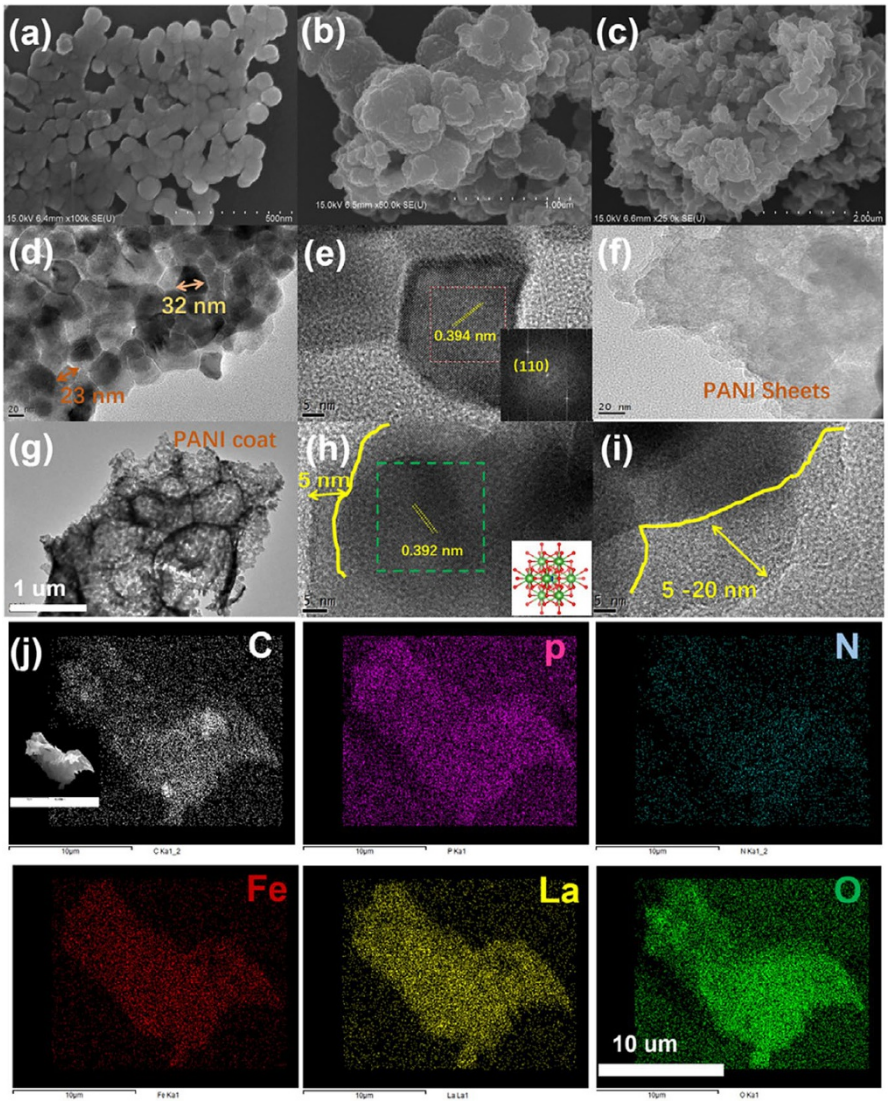

Fig. 12 SEM images of **a** $LaFeO_3$, **b** $LaFeO_3$-0.75PANI, **c** PANI; TEM image of **d**, **e** $LaFeO_3$, **f** PANI, **g–i** $LaFeO_3$-0.75PANI; **j** EDX element mapping of $LaFeO_3$-0.75PANI. Reproduced with permission from Ref. [159]. Copyright Elsevier

synthesis method. The combination of the different factors led to an optimal activity in $La_{0.925}Sr_{0.075}Fe_{0.925}Ti_{0.075}O_3$. Related perovskite lanthanum strontium ferrites in the Ruddlesden–Popper series $(SrO)(LaFeO_3)_n$ ($n = 1$ and 2) were reported as hydrogen evolution photocatalysts from Na_2SO_3 solutions by Chen and co-workers [161], with the $n = 1$ compound ($SrLaFeO_4$) giving rise to a higher hydrogen evolution rate

with Pt as co-catalyst. Anisotropic charge transportation phenomena are invoked to account for the activity of this kind of solid.

As mentioned earlier, photocatalytic CO_2 reduction studies with ferrite catalysts are much scarcer in the literature than hydrogen production ones. Matsumoto and co-workers reported in 1994 the production of methanol and formaldehyde from a CO_2-saturated solution on $CaFe_2O_4$ irradiated with light of different wavelengths [162]. The CH_3OH production followed the same trend versus irradiation wavelength as the photocurrent in a $CaFe_2O_4$ photocathode, proving the photocatalytic character of the reaction. However, in spite of the narrow bandgap of the ferrite (1.9 eV), both photocurrents and CO_2 conversions were significantly higher under UV light. Results with the addition of suspended solid $BaCO_3$ led the authors to propose a mechanism in which CO_3^{2-}/CO_2 activation occurs at the interface between the solid catalyst, the solid carbonate and water. Matsumoto reported 2 years later a screening of photoelectrochemical response and CO_2 reduction to methanol with different ferrites [140]. Both properties were not necessarily related, with some ferrites showing electrochemical but not catalytic activity under irradiation and vice versa. Not only was the mentioned calcium ferrite was photocatalytically active but also some compositions containing magnesium, strontium, barium, lead and bismuth were. The elements forming the oxides as well as the positions of the band edges were found to determine the photocatalytic activity, with $CaFe_2O_4$ and $(Bi, Pb)_2Sr_2BiFe_2O_{9+x}$ giving the best results.

Apparently, as reported by Xiao and co-workers from a combination of UV–Vis and XPS, $ZnFe_2O_4$ has adequate band positions to conduct, under visible light, CO_2 reduction but not water oxidation [163]. Therefore, triethanolamine was used in that study as a sacrificial agent to scavenge photoproduced holes, while conduction band electrons were utilized to reduce aqueous bicarbonate into mainly acetaldehyde and ethanol. However, it remains unclear whether these products result from the oxidation of triethanolamine.

3.2.2 Ferrite-Based Heterojunction Photocatalysts

Either by combining different ferrites or by combining one ferrite with another semiconductor like TiO_2, ZnO or C_3N_4, some works have dealt with the improvement of photocatalytic hydrogen production or carbon dioxide reduction by incorporating these materials into different kinds of heterostructures.

Regarding the combination of different ferrites, Chen et al. reported the fabrication of a $CaFe_2O_4/MgFe_2O_4$ bulk p–n heterojunction for photocatalytic hydrogen evolution from aqueous methanol solutions under visible light, with the use of two co-catalysts, namely RuO_2 and Pt [164]. By *bulk heterojunction*, the authors mean that there are junctions of the two phases distributed along the whole composite material, as investigated by high-resolution TEM, which was prepared by a polymer-complex synthetic method that allowed good crystallinity to be obtained at low temperature as well as an adequate distribution of the composing phases. This heterojunction, whose band structure is shown in Fig. 13, gave rise to a remarkable hydrogen production activity under light with $\lambda \geq 420$ nm, with reported quantum yield of ca. 10%, in contrast with the single phases that showed little activity in the

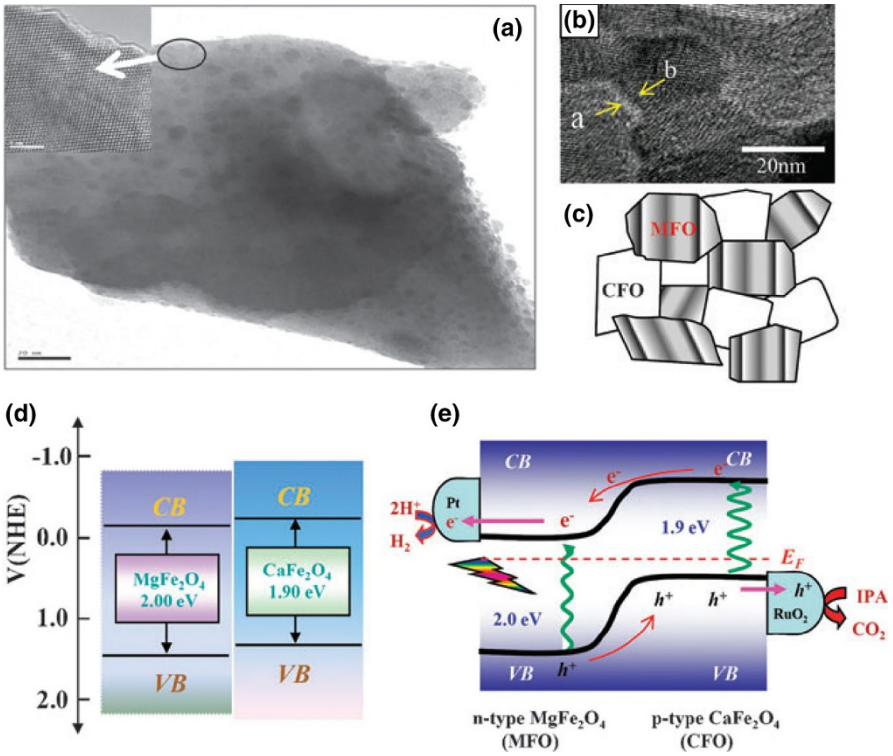

Fig. 13 **a** TEM image of a $CaFe_2O_4/MgFe_2O_4$ particle. **b** High-resolution TEM image of interfaces between semiconductor nanoparticles. **c** Schematic model of interpenetrating domains of $CaFe_2O_4$ (white) and $MgFe_2O_4$ (grey). **d** Energy band diagram showing bandgap energies and band positions of p-$CaFe_2O_4$and n-$MgFe_2O_4$. **e** Operating principle of the formed heterojunction promoted by co-catalysts. Reproduced with permission from Ref. [164]. Copyright Royal Society of Chemistry

same conditions. Compared to a layered heterojunction, the authors ascribed the improved photocatalytic activity to the higher probability of excitons reaching the interfaces and dissociating, particularly for semiconductor particles with sizes in the same range as the exciton diffusion length. In a related work, Vijayaraghavan and co-workers reported a series of photocatalysts based on magnesium and calcium ferrites composed of single phases and mixed compositions of up to four different crystalline structures—$MgFe_2O_4$, cubic and orthorhombic $CaFe_2O_4$ and Fe_2O_3 [165], with activities for hydrogen evolution from glycerol solutions depending mainly on the phase composition of the photocatalyst system, in the absence of co-catalysts. A kind of electron cascade mechanism is proposed by the authors to account for the highest activity displayed by a catalyst composed of the four mentioned phases.

Different ferrites have been combined with TiO_2 in coupled photocatalysts for energy applications. An et al. reported the preparation of Fe_3O_4/TiO_2 composites with varying magnetite loadings supported on nanofibrillated cellulose, and the activity of the obtained systems for hydrogen production from aqueous methanol

solutions [166]. An increase of electron-trapping sites, reducing recombination, is invoked to account for the improved photocatalytic activity of the composite under UV light with respect to cellulose-supported TiO_2, although no scheme of the electronic coupling of both phases is reported. According to previous works though, it is feasible that electrons photo-generated in titania are transferred into the lower lying conduction band of magnetite [167], although this would mean that those transferred electrons would lose reduction potential. In addition to electronic features, these composites were reported to be recyclable by means of an external magnetic field. Recyclability tests showed a loss of activity of ca. 8% after 15 photocatalytic runs [166].

A p–n heterojunction of $CuFe_2O_4$ and TiO_2 supported on reduced graphene oxide (rGO) was reported by Hafeez and co-workers for hydrogen evolution under UV–Vis light using glycerol as hole scavenger [168]. On the basis of optical and electrochemical measurements, a mechanism was proposed in which electrons would flow from the high-energy conduction band of the ferrite phase to the lower-energy one of titania, and from there to the reduced graphene oxide sheets, where they would be transferred to protons to produce hydrogen. In turn, holes would migrate from the valence band of TiO_2 to that of $CuFe_2O_4$ and there be trapped by glycerol molecules. Therefore, $CuFe_2O_4$ and rGO acting as hole traps and electron mediators, respectively, would improve the photocatalytic activity with respect to TiO_2, as shown by the hydrogen evolution results, by largely inhibiting charge carrier recombination. This inhibition is actually supported by the practical disappearance of photoluminescence at wavelengths associated with TiO_2 in the composite system. A similar mechanism, without the use of graphene, was proposed by Uddin and co-workers to account for the visible-light ($\lambda > 400$ nm) activity of $CuFe_2O_4$ heterojunctions for CO_2 reduction into methanol from an aqueous solution of potassium bicarbonate, using sodium sulfide as hole scavenger [169]. The ferrite phase would in this case act as a visible-light sensitizer for titania, which would be inactive in those irradiation conditions, and which does, on the other hand, improve the activity with respect to the ferrite single phase. Again, photoluminescence spectroscopy measurements under UV excitation suggested recombination to be diminished in the composite, although the difference between TiO_2 and the two-phase system was not as dramatic as in the previous case. As is common in photocatalytic CO_2 reduction experiments [136], deactivation of the catalyst was observed in all cases, which the authors associated with the depletion of active sites.

A Z-scheme electronic mechanism was proposed by Song et al. in the photocatalytic reduction of CO_2 in cyclohexanol solution by $ZnFe_2O_4/TiO_2$ composites [170]. With a relative band position arrangement similar to that of the previous heterojunction, $ZnFe_2O_4$ and TiO_2 may couple in such a way that electrons from the conduction band of the latter are transferred into the valence band of the former, while electrons in the ferrite conduction bands reduce CO_2 and holes in titania valence band oxidize the sacrificial agent, in a kind of all-solid Z-scheme without an electron mediator between the distinct phases. This heterojunction, formed by TiO_2 nanobelts decorated with ferrite nanoparticles, showed higher photocatalytic activity than either of the two single phases. Cyclohexyl formate and cyclohexanone were detected as the main products, together with lower amounts of formic acid. This led the authors to

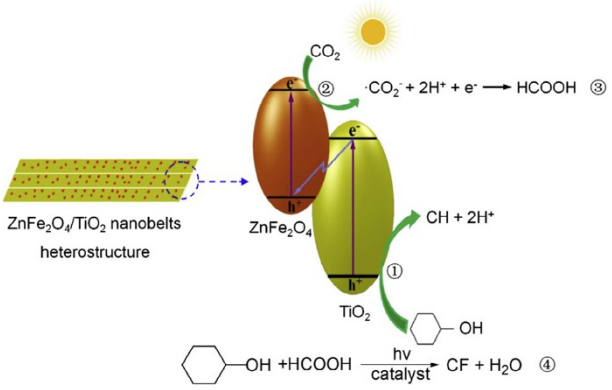

Fig. 14 Schematic diagram for photocatalytic reduction of CO_2 in cyclohexanol over a Z-scheme $ZnFe_2O_4/TiO_2$ heterostructure photocatalyst under UV light irradiation. "CH" stands for cyclohexanone and "CF" for cyclohexyl formate. Reproduced with permission from Ref. [170]. Copyright Elsevier

propose a mechanism in which cyclohexane is oxidized to cyclohexanol, while CO_2 is reduced into formic acid. Esterification between these two intermediates would form cyclohexyl formate, while some of the alcohol would be further oxidized to the ketone (Fig. 14). This research group also reported the combination of the zinc ferrite with bismuth oxychloride, BiOCl, for the same reaction [171, 172]. Apparently, the same type of heterojunction as in the case of the $ZnFe_2O_4/TiO_2$ can be formed with the oxychloride instead of titania, leading to improved photocatalytic activity with respect to the separate semiconductors. The preparation method and the resulting morphology of the particles affected the final photocatalytic activity, in such a way that hydrothermally obtained samples displayed a better performance than physical mixtures of the semiconductors, probably as a result of a more extended interphase contact [172]. In addition, systems with hierarchical microsphere microstructure showed higher photocatalytic activities, apparently owing to a better charge carrier separation than those with non-hierarchical nanosheet morphology [172]. Furthermore, photocatalytic activity in the $ZnFe_2O_4$/BiOCl system is also influenced by the exposed facets of BiOCl. Thus, the yields of cyclohexyl formate and cyclohexanone were higher for the samples with more exposed (001) facets than for the samples with more exposed (010) facets, which the authors attributed to the higher density of oxygen atoms on the (001) facets which enriches the production of electrons under UV irradiation [171].

Soto-Arreola and co-workers combined ZnO with either $CuFe_2O_4$ or $NiFe_2O_4$ to form type II heterojunctions aimed at improved photocatalytic activity for water splitting without any sacrificial reagent under UV light [173]. With an optimum amount of 3 wt% ZnO, both composites, obtained by physical mixing of the single phases, surpassed the activity of the corresponding single-phase ferrites and that of ZnO under the same reaction conditions. In spite of the absence of any sacrificial agent, the reported results are on the same order of magnitude as other works with similar materials that make use of organic hole scavengers. On the basis of fluorescence spectroscopy and (photo)electrochemical measurements, the improvement

in the photocatalytic activity of the heterostructures was attributed to a reduced recombination of the charge carriers, as a result of the transfer of electrons from the conduction band of the metal ferrite to the conduction band of the ZnO. Therefore, the authors proposed a mechanism in which electrons accumulated in the conduction band of ZnO reduce protons to produce hydrogen, while holes remaining in the valence band of the ferrite phase would oxidize water to oxygen. However, no oxygen evolution was reported in the work to account for the electron balance and, as shown by the authors in their electronic scheme, holes in the valence band of both copper and nickel ferrites do not have enough reduction potential to oxidize water. A similar charge transfer mechanism was proposed by Karamian and Sharifnia to account for the visible-light activity of $BiFeO_3$–ZnO p–n junctions for photocatalytic CO_2 reduction using methane as hole scavenger [174], although in this case only the ferrite component is activated by the used irradiation source, thereby acting as an inorganic visible-light sensitizer of the otherwise inactive, wide-bandgap ZnO phase. The charge separation was supported by photoluminescence spectroscopy results, which suggested a hindered recombination in the mixed phases. With an optimized 1:1 molar ratio between the components, ca. 20% CO_2 conversion was reached, which declined to ca. 14% after four runs. However, no other efficiency measure than conversion is given to make the results comparable to other works, nor is it clear what products are obtained.

Regarding other oxides that have been coupled to ferrites, Guo and co-workers [175] reported the preparation of Ce-doped $ZnFe_2O_4$ via a sol–gel method that actually gave rise to biphasic samples composed of a Ce^{3+}-doped $ZnFe_2O_4$ spinel phase together with an additional CeO_2 phase with fluorite structure. These composites displayed higher activity than the pristine zinc ferrite for photocatalytic CO_2 reduction under visible light, with CH_4 and CO as main products, together with hydrogen from the competing reduction of water and oxygen from water oxidation (not shown). The formation of a p–n junction between the two phases induced the establishment of a type II heterojunction that promoted charge separation and reduced recombination, as suggested by a combined study of photoluminescence and UV–Vis absorption spectroscopies with (photo)electrochemical measurements. In addition, temperature-programmed desorption (TPD) and Fourier transform infrared spectroscopy (FTIR) studies revealed that the alkalinity of cerium oxide favours the chemical interaction between CO_2 and photocatalyst surfaces, which occurs via the formation of monodentate and bidentate carbonate and bidentate bicarbonate as the main surface species.

In a similar approach, Khan et al. reported the use of another wide-bandgap alkaline oxide like SrO to promote both charge separation and CO_2 adsorption [176]. However, the electronic matching here is slightly different from those in the previous examples, with the conduction band of SrO lying considerably above that of the ferrite, so that it is only able to extract hot electrons generated in the latter by absorption of relatively high-energy (although still visible) photons. Charge separation is demonstrated by increased signals in the surface photovoltage spectra upon the addition of the strontium oxide phase, as well as by the increased generation of hydroxyl radicals followed by the formation of the fluorescent 7-hydroxycoumarin from coumarin solutions. On the other hand, TPD studies reveal that the alkaline

oxide promotes the adsorption of CO_2 via carbonate species, increasing not only the amount of CO_2 adsorbed but also the strength of the interaction. In this case, carbon monoxide is the main product of CO_2 reduction. According to previous theoretical studies on MO-TiO_2 systems (M = Mg, Ca, Sr, Ba) [177], the improvement of CO_2 adsorption and activation on alkaline earth metal oxide modifications should facilitate the activity for photocatalytic CO_2 reduction, SrO being particularly interesting in that respect since it promotes CO_2 activation and CO desorption.

C_3N_4 has been extensively studied in recent years as a metal-free and visible-light-responsive photocatalyst [178], and some works have extended this study to its combination with ferrites for photocatalytic water splitting. Thus, Chen and co-workers enhanced the photocatalytic activity of graphitic carbon nitride for hydrogen evolution from triethanolamine solutions through the incorporation of $MgFe_2O_4$ by annealing a mixture of ferrite particles obtained by the sol–gel method and melamine as the C_3N_4 precursor [179]. According to static photoluminescence spectra and time-resolved fluorescence decay curves, the ferrite is able extract photoinduced electrons and holes from carbon nitride, which per se leads to a poor activity for hydrogen production due to the low energy of the conduction band of $MgFe_2O_4$. However, if the nitride is modified with both ferrite and platinum, the latter can extract electrons more efficiently, according to the greatly improved activity with respect to both bare C_3N_4 and $MgFeO_4/C_3N_4$. In turn, electrochemical measurements revealed the ferrite to be a good oxidation catalyst, which led the authors to propose a dual effect of $MgFe_2O_4$ in the photocatalytic system as hole extractor and oxidation co-catalyst, with platinum acting as the reduction co-catalyst. The situation is different with nickel and copper ferrites, since both have conduction band levels above that of C_3N_4, according to the same authors [180]. Therefore, under visible irradiation both ferrites can donate electrons from their conduction bands to that of the nitride, while holes can move from the valence band of the latter to that of the ferrite. In line with this, steady-state photoluminescence spectra and fluorescence decay curves suggest in both cases ($CuFe_2O_4/C_3N_4$ and $NiFe_2O_4/C_3N_4$) an inhibited electron–hole recombination, while electrochemical impedance spectroscopy shows a greatly enhanced internal conductivity in the composites compared to the bare nitride. As a result, the activity of the heterojunctions for H_2 production from aqueous triethanolamine increases with respect to the single phases, and is further enhanced in the presence of platinum as reduction co-catalyst. As in the previous work, the authors highlight the dual role of the ferrite as charge separation promoter and oxidation co-catalyst.

The junction of C_3N_4 with the perovskite-structured lanthanum ferrite $LaFeO_3$ has been studied in a few works for photocatalytic hydrogen production. In principle, the relative band positions of both phases would be adequate for the formation of a type II heterojunction. However, as previously described for the zinc ferrite heterojunctions, an all-solid Z-scheme without any electronic mediator seems to occur in the case of $LaFeO_3/C_3N_4$ photocatalysts. Acharya et al. proposed this kind of junction on the basis of thermodynamic considerations [181], given that, in the case of a type II heterojunction, electrons would fall into a conduction band (that of $LaFeO_3$ in this case) with reduction potential slightly below that of the H^+/H_2 redox couple. Even if the presence of Pt as co-catalyst is able to overcome this limitation

in the single-phase ferrite, the observed improvement in hydrogen evolution with respect both to the ferrite and to C_3N_4 would not occur. This mechanism is, according to the authors, supported by the observed increase in photoluminescence in the heterojunction due to the recombination of the electrons in the conduction band of C_3N_4 with the holes in the valence band of the ferrite. However, this evidence does not seem so obvious from the photophysics point of view. The same kind of heterojunction between these two components was proposed by Xu and Feng [182], by which they surpassed the activity of both single phases for hydrogen evolution from triethanolamine solutions under visible light, using platinum (3 wt%) as co-catalyst. The introduction of 2 wt% of Ni_2S improved the photocatalytic activity of the $LaFeO_3/C_3N_4$ heterojunction in the same conditions by a factor of 60, with an apparent quantum yield of 2% at 420 nm [183], although the activity was still lower than that obtained in the previous work with platinum as co-catalyst.

3.3 Ferrite-Based Photoelectrode Materials for Solar Fuels Production

3.3.1 Ferrite Photocathodes

One of the most investigated ferrite photocathodes is p-type calcium ferrite ($CaFe_2O_4$), which has a bandgap of 1.9 eV and suitable band edge positions for water reduction. The first paper using this material was published by Matsumoto et al. [120] using pressed pelletized electrodes sintered at 1200 °C and oxidized under O_2 at 1000 °C. $CaFe_2O_4$ was studied in a N_2 saturated K_2SO_4 solution (0.25 M, pH 6.0), combined in the cell combined with an n-type $Zn_{1.2}Fe_{1.8}O_4$. Photoelectrolysis of water without external bias resulted in a solar-to-hydrogen (STH) conversion efficiency lower than 0.01%. This limited efficiency was ascribed to a low electron concentration in the surface. In addition, Fermi level pinning (FLP) arises because of the presence of surface states associated with the redox pair Fe^{3+}/Fe^{2+}. To improve contact and subsequently the photocurrent, the authors proposed the use of noble metal nanoparticles (Au, Pt–Pd alloy) in the semiconductor/metal interface. Cao et al. [116] investigated the use of p-$CaFe_2O_4$ as photocathode by depositing $CaFe_2O_4$ thin films on fluorine-doped tin oxide (FTO) by pulsed laser deposition method. A photocurrent density of -0.117 mA cm^{-2} at -0.06 V was reported which is significantly larger than the values reported by Matsumoto and co-workers [120, 121], probably as a result of shorter electron transfer distances in the thinner films and higher electrical conductivity. The H_2 evolution rate under visible light irradiation, using a Pt counter electrode without applying any additional bias, was ca. 4.8 μmol m^{-2} h^{-1}. Sekizawa et al. reported several metal-doped $CaFe_2O_4$ electrodes prepared by radio frequency magnetron co-sputtering over antimony-doped tin oxide (ATO) [123]. The doping with Au and Ag leads to an increase in the photocurrent. Particularly, Ag doping triggered an improvement in the symmetry around the Fe atom, which induces high mobility and an increase in activity of 23 times with respect to the undoped ferrite.

Ye et al. investigated the photoelectrochemical performance of p-$CaFe_2O_4$, n-$ZnFe_2O_4$, p-$CaFe_2O_4$/n-$ZnFe_2O_4$ and multiple p–n junction $CaFe_2O_4/ZnFe_2O_4$

photoelectrode materials [122], all of them obtained by pulsed laser deposition. In the FTO/$ZnFe_2O_4$/$CaFe_2O_4$ photoelectrode configuration, negative photocurrent and positive open circuit photovoltage (+0.025 V, $\lambda = 430$ nm, 118 μW cm^{-2}) were described, demonstrating that the p-$CaFe_2O_4$ layer acts as photocathode. In the case of multiple junction FTO/$(ZnFe_2O_4/CaFe_2O_4)_x$ photoelectrodes with similar single-layer thickness between 10 and 15 nm, extending the number of layers (x) led to an improvement in the photocurrent density and the onset potential. The highest photocurrent density (−0.025 mA cm^{-2} at +0.4 V) and the most positive onset potential (+1.3 V) of all four samples were obtained with $x = 20$.

Ida et al. developed a tandem cell (Fig. 15a) without applying an external voltage using (*hk0*)-oriented p-type $CaFe_2O_4$ deposited over FTO (100 nm thick) by pulse layer deposition (PLD) as photocathode and TiO_2 as photoanode with an onset potential of −0.75 V (Fig. 15b) [117]. The open-circuit voltage was 0.97 V and the short-circuit current was about 200 μA cm^{-2} (Fig. 15c), and a H_2 and O_2 evolution of 70 and 4 μmol, respectively, in 48 h was attained (Fig. 15d). After this time, many cracks were observed on the $CaFe_2O_4$ surface as shown in Fig. 15e and the solution contained 2.3 μmol of Fe, indicating a slight corrosion of the $CaFe_2O_4$ electrode. Later, the same authors described the use of n-ZnO as photocathode generating a photovoltage of 0.82 V [118]. In this case, only H_2 was detected and Zn was partially dissolved, which accounted for the absence of O_2. In subsequent work, they also described a modification of p-type $CaFe_2O_4$ with the presence of a $Ca_2Fe_2O_5$ impurity enhancing the short circuit photocurrent density (0.55 mA cm^{-2}) and slightly increasing the photovoltage (1.09 V) [119]. During the reaction a H_2/O_2 ratio of 3.7 was observed which is lower than in the previous paper. In addition, O_2 formation was improved.

One strategy to improve the low quantum efficiency of a pristine p-$CaFe_2O_4$ electrode due to the poor mobility of the photo-generated charge carriers is to dope it with different elements. In this way, Matsumoto et al. used Na and Mg, which have similar ionic radii to Ca and Fe, respectively, to prepare type $Ca_{1-x}Na_xFe_{2-y}Mg_yO_4$ photocathodes [121]. This led to the formation of acceptor levels within the bandgap and to higher electronic conductivity but still low photocurrents.

Rekhila et al. proposed the use of p-$NiFe_2O_4$ pellets prepared by sintering sol–gel synthesized particles at 850 °C [127]. The open-circuit voltage, short-circuit current and efficiency were reported to be, respectively, 0.43 V, 0.71 mA cm^{-2} and 0.28 under irradiation with visible light (50 mW cm^{-2}) with Pt as counter electrode.

Yang et al. prepared porous $CoFe_2O_4$ nanosheets on FTO from aqueous solutions of Co and Fe nitrate using a template-free electrochemical deposition followed by a heat treatment at 933 K [126]. The photocathodes exhibit a small photocurrent of ca. 0.3 μA cm^{-2} in 0.1 M aqueous Na_2S at zero bias voltage under wavelength ≥ 390 nm (30 mW cm^{-2}).

Fan and co-workers reported the preparation of $MgFe_2O_4$ nanofibres and nanowires by electrospinning [184, 185]. Chemical vapour deposition (CVD) coating with MoS_2 created a 1D heterostructure with enhanced charge carrier mobility, which showed 92% photoelectrochemical tetracycline degradation after 2 h. A photoelectrochemical hydrogen evolution rate of 5.8 mmol h^{-1} g^{-1} was found at 0.5 V bias under Xe arc lamp irradiation.

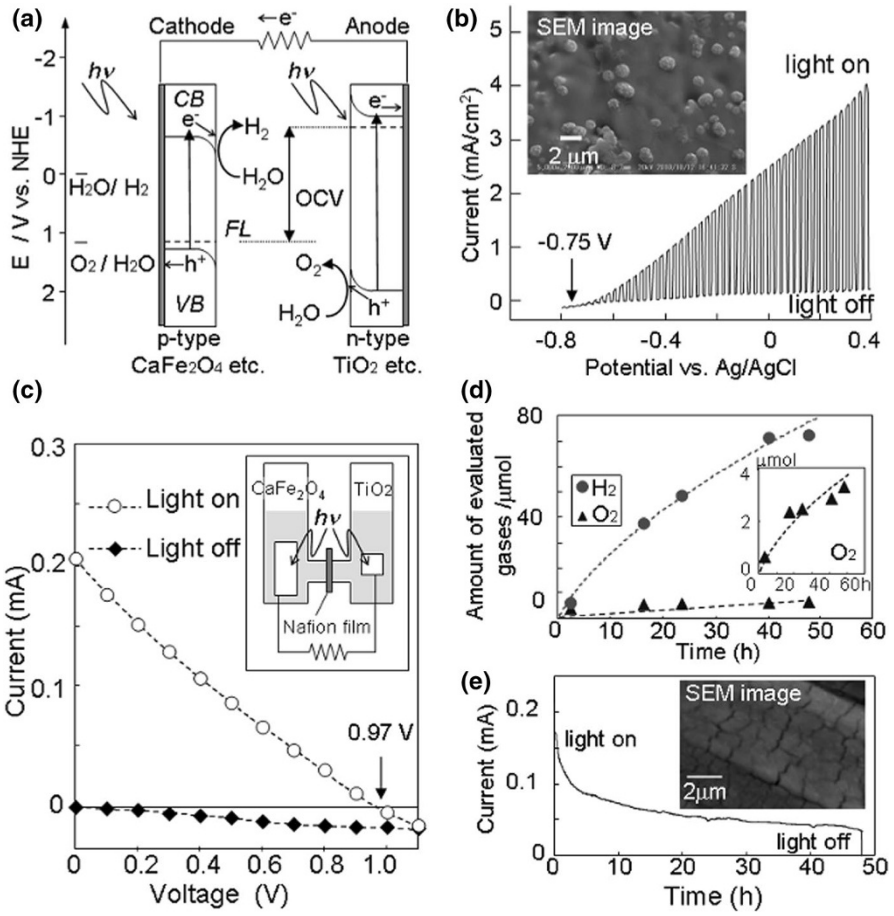

Fig. 15 **a** Reaction and band model in photovoltaic cells using p-type and n-type semiconductor electrodes. **b** Current–potential curve and SEM image of the TiO_2 electrode. **c** Current–potential curve of a photocell with $CaFe_2O_4$ (2 cm^2) and TiO_2 (0.5 cm^2) electrodes and model structure of measurement cell. **d** Amount of hydrogen and oxygen gases generated from the photocell short-circuited by connecting the $CaFe_2O_4$ and TiO_2 electrodes as a function of illumination time. **e** Current–time evolution for the photocell short-circuited by connecting the $CaFe_2O_4$ and TiO_2 electrodes and SEM image of $CaFe_2O_4$ after 48 h reaction. All reactions were carried out in 0.1 M NaOH (aq) under illumination (500 W Xe lamp). Reproduced with permission from Ref. [117]. Copyright American Chemical Society

Guijarro et al. [186] used β-FeOOH as a starting material to obtain $MgFe_2O_4$, $CuFe_2O_4$ and $ZnFe_2O_4$ thin films. After the elimination of MgO, CuO and ZnO impurities by etching in highly acidic (for $CuFe_2O_4$, $MgFe_2O_4$) or alkaline (for $ZnFe_2O_4$) conditions, the activity of the films improved when additional $NiFe_2O_x$ was deposited and a reductive calcination in H_2 was performed after the synthesis. Remarkable faradaic efficiencies were described (97%), albeit with considerable degree of recombination and Fermi level pinning at 0.9 V vs. RHE.

In the case of CO_2 photoreduction, the use of ferrites as photoelectrodes is scarcer. Rezaul Karim et al. [187] developed a p-type $CuFe_2O_4$ photocathode, obtained by sol–gel, for CO_2 photoelectroreduction under visible light (470 nm), starting from a CO_2-saturated $NaHCO_3$ solution. Methanol was detected as the sole reduction product in the liquid phase with a faradaic efficiency of 62% and a quantum efficiency of 14.4%, using a bias potential of 0.5 V (vs. RHE). The comparatively low quantum efficiency was ascribed to the formation of competitive gas products during CO_2 reduction.

3.3.2 Ferrite Photoanodes

Ferrites can also act as n-type semiconductors and are suitable candidates as photoanodes for PECs. Among them, $ZnFe_2O_4$ is a remarkable example. Tahir et al., for instance [133, 134], propose the use of $ZnFe_2O_4$ prepared by aerosol-assisted chemical vapour deposition (AACVD) over FTO as photoanode for water splitting. The obtained photocurrents are highly dependent on the synthesis conditions, with a maximum photocurrent density of 0.35 mA cm^{-2} at 1.23 V vs. RHE using ethanol as solvent and a calcination temperature of 450 °C. An incident photon-to-current conversion efficiency of 13.5% at 350 nm at an applied potential of 1.23 V vs. RHE was observed [133]. The authors attributed this behaviour to the improved collection of the photo-generated minority carriers at the $ZnFe_2O_4$/electrolyte interface as the average feature size gradually decreased with the solvent from ca. 500 nm (methanol) to ca. 100 nm (ethanol) [134].

To decrease the synthesis temperature, Kim et al. propose the use of hybrid microwave annealing (HMA) post-synthetic heat treatment with graphite powder as the susceptor. The synthesis is based on the treatment of β-FeOOH nanorods with a zinc nitrate solution with a thermal treatment at 550 °C for 3 h. After that, $ZnFe_2O_4$ nanorods were calcined at 800 °C (20 min) or subjected to HMA (5 min) to increase the crystallinity. The $ZnFe_2O_4$ nanorods from HMA treatment show a 10- to 15-fold increase in activity compared to conventional thermally treated electrodes and an enhancement of the stability, which is attributed to a higher crystallinity and lower amount of surface defects [188]. In a later work, these authors modified the synthesis atmosphere (vacuum, air or hydrogen) after the first thermal stage (800 °C) [189]. In both H_2 and vacuum an increase of the photoactivity about 20-fold is observed.

Hufnagel et al. [190] prepared mesoporous $ZnFe_2O_4$ thin films on a macroporous ATO scaffold using atomic layer deposition (ALD). These photoanodes show a more negative photocurrent onset (0.9 V vs. RHE) compared to reported values. In addition, these electrodes exhibit a photoresponse 4–5 fold higher than the same material in film conformation.

In order to improve the diffusion length of minority carriers, several strategies have been developed. One of them is the use of structured transparent conductive oxide current collectors to capture and tunnel the photo-generated electrons readily while the large interfacial area allows efficient transfer of the holes to the solution. In this way, Xu et al. developed $ZnFe_2O_4$-decorated Al-doped ZnO (AZO) nanowire films [98]. The Al:ZnO nanowires were first grown on the FTO using hydrothermal synthesis and subsequently treated with $FeCl_3$ and calcined at 550 °C.

The remarkable photoelectrochemical performance (photocurrent density of 1.72 mA cm^{-2} at 1.23 V vs. RHE) was attributed to the synergy of the visible light absorption of $ZnFe_2O_4$ and the of high conductivity of Al:ZnO.

Fe_2O_3 is one of the most studied photoanode materials. There are a number of research works and review articles dealing with the modification strategies of hematite such as morphology control, doping and heterojunction formation to improve the charge transfer efficiency [191, 192]. Regarding the last strategy, ferrites have been also investigated in forming heterojunctions with hematite for photoanodes. The most studied one is the $ZnFe_2O_4/Fe_2O_3$ heterojunction prepared by different synthesis methods. McDonald and Choi employed the electrodeposition route to develop core–shell photoelectrodes composed of α-Fe_2O_3 (core) and $ZnFe_2O_4$ (shell) [193]. β-FeOOH films were first electrodeposited on FTO being transformed into α-Fe_2O_3 by a thermal treatment and a subsequent treatment with a Zn-containing solution covering the iron oxide and annealing to produce the $ZnFe_2O_4$ shell. The best photoelectrochemical performance was obtained for a $ZnFe_2O_4/Fe_2O_3$ ratio of 1. The synergy between $ZnFe_2O_4$ and Fe_2O_3 led to an improved electron hole separation in the heterojunction interface that is responsible for the increase on the photoelectrochemical performance compared with bare iron oxide. In addition, the incorporation of Al^{3+} leads to a thin layer solid solution ($ZnFe_{2-x}Al_xO_4$ or $Fe_{2-x}Al_xO_3$) after heat treatment. This reduces the electron–hole recombination centres, but decreases the catalytic activity for the oxygen evolution reaction (OER). Guo et al. also use hydrothermal synthesis to grow the FeOOH nanorods and subsequent treatment with different concentrations of Zn precursor leading to $ZnFe_2O_4/Fe_2O_3$ nanorods [194]. The photocurrent density for the composite electrode was 0.44 mA cm^{-2} at ca. 1.2 V vs. RHE, which was almost twice as high as that for a Fe_2O_3 electrode (0.24 mA cm^{-2}). On the other hand, Borse et al. used a plasma spray method to deposit an aqueous solution of Zn and Fe salts over stainless steel leading to a $ZnFe_2O_4/Fe_2O_3$ electrode affording a photocurrent fivefold higher than for bare Zinc ferrite. In addition, the hydrogen evolution rates were determined to be 46.3 µmol cm^{-2} (STH conversion = 0.06) and 99.0 µmol cm^{-2} (STH conversion = 0.0125) for $ZnFe_2O_4$ and the $ZnFe_2O_4/Fe_2O_3$ photoanode, respectively [195].

Kim et al. [196, 197] reported the preparation of heterojunction photoanodes using p-$CaFe_2O_4$ with TaON and $BiVO_4$. The selection of these oxides is due to their staggered relative band positions with the ferrite leading to an effective heterojunction for water oxidation reactions. The $CaFe_2O_4$ layer on the surface of a TaON led to an increase in the photocurrent density (1.26 mA cm^{-2}) of about 5.5 times greater than bare TaON. This enhancement in the photoelectrochemical performance is due to a reduction of the resistance of the charge carrier transport and, therefore, an improved electron–hole separation [196]. In the case of $CaFe_2O_4/BiVO_4$ an increase of 65% over that measured at the $BiVO_4$ electrode was observed [197]. In order to improve the photoelectrochemical performance, an OER co-catalyst (cobalt phosphate, Co-Pi) was deposited on $CaFe_2O_4$/TaON. After deposition of Co-Pi, stoichiometric H_2 and O_2 production was obtained (123 µmolH_2 and 59 µmolO_2) by applying a bias of 1.23 V vs. RHE after $\lambda \geq 400$ nm irradiation for 3 h. An STH efficiency of 0.053% at 1.0 V vs. RHE was obtained, which was increased to 0.55% by coupling a photovoltaic cell in a tandem configuration, assuming 0 V applied voltage.

Nevertheless, the initial current declined ca. 50% after 3 h. Similar results were achieved with $CaFe_2O_4/BiVO_4$ compound photoanodes, but with a lower photocurrent and a higher stability. H_2 and O_2 production was 297 and 140 μmol, respectively (after 2 h of visible light irradiation), with a faradic efficiency around 80%.

Another example with a calcium ferrite was reported by Ahmed and co-workers, who prepared a p-$CaFe_2O_4$/n-Fe_2O_3 heterojunction photoanode by anisotropically growing a β-FeOOH film on FTO from an Fe^{3+} and Ca^{2+} aqueous solution and then thermally treating in two steps at 550 °C and 800 °C [198]. This heterojunction showed a photocurrent density of 0.53 mA cm^{-2} at 1.23 V vs. RHE, which doubled the one achieved with Fe_2O_3. This behaviour is explained by a reduction of the resistance for charge transfer at the interface between the electrolyte and the electrode and by improved charge separation.

4 Conclusions

Even if ferrites have displayed some appealing properties that make them promising materials for light-activated applications for energy and the environment like photocatalysis, photo-Fenton and photoelectrochemistry, the amount of scientific literature dealing with such materials is still lower compared to other types of catalysts or semiconductors. Nevertheless, as we have tried to point out here, some works have reported interesting results in the aforementioned processes. However, there is still room for advancement in the way towards the full understanding of the relationships between the physico-chemical properties of these materials and their performance in photoassisted reactions. The possibilities that they display for the modification of their chemical composition, crystalline structure and optoelectronic properties, as well as their versatility for the creation of heterojunction and doped systems, are in our opinion the most relevant characteristics of ferrites for their further development in photoassisted environmental and solar fuels applications.

Acknowledgements The authors want to thank the European Fund for regional development (EFRE/FEDER) for the financial support of the PHOTOPUR project which is performed within the framework of Interreg V and the Sciences Offensive. Financial support from project SOLPAC: ENE2017-89170-R, MCIU/AEI/FEDER, EU from the Spanish Ministry of Science, Innovation and Universities is also gratefully acknowledged.

References

1. Helaïli N, Bessekhouad Y, Bachari K, Trari M (2014) Synthesis and physical properties of the $CuFe_{2-x}Mn_xO4$ ($0 \le x \le 2$) solid solution. Mater Chem Phys 148:734–743
2. Sickafus KE, Wills JM, Grimes NW (1999) Structure of spinel. J Am Ceram Soc 82:3279–3292
3. Levy D, Diella V, Dapiaggi M, Sani A, Gemmi M, Pavese A (2004) Equation of state, structural behaviour and phase diagram of synthetic $MgFe_2O_4$, as a function of pressure and temperature. Phys Chem Miner 31:122–129

4. Candeia RA, Bernardi MIB, Longo E, Santos IMG, Souza AG (2004) Synthesis and characterization of spinel pigment $CaFe_2O_4$ obtained by the polymeric precursor method. Mater Lett 58:569–572
5. Candeia RA, Souza MAF, Bernardi MIB, Maestrelli SC, Santos IMG, Souza AG, Longo E (2007) Monoferrite $BaFe_2O_4$ applied as ceramic pigment. Ceram Int 33:521–525
6. Valenzuela R (2012) Novel applications of ferrites 2012:ID 591839
7. Pullar RC (2012) Hexagonal ferrites: a review of the synthesis, properties and applications of hexaferrite ceramics. Prog Mater Sci 57:1191–1334
8. Structure Type 063: $BaFe_{12}O_{19}$ (magnetoplumbite). http://som.web.cmu.edu/structures/S063-BaFe12O19.html (2019)
9. Taffa DH, Dillert R, Ulpe AC, Bauerfeind KCL, Bredow T, Bahnemann DW, Wark M (2009) Photoelectrochemical and theoretical investigations of spinel type ferrites ($M_xFe_{3-x}O_4$) for water splitting: a mini-review. J Photon Energy 7:1–25
10. Goodenough JB, Longo JM, Hellwege KH (1970) Crystallographic and magnetic properties of perovskite and perovskite-related compounds. Springer, Berlin
11. Dixon CAL, Kavanagh CM, Knight KS, Kockelmann W, Morrison FD, Lightfoot P (2015) Thermal evolution of the crystal structure of the orthorhombic perovskite $LaFeO_3$. J Solid State Chem 230:337–342
12. Yuan SJ, Cao YM, Li L, Qi TF, Cao SX, Zhang JC, DeLong LE, Cao G (2013) First-order spin reorientation transition and specific-heat anomaly in $CeFeO_3$. J Appl Phys 114:113909
13. Kefeni KK, Mamba BB, Msagati TAM (2017) Application of spinel ferrite nanoparticles in water and wastewater treatment: a review. Sep Purif Technol 188:399–422
14. Kefeni KK, Msagati TAM, Mamba BB (2017) Ferrite nanoparticles: synthesis, characterisation and applications in electronic device. Mater Sci Eng B 215:37–55
15. Tatarchuk T, Bououdina M, Judith Vijaya J, John Kennedy L (2017) Spinel ferrite nanoparticles: synthesis, crystal structure, properties, and perspective applications. In: Fesenko O, Yatsenko L (eds) Nanophysics, Nanomaterials, Interface Studies, and Applications. NANO 2016. Springer Proceedings in Physics, vol 195. Springer, Cham, pp 305–325
16. Masunga N, Mmelesi OK, Kefeni KK, Mamba BB (2019) Recent advances in copper ferrite nanoparticles and nanocomposites synthesis, magnetic properties and application in water treatment: review. J Environ Chem Eng 7:103179
17. Dhand C, Dwivedi N, Loh XJ, Jie Ying AN, Verma NK, Beuerman RW, Lakshminarayanan R, Ramakrishna S (2015) Methods and strategies for the synthesis of diverse nanoparticles and their applications: a comprehensive overview. RSC Adv 5:105003–105037
18. Amiri S, Shokrollahi H (2013) Magnetic and structural properties of RE doped Co-ferrite (REåNd, Eu, and Gd) nano-particles synthesized by co-precipitation. J Magn Magn Mater 345:18–23
19. Zi Z, Sun Y, Zhu X, Yang Z, Dai J, Song W (2009) Synthesis and magnetic properties of $CoFe_2O_4$ ferrite nanoparticles. J Magn Magn Mater 321:1251–1255
20. Harzali H, Saida F, Marzouki A, Megriche A, Baillon F, Espitalier F, Mgaidi A (2016) Structural and magnetic properties of nano-sized NiCuZn ferrites synthesized by co-precipitation method with ultrasound irradiation. J Magn Magn Mater 419:50–56
21. Rashmi SK, Bhojya Naik HS, Jayadevappa H, Viswanath R, Patil SB, Madhukara Naik M (2017) Solar light responsive Sm-Zn ferrite nanoparticle as efficient photocatalyst. Mater Sci Eng B 225:86–97
22. Vinosha PA, Das SJ (2018) Investigation on the role of pH for the structural, optical and magnetic properties of cobalt ferrite nanoparticles and its effect on the photo-Fenton activity. Mater Today Proc 5:8662–8671
23. Pereira C, Pereira AM, Fernandes C, Rocha M, Mendes R, Fernandez-Garcia MP, Guedes A, Tavares PB, Greneche J, Araujo JP, Freire C (2012) Superparamagnetic MFe_2O_4 (M = Fe Co, Mn) nanoparticles: tuning the particle size and magnetic properties through a novel one-step coprecipitation route. Chem Mater 24:1496–1504
24. Tatarchuk T, Bououdina M, Vijaya J, John Kennedy L (2017) Spinel ferrite nanoparticles: synthesis, crystal structure, properties, and perspective applications, Chapter 22. In: Fesenko O, Yatsenko L (eds) Nanophysics, nanomaterials, interface studies and applications, Springer Proceedings in Physics, vol 195. Springer, Berlin
25. Sharma R, Bansal S, Singhal S (2015) Tailoring the photo-Fenton activity of spinel ferrites (MFe_2O_4) by incorporating different cations (M = Cu, Zn, Ni and Co) in the structure. RSC Adv 5:6006–6018

26. Zielinska-Jurek A, Bielan Z, Dudziak S, Wolak I, Sobczak Z, Klimczuk T, Nowaczyk G, Hupka J (2017) Design and application of magnetic photocatalysts for water treatment. The effect of particle charge on surface functionality. Catalysts 7:360
27. Kurian M, Nair DS (2015) Heterogeneous Fenton behavior of nano nickel zinc ferrite catalysts in the degradation of 4-chlorophenol from water under neutral conditions. J Water Process Eng 8:e37–e49
28. Li R, Cai M, Xie Z, Zhang Q, Zeng Y, Liu H, Liu G, Lv W (2019) Construction of heterostructured $CuFe_2O_4$/g-C_3N_4 nanocomposite as an efficient visible light photocatalyst with peroxydisulfate for the organic oxidation. Appl Catal B 244:974–982
29. Peng K, Fu L, Yang H, Ouyang J (2016) Perovskite $LaFeO_3$/montmorillonite nanocomposites: synthesis, interface characteristics and enhanced photocatalytic activity. Sci Rep 6:19723
30. Sannino D, Vaiano V, Ciambelli P, Isupova LA (2011) Structured catalysts for photo-Fenton oxidation of acetic acid. Catal Today 161:255–259
31. Soltani T, Lee B (2016) Improving heterogeneous photo-Fenton catalytic degradation of toluene under visible light irradiation through Ba-doping in $BiFeO_3$ nanoparticles. J Mol Catal A Chem 425:199–207
32. Li X, Shi H, Zhu W, Zuo S, Lu X, Luo S, Li Z, Yao C, Chen Y (2018) Nanocomposite $LaFe_{1-x}Ni_xO_3$/palygorskite catalyst for photo-assisted reduction of NO_x: effect of Ni doping. Appl Catal B Environ 231:92–100
33. Li X, Shi H, Yan X, Zuo S, Zhang Y, Wang T, Luo S, Yao C, Ni C (2018) Palygorskite immobilized direct Z-scheme nitrogen-doped carbon quantum dots/$PrFeO_3$ for photo-SCR removal of NO_x. ACS Sustain Chem Eng 6:10616–10627
34. Ansari F, Soofivand F, Salavati-Niasari M (2019) Eco-friendly synthesis of cobalt hexaferrite and improvement of photocatalytic activity by preparation of carbonic-based nanocomposites for waste-water treatment. Compos Part B Eng 165:500–509
35. Pechini MP (1967) Method of preparing lead and alkaline earth titanates and niobates and coating method using the same to form a capacitor. US Patent, 3330697A
36. Danks AE, Hall SR, Schnepp Z (2016) The evolution of sol–gel chemistry as a technique for materials synthesis. Mater Horiz 3:91–112
37. Garcia-Muñoz P, Lefevre C, Robert D, Keller N (2019) Ti-substituted $LaFeO_3$ perovskite as photoassisted CWPO catalyst for water treatment. Appl Catal B 248:120–128
38. Jamil TS, Abbas HA, Nasr RA, Vannier R- (2018) Visible light activity of $BaFe_{1-x}Cu_xO_{3-d}$ as photocatalyst for atrazine degradation. Ecotoxicol Environ Saf 163:620–628
39. Yin J, Liao G, Zhou J, Huang C, Ling Y, Lu P, Li L (2016) High performance of magnetic $BiFeO_3$ nanoparticle-mediated photocatalytic ozonation for wastewater decontamination. Sep Purif Technol 168:134–140
40. Luo J, Li R, Chen Y, Zhou X, Ning X, Zhan L, Ma L, Xu X, Xu L, Zhang L (2019) Rational design of Z-scheme $LaFeO_3/SnS_2$ hybrid with boosted visible light photocatalytic activity towards tetracycline degradation. Sep Purif Technol 210:417–430
41. Liu Q, Xu Y, Wang J, Xie M, Wei W, Huang L, Xu H, Song Y, Li H (2018) Fabrication of Ag/AgCl/$ZnFe_2O_4$ composites with enhanced photocatalytic activity for pollutant degradation and *E. coli* disinfection. Colloids Surf A Physicochem Eng Asp 553:114–124
42. Liu Z, Feng H, Xue S, Xie P, Li L, Hou X, Gong J, Wei X, Huang J, Wu D (2018) The triple-component Ag_3PO_4-$CoFe_2O_4$-GO synthesis and visible light photocatalytic performance. Appl Surf Sci 458:880–892
43. Diao Y, Yan Z, Guo M, Wang X (2018) Magnetic multi-metal co-doped magnesium ferrite nanoparticles: an efficient visible light-assisted heterogeneous Fenton-like catalyst synthesized from saprolite laterite ore. J Hazard Mater 344:829–838
44. Casbeer E, Sharma VK, Li X (2012) Synthesis and photocatalytic activity of ferrites under visible light: a review. Sep Purif Technol 87:1–14
45. Ameer S, Gul IH, Mujahid M (2015) Ultra low permittivity/loss $CoFe_2O_4$ and $CoFe_2O_4$–rGO nanohybrids by novel 1-hexanol assisted solvothermal process. J Alloy Compd 642:78–82
46. Marinca TF, Chicinaş I, Isnard O (2013) Structural and magnetic properties of the copper ferrite obtained by reactive milling and heat treatment. Ceram Int 39:4179–4186
47. Zhang Z, Yao G, Zhang X, Ma J, Lin H (2015) Synthesis and characterization of nickel ferrite nanoparticles via planetary ball milling assisted solid-state reaction. Ceram Int 41:4523–4530

48. Manova E, Kunev B, Paneva D, Mitov I, Petrov L, Estournès C, D'Orléan C, Rehspringer J, Kurmoo M (2004) Mechano-synthesis, characterization, and magnetic properties of nanoparticles of cobalt ferrite, $CoFe_2O_4$. Chem Mater 16:5689–5696
49. Yan Z, Gao J, Li Y, Zhang M, Guo M (2015) Hydrothermal synthesis and structure evolution of metal-doped magnesium ferrite from saprolite laterite. RSC Adv 5:92778–92787
50. Thomson WT (2011) Uhlig's corrosion handbook. Wiley, Hoboken
51. Hemmi Y, Ichikawa N, Saito N, Masuda T (1994) Electrochemical considerations regarding general corrosion of materials in a BWR primary circuit. J Nucl Sci Technol 31:1202–1213
52. Ramankutty CG, Sugunan S (2001) Surface properties and catalytic activity of ferrospinels of nickel, cobalt and copper, prepared by soft chemical methods. Appl Catal A 218:39–51
53. Reddy GK, Gunasekara K, Boolchand P, Smirniotis PG (2011) Cr- and Ce-doped ferrite catalysts for the high temperature water–gas shift reaction: TPR and Mossbauer spectroscopic study. J Phys Chem C 115:920–930
54. Šimša Z, Široký P, Koláček J, Brabers VAM (1980) Optical and magneto-optical properties of magnetite and manganese ferrites. J Magn Magn Mater 15–18:775–776
55. Balaji S, Kalai Selvan R, John Berchmans L, Angappan S, Subramanian K, Augustin CO (2005) Combustion synthesis and characterization of Sn^{4+} substituted nanocrystalline $NiFe_2O_4$. Mater Sci Eng B 119:119–124
56. Harish KN, Bhojya Naik HS, Prashanth Kumar PN, Viswanath R (2012) Synthesis, enhanced optical and photocatalytic study of Cd–Zn ferrites under sunlight. Catal Sci Technol 2:1033–1039
57. Archer MD, Morris GC, Yim GK (1981) Electrochemical approaches to solar energy conversion: a brief overview and preliminary results obtained with n-type cobalt ferrite. J Electroanal Chem Interfacial Electrochem 118:89–100
58. Antonious MS, Etman M, Guyot M, Merceron T (1986) Photoelectrochemical characteristics of p- and n- type polycrystalline Ni-ferrite electrodes in aqueous solutions. Mater Res Bull 21:1515–1523
59. Vinodgopal K, Kamat PV (1995) Enhanced rates of photocatalytic degradation of an azo dye using SnO_2/TiO_2 coupled semiconductor thin films. Environ Sci Technol 29:841–845
60. Ranjit KT, Viswanathan B (1997) Synthesis, characterization and photocatalytic properties of iron-doped TiO_2 catalysts. J Photochem Photobiol A 108:79–84
61. Bard AJ (1979) Photoelectrochemistry and heterogeneous photo-catalysis at semiconductors. J Photochem 10:59–75
62. Low J, Yu J, Jaroniec M, Wageh S, Al-Ghamdi A (2017) Heterojunction photocatalysts. Adv Mater 29:1601694
63. Jang JS, Kim HG, Lee JS (2012) Heterojunction semiconductors: a strategy to develop efficient photocatalytic materials for visible light water splitting. Catal Today 185:270–277
64. Jang JS, Choi SH, Kim HG, Lee JS (2008) Location and state of Pt in platinized CdS/TiO_2 photocatalysts for hydrogen production from water under visible light. J Phys Chem C 112:17200–17205
65. Jang JS, Yoon KY, Xiao X, Fan FF, Bard AJ (2009) Development of a potential Fe_2O_3-based photocatalyst thin film for water oxidation by scanning electrochemical microscopy: effects of Ag–Fe_2O_3 nanocomposite and Sn doping. Chem Mater 21:4803–4810
66. Tu Y, You C, Chang C, Wang S, Chan T (2013) Adsorption behavior of As(III) onto a copper ferrite generated from printed circuit board industry. Chem Eng J 225:433–439
67. Tu Y, You C, Chang C, Wang S, Chan T (2012) Arsenate adsorption from water using a novel fabricated copper ferrite. Chem Eng J 198–199:440–448
68. Tu Y, You C (2014) Phosphorus adsorption onto green synthesized nano-bimetal ferrites: equilibrium, kinetic and thermodynamic investigation. Chem Eng J 251:285–292
69. Rehman MA, Yusoff I, Alias Y (2015) Fluoride adsorption by doped and un-doped magnetic ferrites $CuCe_xFe_{2-x}O_4$: preparation, characterization, optimization and modeling for effectual remediation technologies. J Hazard Mater 299:316–324
70. Sun W, Pan W, Wang F, Xu N (2015) Removal of Se(IV) and Se(VI) by MFe_2O_4 nanoparticles from aqueous solution. Chem Eng J 273:353–362
71. Duan S, Tang R, Xue Z, Zhang X, Zhao Y, Zhang W, Zhang J, Wang B, Zeng S, Sun D (2015) Effective removal of Pb(II) using magnetic $Co_{0.6}Fe_{2.4}O_4$ micro-particles as the adsorbent: synthesis and study on the kinetic and thermodynamic behaviors for its adsorption. Colloids Surf A 469:211–223

72. Li J, Ng DHL, Song P, Song Y, Kong C (2015) Bio-inspired synthesis and characterization of mesoporous $ZnFe_2O_4$ hollow fibers with enhancement of adsorption capacity for acid dye. J Ind Eng Chem 23:290–298
73. Srivastava V, Sharma YC, Sillanpää M (2015) Application of nano-magnesso ferrite (n-$MgFe_2O_4$) for the removal of Co_{2+} ions from synthetic wastewater: kinetic, equilibrium and thermodynamic studies. Appl Surf Sci 338:42–54
74. Yang L, Zhang Y, Liu X, Jiang X, Zhang Z, Zhang T, Zhang L (2014) The investigation of synergistic and competitive interaction between dye Congo red and methyl blue on magnetic $MnFe_2O_4$. Chem Eng J 246:88–96
75. Zhang S, Niu H, Cai Y, Zhao X, Shi Y (2010) Arsenite and arsenate adsorption on coprecipitated bimetal oxide magnetic nanomaterials: $MnFe_2O_4$ and $CoFe_2O_4$. Chem Eng J 158:599–607
76. An S, Liu X, Yang L, Zhang L (2015) Enhancement removal of crystal violet dye using magnetic calcium ferrite nanoparticle: study in single- and binary-solute systems. Chem Eng Res Des 94:726–735
77. Zeng S, Duan S, Tang R, Li L, Liu C, Sun D (2014) Magnetically separable $Ni_{0.6}Fe_{2.4}O_4$ nanoparticles as an effective adsorbent for dye removal: synthesis and study on the kinetic and thermodynamic behaviors for dye adsorption. Chem Eng J 258:218–228
78. Liu R, Fu H, Yin H, Wang P, Lu L, Tao Y (2015) A facile sol combustion and calcination process for the preparation of magnetic $Ni_{0.5}Zn_{0.5}Fe_2O_4$ nanopowders and their adsorption behaviors of Congo red. Powder Technol 274:418–425
79. Gao F, Chen X, Yin K, Dong S, Ren Z, Yuan F, Yu T, Zou Z, Liu J- (2007) Visible-light photocatalytic properties of weak magnetic $BiFeO_3$ nanoparticles. Adv Mater 19:2889–2892
80. Li S, Jing L, Fu W, Yang L, Xin B, Fu H (2007) Photoinduced charge property of nanosized perovskite-type $LaFeO_3$ and its relationships with photocatalytic activity under visible irradiation. Mater Res Bull 42:203–212
81. Thirumalairajan S, Girija K, Ganesh V, Mangalaraj D, Viswanathan C, Ponpandian N (2013) Novel synthesis of $LaFeO_3$ nanostructure dendrites: a systematic investigation of growth mechanism, properties, and biosensing for highly selective determination of neurotransmitter compounds. Cryst Growth Des 13:291–302
82. Ismael M, Wark M (2019) Perovskite-type $LaFeO_3$: photoelectrochemical properties and photocatalytic degradation of organic pollutants under visible light irradiation. Catalysts 9:4
83. Parida KM, Reddy KH, Martha S, Das DP, Biswal N (2010) Fabrication of nanocrystalline $LaFeO_3$: an efficient sol–gel auto-combustion assisted visible light responsive photocatalyst for water decomposition. Int J Hydrogen Energy 35:12161–12168
84. Gong S, Xie Z, Li W, Wu X, Han N, Chen Y (2019) Highly active and humidity resistive perovskite $LaFeO_3$ based catalysts for efficient ozone decomposition. Appl Catal B 241:578–587
85. Zaharieva K, Rives V, Tsvetkov M, Cherkezova-Zheleva Z, Kunev B, Trujillano R, Mitov I, Milanova M (2015) Preparation, characterization and application of nanosized copper ferrite photocatalysts for dye degradation under UV irradiation. Mater Chem Phys 160:271–278
86. Mahto TK, Roy A, Sahoo B, Sahu SK (2015) Citric acid fuctionalized magnetic ferrite nanoparticles for photocatalytic degradation of azo dye. J Nanosci Nanotechnol 15:273–280
87. El-Rafei AM, El-Kalliny AS, Gad-Allah TA (2017) Electrospun magnetically separable calcium ferrite nanofibers for photocatalytic water purification. J Magn Magn Mater 428:92–98
88. Patil SB, Bhojya Naik HS, Nagaraju G, Viswanath R, Rashmi SK, Vijay Kumar M (2018) Sugarcane juice mediated eco-friendly synthesis of visible light active zinc ferrite nanoparticles: application to degradation of mixed dyes and antibacterial activities. Mater Chem Phys 212:351–362
89. Roonasi P, Mazinani M (2017) Synthesis and application of barium ferrite/activated carbon composite as an effective solar photocatalyst for discoloration of organic dye contaminants in wastewater. J Environ Chem Eng 5:3822–3827
90. Song Y, Xue S, Wang G, Jin J, Liang Q, Li Z, Xu S (2018) Enhanced photocatalytic decomposition of an organic dye under visible light with a stable $LaFeO_3$/AgBr heterostructured photocatalyst. J Phys Chem Solids 121:329–338
91. Malathi A, Arunachalam P, Kirankumar VS, Madhavan J, Al-Mayouf AM (2018) An efficient visible light driven bismuth ferrite incorporated bismuth oxyiodide ($BiFeO_3$/BiOI) composite photocatalytic material for degradation of pollutants. Opt Mater 84:227–235
92. Bhoi YP, Mishra BG (2018) Photocatalytic degradation of alachlor using type-II CuS/$BiFeO_3$ heterojunctions as novel photocatalyst under visible light irradiation. Chem Eng J 344:391–401

93. Zhu K, Wang J, Wang Y, Jin C, Ganeshraja AS (2016) Visible-light-induced photocatalysis and peroxymonosulfate activation over $ZnFe_2O_4$ fine nanoparticles for degradation of Orange II. Catal Sci Technol 6:2296–2304
94. Li C, Wang J, Wang B, Gong J, Lin Z (2012) Direct formation of reusable $TiO_2/CoFe_2O_4$ heterogeneous photocatalytic fibers via two-spinneret electrospinning. J Nanosci Nanotechnol 12:2496–2502
95. Mandal S, Natarajan S, Tamilselvi A, Mayadevi S (2016) Photocatalytic and antimicrobial activities of zinc ferrite nanoparticles synthesized through soft chemical route: a magnetically recyclable catalyst for water/wastewater treatment. J Environ Chem Eng 4:2706–2712
96. Chen C, Butler E, Ahmad MA, Hung Y, Fu Y (2014) Characterizations of TiO_2@Mn-Zn ferrite powders for magnetic photocatalyst prepared from used alkaline batteries and waste steel pickling liquor. Mater Res Bull 50:178–182
97. Meng W, Hu R, Yang J, Du Y, Li J, Wang H (2016) Influence of lanthanum-doping on photocatalytic properties of $BiFeO_3$ for phenol degradation. Cuihua Xuebao Chin J Catal 37:1283–1292
98. Xu Y-, Rao H-, Wang X-, Chen H-, Kuang D-, Su C- (2016) In situ formation of zinc ferrite modified Al-doped ZnO nanowire arrays for solar water splitting. J Mater Chem A 4:5124–5129
99. Li R, Cai M, Xie Z, Zhang Q, Zeng Y, Liu H, Liu G, Lv W (2019) Construction of heterostructured $CuFe_2O_4/g\text{-}C_3N_4$ nanocomposite as an efficient visible light photocatalyst with peroxydisulfate for the organic oxidation. Appl Catal B Environ 244:974–982
100. Dumitru R, Ianculescu A, Păcurariu C, Lupa L, Pop A, Vasile B, Surdu A, Manea F (2019) $BiFeO_3$-synthesis, characterization and its photocatalytic activity towards doxorubicin degradation from water. Ceram Int 45:2789–2802
101. Aghdam TR, Mehrizadeh H, Salari D, Tseng H-, Niaei A, Amini A (2018) Photocatalytic removal of NO_x over immobilized $BiFeO_3$ nanoparticles and effect of operational parameters. Korean J Chem Eng 35:994–999
102. Gao J, Wu S, Han Y, Tan F, Shi Y, Liu M, Li X (2018) 3D mesoporous $CuFe_2O_4$ as a catalyst for photo-Fenton removal of sulfonamide antibiotics at near neutral pH. J Colloid Interface Sci 524:409–416
103. Samoila P, Cojocaru C, Sacarescu L, Dorneanu PP, Domocos A, Rotaru A (2017) Remarkable catalytic properties of rare-earth doped nickel ferrites synthesized by sol–gel auto-combustion with maleic acid as fuel for CWPO of dyes. Appl Catal B 202:21–32
104. Phan TTN, Nikoloski AN, Bahri PA, Li D (2018) Heterogeneous photo-Fenton degradation of organics using highly efficient Cu-doped $LaFeO_3$ under visible light. J Ind Eng Chem 61:53–64
105. Li Y, Chen D, Fan S, Yang T (2019) Enhanced visible light assisted Fenton-like degradation of dye via metal-doped zinc ferrite nanosphere prepared from metal-rich industrial wastewater. J Taiwan Inst Chem Eng 96:185–192
106. Garcia-Muñoz P, Fresno F, Lefevre C, Robert D, Keller N (2020) Highly robust $La_{1-x}Ti_xFeO_3$ dual catalyst with combined photocatalytic and photo-CWPO activity under visible light for 4-chlorophenol removal in water. Appl Catal B Environ 262:118310
107. Yang X, Wang D (2018) Photocatalysis: from fundamental principles to materials and applications. ACS Appl Energy Mater 1:6657–6693
108. Armaroli N, Balzani V (2011) The hydrogen issue. ChemSusChem 4:21–36
109. Christoforidis KC, Fornasiero P (2017) Photocatalytic hydrogen production: a rift into the future energy supply. ChemCatChem 9:1523–1544
110. Colmenares JC (2019) Selective redox photocatalysis: is there any chance for solar bio-refineries? Curr Opin Green Sustain Chem 15:38–46
111. Kudo A, Miseki Y (2009) Heterogeneous photocatalyst materials for water splitting. Chem Soc Rev 38:253–278
112. Coronado JM, Fresno F, Hernández-Alonso MD, Portela R (2013) Design of advanced photocatalytic materials for energy and environmental applications. Green energy and technology, vol 71. Springer, Berlin
113. Osterloh FE (2008) Inorganic materials as catalysts for photochemical splitting of water. Chem Mater 20:35–54
114. Dillert R, Taffa DH, Wark M, Bredow T, Bahnemann DW (2015) Research Update: photoelectrochemical water splitting and photocatalytic hydrogen production using ferrites (MFe_2O_4) under visible light irradiation. APL Mater. https://doi.org/10.1063/1.4931763

115. Taffa DH, Dillert R, Ulpe AC, Bauerfeind KCL, Bredow T, Bahnemann DW, Wark M (2017) Photoelectrochemical and theoretical investigations of spinel type ferrites ($M_xFe_{3-x}O_4$) for water splitting: a mini-review. J Photon Energy 7:012009
116. Cao J, Kako T, Li P, Ouyang S, Ye J (2011) Fabrication of p-type $CaFe_2O_4$ nanofilms for photoelectrochemical hydrogen generation. Electrochem Commun 13:275–278
117. Ida S, Yamada K, Matsunaga T, Hagiwara H, Matsumoto Y, Ishihara T (2010) Preparation of p-type $CaFe_2O_4$ photocathodes for producing hydrogen from water. J Am Chem Soc 132:17343–17345
118. Ida S, Yamada K, Matsunaga T, Hagiwara H, Ishihara T, Taniguchi T, Koinuma M, Matsumoto Y (2011) Photoelectrochemical hydrogen production from water using p-type $CaFe_2O_4$ and n-type ZnO. Electrochemistry 79:797–800
119. Ida S, Yamada K, Matsuka M, Hagiwara H, Ishihara T (2012) Photoelectrochemical hydrogen production from water using p-type and n-type oxide semiconductor electrodes. Electrochim Acta 82:397–401
120. Matsumoto Y, Omae M, Sugiyama K, Sato E- (1987) New photocathode materials for hydrogen evolution: $CaFe_2O_4$ and $Sr_7Fe_{10}O_{22}$. J Phys Chem 91:577–581
121. Matsumoto Y, Sugiyama K, Sato E- (1988) Improvement of $CaFe_2O_4$ photocathode by doping with Na and Mg. J Solid State Chem 74:117–125
122. Cao J, Xing J, Zhang Y, Tong H, Bi Y, Kako T, Takeguchi M, Ye J (2013) Photoelectrochemical properties of nanomultiple $CaFe_2O_4/ZnFe_2O_4$ pn junction photoelectrodes. Langmuir 29:3116–3124
123. Sekizawa K, Nonaka T, Arai T, Morikawa T (2014) Structural improvement of $CaFe_2O_4$ by metal doping toward enhanced cathodic photocurrent. ACS Appl Mater Interfaces 6:10969–10973
124. Kung HH, Jarrett HS, Sleight AW, Ferretti A (1977) Semiconducting oxide anodes in photoassisted electrolysis of water. J Appl Phys 48:2463–2469
125. Archer MD, Morris GC, Yim GK (1981) Electrochemical approaches to solar energy conversion: a brief overview and preliminary results obtained with n-type cobalt ferrite. J Electroanal Chem 118:89–100
126. Yang H, Mao Y, Li M, Liu P, Tong Y (2013) Electrochemical synthesis of $CoFe_2O_4$ porous nanosheets for visible light driven photoelectrochemical applications. New J Chem 37:2965–2968
127. Rekhila G, Bessekhouad Y, Trari M (2013) Visible light hydrogen production on the novel ferrite $NiFe_2O_4$. Int J Hydrogen Energy 38:6335–6343
128. de Haart LGJ, Blasse G (1985) Photoelectrochemical properties of ferrites with the spinel structure. J Electrochem Soc 132:2933–2938
129. Benko FA, Koffyberg FP (1986) The effect of defects on some photoelectrochemical properties of semiconducting $MgFe_2O_4$. Mater Res Bull 21:1183–1188
130. Zazoua H, Boudjemaa A, Chebout R, Bachari K (2014) Enhanced photocatalytic hydrogen production under visible light over a material based on magnesium ferrite derived from layered double hydroxides (LDHs). Int J Energy Res 38:2010–2018
131. Chang BT, Jakani M, Campet G, Claverie J (1988) Photoelectrochemical study of a spinel-type titanomagnetite. J Solid State Chem 72:201–208
132. Matsumoto Y, Omae M, Watanabe I, Sato E- (1986) Photoelectrochemical properties of the Zn-Ti-Fe spinel oxides. J Electrochem Soc 133:711–716
133. Tahir AA, Wijayantha KGU (2010) Photoelectrochemical water splitting at nanostructured $ZnFe_2O_4$ electrodes. J Photochem Photobiol A Chem 216:119–125
134. Tahir AA, Burch HA, Wijayantha KGU, Pollet BG (2013) A new route to control texture of materials: nanostructured $ZnFe_2O_4$ photoelectrodes. Int J Hydrogen Energy 38:4315–4323
135. Senftle TP, Carter EA (2017) The holy grail: chemistry enabling an economically viable CO_2 capture, utilization, and storage strategy. Acc Chem Res 50:472–475
136. Fresno F, Villar-García IJ, Collado L, Alfonso-González E, Renones P, Barawi M, De La Pena O'Shea VA (2018) Mechanistic view of the main current issues in photocatalytic CO_2 reduction. J Phys Chem Lett 9:7192–7204
137. Mota FM, Kim DH (2019) From CO_2 methanation to ambitious long-chain hydrocarbons: alternative fuels paving the path to sustainability. Chem Soc Rev 48:205–259
138. Ran J, Jaroniec M, Qiao S (2018) Cocatalysts in semiconductor-based photocatalytic CO_2 reduction: achievements, challenges, and opportunities. Adv Mater. https://doi.org/10.1002/adma.201704649
139. Lais A, Gondal MA, Dastageer MA (2018) Semiconducting oxide photocatalysts for reduction of CO_2 to methanol. Environ Chem Lett 16:183–210

140. Matsumoto Y (1996) Energy positions of oxide semiconductors and photocatalysis with iron complex oxides. J Solid State Chem 126:227–234
141. Neudeck C, Kim Y-, Ogasawara W, Shida Y, Meldrum F, Walsh D (2011) General route to functional metal oxide nanosuspensions, enzymatically deshelled nanoparticles, and their application in photocatalytic water splitting. Small 7:869–873
142. Mangrulkar PA, Joshi MM, Tijare SN, Polshettiwar V, Labhsetwar NK, Rayalu SS (2012) Nano cobalt oxides for photocatalytic hydrogen production. Int J Hydrogen Energy 37:10462–10466
143. Büchler M, Schmuki P, Böhni H, Stenberg T, Mäntylä T (1998) Comparison of the semiconductive properties of sputter-deposited iron oxides with the passive film on iron. J Electrochem Soc 145:378–385
144. Gobara HM, Nassar IM, El Naggar AMA, Eshaq G (2017) Nanocrystalline spinel ferrite for an enriched production of hydrogen through a solar energy stimulated water splitting process. Energy 118:1234–1242
145. Peng T, Zhang X, Lv H, Zan L (2012) Preparation of $NiFe_2O_4$ nanoparticles and its visible-light-driven photoactivity for hydrogen production. Catal Commun 28:116–119
146. Hong D, Yamada Y, Sheehan M, Shikano S, Kuo C-, Tian M, Tsung C-, Fukuzumi S (2014) Mesoporous nickel ferrites with spinel structure prepared by an aerosol spray pyrolysis method for photocatalytic hydrogen evolution. ACS Sustain Chem Eng 2:2588–2594
147. Domínguez-Arvizu JL, Jiménez-Miramontes JA, Salinas-Gutiérrez JM, Meléndez-Zaragoza MJ, López-Ortiz A, Collins-Martínez V (2017) Optical properties determination of $NiFe_2O_4$ nanoparticles and their photocatalytic evaluation towards hydrogen production. Int J Hydrogen Energy 42:30242–30248
148. Núñez J, Fresno F, Platero-Prats AE, Jana P, Fierro JLG, Coronado JM, Serrano DP, De La Peña O'Shea VA (2016) Ga-promoted photocatalytic H_2 production over Pt/ZnO nanostructures. ACS Appl Mater Interfaces 8:23729–23738
149. Zeng J, Zeng W, Zeng H (2017) In situ plasmonic Au nanoparticle anchored nickel ferrite: an efficient plasmonic photocatalyst for fluorescein-sensitized hydrogen evolution under visible light irradiation. J Solid State Chem 253:294–304
150. Rodríguez-Rodríguez AA, Moreno-Trejo MB, Meléndez-Zaragoza MJ, Collins-Martínez V, López-Ortiz A, Martínez-Guerra E, Sánchez-Domínguez M (2018) Spinel-type ferrite nanoparticles: synthesis by the oil-in-water microemulsion reaction method and photocatalytic water-splitting evaluation. Int J Hydrogen Energy 44:12421–12429
151. Dom R, Subasri R, Hebalkar NY, Chary AS, Borse PH (2012) Synthesis of a hydrogen producing nanocrystalline $ZnFe_2O_4$ visible light photocatalyst using a rapid microwave irradiation method. RSC Adv 2:12782–12791
152. Boudjemaa A, Popescu I, Juzsakova T, Kebir M, Helaili N, Bachari K, Marcu I- (2016) M-substituted (M = Co, Ni and Cu) zinc ferrite photo-catalysts for hydrogen production by water photoreduction. Int J Hydrogen Energy 41:11108–11118
153. Ortega López Y, Medina Vázquez H, Salinas Gutiérrez J, Guzmán Velderrain V, López Ortiz A, Collins Martínez V (2015) Synthesis method effect of $CoFe_2O_4$ on its photocatalytic properties for H_2 production from water and visible light. J Nanomater 2015:985872
154. Yang H, Yan J, Lu Z, Cheng X, Tang Y (2009) Photocatalytic activity evaluation of tetragonal $CuFe_2O_4$ nanoparticles for the H_2 evolution under visible light irradiation. J Alloys Compd 476:715–719
155. Dom R, Kim HG, Borse PH (2017) Photo chemical hydrogen generation from orthorhombic $CaFe_2O_4$ nanoparticles synthesized by different methods. Chem Select 2:2556–2564
156. Jiménez-Miramontes JA, Domínguez-Arvizu JL, Salinas-Gutiérrez JM, Meléndez-Zaragoza MJ, López-Ortiz A, Collins-Martínez V (2017) Synthesis, characterization and photocatalytic evaluation of strontium ferrites towards H_2 production by water splitting under visible light irradiation. Int J Hydrogen Energy 42:30257–30266
157. Tijare SN, Joshi MV, Padole PS, Mangrulkar PA, Rayalu SS, Labhsetwar NK (2012) Photocatalytic hydrogen generation through water splitting on nano-crystalline $LaFeO_3$ perovskite. Int J Hydrogen Energy 37:10451–10456
158. Iervolino G, Vaiano V, Sannino D, Rizzo L, Ciambelli P (2016) Production of hydrogen from glucose by $LaFeO_3$ based photocatalytic process during water treatment. Int J Hydrogen Energy 41:959–966

159. Chen Z, Fan T, Zhang Q, He J, Fan H, Sun Y, Yi X, Li J (2019) Interface engineering: surface hydrophilic regulation of $LaFeO_3$ towards enhanced visible light photocatalytic hydrogen evolution. J Colloid Interface Sci 536:105–111
160. Hojamberdiev M, Kawashima K, Kumar M, Yamakata A, Yubuta K, Gurlo A, Hasegawa M, Domen K, Teshima K (2017) Engaging the flux-grown $La_{1-x}Sr_xFe_{1-y}Ti_yO_3$ crystals in visible-light-driven photocatalytic hydrogen generation. Int J Hydrogen Energy 42:27024–27033
161. Chen D, Zhang F, Li Q, Wang W, Qian G, Jin Y, Xu Z (2017) A promising synergistic effect of nickel ferrite loaded on the layered double hydroxide-derived carrier for enhanced photocatalytic hydrogen evolution. Int J Hydrogen Energy 42:867–875
162. Matsumoto Y, Obata M, Hombo J (1994) Photocatalytic reduction of carbon dioxide on p-type $CaFe_2O_4$ powder. J Phys Chem 98:2950–2951
163. Xiao J, Yang W, Gao S, Sun C, Li Q (2018) Fabrication of ultrafine $ZnFe_2O_4$ nanoparticles for efficient photocatalytic reduction CO_2 under visible light illumination. J Mater Sci Technol 34:2331–2336
164. Kim HG, Borse PH, Jang JS, Jeong ED, Jung O-, Suh YJ, Lee JS (2009) Fabrication of $CaFe_2O_4/MgFe_2O_4$ bulk heterojunction for enhanced visible light photocatalysis. Chem Commun 39:5889–5891
165. Vijayaraghavan T, Lakshmana Reddy N, Shankar MV, Vadivel S, Ashok A (2018) A co-catalyst free, eco-friendly, novel visible light absorbing iron based complex oxide nanocomposites for enhanced photocatalytic hydrogen evolution. Int J Hydrogen Energy 43:14417–14426
166. An X, Cheng D, Dai L, Wang B, Ocampo HJ, Nasrallah J, Jia X, Zou J, Long Y, Ni Y (2017) Synthesis of nano-fibrillated cellulose/magnetite/titanium dioxide (NFC@Fe_3O_4@TNP) nanocomposites and their application in the photocatalytic hydrogen generation. Appl Catal B Environ 206:53–64
167. Beydoun D, Amal R, Low GK-, McEvoy S (2000) Novel photocatalyst: titania-coated magnetite. activity and photodissolution. J Phys Chem B 104:4387–4396
168. Hafeez HY, Lakhera SK, Karthik P, Anpo M, Neppolian B (2018) Facile construction of ternary $CuFe_2O_4$–TiO_2 nanocomposite supported reduced graphene oxide (rGO) photocatalysts for the efficient hydrogen production. Appl Surf Sci 449:772–779
169. Uddin MR, Khan MR, Rahman MW, Yousuf A, Cheng CK (2015) Photocatalytic reduction of CO_2 into methanol over $CuFe_2O_4/TiO_2$ under visible light irradiation. React Kinet Mech Catal 116:589–604
170. Song G, Xin F, Yin X (2015) Photocatalytic reduction of carbon dioxide over $ZnFe_2O_4/TiO_2$ nanobelts heterostructure in cyclohexanol. J Colloid Interface Sci 442:60–66
171. Song G, Wu X, Xin F, Yin X (2017) $ZnFe_2O_4$ deposited on BiOCl with exposed (001) and (010) facets for photocatalytic reduction of CO_2 in cyclohexanol. Front Chem Sci Eng 11:197–204
172. Song G, Wu X, Xin F, Yin X (2017) Synthesis of different shapes $ZnFe_2O_4$-BiOCl nanocomposites for photocatalytic reduction of CO_2 in cyclohexanol. J Nanosci Nanotechnol 17:2438–2446
173. Soto-Arreola A, Huerta-Flores AM, Mora-Hernández JM, Torres-Martínez LM (2018) Improved photocatalytic activity for water splitting over MFe_2O_4–ZnO (M = Cu and Ni) type-ll heterostructures. J Photochem Photobiol A Chem 364:433–442
174. Karamian E, Sharifnia S (2018) Enhanced visible light photocatalytic activity of $BiFeO_3$-ZnO p–n heterojunction for CO_2 reduction. Mater Sci Eng B Solid State Adv Technol 238–239:142–148
175. Guo J, Wang K, Wang X (2017) Photocatalytic reduction of CO_2 with H_2O vapor under visible light over Ce doped $ZnFe_2O_4$. Catal Sci Technol 7:6013–6025
176. Khan I, Sun N, Zhang Z, Li Z, Humayun M, Ali S, Qu Y, Jing L (2019) Improved visible-light photoactivities of porous $LaFeO_3$ by coupling with nanosized alkaline earth metal oxides and mechanism insight. Catal Sci Technol 9:3149–3157
177. Kwon S, Liao P, Stair PC, Snurr RQ (2016) Alkaline-earth metal-oxide overlayers on TiO_2: application toward CO_2 photoreduction. Catal Sci Technol 6:7885–7895
178. Ong W-, Tan L-, Ng YH, Yong S-, Chai S- (2016) Graphitic carbon nitride ($g\text{-}C_3N_4$)-based photocatalysts for artificial photosynthesis and environmental remediation: are we a step closer to achieving sustainability? Chem Rev 116:7159–7329
179. Chen J, Zhao D, Diao Z, Wang M, Guo L, Shen S (2015) Bifunctional modification of graphitic carbon nitride with $MgFe_2O_4$ for enhanced photocatalytic hydrogen generation. ACS Appl Mater Interfaces 7:18843–18848

180. Chen J, Zhao D, Diao Z, Wang M, Shen S (2016) Ferrites boosting photocatalytic hydrogen evolution over graphitic carbon nitride: a case study of (Co, Ni)Fe_2O_4 modification. Sci Bull 61:292–301
181. Acharya S, Mansingh S, Parida KM (2017) The enhanced photocatalytic activity of g-C_3N_4-$LaFeO_3$ for the water reduction reaction through a mediator free Z-scheme mechanism. Inorg Chem Front 4:1022–1032
182. Xu K, Feng J (2017) Superior photocatalytic performance of $LaFeO_3$/g-C_3N_4 heterojunction nanocomposites under visible light irradiation. RSC Adv 7:45369–45376
183. Xu K, Xu H, Feng G, Feng J (2017) Photocatalytic hydrogen evolution performance of NiS cocatalyst modified $LaFeO_3$/g-C_3N_4 heterojunctions. New J Chem 41:14602–14609
184. Fan W, Li M, Bai H, Xu D, Chen C, Li C, Ge Y, Shi W (2016) Fabrication of $MgFe_2O_4$/MoS_2 heterostructure nanowires for photoelectrochemical catalysis. Langmuir 32:1629–1636
185. Jiang J, Fan W, Zhang X, Bai H, Liu Y, Huang S, Mao B, Yuan S, Liu C, Shi W (2016) Rod-in-tube nanostructure of $MgFe_2O_4$: electrospinning synthesis and photocatalytic activities of tetracycline. New J Chem 40:538–544
186. Guijarro N, Bornoz P, Prévot M, Yu X, Zhu X, Johnson M, Jeanbourquin X, Le Formal F, Sivula K (2018) Evaluating spinel ferrites MFe_2O_4 (M = Cu, Mg, Zn) as photoanodes for solar water oxidation: prospects and limitations. Sustain Energy Fuels 2:103–117
187. Rezaul Karim KM, Ong HR, Abdullah H, Yousuf A, Cheng CK, Rahman Khan MM (2018) Photoelectrochemical reduction of carbon dioxide to methanol on p-type $CuFe_2O_4$ under visible light irradiation. Int J Hydrogen Energy 43:18185–18193
188. Kim JH, Kim JH, Jang J-, Kim JY, Choi SH, Magesh G, Lee J, Lee JS (2015) Awakening solar water-splitting activity of $ZnFe_2O_4$ nanorods by hybrid microwave annealing. Adv Energy Mater. https://doi.org/10.1002/aenm.201401933
189. Kim JH, Jang YJ, Kim JH, Jang J-, Choi SH, Lee JS (2015) Defective $ZnFe_2O_4$ nanorods with oxygen vacancy for photoelectrochemical water splitting. Nanoscale 7:19144–19151
190. Hufnagel AG, Peters K, Müller A, Scheu C, Fattakhova-Rohlfing D, Bein T (2016) Zinc ferrite photoanode nanomorphologies with favorable kinetics for water-splitting. Adv Funct Mater 26:4435–4443
191. Sharma P, Jang J, Lee JS (2019) Key strategies to advance the photoelectrochemical water splitting performance of α-Fe_2O_3 photoanode. ChemCatChem 11:157–179
192. Sivula K (2013) Metal oxide photoelectrodes for solar fuel production, surface traps, and catalysis. J Phys Chem Lett 4:1624–1633
193. McDonald KJ, Choi KS (2011) Synthesis and photoelectrochemical properties of Fe_2O_3/$ZnFe_2O_4$ composite photoanodes for use in solar water oxidation. Chem Mater 23:4863–4869
194. Guo Y, Fu Y, Liu Y, Shen S (2014) Photoelectrochemical activity of $ZnFe_2O_4$ modified a-Fe_2O_3 nanorod array films. RSC Adv 4:36967–36972
195. Dom R, Kumar GS, Hebalkar NY, Joshi SV, Borse PH (2013) Eco-friendly ferrite nanocomposite photoelectrode for improved solar hydrogen generation. RSC Adv 3:15217–15224
196. Kim JY, Magesh G, Youn DH, Jang J-, Kubota J, Domen K, Lee JS (2013) Single-crystalline, wormlike hematite photoanodes for efficient solar water splitting. Sci Rep 3:2681
197. Kim ES, Kang HJ, Magesh G, Kim JY, Jang J-, Lee JS (2014) Improved photoelectrochemical activity of $CaFe_2O_4$/$BiVO_4$ heterojunction photoanode by reduced surface recombination in solar water oxidation. ACS Appl Mater Interfaces 6:17762–17769
198. Ahmed MG, Kandiel TA, Ahmed AY, Kretschmer I, Rashwan F, Bahnemann D (2015) Enhanced photoelectrochemical water oxidation on nanostructured hematite photoanodes via p-$CaFe_2O_4$/n-Fe_2O_3 heterojunction formation. J Phys Chem C 119:5864–5871
199. Iervolino G, Vaiano V, Sannino D, Rizzo L, Palma V (2017) Enhanced photocatalytic hydrogen production from glucose aqueous matrices on Ru-doped $LaFeO_3$. Appl Catal B 207:182–194
200. Chen H, Sun X, Xu X (2017) Ruddlesden-Popper compounds $(SrO)(LaFeO_3)_n$ ($n = 1$ and 2) as p-type semiconductors for photocatalytic hydrogen production. Electrochim Acta 252:138–146

Topics in Current Chemistry (2019) 377:24
https://doi.org/10.1007/s41061-019-0248-1

REVIEW

Characterization of Photo-catalysts: From Traditional to Advanced Approaches

Uriel Caudillo-Flores[1] · Irene Barba-Nieto[1] · Mario J. Muñoz-Batista[2] · Anna Kubacka[1] · Marcos Fernández-García[1]

Received: 2 March 2019 / Accepted: 16 August 2019 / Published online: 29 August 2019

Abstract

The article provides an overview of the most relevant characterization results of heterogeneous photo-catalytic materials available in the literature. First, we present a summary of the ex situ utilization of physico-chemical characterization techniques. In the majority of current works, pre and post-reaction samples are subjected to ex situ analysis using a multitechnique approach which attempts to render information about the morphological, structural, and electronic properties of relevance to interpret photoactivity. Details of the effects on physico-chemical observables of the nanostructure and the complex chemical nature (considering mono and multiphase materials with presence of several chemical elements) of typical photo-catalysts will be analyzed. Modern studies however emphasize the use of in situ tools in order to establish activity–structure links. To this end, the first point to pay attention to is to consider carefully the interaction between light and matter at the reaction cell where the characterization is carried out. Operando and spectro-kinetic methodologies will be reviewed as they would render valuable and trusting results and thus will pave the way for the future developments in photocatalysis.

Keywords Spectroscopy · Kinetics · In situ · Operando · Spectro-kinetic · Multitechnique approach

Chapter 5 was originally published as Caudillo-Flores, U., Barba-Nieto, I., Muñoz-Batista, M. J., Kubacka, A. & Fernández-García, M. Topics in Current Chemistry (2019) 377: 24. https://doi.org/10.1007/s41061-019-0248-1.

✉ Anna Kubacka
ak@icp.csic.es

✉ Marcos Fernández-García
mfg@icp.csic.es

[1] Instituto de Catálisis y Petroleoquímica CSIC, Marie Curie 2, 28049 Madrid, Spain

[2] Departamento de Química Orgánica, Universidad de Córdoba, Edif. Marie Curie, Ctra Nnal IV-A, Km 396, 14014 Córdoba, Spain

1 Introduction

Heterogeneous photo-catalysis is a field of research intensively investigated which includes both energy and environmental applications. This field is essentially defined by the use of photons as the energy source to drive the chemical reaction(s) of interest [1, 2]. An inherent part of the research in this and, in general, in any field related to catalysis, concerns the physico-chemical characterization of the materials. Heterogeneous photocatalysts are frequently nanostructured materials in the form of powders or films. Moreover, such materials are dominantly constituted by semiconductors that can handle light and transform photons into chemical energy but also by other nanosized materials such as metals, and, more frequently, by composite materials having several components of different chemical nature [1, 3]. In all active photo-catalytic materials, light is transformed in hole and electron-related charge carrier species after absorption. Such species would interact with chemical reactants in subsequent steps of the process but such chemical steps always compete with the recombination of charge [1, 2]. Both the nanostructure as well as the composite nature of the materials posse important challenges to the characterization of photo-catalysts and here we will attempt to provide a general view of the problem and the current status of the research.

Traditionally, the characterization of such materials was performed in pre and post-reaction specimens and was focused on obtaining pertinent morphological, structural, and electronic information of the photo-catalysts. Nowadays, such a characterization is a pillar of any investigation in photo-catalysis but a push for operando studies can be noticed [4, 5]. Moreover, further to such works, there are some interesting contributions that try to combine operando spectroscopic tools and kinetic studies under the so-called spectro-kinetic approach [6]. Considering these points, here we will provide a first look into the traditional studies but will emphasize results corresponding to more detailed analyses or examples concerning advanced methods closely connected with operando or spectro-kinetic approaches. Operando studies mainly (although not exclusively) focus on the analysis of the (surface and/or bulk) of the catalyst while spectro-kinetic approaches complete the information attempting to obtain mechanistic and relevant kinetic information of the process under investigation.

The combination of the information from characterization studies attempts to give an answer to the most challenging question in catalysis; the settlement of activity–structure links that can rationalize and, more importantly, predict activity, setting up the bases for the future developments in the field.

2 Static View of the Photo-Catalysts: Traditional Characterization

As mentioned, the use of light to trigger a photo-catalytic process makes that a significant number of scientific contributions carried out characterization studies of the samples before and after reaction. This may render a restrictive view of the

key properties controlling activity. In spite of this, such characterization has been shown fundamental to establishing the scientific ground of the field.

There are a significant number of techniques to extract information about heterogeneous photo-catalysts, but a simple classification procedure can be based on the type of information. Mostly morphological, structural, and electronic types of information are relevant to any photo-catalyst. Morphology is frequently analyzed by physisorption of gases (nitrogen, carbon dioxide) and mercury, although in recent times this is combined with information from other techniques such as X-ray diffraction, nuclear magnetic resonance, or microscopy [7, 8]. Most frequent morphological properties analyzed consider primary and secondary (or aggregate) size and porosity. A challenge is to have a complete view of the full distribution of the observable(s) in the highly heterogeneous samples or at least rigorous information about a few moments (aside the order zero one) of the corresponding observable distribution.

Such basic morphological information is combined with structural and electronic information. To illustrate the most relevant techniques used to achieve these two types of physico-chemical characterizations, we selected a number of techniques applied to an anatase-TiO_2 material in the presence of a heterocation (tungsten). A first challenge when the two cations (Ti and W) coexist in the solid matrix is to distinguish between a true doped, single-phase material, and a composite material, even in the case of diffraction (and Raman) silent surface species, which may be present over a dominant anatase phase [9]. The general system consisting of a dominant anatase material having a heteroatom dopand at bulk or surface position(s) and thus rendering single or multiple (composite) phase materials can therefore provide a general view of the complex task pursued when characterizing a solid photo-catalyst.

Figure 1 contains a summary of the most common techniques applied to obtain structural information. Customary, structural information is divided into that intrinsic to long-range order, requiring periodicity in atomic arrangement above a few nanometers, and characteristic of crystalline materials, and that taking place at a local level, below 1 nm, describing the atom organization around a specific position and existing in all (amorphous, nano of fully crystalline) materials. As a primary source of information, X-ray or neutron diffraction and Raman spectroscopy renders information about existent crystalline phases. As is well known, diffraction comes from the in-phase sum of the elastically scattered photons taking place by interaction with the electron cloud of the solid while Raman is an inelastic scattering process of photons controlled by the polarizability of the electronic cloud. Such techniques can detect a contribution from a solid phase if superior to roughly 0.5 weight percentage. Both techniques can inform about the properties of the crystalline domains present in the materials. Concerning nanomaterials, the signal of both techniques is sensitive to particle size (crystalline domain), a fact typically detected in the peak(s) positions and/or line widths [10]. The complete analysis of such techniques by specific mathematical procedures (such as the well-known Rietveld refinement for diffraction techniques) can render insights into the unit cell parameters and volume, tetragonallity in the case of anatase, defect nature and distribution, strain, and cation/anion fractional occupation. Information relative to the crystalline size (somehow related to the primary particle size) and shape is also accessed from both

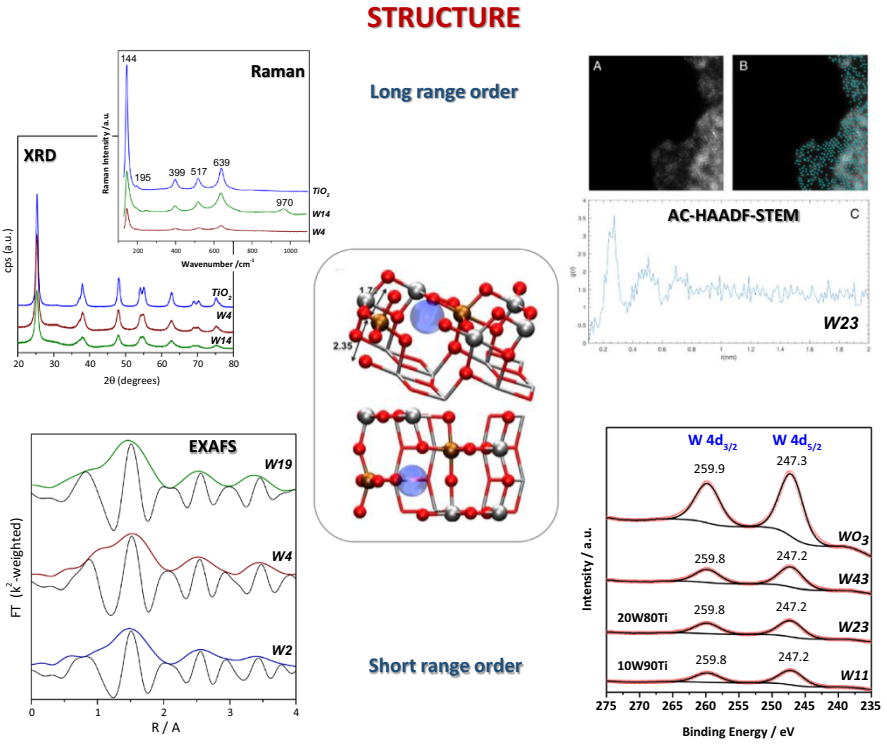

Fig. 1 Results from experimental techniques used for structural characterization of catalytic solids; anatase-based W–Ti mixed or composite oxides with names presenting the W atomic percentage in cationic basis. *Center*: schematic representation of the structural situation in the case of W doping of the anatase structure. See text for details

techniques, although these are morphological parameters mentioned in the previous paragraph. Defect nature and distribution is additionally analyzed with the combination of diffraction and Raman with electron paramagnetic resonance (EPR) and other less common techniques [11]. In Fig. 1, analysis of XRD and Raman results indicates the presence of a single anatase phase, characteristic of the titania oxide, in all the materials presented. The presence of W at the nano materials is shown to occupy cation positions of the anatase structure up to a doping level of ca. 25 at.%, producing cation (Ti) vacancies to achieve charge neutrality, and altering anatase unit cell parameters in a way that mostly tetragonallity (and not cell volume) is notably affected. So, below a 25 at.% substitution of Ti by W results in the formation of substitutionally disordered mixed oxides. Above that limit, W at the surface starts to form W–O–W links detectable by Raman and indicative of the formation of (diffraction silent) surface clusters [9, 12, 13].

The structural properties of a material can be further studied with microscopy techniques. There are a number of significant microscopy techniques among which transmission (TEM) and scanning (SEM) electron microscopy are the most

frequently utilized in catalysis. They are frequently combined with electron diffraction and X-ray energy dispersive spectroscopy in order to complete the structural information already described and extracted from XRD or Raman [14, 15]. In particular, in the system under investigation (Fig. 1), the use of STEM (scanning transmission electron microscopy here with a high angle annular dark field detector) was able to identify tungsten atoms at the materials. They are located at the more brilliant spots in the image(s) included in Fig. 1. The use of mathematical tools (classification techniques based in a K-means clustering algorithm) allow to obtain the W–W distance(s) taking place in a material having ca. 20 atomic (cation basis) tungsten content. The plot of such an observable (see bottom of Fig. 1) shows well-defined distance(s) between tungsten atoms, which are exclusively located at specific (bulk and surface positions) of anatase planes, showing the true doped nature of the sample [9]. Of course, microscopy can capture additional details concerning the presence of amorphous phases (frequently occurring at surface positions) and/or details of the defect nature and distribution. Apart from point defects, dislocations, twinning and stacking faults, and antiphase domains are subjects of microscopy studies [14, 15].

In a brief comment, here we can mention some techniques specifically dedicated to analyzing surface groups present at photo-catalytic materials. Among them, infrared spectroscopy is the most utilized, although it can also provide structural (and electronic) information coming from the phonon modes of the solids [16, 17]. Surface species, particularly surface hydroxyl groups, are analyzed in photo-catalysts with the help of infrared (but also with EPR under light excitation) using or not probe molecules [11, 16, 17]. In addition, surface chemical composition can be analyzed using low-energy surface scattering (LEIS) [18]. In the case of Ti–W systems, the Raman band at ca. 970 cm^{-1} (Fig. 1) is indicative of the presence of surface tungsten atoms detected by the formation of W=O bonds [9, 13]. Raman is sensitive to the formation of different M–O and (as previously mentioned) M–O–M bonds originated by the presence of cations at surface (and bulk) positions in a significant number of mixed or composite oxides. Similarly, Raman can detect bonds of other (sulfides, nitrides, etc.) chemical compounds [10].

The structural characterization of the solid photo-catalysts is completed with the study of the local order of the materials. Typical techniques (which, as mentioned, can allow the study of amorphous, nanocrystalline, and crystalline samples) to handle this issue are extended X-ray absorption fine structure (EXAFS) and X-ray photoelectron spectroscopy (XPS). EXAFS is a technique mostly carried out in synchrotrons which analyze the signal coming from the interference between the incident and scattered photo-electron(s), and gives a picture of the local order for atoms (shells) at distances below ca. 6–7 Angstroms from the absorber atom [19, 20]. In recent times, X-ray total scattering techniques are also utilized to study the local order as they offer information at essentially all (local) distances present in the nanostructured material [21]. Both techniques differ in the maximum distance achievable but also in the fact that EXAFS describes the local structure around the absorbing atom (allowing to study all atoms of the sample) while total scatting signal contains the sum of all pairs of atoms present at the structure. On the other hand, XPS scans the unoccupied density of state (far from the edge) as a function of the

kinetic energy of the ejected photoelectron and is sensitive to the local arrangement around the absorbing atom. It can have a penetration depth between 1 and ca. 3 nm, depending on the excitation wavelength. Thus, XPS is considered a surface-sensitive technique for most materials [10].

Figure 1 contains information from XAS and XPS techniques in the Ti–W samples. The Fourier transform of the EXAFS signals of the W L_{III}-edge presents peaks at shell pseudo-radial distances from the tungsten atom absorbing the X-ray radiation in binary Ti–W oxides. Mathematical analysis of the signal shows, as expected, that oxygen occupies the first shell in the oxide but only Ti occupies the second. Complete information comes from the shell coordination numbers and distances. These observables showed that the first shell has a local structure resembling the tungsten oxide local environment (has two subshells at distances differing up to ca. 0.6 Angstroms) in spite of being at the anatase structure. The second shell shows the strong driving force to have M–O–M hetero and not homo-bonds at such structure. This second shell changes coordination number drastically with tungsten content in the materials. The chemical nature of the second (first metal) neighbor is always Ti, a fact that has probes the mixed oxide nature of the samples and has strong implications in the electronic properties of the nanostructured Ti–W anatase-based materials. The local environment picture obtained from EXAFS can be combined thus with XPS (Fig. 1 includes the W3d region, showing a signal profile compatible with the W–O local arrangement already described) to confirm the substitutional position of the tungsten cations [22, 23].

So, as a summary of the outcome resulting from the structural characterization of photo-catalysts, the center of Fig. 1 gives a pictorial interpretation of the experimental result concerning the structure, presenting the local and middle range order around the tungsten atom located in an anatase structure. Of course, such experimental information can be always accompanied and frequently interpreted using theoretical results from DFT or similar calculation tools [22, 24, 25]. While at the surface, tungsten forms the already-described W=O bonds and, at increasing loadings (well above the solubility limit at the anatase structure) W–O–W bonds characteristic of oligo-sized entities [9, 12, 13].

It is also evident that XPS (after now consider within the framework of the structural characterization) can provide electronic information. XPS and the X-ray near edge structure (XANES) technique are frequent techniques applied to investigate the electronic information of the solid constituents. The latter technique has the same physical origin as EXAFS, but is dominated by multiple scattering effects, while EXAFS is dominated by single scattering events. XANES informs about the local (symmetry projected) unoccupied electronic density states near or about the edge scanned. Again, local means in the close vicinity of the atom absorbing the X-ray photons and the electronic transitions occurring in a XANES spectrum are defined (in a first approximation) by the Fermi Golden rule [26, 27]. A somewhat similar technique corresponds to the electron energy loss spectroscopy (EELS), although here the excitation of the catalyst takes place using electrons. EELS can analyze inner-shell ionization processes (as XANES) but also plasmon or phonon excitations and other physical phenomena [28]. Close information, now corresponding to the occupied density of states, can be obtained using X-ray emission techniques (XES)

[29]. Finally, XPS can render information about the oxidation state of the cations and anions of the material [30, 31].

In Fig. 2, we show the W L_I-edge XANES spectra of tungsten cations at the anatase structure together with the W3d XPS peaks. The analysis of the XANES edge and XPS binding energy positions for these W-related signals indicates the presence of W(VI) species in all Ti–W solid samples. The pre-edge of the XANES spectra (located at ca. 12107.1 eV) shows differences with respect to an octahedral W reference indicative of tetrahedral type local symmetry (which can be further detailed combining the data with EXAFS results, see above), as well as minor changes in the sp electronic density, which can be finely analyzed using the continuum resonances (peaks after the edge). Combined with an analysis of the W L_{III}-edge XANES spectra, we can obtain a complete picture of the spd (cation) electronic density and how it evolves in the Ti–W mixed oxide materials as a function of the tungsten content. This can be contrasted or combined with the information coming from an analysis of the valence band by XPS or by a combination of UPS (ultraviolet photoelectron spectroscopy) and XPS. The result is that a W(VI) cation has a

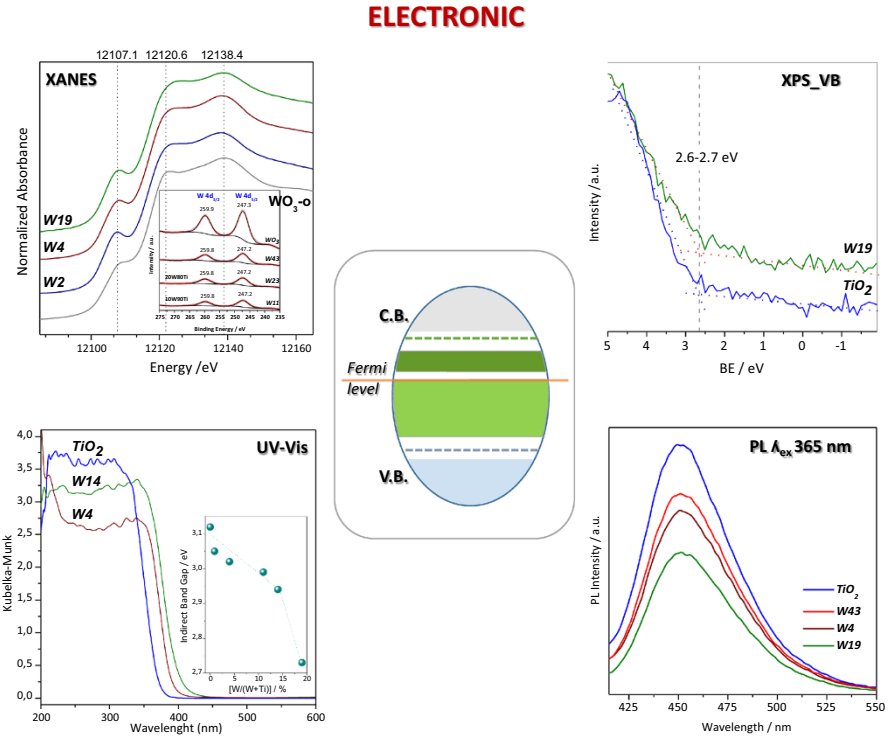

Fig. 2 Results from experimental techniques used for electronic characterization of catalytic solids; anatase-based W–Ti mixed or composite oxides with names presenting the W atomic percentage in cationic basis. *Center*: schematic representation of main electronic bands and localized states at anatase. See text for details

modest increasing electronic charge (with respect to their pure oxide state), mostly localized into the d band, as the tungsten content of the mixed oxide increases. This happens without altering substantially the energy position of the valence band end [13, 22, 23]. Once tungsten is at the surface forming composite oxide systems, the electronic properties depend on the size of the aggregates as they differ in the amount of tungsten to oxygen single and double bonds (which is also related to the formation of W–O–W connections) as well as the sharing of oxygen atoms with anatase [9, 12, 13, 23].

Relevant electronic information for photo-catalysis can come from UV–visible spectroscopy, which analyzes the absorption of light in the UV-visble-near-IR region. Aside from providing further details of some cation(s) electronic structure, information on the band gap can be obtained. Note than band gap is strongly affected by nanostructure [10, 32]. Numerical analysis of direct/indirect gap semiconductors obtained from UV–visible spectroscopy can be combined with the above-described UPS/XPS study of the valence band to settle down the position of the conduction and valence band(s) of any photo-catalyst. Interpretation of the position can be obtained by theoretical calculations. In the case of Ti–W mixed oxides described in Fig. 2, the combination of experimental and theoretical tools indicate that the band gap energy modification with tungsten content is a result of a dominant change in the conduction band position. As mentioned above, the band gap change trough the Ti–W mixed oxide samples lacks a linear trend with tungsten content as the modification of the local order around the tungsten cation occurring around 15 at.% has a "disrupting" effect in the conduction band [22, 23].

Finally, we can consider the analysis of the de-excitation process taking place after light excitation. This is a key piece to interpret the electronic behavior of the photo-catalytic materials. De-excitation of charge carriers after light absorption is a complex process having non-radiative and radiative processes. Non-radiative processes can be analyzed using calorimetric techniques [33] but literature reports concentrate on the use of photoluminescence to analyze the radiative processes [34]. For our purposes, most relevant information is related to the analysis of the localized gap states presented in any nanostructure material as well as the annihilation of charge carrier species. In the case of Fig. 2, the photoluminescence intensity (obtained under UV excitation) is dominated by the anatase characteristics displaying annihilation processes concerning electron/hole species. The addition of tungsten to the structure decreases the intensity of the photoluminescence spectrum of the pure oxide without significant changes. This is proof that the recombination markedly decreased in the doped materials. When tungsten is at the surface of the samples, a larger intensity with respect to the doped materials is commonly observed, but such intensity is also lower than the one of the pure oxide. This indicates that recombination of charge carriers is also decreased, although not to the extent of doped materials [9, 12, 13, 23, 24].

The center of Fig. 2 summarizes the most interesting electronic characterization results in the field coming from the described experimental techniques as well as from theoretical calculations. Such information concerns (for a semiconductor) the valance and conduction band positions, the existence of localized (gap) electronic states, and the ability of band-type and localized electronic levels to accept

and handle (electron and hole) charge carriers after excitation. In the case of Ti–W mixed oxides, the presence of W mostly affects the band gap energy (as mentioned in non-linear way with tungsten content) and the conduction band edge, detecting minor effects in the valence band and relatively minor localized gap states mostly related to surface defects. When tungsten exceeds the solubility limit at the anatase structure, the presence of W–O–W bonds are behind electronic properties, triggering changes in the surface redox and acid–base properties of the solids [9, 12, 13, 22, 23].

3 Advanced Characterization

Recently, the need for obtaining information on interpreting photo-catalyst behavior under reaction conditions has lead to the development of operando studies as well as spectro-kinetic approaches. Although both types of experiments are closely connected, contributions in the literature can be ascribed usually to one of these categories. Therefore, and for practical reasons, we will analyze both in separate sections.

A first (and common to all novel or advanced approaches) point to study active materials under the effect of light and the reactive mixture is to define adequately the experimental conditions to measure the catalyst portion illuminated. If this is not the case, misleading results are likely to come for the corresponding experimental observations. This constrain adds to the normal ones in any operando or kinetic catalytic study, e.g., efficient reactant–catalyst contact to avoid internal/external mass transfer and near-zero dead volume. Analysis of the light–matter interaction is thus mandatory for gas and liquid phase photo-catalytic processes if advanced methodologies are to be used. A primary result from that would be the catalyst volume under illumination and, consequently, the mean free path of light across the sample.

Analysis of the mean free path in a gas phase catalyst (or if a film is used in liquid phase) requires calculating the intensity decay through the solid. For a uniform on-top illumination of an in situ (spectroscopic) cell, we first calculated the value of the light intensity at the surface of the material, $I_{S,\lambda}$ [35]:

$$I_{S,\lambda} = (1 - F_{R,\lambda}) \cdot \int_{\Omega} I_{\lambda}(x, y, z; \underline{\Omega}) \underline{\Omega} \cdot \underline{n}_{G} \mathrm{d}\Omega \mathrm{d}\lambda \tag{1}$$

where $\underline{n}_{G}$ is the outwardly directed unit vector normal to the catalytic surface. This observable is a function of the spectral photon flux of the lamp (together with other elements located in the optical path between the source and the catalyst) $I_{\lambda}(x, y, z; \underline{\Omega})$ measured at the direction of the solid angle unit vector $\underline{\Omega}$ as a function of the incident light wavelength (λ). Equation (1) eliminates the reflectance of the solid ($F_{R,\lambda}$) to calculate the available flux and renders the number (moles) of photons available per unit area normal to the solid surface and unit time. At the solid surface of a "volumetric" sample (i.e., thickness ensuring complete light absorption) this corresponds to the so-called superficial rate of photon absorption, $e^{a,s}$. From this point, and using the solid absorption coefficient κ_{λ} applied to any point of the solid volume, we can calculate the corresponding observable for all positions of the sample [35].

In Fig. 3 we plot results of the $e^{a,s}$ variation in perpendicular to the solid surface corresponding to three broadly used photo-catalysts, commercial P25 (ca. 80% anatase and 20% rutile), pure anatase and graphitic carbon nitride g-C_3N_4 using a typical UV illumination source (250–450-nm range, flat intensity) and power (10 mW cm^{-2}). Results shown the two extreme values of the absorption coefficient reported in literature for each of the above mentioned solids [35, 36]. It can be observed that for low-density powder materials or films, light is essentially absorbed within the "first" 2 or 3 μm, while in dense powder materials or films it is essentially confined to the first micron.

For a liquid phase (solid suspension) process, we need to calculate the volumetric rate of photon absorption ($e^{a,v}$) at each position of the reaction volume [37]:

$$e^{a,v} = \int_{\lambda} \kappa_{\lambda} \cdot \int_{\Omega=4\pi} I_{\lambda,\Omega}\left(\underline{x}, \underline{\Omega}\right) \mathrm{d}\Omega \mathrm{d}\lambda \tag{2}$$

The $e^{a,v}$ requires solving the radiative transfer equation (RTE) to obtain $I_{\lambda,\Omega}$ (now the intensity at each point of the in situ cell volume) and the measurement of the spectral absorption coefficient (κ_{λ}). Solving the RTE in turn requires the complete knowledge of the optical properties of the catalyst suspension at the liquid phase; the spectral absorption coefficient (κ_{λ}), the spectral scattering coefficient (σ_{λ}), and the scattering phase function (($p(\underline{\Omega}' \rightarrow \underline{\Omega})$)) [37]. The liquid phase differs radically from the gas phase in the point that (liquid phase) scattering of light can occur within all spatial directions and thus the intensity at each position of the cell cannot be obtained in a straightforward way from the illumination source (and solid) properties.

In Fig. 4, we plot the $e^{a,v}$ decay from an illuminated surface ("light" progressing along the OX coordinate) in a rectangular cell having two (typical) parallel windows for spectroscopy and variable distance between them (the OX coordinate). Light spectral distribution and intensity for on-top illumination are equal to those used in Fig. 3. To illustrate the situation, four solids, Degussa P25, pure anatase, g-C_3N_4, as well as SnS_2 (all typical photo-catalytic semiconductors) were used. For each solid, four concentrations (from 0.1 to 2 g l^{-1}) are presented, covering the concentrations typically used in experimental catalytic experiments. Figure 4 shows than the different optical properties of the solids makes than even at relatively low concentrations (0.5 g l^{-1}) some of the samples (P25 and SnS_2) render a significant decrease of light. In any case, for all samples, the optimal concentration of the samples is around 1 g l^{-1} and the decay profile shows that almost all photons are utilized well below 1 mm away from the illumination surface.

Summarizing, to perform operando or spectro-kinetic studies, we have to be very careful with the volume and path probe by the beam of each spectroscopy. They need to match the one fully illuminated. Light penetration is, as a rule of thumb, in the order of a few (typically less than 5) microns in the gas phase and well below 1 mm in the liquid phase. Here we will describe experiments taking into consideration this point (with specificities for each experimental technique) or mention the potential weaknesses of others that did not take this point fully into account. Of course, such a point has peculiarities specific for each spectroscopy, which will be detailed in subsequent sections.

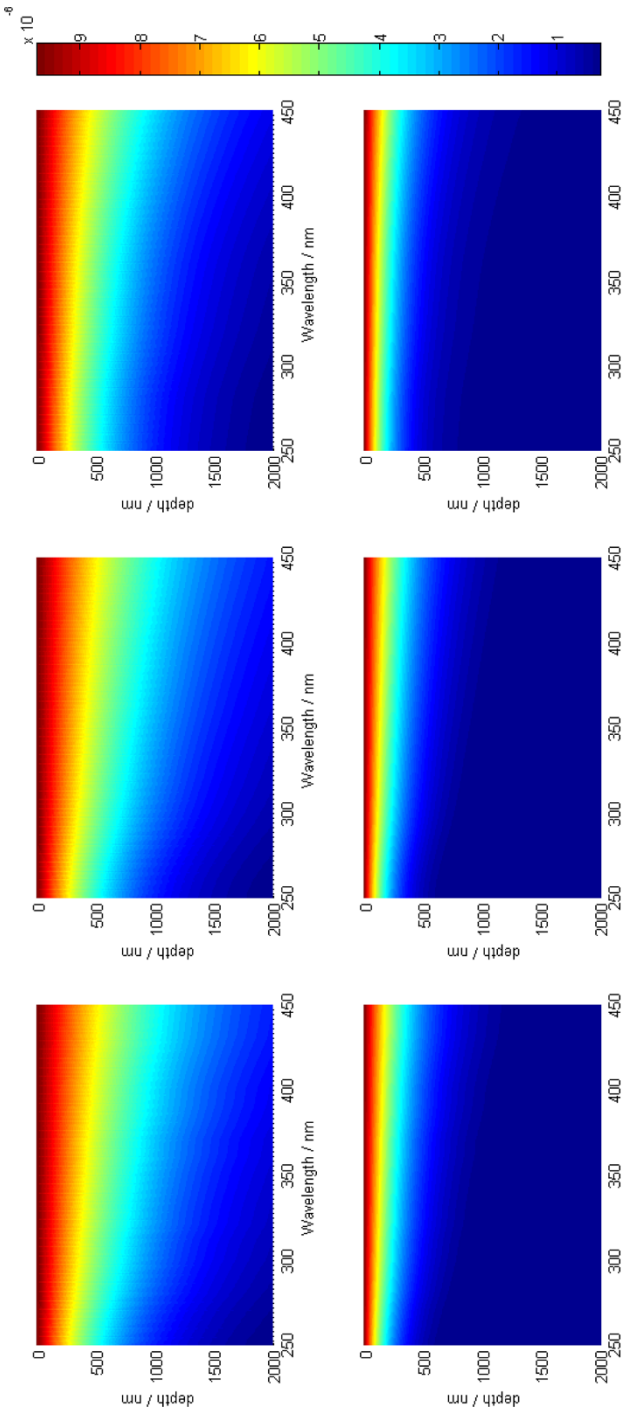

Fig. 3 Light absorption decay (Einstein cm^{-2} s^{-1}) occurring as a function of depth from the surface in a gas-phase reaction for two absorption coefficient values (Eq. 1). *Left column*: Degussa P25 sample; *middle column*: Anatase sample; *right column*: g-C_3N_4 sample. See text for details

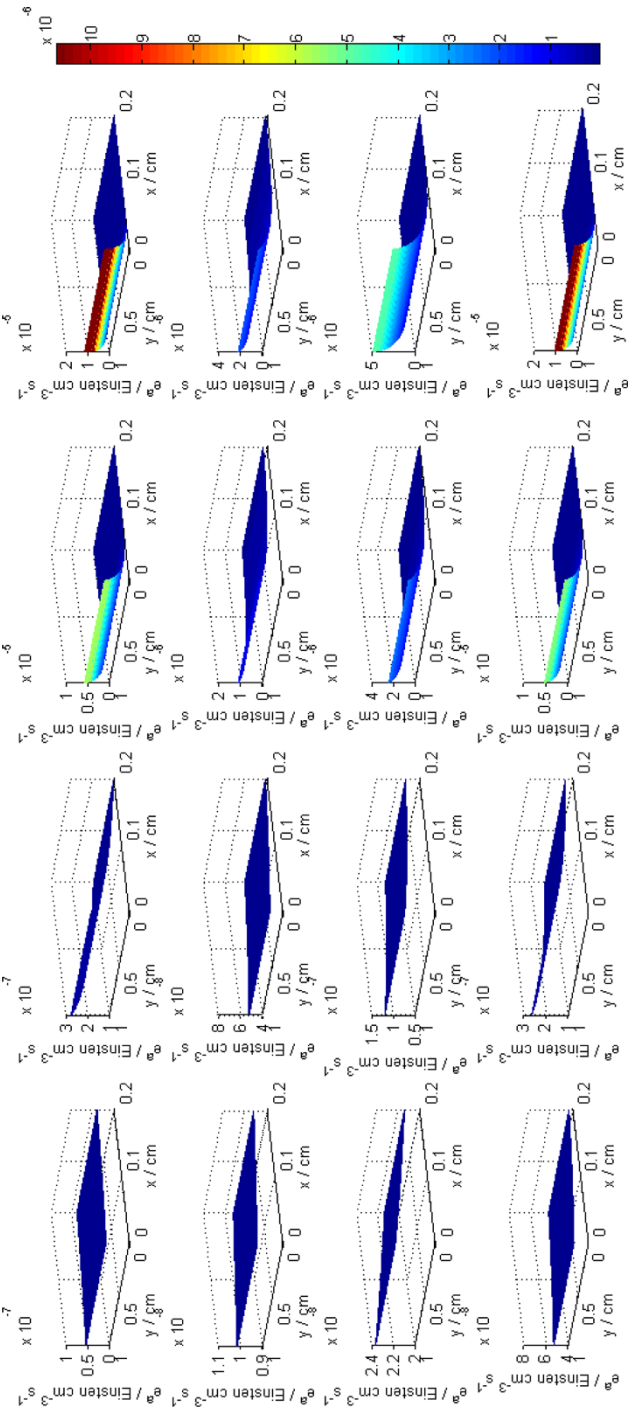

Fig. 4 Light absorption evolution (Einstein cm^{-3} s^{-1}) though a liquid phase (rectangular) reactor as a function of the catalyst content for; (1) *first and upper line*, Degussa P25 sample; (2) *second line*, a anatase sample; (3) *third line*, a g-C_3N_4 sample; and (4) four and *lower line*, a SnS_2 sampled. The four columns correspond to catalyst concentrations (*from left to right*) of 0.1, 0.5, 1, and 2 g l^{-1}. See text for details

3.1 Operando Spectroscopy

Studies focusing on photo-catalytic solid samples at reaction conditions were mostly performed using X-ray absorption spectroscopy (XAS) with a limited number considering the use of Raman and XPS. Both X-ray absorption near edge (XANES) and X-ray extended absorption fine structure (EXAFS) have been used to follow the evolution of a catalyst under the simultaneous influence of light and reactants.

XAS studies using pump and probe procedures were mostly aimed at understanding charge carrier capture and transfer processes. In the case of titanium [38] and tungsten [39] oxides, the photoabsorption process occurs with partial reduction of (mostly surface) cation species form their initial Ti^{4+} and W^{6+} chemical states, followed by a local structural distortion in the tungsten case. The studies thus established a way to analyze the trapping of excited electrons in the solids. Also, the charge transfer process between semiconductors and metals has been analyzed using pump and probe XAS. The process of charge transfer between gold and titania under visible light excitation was the objective of several works using X-ray absorption and emission techniques. In particular, they analyzed the electron transfer and capture occurring after visible light excitation in materials having metallic gold species deposited over titania. A rather interesting study pointed out the key role played by Ti surface centers in the vicinity of the metal particles. Such Ti cations behave as long-lived trapping charge centers allowing the transfer of charge from the noble metal particles to titania after light excitation of the metal component with visible light [40]. The same subject was investigated in other publications that analyzed electronic details concerning the formation of electron–hole pairs after light excitation in gold as well as the subsequent transfer to the titania semiconductor [41]. A similar procedure was carried out to investigate Cu doping of a InP nanostructure material, detecting the capture of a hole by copper after light excitation, relaxation differences between bulk and surface copper species, and the annihilation of charge localized at copper with initially trapped electrons [42].

XAS has also been utilized in situ to study the behavior of different photo-catalysts during reaction. A recent contribution considers the Co-Ru-UIO-67(bpy) photo-catalyst, based on a metal organic framework platform with incorporated molecular photosensitizer (bpy; bipyridine) and “active” Co and Ru species. The XAS analysis (Fig. 5) showed that the reduction of Co^{2+} to Co^{1+} with electrons coming from the sensitizer (bpy) has a relevant role in driving activity in hydrogen photo-production under visible light. This process occurs after an induction period, which suggests that a local reordering around or connected with Co centers is required to achieve photo-activity [43]. Although MOFs and other novel systems are analyzed using XAS, most results reported correspond to oxide or metal parts of composite photo-catalysts. Studies of non-noble metal atoms like Cu or Ni showed the dominant presence of oxidized phases, which evolves in a limited quantity (typically the fraction of atoms evolving is well below 10%) to a reduced state. This has been analyzed for the photo-oxidation of 2-propanol [44] as well as the reduction of CO_2 in presence of water [45]. However, a recent contribution taking into account the matching of spectroscopic and illuminated sample volumes uncovered a more complex evolution of the non-noble metal component for titania-based materials

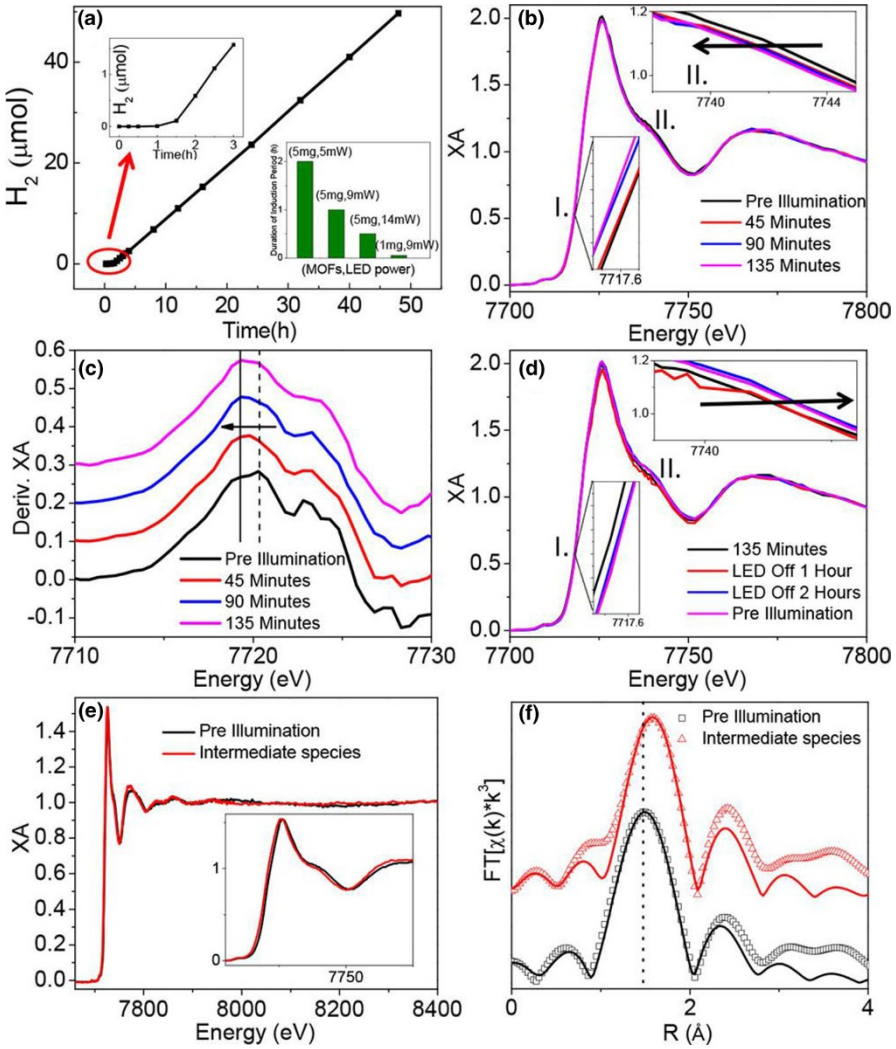

Fig. 5 **a** Time profile of H_2 production by Co-Ru-UIO-67(bpy) under 447 nm LED illumination at 9 mW in the presence of TEOA (0.3 ml) and H_2O (0.4 ml) in acetonitrile solution (3 ml). The *inset* is the duration of induction period as a function of Co-Ru-UIO-67(bpy) concentration and LED power. **b** In situ XANES spectra of Co–Ru–UIO-67(bpy) as a function of irradiation times. The *insets* are enlarged regions I and II. **c** The offset first derivative of in situ XANES spectra. **d** In situ XANES spectra of Co-Ru-UIO-67(bpy) after LED was switched off to observe change back to the original spectrum. The comparison of XANES (**e**), EXAFS (*inset* of **e**), and EXAFS spectra in R space **f** of Co-Ru-UIO-67(bpy) before illumination and the intermediate species formed after the induction period ends. Reproduced with permission from Ref. [43]

used for gas-phase hydrogen photo-production from bio-alcohols [36]. The use of micro-XAS techniques for Cu, Ni, and CuNi titania-supported materials provided evidence of the different physico-chemical properties of the non-noble components as a function of the depth from the illuminated surface of the experiment. Figure 6

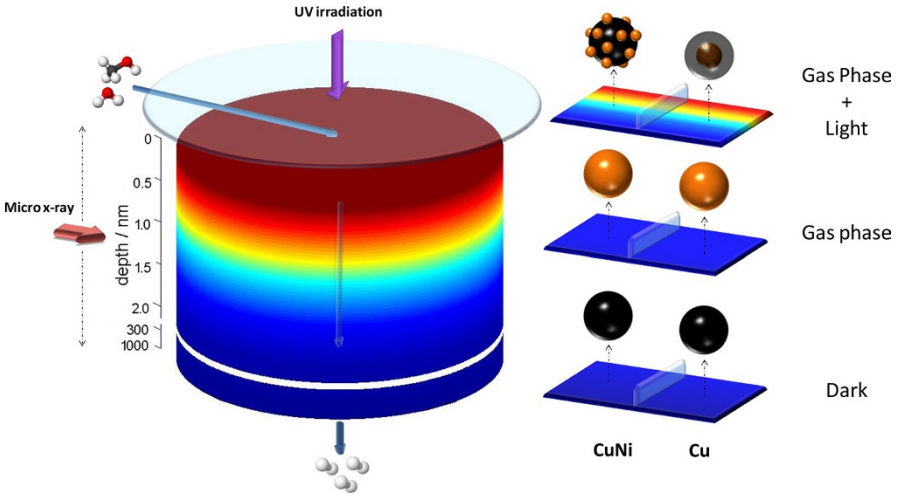

Fig. 6 Schematic view of the sample and experimental conditions. The sample is confined in a cell, which allows simultaneous gas phase treatment and illumination from to top side. *Arrows* show the direction of the gas flow, illumination, and incident X-ray micro-beam. The X-ray micro-beam probes non-noble metal chemical states and structure as a function of the depth from the surface. Panels at the right hand depict the most relevant metal-containing phases (Cu(0) *brown color*; Cu(II) *black color*) for different depths described by the light intensity received. Cu and CuNi samples are considered. Reproduced with permission from Ref. [36]

schematically summarizes the results concerning the Cu component as Ni only suffers rather modest variations in the mono and bimetallic catalysts. At the bottom part of Fig. 6, we can see the chemical state of the Cu and CuNi-containing materials at dark conditions. Copper is fully oxidized in both samples as a consequence of the preparation stage triggered by the calcination treatment of the materials. Under reaction, at positions of the cell where light absorption by the catalysts does not essentially occur, the Cu component appears fully reduced in both samples. This is an effect of the alcohol acting as a reductant at room temperature. Some differences take place between the mono and bimetallic catalysts as a small fraction of Ni is co-reduced with copper in the binary sample. However, the most important result appears when scanning the zone of the catalyst within the simultaneous action of the light and the reactants. In this case, copper is partially oxidized in both (mono and bimetallic) materials with respect to the exclusive effect of the reactants. In the case of the monometallic catalyst, this oxidation process leads to the formation of a core–shell structure with a metallic kernel. In the case of the bimetallic material, the oxidation process progresses in a more important way, leaving only rather small metallic entities (of a few atoms) "deposited" onto the dominant oxidized phase. So, fundamental physico-chemical aspects of the non-noble metal catalysts are only uncovered with the utilization of the appropriate micrometric X-ray beam to obtain XAS data. On the other hand, such a study was also able to show and rationalize the significant differences in the behavior of mono and bimetallic non-noble phases, originated from the different non-noble metal-containing structures stabilized under operation conditions.

In absence of reactants, Pt and Ir showed changes in the interaction between the metallic state (obtained during the preparation stage of the materials) and the support under UV illumination [46]. The metallic state was also detected under operando conditions and assumed to be responsible for visible-light-driven hydrogen photo-reforming from methanol in monometallic Au and Cu as well as bimetallic AuCu catalysts. Optimum activity for the bimetallic system was achieved in cases where an effective interaction (alloying) between the two metals takes place [47]. Another study of Pt but in oxidized form (PtO) was carried out during the water splitting process. Although the work uses co-catalyst concentrations far from those required for a photo-catalytic process, it showed changes in both Pt-O bond distance and coordination number under reaction conditions. Such changes likely relate to a modification of the interaction with the support. Metallic Pt was not detected or generated under reaction conditions [48]. Recently, Pt-based materials were analyzed by absorption and emission spectroscopies under photo-thermal conditions for CO oxidation. As occurs with some of the previous reports, Pt appears more oxidized under illumination and together with the combined effect of temperature controlling noble metal surface CO coverage drive to a significant increase in activity with respect to dark (thermal-alone) conditions [49].

As mentioned, other experimental techniques focusing on analyzing the solid response under photo-catalytic conditions concerns the use of Raman or XPS. These two techniques are only occasionally used in the field of photo-catalysis. Raman has been utilized to study the face-dependent response of the $K_3B_6O_{10}Br$ materials used in chlorophenol degradation under visible light [50] as well as the response of a core–shell CdS-TiO_2 structure for hydrogen photo-production under both UV and visible light illumination conditions [51]. The first contribution (see Fig. 7) follows the evolution of the (211), (110), and (101) facets of a $K_3B_6O_{10}Br$ single crystallite (having all these faces) under reaction conditions, showing that only the first suffers evolution and at the same time provides higher photo-catalytic activity, a fact likely related to the higher OH density (in turn promoted by the higher presence of K) and surface interaction with the pollutant [50]. Raman showed, on the other hand, that the oxide layer of the CdS-TiO_2 catalyst(s) confers stability to the system under reaction conditions concerning hydrogen photo-production, inhibiting the typically corrosion process suffered by the sulphide [51]. A few other examples of using Raman consider the analysis of the gas or liquid phase–catalyst interface and will be presented in following pages.

XPS studies concentrate on the analysis of the surface and near-surface regions of the materials in the field of photo-catalysis. As mentioned, XPS can sample different depths of the solid depending of the energy of excitation, the usual Mo, Mg, or Al K-alpha sources allow sampling a few nanometers of typical photo-catalysts [30, 31]. A nice work described the response of titania, alumina, and silica materials modified with 5 wt% of uranyl nitrate and tested in the oxidation of acetone vapor under visible light. The use of XPS (Fig. 8) was able to show that the surface uranium species was slowly reduced from U^{6+} to the U^{5+} on the Al_2O_3 and SiO_2 surfaces but an easier reduction to the U^{4+} state was observed on the TiO_2 surface. The catalyst based on TiO_2 revealed a substantially higher activity compared to other oxides, which was ascribed to the easy redox handling

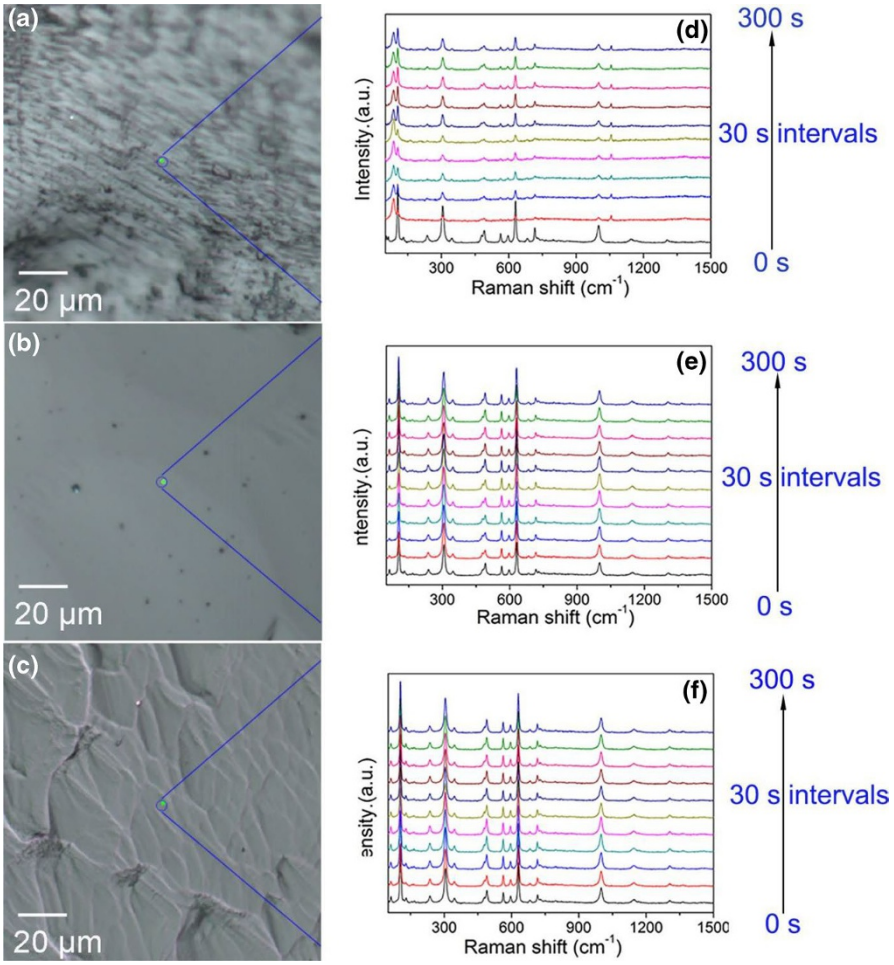

Fig. 7 Images of the three facets from Raman microscope (**a**–**c**), and the corresponding Raman spectrum (**d**–**f**) for (211), (110), and (101) facets, respectively. Reproduced with permission from Ref. [50]

properties of the uranium species [52]. The same technique was used to follow the evolution of Bi nanoparticles supported in titania nanotubes. Initially, a surface passivation of the Bi nanoparticles is detected by XPS under air. As shown in Fig. 9, after excitation of the Bi nanoparticles surface plasmon by visible light absorption, a charge transfer process takes place, reducing the bismuth oxide overlayer located at the surface of the particles. The process does not take place in the absence of titania, which acts as a bridge in the electron handling, likely due to the existence of long-lived trap states at the titania semiconductor. This favors charge separation and photo-activity [53]. Earlier XPS experiments tested the C/Ti ratio in titania materials to show that light excitation effectively triggers the decomposition of dyes [54].

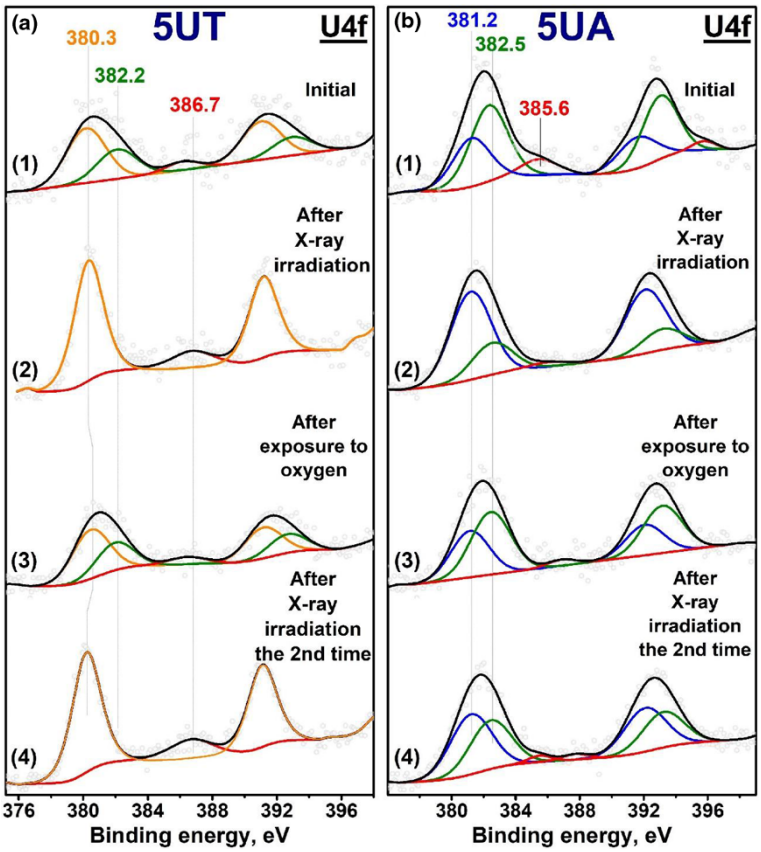

Fig. 8 Photoelectron U4f spectral regions for 5UT (uranium/titania) (**a**) and 5UA (uranium/alumina) (**b**) catalysts during in situ experiments. The plots correspond to: the initial samples (1); after 450-nm LED irradiation for different time periods (2–4). Reprinted with permission from Ref. [52]

The characterization of materials makes use of other techniques than the ones previously described (with the exception of Raman) to focus on the analysis of the reactant–catalyst interface. The study of the interaction of solids with reactants and the formation of reaction intermediates and products is followed by vibrational spectroscopies, infrared and Raman, and nuclear magnetic resonance (NMR). Raman was utilized to follow the photo-degradation of *p*-aminonitrophenol with a titania material and visible light. The study followed the formation of several azo compounds described as kinetically relevant intermediates in the degradation process [55]. NMR was used to analyze the formation of C-containing intermediates in hydrogen photo-production through alcohol reforming, indicating that the reaction occurs through a chain of consecutive reactions [56].

Infrared spectroscopy has been profusely utilized in operando or spectro-kinetic studies and here we first described the operando studies dedicated to describe the interaction and evolution of reactants at the photo-catalyst surface.

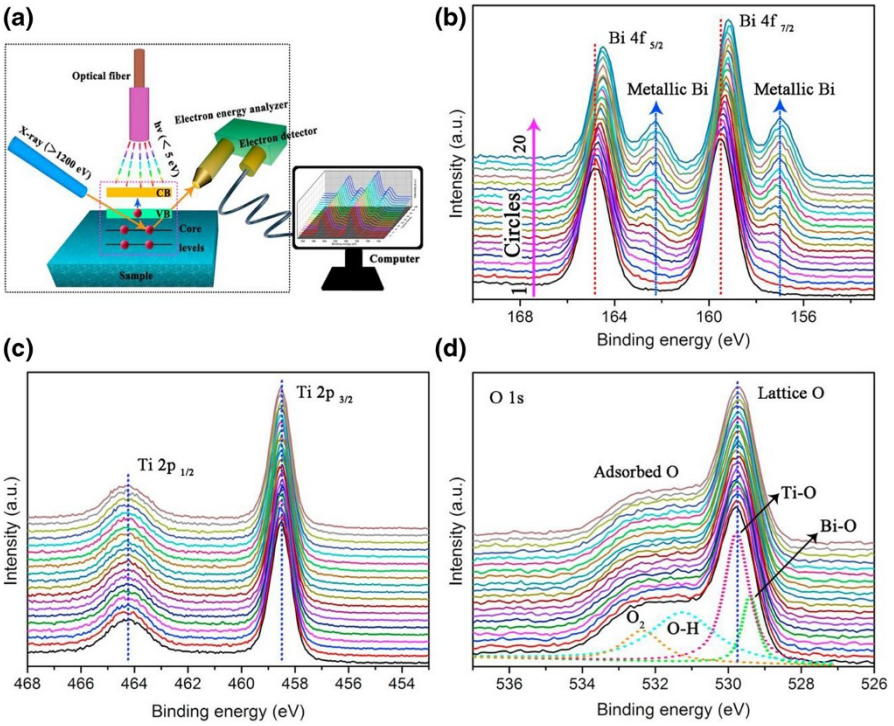

Fig. 9 Schematic illustration of the in situ XPS test procedure, which introduces an optical fiber into the vacuum chamber (**a**). The in situ XPS spectra of **b** Bi 4f, **c** Ti 2p, and **d** O1 s under visible light illumination. Reprinted with permission from Ref. [53]

Traditional infrared works carried out studies investigating the photo-oxidation (or less typically photo-reduction as, for example, the case of NO reduction to nitrogen) of several pollutants such as hydrocarbons [57, 58], alcohols [59–63], aldehydes and ketones [64, 65], acids [66–68], dyes [69, 70], NO, CO, and inorganic molecules [71–74]. More recently, interest has been focused on the analysis of hydrogen production from water or using alcohols as sacrificial agents, as well as the reduction of carbon dioxide using water or hydrogen as reducing agents.

Hydrogen photo-production is a key technology for a greener future. The use of sacrificial molecules and particularly alcohols which can come from natural resources has been subjected to intensive research within the context of this reaction. Infrared spectroscopy results using methanol, ethanol, and iso-propanol showed the adsorption over titania of the alcohol as both neutral molecule and (for methanol and ethanol) alcoxy entities [75–78]. Figure 10 displays a representative example, which concerns the methanol photo-reforming reaction over Pt-promoted (Degussa) P25 catalysts [75]. As mentioned, Fig. 10b, g provide evidence of the adsorption of the methanol and methoxy species at dark conditions through the analysis of C–H bond contributions. After illumination, negative bands indicate that these species (as well as molecular water) are eliminated from

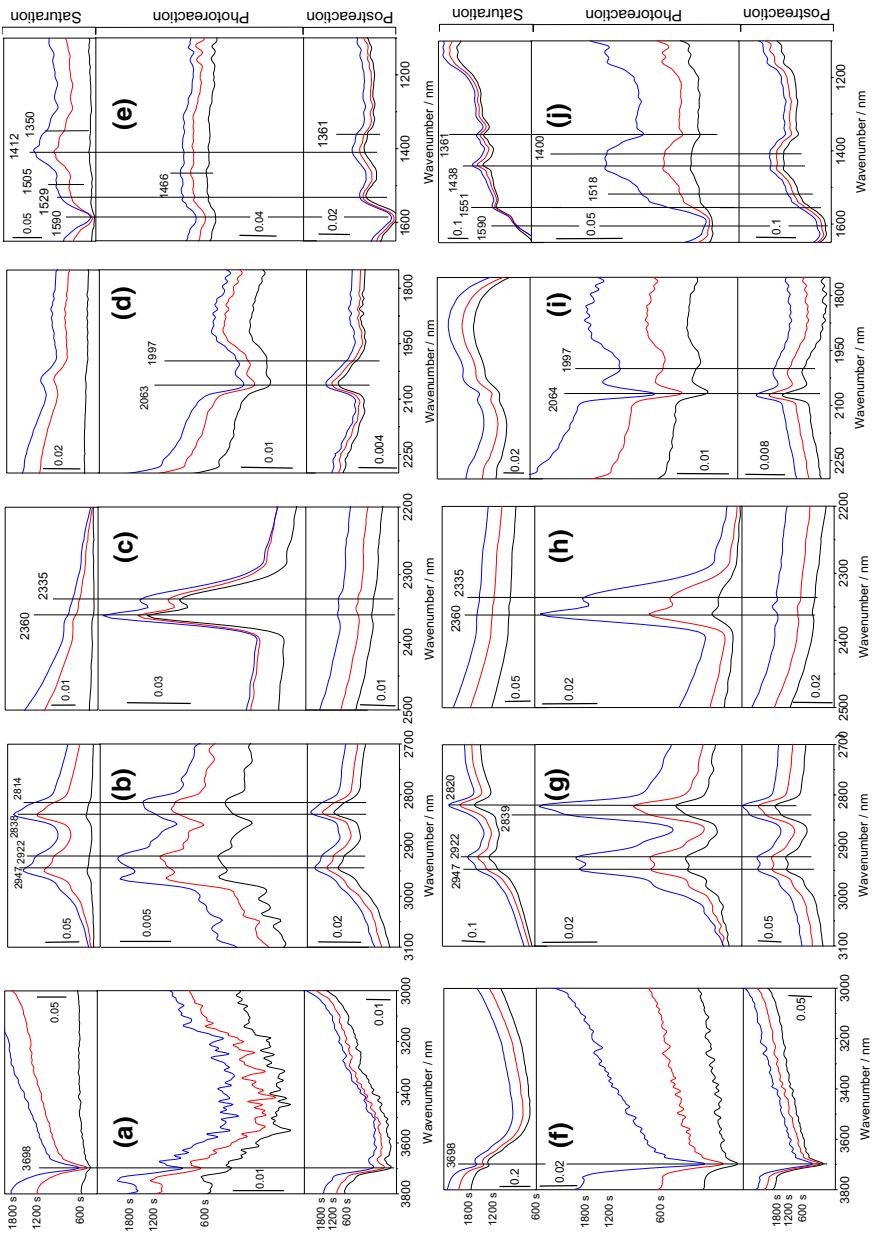
Saturation
Photoreaction
Postreaction
(a)
(b)
(c)
(d)
(e)
(f)
(g)
(h)
(i)
(j)
Wavenumber / nm
1800 s
1200 s
600 s

◀ **Fig. 10** DRIFTS spectra for the in situ analysis of the methanol photo-transformation occurring under reaction conditions: *upper panel*, P25-5Pt (0.5 wt% Pt onto P25 prepared by chemical deposition with a metal/reductant ratio of 5); *lower panel*, P25-10Pt (0.5 wt% Pt onto P25 prepared by chemical deposition with a metal/reductant ratio of 10) samples. Difference spectra obtained during saturation with the alcohol:water mixture (*upper zone of each panel*), under reaction-illumination conditions (*middle part*) and subsequently at dark conditions (*bottom part*) are presented. Reproduced with permission from Ref. [75]

the surface or consumed with concomitant formation (positive bands) of carbon dioxide (Fig. 10c, h). There is also parallel formation of several carboxylate moieties (positive bands at Fig. 10e, j). The more interesting point of the study is the appearance of carbon monoxide (Fig. 10d, i), which appears strongly correlated with the activity of the materials. Larger intensity of the carbon monoxide signal(s) leads to larger activity, evidenced by the behavior of the gas-phase carbon dioxide signal(s) concomitantly detected in the infrared spectra. The adsorption of the CO species seems relatively weak, as they decrease under a subsequent dark period. CO is likely formed from the carboxylate species detected by a water gas-shift type reaction with hydroxyl entities from the support. The positive or negative role of CO on the reaction depends on its degree of interaction with the metal, the efficiency of its handling by the metal-support interface (and thus its removal from the metal surface) but also relates to the nature of the carboxylate (or other) species from which it evolves. The key issue of the study is that the alcohol molecule is activated by a series of steps (which concomitantly lead to carbon-containing products and hydrogen ions leading to hydrogen at the metal surface) up to the production of surface formates and that the evolution of such species occurs with a critical involvement of the metal–support interface through a water gas shift-type step. This step would control kinetically the activity of the two noble metal P25 but also anatase-based noble metal promoted materials [75, 76, 78].

The transformation of carbon dioxide is of importance in the controlling of global warning. The reduction of this molecule can render useful chemicals such as carbon monoxide, methane, and, in optimal conditions, methanol, providing a nice route to synthesize valuable chemicals within the context of a circular economy. Infrared studies look into such a reaction, with particular emphasis in the analysis of the CO_2 activation step(s) using titania-, carbon nitride-, sulphide-based and others catalysts [79–82]. As shown in Fig. 11, titania materials are able to adsorb carbon dioxide in several different forms in the presence of water. Monodentate, bidentate y chelating brigde carbonates are usually formed but are commonly considered as expectator species without kinetic significance. Apart from that, the negatively charged CO_2 entity as well as formate ions (also connected with some surface species detected in Fig. 11) are considered true intermediates of different reaction products formed in the photo-reduction reaction. In fact, the first is described as directly related to the production of methane in titania-based materials; a linear relationship was presented between the intensity of IR bands of such entities (negatively charged carbon dioxide) and the rate of methane production [82]. On the other hand, the second, formate species is described by a combination of infrared and theoretical results as the intermediate leading to CO production in SnS_x-based photo-catalysts [81].

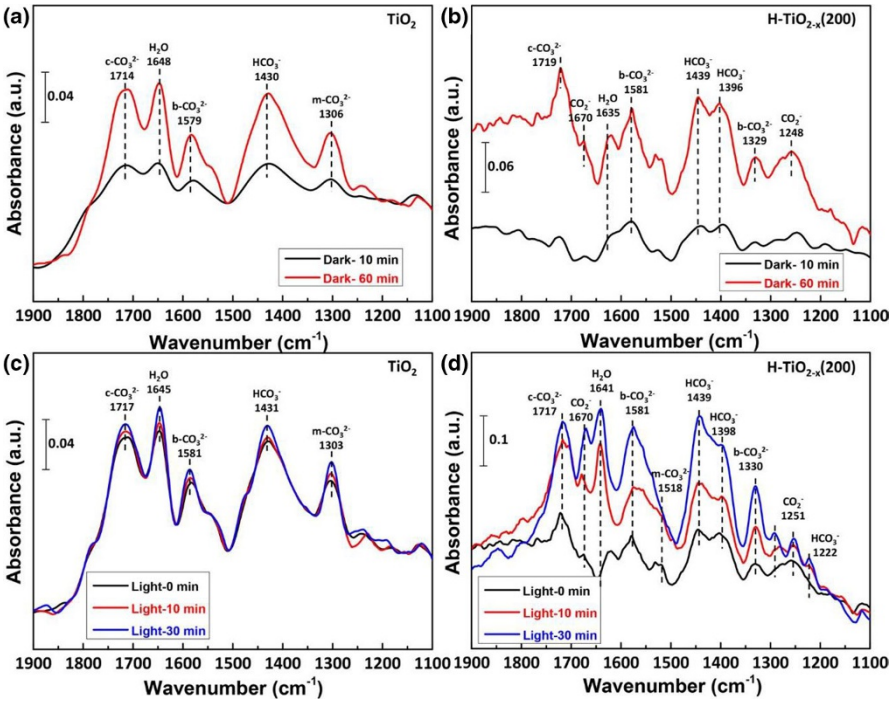

Fig. 11 DRIFTS spectra for the in situ analysis of the carbon dioxide reduction with water for titania (TiO_2) and back-titania ($H\text{-}TiO_{2-x}$) samples at dark (**a**, **b**) and under visible illumination (**c**, **d**). Reproduced with permission from Ref. [82]

3.2 Spectro-Kinetic Studies

A well-described experimental methodology in catalysis is related to the study of the mechanism and kinetics of a reaction using spectroscopic tools. In photocatalysis, such a task has complications coming from the necessity of including light into the mechanistic framework, leading to what is called light-triggered intrinsic kinetic formalisms [6, 83–85]. Spectro-kinetic schemes have been utilized in photo-catalysis to answer two main questions; first the study of the kinetic significance of radical species, and second to detail or analyze the potential mechanism of different photo-reactions.

Photo-catalytic reactions are initiated by radical species produced after light absorption but the analysis of their kinetic relevance is relatively complex. Some simple kinetic analysis worked out relationships between the amount of radical species, typically measured with electron spin resonance (EPR) or optical spectroscopies with the help of probe molecules, and the reaction rate. More concretely, the hydroxyl radical species was found kinetically significant through this methodology for a series of reactions. This is the case of Fe(III)-deposited Ru-doped TiO_2 photo-catalysts used for the liquid-phase photo-degradation

acetaldehyde using visible light [86] as well as the production hydrogen from biomass molecules using Sn-grafted Ru:TiO_2 photo-catalysts [87]. A more elaborated analysis considers the measurement of the rate of radical (hydroxyl) species normalized per rate of photon absorption [83]. Such an observable can be obtained from joined EPR and optical measurements and is shown to be proportional to the ratio between the rate constants of creation of hydroxyl-type radicals and the electron–hole recombination process. This is a measure of the rate at which such species are available at the surface of the photo-catalyst. In Fig. 12, this observable (called EPR parameter) is conformed against the reaction rate for different series of catalysts. An additional measurement of the rate of hydroxyl availability at the surface using a kinetic approach is also conformed (so-called kinetic parameter) with the reaction rate in Fig. 12. The two different experimental measurements allow to validate each other and, at the same time, render a robust procedure to check if hydroxyl-radical species can be kinetically significant in photo-catalytic reactions. The application of this methodology in Fig. 12 concerns the use of binary ceria–titania and carbon nitride–titania materials to investigate UV and sunlight triggered photo-oxidation of acetaldehyde [88] and toluene [89, 90], as well as quaternary MnOx-carbon nitride/ceria-titania powders used in toluene photo-elimination [91]. Both UV and visible illumination conditions are considered. Results in Fig. 12 show that binary and quaternary titania-based materials and their (single phase or component) counterparts display linear relationships between the rate of surface hydroxyl availability and the reaction rate, yielding a demonstration that the mechanism is hole-mediated and that composite materials has physical effects influencing activity by increasing the hydroxyl-related rate. This provides experimental evidence of the type of mechanism and informs about the potential key kinetic steps.

The study of intermediates and, in general, of the reaction mechanism is typically followed with infrared spectroscopic using micro-kinetic schemes. The photo-oxidation of 2-propanol is a frequent subject, showing always the production of acetone as a key intermediate [92]. The surface of titania-based catalysts has a rather high coverage of 2-propanol, which limits the reaction rate and also complicates the progression of the reaction from acetone to generate further oxidized carbon-containing species [60, 93, 94]. Figure 13 displays results concerning a thorough analysis of the photo-oxidation of acetaldehyde using titania catalysts having or not sulfate surface groups [95]. Panels A1 and A2 exemplify the evolution of the IR signal corresponding to the target pollutant in a step-wise, cycled experiment consisting in gas dosing, purging in synthetic air, and UV irradiation. A drifting background (as a consequence of the conduction band electrons) was subtracted to isolate the IR peaks, which were subsequently modeled within a micro-kinetic analysis. Acetaldehyde, crotonaldehyde (depending on the surface properties of titania, only appearing in absence of sulfate species), other intermediates such as formates and CO_2 (panels C1 and C2 of Fig. 13) were analyzed using a (sequential) mechanistic scheme such as $CH_3CHO_{ads} \rightarrow CH_3(CH)_2CHO_{ads} \rightarrow HCOO_{ads} \rightarrow CO_2$. The modeling describes the spontaneous formation of crotonaldehyde in the bare titania surface, which is hindered by interaction of the acetaldehyde with sulfate groups. Such groups also

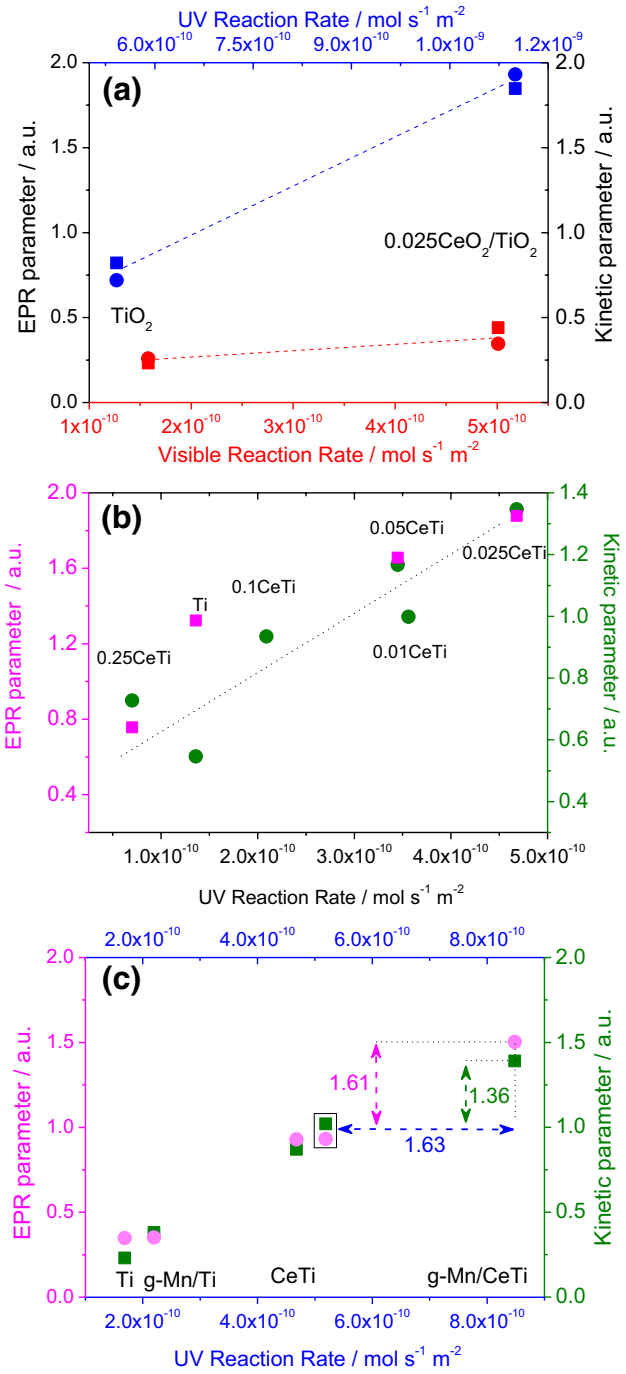
UV Reaction Rate / mol s-1 m-2
6.0x10-10
7.5x10-10
9.0x10-10
1.0x10-9
1.2x10-9
(a)
EPR parameter / a.u.
Kinetic parameter / a.u.
0.025CeO2/TiO2
TiO2
1x10-10
2x10-10
3x10-10
4x10-10
5x10-10
Visible Reaction Rate / mol s-1 m-2
(b)
0.05CeTi
0.025CeTi
0.1CeTi
Ti
0.25CeTi
0.01CeTi
EPR parameter / a.u.
Kinetic parameter / a.u.
1.0x10-10
2.0x10-10
3.0x10-10
4.0x10-10
5.0x10-10
UV Reaction Rate / mol s-1 m-2
2.0x10-10
4.0x10-10
6.0x10-10
8.0x10-10
(c)
1.61
1.36
1.63
Ti
g-Mn/Ti
CeTi
g-Mn/CeTi
EPR parameter / a.u.
Kinetic parameter / a.u.
UV Reaction Rate / mol s-1 m-2

◀ **Fig. 12** **a** Correlation plot of the normalized kinetic parameter ratio (*squares*) and the EPR normalized rate of hydroxyl-type radical formation (*circles*) vs. the reaction rate for acetaldehyde degradation using a pure anatase (Ti) sample and a titania-ceria composite (0.025 mol% ceria; 0.025 CeTi) sample. *Blue*: UV irradiation, *red*: visible irradiation. Reprinted with permission from Ref. [88] © 2014. **b** Correlation plot of the normalized kinetic parameter ratio (*squares*; olive color) and the EPR normalized rate of hydroxyl-type radical formation (*circles*; magenta color) vs. the reaction rate for toluene degradation using a pure anatase (Ti) sample and a titania-ceria composite (xCeTi) sample. Reprinted with permission from Ref. 89 © 2014. **c** Correlation plot of the normalized kinetic parameter ratio (*squares*; olive color) and the EPR normalized rate of hydroxyl-type radical formation (*circles*; magenta color) vs. the reaction rate for toluene degradation using a pure anatase (Ti) sample, titania-ceria (CeTi), Mn: carbon nitride-titania (g-Mn/Ti), and Mn: carbon nitride–ceria–titania (g-Mn/CeTi) composite samples. Reprinted with permission from Ref. [91] © 2014

weaken the interaction of the catalyst with some aldehyde and carboxylate species. The study concludes that the sulfate surface groups have a positive catalytic role mostly related to the modification of the pollutant adsorption (enhanced surface coverage related to the absence of crotonaldehyde) and a diminished poisoning (carbonate-related) of the surface, with relative minor effects in the coverage and rate of the carboxylate-type reaction intermediates. This affects activity as well as the stability of the catalyst.

4 Conclusions

The characterization of photo-catalytic materials is here analyzed through the review of ex situ and in situ results coming from a survey analysis of the literature. Characterization aims to provide the relevant information to establish structure–activity relationships, which can interpret the functional properties of photo-catalysts and can allow future improvements of the field.

Up to date, the ex situ study of pre and post-reaction photo-catalysts is the most common way of analyzing the physico-chemical properties of the solids. Multitechnique approaches leading to complete information concerning morphological, structural, and electronic properties are required to provide insightful results. We described the most common techniques for such purpose and provided a brief summary of the information extracted using as a representative example Ti–W binary materials leading to doped or composite materials after calcination treatments.

However, this review article put more emphasis on presenting advanced characterization methodologies. Axiomatic to such approaches is the analysis of the interaction of the catalysts with light at the reaction cell where the physico-chemical characterization is performed. Such analysis leads to information about the catalyst volume (or depth from the illuminated surface), which is illuminated and which would need to the (exclusively) probed by advanced characterization tools. For UV and visible wavelengths, the mentioned deep is of a few micrometers (below 5) in the case of reactions using solid powders or films and of the order of 1 mm for reactions using catalyst suspensions. Dismissing this information could drive

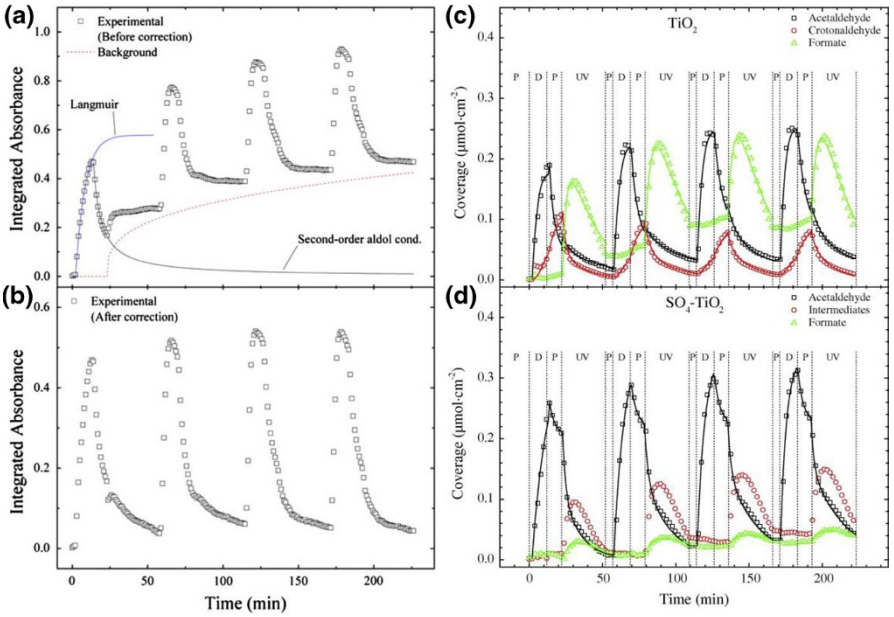

Fig. 13 Integrated FTIR absorbance bands between 1680 and 1708 cm^{-1} for acetaldehyde on a TiO_2 surface without (**a**) and with (**b**) baseline corrections. Surface coverage of adsorbed acetaldehyde, crotonaldehyde, and formate as a function of reaction time during four consecutive cycles of acetaldehyde gas dosing (D), purging in synthetic air (P), and UV irradiation (UV), respectively, on **c** TiO_2, and **d** SO_4–TiO_2 films. *Solid curves* represent results from the micro-kinetic modeling. Reprinted with permission from Ref. [95]

to misleading results coming from the characterization. Both operando and spectro-kinetic approaches are described as advanced tools for the settlement of structure–activity in photo-catalysis. Such tools are used to obtain information about the catalytic active phases as well as for interpreting the mechanism and relevant kinetic steps of the catalytic processes. In these cases, we reviewed more exciting results coming from the application of characterization techniques such as infrared and Raman, electron paramagnetic, X-ray photoelectron and absorption, and nuclear magnetic resonance spectroscopies.

Acknowledgments We thank MINECO (Spain) for financial support through the ENE2016-77798-C4-1-R Grant. The support by Secretaria de Ciencia Tecnología e Innovación of CDMX (SECTEI, México. U. Caudillo-Flores) is also acknowledged. I. Barba-Nieto thanks MINECO for a FPI doctoral fellowship (BES-2017-080069).

References

1. Kubacka A, Fernández-García M, Colón G (2012) Chem Rev 112:1555–1614
2. Colmenares JC, Luque R (2014) Chem Soc Rev 43:765–778
3. Bai S, Jian J, Zhang Q, Xiong Y (2015) Chem Soc Rev 44:2893–2939

4. Caudillo-Flores U, Muñoz-Batista MJ, Kubacka A, Fernández-García M (2018) Chem Photo Chem 2:777–785
5. Fracchia M, Ghigna P, Vertova A, Rondinini S, Mijnguzzi A (2018) Surfaces 1:138–150
6. Muñoz-Batista MJ, Ballari MM, Kubacka A, Alfano OM, Fernández-García M (2019) Chem Soc Rev 48:637l–682l
7. Weidenthaler C (2011) Nanoscale 3:792–810
8. Thommas M, Keneko K, Neimarrk AV, Olivier JP, Rodríguez-Reionoso F, Rouquerol J, Sing SK (2015) Pure Appl Chem 87:1051–1069
9. Caudillo-Flores U, Muñoz-Batista MJ, Hungría AB, López-Haro M, Fernández-García M, Kubacka A (2019) Appl Catal B 245:49–61
10. Fernández-García M, Martínez-Arias A, Hanson JC, Rodriguez JA (2004) Chem Rev 104:4063–4104
11. Nosaka Y, Nosaka AY (2017) Chem Rev 117:11302–11336
12. Fuerte A, Hernández-Alonso MD, Maira J, Martínez-Arias A, Fernández-García M, Conesa JC, Soria J, Munuera G (2002) J Catal 212:1–9
13. Kubacka A, Fernández-García M, Colón G (2008) J Catal 254:272–284
14. Yang J, Small MW, Grieshaber RV, Nuzzo R (2012) Chem Soc Rev 41:8179–8194
15. Jinschek JR (2013) Chem Commun 50:2696–2706
16. Lamberti C, Zecchina A, Groppo E, Bordiga S (2010) Chem Soc Rev 39:4951–5001
17. McCue AJ, Mutch GA, McNab AI, Campbell S, Anderson JA (2015) Catal Today 259:19–26
18. Ter Veen HRJ, Kim T, Wachs IE, Brongersma HH (2009) Catal Today 104:197–2001
19. Frenkel AI, Yevick A, Cooper C, Vasic R (2011) Annual. Rev Anal Chem 4:23–39
20. Lamberti C, Bokhoven JA (2016) Chapter 13. In: Lamberti C, Bokhoven JA (eds) X-ray absorption and X-ray emission spectroscopy. Wiley, New York
21. Lamberti C, Borfecchia E, Bokhoven JA, Fernández-García M (2016) Chapter 12. In: Lamberti C, Bokhoven JA (eds) X-ray absorption and X-ray emission spectroscopy. Wiley, New York
22. Fernández-García M, Martínez-Arias A, Fuerte A, Conesa JC (2005) J Phys Chem B 109:6075–6083
23. Kubacka A, Colón G, Fernández-García M (2009) Catal Today 143:286–292
24. Márquez AM, Plata JJ, Fdez SJ, Colon G, Kubacka A, Fernández-García M (2012) J Phys Chem C 116:18759-18767
25. Czelej K, Cwieka K, Colmenares JC, Kurzydlowski KJ, Xu T-J (2017) ACS Appl Mater Interf 9:31825–31833
26. Fernández-García M (2002) Catal. Reviews 44:59–121
27. Yamamoto T (2008) X-Ray Spectrom 37:572–584
28. Egerton RF (2009) Rep Prog Phys 72:016502
29. Glatzel P, Sikora M, Smolentsev G, Fernández-García M (2009) Catal Today 145:294–299
30. Biesinger MC, Lau LWM, Gerson AR, Smart RSC (2010) Appl Surf Sci 257:887–898
31. Sarma DD, Santra PK, Mukherjee S, Nag A (2013) Chem Mater 25:1222–1232
32. Jentoft FC (2009) Adv Catal 52:129–211
33. Li X, Wan T, Qui J, Wei H, Qin F, Wang Y, Liao Y, Huang z, Tan X (2017) Appl Catal B 217:591–602
34. Anpo M, Dzwigaj S, Che M (2009) Adv Catal 52:1–42
35. Muñoz-Batista MJ, Kubacka A, Hungría AB, Fernández-García M (2015) J Catal 330:154–166
36. Muñoz-Batista MJ, Motta-Meira D, Colón G, Kubacka A, Fernández-García M (2018) Angew Chem Int Ed 55:1199–1203
37. Cabrera MI, Alfano OM, Cassano AE (1996) J Phys Chem 100:20043–20050
38. Santomauro FG, Lübcke A, Rittmann J, Baldini E, Ferrer A, Silatani M, Zimmermann P, Grübel S, Johnson JA, Mariager SO (2015) Sci Rep 5:14834–14840
39. Uemura Y, Kido D, Wakisaka Y, Uehara H, Ohba T, Niwa Y, Nozawa S, Sato T, Ichiyanagi K, Fukaya R (2016) Angw Chem Int Ed 55:1364–1367
40. Amidani L, Naldon A, Malvestuto M, del Santo V, Boscherini F (2015) Angew Chem Int Ed 54:5413–5416
41. Sá J, Tagliabue G, Friedli P, Szlachetko J, Rittmann-Frank MH, Santomauro FG, Milne CJ, Sigg H (2013) Energ. Environ Sci 6:3584–3588
42. Hassan A, Zhang X, Liu C, Snee PT (2018) J Phys Chem C 122:11145–11151
43. Yang S, Pattengale B, Lee S, Huang J (2018) ACS Energy Lett 3:532–539

44. Irie H, Kamiya K, Shibanona T, Miura S, Tryck DA, Yokoyama T, Hashimoto K (2009) J Phys Chem C 113:10761–10766
45. Liu L, Zhao C, Miller JT, Li Y (2017) J Phys Chem C 121:490–499
46. Lahiri D, Subramanian Y, Bunker BA, Kamat PV (2006) J Phys Chem C 124:20420–20427
47. Priebe JB, Radnik J, Kreyenschulte C, Lennox A, Junge H, Beller M, Brückner A (2017) ChemCatChem 9:1025–1031
48. Li YH, Li C, Yang HG (2017) J Mater Chem A 5:20631–20635
49. Zhou Y, Doronkin DR, Zhao Z, Plessow PN, Jelic J, Detlefs B, Pruessmann T, Studt F, Grunwaldt JD (2018) ACS Catal 8:11398–11406
50. Fan X, Yue X, Jia H (2018) J Phys Chem C 122:14574–14581
51. Ma L, Zhang T, Guo L (2018) Int. J. Hydr. Energ. 43:13778–13787
52. Filippov TN, Svintsitskiy DA, Chetyrin IA, Prosvirin IP, Selishchev DS, Kozlov DV (2018) Appl Catal A: Gen 558:81–90
53. Jiao Z, Shang M, Liu J, Liu G, Wang X, Bi Y (2017) Nano Energy 31:96–104
54. Ohtsu N, Masahashi N, Mizukoshi Y, Wagatsuma K (2009) Langmuir 25:11586–11591
55. Wang X, Xin Y, Tian B, Lei J, Zhang J (2018) Appl Catal B 224:305–309
56. Wang XL, Liu W, Yu Y-Y, Song Y, Fang WQ, Wie D, Gong Z-Q, Yao Y-F, Yang HG (2015) Nat Commun 7:11918–11926
57. Meulen T, Mattson A, Österlund L (2007) J Catal 251:131–144
58. Almeida AR, Moulijn JA, Mul G (2011) J Phys Chem C 115:1330–1338
59. Coronado JM, Kataoka S, Tejedor-Tejedor I, Anderson MA (2003) J Catal 219:219–230
60. Arsac F, Bianchi D, Chovelon JM, Ferronato C, Herrmann JM (2006) J Phys Chem A 110:4213–4222
61. Chen T, Feng Z, Wu G, Shi J, Ma G, Ying P, Li C (2007) J Phys Chem C 111:8005–8014
62. Augugliaro V, Kisch H, Loddo V, López-Muñoz MJ, Márquez-Alvarez C, Palmisano G, Palmisano L, Parrino F, Yurdakal S (2008) Appl Catal A: Gen 349:189–197
63. Muñoz-Batista MJ, Caudillo-Flores U, Ung-Medina F, Chávez-Parga MC, Cortés JA, Kubacka A, Fernández-García M (2017) Appl Catal B 201:400–410
64. Hernández-Alonso M, Tejedor-Tejedor I, Coronado JM, Anderson MA, Soria J (2009) Catal Today 143:364–373
65. Zhu X, Jin C, Li X-S, Liu J-L, Sun Z-C, Li CS, Li X, Zhu A-M (2017) ACS Catal 7:65124–66524
66. Kraeutler B, Bard AJ (1978) J Am Chem Soc 100:5985
67. Dolamic I, Bürgi T (2007) J Catal 248:268–276
68. Mattsson A, Österlund L (2010) J Phys Chem C 114:14121–14132
69. Yanga TC-K, Wang S-F, Tsaic SH-Y, Lin S-Y (2001) Appl Catal B: Environ 30:293–301
70. Yu Z, Chuang SSC (2007) J Phys Chem C 111:13813–13820
71. Wu JCS, Cheng Y-T (2006) J Catal 237:393–404
72. Shanda M, Anderson JA (2013) Catal. Sci Technol 3:879–899
73. Dong X, Zhand W, Sun Y, Li J, Chen W, Cui Z, Huang H (2018) J Catal 357:41–50
74. Li X, Zhang W, Cui W, Sun Y, Jiang G, Zhang Y, Huang H, Dong F (2018) Appl Catal B 221:482–489
75. Fontelles-Carceller O, Muñoz-Batista MJ, Rodríguez-Castellón E, Conesa JC, Fernández-García M, Kubacka A (2017) J Catal 347:157–169
76. Fontelles-Carceller O, Muñoz-Batista MJ, Conesa JC, Kubacka A, Fernández-García M (2018) Mol Catal 446:88–97
77. Chiarello GL, Ferri D, Selli E (2018) Appl Surf Sci 450:146–1543
78. Caudillo-Flores U, Muñoz-Batista MJ, Fernández-García M, Kubacka A (2018) Appl Catal B 238:533–545
79. Wang Y, Zhao J, Wang T, Li Y, Li X, Yin J, Wang C (2016) J Catal 337:293–302
80. Li Q, Sun Z, Wang H, Wu Z (2018) J CO2 Util 28:126–136
81. Jiao X, Li X, Jin X, Sun Y, Xu J, Liang L, Ju H, Zhu J, Pan Y, Yan W, Lin Y, Xie Y (2017) J Am Chem Soc 139:18044–18051
82. Yin G, Huang X, Chen T, Zhao W, Bi Q, Xu J, Han Y, Huang F (2018) ACS Catal 8:1009–1017
83. Mills A, Rourke CO, Moore K (2015) J Photochem Photobiol A 310:66–105
84. Nosaka Y, Nosaka AY (2018) J Phys Chem C 122:28748–28756
85. Muñoz-Batista M, Eslava-Castillo AM, Kubacka A, Fernández-García M (2018) Appl Catal B 225:298–306
86. Zhang J, Nosaka Y (2013) J Phys Chem C 117:1383–1391

87. Gu G, Long J, Fan L, Chen L, Zhao L, Lin H, Wang X (2013) J Catal 303:141–155
88. Muñoz-Batista M, Ballari MM, Cassano AE, Alfano OM, Kubacka A, Fernández-García M (2014) Catal. Sci Technol 5:1521–1531
89. Muñoz-Batista M, Gómez-Cerezo MN, Kubacka A, Tudela D, Fernández-García M (2014) ACS Catal 4:63–72
90. Caudillo-Flores U, Muñoz-Batista M, Luque R, Kubacka A, Fernández-García M (2019) Chem Eng J 378:122228
91. Muñoz-Batista M, Kubacka A, Fernández-García M (2014) ACS Catal. 4:4277–4288
92. López-Tenllado FJ, Marinas A, Urbano FJ, Colmenares JC, Hidalgo MC, Marinas JM, Moreno JM (2012) Appl Catal B 128:150–158
93. Xu W, Raferty D, Francisco JS (2003) J Phys Chem B 107:4537–4544
94. Caudillo-Flores U, Agostini G, Marini C, Kubacka A, Fernández-García M (2019) Appl Catal B: Environ 256:117790
95. Topalian Z, Stefanov BI, Granqvist CG, Österlund L (2013) J Catal 307:265–274

Topics in Current Chemistry (2019) 377:27
https://doi.org/10.1007/s41061-019-0253-4

REVIEW

Photocatalytic Approaches for Hydrogen Production via Formic Acid Decomposition

Miriam Navlani-García[1,2] · David Salinas-Torres[1,2] · Kohsuke Mori[1,3] · Yasutaka Kuwahara[1,3] · Hiromi Yamashita[1,3]

Received: 31 May 2019 / Accepted: 10 September 2019 / Published online: 26 September 2019

Abstract

The photocatalytic dehydrogenation of formic acid has recently emerged as an outstanding alternative to the traditional thermal catalysts widely applied in this reaction. The utilization of photocatalytic processes for the production of hydrogen is an appealing strategy that perfectly matches with the idea of a green and sustainable future energy scenario. However, it sounds easier than it is, and great efforts have been needed to design and develop highly efficient photocatalysts for the production of hydrogen from formic acid. In this work, some of the most representative strategies adopted for this application are reviewed, paying particular attention to systems based on TiO_2, CdS and C_3N_4.

Keywords Hydrogen production · Formic acid · Photocatalyst · Semiconductor · Heterojunction

1 Introduction

Hydrogen holds great hope in the current energy scenario as a promising energy vector able to replace the widely used vectors based on fossil fuels (coal, oil, and gas). This is due not only to the rapid depletion of fossil fuel reserves, but also to the increasing energy demand experienced in the last decades and the negative impact

Chapter 6 was originally published as Navlani-Garcia, M., Salinas-Torres, D., Mori, K., Kuwahara, Y. & Yamashita, H. Topics in Current Chemistry (2019) 377: 27. https://doi.org/10.1007/s41061-019-0253-4.

✉ Kohsuke Mori
mori@mat.eng.osaka-u.ac.jp

✉ Hiromi Yamashita
yamashita@mat.eng.osaka-u.ac.jp

[1] Division of Materials and Manufacturing Science, Graduate School of Engineering, Osaka University, 2-1 Yamada-oka, Suita, Osaka 565-0871, Japan

[2] University Materials Institute of Alicante (IUMA), University of Alicante (UA), Ap. 99, 03080 Alicante, Spain

[3] Unit of Elements Strategy Initiative for Catalysts and Batteries (ESICB), Kyoto University, Katsura, Kyoto 615-8520, Japan

of the use of such fuels due to the generation of greenhouse gases [1]. Among greenhouse gases, carbon dioxide (CO_2) is the largest contributor to climate change [2]. As a proof of the impact of anthropogenic activities in the emission of CO_2, its concentration in the atmosphere has increased greatly since the Industrial Revolution (270–275 ppm in 1750; 310 ppm in 1950; 408 ppm in 2018), with a total emission of 36 Gt CO_2 per year, 91% of it being generated by anthropogenic activities [3].

The worldwide concern regarding climate change has resulted in global agreements to combat its tragic consequences. For example, the Kyoto Protocol and the more recent Paris Agreement (United Nations Framework Convention on Climate Change; UNFCCC) [4], aim to keep global warming below 2 °C. In such an energy context, the role of renewable and clean energy is gaining more and more importance. Among renewable resources, the use of solar and wind energy as well as hydropower are green energy power sources of interest in the quest to satisfy global energy demand. Such renewable sources have several advantages compared to fossil fuels and nuclear-based energy: (1) low variable cost of production; (2) no production of waste linked to the generation of power; and (3) suitable for decentralized power generation [5].

However, their obvious advantages come with important drawbacks related to their intrinsical dependence on day–night intervals, seasons, and fluctuating environmental conditions, which result in periods of deficit and surplus of energy output [6, 7]. In such a complicated energy scenario, hydrogen, as a never-ending and renewable source of energy, emerges as an outstanding energy vector for mobile and stationary applications. Hydrogen was recently defined by the International Energy Agency (IEA) as a flexible energy carrier, which can be produced from any energy source, and which can be converted into various energy forms [8].

The widespread implementation of the so-called "hydrogen economy" faces not only technical barriers, but also headwinds related to the political and economic interests of using fossil fuels. However, the scientific community has a moral obligation to search for possible solutions to issues related to the production, storage, and transportation of hydrogen. The production of hydrogen can be carried out through both renewable and non-renewable means; currently, steam methane reforming of natural gas is the main process used, accounting for approximately 48% of total production [9]. However, this process is linked to the generation of CO_2 emissions, which tarnishes the concept of "green hydrogen production" [10]. Aside from that, safety issues related to the physical storage of hydrogen by compression and cooling are also a focus of discussion because of the very high pressure levels (up to 700–800 bar) or very low temperatures (−252 °C) required [11–15].

The generation of molecular hydrogen (H_2) from hydrogen carrier molecules that contain it in their structure has recently been claimed as an auspicious option. Such molecules provide a unique way to deliver molecular hydrogen in a reversible way by means of chemical reactions, and, although hydrogen production by these means is not as mature as the classical alternatives, there are already a number of potential candidates that show interesting characteristics [16–25]. Among them, liquid organic hydrogen carriers (LOHC) are recognized as an ideal option in terms of cost, safety and manageability [26, 27]. Included within LOHC are all hydrogen storage systems that are liquid in their hydrogen-rich form [11]. Such molecules

can be dehydrogenated and re-hydrogenated, and show great potential for use in stationary and transportation applications [5, 28]. Among LOHC investigated for this application (e.g., *N*-ethylcarbazole, dibenzyltoluene, naphthalene, methanol, toluene, etc. [26, 27]), the suitability of formic acid (HCOOH, FA) has been highlighted by a plethora of recent publications reporting the investigation of H_2 production from FA via dehydrogenation reaction ($HCOOH \leftrightarrow H_2 + CO_2$) [29–35]. FA is the simplest carboxylic acid and has attracted great attention due to its non-toxic character, stability, and high hydrogen content (4.4 wt% and 53 g L^{-1}) [30, 31]. Furthermore, FA is readily available from sources such as oxidation of biomass, and it is an intermediate, byproduct, and product of the chemical industry, as well as a product of the hydrogenation of CO_2 [36].

The $HCOOH/CO_2$ system has been claimed to be an ideal environmentally friendly system for hydrogen storage, with the CO_2 produced in the dehydrogenation reaction being re-hydrogenated to HCOOH in a carbon-free emission process [37]. The use of catalysts is vital in the reactions involved in hydrogen storage and release. Traditionally, homogeneous systems have been used to boost the dehydrogenation of FA, starting with the pioneering investigation reported by Coffey in 1967, in which Pt, Ru and Ir phosphine complexes were used [38]. Although FA has attracted interest for the H_2 production for more than five decades, its use as a LOHC was not claimed until 2008 by the independent investigations of Laurenczy [39] and Beller [40, 41].

The more convenient use of heterogeneous catalysts has motivated the search for new alternatives to achieve competitive and selective heterogeneous systems able to catalyze the dehydrogenation of FA under mild or moderate conditions. Significant breakthroughs in the field have been achieved while exploring aspects such as the features of the metallic active phase [42–46] or the properties of the support [44, 47–50]. Most investigations reported so far use relatively high temperatures to achieve acceptable conversion of FA into H_2. However, CO can be also produced from FA at high temperatures by following the dehydration reaction ($HCOOH \rightarrow CO + H_2O$), which is a poison of the catalysts used in fuel cells [51].

Recently, the photocatalytic dehydrogenation of FA has also attracted great attention as a promising option for the generation of H_2 at room temperature. In most cases, the catalysts used are Mott–Schottky photocatalysts, which use a semiconductor support and metal nanoparticles of diverse composition (i.e., Pd, Pt, Au, Ag, etc.) [52].

The use of sunlight, as a green and abundant energy source, is of great interest in the current energy scenario. In particular, the use of sunlight for the production of H_2 unites two pillars of research aimed at the realization of a sustainable energy future. Most solar-to-hydrogen production is based on the water splitting reaction [53, 54], but photocatalytic processes have also been utilized for the production of H_2 from other molecules, such as ethanol [55, 56], methanol [57, 58], glycerol [59, 60], hydrazine [61], ammonia [62, 63], ammonia borane [17, 20, 64, 65], etc.

Here, we review some of the most representative investigations dealing with the production of H_2 from the photocatalytic decomposition of FA. The photodecomposition of FA has frequently been investigated from other points of view, such as the degradation of pollutants, the use of FA in photoelectrochemical cells, or the

role of FA as an intermediate in the photocatalytic oxidation of other molecules (i.e., formaldehyde, acetaldehyde, ethanol, and acetic acid) [66, 67]. For that reason, the mechanism involved in the photodecomposition of FA has been studied widely by both experimental and theoretical researchers. However, uncertainty remains because of the various possible adsorption configurations of FA on the surface of photocatalysts. Ji and Luo [66] reported that FA photodecomposition can take place via either a one-step mechanism (without any reaction intermediate), or a two-reaction mechanism in which FA first forms a formate radical and subsequently forms CO_2 with an electron injected into the conduction band of the semiconductor.

- One-step mechanism:

$$HCOOH + h^+ \rightarrow CO_2 + 2H^+ + e^-_{cb}$$

- Two-step mechanism:

$$HCOOH + h^+ \rightarrow HCOO^{\cdot} + H^+$$

$$HCOO^{\cdot} \rightarrow CO_2 + H^+ + e^-_{cb}$$

In order to review the most important breakthroughs achieved in the field, the following sections are divided according to the main component of the photocatalytic system (i.e., TiO_2, CdS, C_3N_4, etc.).

2 Photocatalytic Systems Based on TiO_2

Starting a review on photocatalytic applications by highlighting the importance of titanium dioxide is a must. Although the investigation of TiO_2 in photocatalysis has long since begun, it remains one of the most important photocatalytic materials because of the great performance shown in multiple applications by virtue of features such as its low cost, chemical inertness, low toxicity, excellent thermal and photo stability, and scalability [68, 69]. The great potential of TiO_2 for a photocatalytic application was firstly discovered by Akira Fujishima in the late 1960s with his investigation into the photo-splitting of water [70, 71]. After that, TiO_2 became the semiconductor material most often used for photocatalysis, and it has been utilized for countless applications [72–76]. The application of TiO_2 for the production of H_2 from FA has also attracted great attention. Some of the strategies found in the literature towards the design of high-performing photocatalysts for the decomposition of FA using TiO_2 are based on the modification of its properties by means of doping or creating hybrid nanostructures with metal nanoparticles, synthesizing shape-controlled TiO_2 nanoparticles, etc. Such approaches found in the literature are briefly reviewed here.

It is well-known that most photocatalytic processes are carried out at room temperature by excluding the heat generated by the infrared part of the solar spectrum using external cooling systems. In an attempt to fully use the solar energy, i.e., both photo and thermal contributions, thereby maximizing the process from an economic

viewpoint, Liu and co-workers explored the effect of both energies in the decomposition of FA [77]. For this purpose, Pt/TiO_2 catalysts prepared by photodeposition and with $H_2PtCl_6{\cdot}6H_2O$ as the metal precursor were used as model to study the photothermal generation of hydrogen up to 90 °C (i.e. 35, 70, 80, and 90 °C). The impact of the photo and thermal effects was differentiated by using LEDs emitting purple, blue and white light. The sets of catalytic tests consisted of: (1) photocatalytic test at 35 °C (Pt/TiO_2-P); (2) thermal reaction at 90 °C (Pt/TiO_2-P); (3) photothermal coupling reaction (photo + 35 °C, photo + 70 °C, photo + 80 °C, and photo + 90 °C, Pt/TiO_2-PT). The results obtained are summarized in Fig. 1. As expected, the thermal tests gave higher H_2 yield with increasing temperature. As for the results achieved with photothermal experiments, a more pronounced dependence with temperature was observed, and the H_2 yield was 8.1 and 4.2 times than that obtained with photo and thermal experiments, respectively. This effect was ascribed to a synergetic effect of the photo and thermal contributions in Pt/TiO_2 catalysts. After performing the test with different LED light irradiations, it was concluded that the H_2 yield followed the order white > blue > purple, confirming the synergistic effect between the thermal catalytic and photocatalytic processes under blue and purple illumination conditions.

The catalysts were characterized in depth, and the tentative mechanism displayed in Fig. 2 was proposed. According to research findings, the photothermal activity was due to the presence of both non-plasmonic Pt and TiO_2 nanoparticles. According to the proposed mechanism, the production of H_2 takes place mainly on the Pt nanoparticles, and the adsorbates derived from FA are mainly responsible for the consumption of holes. When the sample is irradiated with UV light, electrons transfer from the valence band to the conduction band, and rapidly transfer to Pt nanoparticles. The adsorbates derived from FA are oxidized by the holes and release hydrogen protons (H_f^+), which are accepted by the water species ($H_2H_fO^+$). Such $H_2H_fO^+$ species diffuse on the surface of the catalyst and exchange the protons with

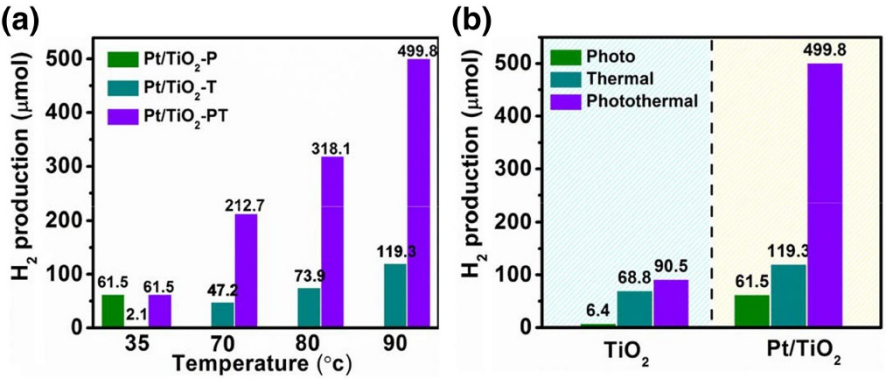

Fig. 1 **a** Total amount of H_2 generated in 8 h under photo (35 °C), thermal (35, 70, 80, and 90 °C) and photothermal (photo + 35 °C, photo + 70 °C, photo + 80 °C, and photo + 90 °C) condition over Pt/TiO_2 in the presence of formic acid (FA; 10 vol%). **b** Comparison of 8 h H_2 generation over TiO_2 and Pt/TiO_2 under photo (35 °C), thermal (90 °C), and photothermal (photo + 90 °C) reaction conditions. Reprinted with permission from [77]

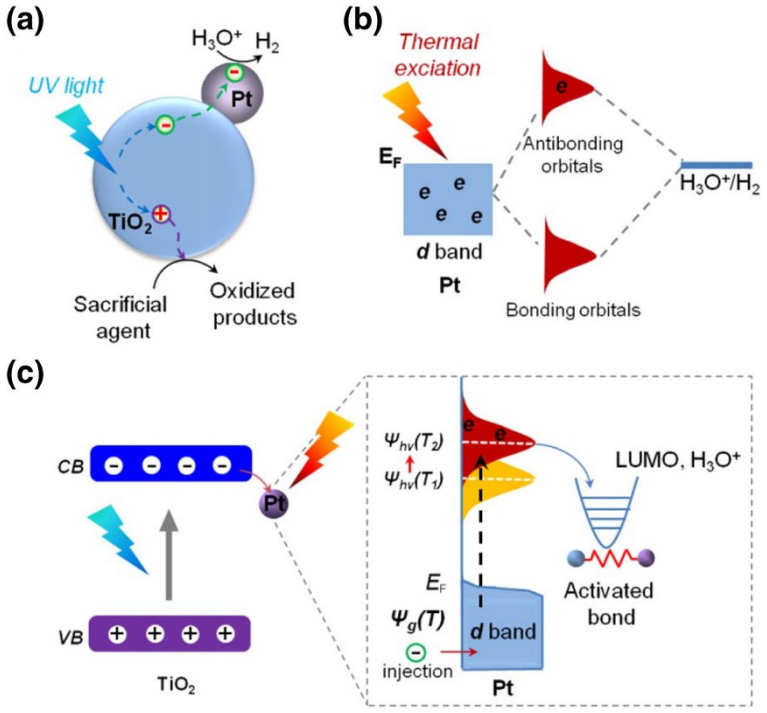

Fig. 2 Proposed mechanism of the photothermal catalytic reaction with Pt/TiO_2 nanocatalysts. Reprinted with permission from [77]

other molecules of water, forming H_3O^+. After that, when H_3O^+ reaches the metal nanoparticles, electrons go to the LUMO of the molecules adsorbed, and H_2 is produced (Fig. 2a). On the other hand, the non-plasmonic Pt nanoparticles can use heat energy, creating a chemical bond with the adsorbed reactants. Bonding and antibonding orbitals of the adsorbed molecules result from the interaction of the molecular orbital of the adsorbed species and the *d* electron states of the nanoparticles (Fig. 2b). Then, hydrogen can be formed from FA by the d band electrons of Pt that are excited upon heating. In the case proposed in that study, irradiation of Pt/TiO_2 causes excitation of the bound electrons of Pt nanoparticles. Such excited electrons inject into the LUMO of the reactants adsorbed to form protons. Upon heating, the excited electrons on the Pt nanoparticles go to higher energy levels, facilitating the activation of the adsorbed reactants and inducing the reaction (Fig. 2c).

In line with the investigations reporting thermal decomposition of FA, in which most of the alternatives used are based on Pd-catalysts, Xiong et al. [78] reported the photocatalytic decomposition of FA with Pd-TiO_2. In that study, the electronic state of the active site was modified by depositing foreign atoms on Pd-tetrahedron–TiO_2. First, Pd loading was optimizing by checking the activity of catalysts with 5, 10, 18, and 40 wt% Pd, the sample with 18 wt% being the most active. Characterization of the samples indicated that Pd nanocrystals had an average length of 6.3 nm and were covered by {111} facets. The photocatalytic activity in liquid phase was evaluated

under various light intensities while collecting the gas generated with a gas burette system (Fig. 3).

According to the results, the improvement in activity was ascribed to the increased electron density of Pd by the Mott–Schottky effect. Two effects were considered to explain the photocatalytic tendencies. On the one hand, plasmonic hot electrons generated in Pd particles can inject into the conduction band of TiO_2, which would reduce the electron density of Pd. On the other hand, photoexcitation electrons transfer from TiO_2 to Pd, thereby increasing its electron density. The authors claimed that photoexcitation of TiO_2 and the increase in electron density on Pd were the main contributions at low light intensities, due to the low plasmonic coefficient of Pd. On the contrary, for higher light intensities (beyond 4.5 mW cm^{-2}), generation of plasmonic electrons was promoted, while photoexcitation in TiO_2 was saturated, making injection of plasmonic electrons from Pd to TiO_2, and the subsequent decrease in electron density of Pd, the predominant process. After that, foreign metals (i.e., M = Ag^+, Cu^{2+}, Au^{3+} or Pt^{4+}) were deposited on the surface of Pd tetrahedrons so that their surface was partially covered by a layer of PdM alloy. The photocatalytic

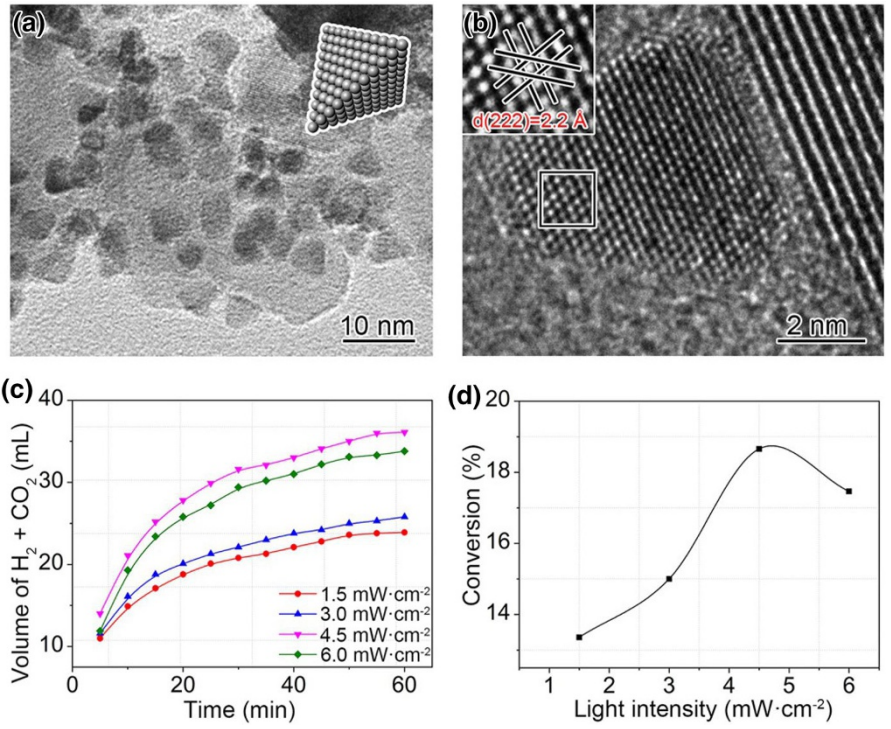

Fig. 3 **a** Transmission elecetron microscopy (TEM) and **b** high resoution TEM (HRTEM) images of Pd-tetrahedron–TiO_2 hybrid nanostructures. **c** Volume of H_2 and CO_2 produced by the decomposition of FA catalyzed by Pd-tetrahedron–TiO_2 hybrid nanostructures at different light intensities. **d** Dependence of catalytic conversion on light intensity. Conditions: 0.5 m aq. HCOOH solution (5 mL), Pd-tetrahedron–TiO_2 (Pd: 7.74 mg), 90 °C. Reprinted with permission from [78]

activity of the resulting samples with a light intensity of 4.5 mW cm^{-2} was assessed. It was observed that the activity in the dehydrogenation of FA was strongly dependent on the foreign metal used. The best performance was achieved with Pd@Ag5%-tetrahedron–TiO_2, with a conversion of 98.7%, while 63.2% and 35.5% of conversion was achieved with Cu- and Au-modified Pd-tetrahedron–TiO_2, respectively. A sample modified with Pt displayed reduced activity. According to the results of DRIFT analysis and the work function of the metals used, this catalytic trend was explained mainly in terms of CO interaction strength and poisoning effect.

Ago et al. [79] also reported on the photocatalytic activity of PdAg–TiO_2 catalysts (AgPd@Pd/TiO_2). In that case, the desired composition of the metal phase was achieved by dealloying the AgPd core. Samples with various compositions (i.e., $Ag_{100-x}Pd_x$@Pd/TiO_2, with $x=7$, 10, 15) were prepared by microwave heating at 100 °C during 30 min, 1 h, and 2 h, respectively. The best composition of the catalysts was determined to be $Ag_{93}Pd_7$@Pd/TiO_2. Furthermore, the effect of TiO_2 was also analyzed by using anatase (A) and P25 (P). The characterization of the catalysts indicated that 0.8 nm-thick Pd shells were achieved on the AgPd cores for both TiO_2 supports, and the composition, sizes, and morphology did not depend on the TiO_2 used. The photocatalytic activity was monitored by measuring the gas generated while irradiating with a Xe lamp and heating at various temperatures (from 27 °C to 90 °C). The profiles of the gas evolution with and without illumination are plotted in Fig. 4. Analysis of the profiles indicated that the initial reaction rate was improved by a factor of 1.5–1.6 for AgPd@Pd/TiO_2 (A) and AgPd@Pd/TiO_2 (P) at 27 °C, respectively, while that factor was 1.1–1.2 at 90 °C. Such differences observed with the temperature were explained on the basis of the migration of photogenerated electrons from TiO_2 to Pd. At low temperatures, the photogenerated electrons transfer from the conduction band of TiO_2 to Pd shell with larger work function (5.1, 4.7, and 4.0 eV for Pd, Ag, and TiO_2, respectively). The electron-rich Pd species formed upon irradiation were responsible for enhancement of FA decomposition ability. However, at higher temperatures, photogenerated electrons have a higher migration rate, but, at the same time, electron–hole pairs recombination is also favored, which eventually results in a lower number of electrons reaching the surface of Pd. As for the TiO_2 support, it was observed that AgPd@Pd/TiO_2 (A) displayed better activity than AgPd@Pd/TiO_2 (P) under both light and dark conditions, which was ascribed to the slower electron–hole recombination rate of anatase in comparison to the rutile phase present in P25, as well as to its higher specific surface area and strong interaction of anatase phase with AgPd@Pd particles.

Apart from the most commonly investigated PdAg-based catalysts, other compositions have been studied for this application. For instance, Xue el al. [80] reported selective photocatalytic decomposition of FA over AuPd nanoparticle-decorated TiO_2 nanofibers under simulated sunlight irradiation, which were expected to combine the optimum ability of Pd to boost the decomposition of FA with the surface plasmon resonance (SPR) of Au, as well as the optimized features of the three-dimensional (3D) TiO_2 structure. Samples with various Au/Pd ratios were prepared by electrospinning from a solution containing $HAuCl_4$, $Pd(C_2H_3O_2)_2$, tetrabutyl titanate [$Ti(OC_4H_9)_4$], and poly(vinylpyrrolidone) (PVP). Pd_1/TiO_2 and Au_1/TiO_2 were synthesized as control samples. Among those investigated, sample

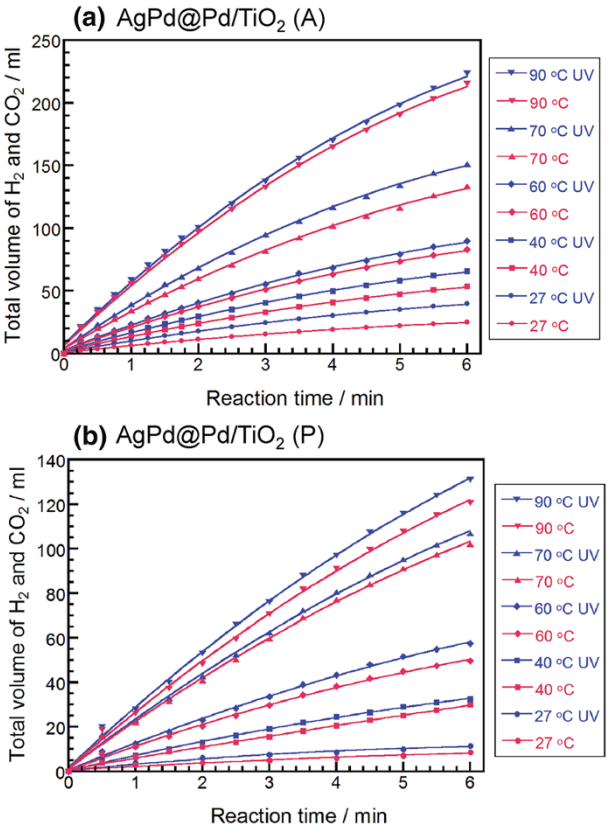

Fig. 4 **a** Gas generation by decomposition of FA (0.25 M, 20 mL) vs. time in the presence of **a** AgPd@Pd/TiO_2 and **b** AgPd@Pd/TiO_2 (P) nanocatalysts at 27–90 °C with and without photoirradiation. Reprinted with permission from [79]

$Au_{0.75}Pd_{0.25}/TiO_2$ displayed the highest H_2 production rate. The presence of alloyed nanoparticles was confirmed by high resolution transmission electron microscopy (TEM), X-ray photoelectron spectroscopy (XPS), and UV–Vis spectra. Samples with Au nanoparticles showed an absorption band at 590 nm, corresponding to the SPR of Au, while the AuPd-based catalysts displayed a blue-shift to 540 nm with lower intensity due to the increase of electron density in Au particles.

The photocatalytic tests were carried out under simulated sunlight irradiation, with a light intensity of 100 mW cm^{-2}. The results of the photocatalytic test are depicted in Fig. 5. The hydrogen generation rate was calculated to be 4.0, 19.5, 54.5, and 88.5 μmol h^{-1}, for TiO_2, Au_1/TiO_2, Pd_1/TiO_2, and $Au_{0.75}Pd_{0.25}/TiO_2$, respectively. This tendency confirms the ability of Au and Pd to hold the photogenerated electrons from TiO_2 and act as an active site for the dehydrogenation reaction. The test under visible light irradiation did not show generation of H_2 for the alloy catalysts, which suggested that TiO_2 excitation is mainly responsible for the photocatalytic activity of the sample. Furthermore, the cyclability tests showed a high stability

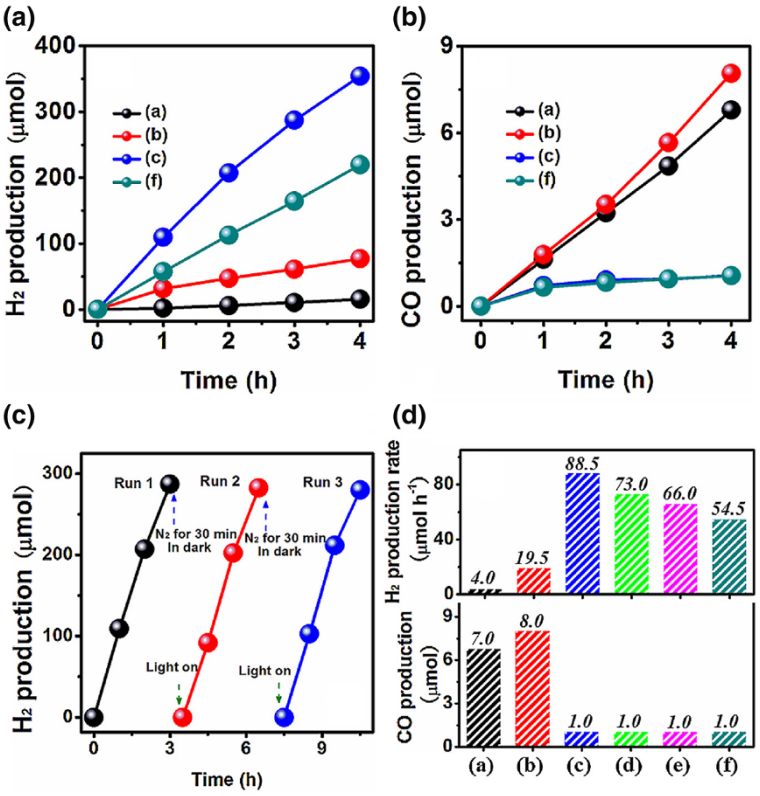

Fig. 5a–d Results of photocatalytic FA decomposition under simulated sunlight irradiation over different nanofibers. *(a)* TiO_2; *(b)* Au_1/TiO_2; *(c)* $Au_{0.75}Pd_{0.25}/TiO_2$; *(d)* $Au_{0.5}Pd_{0.2}/TiO_2$, *(e)* $Au_{0.25}Pd_{0.75}/TiO_2$; *(f)* Pd_1/TiO_2 nanofibers. **a** Photocatalytic H_2 production amount versus irradiation time; **b** photocatalytic CO production amount versus irradiation time; **c** cycling test of photocatalytic H_2 production over the $Au_{0.75}Pd_{0.25}/TiO_2$ nanofibers; **d** H_2 production rates and CO production amounts (after 4 h). Reprinted with permission from [80]

of the alloy photocatalysts during 9 h of reaction. The higher activity displayed by the alloy AuPd-based catalysts was ascribed to the stronger electron-sink effect, which reduced the recombination of electron–hole pairs, as confirmed by photoelectrochemical tests and photoluminescence measurements. Interestingly, it was demonstrated that the CO-poisoned metal surface could be reactivated by means of light excitation of the TiO_2 support upon sunlight irradiation, while such reactivation was not effective under visible light irradiation.

Liu et al. [81] also reported an investigation of Au–TiO_2 photocatalysts. In that study, a more complex visible-light-responsive system formed by Au–La_2O_3/TiO_2 (ALT) hybrid was prepared by a sol–gel method and using different atmospheres (i.e., H_2/CO_2, H_2, CO_2, and N_2; samples denoted as ALT-H_2/CO_2, ALT-H_2, ALT-CO_2, and ALT-N_2, respectively). It was observed that the presence of La inhibited the transformation of anatase to rutile phase. Furthermore, $La_2O_2CO_3$ was

formed upon treatment under H_2/CO_2 atmosphere, which was claimed to be able to decompose to La_2O_3. As for the morphology of the samples, it was observed that Au nanoparticles were embedded in sample ALT-H_2/CO_2, that they interacted strongly with TiO_2 and La_2O_3 phases, and had an average size of 5–6 nm, while larger nanoparticles with hemispherical shape were identified in sample ALT-H_2. The presence of $La_2O_2CO_3$ in samples treated under H_2/CO_2 atmosphere and its dynamic formation and decomposition was found to be responsible for the good dispersion of nanoparticles observed in ALT-H_2/CO_2. However, Au nanoparticles were not detected in ALT-CO_2 and ALT-N_2, possibly due to the absence of reducing agent in the calcination step. UV–Vis characterization of the catalysts revealed that co-doping of La and Au provoked a reduction in the band gap, following the order ALT-H_2 (2.56 eV) < ALT-H_2/CO_2 (2.66 eV) < ALT-CO_2 (2.77 eV) < ALT-N_2 (2.84 eV), which was ascribed to a synergistic effect between Au and La under the different atmospheres used. In addition, photoluminescence analysis demonstrated the prolonged lifetime of electron–hole pairs in sample ALT-H_2/CO_2. As expected, after all the results of characterization of the samples, ALT-H_2/CO_2 displayed the best photocatalytic performance among investigated, with a H_2 production rate of 178.4 μmol g_{cat}^{-1} h^{-1}, which was much higher than those rates achieved with the catalysts prepared under the other atmospheres under study. A plausible mechanism for the decomposition of FA was proposed, which is schematized in Fig. 6. The photon absorbed by La-doped TiO_2 excite photogenerated electrons to the conduction band and generate holes in the valence band. First, electrons are transferred to Au nanoparticles promoting the decomposition of HCOOH into $HCOO^-$ and H^+. H^+ can then produce H_2 by reduction with an electron, and $HCOO^-$ reacts with a photogenerated hole in TiO_2 forming a free radical ($HCOO^-$). Subsequently, $HCOO^-$ is oxidized by holes and produces CO_2 by releasing a H^+. In the mechanism proposed, $La_2O_2CO_3$ plays a vital role in promoting the decomposition of FA and the desorption of CO_2 from the surface of the catalyst.

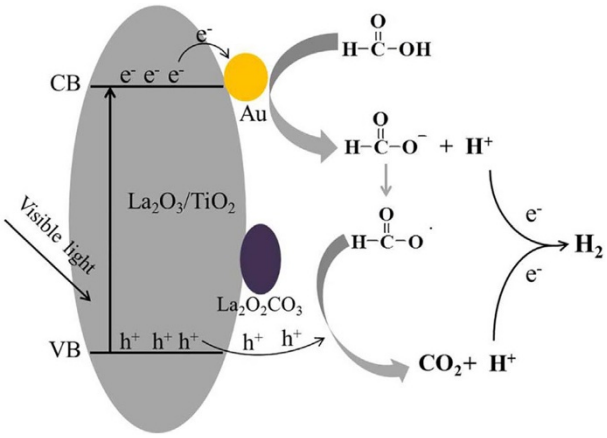

Fig. 6 Schematic illustration for the reaction mechanism of photocatalytic decomposition over ALT-H_2/CO_2 photocatalyst. Reprinted with permission from [81]

As for noble-metal-free photocatalysts, some nice works can also be found in the literature. For instance, Clarizia et al. [82] reported on novel nano-TiO_2 photocatalytic system based on the solar reforming of FA in presence of cupric ions and chlorides, in a study in which the effect of the pH values, initial concentration of FA, chloride and cupric ion in the H_2 production ability was investigated. The H_2 production was suggested to proceed via the following steps:

- Step 1: reduction of cupric ions to cuprous with a simultaneous oxidation of formic acid.

$$\text{Cu (II)} \xrightarrow{e^-_{CB}} \text{Cu (I)} \xrightarrow{e^-_{CB}} \text{Cu (0)}$$

$$\text{HCOOH} \xrightarrow{h^+_{VB}} CO_2^{\cdot -} + 2H^+$$

- Step 2: photolysis of some chloride complexes of cuprous ions.

$$CuCl_2^- + H^+ \xrightarrow{h\upsilon} Cu^{2+} + 2Cl^- + e_s^-,$$

$$CuCl_3^{2-} + H^+ \xrightarrow{h\upsilon} Cu^{2+} + 3Cl^- + e_s^-.$$

Dong et al. [83] investigated the engineering of binary CuO/TiO_2 heterojunction nanofibers prepared from electrospinning and followed calcination treatment. It was found that, after irradiation for 30 min during the photodecomposition of FA, the binary heteroconjunction (CuO/TiO_2) changed to a heteroconjunction formed by four components (Cu/Cu_2O/CuO/TiO_2) originated by a photo-assisted recrystallization reaction (Fig. 7), enhancing the separation of electron and hole pairs. This aspect is crucial, because the production of H_2 takes place in a two-steps photoreaction: the generation of H^+ via photocatalytic oxidation of HCOOH by the holes in the valence band, and formation of H_2 via photocatalytic reduction of H^+ with photoinduced electrons in the conduction band. Then, as the oxidation reaction by the holes occurs before the reduction, the lifetime of the electrons should be longer than that of the holes. In this particular case, HCOOH can be oxidized to H^+ by the holes accumulated in the valence band of CuO, because of their higher potential ($\sim +2.05$ V) than those of the pair CO_2/HCOOH (~ -0.61 V). However, the position of the conduction band of CuO is below the reduction potential of the pair H^+/H_2 ($\sim +0.36$ V and ~ -0.42 V, respectively), meaning that the reduction of H^+ to H_2 by the photoinduced electrons is not thermodynamically favored. For that reason, Cu_2O and Cu species, which are visible-light responsive and inexpensive co-catalysts, respectively, are formed from the reduction of CuO. As a result, the quaternary multi-heterojunction photocatalysts (Cu/Cu_2O/CuO/TiO_2) displayed 40 times higher production of H_2 from FA than their pure TiO_2 nanofibers counterpart.

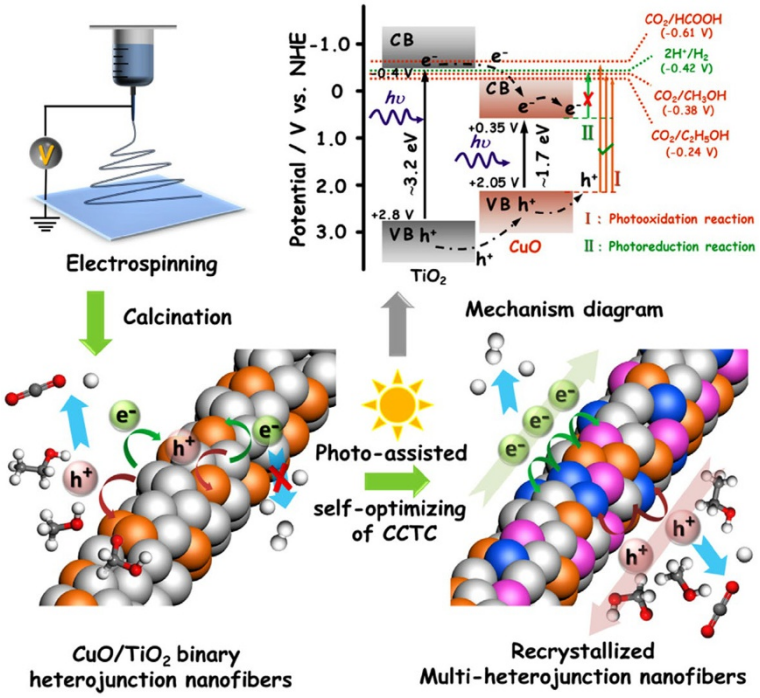

Fig. 7 Schematic diagrams for the synthesis route of CuO/TiO_2 binary heterojunction nanofibers and the photo-assisted self-optimizing of charge-carriers transport channel (CCTC) through a recrystallization process during the photocatalytic decomposition of organic hydrogen-carrier molecules. Reprinted with permission from [83]

3 Photocatalytic Systems Based on CdS

The previous section mentioned some benefits of TiO_2 in photocatalytic reactions, and summarized some examples of TiO_2-based catalysts for FA decomposition. However, their limitation in the visible-light range makes it necessary to search for photocatalysts with a wider light responsive range. In this sense, metal sulphides have been studied extensively because they exhibit an important visible-light response although their efficiency is poor. As mentioned before, recombination between electron and hole is related to efficiency. An approach to limit such recombination is the use of photocatalysts with a high CB position, which present an interesting reduction capability. At this point, CdS (with a band gap of ~ 2.5 eV) is an interesting option that has attracted much attention due to its wide visible-light range together with its simple synthesis and low cost. Furthermore, it fulfils the thermodynamic aspects of some of the most studied photocatalytic reactions [84, 85]. Regarding the photocatalytic decomposition of FA, a few studies on CdS-based photocatalysts have also been reported to date. In 1968, Willner and Goren [86] reported on semiconductor CdS particles for the generation of H_2 from the FA decomposition. In this particular case, they used

both formate solution and its deuterated counterpart to evaluate photodecomposition to produce H_2. The yield of H_2 was higher than 90% for the formate solution, while the deuterated solution displayed a lower H_2 evolution rate, indicating that the limiting step of the formate oxidation reaction was the generation of holes in CdS particles ($h^+ + HCO_2^- \rightarrow CO_2^- + H^+$), and that water was the source of H^+ for the H_2 formation. Moreover, they realized that the formation of CO_2^- (reducing agent) after the photodecomposition promoted the presence of Cd metal in the system. Nedoluzhko et al. [87] also reported that Cd^0 was involved in the photoformation of H_2. In that study, a solution of CdS particles (~ 1.5 μm), FA and buffer was irradiated under anaerobic conditions. Among evolved gases, the H_2 profile exhibited an induction time and the rate of H_2 evolution increased rapidly. This turning point was related to the generation of Cd^0 from CdS. The formation of cadmium (metallic state) was first attributed to the presence of formate; the authors proposed that two CO_2^- anion radicals, which acted as reducing agents, are involved in the reduction process of CdS.

$$CdS + 2CO_2^{\cdot -} \rightarrow Cd^0 + S^{2-} + 2CO_2$$

During this process, electrons present in the conduction band reduced water to form H_2. However, the authors noted that H_2 gas evolution did not happen at the beginning of the photoreaction, and they claimed that one equivalent of CO_2^- participated to reduce the lattice Cd^{2+}. Therefore, the proposed mechanism consisted of trapping of electrons, followed by a reduction.

$$CdS + e_{cb}^- \rightarrow \left(Cd^{2+}e^-S^{2-}\right),$$

$$\left(Cd^{2+}e^-S^{2-}\right) + CO_2^{\cdot -} \rightarrow Cd^0 + CO_2 + S^{2-}$$

According to the standard reduction potential values, it was stated that electrons of the CdS conduction band could not reduce the lattice Cd^{2+} to Cd^0. Once a determined amount of the lattice Cd^{2+} was converted to Cd^0, H_2 gas evolution commenced following the suggested pathways.

$$(1)\ COOH^- + h^+ \rightarrow CO_2^{\cdot -} + H^+,$$

$$CO_2^{\cdot -} + h^+ \rightarrow CO_2$$

$$2H^+ + 2e^- \rightarrow H_2$$

$$(2)\ CO_2^{\cdot -} + H^+ \rightarrow CO_2 + \frac{1}{2}H_2$$

$$H^+ + e^- \rightarrow \frac{1}{2}H_2$$

Although CdS exhibited photocatalytic activity towards FA decomposition, it was restricted to CdS in powder form. For instance, Nedoluzhko et al. [87] also observed that the formation of Cd^0, which played a pivotal role in the H_2 formation from FA

decomposition, depended on a limited amount of Cd^{2+}. Therefore, different strategies based on CdS have been explored to enhance the photocatalytic activity in the FA decomposition. Chen et al. [88] reported that CdS particles were embedded on titanate nanotubes (TNTs) using a hydrothermal synthesis. From TEM images, confined CdS particles as well as CdS particles suported on the surface of TNTs were observed. Moreover, XRD patterns and UV spectra confirmed the presence of CdS particles. The photocatalytic activity towards H_2 production was evaluated in a 10 vol% FA solution. CdS/TNTs produced 179.4 μmol of H_2 after 3 h while TNTs generated only 0.09 μmol. This enhancement could be related to the transfer of photogenerated electrons from the valence band to the conduction band. These electrons could be transferred to TNTs because both valence band and conduction band positions of CdS are higher compared to TNTs. Recently, Liou et al. [89] published a composite that consisted of Pt, CdS, and TNTs synthesized by microwave hydrothermal method. The H_2 evolution rate for different catalysts were assessed in an aqueous FA solution (10 vol%) under visible light. Neither TiO_2 nor TNTs catalysts displayed activity towards the FA decomposition. However, the addition of CdS into titania structures promoted photocatalytic activity, being more active in the case of Cds/TNTs (295.0 μmol h^{-1}) than CdS/TiO_2 (118.7 μmol h^{-1}). This effect was attributted to a higher active surface area for TNTs compared to TiO_2, which boosted the adsorption of FA onto the active sites and reduced recombination of the electron–hole pair. After this, Pt was loaded on titania-based photocatalysts in order to trap the photogenerated electrons, resulting in photocatalysts that were more active towards FA decomposition. To do that, impregnation and photodeposition methods were carried out, leading to Pt-CdS/TNT samples prepared by the thermal impregnation method with different Pt loadings, which exhibited poorer photocatalytic activities compared to that of CdS/TNT photocatalyst. This decline in H_2 production was related to agglomeration after thermal impregnation. However, Pt-CdS/TNT synthesized by photodeposition of Pt displayed a remarkable photocatalytic activity for H_2 production (661.1 μmol h^{-1}). The enhancement of H_2 production was due to a smaller Pt nanoparticle size and better distribution of nanoparticles onto CdS/TNT, resulting in better contact between Pt and TNTs, which improved separation of the electron–hole pair. Concerning the mechanism, it was suggested that the photogenerated electrons were transferred from the valence band to the conduction band of CdS, and therefore the concentration of holes increased in the valence band. According to the band gap of TNTs, the photoelectrons in CdS jumped quickly into TNTs. Moreover, it was indicated that Ti^{3+} species present in TNTs (due to the oxygen vacancy) may capture electrons, and that Pt nanoparticles act as active sites for H_2 production. Additionally, Ti^{4+} species were suggested as hole co-catalysts because the photogenerated holes in the CdS surface can be trapped by Ti^{4+} species, avoiding the CdS photocorrosion.

A different strategy was tackled by Li et al. [90], who reported the use of visible light-driven photocatalysts based on a CdS–ZnS composite with heterogeneous structure. In this system, CdS, with a narrow band gap and high photo-sensitivity, showed great reactivity for the production of H_2, while ZnS, with a wider band gap, reduced the recombination of electron–hole pairs. The nanoparticles of the CdS–ZnS photocatalyst were prepared by a microemulsion technique in a system composed of water/

Triton X-100/1-butanol/*n*-hexane, and using $Cd(NO_3)_2$, $Zn(NO_3)_2$, and $Na_2S{\cdot}xH_2O$, as precursors of Cd, Zn and S^{2-}, respectively. The heterogeneous solid formed was composed by ZnS deposited on the surface of crystals of CdS. The obtained photocatalysts were evaluated in the production of H_2 and it was shown that only 13.7 μmol h^{-1} of H_2 was generated from CdS, while 189.5 μmol h^{-1} was produced from the CdS–ZnS; no H_2 was detected using bare ZnS. The enhancement observed for the heterogeneous CdS–ZnS system was claimed to be due to the suppression of electron–hole pairs recombination due to the presence of ZnS, which makes electrons available for the evolution of H_2. It was proved that, aside from that effect, the addition of ZnS was responsible for the good stability against photo-corrosion displayed by CdS–ZnS. Moreover, it was observed that the ZnS coating avoided Cd^{2+} leaching from the photocatalysts, which also helped maintain reactivity of the samples (Fig. 8).

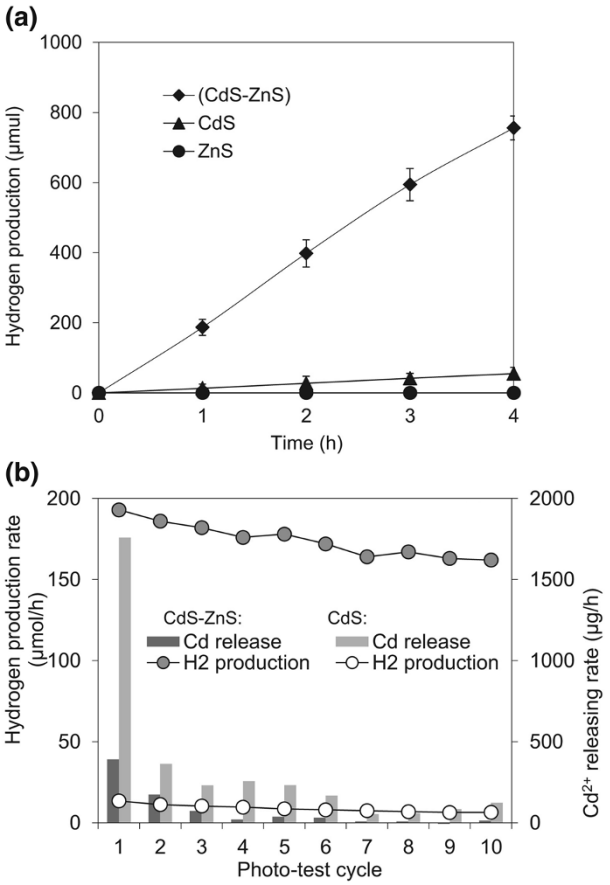

Fig. 8 **a** Hydrogen production in FA solution (10%) by composite CdS–ZnS, bare CdS and bare ZnS, under visible light. **b** Stability of CdS–ZnS and bare CdS in terms of the hydrogen production rate and leaching of Cd^{2+} from the catalysts during repeated photocatalytic tests (at least 4 h for each test cycle). Reprinted with permission from [90]

Following heterogeneous systems based on CdS, Xu et al. [91] reported multi-core–shell CdS@ZIF-8 structures prepared by a two-step method. In the synthetic protocol used in that study, polyvinylpyrrolidone (PVP) was used to stabilize the nanoparticles of CdS and ZIF-8 shells with controlled thickness (from 13.6 to 102 nm) were formed on the surface of CdS. The photocatalytic performance evidenced the superiority of the core–shell structure compared to bare CdS nanoparticles. It was observed that core–shell structures showed better selectivity towards the production of H_2 via the FA dehydrogenation reaction.

Zhang et al. [92] reported the preparation of composite aluminium-substituted mesoporous silica (Al-HMS) molecular sieves coupled with CdS (CdS/Al-HMS). The addition of Ru enhanced the photocatalytic activity as a consequence of the separation of photogenerated charge-carrier. Among the samples investigated, 0.07Ru/CdS/Al-HMS exhibited the highest H_2 evolution activity (3.7 mL h^{-1}).

Reisner et al. [93] investigated a CdS-based photocatalyst that efficiently converted FA into H_2 or CO by boosting the dehydrogenation or dehydration reaction, respectively, by means of controlling selectivity of the reaction by using 3-mercaptopro-pionic acid (MPA) as a capping ligand (QD-MPA). Under visible-light irradiation, 52.1 mmol H_2 g_{cat}^{-1} h^{-1} was generated with QD-MPA, which was enhanced by the addition of Co (QD-MPA/$CoCl_2$; 116 mmol H_2 g_{cat}^{-1} h^{-1}). However, 218 H_2 g_{cat}^{-1} h^{-1} was achieved upon utilization of the full solar spectrum. Aside from the effect of Co species in boosting catalytic performance, the latter study also proved that selectivity of FA decomposition towards either H_2 or CO could be modified by means of modifying the surface of CdS with ligands, such as $[Me_3O]BF_4$.

Piao et al. [94] reported on the use of ultrasmall cobalt phosphide nanoparticle (CoP) as efficient cocatalysts for photocatalytic dehydrogenation of FA, in a study in which a CdS/CoP@RGO hybrid was evaluated. In order to obtain the final catalysts, Co_3O_4@SiO_2 nanospheres were first prepared using a microemulsion method, and subsequently decorated by polyethyleneimine (PEI) and loaded on graphene oxide (GO). After that, SiO_2 was removed to obtain Co_3O_4 dispersed on RGO, and the final CdS/CoP@RGO photocatalyst was prepared by phosphidation and loading CdS nanoparticles by ultrasonic treatment. The performance of CoP was assessed by comparison with the counterpart noble-metal based catalysts (CdS/Pt@RGO, CdS/Pd@RGO, CdS/Au@RGO, and CdS/Ru@RGO). The time of flight (TOF) values were 196, 244, 106, 107, and 63 h^{-1}, for CoP, Pt, Pd, Au, and Ru, respectively, which evidenced the promising behavior of CoP as a cocatalyst for the photocatalytic dehydrogenation of FA. Following with the non-noble-free photocatalysts, Khan et al. [95] reported a system based on Ni and Co loaded on CdS nanorods (NRs), that were synthetized via controlled thermolysis of cadmium (II) bis(dibutylcarbamodithioate) in ethylenediamine. Using this system, and due to the redox potentials of Ni and Co in relation to the band positions of CdS NRs, electron and holes were shuttled from CdS to Ni and $CoCl_2$ species, respectively, which led to higher stability and photocatalytic performance. Evaluation of catalytic performance under visible-light irradiation revealed that H_2 production ability followed the order CdS < Co/CdS < Ni/CdS < Co–Ni/CdS.

4 Photocatalytic Systems Based on C_3N_4

Graphitic carbon nitride (g-C_3N_4)—a polymeric semiconductor—has elicited great attention in the context of the search for robust and visible-light-active semiconductor photocatalysts. It is formed by ordered *tri*-s-triazine subunits connected through planar tertiary amino groups within layers and weak van der Waals force between layers. It shows appealing electronic properties, high physicochemical stability, and easy synthesis from N-containing precursors (i.e. urea, cyanamide, dicyandiamide, melamine, etc.). It has a moderate band gap (2.4–2.8 eV) that results in an onset visible light absorption of ~ 450 nm [96, 97]. Although the history of C_3N_4-based polymers started in the nineteenth century by the investigation of Berzelius and Liebig [98], its use in heterogeneous catalysis started much later, in 2006 [99], and its properties as a metal-free conjugated semiconductor photocatalyst for the evolution of H_2 was pioneered by Wang just 10 years ago [100].

Since then, g-C_3N_4 has been used widely in numerous photocatalytic applications, such as water splitting, CO_2 reduction, and degradation of pollutants, etc. [101–103]. Recently, g-C_3N_4 has also received attention as a catalyst for H_2 production from hydrogen carrier molecules [20, 44, 50, 104]. g-C_3N_4-photocatalysts used for decomposition of FA contain metal nanoparticles so as to construct Mott–Schottky photocatalysts, in which charge separation is enhanced. This was the case in the study reported by Chen et al. [105], in which Mott–Schottky type Pd-C_3N_4 photocatalysts, with mesoporous C_3N_4 (mpg-C_3N_4) as support, were prepared by wet impregnation; the resulting material was denoted Pd@CN. For this, mpg-C_3N_4 was first synthetized from cyanamide and a Ludox HS40 solution, and subsequently impregnated with $PdCl_2$ to give a final metal loading of 8%. Furthermore, reference samples with N-doped layered carbon and carbon black (Pd@N-LC and Pd@CB, respectively) were also synthetized. The average nanoparticle size was determined to be 3–5 nm for Pd@CN and Pd@N-LC, and 10 nm for Pd@CB. In order to assess the performance of the samples, catalytic and photocatalytic tests were monitored. It was observed that, in dark conditions (i.e. catalytic test at 15 °C), Pd@CN displayed the highest TOF number among investigated (49.8 mol H_2 mol^{-1} Pd h^{-1}), which was attributed to the Mott–Schottky effect (i.e. support effect). This effect was confirmed by the decreased intensity of the photoluminescence spectra after loading of Pd nanoparticles on mpg-C_3N_4. In addition, the good catalytic activity found was increased further upon visible-light irradiation (71.0 mol H_2 mol^{-1} Pd h^{-1}). It was claimed that the enhancement observed in the catalytic activity under light irradiation conditions was due to the electron enrichment of Pd nanoparticles, which, in turn, was strongly dependent on the wavelength of the light used (see Fig. 9).

Yu et al. also reported on the application of Mott–Schottky heterojunctions [106]. In that case, PdAg nanowires (NWs) with various Pd/Ag compositions (Pd_7Ag_3 NWs@g-C_3N_4, Pd_5Ag_5 NWs@g-C_3N_4, Pd_3Ag_7 NWs@g-C_3N_4, and Pd NWs@g-C_3N_4) were formed in situ on g-C_3N_4. XPS analysis confirmed the electron transfer from Ag and g-C_3N_4 to Pd of the Pd_5Ag_5 NWs@g-C_3N_4

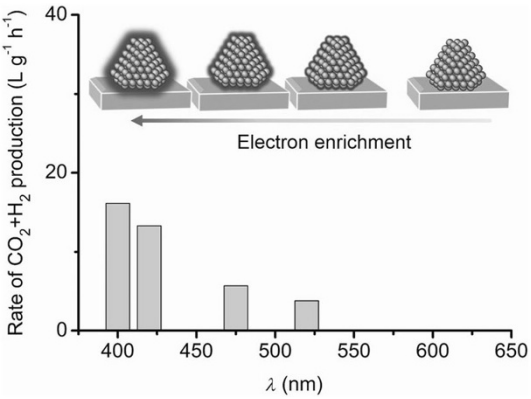

Fig. 9 Dependence of the activity of Pd@CN on the irradiation wavelength for the photocatalytic decomposition of FA. Reaction conditions: 1 m aqueous FA solution (10 mL), Pd@CN-1% (20 mg), 1 h, 15 °C. Reprinted with permission from [105]

Mott–Schottky heterojunction, creating electron-rich Pd species that are favorable for facilitating the O–H cleavage and strengthening the adsorption of formate. From its side, the support serves as a proton scavenger for the dissociation of O–H, forming protonated g-C_3N_4, which facilitates the production of H_2 and CO_2 via β-hydride elimination of Pd-formate. The catalytic activity displayed dependence with the composition of the nanoparticles, with initial TOF of 346, 420, 242, and 105 h^{-1}, Pd_7Ag_3 NWs@g-C_3N_4, Pd_5Ag_5 NWs@g-C_3N_4, Pd_3Ag_7 NWs@g-C_3N_4 and Pd NWs@g-C_3N_4, respectively. Furthermore, the performance of some control samples was also assessed to point out the effect of the Mott–Schottky heterojunction. The effect of the visible-light intensity on the photocatalytic activity of Pd_5Ag_5 NWs@g-C_3N_4 was also investigated, which showed increasing dehydrogenation rate with light intensity.

Stucky et al. [104] also investigated AgPd nanocatalysts supported on g-C_3N_4 (denoted as AgPd/CN). In that case, microsized mesoporous carbon nitride hollow spheres were synthetized from a melamine–cyanuric acid network, and subsequently impregnated with K_2PdCl_4 and $AgNO_3$. As indicated by the characterization results, the resulting nanoparticles had an average size of 7.5 ± 1.0 nm and a Ag/Pd ratio of 1/1. Comparison with reference samples prepared from SiO_2 and activated carbon demonstrated the vital role of N-functional groups in C_3N_4 in achieving highly dispersed alloy AgPd nanoparticles. The electron density enrichment of Pd species via electron donation from C_3N_4 and Ag to Pd was also demonstrated by XPS analysis. It was also claimed that the electron density of Pd could be further increased by photoexcited electron transfer from the semiconductor support, which, in turn, would suppress recombination of the electron–hole pairs. As a consequence of the resulting unique electronic features, AgPd/CN displayed much higher activities than its Ag/CN and Pd/CN counterparts, and activity was further enhanced under visible-light irradiation. H/D isotope experiments were also followed using D_2O to investigate the contribution of the semiconductor and the direction of the charge carrier in components of the photocatalysts. The results of the relative atomic amount and atomic ratio of H and D in the gas produced from FA decomposition at 30 °C is depicted in Fig. 10.

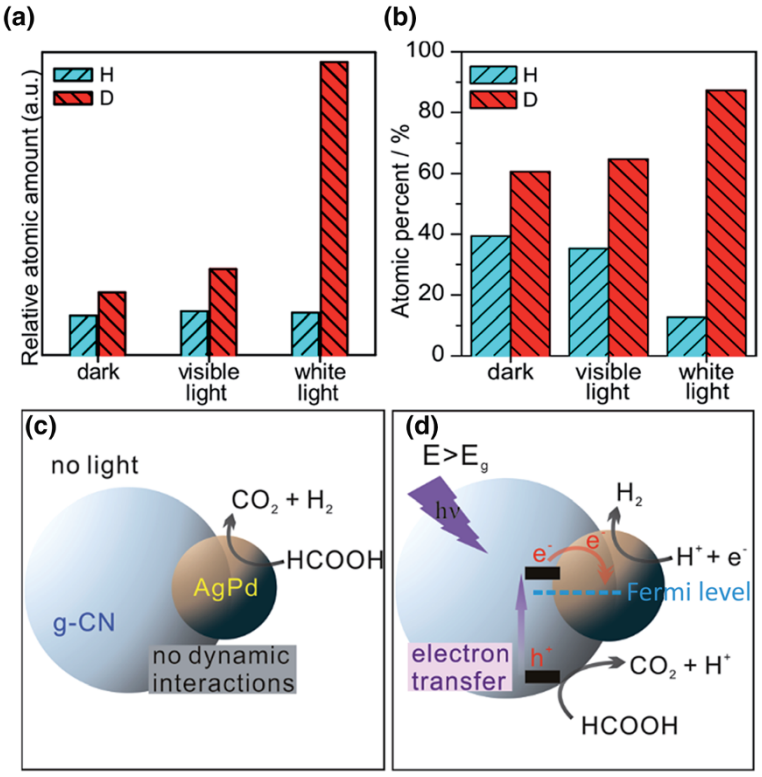

Fig. 10a–d **a**, **b** Kinetic isotope effects for FA decomposition with AgPd/CN-3% catalyst in D_2O at 30 °C under different conditions. **a** Relative atomic amount, **b** atomic ratio of deuterium/hydrogen to the total amount of hydrogen and deuterium. The reaction pathway and mechanism for **c** catalytic route in the dark or **d** photoelectrochemical route in the light with incident energy higher than bandgap of CN. Reprinted with permission from [104]

The atomic percentage of D under visible-light was observed to be slightly higher than under dark conditions (64.7 and 60.6%, respectively), while it increased to 87.3% under UV-light, indicating that the photocatalytic activity was wavelength-dependent. Under UV-light, the energy of the photon is able to excite the electron–hole pair directly, and water splitting occurs in the different components of the catalysts (i.e., photocathode: AgPd for reduction of water; photoanode: C_3N_4 for the oxidation of FA), so that FA serves as electron donor and D_2O acts as electron acceptor. The higher content of D observed in the gas product demonstrated that D_2O is the source of D, due to the photoelectrochemistry with half reaction separated. However, for very short wavelengths, FA photolysis to CO can take place.

Following Mott–Schottky photocatalysts, Liu et al. [52] recently reported the application of plasmonic AuPd alloy nanoparticles supported on super small carbon nitride nanospheres (Au_xPd_y/CNS) for H_2 production. The catalysts were designed so that Au could capture the irradiation energy, which results in electrons with high density on their surface by the localized surface plasmon resonance (LSPR) effect.

Such high energy electrons can migrate to Pd active sites and result in enhanced photocatalytic performances. For the preparation of catalysts, carbon nitride nanospheres were first synthetized from cyanamide using SiO_2 as a template. They were subsequently impregnated with $HAuCl_4$ and H_2PdCl_4 at various mole ratios (i.e. 1:0, 2:1, 1:1, 1:2, and 0:1) to achieve different compositions of the alloy nanoparticles. The resulting photocatalysts were denoted as Au/CNS, Au_2Pd_1/CNS, AuPd/CNS, Au_1Pd_2/CNS and Pd/CNS, respectively, according to the composition of the nanoparticles. A sample prepared from bulk C_3N_4 (AuPd/Bulk CN) was also prepared as a reference material. TEM analysis revealed that the average size of g-C_3N_4 nanospheres and AuPd nanoparticles was 20 and 3 nm, respectively. Once again, the fine distribution of AuPd nanoparticles on the nanospheres was attributed to the anchoring effect of the uncondensed amine groups on the surface g-C_3N_4. XPS analysis confirmed the strong interaction and distribution of charge from Au to Pd in the AuPd nanoparticles, as well as electron donation from the support to Pd species. As for the catalytic results (see Fig. 11), it was observed that, under dark conditions, the generation of gas was equal to 86 mL, 137 mL and 171 mL for Pd/CNS, AuPd/Bulk CN, and AuPd/CNS, respectively, confirming the beneficial effect of the alloyed nanoparticles. All Pd-containing showed improved activity under visible light as compared to that under dark conditions, being more marked in sample AuPd/CNS, which displayed the highest activity (TOF value of 1017.8 h^{-1}). Such enhancement was attributed to the donation of electrons from CNS to the nanoparticles due to the Mott–Schottky effect, as well as to the alloying and plasmonic effects that lead to the

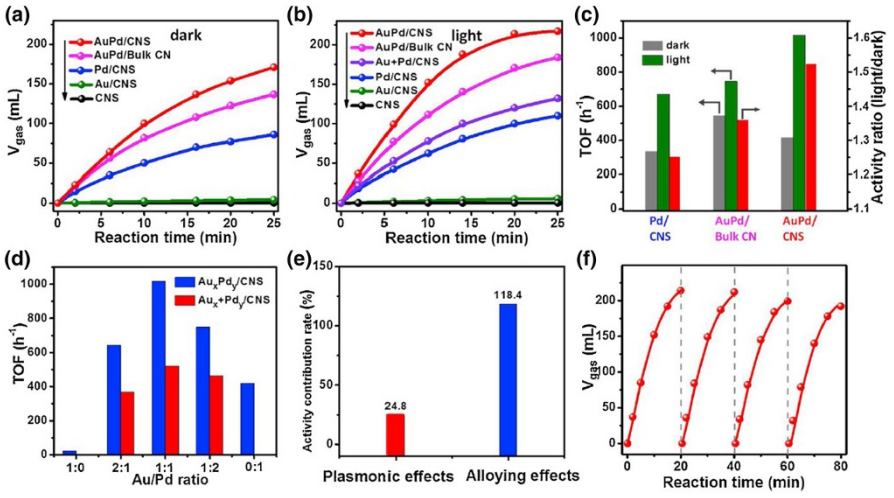

Fig. 11 Time-dependent gas (H_2 and CO_2) evolution curves from FA of all the as-prepared materials **a** in the dark at 25 °C and **b** under visible light irradiation ($\lambda > 420$ nm) at 25 °C. **c** The TOFs and activity ratio of different catalysts in the dark and under visible light irradiation [time of flight (TOF) was calculated from the data within the first 10 min according to the following equation: TOF = mmol gas produced/(mmolAuPd × h)]. **d** The TOFs of Au_xPd_y/CNS and $Au_x + Pd_y$/CNS under visible light irradiation. **e** The activity contribution rate of alloying effects and plasmonic effects under visible light irradiation. **f** The recycling performance of AuPd/CNS under visible light irradiation ($\lambda > 420$ nm). Reprinted with permission from [52]

redistribution of charge under visible-light irradiation. The contribution of alloying and plasmonic effects was confirmed by assessing the performance of samples with various composition of the alloy nanoparticles (Au_2Pd_1/CNS, AuPd/CNS, Au_1Pd_2/CNS, and Au_1Pd_2/CNS) and the physically mixed counterpart catalysts (Au_2+Pd_1/CNS, Au + Pd/CNS, and Au_1+Pd_2/CNS).

Considering that Pd is the active phase, a decrease in activity with increasing Au content could be expected. However, the positive alloying and plasmonic effect was confirmed by the enhancement achieved by the AuPd-based catalysts. Samples Au + Pd/CNS and AuPd/CNS,displayed the best performances among physically mixed and alloy catalysts, respectively. The comparison between Pd/CNS and Au + Pd/CNS revealed an increasing rate of 24.8%, which corresponds to the plasmonic effect. The increasing rate in the case of the alloy catalysts was of 143.2%, indicating that the alloy effect is much more important than the plasmonic effect.

Furthermore, the reaction mechanism summarized in Fig. 12 was also proposed in that study. In dark conditions, FA is auto-oxidized and reduction to H_2 and CO_2 takes place on Pd active sites of the alloy system by means of thermal power. Under visible-light irradiation conditions, electron–electron collisions and electron distribution between Au and Pd occur due to the alloying and plasmonic effects. Furthermore, the photogenerated electron of CNS transfer to Pd sites, leading to the formation of electron-rich Pd species. FA is oxidized to form CO_2 and H^+ by the holes on CNS, and such H^+ are reduced to H_2 by the electron-rich Pd species.

5 Other Photocatalytic Systems

Aside from the most commonly photocatalytic systems based on TiO_2, CdS, and C_3N_4, some other nice works aimed at catalyzing photodecomposition of FA have also been reported in the recent literature.

For instance, Tabata et al. [107] investigated the use of silicon-base material for the production of H_2 under visible-light irradiation. Pure Si powder and

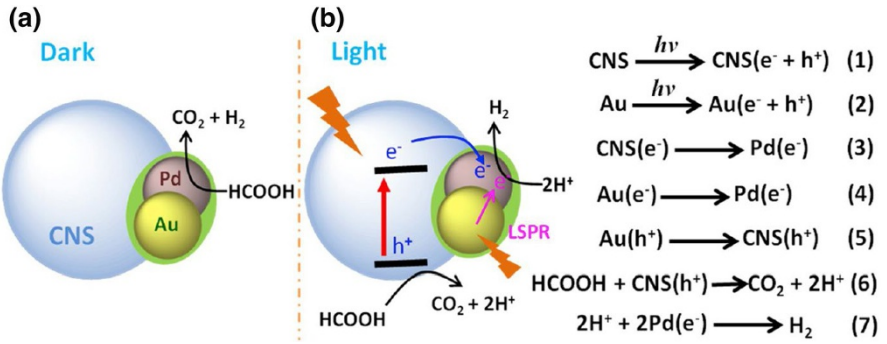

Fig. 12 Schematic illustration of photocatalytic hydrogen evolution from FA for AuPd/CNS under **a** dark and **b** light. Reprinted with permission from [52]

metal-containing catalysts (Pt, Pd, or Ru) were evaluated. In that case, the catalytic ability was shown to follow the order Ru/Si > Pd/Si > Pt/Si > Si.

Moskovits et al. [108] prepared a series of Pd nanostructures to serve as plasmon-mediated photocatalytic for the decomposition of FA. The investigated nanostructures were nanocubes (average edge length of 10 nm) and hexagonal nanosheets (average edge lengths of 22 nm and thickness of 2.9 nm) with the same surface-to-volume ratio.

Kakuta and Abe [109] reported the use of Cu_2O and Pt-Cu_2O as visible-light-responsive photocatalysts to boost the decomposition of FA. According to the valence and conduction band edge of Cu_2O (+ 0.844 V and − 1.16 V, vs. SHE (pH 7), respectively), the oxidation of FA ($HCOOH + 2h^+ \rightarrow CO_2 + 2H^+$) and the generation of H_2 was determined as feasible ($2h^+ + 2e^- \rightarrow H_2$). The catalytic test under dark conditions did not produce gas, indicating that, using such systems, the decomposition of FA takes place via photocatalytic processes. Upon irradiation, the production of H_2 with both Cu_2O and Pt–Cu_2O showed a linear trend with the irradiation time, and was larger for Pt–Cu_2O. That study claimed to be the first instance of reporting the selective and stoichiometric decomposition of FA to H_2 and CO_2 with a visible-light-responsive photocatalyst.

Wang et al. [110] recently reported on Pt Single Atoms on Te nanowires (Te NWs) for plasmon-enhanced dehydrogenation of FA. Initially, Te NWs were prepared from Na_2TeO_3 and were loaded with Pt contents of 1.1, 4.6, and 32.0 wt%, resulting in the formation of Pt single atoms, nanoclusters and nanocrystals (average size of ~ 4 nm), 1.1%Pt/Te, 4.6%Pt/Te, and 32.0%Pt/Te, respectively. Furthermore, a commercial Pt/C sample with an average nanoparticle size of ~ 4 to 5 nm was also assessed. The reaction tests revealed that, while the decomposition of FA was almost negligible under dark conditions, the performance was greatly enhanced under light irradiation, reaching TOF values of TOFs 3070, 1205, 580, and 363 h^{-1} for 1.1%Pt/Te, 4.6%Pt/Te, 32.0%Pt/Te, and Pt/C, respectively. In addition, the photocatalysts were evaluated under various light wavelengths. It was observed that, in the case of 1.1%Pt/Te ad 4.6%Pt/Te, the apparent quantum efficiency (AQE) irradiated by light with different wavelength followed the same tendency as the UV–Vis spectrum, being such tendency deviated for the sample with the highest Pt content. Additional tests were conducted to elucidate the plasmonic electron-driven mechanism and photothermal effect accompanied by plasmonic effect factors. The linear dependence of TOF values on light intensity observed for 1.1%Pt/Te confirmed the importance of the plasmonic electron-driven mechanism for photocatalysts with low Pt content, while photothermal effects gain importance for higher Pt content.

Su et al. [111] reported the visible-light-driven catalytic activity enhancement of Pd in AuPd nanoparticles supported on graphene oxide (AuPd/GO). As previously mentioned for some other bimetallic AuPd systems, the significant effect of electron transfer from Au to Pd was claimed to be crucial for the enhancement achieved by the AuPd-system under visible-light irradiation. Wen et al. [112] also reported on AuPd-based photocatalysts for the decomposition of FA using a more sophisticated photocatalyst formed by plasmonic Au@Pd nanoparticles supported on titanium-doped zirconium-based amine functionalized metal–organic frameworks (MOFs) [UiO-66($Zr_{100-x}Ti_x$)]. It was observed that integration of the components of the

catalyst resulted in a highly effective light energy harvesting system able to catalyze dehydrogenation of FA under visible-light irradiation without any additive.

As for the case of thermal catalysts used in the FA decomposition [47, 49], the beneficial role of N-doped materials in achieved enhanced performances has also been indicated for photocatalytic processes. In this context, the photocatalytic activity of N-doped carbon quantum dots (NCQDs) in the production of H_2 from FA was evaluated by Li et al. [113]. In that study, NCQDs of an average diameter of 2.5 nm were obtained from shrimp waste by hydrothermal treatment and washing, and their photoactivity was evaluated using external sunlight irradiation.

As can be seen from the results summarized above, diverse strategies are being considered for the preparation of photocatalytic systems used in the photodecomposition of FA. To allow readers to compare the performances achieved, the results of some representative photocatalysts are listed in Table 1.

6 Conclusion and Outlook

The present review highlights the promising role of hydrogen as an energy vector able to replace the widely used vectors based on fossil fuels. Furthermore, the suitability of FA as a LOHC is highlighted by summarizing its features and some of the

Table 1 Comparison of the performance of various photocatalytic systems in the conversion of FA to H_2

Photocatalyst	Production of H_2 (mmol H_2 g catalyst^{-1} h^{-1})	Selectivity to H_2	Light	Reference
TiO_2 nanofibers	0.80	69.6	AM1.5, 1 sun	[80]
Pd–TiO_2 nanofibers	10.9	98.2	AM1.5, 1 sun	[80]
Au–TiO_2 nanofibers	3.9	90.7	AM1.5, 1 sun	[80]
AuPd–TiO_2 nanofibers	17.7	99.7	AM1.5, 1 sun	[80]
Pt–TiO_2	1.62	n/a	UV	[114]
Cu–TiO_2	0.83	n/a	UV	[115]
Rh–N–TiO_2	0.75	98	230–440 nm	[116]
Bulk CdS	0.08	n/a	> 400 nm	[86]
Pt–CdS	0.85	83	> 400 nm	[117]
CdS nanorods	0.22	n/a	> 420 nm	[118]
Pt–CdS nanorods	4.46	n/a	> 420 nm	[118]
Pt–CdS–TNT	4.26	n/a	> 420 nm	[88]
CdS–TNT + WO_3	0.62	n/a	> 420 nm	[88]
Pt–CdS–QD	1.22	n/a	> 420 nm	[119]
CdS@Al-HMS	0.13	n/a	> 420 nm	[120]
Ru–CdS@Al-HMS	0.54	n/a	> 420 nm	[120]
CdS/ZnS nanoparticles	1.24	n/a	> 420 nm	[90]
Ru–CdS/ZnS nanoparticles	5.85	n/a	> 420 nm	[90]
Pd@C_3N_4	53.4	100	> 400 nm	[105]

most representative studies aiming at reporting on the photocatalytic decomposition of FA. In order to consider the most widely investigated photocatalytic systems studies for the present application, sections on TiO_2, CdS and C_3N_4-based photocatalysts have been included in this manuscript. These sections cite evidence that, as in the case of the thermal decomposition of FA, the addition of metal nanoparticles is vital to accelerate the photocatalytic process. In this context, Mott–Schottky photocatalysts have shown to be a very promising approach to adjust the surface charge density of the active metal phase, while decreasing the recombination of electron–holes pairs by transferring photogenerated electrons from the semiconductor supports to the metal active phase. Such electron-rich metal species are, in turn, more active in boosting hydrogen production from FA. This is particularly important for Pd-based catalysts. Moreover, it has been observed that the use of alloy nanoparticles further promotes the formation of electron-rich Pd species. In addition, the incorporation of agents to control the size and shape of nanoparticles are a useful resource to afford optimized performances. Particular attention has been paid to those systems containing plasmonic nanoparticles (PdAg and PdAu).

Aside from noble metal-containing photocatalysts, noble-metal-free systems have also been studied in this application. For instance, the utilization of heterojunction (i.e., CuO/TiO_2, CdS/Fe_2O_3, MoS_2/CdS, etc.) or core–shell structures (i.e. CdS@ ZIF-8, CdS–ZnS, etc.) has been shown to afford enhanced performances ascribed to efficient electron–hole pair separation at the interface. Such systems are also promising from an economic viewpoint. Furthermore, the importance of some other photocatalytic systems (i.e., MOFs, GO, NCQDs, etc.) has also been briefly mentioned.

This review highlights the applicability of photocatalysts in hydrogen production from LOHC. It is expected to provide the reader with an overview of the most representative approaches used so far for this application at a time when the research community is encouraged to further explore the exciting and barely investigated photocatalytic decomposition of FA. Although important breakthroughs have recently been achieved in the photodecomposition of FA, the materials used to date are far from being as sophisticated as those used for some other traditional photocatalytic applications. It could be envisaged that such important application will soon deserve new efforts towards the design of efficient photocatalytic systems. A point to consider in this respect is improvement of the stability of the photocatalysts, which has been shown to be lacking until now. Such aspects could be enhanced by engineering the optical properties of the materials used, as well as by controlling the adsorption of the reaction intermediates, which would eventually block the active sites. Furthermore, another point to consider is the development of photocatalysts with higher surface area that are able to provide a higher dispersion of the active sites. In this line, the combination of the traditionally used photocatalytic materials (i.e. TiO_2, CdS, *g*-C_3N_4) with a second component with a higher developed porosity (i.e., carbon materials, etc.) could be a resourceful alternative to afford highly efficient systems for the photodecomposition of FA.

Acknowledgments The present work was supported by JST, PRESTO (JPMJPR1544) and by Grants-in-Aid for Scientific Research (nos. 26220911, 25289289, and 26630409, 26620194) from the Japan Society for the Promotion of Science (JSPS) and MEXT and "Elemental Strategy Initiative to Form Core

Research Center". MNG gratefully acknowledge the financial support by the Generalitat Valenciana and Plan GenT (CDEIGENT/2018/027) for the financial support. DST thanks MICINN for a "Juan de la Cierva" contract (IJCI-2016-27636).

References

1. Kothandaraman J, Kar S, Sen R et al (2017) Efficient reversible hydrogen carrier system based on amine reforming of methanol. J Am Chem Soc 139:2549–2552
2. https://www.epa.gov/ghgemissions/understanding-global-warming-potentials. Accessed 7 May 2019
3. Pires JCM (2019) Negative emissions technologies: a complementary solution for climate change mitigation. Sci Total Environ 672:502–514
4. http://unfccc.int/paris_agreement/items/9485.php. Accessed 7 May 2019
5. Markiewicz M, Zhang YQ, Bösmann A et al (2015) Environmental and health impact assessment of Liquid Organic Hydrogen Carrier (LOHC) systems—challenges and preliminary results. Energy Environ Sci 8:1035–1045
6. Gahleitner G (2013) Hydrogen from renewable electricity: an international review of power-to-gas pilot plants for stationary applications. Int J Hydrogen Energy 38:2039–2061
7. Kousksou T, Bruel P, Jamil A et al (2014) Energy storage: applications and challenges. Sol Energy Mater Sol Cells 120:59–80
8. https://www.iea.org/publications/freepublications/publication/TechnologyRoadmapHydrogenandFuelCells.pdf. Accessed 7 May 2019
9. Aakko-Saksa PT, Cook C, Kiviaho J, Repo T (2018) Liquid organic hydrogen carriers for transportation and storing of renewable energy—review and discussion. J Power Sources 396:803–823
10. Dincer I, Acar C (2015) Review and evaluation of hydrogen production methods for better sustainability. Int J Hydrogen Energy 40:11094–11111
11. Niermann M, Drünert S, Kaltschmitt M, Bonhoff K (2019) Liquid organic hydrogen carriers (LOHCs)—techno-economic analysis of LOHCs in a defined process chain. Energy Environ Sci 12:290–307
12. Rigas F, Sklavounos S (2005) Evaluation of hazards associated with hydrogen storage facilities. Int J Hydrogen Energy 30:1501–1510
13. Edwards PP, Kuznetsov VL, David WIF, Brandon NP (2008) Hydrogen and fuel cells: towards a sustainable energy future. Energy Policy 36:4356–4362
14. Zheng J, Liu X, Xu P et al (2012) Development of high pressure gaseous hydrogen storage technologies. Int J Hydrogen Energy 37:1048–1057
15. Dadashzadeh M, Kashkarov S, Makarov D, Molkov V (2018) Risk assessment methodology for onboard hydrogen storage. Int J Hydrogen Energy 43:6462–6475
16. Lillo-Ródenas MA, Guo ZX, Aguey-Zinsou KF et al (2008) Effects of different carbon materials on MgH_2 decomposition. Carbon 46:126–137
17. Shi J, Kuwahara Y, Wen M et al (2016) Room-temperature and aqueous-phase synthesis of plasmonic molybdenum oxide nanoparticles for visible-light-enhanced hydrogen generation. Chem Asian J 11:2377–2381
18. Salinas-Torres D, Navlani-García M, Kuwahara Y et al (2019) Non-noble metal doped perovskite as a promising catalyst for ammonia borane dehydrogenation. Catal Today. https://doi.org/10.1016/j.cattod.2019.03.072
19. García-Aguilar J, Navlani-García M, Berenguer-Murcia Á et al (2016) Enhanced ammonia-borane decomposition by synergistic catalysis using CoPd nanoparticles supported on titano-silicates. RSC Adv 6:91768–91772
20. Navlani-garcía M, Verma P, Kuwahara Y et al (2018) Visible-light-enhanced catalytic activity of Ru nanoparticles over carbon modified g-C3N4. J Photochem Photobiol A 358:327–333
21. Fuku K, Kamegawa T, Mori K, Yamashita H (2012) Highly dispersed platinum nanoparticles on TiO_2 prepared by using the microwave-assisted deposition method: an efficient photocatalyst for the formation of H_2 and N_2 from aqueous NH_3. Chem Asian J 7:1366–1371
22. Lan R, Irvine JTS, Tao S (2012) Ammonia and related chemicals as potential indirect hydrogen storage materials. Int J Hydrogen Energy 37:1482–1494

23. Afif A, Radenahmad N, Cheok Q et al (2016) Ammonia-fed fuel cells: a comprehensive review. Renew Sustain Energy Rev 60:822–835
24. Chowdhury AD, Agnihotri N, De A (2015) Hydrolysis of sodium borohydride using Ru-Co-PEDOT nanocomposites as catalyst. Chem Eng J 264:531–537
25. Dalebrook AF, Gan W, Grasemann M et al (2013) Hydrogen storage: beyond conventional methods. Chem Commun 49:8735–8751
26. Preuster P, Papp C, Wasserscheid P (2017) Liquid Organic Hydrogen Carriers (LOHCs): toward a hydrogen-free hydrogen economy. Acc Chem Res 50:74–85
27. Niermann M, Beckendorff A, Kaltschmitt M, Bonhoff K (2019) Liquid Organic Hydrogen Carrier (LOHC)—assessment based on chemical and economic properties. Int J Hydrogen Energy 44:6631–6654
28. Hu P, Fogler E, Diskin-Posner Y et al (2015) A novel liquid organic hydrogen carrier system based on catalytic peptide formation and hydrogenation. Nat Commun 6:6859
29. Mori K, Dojo M, Yamashita H (2013) Pd and Pd–Ag nanoparticles within a macroreticular basic resin: an efficient catalyst for hydrogen production from formic acid decomposition. ACS Catal 3:1114–1119
30. Navlani-García M, Mori K, Kuwahara Y, Yamashita H (2018) Recent strategies targeting efficient hydrogen production from chemical hydrogen storage materials over carbon-supported catalysts. NPG Asia Mater 2018:1–16
31. Navlani-García M, Mori K, Salinas-Torres D et al (2019) New approaches toward the hydrogen production from formic acid dehydrogenation over Pd-based heterogeneous catalysts. Front Mater 6:44
32. García-Aguilar J, Navlani-García M, Berenguer-Murcia Á et al (2016) Evolution of the PVP–Pd surface interaction in nanoparticles through the case study of formic acid decomposition. Langmuir 32:12110–12118
33. Podyacheva OY, Bulushev DA, Suboch AN et al (2018) Highly stable single-atom catalyst with ionic Pd active sites supported on N-doped carbon nanotubes for formic acid decomposition. Chemsuschem 11:3724–3727
34. Bulushev DA, Zacharska M, Shlyakhova EV et al (2016) Single isolated Pd^{2+} cations supported on N-doped carbon as active sites for hydrogen production from formic acid decomposition. ACS Catal 6:681–691
35. Bulushev DA, Bulusheva LG, Beloshapkin S et al (2015) Pd clusters supported on amorphous, low-porosity carbon spheres for hydrogen production from formic acid. ACS Appl Mater Interfaces 7:8719–8726
36. Mellmann D, Sponholz P, Junge H, Beller M (2016) Formic acid as a hydrogen storage material-development of homogeneous catalysts for selective hydrogen release. Chem Soc Rev 45:3954–3988
37. Enthaler S, Von Langermann J, Schmidt T (2010) Carbon dioxide and formic acid—the couple for environmental-friendly hydrogen storage? Energy Environ Sci 3:1207–1217
38. Coffey RS (1967) The decomposition of formic acid catalysed by soluble metal complexes. Chem Commun 1967:923–924
39. Fellay C, Dyson PJ, Laurenczy G (2008) A viable hydrogen-storage system based on selective formic acid decomposition with a ruthenium catalyst. Angew Chemie Int Ed 47:3966–3968
40. Loges B, Boddien A, Junge H, Beller M (2008) Controlled generation of hydrogen from formic acid amine adducts at room temperature and application in H_2/O_2 fuel cells. Angew Chem Int Ed 47:3962–3965
41. Iglesias M, Oro LA (2018) Mechanistic considerations on homogeneously catalyzed formic acid dehydrogenation. Eur J Inorg Chem 2018:2125–2138
42. Navlani-García M, Mori K, Nozaki A et al (2016) Investigation of size sensitivity in the hydrogen production from formic acid over carbon-supported Pd nanoparticles. Chem Sel 1:1879–1886
43. Navlani-García M, Mori K, Nozaki A et al (2016) Screening of carbon-supported PdAg nanoparticles in the hydrogen production from formic acid. Ind Eng Chem Res 55:7612–7620
44. Navlani-García M, Salinas-Torres D, Mori K et al (2018) Enhanced formic acid dehydrogenation by the synergistic alloying effect of PdCo catalysts supported on graphitic carbon nitride. Int J Hydrogen Energy (in press) https://doi.org/10.1016/j.ijhydene.2018.11.057
45. Sun J, Qiu H, Cao W et al (2019) Ultrafine Pd particles embedded in nitrogen-enriched mesoporous carbon for efficient H_2 production from formic acid decomposition. ACS Sustain Chem Eng 7:1963–1972

46. Mori K, Sano T, Kobayashi H, Yamashita H (2018) Surface engineering of a supported PdAg catalyst for hydrogenation of CO_2 to formic acid: elucidating the active Pd atoms in alloy nanoparticles. J Am Chem Soc 140:8902–8909
47. Salinas-Torres D, Navlani-García M, Mori K et al (2019) Nitrogen-doped carbon materials as a promising platform toward the efficient catalysis for hydrogen generation. Appl Catal A Gen 571:25–41
48. Navlani-García M, Martis M, Lozano-Castelló D et al (2015) Investigation of Pd nanoparticles supported on zeolites for hydrogen production from formic acid dehydrogenation. Catal Sci Technol 5:364–371
49. Navlani-García M, Salinas-Torres D, Mori K et al (2019) Insights on palladium decorated nitrogen-doped carbon xerogels for the hydrogen production from formic acid. Catal Today 324:90–96
50. Wu Y, Wen M, Navlani-García M et al (2017) Palladium nanoparticles supported on titanium doped graphitic carbon nitride for formic acid dehydrogenation. Chem Asian J 12:860–867
51. Navlani-García M, Miguel-García I, Berenguer-Murcia Á et al (2016) Pd/zeolite-based catalysts for the preferential CO oxidation reaction: ion-exchange, Si/Al and structure effect. Catal Sci Technol 6:2623–2632
52. Zhang S, Li M, Zhao J et al (2019) Plasmonic AuPd-based Mott–Schottky photocatalyst for synergistically enhanced hydrogen evolution from formic acid and aldehyde. Appl Catal B Environ 252:24–32
53. Kim JH, Hansora D, Sharma P et al (2019) Toward practical solar hydrogen production—an artificial photosynthetic leaf-to-farm challenge. Chem Soc Rev 48:1908–1971
54. Takata T, Domen K (2019) Particulate photocatalysts for water splitting: recent advances and future prospects. ACS Energy Lett 4:542–549
55. Murdoch, Waterhouse, Nadeem et al (2010) Photocatalytic hydrogen production from ethanol over Au/TiO_2 anatase and rutile nanoparticles: effect of Au particle size. ACS Natl Meet B Abstr 3:1
56. Gallo A, Marelli M, Psaro R et al (2012) Bimetallic Au–Pt/TiO_2 photocatalysts active under UV-A and simulated sunlight for H_2 production from ethanol. Green Chem 14:330–333
57. Wu N-L, Lee M-S (2004) Enhanced TiO_2 photocatalysis by Cu in hydrogen production from aqueous methanol solution. Int J Hydrogen Energy 29:1601–1605
58. Jing D, Guo L (2007) Hydrogen production over Fe-doped tantalum oxide from an aqueous methanol solution under the light irradiation. J Phys Chem Solids 68:2363–2369
59. Montini T, Monai M, Beltram A et al (2016) H_2 production by photocatalytic reforming of oxygenated compounds using TiO_2-based materials. Mater Sci Semicond Process 42:122–130
60. de Oliveira Melo M, Silva LA (2011) Visible light-induced hydrogen production from glycerol aqueous solution on hybrid Pt–CdS–TiO_2 photocatalysts. J Photochem Photobiol A Chem 226:36–41
61. Jana MK, Gupta U, Rao CNR (2016) Hydrazine as a hydrogen carrier in the photocatalytic generation of H2 using CdS quantum dots. Dalt Trans 45:15137–15141
62. Yuzawa H, Mori T, Itoh H, Yoshida H (2012) Reaction mechanism of ammonia decomposition to nitrogen and hydrogen over metal loaded titanium oxide photocatalyst. J Phys Chem C 116:4126–4136
63. Reli M, Ambrožová N, Šihor M et al (2015) Novel cerium doped titania catalysts for photocatalytic decomposition of ammonia. Appl Catal B Environ 178:108–116
64. Liu P-H, Wen M, Tan C-S et al (2017) Surface plasmon resonance enhancement of production of H_2 from ammonia borane solution with tunable $Cu_{2-x}S$ nanowires decorated by Pd nanoparticles. Nano Energy 31:57–63
65. Verma P, Yuan K, Kuwahara Y et al (2018) Enhancement of plasmonic activity by Pt/Ag bimetallic nanocatalyst supported on mesoporous silica in the hydrogen production from hydrogen storage material. Appl Catal B Environ 223:10–15
66. Ji Y, Luo Y (2016) Structure-dependent photocatalytic decomposition of formic acid on the anatase TiO_2(101) surface and strategies to increase its reaction rate. J Power Sources 306:208–212
67. Civiš S, Ferus M, Zukalová M et al (2012) Photochemistry and gas-phase FTIR spectroscopy of formic acid interaction with anatase $Ti_{18}O_2$ nanoparticles. J Phys Chem C 116:11200–11205
68. Liu S, Yu J, Jaroniec M (2011) Anatase TiO_2 with dominant high-energy 001 facets: synthesis, properties, and applications. Chem Mater 23:4085–4093
69. Roy P, Berger S, Schmuki P (2011) TiO_2 nanotubes: synthesis and applications. Angew Chem Int Ed 50:2904–2939

70. Fujishima A, Honda K (1972) Electrochemical photolysis of water at a semiconductor electrode. Nature 238:37–38
71. Fujishima A, Zhang X (2006) Titanium dioxide photocatalysis: present situation and future approaches. Comptes Rendus Chim 9:750–760
72. Kumaravel V, Mathew S, Bartlett J, Pillai SC (2019) Photocatalytic hydrogen production using metal doped TiO_2: a review of recent advances. Appl Catal B Environ 244:1021–1064
73. Ma D, Liu A, Li S et al (2018) TiO_2 photocatalysis for C–C bond formation. Catal Sci Technol 8:2030–2045
74. Fernández-Catalá J, Cazorla-Amorós D, Berenguer-Murcia Á (2018) Facile encapsulation of P25 (TiO_2) in spherical silica with hierarchical porosity with enhanced photocatalytic properties for gas-phase propene oxidation. Appl Catal A Gen 564:123–132
75. Cano-Casanova L, Amorós-Pérez A, Ouzzine M et al (2018) One step hydrothermal synthesis of TiO_2 with variable HCl concentration: detailed characterization and photocatalytic activity in propene oxidation. Appl Catal B Environ 220:645–653
76. Amorós-Pérez A, Cano-Casanova L, Lillo-Ródenas MÁ, Román-Martínez MC (2017) Cu/TiO_2 photocatalysts for the conversion of acetic acid into biogas and hydrogen. Catal Today 287:78–84
77. Song R, Luo B, Liu M et al (2017) Synergetic coupling of photo and thermal energy for efficient hydrogen production by formic acid reforming. AIChE J 63:2916–2925
78. Liu P, Cai Z, You Y et al (2018) Surface modification on Pd–TiO_2 hybrid nanostructures towards highly efficient H_2 production from catalytic formic acid decomposition. Chem A Eur J 24:18398–18402
79. Tsuji M, Shimamoto D, Uto K et al (2016) Enhancement of catalytic activity of AgPd@Pd/TiO_2 nanoparticles under UV and visible photoirradiation. J Mater Chem A 4:14649–14656
80. Zhang Z, Cao S, Liao Y, Xue C (2015) Selective photocatalytic decomposition of formic acid over AuPd nanoparticle-decorated TiO_2 nanofibers toward high-yield hydrogen production. Appl Catal B Environ 162:204–209
81. Wu M, Zhang M, Lv T et al (2017) The effect of calcination atmosphere upon the photocatalytic performance of Au–La_2O_3/TiO_2 for hydrogen production from formic acid. Appl Catal A Gen 547:96–104
82. Clarizia L, Di Somma I, Marotta R, Minutolo P, Villamaina R, Andreozzi R (2016) Photocatalytic reforming of formic acid for hydrogen production in Aqueous solutions containing cupric ions and TiO2 suspended nanoparticles under UV-simulated solar radiation. Appl Catal A Gen 518:181–188
83. Zhang Z, Liu K, Bao Y, Dong B (2017) Photo-assisted self-optimizing of charge-carriers transport channel in the recrystallized multi-heterojunction nanofibers for highly efficient photocatalytic H_2 generation. Appl Catal B Environ 203:599–606
84. Li Q, Li X, Wageh S et al (2015) CdS/graphene nanocomposite photocatalysts. Adv Energy Mater 5:1500010
85. Tada H, Naya S-I, Fujishima M (2018) Water splitting by plasmonic photocatalysts with a gold nanoparticle/cadmium sulfide heteroepitaxial junction: a mini review. Electrochem Commun 97:22–26
86. Willner I, Goren Z (1986) Photodecomposition of formic acid by cadmium sulphide semiconductor particles. J Chem Soc Chem Commun 1986:172–173
87. Nedoluzhko AI, Shumilin IA, Nikandrov VV (1996) Coupled action of cadmium metal and hydrogenase in formate photodecomposition sensitized by CdS. J Phys Chem 100:17544–17550
88. Yeh HM, Lo SL, Chen MJ, Chen HY (2014) Hydrogen production from formic acid solution by modified TiO_2 and titanate nanotubes in a two-step system under visible light irradiation. Water Sci Technol 69:1676–1681
89. Chen H-Y, Lo S-L, Lai Y-C, Liou Y-H (2018) Titanate nanotubes coupled with Pt nanoparticles for the inhibition of CdS photocorrosion during visible-light-driven hydrogen production from formic acid. Mater Res Express 5:9
90. Wang X, Peng W-C, Li X-Y (2014) Photocatalytic hydrogen generation with simultaneous organic degradation by composite CdS–ZnS nanoparticles under visible light. Int J Hydrogen Energy 39:13454–13461
91. Zeng M, Chai Z, Deng X et al (2016) Core–shell CdS@ZIF-8 structures for improved selectivity in photocatalytic H_2 generation from formic acid. Nano Res 9:2729–2734
92. Zhang YJ, Zhang L (2009) Preparation of Ru-loaded CdS/Al-HMS nanocomposites and production of hydrogen by photocatalytic degradation of formic acid. Appl Surf Sci 255:4863–4866

93. Kuehnel MF, Wakerley DW, Orchard KL, Reisner E (2015) Photocatalytic formic acid conversion on CdS nanocrystals with controllable selectivity for H_2 or CO. Angew Chem Int Ed 54:9627–9631
94. Cao S, Chen Y, Wang H et al (2018) Ultrasmall CoP nanoparticles as efficient cocatalysts for photocatalytic formic acid dehydrogenation. Joule 2:549–557
95. Nasir JA, Hafeez M, Arshad M et al (2018) Photocatalytic dehydrogenation of formic acid on CdS nanorods through Ni and Co redox mediation under mild conditions. Chemsuschem 11:2587–2592
96. Dong F, Zhao Z, Xiong T et al (2013) In situ construction of g-C_3N_4/g-C_3N_4 metal-free heterojunction for enhanced visible-light photocatalysis. ACS Appl Mater Interfaces 5:11392–11401
97. Huang H, Yang S, Vajtai R et al (2014) Pt-decorated 3D architectures built from graphene and graphitic carbon nitride nanosheets as efficient methanol oxidation catalysts. Adv Mater 26:5160–5165
98. Ong W-J, Tan L-L, Ng YH et al (2016) Graphitic carbon nitride (g-C_3N_4)-based photocatalysts for artificial photosynthesis and environmental remediation: are we a step closer to achieving sustainability? Chem Rev 116:7159–7329
99. Goettmann F, Fischer A, Antonietti M, Thomas A (2006) Metal-free catalysis of sustainable Friedel–Crafts reactions: direct activation of benzene by carbon nitrides to avoid the use of metal chlorides and halogenated compounds. Chem Commun 2006:4530–4532
100. Wang X, Maeda K, Thomas A et al (2009) A metal-free polymeric photocatalyst for hydrogen production from water under visible light. Nat Mater 8:76–80
101. Fu J, Yu J, Jiang C, Cheng B (2018) g-C_3N_4-based heterostructured photocatalysts. Adv Energy Mater 8:1701503
102. Mamba G, Mishra AK (2016) Graphitic carbon nitride (g-C_3N_4) nanocomposites: a new and exciting generation of visible light driven photocatalysts for environmental pollution remediation. Appl Catal B Environ 198:347–377
103. Fajrina N, Tahir M (2019) A critical review in strategies to improve photocatalytic water splitting towards hydrogen production. Int J Hydrogen Energy 44:540–577
104. Xiao L, Jun Y-S, Wu B et al (2017) Carbon nitride supported AgPd alloy nanocatalysts for dehydrogenation of formic acid under visible light. J Mater Chem A 5:6382–6387
105. Photocatalyst NMS, Cai Y, Li X et al (2013) Highly efficient dehydrogenation of formic acid over a palladium. Angew Chem 125:1–5
106. Liu H, Liu X, Yang W et al (2019) Photocatalytic dehydrogenation of formic acid promoted by a superior PdAg@g-C3N4 Mott–Schottky heterojunction. J Mater Chem A 7:2022
107. Tsutsumi K, Kashimura N, Tabata K (2015) Photo-assisted hydrogen evolution in aqueous solution of formic acid with silicon which is supported with noble metals. Silicon 7:43–48
108. Wu B, Lee J, Mubeen S et al (2016) Plasmon-mediated photocatalytic decomposition of formic acid on palladium. Nanostructures 4:1041–1046
109. Kakuta S, Abe T (2009) A novel example of molecular hydrogen generation from formic acid at visible-light-responsive photocatalyst. ACS Appl Mater Interfaces 1:2707–2710
110. Han L, Zhang L, Wu H et al (2019) Anchoring Pt single atoms on Te nanowires for plasmon-enhanced dehydrogenation of formic acid at room temperature. Adv Sci. https://doi.org/10.1002/advs.201900006
111. Liu P, Gu X, Zhang H et al (2017) Visible-light-driven catalytic activity enhancement of Pd in AuPd nanoparticles for hydrogen evolution from formic acid at room temperature. Appl Catal B Environ 204:497–504
112. Wen M, Mori K, Kuwahara Y, Yamashita H (2017) Plasmonic Au@Pd nanoparticles supported on a basic metal-organic framework: synergic boosting of H_2 production from formic acid. ACS Energy Lett 2:1–7
113. Wei J, Wang H, Zhang Q, Li Y (2015) One-pot hydrothermal synthesis of N-doped carbon quantum dots using the waste of shrimp for hydrogen evolution from formic acid. Chem Lett 44:241–243
114. Li Y, He F, Peng S et al (2011) Effects of electrolyte NaCl on photocatalytic hydrogen evolution in the presence of electron donors over Pt/TiO_2. J Mol Catal A Chem 341:71–76
115. Lanese V, Spasiano D, Marotta R et al (2013) Hydrogen production by photoreforming of formic acid in aqueous copper/TiO_2 suspensions under UV-simulated solar radiation at room temperature. Int J Hydrogen Energy 38:9644–9654
116. Halasi G, Schubert G, Solymosi F (2012) Photolysis of HCOOH over Rh deposited on pure and N-modified TiO_2: production of pure H_2. Catal Lett 142:218–223
117. Matsumura M, Hiramoto M, Iehara T, Tsubomura H (1984) Photocatalytic and photoelectrochemical reactions of aqueous solutions of formic acid, formaldehyde, and methanol on platinized CdS powder and at a CdS electrode. J Phys Chem 88:248–250

118. Li Y, Hu Y, Peng S et al (2009) Synthesis of CdS nanorods by an ethylenediamine assisted hydrothermal method for photocatalytic hydrogen evolution. J Phys Chem C 113:9352–9358
119. Li Y, Tang L, Peng S et al (2012) Phosphate-assisted hydrothermal synthesis of hexagonal CdS for efficient photocatalytic hydrogen evolution. Cryst Eng Comm 14:6974–6982
120. Zhang YJ, Zhang L, Li S (2010) Synthesis of Al-substituted mesoporous silica coupled with CdS nanoparticles for photocatalytic generation of hydrogen. Int J Hydrogen Energy 35:438–444

Topics in Current Chemistry (2020) 378:7
https://doi.org/10.1007/s41061-019-0272-1

REVIEW

Limitations and Prospects for Wastewater Treatment by UV and Visible-Light-Active Heterogeneous Photocatalysis: A Critical Review

Giuseppina Iervolino[1] · Ian Zammit[2] · Vincenzo Vaiano[1] · Luigi Rizzo[2]

Received: 12 July 2019 / Accepted: 26 November 2019 / Published online: 16 December 2019

Abstract

Heterogeneous photocatalysis (HPC) has been widely investigated in recent decades for the removal of a number of contaminants from aqueous matrices, but its application in real wastewater treatment at full scale is still scarce. Indeed, process and technological limitations have made HPC uncompetitive with respect to consolidated processes/technologies so far. In this manuscript, these issues are critically discussed and reviewed with the aim of providing the reader with a realistic picture of the prospective application of HPC in wastewater treatment. Accordingly, consolidated and new photocatalysts (among which the visible active ones are attracting increasing interest among the scientific community), along with preparation methods, are reviewed to understand whether, with increased process efficiency, these methods can be realistically and competitively developed at industrial scale. Precipitation is considered as an attractive method for photocatalyst preparation at the industrial scale; sol–gel and ultrasound may be feasible only if no expensive metal precursor is used, while hydrothermal and solution combustion synthesis are expected to be difficult (expensive) to scale up. The application of HPC in urban and industrial wastewater treatment and possible energy recovery by hydrogen production are discussed in terms of current limitations and future prospects. Despite the fact that HPC has been studied for the removal of pollutants in aqueous matrices for two decades, its use in wastewater treatment is still at a "technological research" stage. In order to accelerate the adoption of HPC at full scale, it is advisable to focus on investigations under real conditions and on developing/improving pilot-scale reactors to better investigate scale-up conditions and the potential to successfully address specific challenges in wastewater treatment through HPC. In realistic terms, the prospective use of HPC is more likely as a tertiary treatment of wastewater, particularly if more stringent regulations come into force, than as pretreatment for industrial wastewater to improve biodegradability.

Chapter 7 was originally published as Iervolino, G., Zammit, I., Vaiano, V. & Rizzo, L. Topics in Current Chemistry (2020) 378: 7. https://doi.org/10.1007/s41061-019-0272-1.

Extended author information available on the last page of the article

Keywords Energy recovery · Hydrogen production · Industrial wastewater · Photocatalysis · Technology readiness level · Urban wastewater

1 Introduction

New challenges in wastewater treatment [e.g., the removal of contaminants of emerging concern (CECs) from municipal wastewater treatment plant effluents], the increasing interest/demand for sustainable wastewater treatment methods, and a circular economic approach (e.g., energy saving and recovery, mass recovery from waste, and water reuse) are leading to the investigation and development of increasingly effective wastewater treatment processes and technologies. The main problem is related to the presence of non-biodegradable substances (organic and inorganic) including metals, pharmaceutical compounds, and personal care products, which persist in water and in the environment, causing serious damage to the ecosystem and to human health. For this reason, the study of advanced oxidation processes (AOPs) has increased significantly in recent years. AOPs are characterized by the presence of highly reactive species able to remove and mineralize refractory organic compounds, water pathogens, and disinfection by-products [1]. Among these processes, heterogeneous photocatalysis (HPC) has been proven to be effective in the degradation of a wide range of refractory organic compounds. However, its application in water and wastewater treatment at full scale is far from being successfully implemented due to the complexity of the various real aqueous matrices as well as limitations in the process (e.g., low photoconversion efficiency) and technological limitations (i.e., catalyst preparation method, slurry vs. supported system, reactor design, energy consumption, etc.). In an effort to improve process efficiency while minimizing energy cost, the new trend in HPC research deals with the formulation of semiconductors active in the presence of visible light. In this review these issues were addressed with regard to the application of HPC in urban and industrial wastewater treatment as well as energy recovery through hydrogen production during treatment, by explaining and critically discussing possible advantages and disadvantages of the process. The scope was to provide the reader with some information and tools to understand the current knowledge gaps as well as to evaluate prospective applications of HPC in the treatment of wastewater.

2 Heterogeneous Photocatalysis: An Overview of Consolidated and New Photocatalysts as well as Preparation Methods

Heterogeneous photocatalysis relies on the interaction between a light source and a solid semiconductor in an aqueous matrix. Depending on the emission spectrum of the light source and the characteristics of the semiconductor (photocatalyst), electrons are promoted from the valence band to the conduction band of the photocatalyst, thus initiating a surface reaction will ultimately result in the formation of highly oxidizing agents, such as hydroxyl radicals ($^{\cdot}$OH). The efficiency of the HPC process in water/wastewater treatment will depend on the capacity of the system to

effectively produce such radicals, which can degrade/oxidize a wide range of contaminants as well as effectively inactivate microorganisms.

The development of photocatalysts should take into account the typical characteristics and requirements for photocatalytic materials. In particular, a photocatalyst must be photoactive, inert, stable, non-toxic, and relatively cheap [2]. One of the most studied photocatalyst for water/wastewater treatment is titanium dioxide (TiO_2). TiO_2 has been widely investigated because of its very high ultraviolet absorption and high stability. These properties made this photocatalyst ideal for different applications, such as electroceramics, glass, and photocatalytic degradation of chemicals in water and air. It has been investigated in powdered form suspended in aqueous matrices (slurry reactor) or as thin film. TiO_2 presents three different crystalline forms: anatase, rutile (more stable), and brookite (uncommon and unstable). Degussa P25 titania is commercially available and consists of 25% rutile and 75% anatase crystalline phases [3]. P25 is used as a benchmark in water and wastewater treatment by TiO_2 photocatalysis due to its easy availability, reproducibility, chemical stability, and high photoactivity [4–8]. Beyond TiO_2, another interesting photocatalyst with properties similar to titania is ZnO. This photocatalyst has recently attracted increasing attention from the scientific community for its characteristics that include strong oxidation ability, good photocatalytic properties large free-exciton binding energy, and low cost (cheaper than TiO_2) [9]. Another category of semiconductors that has found success in photocatalytic applications for water treatment is represented by perovskites, in particular $LaFeO_3$ [10, 11]. $LaFeO_3$ is one of the most common perovskite-type oxides, and it is a promising material with different functionalities, having a general formula ABO_3, where position *A* is the rare earth ion and position *B* is represented by metal ion. This material is characterized by high stability, non-toxicity, and small bandgap energy (2.07 eV), making perovskite an interesting visible-light-active photocatalyst [12].

2.1 Methods for Improving Photocatalyst Activity

The application of photocatalysts such as TiO_2 and ZnO is limited by the fact that ultraviolet (UV) activation is needed (the bandgap energy is about 3.2 eV, and this means that less than 5% of the solar spectrum has sufficient energy to activate the photocatalyst) and by the fast recombination rate of the electron–hole pairs generated [13]. Hence, modification of photocatalysts through metal or non-metal doping or their combination with another semiconductor are common methods used to improve the photocatalytic performance and for activation by visible light irradiation. The particle size and morphology of nanoscale photocatalysts is also a problem in full-scale application for water and wastewater treatment, because the particles should be removed/recovered after treatment. To overcome this drawback, the application of photocatalytic membranes or the use of other photocatalyst-supporting materials has been proposed [14–16]. For example, photocatalysts have been supported on activated carbon [14], fibers, [17, 18] membranes, [19, 20] metal [5], and plastics [21]. In this section, the main methods for the synthesis of modified photocatalysts used in wastewater treatment are introduced, along with the methods

developed for supporting photocatalysts on suitable materials in order to make them usable on a large scale.

A number of methods can be used to extend the light absorption properties of traditional semiconductors (e.g., ZnO or TiO_2) into the visible range, including:

- Coupling a primary photocatalyst with different semiconductors with a smaller bandgap or through sensitization with dyes.
- Doping the photocatalyst with metals (second-generation photocatalysts).
- Doping the photocatalyst with non-metals (third-generation photocatalysts).

2.1.1 Coupling a Primary Photocatalyst with Smaller-Bandgap Semiconductor or Its Sensitization with Dye

As a semiconductor (e.g., TiO_2 or ZnO) with a wide bandgap is coupled with other semiconductors having a lower bandgap or is sensitized with specific types of dyes, the absorption properties of the obtained composite are extended into the visible region. This phenomenon is induced either by the light absorption characteristics of the dye or by the other semiconductor coupled with TiO_2 or ZnO. When a semiconductor is sensitized with a dye, the visible light is absorbed by the dye molecules bridged to the semiconductor surface, and the electrons pass from the dye's ground state to an excited state. These excited electrons are then transferred to the conduction band of ZnO or TiO_2, which results in a modified photocatalyst with improved photoactivity under visible light. Dyes that have been used for this purpose include ruthenium polypyridyl complexes [22] and different metal-free organic dye molecules such as hemicyanine [23] and indoline [24]. However, it is worth noting that the low stability of the dye used for the sensitization of semiconductors in water/wastewater is the main drawback of this method.

With regard to the coupling of two semiconductors, the aim is to form a heterojunction structure between TiO_2 or ZnO and a narrow-bandgap semiconductor such as CdS, MoS_2, or In_2S_3 [25]. The electrons excited by visible light are transferred to TiO_2 or ZnO from the narrow-bandgap semiconductor, thus promoting charge carrier separation and, consequently, improving the visible-light photocatalytic activity of the composite [25]. In order to improve ZnO (bandgap of 3.2 eV) activity under visible light, photocatalysts have also been coupled with $LaFeO_3$. This composite was prepared by a process known as solution combustion synthesis, using citric acid as the organic fuel and metal nitrates, thus drastically affecting the bandgap energy, which decreased from 3.2 to 1.94 eV [26]. However, although this method might represent a suitable approach for preparing photocatalysts that work effectively under visible light, the coupling between semiconductors can suffer from the photocorrosion phenomenon, negatively affecting the photocatalytic activity [27–29].

2.1.2 Photocatalyst Doping with Metals

In order to improve the photocatalytic efficiency of primary photocatalysts under visible light, TiO_2 and ZnO were also doped with metals (second-generation visible-light-active photocatalysts), by inserting a metal ion in the crystalline structure

of the semiconductor. Generally, doping with metal ions is able to generate further energy levels between the valence band and conduction band of the undoped semiconductor, shifting the absorption properties in the visible region due to the decrease in bandgap energy of TiO_2 or ZnO. Several metals have been investigated in the synthesis of second-generation visible active photocatalysts, such as Mn, Fe, Co, Ni, Cu for ZnO [5, 30, 31] or Mo, Cr, La, Er, Ce for TiO_2 [32]. The main drawback of this type of doping is that metal ions could act as recombination centers of electron–hole pairs, reducing the photocatalytic activity [33, 34].

2.1.3 Photocatalyst Doping with Non-Metals

With together the second-generation visible active photocatalysts are of concern, ZnO or TiO_2 doped with non-metals element (third-generation visible active photocatalysts) have been widely investigated. The doping with non-metals can significantly extend the visible light absorption of the doped-photocatalysts and minimize photogenerated charge recombination [35]. Doping process with non-metals (mainly anion of C, N, F, P or S) aims to replace oxygen atoms with these elements in the semiconductor lattice. The high activity under visible light irradiation of the third-generation visible active photocatalysts is due to the decrease of their bandgap by mixing *p* orbital of the anions with 2*p* orbital of oxygen [32, 36]. Moreover, the inclusion of these elements in the semiconductor crystalline structure causes the formation of some defects that delay the recombination of the photo-excited species [37, 38].

2.2 Photocatalyst Preparation Methods

One of the main limitations of the application of photocatalytic processes to wastewater treatment at full scale is related to the preparation of the photocatalysts, which significantly affects the cost of the process, particularly compared with homogenous photo-driven AOPs [103, 150]. Unlike HPC technology, which is expensive to produce in terms of photocatalyst preparation and reactor design, UV/H_2O_2 is easy to implement, and H_2O_2 is widely available commercially. In order to provide a contribution to fill this gap, the easiest and possibly most cost-effective preparation methods for the synthesis of pure or doped semiconductors are summarized and discussed in the following subsections. A comparison summarizing the main advantages, disadvantages, and prospective applications at large industrial scale is also proposed.

2.2.1 Sol–Gel Method

Sol–gel is the most commonly used method for the preparation of photocatalysts. A sol is made by solid particles homogeneously dispersed in a liquid medium in colloidal form, whereas a gel is an organized three-dimensional continuous solid arrangement having sub-micrometer-sized pores in which the liquid phase is present. During sol–gel synthesis, the sol is produced from the hydrolysis and polymerization

reactions of the precursors (usually metal alkoxides). Briefly, the sol–gel method involves four basic steps: hydrolysis, polycondensation, drying, and thermal decomposition of precursors. A schematic of the sol–gel process for the preparation of TiO_2-based photocatalysts is showed in Fig. 1 [32].

Typically, a solution containing a precursor salt of the doping element (metal or non-metal) is added as the sol is formed. In this way, strong covalent bonds are created between the dopant element and the very reactive monomeric species of the precursor of the semiconductor (e.g., TiO_2 or ZnO). Several photocatalysts active under visible light have been prepared by the sol–gel process, including TiO_2 doped with nitrogen, boron [39], cerium [40], fluorine [41], iron, zinc [42], molybdenum, and chromium [43]. In addition, ZnO has been doped with different metals and non-metals (e.g., nitrogen, aluminum, silver, copper, cobalt) [44–48].

A Sol–gel method was also recently used for doping ZrO_2, a metal oxide with a very large bandgap (about 5 eV), an energy corresponding to a negligible fraction of the solar light at the earth's surface [49]. In this case, sol–gel synthesis was carried out using Ce isopropoxide and Zr propoxide solutions. Sol–gel synthesis has also been coupled with a dip-coating procedure to immobilize visible active photocatalysts on macroscopic and transparent supports in order to formulate structured photocatalysts for use in water/wastewater treatment applications. For example, an N-doped photocatalyst was immobilized on glass spheres and tested for the removal of organic dyes from wastewater under visible light irradiation [50]. In the preparation procedure, triton X-100 (used as binder) was dissolved in isopropyl alcohol, and the pH of the solution was adjusted with nitric acid to about pH 2. Titanium isopropoxide, used as titanium precursor, was then added to the mixture [50]. The N-doped TiO_2 coating was achieved by leaving the glass spheres in the solution for 10 min, with subsequent calcination for 30 min at 450 °C. This method was able to obtain N-doped TiO_2 nanoparticles which were well dispersed on a glass substrate.

2.2.2 Hydrothermal Synthesis

Hydrothermal synthesis requires the use of high temperature and water pressure. When another solvent is used instead of water, this method is known as "solvothermal" [51]. The synthesis of photocatalysts with this method is typically carried out in steel vessels operating at high pressure (autoclaves) under controlled temperature, and the formation of nano-catalysts takes place in the liquid medium [52].

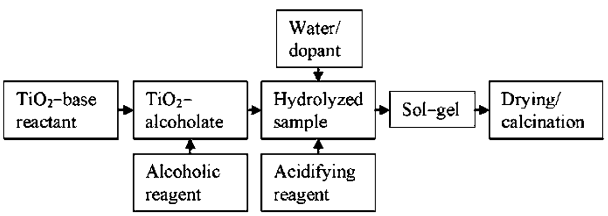

Fig. 1 Preparation of TiO_2-based photocatalysts by sol–gel method [32]

This method has been found to be very effective for incorporating dopants into the crystalline structure of TiO_2 or ZnO. Because of the high photocatalytic activity achieved by the controlled synthesis of hollow TiO_2 particles, it has attracted much interest among the scientific community [53]. For example, Zhou et al. prepared flower-like F-doped TiO_2 hollow microspheres using a hydrothermal synthesis method by controlling the hydrolysis of TiF_4 in a autoclave lined with Teflon at a reaction temperature of 180 °C [54].

2.2.3 Precipitation Method

The preparation of photocatalysts through the precipitation method consists of the chemical transformation of a highly soluble metal precursor into another substance of lower solubility, which precipitates in solution. The conversion into the low-solubility compound (and then into the precipitate) is usually obtained by changing (generally by increasing) the pH of the solution [55]. To avoid a rapid precipitation in solution (that can cause a strong increase in particle size), it is better if the mixing and the generation of the precipitant are carried out separately. At the laboratory scale, this is possible through the use of a base. The precipitation method using a base has been applied for the preparation of various catalysts. Upon increasing the pH of the solution, the precipitation of a hydroxide is induced. The semiconductor typically prepared through this method is ZnO. In particular, the preparation involves the reaction of zinc salts such as $Zn(NO_3)_2$, $Zn(CH_3COO)_2$, or $ZnSO_4$ with solutions containing NH_4OH, NaOH, etc. [56, 57]. For the doping of ZnO with metals in order to shift its absorption to the visible region, the precursor salt of the doping element can be added to the solution of the zinc precursor before inducing precipitation [9, 58, 59]. The obtained precipitate is then transformed into the ZnO-doped photocatalyst through thermal treatment.

2.2.4 Solution Combustion Synthesis

Solution combustion synthesis (SCS) is a well-known synthesis method used for the preparation of inorganic compounds for many catalytic, photocatalytic, and electrocatalytic applications. The method is based on the redox reactions that take place between a fuel and an oxidant in the presence of metal cations. Oxidants are metal precursors such as metal nitrates, while fuel is an organic material such as glycine, urea or citric acid. The final products of this synthesis are characterized by high purity, narrow particle distribution, and good agglomeration [60, 61]. Another advantage is the possibility of using different precursors, both soluble and insoluble. Solution combustion synthesis is characterized by three main steps: (1) the formation of the combustion mixture, (2) the formation of the gel, and (3) the gel combustion [62]. A schematic description of these three steps is shown in Fig. 2 [62]. The metal precursors are mixed in water solution with an organic fuel. The product obtained at the end of the combustion process is a soft powder, typical of combustion synthesis processes whose characteristics depend on the parameters chosen for the synthesis, such as the type of fuel.

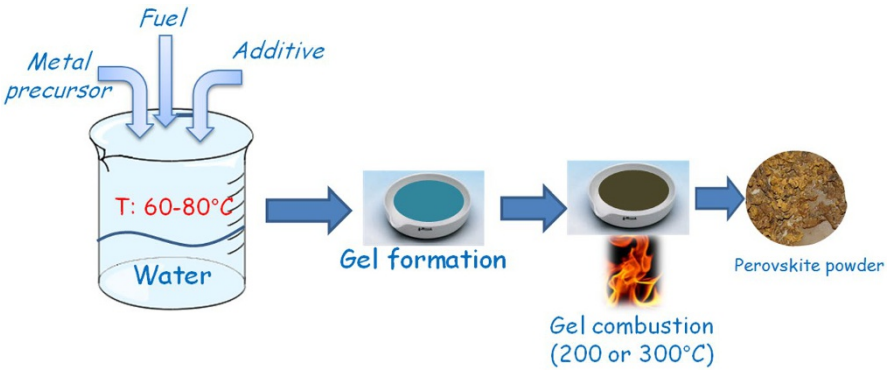

Fig. 2 Schematic representation of the three main steps of solution combustion synthesis (SCS) (Adapted from [62])

The SCS process is very fast. Fast kinetics inhibits the sintering of the particles and guarantees a certain degree of porosity in the powder obtained. The microstructure of the material can change in relation to the type and quantity of fuel. It was also observed that the interaction of citric acid (fuel) with metal cations occurs through formation of metal chelates forming a gel network, where metal cations are uniformly distributed [63].

One of the most well-studied and commonly used perovskites for wastewater and water treatment purposes is $LaFeO_3$ [64, 65]. The characteristics of $LaFeO_3$ photocatalysts prepared with SCS using different amounts of citric acid have been reported in the literature [11]. The results in terms of X-ray diffraction (XRD) patterns showed well-indexed diffraction peaks, clearly indicating the formation of an orthorhombic perovskite-type structure. Moreover, it was possible to observe from the XRD that the crystallite size of perovskite decreased as the amount of citric acid used in the synthesis was increased. On the other hand, different amounts of citric acid caused changes in the crystalline structure of perovskites [11]. When $LaFeO_3$ was prepared with the highest amount of citric acid (2.15 g in 100 mL of distilled water), a partially amorphous structure with respect to the $LaFeO_3$ synthesized using the lowest fuel content was observed. It is worth noting that the SCS method was also applied for the preparation of an $LaFeO_3$ layer on corundum or cordierite honeycomb monoliths and studied as a structured catalytic system for the photo-Fenton oxidation of organic pollutants in aqueous solution [66, 67]. The thin walls of the monolithic supports (triangular channel) were treated with aqueous solutions of iron and lanthanum nitrate in the presence of citric acid and ethylene glycol. The samples were dried and calcined in air at 900 °C for 4 h to form a grainy porous $LaFeO_3$-supported layer [68].

2.2.5 Ultrasound (or Sonochemical)-Assisted Synthesis

Sonochemical synthesis is a method that uses the principles of sonochemistry for the synthesis of new molecules or particles by the application of ultrasound. The

chemical effects of ultrasound derive from acoustic cavitation. The collapse of the bubbles in the liquid generates a huge amount of energy from the conversion of the kinetic energy of the liquid motion into heating. The high local temperature and pressure, combined with extraordinarily rapid cooling, provide a unique means of driving chemical reactions under extreme conditions [69]. The implosion of the bubbles creates extreme conditions that enable synthesis to be conducted on the benchtop in liquid at room temperature that in other cases would have required high temperature and pressure or long reaction times [70]. During the preparation of nanomaterials with ultrasonic irradiation, the phenomena responsible for sonochemistry can be characterized under "primary sonochemistry", "secondary sonochemistry", and "physical modifications" [71]. Xu et al. reported "primary sonochemistry" as the reaction occurring inside the collapsing bubbles and "secondary sonochemistry" as the reaction in solution phase occurring outside the bubbles. These phenomena are responsible for the chemical effect of ultrasound and occur only if the reaction is sonication-sensitive or when the energy released during cavitation collapse participates as reaction intermediate [70]. In particular, sonolysis of water produces highly reactive $H^{\cdot}$ and $OH^{\cdot}$ radicals, which can be utilized for various sonochemical reactions. These generated free radicals can further react with each other to form new molecules and radicals or diffuse into the bulk liquid to serve as oxidants. The reaction that produces free radicals can occur within the collapsing bubble (thermolytic center), at the interface between the bubble and bulk liquid, or in the adjacent liquid. Several studies have reported that the predominant effect in heterogeneous sonochemical reactions used for the production or modification of semiconductors is the physical one [72]. In particular, it is the impact of jets of liquid at high speed on the particle surface that can cause erosion and corrosion phenomena, by modifying the particle surfaces. In this way, surface nanostructures or disaggregated particles can be generated [71].

The mechanisms governing ultrasound applications can be summarized as follows [73].

- Homogeneous reactions that proceed via radical mechanisms are affected by sonication, while ionic reactions are not affected by ultrasound.
- Heterogeneous reactions involving ionic species are influenced mainly by the physical effects of cavitation (e.g., by the reduction in particle size). In this type of reaction, the chemical effects are not dominant, so it is important to select the appropriate operating parameters.
- Heterogeneous reactions involving radicals or combined mechanisms (ionic and radical) are significantly influenced by the ultrasound effect. The radical reactions are intensified by the presence of ultrasound, but the physical effects also greatly affect the mass transfer rate, improving its efficiency.

As regards the ultrasonic application for photocatalyst synthesis, the preparation of anatase and rutile TiO_2 was reported by Huang et al. [74]. The authors compared the sol–gel method with the sonochemistry procedure, highlighting that the ultrasound process resulted in a perfectly crystalline TiO_2 structure. The procedure used to obtain the titania photocatalyst typically involves the treatment of the precursor

deionized water solution by ultrasound. During the process, the precipitates are separated by centrifugation, then washed and vacuum-dried overnight until the final product is obtained. In addition, the application of high-intensity ultrasound irradiation allows a mesoporous TiO_2 to be obtained without the addition of surfactant compounds [75]. According to the scientific literature, this method has the capacity to (1) increase crystal growth rate, (2) decrease induction periods and metastable zone width, (3) improve particle size distribution and morphology, and (4) achieve higher control of the nucleation process [76]. Moreover, the synthesis of photocatalysts by ultrasound is considered a "green technology", as it is a fast, clean, and efficient option that enables the formation of reaction conditions at ambient temperatures in cases that would otherwise require high temperature and pressure to yield the same results. An additional benefit is that it is an extremely versatile synthetic procedure that cab be used for the development of various photocatalysts. The materials synthesized by this method show clear improvements in terms of photocatalytic performance over photocatalysts synthesized using traditional methods.

2.2.6 Comparison of Photocatalyst Preparation Methods

Table 1 summarizes the main advantages, disadvantages, and feasibility of large-scale application of the photocatalyst preparation methods discussed in the previous paragraphs.

Although all of the methods described can generate effective photocatalysts, from a large-scale application point of view, it appears that SCS and hydrothermal synthesis are less strongly recommended methods, as they require high thermal energy and high pressure [83]. On the other hand, sol–gel and precipitation methods may be feasible at a large scale if no expensive metal precursors are required.

3 Wastewater Treatment by HPC: Great Potential but Some Limitations and Drawbacks

The efficiency of photocatalytic processes in water and wastewater treatment can be negatively affected by different factors, including low photoconversion efficiency and the occurrence of reactive oxygen species (ROS)-scavenging substances in the target water/wastewater matrix. Moreover, technological limitations such as the selection of a more suitable photocatalyst and preparation method or the choice between slurry (need to recovery the powder photocatalyst after treatment) and supported photocatalyst systems have thus far discouraged the application of heterogeneous photocatalysis for water and wastewater treatment at full scale.

3.1 Photoconversion Efficiency

Low photoconversion efficiency is a major limiting factor in the application of photocatalytic processes, even when compared with other AOPs. Quantum yield can vary widely depending on the photocatalyst, experimental conditions, and

Table 1 Advantages, disadvantages, and feasibility of large-scale application of photocatalyst preparation methods

Synthesis method	Advantages	Disadvantages	Large-scale application	Bibliographic references
Sol–gel	High purity Uniform nanostructure Low temperatures Lower energy consumption compared with other methods No expensive equipment required	Expensive metal precursors in some cases (this technique is "substrate-dependent"; metal alkoxides are the most preferred precursors, but they are expensive) Lengthy processing times, low yields Expensive special reagents may be required	Possible, if no expensive metal precursors are used	[77–80]
Precipitation	Homogeneous mixing of reactant precipitates No use of specific solvent Low reaction temperature Short reaction time No solid waste Effective and proven technologies	Process not suitable for the high pure and accurate stoichiometric phase preparation The method is affected by the solubility of the reagents. If they have different levels of solubility, it does not work well No universal experimental conditions Insufficient size control distribution Uncontrolled shape Readjustment of pH may be necessary	Possible, no particular restriction given the simple application and no use of specific solvent	[79]
Hydrothermal synthesis	Possibility to grow crystals of compounds with high melting points at lower temperatures Possibility to also apply the method to materials with high vapor pressure near their melting points Method particularly suitable for the growth of large good-quality crystals while maintaining control over their composition	Need for expensive autoclaves Not possible to observe the crystal as it grows	No prospective feasibility due to the need for autoclaves and high pressure	[81, 82]

Table 1 (continued)

Synthesis method	Advantages	Disadvantages	Large-scale application	Bibliographic references
Solution combustion synthesis	Short reaction times of synthesis Ability to fabricate nanoscale powders with the desired crystal structure in one step	Wide size distribution (from nano- to sub-micrometer irregular particles) Particle aggregation High energy consumption	No prospective feasibility, due to the high energy demand	[80, 83, 84]
Ultrasound	No chemical reducing agent is needed Reaction rates are reasonably fast Very small catalyst particles are produced	High energy consumption	Possible, if no expensive metal precursor are used	[85]

wastewater matrix [86]. Taking UV/H_2O_2 AOPs as an example, the photolytic decomposition of H_2O_2 is characterized by a quite high Φ and ·OH production yield [87], making HPC not so competitive in terms of energy efficiency. However, it is worth noting that TiO_2 can also be effective under sunlight, and more effective than sunlight/H_2O_2 [88].

3.2 Interfering Substances

A wastewater matrix can significantly affect HPC efficiency due to the presence of natural organic matter (NOM), carbonate species, and other background constituents that can scavenge ROS and absorb light [89, 90]. Indeed, HPC is susceptible to the differences in the light absorption factors of the wastewater. The UVA or solar radiation supplied to the reactor needs to travel through a column of water (path length). The presence of total suspended solids (TSS) and numerous soluble substances in the wastewater results in a loss of transmittance, via absorption but also scattering and reflection. This results in energy loss from light that does not reach the photocatalyst's surface. At wavelengths relevant for UVA photocatalysis (365 nm), there is considerable absorption (Fig. 3).

The path length that the electromagnetic radiation has to travel is also crucial. According to Beer–Lambert's law (Eq. 1), a directly proportional relationship between path length and absorption exists, and doubling of the path length results in doubling of the absorption (logarithmic units). The molar absorption coefficient (ε) is a constant specific for each chemical compound and the wavelength at which it is measured, while l is the path length and c is the concentration of the compound in question. In wastewater, the measured absorbance is the summed absorbance of all compounds in the wastewater

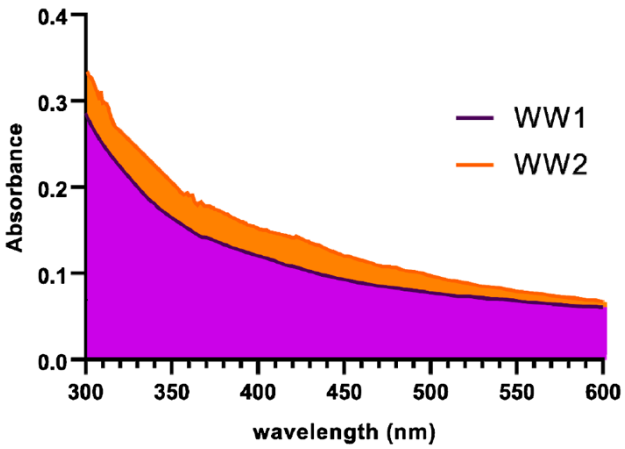

Fig. 3 UV–Vis absorption spectrum of secondary treated wastewater. Under CC 4.0 from supplementary information of [5]

$$A_\lambda = \log \frac{I_0}{I} = \varepsilon \cdot l \cdot c \tag{1}$$

This limits reactor design, especially for reactors with immobilized photocatalysts versus suspended (slurry) photocatalysts, since in the former light is absorbed only after passing through the entire path length, not throughout, as would happen in a suspended photocatalyst reactor.

3.3 Suspended Versus Immobilized HPC

HPC for wastewater treatment in a lab setting is commonly studied as a suspended powder. Maintaining a powder in suspension in a large body of water is very energy-intensive. It is also important that the water is somewhat aerated, since an external source of dissolved oxygen enhances the generation of ROS via electron–hole pairs. Anoxic conditions [i.e., lack of $O_{2(aq.)}$] prevent the generation of both hydroxyl radicals and superoxide radicals, as the electron promoted to the conduction band does not transfer to dissolved oxygen to form superoxide but recombines with the hole [91]. Precipitation of the suspended photocatalyst to the bottom of the tank would be extremely detrimental to the efficiency of the process, since light adsorption would be at a minimum and contact between targeted compounds/bacteria and the catalyst low. Thus, the cost of circulating the wastewater during treatment in a suspended reactor is essential and should be accounted for. Using the photocatalyst in powder form adds a further processing step to remove the catalyst and recover it for reuse. This can be by gravity precipitation, induced agglomeration and precipitation or filtration, all of which further increase operating costs. In an effort to circumvent these costs, catalyst immobilization has been proposed [5, 92–94]. Immobilization of a photocatalyst is the coating of the macrostructure with a layer of photocatalyst that is exposed to the water and that can receive UVA/visible light. Numerous materials (glass, alumina, silica, metal, fibers) have been successfully coated with a photocatalyst [95]. This serves the dual purpose of reducing the energy expenditure for keeping a powder in suspension and eliminating the catalyst recovery step. Utilizing immobilized photocatalysts does have its drawbacks. Reactor design in intrinsically more complex and ultimately is a compromise between maximizing the illuminated catalyst-coated surface area and reactor volume while minimizing the path length of wastewater above the coated surface from the light source. The processes used to immobilize a photocatalysts can also be complex or costly. Despite the limitations, pilot-scale reactors with immobilized catalysts are reported in the literature and have been successfully employed for both CEC removal and bacterial inactivation [96, 97].

4 Application of Heterogeneous Photocatalysis to Wastewater Treatment

4.1 Tertiary Treatment of Urban Wastewater

The three conventional stages of urban wastewater treatment consist of a primary stage of physical separation by sedimentation of solids and skimming off of floating contaminants, a secondary stage for reducing biodegradable organic load by bacterial growth, and a tertiary stage of nutrient removal (typically achieved by biological processes) and/or disinfection and/or removal of micropollutants such as CECs (including pharmaceuticals, pesticides, personal care products, and any other pollutant that is found in micrograms-per-liter or lower quantities in wastewater). The tertiary stage is not considered essential, and only a few countries have regulation that require the use of tertiary treatment to remove one or more of the contaminants explained above. When tertiary treatment is used, the main factors driving the choice of treatment are the efficiency in removing the target contaminants set by the local/national regulation and the cost. The tertiary treatment applied depends on the target parameter(s) that need to be brought within regulatory limits. If such a target is the reduction of bacterial load, then chlorination, peracetic acid, or UVC disinfection is commonly employed [98–100]. On the other hand, if CECs should be removed, disinfection processes are no longer effective, and advanced treatment methods are necessary [101]. Indeed, in Switzerland, according to the new national water act (Swiss Federal Council Waters Protection Ordinance) [102], 70% of the urban wastewater treatment plants (UWTPs) must be upgraded with ozonation or adsorption treatment methods to remove 14 selected CECs by 80% of inflow levels. In such a context, homogeneous photo-driven AOPs may be competitive with consolidated technologies in the short term, and HPC may be feasible if some limitations/drawbacks are successfully addressed [103].

4.1.1 HPC for Micropollutant Removal and Bacterial Inactivation

HPC has been intensively studied as a potential technology for the mineralization of organic contaminants and the inactivation of bacteria in the effluents of secondary treated urban wastewater. While full mineralization is not considered feasible for urban wastewater, a wide variety of catalysts have been employed for pollutant degradation and disinfection. These include dyes, [104, 105] endocrine disruptors [106], pharmaceuticals [107] including specifically antibiotics [108, 109], and agricultural chemicals [110, 111], and for bacterial inactivation [112, 113. The most imposing obstacle hindering widespread use of heterogeneous photocatalysis as a tertiary treatment in UWTPs is the high cost associated with photocatalysis, which can be more than an order of magnitude greater than established AOPs [103]. Nevertheless, HPC could find application in the treatment of wastewater intended for reuse, which has stricter water quality requirements than

current requirements. The need to achieve higher requirements could outweigh the limitations of HPC when compared with other available treatments, especially when considering degradation of organic chemical pollutants, toxic disinfection by-product formation, and antibiotic resistance concerns in wastewater reuse.

4.1.2 Variability in Wastewater Loads and Its Effect on Treatment

As for challenges of a technical nature, the variability in wastewater in terms of organic contaminant load (COD/DOC) has major effects on the process and the duration required for treatment. ROS generated by photocatalysis, such as hydroxyl radicals, are highly reactive but also highly unselective. This translates to reactions between any form of organic matter, whether harmless humic acids or chemical pollutants that are the target of the treatment. Choi et al. measured the pseudo-first-order rate constants of degradation for acetaminophen and carbamazepine in distilled water and real wastewater from different wastewater treatment plants (WWTPs) having different DOC loads [114]. Relative to distilled water, i.e., where DOC is entirely due to the contaminants of interest, real wastewater showed slower degradation of these two drugs by factors of 3–6. While concentrations of ions such as bicarbonate, chloride, and nitrate in low milligrams-per-liter quantities have a negligible effect on the rate constant, humic acid load drastically reduces the rate of removal (Fig. 4). It should also be noted that slowing of removal kinetics is not linear with DOC load, but rather plateaus after a certain load DOC [114].

The rate constants of hydroxyl radicals, the dominant radical in HPC, with most organic compounds approach the theoretical maximum imposed by diffusion-controlled reaction kinetics [115]. This means that while there are differences in reactivity between different organic compounds in water, these differences tend to be mostly of the same order of magnitude ($\log k_{OH}$ 9.5 ± 1) [116]. As CECs occur at concentrations many orders of magnitude lower than interfering substances, but both have a rate constant within one order of magnitude, this results in a very small fraction of the ROS probabilistically reacting with CECs as dictated by competitive kinetics between the ROS formed and organic compounds in the water phase. The reduction in the rate of pollutant removal due to high contaminant load and/or the presence of scavengers is a well-established fact [117]. However, such an interfering effect can be overcome to a certain extent in some AOPs, such as ozonation or UVC/H_2O_2, where the concentration of the oxidant can be increased to achieve a suitable ratio between oxidant and total DOC load. By increasing the oxidant load (ozone, hydrogen peroxide, etc.), the concentration of hydroxyl radicals increases, yield a higher rate. The rate constant (k) is not affected by the concentration of reactants; thus, at the same temperature, increasing the concentration of the reactants increases the overall reaction rate of both CECs and DOC (since they compete for reaction with ·OH as per Eqs. 2 and 3).

$$\text{rate} = k \cdot [\text{CEC}] \cdot [\cdot\text{OH}] \tag{2}$$

$$\text{rate} = k' \cdot [\text{DOC}] \cdot [\cdot\text{OH}] \tag{3}$$

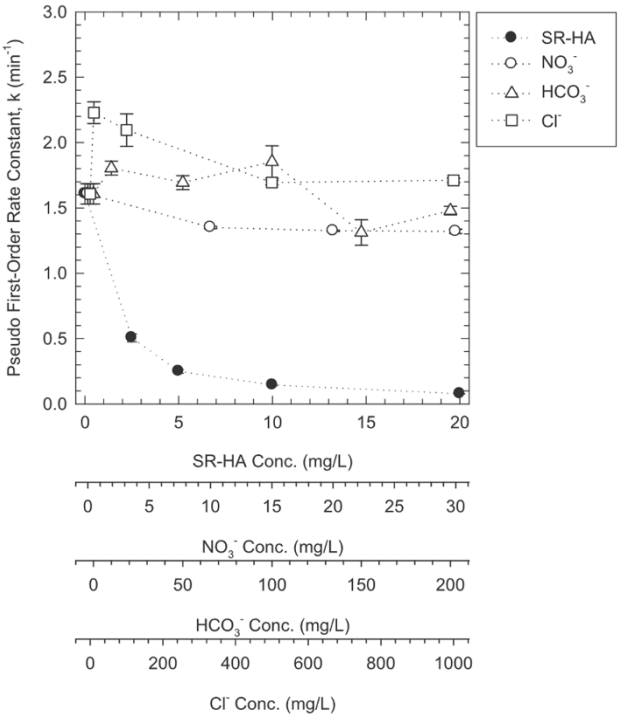

Fig. 4 Effect of initial concentration of humic acid (SR-HA), bicarbonate (HCO_3^-), nitrate (NO_3^-), and chloride (Cl^-) on the rate constant for the degradation of carbamazepine. Reproduced with permission from [114]

Fixing the rate of oxidant to the [DOC] (concentration of DOC) thus aids in stabilizing the reaction rate.

The performance of the catalyst in the application of HPC to water/wastewater treatment peaks at a certain catalyst load. A further increase in catalyst loading would be counterproductive, resulting in reduced efficiency due to the increased opacity of the aqueous matrix. Other factors such as light intensity can be increased, but only up to a certain threshold of saturation. Additionally, commonly used low-pressure mercury lamps are not dimmable, and increasing the intensity would require increasing the number of active bulbs. Moreover, adsorption and electrostatic forces should not be underestimated in heterogeneous photocatalytic process. HPC involves reaction between two materials in different states of matter, and pollutant adsorption on the surface of the catalyst has a drastic effect on removal efficiency. This is because radicals are generated at the semiconductor–water interface, and these species have a very short half-life due to their very high reactivity. Having compounds adsorbed at the site of radical generation increases the probability of reaction of these radicals with the adsorbed species. This is also applicable for HPC for water disinfection, as *E. coli* and other Gram-negative bacteria are negatively charged due to the ionized phosphoryl and

carboxylate components in the cell wall [118, 119], and consequently they are attracted to positively charged semiconductor photocatalysts. These effects also influence the rate of removal/inactivation in other ways; for example, bicarbonate ions are known to adsorb to titania, reducing its activity [120] by preventing electron transfers that generate ROS to take place at the site of adsorption.

4.1.3 Irradiance and Transmittance Through Wastewater

The presence of TSS/turbidity and light-absorbing substances in wastewater results in a loss of transmittance (via absorption but also scattering and reflection) and, consequently, a loss of energy because of the reduced light intensity that will reach the photocatalyst's surface (as we already saw in Fig. 3). In the day-to-day operation of an HPC tertiary treatment process, the additional variability resulting from this issue can negatively affect process efficiency. Just like ozone content is dosed relative to the DOC load in water, some HPC process parameters can be modified depending on the type of reactor utilized. An online measure of UV–Vis transmittance at appropriate wavelengths has been suggested as a proxy measure for contaminant load [121]. Thus, this can be used to adjust some HPC parameters, e.g., in semi-batch reactors such as raceway reactors [122] the volume of wastewater treated can be increased and decreased accordingly. A lower volume in a fixed reactor results in a shorter water column and thus higher transmittance. Batch reactor residence time can be adjusted as well.

4.1.4 Requirements for Widespread Adoption of Photocatalysis: A Technological Niche for HPC?

Photocatalytic reactors, including solar reactors, have been reviewed in detail in other publications (see [123, 124]), and the obstacles to widespread use are not so much technological, but rather a lack of market demand given the higher costs and levels of treatment obtained by HPC-treated wastewater.

The most critical requirement for widespread adoption of HPC is the establishment of regulations mandating reduced CEC load in discharged effluents and/or water intended for reuse. The case for reducing CECs in water intended for reuse, specifically agricultural irrigation, is especially strong. Paltiel et al. demonstrated that persons consuming crops irrigated with reused wastewater had significantly higher blood levels of carbamazepine compared with those who consumed vegetables irrigated with fresh water [125]. While the levels recorded are orders of magnitudes less than therapeutic levels, there is still cause for concern, both because of chronic exposure to such compounds and due to the cocktail effects from the presence of numerous compounds and their transformation products, many of which are not known. High-level treatment of wastewater intended for food crop irrigation would thus be required if one were applying precautionary measures.

Another potential issue that might make HPC a necessity is the environmental dimension of antibiotic resistance. Conventional tertiary treatment processes and ozonation are both associated with an increased prevalence of antibiotic-resistant bacteria (ARB) and antibiotic resistant genes (ARGs) [126]. Such an increase

in prevalence results a process of natural selection in bacterial mortality, that is, when non-resistant bacteria are more susceptible to treatment than resistant bacteria. Therefore, while the overall bacterial loads decrease, the percentage of resistant bacteria within the total bacterial load increases [127–129]. This shift in population dynamics introduces risks in the downstream environment such that the more prevalent resistance is now more likely to thrive in the environment. Chlorination and UVC treatments are known to cause resistance selection [127, 129]. Ozonation, which is also an AOP with high operating costs, is associated with increased ARB and ARGs as well [126]. Since HPC application for AR resistance mitigation is largely in its early stages, most studies on the matter have dealt with its ability to reduce the absolute number of ARB and ARGs, not specifically on reducing relative abundance [94, 112, 130]. Other studies have targeted abundance [5, 131], but because of the lack of full-scale application in WWTPs, it has not been fully established whether HPC also increases prevalence. If antibiotic resistance associated with wastewater reuse is deemed a high risk in need of regulation by the authorities, and HPC is found to be an effective technology for AR mitigation, the high cost of HPC could be justified by its efficacy and by the lack of suitable alternative treatment methods.

Without fulfilling such a need, photocatalysis needs to become at least one order of magnitude more efficient [103], an obstacle that as yet has not been overcome despite the intense level of research on the matter. The preferential use of modified catalysts over commercially available ones can play a pivotal role. These modifications must result in both higher efficiency in the generation of radicals (i.e., quantum yields for hydroxyl radical generation) and the ability to harness photonic energy beyond the UV range and into the visible range, thus enabling solar treatment. Energy production in a power plant and the transport and powering of UVA lamps involve substantial energy losses at each stage, which can be avoided by using solar reactors as a cost-effective strategy. However, solar-driven treatments have problems as well. Even if future engineering modifications result in a sufficiently efficient visible-light-active photocatalyst that makes HPC competitive with other AOPs, solar treatments are still limited by the actual duration of daylight and by the fact that solar reactors need a large footprint in terms of land area. Thus, they are more feasible in smaller, less densely populated cities, where the value of land is not as high as it is close to major cities. Additionally, solar treatments are limited seasonally, with lower treatment potential in winter, as well as geographically, with latitudes farther from the equator having lower insolation and hence treatment potential. While this limits solar-based technologies for the treatment of all types of wastewater, it is much less an issue for solar-based treatment of water specifically for agricultural reuse. Firstly, areas with intense agriculture activity are located far from major cities, and thus the value of land is low allowing for larger footprints. Additionally, the need for irrigation is stronger in latitudes and seasons where insolation is higher. A wide variety of solar reactors have been proposed, including parabolic-based reactors and raceway pond reactors [124, 132]. Parabolic reactors are more suitable in low-insolation conditions but are more expensive than raceway pond reactors. The latter have been used mostly for homogenous AOP processes [133], since the low flow

rate of the water inside the reactors would require a catalyst to be immobilized to avoid powdered catalyst sedimentation.

In summary, there are tangible benefits in risk reduction with tertiary treating to a high standard, especially for the case of wastewater for agricultural reuse. The ripest area for development is the combination of cheap raceway pond reactors with immobilized solar-active photocatalysts being employed as the need arises to alleviate temporal water scarcity bouts.

Even at equivalent outcomes, a consolidated system is always favorable to a newer system. Thus, for HPC to be competitive and turn the tide on other AOPs, it does not need to simply match the benefits of currently employed AOPs, but to exceed them. A possible strong point for immobilized solar HPC is that it would not require additional material input, and would require low energy input only for mixing, as opposed to the more consolidated ozonation or Fenton processes which have these requirements.

Another pathway that can lead to increased acceptance of photocatalysis as a treatment is by combining it with other treatments. There are two main ways to combine treatments: simultaneously and in cascade/sequentially. The most common simultaneous use of HPC is its coupling with ozonation. This type of treatment was recently reviewed [134]. The premise of such a combination is that the combined process is more efficient than either of the separate processes, by means of additional pathways that lead to ROS formation through the interaction of the photocatalyst and dissolved ozone as well as direct reactions with molecular ozone [134]. Sequential applications of HPC and other water treatments are not at all well studied. Examples exist of other AOPs that are applied in combination with or after another treatment such as chlorination exist [135, 136], but no suitable examples for HPC have been noted. The benefit of using HPC in a cascade with other treatments includes the fact that the intensity of treatments can be lower than what would be used individually; for example, if chlorination is to be used prior to a photocatalytic process, it is possible to reduce the quantity of chlorine applied and thus reduce the concentration of chlorinated by-products, while meeting the same targets that would not be possible with only one of the sequential treatments. An additional benefit, due to the different oxidation mechanisms, is that one process may be more active on a certain type of contaminant, while the other process is more active on another type; thus when used in cascade, the overall efficiency is higher.

A different approach for improving photocatalytic performance is to reduce the recombination of electron–hole pairs. A particularly interesting solution, in contrast to doping with metals, is represented by the modification (or combination) of the semiconductor with graphitic materials [137]. These materials are interesting because they have excellent electrical conductivity and are considered promising materials for photocatalysis [138]. In recent years, graphene-based photocatalytic processes have also been implemented through the combination of photocatalysis with other techniques. In particular, several studies report interesting results regarding the application of photoelectrocatalysis as an effective process used to suppress the recombination of charges [137]. In an photoelectrocatalytic process, an external bias potential is used. The electrons generated are accumulated on the external cathode and the holes on the photocatalyst. The electrodes used in

photoelectrocatalysis are generally composed of photocatalyst and co-catalyst deposited on conductive glass. Different photocatalytic materials have been used in photoelectrocatalysis, among which TiO_2 is one of the most widely studied semiconductors and is used as photoanode. Other materials active in the presence of visible light have also been used for their good performance as photoanodes [139].

However, if the photoanode consists of only one component, it is characterized by the problem of recombination of the charges. For this reason, making changes to the composition of the photoanode can be useful. In particular, an interesting approach is the use of co-catalysts, and among these, graphitic materials are very promising. Graphitic materials with two-dimensional structures are characterized by excellent electrical conductivity and can be used as electron transporters in order to improve the separation of photogenerated charge carriers and to enhance photoelectrocatalytic activity [137]. Various studies have investigated the ability of graphene to attract and transport electrons, improve the adsorption of reagents, and confer the ability to absorb light in the visible field to semiconductors [140–144].

4.2 Gray- and Stormwater Treatment

Gray water includes wastewater generated by households from sources such as sinks, showers, baths, laundry washing machines, and dishwashers, but does not include fecal-contaminated sources. Stormwater originates from precipitation events, including snow and ice melt. Stormwater can be absorbed in soil, stored in water bodies as surface water (e.g., in ponds and lakes), evaporate, or be transported via streams and rivers. HPC has seen some research applications in gray-water and harvested stormwater treatment. Wang et al. [145] used TiO_2-graphene oxide composites at various percentages in artificial stormwater for the disinfection of spiked *E. coli* under solar light. While the catalyst showed good reusability, even after ten cycles, in the optimal case only up to 1 log removal was reported from an initial bacterial load of 10^4 CFU/mL. The catalyst, due to its surface charge, was very efficient in reducing TSS by co-sedimentation of any waterborne particles with the photocatalyst. The authors suggest that such a treatment could take place with photocatalysis during daytime, coupled with a long period of sedimentation for catalyst recovery and TSS reduction overnight. However, the application of HPC for gray-water or stormwater is not ideal—HPC, as a process that is reactive to virtually all organic compounds, would benefit from an initial biological process in order to remove biodegradable organic compounds. Such a setup was demonstrated by Garcia et al. following the removal of TOC in rainwater using a combined ozonation-photocatalytic system, but only after treatment in a bioreactor for the removal of biodegradable compounds [146]. Other examples of gray-water treatment by HPC have also been reported [147, 148]. While research on HPC treatment of gray/stormwater has been published, it is a very small part of water treatment. Both in terms of microbial contamination and potentially toxic compounds, gray/stormwater is of negligible importance relative to wastewater.

4.3 Industrial Wastewater Treatment and Energy Recovery from Hydrogen Production

Industrial processes utilize water that can be contaminated by any organic or inorganic compounds used in the process. Thus, the characteristics of urban wastewater are completely different from those of industrial wastewater. The role of AOPs in industrial wastewater treatment is often to improve its biodegradability and/or reduce toxicity, before applying a biological process. AOPs can also be used after biological treatment of industrial wastewater to further reduce residual contaminants to meet the standards for effluent disposal or reuse. In the following subsections, the application of HPC to various types of industrial wastewater (food, textile, tanning, and pharmaceutical/pesticide) are critically reviewed by discussing its potential, limitations, and prospects.

4.3.1 Pharmaceutical and Pesticide Industry Wastewater

Pharmaceutical compounds are typically detected in urban wastewater at concentrations in the range of nanograms to micrograms per liter [149], with TOC levels in the low milligrams-per-liter range [150]. Although pharmaceuticals can be resistant to treatment and have deleterious effects downstream, at the levels they are found in urban wastewater they do not cause operational problems to the UWTPs. However, wastewater from pharmaceutical industries presents a distinctive case. These wastewater effluents contain high levels of TOC, with concentrations even reaching grams per liter [151], and high levels of compounds that are specifically designed to be bioactive and hence have a high potential for toxicity. Because the volumes of water are much lower than in urban wastewater, Fenton processes are more commonly used to treat pharmaceutical wastewater, as the high TOC load and lower water volumes make it feasible to alter the pH to meet the requirements for Fenton processes. However, photocatalysis has also been studied at the lab scale for treatment of pharmaceutical industrial wastewater. Ahmadi et al. used a TiO_2 coupled with carbon nanotubes to treat pharmaceutical wastewater; 0.2 g/L of catalyst was able to reduce the TOC from 1295 to 228 mg/L in 240 min of irradiation. Deng et al. utilized a silver-based photocatalyst to reduce the TOC of real pharmaceutical wastewater from 25 to 10 g/L in 500 min [152], while Verma et al. used a commercial TiO_2 preparation to reduce the COD by approximately 90% after 7 h from an initial load of 2.5 g/L.

Industrial wastewater from the pesticide industry is in many ways identical to that from the pharmaceutical industry. Pesticides, like pharmaceuticals, are bioactive compounds, are designed to be stable in order to perform their designed function, and can interfere with biological treatments. HPC has also been studied for the treatment of industrial wastewater from the pesticide industry. Alalm et al. [153] compared the efficiency and cost of using HPC (commercial TiO_2) versus a solar photo-Fenton process for treating real agrochemical/pesticide wastewater with a high COD load of 7 g/L. The wastewater was treated using parabolic solar collectors and showed very high efficacy for both processes, especially when taking into account the COD load present. Under the optimal conditions studied, solar HPC was able to reduce the COD load by 80%, while the photo-Fenton process reached 91%. As

already mentioned for pharmaceutical wastewater, Fenton processes are generally preferred for industrial wastewater of this type, since the lower water volumes make pH alteration economically feasible. The authors reached the same conclusion, since they estimated that the best-performing HPC treatment was 1.5 times as expensive as solar photo-Fenton per unit volume of wastewater treated. Other research has been carried out on in situ treatment of wastewater from the agro-industry using innovative solar photocatalytic reactors [154]. Wastewater generated from the washing of equipment used for agricultural pesticide application was treated using commercial titania. While the COD loads of the treated wastewater were not high, in the range of 0.1 g/L, the treatment was able to reduce it by more than 75% of the initial value, with contained costs of operation. Kushniarou et al. also applied a photocatalytic treatment for agro-industry wastewater generated from washing equipment that had been in direct contact with pesticides. With the use of commercial TiO_2-P25 and 150 mg/L of persulfate, the grouped concentration of 12 selected pesticides was reduced by $>99\%$ in 1 h [155].

In all cases, commercial unmodified titania was used as the photocatalyst under solar or solar-simulated conditions. This catalyst, with a bandgap of about 3.2 eV, is mostly active under UV radiation, which is a minor fraction of the solar spectrum. This presents an opportunity to further enhance the photocatalytic process in the removal of pesticides from agro-industry wastewater, since the use of a doped photocatalyst with a lower bandgap would result in the utilization of a higher fraction of the solar spectrum and higher expected rates of removals. This improvement might be enough to reduce the cost while also having a major advantage over solar photo-Fenton processes in ease of automation, as it does not require the addition of an oxidant such as hydrogen peroxide.

4.3.2 Food Industry Wastewater Treatment and Energy Recovery

Food industry wastewater, in addition to biodegradable organic substances, can also include organic substances that are not easily biodegradable, such as food dyes.

Synthetic dyes are the largest group of additives used in the food industry, and their by-products, such as phenolic compounds and aromatic amines, are toxic to the aquatic environment because of their carcinogenic and mutagenic nature [156]. These dyes generally contain recalcitrant organic and inorganic groups, and their release into the aquatic environment results in a reduction in light transmittance, thus reducing the penetration of solar radiation through the receiving body of water. Dyes have high thermal and photo-stability, and this makes them resistant to biodegradation [157]. For this reason, they are persistent molecules which remain in the environment for long periods. The main consequence of the presence of dyes in aquatic environments is on plants, since the light absorption by the dye present in the water reduces photosynthesis activity and influences the food chain [157]. Furthermore, some dyes can cause carcinogenic and genotoxic effects on humans [67, 158], and AOPs appear to be an attractive option for removing such pollutants from wastewater.

Although homogeneous Fenton reaction is effective in the oxidation of several recalcitrant pollutants and is used in industrial wastewater treatment as a

pre-oxidation step before a biological process, it has some drawbacks. One of the main limitations is that the process relies on acidic operating conditions (optimal at pH < 3) to avoid catalyst precipitation. Thus conventional homogeneous photo-Fenton can improve process efficiency but does not solve pH-related problems (pH pre-acidification, pH post-neutralization, and sludge production, treatment, and disposal). This restriction makes this option attractive only for the treatment of acidic wastewater, because application to neutral or alkaline wastewater would increase operating costs. The improvement of photo-Fenton performance under neutral conditions has been a subject of high interest among the scientific community in recent years. In particular, photo-Fenton has been investigated for the removal of CECs from urban wastewater and inactivation of bacteria, and its operation under mild conditions (pH 5–6) resulted in good efficiency [159, 160]. Other possible approaches include the use of heterogeneous and homogeneous (photo)-Fenton-like processes. In homogeneous processes, Fe^{2+} is replaced by other metals or possibly combined with organic or inorganic ligands to form complexes and/or to stabilize the metals over a wide pH range [161]. Different ligands including nitriloacetic acid, ethylenediaminetetraacetic acid, oxalic acid, tartaric acid [162], and ethylenediamine-*N*-N0-disuccinic acid [163], as well as metal–organic complexes, have been investigated so far. Another option for overcoming homogeneous photo-Fenton drawbacks includes heterogeneous catalytic systems based on macroscopic supports (such as corundum, cordierite) [164]. Heterogeneous photo-Fenton methods have been investigated for the removal of dyes from aqueous matrices [165] through the immobilization of Fe ions on clays, bentonite, and laponite [166], or by using iron oxides such as goethite or hematite under non-controlled pH conditions [167]. To overcome the drawback of powder catalyst removal after treatment, macroscopic supports appear to be an attractive alternative. Structured catalysts can be purposefully designed to optimize fluid dynamics. The application of such a catalyst (i.e., $LaFeO_3$ loaded on corundum honeycomb monolithic support) for the removal of food azo dyes from aqueous solutions resulted in complete discoloration and mineralization (evaluated in terms of TOC removal) of two food dyes [Allura Red (RED) and tartrazine (TRZ)] (Fig. 5); notably, the process proved to be extremely efficient at spontaneous pH values (equal to 6) [67].

Among food industrial wastewater, dairy wastewater is a category not easily managed through conventional biological process alone [168]. While it does not contain particularly toxic substances, dairy wastewater is characterized by high organic content including fats and proteins, which can decompose. Their treatment is generally managed through biological processes, but several problems have been noted related to operating pH, variations in the organic loading, and high sludge volume produced [169]. Some attempts to treat such wastewater by HPC have been carried out but were not so successful.

HPC was combined with a flocculation process to remove COD and inactivate bacteria from dairy wastewater [170]. Although a TiO_2 P25 Evonik photocatalyst resulted in total inactivation of *E. Coli* after 5 h of treatment (120 W/m^2 of UV–Vis light intensity), an increase in COD and TOC was also observed, which the authors attributed to the formation of organic oxidation intermediaries.

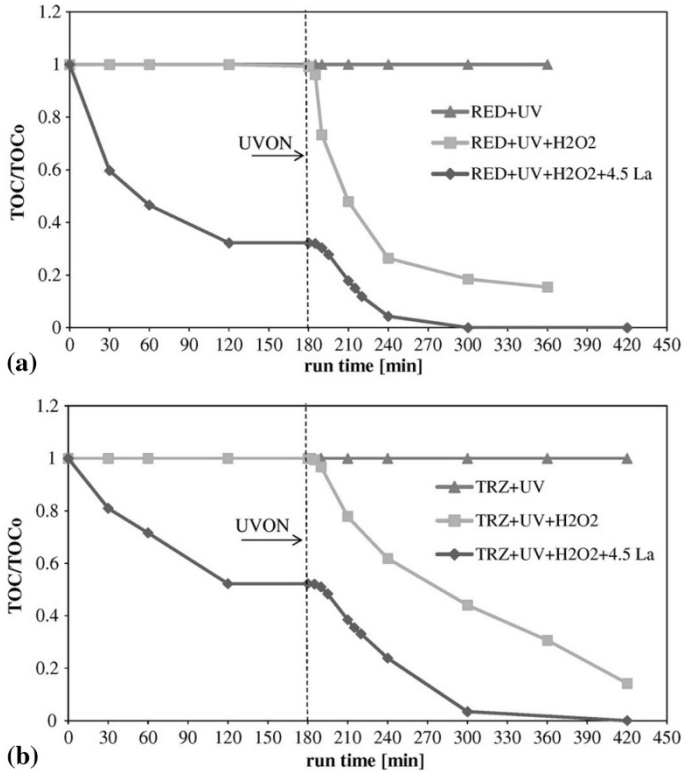

Fig. 5 Effects of $LaFeO_3$ structured photocatalyst for photo-Fenton reaction on TOC removal over the run time for **a** RED and **b** TRZ dyes [67]

An HPC technique using ZnO thin film as photocatalyst immobilized on a metal plate (800 × 250 mm) was investigated as possible pretreatment (before biological processing) of dairy wastewater [171]. The experiments were carried out using a solar reactor with a fixed dairy wastewater volume (3 L) and a liquid flow rate of 13 L/min. According to the Taguchi L8 orthogonal array used in the experimental design, an effective TOC percentage degradation as low as 14.23% for all conditions at an optimal level was recorded (max degradation percentage of 31.42%). Although the authors recommend the process as a possible pre-oxidation step to improve dairy wastewater biodegradability, taking into account wastewater characteristics (turbidity 2786 NTU, COD 6032 mg/L, total solids 10,720 mg/L, oil and grease 2002 mg/L) as well as initial biodegradability (as $BOD_5/COD = 0.368$), it appears to be more appropriate as a post-treatment method after biological processes, assuming that the reactor can be scaled up.

The possibility of energy recovery from agrifood wastewater has attracted increasing interest among the scientific community due to the potential for organic pollutants to be transformed into useful fuels such as methane and hydrogen. The purification of wastewater with simultaneous energy conversion is an

attractive strategy in the context of a circular economy. The use of photocatalysis for hydrogen production is one of the most widely investigated and interesting approaches for simultaneously treating and deriving value (through renewable energy production) from wastewater [172]. For example, hydrogen recovery through photocatalytic treatment of wastewater containing high concentrations of sugars (particularly glucose) has been increasingly investigated [11, 173–175]. In particular, for the photocatalytic production of hydrogen, the use of suspended and dispersed photocatalysts has unique advantages such as efficient utilization of light energy and fast transport of pollutants between the powder surface and the aqueous medium. An interesting solution for overcoming photocatalyst recovery problems, while at the same time preserving the characteristics and advantages of a slurry reactor configuration with the photocatalyst dispersed in solution, is the use of magnetic particles as catalyst support materials [176]. For example, a Ru-doped $LaFeO_3$ photocatalyst coupled with magnetic Fe_2O_3 particles was proposed for the photocatalytic production of hydrogen (5460 µmol/L) from glucose degradation (complete removal after 4 h treatment) under visible light irradiation [176]. Notably, the photocatalyst recovered from the photoreactor using an external magnetic force showed high stability, and its activity did not change even after seven cycles of use (Fig. 6).

The hydrogen production observed was competitive relative to the results of other studies in the literature (e.g., 1580 µmol/L under UV irradiation in the presence of ethanol as sacrificial agent and using a perovskite-based catalyst) [177]. It is not possible to make a comparison in the case of glucose as sacrificial agent, since this last compound has thus far been investigated only in the presence of noble metal-based catalysts [178, 179]. Moreover, the magnetic photocatalyst was also tested on real agrifood industrial wastewater (cherry washing process), yielding significant hydrogen production (12,344 µmol/L).

4.3.3 Tannery Wastewater

The tannery industry is one of the most productive sectors for the economies of some countries, but also one of the most environmentally impacting processes due to the huge consumption of water resources and chemicals and the high-polluting wastewater [180]. Tannery wastewater is characterized by a dark brown color, high COD and BOD_5, and the presence of chromium(III) and phenols [181]. The application of HPC with different semiconductors has been intensively studied because of its ability to degrade the pollutants into nontoxic molecules [182, 183]. ZnO supported on glass spheres, through dip-coating technique without using complexing chemicals, have been effective in the discoloration and mineralization of non-biodegradable tannery dyes under UV light irradiation, reaching discoloration and mineralization values higher than 70% [184]. Moreover, the developed structured photocatalyst was also effective in the treatment of real wastewater characterized as having a high COD value (11 g/L) (Fig. 7). COD removal as high as 70% was achieved after 180 min of UV irradiation [184].

Another reported application of ZnO-based photocatalysts (doped with rare earth praseodymium) is in the purification of industrial wastewater from the dyeing and

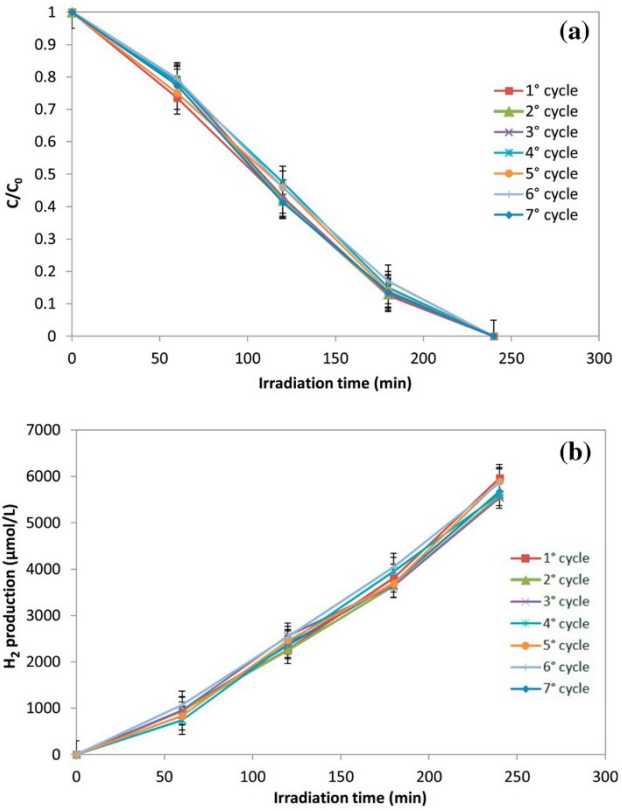

Fig. 6 Photocatalytic degradation (**a**) and hydrogen production (**b**) for Ru-$LaFeO_3$/Fe_2O_3 photocatalysts for different cycles. Initial glucose concentration: 1000 mg/L; catalyst dosage: 1.5 g/L [176]

finishing processes of the leather industry [185]. In particular, a Pr-doped ZnO photocatalyst was able to obtain a discoloration degree higher than 50% after 240 min of UV irradiation, with a TOC removal rate of about 40% (TOC initial values in the range 540–1200 mg/L) after 180 min of UV irradiation.

4.4 What are HPC Prospective Uses for Wastewater Treatment?

According to the results available in the scientific literature and discussed in the sections above, the application of HPC to wastewater treatment is basically at a "technological research" level, which is a technology readiness level (TRL) between 2 and 6 (Fig. 8). A number of disadvantages remain, including (1) technological limitations, (2) lack of regulations limiting the release of specific contaminants into the environment (namely CECs from urban WWTPs), and (3) still low efficiency relative to other consolidated technologies in treating some refractory (industrial) wastewater (Table 2).

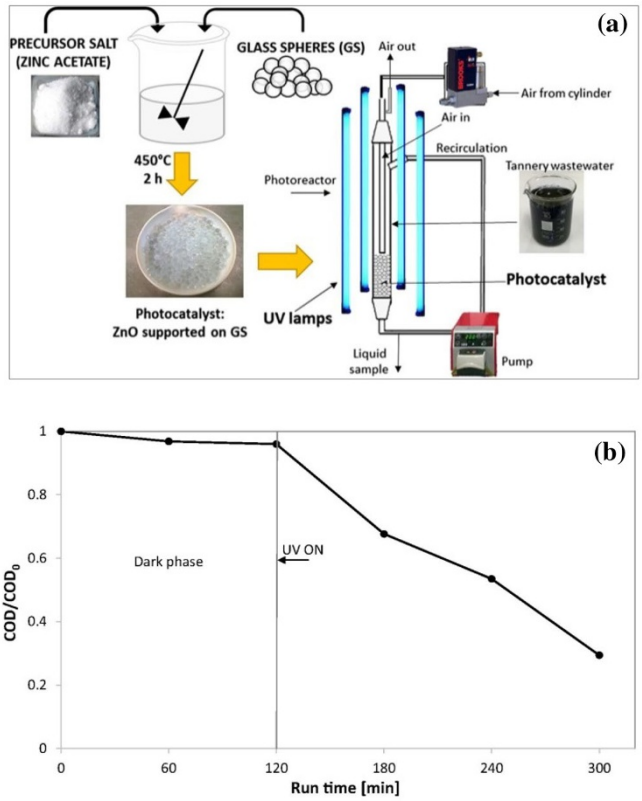

Fig. 7 **a** Schematic representation of synthesis and photocatalytic tests using ZnO on glass spheres. **b** COD behavior as a function of run time during the treatment of tannery real wastewater using ZnO on glass spheres [184]

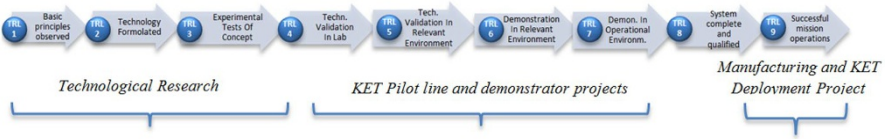

Fig. 8 Technology readiness level scale [185]

Although HPC was found to be effective for the inactivation of pathogens and the degradation of CECs in secondary treated urban wastewater, it is not competitive with consolidated technologies (namely ozonation) due to technological limitations [103, 150], which rank it at TRL 4. Even if such technological limitations are successfully addressed in the future, the absence of a specific regulation on the release of CECs into the environment (except in Switzerland) or in wastewater treated for reused discourages urban WWTP managers from replacing conventional tertiary treatments (mainly disinfection by chlorine, peracetic acid or UV radiation)

Table 2 Summary of advantages, limitations, technology readiness level, and prospects for HPC application to wastewater treatment

Wastewater	Advantages	Limitations	Technology readiness level	Prospects
Urban	Active for both bacterial inactivation and CEC removal Does not involve the addition of an oxidant With suitable modifications can use solar energy Photocatalyst recoverable and reusable, which is very significant given the large volumes of wastewater treated and hence large quantity of catalyst needed	High cost when compared with competing technologies More complex process compared with other possible alternatives	4	Feasible at full scale only if regulations on the removal of CECs come into force (such as in Switzerland) Solar: ripe for development of real scale systems for treatment of wastewater intended for agricultural reuse of specifically edible crops where high quality is essential Non-solar: medium term for reuse scenarios necessitating high water quality Not feasible for treating wastewater intended for discharge in non-sensitive downstream environments
Pharmaceutical industry	The high cost of HPC is justified by the high toxicity of components in this type of wastewater HPC can be used to reduce COD and toxicity and allow the subsequent use of biological treatments	Very high TOC/COD loads The non-specificity of HPC here can be a limitation, since it does not allow targeted treatment based on the chemistry of the wastewater, e.g., if the wastewater is known to have high content of aromatic compounds, ozonation is likely a more efficient treatment	2	HPC needs to be very well established before it will be adopted by the pharmaceutical industry Ozonation and (photo)-Fenton processes are more dependable and have lower reaction times
Pesticide industry	High activity in reducing DOC in wastewater that is often too toxic to be treated by biological means, without any pretreatment Using solar photocatalysis, wastewater can be treated directly on-site, since land area use is generally not an issue in the agricultural sector	Pesticide use is specific to the category of crops grown, season, and region. This introduces a high variability of the components in the wastewater	6	Pilot-level solar reactors have proven to be effective at a competitive cost Adoption of doped catalyst to enhance removal rates under solar radiation could potentially lead to widespread adoption of this technology in the agriculture industry

Table 2 (continued)

Wastewater	Advantages	Limitations	Technology readiness level	Prospects
Tannery and textile	Effective for discoloration of pollutants and COD removal Can improve biodegradability before biological process	Photocatalysts active only under UV light	4	Not yet competitive with consolidated technologies such as Fenton and ozonation to improve wastewater biodegradability. Higher probability of being used as tertiary treatment (after biological process) to remove specific contaminants Development of visible-light-active photocatalysts
Dairy	–	High organic and suspended solids content negatively affect process efficiency	2	Low probability of being used at full scale. The wastewater characteristics make other processes more reliable and effective
Olive mill	Phenols can be degraded and organic load reduced	High organic and suspended solids content negatively affect process efficiency	2	Low probability of being used at full scale to improve biodegradability compared with consolidated technologies such as Fenton and ozonation More likely to be applied as a tertiary treatment for phenol removal if technological developments will make it competitive with consolidated technologies.
Food industry	Possible recovery of energy from the conversion of carbohydrates present in wastewater	Developed only at lab scale	3	Development of photoreactor systems able to produce an amount of hydrogen competitive with the consolidated technologies for energy purposes

with more expensive processes such as AOP, and particularly HPC. The treatment of industrial wastewater is a more complex matter, and process efficiency strongly depends on the specific industrial process. In such a case, wastewater characteristics can change substantially in terms of organic loading (from tens of milligrams to tens of grams per liter of COD) and in quantity of toxic/refractory contaminants. As high organic loads in wastewater are of concern, HPC is less effective than more consolidated processes (namely ozonation and Fenton) as a pre-oxidation step to improve wastewater biodegradability before a less expensive biological treatment step. Nevertheless, HPC could become competitive provided that certain technological limitations are resolved (e.g., reactor design, synthesis, and development of effective supported photocatalysts), as an advanced treatment of industrial wastewater (after biological treatment) to remove specific contaminants not effectively removed by biological processes (e.g., phenols in olive oil wastewater treatment).

5 Conclusions

Although HPC has been widely investigated in recent decades for the removal of several contaminants from aqueous matrices, due to the several issues outlined herein, its application in real wastewater treatment at full scale is still far from becoming a consolidated technology. However, (1) continuing technological developments in terms of increasingly effective photocatalysts (even under visible light) and easily scalable synthesis methods, along with the design of new reactors and the identification of specific applications in wastewater treatment where HPC can be competitive with consolidated technologies, may promote its application at full scale in the mid- to long term. A contribution in that direction can come from an increasing number of investigations under real conditions, developing more reactors at a pilot scale to better investigate their feasibility, and possible scale-up conditions to successfully address specific challenges in wastewater treatment.

Acknowledgements This work is part of a project that has received funding from the European Union's Horizon 2020 under the Innovative Training Networks (ITN-ETN) programme Marie Skłodowska-Curie Grant (ANtibioticS and mobile resistance elements in WastEwater Reuse applications: risks and innovative solutions) agreement no. 675530.

References

1. Esplugas S, Gimenez J Contreras S, Pascual E, Rodríguez M (2002) Comparison of different advanced oxidation processes for phenol degradation. Water Res 36:1034–1042
2. Bhatkhande DS, Pangarkar VG, Beenackers AACM (2002) Photocatalytic degradation for environmental applications–a review. J Chem Technol Biotechnol Int Res Process Environ Clean Technol 77:102–116
3. Ohno T, Sarukawa K, Tokieda K, Matsumura M (2001) Morphology of a TiO_2 photocatalyst (Degussa, P-25) consisting of anatase and rutile crystalline phases. J Catal 203:82–86
4. Bekbölet M, Boyacioglu Z, Özkaraova B (1998) The influence of solution matrix on the photocatalytic removal of color from natural waters. Water Sci Technol 38:155–162

5. Zammit I, Vaiano V, Ribeiro AR, Silva AM, Manaia CM, Rizzo L (2019) Photocatalyst for the degradation of antibiotics and the inactivation of antibiotic-resistant bacteria. Catalysts 9:222
6. Zhang H, Lv X, Li Y, Wang Y, Li J (2009) P25-graphene composite as a high performance photocatalyst. ACS Nano 4:380–386
7. Yang L, Liu B, Liu T, Ma X, Li H, Yin S, Sato T, Wang Y (2017) A P25/$(NH_4)_x WO_3$ hybrid photocatalyst with broad spectrum photocatalytic properties under UV, visible, and near-infrared irradiation. Sci Rep 7:45715
8. Hashimoto K, Irie H, Fujishima A (2005) TiO_2 photocatalysis: a historical overview and future prospects. Jpn J Appl Phys 44:8269–8285
9. Vaiano V, Iervolino G, Rizzo L (2018) Cu-doped ZnO as efficient photocatalyst for the oxidation of arsenite to arsenate under visible light. Appl Catal B 238:471–479
10. Su H, Jing L, Shi K, Yao C, Fu H (2010) Synthesis of large surface area $LaFeO_3$ nanoparticles by SBA-16 template method as high active visible photocatalysts. J Nanopart Res 12:967–974
11. Iervolino G, Vaiano V, Sannino D, Rizzo L, Ciambelli P (2016) Production of hydrogen from glucose by $LaFeO_3$ based photocatalytic process during water treatment. Int J Hydrogen Energy 41:959–966
12. Li S, Jing L, Fu W, Yang L, Xin B, Fu H (2007) Photoinduced charge property of nanosized perovskite-type $LaFeO_3$ and its relationships with photocatalytic activity under visible irradiation. Mater Res Bull 42:203–212
13. Huang L, Fu W, Fu X, Zong B, Liu H, Bala H et al (2017) Facile and large-scale preparation of N doped TiO_2 photocatalyst with high visible light photocatalytic activity. Mater Lett 209:585–588
14. Lee D-K, Kim S-C, Cho I-C, Kim S-J, Kim S-W (2004) Photocatalytic oxidation of microcystin-LR in a fluidized bed reactor having TiO_2-coated activated carbon. Sep Purif Technol 34:59–66
15. Chong MN, Vimonses V, Lei S, Jin B, Chow C, Saint C (2009) Synthesis and characterisation of novel titania impregnated kaolinite nano-photocatalyst. Microporous Mesoporous Mater 117:233–242
16. Argurio P, Fontananova E, Molinari R, Drioli E (2018) Photocatalytic membranes in photocatalytic membrane reactors. Processes 6:162–189
17. Zhu H, Gao X, Lan Y, Song D, Xi Y, Zhao J (2004) Hydrogen titanate nanofibers covered with anatase nanocrystals: a delicate structure achieved by the wet chemistry reaction of the titanate nanofibers. J Am Chem Soc 126:8380–8381
18. Hatat-Fraile M, Liang R, Arlos MJ, He RX, Peng P, Servos MR et al (2017) Concurrent photocatalytic and filtration processes using doped TiO_2 coated quartz fiber membranes in a photocatalytic membrane reactor. Chem Eng J 330:531–540
19. Kwak S-Y, Kim SH, Kim SS (2001) Hybrid organic/inorganic reverse osmosis (RO) membrane for bactericidal anti-fouling. 1. Preparation and characterization of TiO_2 nanoparticle self-assembled aromatic polyamide thin-film-composite (TFC) membrane. Environ Sci Technol 35:2388–2394
20. Dzinun H, Othman MHD, Ismail AF, Puteh MH, Rahman MA, Jaafar J (2015) Photocatalytic degradation of nonylphenol by immobilized TiO_2 in dual layer hollow fibre membranes. Chem Eng J 269:255–261
21. Cantarella M, Sanz R, Buccheri MA, Ruffino F, Rappazzo G, Scalese S et al (2016) Immobilization of nanomaterials in PMMA composites for photocatalytic removal of dyes, phenols and bacteria from water. J Photochem Photobiol A 321:1–11
22. Chen C-Y, Wang M, Li J-Y, Pootrakulchote N, Alibabaei L, Ngoc-le C-h et al (2009) Highly efficient light-harvesting ruthenium sensitizer for thin-film dyesensitized solar cells. ACS nano 3:3103–3109
23. Chen Z, Li F, Huang C (2007) Organic D-π-A dyes for dye-sensitized solar cell. Curr Org Chem 11:1241–1258
24. Ito S, Miura H, Uchida S, Takata M, Sumioka K, Liska P et al (2008) High-conversion-efficiency organic dye-sensitized solar cells with a novel indoline dye. Chem Commun 44(41):5194–5196
25. Zhang Z, Wang W, Wang L, Sun S (2012) Enhancement of visible-light photocatalysis by coupling with narrow-band-gap semiconductor: a case study on Bi_2S_3/Bi_2WO_6. ACS Appl Mater Interfaces 4:593–597
26. Vaiano V, Iervolino G, Sannino D (2016) Photocatalytic Removal of Tartrazine Dye from Aqueous Samples on $LaFeO_3$/ZnO Photocatalysts. Chem Eng Trans 52:847–852
27. Abe R, Sayama K, Arakawa H (2002) Efficient hydrogen evolution from aqueous mixture of I^- and acetonitrile using a merocyanine dye-sensitized Pt/TiO_2 photocatalyst under visible light irradiation. Chem Phys Lett 362:441–444

28. Boschloo G, Hagfeldt A (2005) Activation energy of electron transport in dye-sensitized TiO_2 solar cells. J Phys Chem B 109:12093–12098
29. Tae EL, Lee SH, Lee JK, Yoo SS, Kang EJ, Yoon KB (2005) A strategy to increase the efficiency of the dye-sensitized TiO2 solar cells operated by photoexcitation of dye-to-TiO_2 charge-transfer bands. J Phys Chem B 109:22513–22522
30. Pearton SJ, Norton DP, Ivill MP, Hebard AF, Zavada JM, Chen WM et al (2007) ZnO Doped With Transition Metal Ions. IEEE Trans Electron Devices 54:1040–1048
31. Iervolino G, Vaiano V, Rizzo L (2018) Visible light active Fe-doped TiO_2 for the oxidation of arsenite to arsenate in drinking water. Chem Eng Trans 70:1573–1578
32. Akpan UG, Hameed BH (2010) The advancements in sol–gel method of doped-TiO_2 photocatalysts. Appl Catal A 375:1–11
33. Hoffmann MR, Martin ST, Choi W, Bahnemann DW (1995) Environmental applications of semiconductor photocatalysis. Chem Rev 95:69–96
34. Anpo M, Takeuchi M (2003) The design and development of highly reactive titanium oxide photocatalysts operating under visible light irradiation. J Catal 216:505–516
35. Alshammari AS, Chi L, Chen X, Bagabas A, Kramer D, Alromaeh A et al (2015) Visible-light photocatalysis on C-doped ZnO derived from polymer-assisted pyrolysis. RSC Advances. 5:27690–27698
36. Vaiano V, Sacco O, Sannino D, Ciambelli P (2016) N-doped ZnO nanoparticles supported on ZnS based blue phosphors in the photocatalytic removal of eriochrome black-T dye. Chem Eng Trans 47:187–192
37. Thompson TL, Yates JT (2006) Surface science studies of the photoactivation of TiO_2 new photochemical processes. Chem Rev 106:4428–4453
38. Di Valentin C, Pacchioni G, Selloni A, Livraghi S, Giamello E (2005) Characterization of paramagnetic species in N-doped TiO_2 powders by EPR spectroscopy and DFT calculations. J Phys Chem B 109:11414–11419
39. Gombac V, De Rogatis L, Gasparotto A, Vicario G, Montini T, Barreca D et al (2007) TiO_2 nanopowders doped with boron and nitrogen for photocatalytic applications. Chem Phys 339:111–123
40. Zhang X, Liu Q (2008) Preparation and characterization of titania photocatalyst co-doped with boron, nickel, and cerium. Mater Lett 62:2589–2592
41. Huang D-G, Liao S-J, Liu J-M, Dang Z, Petrik L (2006) Preparation of visible-light responsive N-F-codoped TiO_2 photocatalyst by a sol–gel-solvothermal method. J Photochem Photobiol A 184:282–288
42. Srinivasan SS, Wade J, Stefanakos EK, Goswami Y (2006) Synergistic effects of sulfation and co-doping on the visible light photocatalysis of TiO_2. J Alloy Compd 424:322–326
43. Wilke K, Breuer H (1999) The influence of transition metal doping on the physical and photocatalytic properties of titania. J Photochem Photobiol A 121:49–53
44. Macías-Sánchez J, Hinojosa-Reyes L, Caballero-Quintero Ad, De La Cruz W, Ruiz-Ruiz E, Hernández-Ramírez A et al (2015) Synthesis of nitrogen-doped ZnO by sol–gel method: characterization and its application on visible photocatalytic degradation of 2, 4-D and picloram herbicides. Photochem Photobiol Sci 14:536–542
45. Pal M, Bera S, Sarkar S, Jana S (2014) Influence of Al doping on microstructural, optical and photocatalytic properties of sol–gel based nanostructured zinc oxide films on glass. Rsc Advances 4:11552–11563
46. Thongsuriwong K, Amornpitoksuk P, Suwanboon S (2012) Photocatalytic and antibacterial activities of Ag-doped ZnO thin films prepared by a sol–gel dip-coating method. J Sol-Gel Sci Technol 62:304–312
47. Fu M, Li Y, Lu P, Liu J, Dong F (2011) Sol–gel preparation and enhanced photocatalytic performance of Cu-doped ZnO nanoparticles. Appl Surf Sci 258:1587–1591
48. Lima MK, Fernandes DM, Silva MF, Baesso ML, Neto AM, de Morais GR et al (2014) Co-doped ZnO nanoparticles synthesized by an adapted sol–gel method: effects on the structural, optical, photocatalytic and antibacterial properties. J Sol-Gel Sci Technol 72:301–309
49. Gionco C, Paganini MC, Giamello E, Burgess R, Di Valentin C, Pacchioni G (2014) Cerium-doped zirconium dioxide, a visible-light-sensitive photoactive material of third generation. J Phys Chem Lett 5:447–451
50. Vaiano V, Sacco O, Sannino D, Ciambelli P (2015) Nanostructured N-doped TiO_2 coated on glass spheres for the photocatalytic removal of organic dyes under UV or visible light irradiation. Appl Catal B 170–171:153–161

51. Sōmiya S, Roy R (2000) Hydrothermal synthesis of fine oxide powders. Bull Mater Sci 23:453–460
52. Einarsrud M-A, Grande T (2014) 1D oxide nanostructures from chemical solutions. Chem Soc Rev 43:2187–2199
53. Anpo M, Kamat PV (2010) Environmentally benign photocatalysts: applications of titanium oxide-based materials, Chap 1. Springer Science & Business Media
54. Zhou JK, Lv L, Yu J, Li HL, Guo P-Z, Sun H et al (2008) Synthesis of self-organized polycrystalline F-doped TiO2 hollow microspheres and their photocatalytic activity under visible light. J Phys Chem C 112:5316–5321
55. Regalbuto J (2016) Catalyst preparation: science and engineering, Chap 8. CRC press
56. Nejati K, Rezvani Z, Pakizevand R (2011) Synthesis of ZnO nanoparticles and investigation of the ionic template effect on their size and shape. Int Nano Lett 1:75–81
57. Vaiano V, Sacco O, Sannino D, Ciambelli P (2015) Process intensification in the removal of organic pollutants from wastewater using innovative photocatalysts obtained coupling Zinc Sulfide based phosphors with nitrogen doped semiconductors. J Clean Prod 100:208–211
58. Mittal M, Sharma M, Pandey O (2014) UV–Visible light induced photocatalytic studies of Cu doped ZnO nanoparticles prepared by co-precipitation method. Sol Energy 110:386–397
59. Amornpitoksuk P, Suwanboon S, Sangkanu S, Sukhoom A, Muensit N, Baltrusaitis J (2012) Synthesis, characterization, photocatalytic and antibacterial activities of Ag-doped ZnO powders modified with a diblock copolymer. Powder Technol 219:158–164
60. Zhang Y, Stangle GC (1994) Preparation of fine multicomponent oxide ceramic powder by a combustion synthesis process. J Mater Res 9:1997–2004
61. Manoharan SS, Kumar N, Patil K (1990) Preparation of fine particle chromites: a combustion approach. Mater Res Bull 25:731–738
62. Deganello F, Tyagi AK (2018) Solution combustion synthesis, energy and environment: Best parameters for better materials. Prog Cryst Growth Charact Mater 64:23–61
63. Danks AE, Hall SR, Schnepp Z (2016) The evolution of 'sol–gel' chemistry as a technique for materials synthesis. Mater Horiz 3:91–112
64. Peng K, Fu L, Yang H, Ouyang J (2016) Perovskite $LaFeO_3$/montmorillonite nanocomposites: synthesis, interface characteristics and enhanced photocatalytic activity. Sci Rep 6:19723–19733
65. Parida K, Reddy K, Martha S, Das D, Biswal N (2010) Fabrication of nanocrystalline $LaFeO_3$: an efficient sol–gel auto-combustion assisted visible light responsive photocatalyst for water decomposition. Int J Hydrogen Energy 35:12161–12168
66. Sannino D, Vaiano V, Ciambelli P, Isupova LA (2011) Structured catalysts for photo-Fenton oxidation of acetic acid. Catal Today 161:255–259
67. Vaiano V, Iervolino G, Sannino D, Rizzo L, Sarno G, Ciambelli P et al (2015) Food Azo-Dyes removal from water by heterogeneous photo-fenton with $LaFeO_3$ supported on honeycomb corundum monoliths. J Environ Eng 141(12):04015038
68. Sannino D, Vaiano V, Ciambelli P, Isupova L (2013) Mathematical modelling of the heterogeneous photo-Fenton oxidation of acetic acid on structured catalysts. Chem Eng J 224:53–58
69. Suslick KS, Price GJ (1999) Applications of ultrasound to materials chemistry. Annu Rev Mater Sci 29:295–326
70. Xu H, Zeiger BW, Suslick KS (2013) Sonochemical synthesis of nanomaterials. Chem Soc Rev 42:2555–2567
71. Teh CY, Wu TY, Juan JC (2017) An application of ultrasound technology in synthesis of titania-based photocatalyst for degrading pollutant. Chem Eng J 317:586–612
72. Moholkar VS, Sivasankar T, Nalajala VS (2012) 20 Mechanistic aspects of ultrasound-enhanced physical and chemical processes. In: Handbook on applications of, pp 501–531
73. Sancheti SV, Gogate PR (2017) A review of engineering aspects of intensification of chemical synthesis using ultrasound. Ultrason Sonochem 36:527–543
74. Huang W, Tang X, Wang Y, Koltypin Y, Gedanken A (2000) Selective synthesis of anatase and rutile via ultrasound irradiation. Chem Commun 15(15):1415–1416
75. Jimmy CY, Zhang L, Yu J (2002) Rapid synthesis of mesoporous TiO_2 with high photocatalytic activity by ultrasound-induced agglomeration. New J Chem 26:416–420
76. Boels L, Wagterveld R, Mayer M, Witkamp G (2010) Seeded calcite sonocrystallization. J Cryst Growth 312:961–966
77. Tian C, Zhang Q, Wu A, Jiang M, Liang Z, Jiang B et al (2012) Cost-effective large-scale synthesis of ZnO photocatalyst with excellent performance for dye photodegradation. Chem Commun 48:2858–2860

78. Thiagarajan S, Sanmugam A, Vikraman D (2017) Facile methodology of Sol-Gel synthesis for metal oxide nanostructures. In: Recent applications in sol–gel synthesis, Chap 1, IntechOpen
79. Macwan D, Dave PN, Chaturvedi S (2011) A review on nano-TiO_2 sol–gel type syntheses and its applications. J Mater Sci 46:3669–3686
80. Lin K, Wu C, Chang J (2014) Advances in synthesis of calcium phosphate crystals with controlled size and shape. Acta Biomater 10:4071–4102
81. O'Donoghue M (1983) A guide to man-made gemstones. Van Nostrand Reinhold Company
82. Khalil I, Julkapli N, Yehye W, Basirun W, Bhargava S (2016) Graphene–gold nanoparticles hybrid—synthesis, functionalization, and application in a electrochemical and surface-enhanced raman scattering biosensor. Materials 9:406–444
83. Varma A, Mukasyan AS, Rogachev AS, Manukyan KV (2016) Solution combustion synthesis of nanoscale materials. Chem Rev 116:14493–14586
84. Aghayan M, Rodríguez M (2012) Influence of fuels and combustion aids on solution combustion synthesis of bi-phasic calcium phosphates (BCP). Mater Sci Eng C 32:2464–2468
85. Bang JH, Suslick KS (2010) Applications of ultrasound to the synthesis of nanostructured materials. Adv Mater 22:1039–1059
86. Loeb SK, Alvarez PJ, Brame JA, Cates EL, Choi W, Crittenden J et al (2019) The technology horizon for photocatalytic water treatment: sunrise or sunset? : ACS Publications. Environ Sci Technol 53:2937–2947
87. Liao C-H, Gurol MD (1995) Chemical oxidation by photolytic decomposition of hydrogen peroxide. Environ Sci Technol 29:3007–3014
88. Fiorentino A, Ferro G, Alferez MC, Polo-López MI, Fernández-Ibañez P, Rizzo L (2015) Inactivation and regrowth of multidrug resistant bacteria in urban wastewater after disinfection by solar-driven and chlorination processes. J Photochem Photobiol B 148:43–50
89. Rizzo L, Lofrano G, Grassi M, Belgiorno V (2008) Pre-treatment of olive mill wastewater by chitosan coagulation and advanced oxidation processes. Sep Purif Technol 63:648–653
90. Haroune L, Salaun M, Ménard A, Legault CY, Bellenger J-P (2014) Photocatalytic degradation of carbamazepine and three derivatives using TiO2 and ZnO: Effect of pH, ionic strength, and natural organic matter. Sci Total Environ 475:16–22
91. Qin G, Sun Z, Wu Q, Lin L, Liang M, Xue S (2011) Dye-sensitized TiO2 film with bifunctionalized zones for photocatalytic degradation of 4-cholophenol. J Hazard Mater 192:599–604
92. Adán C, Magnet A, Fenoy S, Pablos C, Del Águila C, Marugán J (2018) Concomitant inactivation of *Acanthamoeba* spp. and Escherichia coli using suspended and immobilized TiO_2. Water Res 144:512–521
93. Lalhriatpuia C, Tiwari D, Tiwari A, Lee SM (2015) Immobilized Nanopillars-TiO_2 in the efficient removal of micro-pollutants from aqueous solutions: physicochemical studies. Chem Eng J 281:782–792
94. Xiong P, Hu J (2013) Inactivation/reactivation of antibiotic-resistant bacteria by a novel UVA/LED/TiO_2 system. Water Res 47:4547–4555
95. Coronado JM, Fresno F, Hernández-Alonso MD, Portela R (2013) Design of advanced photocatalytic materials for energy and environmental applications, Springer, pp 123–156
96. Yu H, Song L, Hao Y, Lu N, Quan X, Chen S et al (2016) Fabrication of pilot-scale photocatalytic disinfection device by installing TiO_2 coated helical support into UV annular reactor for strengthening sterilization. Chem Eng J 283:1506–1513
97. Borges M, Sierra M, Esparza P (2017) Solar photocatalysis at semi-pilot scale: wastewater decontamination in a packed-bed photocatalytic reactor system with a visible-solar-light-driven photocatalyst. Clean Technol Environ Policy 19:1239–1245
98. Antonelli M, Turolla A, Mezzanotte V, Nurizzo C (2013) Peracetic acid for secondary effluent disinfection: a comprehensive performance assessment. Water Sci Technol 68:2638–2644
99. Da Costa JB, Rodgher S, Daniel LA, Espíndola ELG (2014) Toxicity on aquatic organisms exposed to secondary effluent disinfected with chlorine, peracetic acid, ozone and UV radiation. Ecotoxicology 23:1803–1813
100. Di Cesare A, Eckert EM, D'Urso S, Bertoni R, Gillan DC, Wattiez R et al (2016) Co-occurrence of integrase 1, antibiotic and heavy metal resistance genes in municipal wastewater treatment plants. Water Res 94:208–214
101. McArdell C (2015) The first full-scale advanced ozonation plant in the Dübendorf WWTP running; the new Swiss water protection act approved. Norman Bulletin 4:36–37

102. Rizzo L, Malato S, Antakyali D, Beretsou VG, Đolić MB, Gernjak W et al (2019) Consolidated vs new advanced treatment methods for the removal of contaminants of emerging concern from urban wastewater. Sci Total Environ 655:986–1008
103. Vaiano V, Matarangolo M, Sacco O, Sannino D (2017) Photocatalytic treatment of aqueous solutions at high dye concentration using praseodymium-doped ZnO catalysts. Appl Catal B 209:621–630
104. .Konstantinou I, Albanis T (2004) TiO_2-Assisted photocatalytic degradation of azo dyes in aqueous solution: kinetic and mechanistic investigations: a review 49:1-14
105. Chiang L-F, Doong R-A (2014) Cu-TiO_2 nanorods with enhanced ultraviolet- and visible-light photoactivity for bisphenol A degradation. J Hazard Mater 277:84–92
106. Calza P, Sakkas VA, Medana C, Baiocchi C, Dimou A, Pelizzetti E et al (2006) Photocatalytic degradation study of diclofenac over aqueous TiO_2 suspensions. Appl Catal B 67:197–205
107. Reyes C, Fernández J, Freer J, Mondaca MA, Zaror C, Malato S et al (2006) Degradation and inactivation of tetracycline by TiO_2 photocatalysis. J Photochem Photobiol, A 184:141–146
108. Elmolla ES, Chaudhuri M (2010) Degradation of amoxicillin, ampicillin and cloxacillin antibiotics in aqueous solution by the UV/ZnO photocatalytic process. J Hazard Mater 173:445–449
109. Mijin D, Savić M, Snežana P, Smiljanić A, Glavaški O, Jovanović M et al (2009) A study of the photocatalytic degradation of metamitron in ZnO water suspensions. Desalination 249:286–292
110. Ahmed S, Rasul MG, Brown R, Hashib MA (2011) Influence of parameters on the heterogeneous photocatalytic degradation of pesticides and phenolic contaminants in wastewater: A short review. J Environ Manage 92:311–330
111. Rizzo L, Della Sala A, Fiorentino A, Li Puma G (2014) Disinfection of urban wastewater by solar driven and UV lamp – TiO_2 photocatalysis: effect on a multi drug resistant Escherichia coli strain. Water Res 53:145–152
112. Wang W, Huang G, Yu JC, Wong PK (2015) Advances in photocatalytic disinfection of bacteria: development of photocatalysts and mechanisms. J Environ Sci 34:232–247
113. Choi J, Lee H, Choi Y, Kim S, Lee S, Lee S et al (2014) Heterogeneous photocatalytic treatment of pharmaceutical micropollutants: effects of wastewater effluent matrix and catalyst modifications. Appl Catal B 147:8–16
114. Buxton GV, Greenstock CL, Helman WP, Ross AB (1988) Critical review of rate constants for reactions of hydrated electrons, hydrogen atoms and hydroxyl radicals ($\cdot OH/\cdot O^-$) in aqueous solution. J Phys Chem Ref Data 17:513–886
115. Luo X, Yang X, Qiao X, Wang Y, Chen J, Wei X et al (2017) Development of a QSAR model for predicting aqueous reaction rate constants of organic chemicals with hydroxyl radicals. Environmental Science: Processes & Impacts. 19:350–356
116. Jallouli N, Pastrana Martinez L, Ribeiro A, Moreira N, L Faria J, Hentati O, et al (2018) Heterogeneous photocatalytic degradation of ibuprofen in ultrapure water, municipal and pharmaceutical industry wastewaters using a TiO_2/UV-LED system. 334:976–984
117. Wilson WW, Wade MM, Holman SC, Champlin FR (2001) Status of methods for assessing bacterial cell surface charge properties based on zeta potential measurements. J Microbiol Methods 43:153–164
118. Gottenbos B, Grijpma DW, van der Mei HC, Feijen J, Busscher HJ (2001) Antimicrobial effects of positively charged surfaces on adhering Gram-positive and Gram-negative bacteria. J Antimicrob Chemother 48:7–13
119. Coleman HM, Marquis CP, Scott JA, Chin SS, Amal R (2005) Bactericidal effects of titanium dioxide-based photocatalysts. Chem Eng J 113:55–63
120. Thomas O, Causse J, Thomas M-F (2017) Aggregate organic constituents. Chap 4
121. Fiorentino A, Esteban B, Garrido-Cardenas JA, Kowalska K, Rizzo L, Aguera A et al (2019) Effect of solar photo-Fenton process in raceway pond reactors at neutral pH on antibiotic resistance determinants in secondary treated urban wastewater. J Hazard Mater 378:120737–120746
122. McCullagh C, Skillen N, Adams M, Robertson PKJ (2011) Photocatalytic reactors for environmental remediation: a review. J Chem Technol Biotechnol 86:1002–1017
123. Braham RJ, Harris AT (2009) Review of major design and scale-up considerations for solar photocatalytic reactors. Ind Eng Chem Res 48:8890–8905
124. Paltiel O, Fedorova G, Tadmor G, Kleinstern G, Maor Y, Chefetz B (2016) Human exposure to wastewater-derived pharmaceuticals in fresh produce: a randomized controlled trial focusing on carbamazepine. Environ Sci Technol 50:4476–4482

125. Alexander J, Knopp G, Dötsch A, Wieland A, Schwartz T (2016) Ozone treatment of conditioned wastewater selects antibiotic resistance genes, opportunistic bacteria, and induce strong population shifts. Sci Total Environ 559:103–112
126. Liu S-S, Qu H-M, Yang D, Hu H, Liu W-L, Qiu Z-G et al (2018) Chlorine disinfection increases both intracellular and extracellular antibiotic resistance genes in a full-scale wastewater treatment plant. Water Res 136:131–136
127. Murray GE, Tobin RS, Junkins B, Kushner DJ (1984) Effect of chlorination on antibiotic resistance profiles of sewage-related bacteria. Appl Environ Microbiol 48:73–77
128. Zheng J, Su C, Zhou J, Xu L, Qian Y, Chen H (2017) Effects and mechanisms of ultraviolet, chlorination, and ozone disinfection on antibiotic resistance genes in secondary effluents of municipal wastewater treatment plants. Chem Eng J 317:309–316
129. Karaolia P, Michael-Kordatou I, Hapeshi E, Drosou C, Bertakis Y, Christofilos D et al (2018) Removal of antibiotics, antibiotic-resistant bacteria and their associated genes by graphene-based TiO2 composite photocatalysts under solar radiation in urban wastewaters. Appl Catal B 224:810–824
130. Moreira NFF, Sousa JM, Macedo G, Ribeiro AR, Barreiros L, Pedrosa M et al (2016) Photocatalytic ozonation of urban wastewater and surface water using immobilized TiO2 with LEDs: Micropollutants, antibiotic resistance genes and estrogenic activity. Water Res 94:10–22
131. Amiri H, Nabizadeh R, Silva Martinez S, Jamaleddin Shahtaheri S, Yaghmaeian K, Badiei A et al (2018) Response surface methodology modeling to improve degradation of Chlorpyrifos in agriculture runoff using TiO_2 solar photocatalytic in a raceway pond reactor. Ecotoxicol Environ Saf 147:919–925
132. Carra I, Santos-Juanes L, Acién Fernández FG, Malato S, Sánchez Pérez JA. New approach to solar photo-Fenton operation. Raceway ponds as tertiary treatment technology. Journal of Hazardous Materials. 2014;279:322-9.
133. Mehrjouei M, Müller S, Möller D (2015) A review on photocatalytic ozonation used for the treatment of water and wastewater. Chem Eng J 263:209–219
134. Cho M, Gandhi V, Hwang T-M, Lee S, Kim J-H (2011) Investigating synergism during sequential inactivation of MS-2 phage and Bacillus subtilis spores with UV/H_2O_2 followed by free chlorine. Water Res 45:1063–1070
135. Bandala ER, González L, Sanchez-Salas JL, Castillo JH (2011) Inactivation of Ascaris eggs in water using sequential solar driven photo-Fenton and free chlorine. J Water Health 10:20–30
136. Meng X, Zhang Z (2018) Two dimensional graphitic materials for photoelectrocatalysis: a short review. Catal Today 315:2–8
137. Li X, Yu J, Wageh S, Al-Ghamdi AA, Xie J (2016) Graphene in photocatalysis: a review. Small 12:6640–6696
138. Georgieva J, Valova E, Armyanov S, Philippidis N, Poulios I, Sotiropoulos S (2012) Bi-component semiconductor oxide photoanodes for the photoelectrocatalytic oxidation of organic solutes and vapours: a short review with emphasis to TiO_2–WO_3 photoanodes. J Hazard Mater 211:30–46
139. Yang M-Q, Zhang N, Pagliaro M, Xu Y-J (2014) Artificial photosynthesis over graphene–semiconductor composites. Are we getting better? Chem Soc Rev 43:8240–8254
140. Kakaei K (2013) One-pot electrochemical synthesis of graphene by the exfoliation of graphite powder in sodium dodecyl sulfate and its decoration with platinum nanoparticles for methanol oxidation. Carbon 51:195–201
141. Liu C, Zhang L, Liu R, Gao Z, Yang X, Tu Z et al (2016) Hydrothermal synthesis of N-doped TiO_2 nanowires and N-doped graphene heterostructures with enhanced photocatalytic properties. J Alloy Compd 656:24–32
142. Jin Z, Zhang Q, Yuan S, Ohno T (2015) Synthesis high specific surface area nanotube gC_3N_4 with two-step condensation treatment of melamine to enhance photocatalysis properties. RSC Adv 5:4026–4029
143. Ozer LY, Garlisi C, Oladipo H, Pagliaro M, Sharief SA, Yusuf A et al (2017) Inorganic semiconductors-graphene composites in photo (electro) catalysis: synthetic strategies, interaction mechanisms and applications. J Photochem Photobiol C 33:132–164
144. Wang G, Feng W, Zeng X, Wang Z, Feng C, McCarthy DT et al (2016) Highly recoverable TiO_2–GO nanocomposites for stormwater disinfection. Water Res 94:363–370
145. Garcia DT, Ozer LY, Parrino F, Ahmed M, Brudecki GP, Hasan SW et al (2018) Photocatalytic ozonation under visible light for the remediation of water effluents and its integration with an electro-membrane bioreactor. Chemosphere 209:534–541

146. Sanchez M, Rivero M, Ortiz I (2010) Photocatalytic oxidation of grey water over titanium dioxide suspensions. Desalination 262:141–146
147. Armanious A, Özkan A, Sohmen U, Gulyas H (2011) Inorganic greywater matrix impact on photocatalytic oxidation: does flocculation of TiO_2 nanoparticles impair process efficiency? Water Sci Technol 63:2808–2813
148. Michael I, Rizzo L, McArdell CS, Manaia CM, Merlin C, Schwartz T et al (2013) Urban wastewater treatment plants as hotspots for the release of antibiotics in the environment: a review. Water Res 47:957–995
149. Rizzo L, Meric S, Guida M, Kassinos D, Belgiorno V (2009) Heterogenous photocatalytic degradation kinetics and detoxification of an urban wastewater treatment plant effluent contaminated with pharmaceuticals. Water Res 43:4070–4078
150. Mascolo G, Balest L, Cassano D, Laera G, Lopez A, Pollice A et al (2010) Biodegradability of pharmaceutical industrial wastewater and formation of recalcitrant organic compounds during aerobic biological treatment. Biores Technol 101:2585–2591
151. Deng F, Zhao L, Luo X, Luo S, Dionysiou DD (2018) Highly efficient visible-light photocatalytic performance of Ag/AgIn5S8 for degradation of tetracycline hydrochloride and treatment of real pharmaceutical industry wastewater. Chem Eng J 333:423–433
152. Alalm MG, Tawfik A, Ookawara S (2015) Comparison of solar TiO_2 photocatalysis and solar photo-Fenton for treatment of pesticides industry wastewater: operational conditions, kinetics, and costs. J Water Process Eng 8:55–63
153. Fenoll J, Garrido I, Flores P, Hellín P, Vela N, Navarro G et al (2019) Implementation of a new modular facility to detoxify agro-wastewater polluted with neonicotinoid insecticides in farms by solar photocatalysis. Energy 175:722–729
154. Kushniarou A, Garrido I, Fenoll J, Vela N, Flores P, Navarro G et al (2019) Solar photocatalytic reclamation of agro-waste water polluted with twelve pesticides for agricultural reuse. Chemosphere 214:839–845
155. Singh P, Lakhan Singh R (2017) Bio-removal of azo dyes: a review. Int J Appl Sci Biotechnol 5(2):108–126
156. Gita S, Hussan A, Choudhury T (2017) Impact of textile dyes waste on aquatic environments and its treatment. Environ Ecol. 35:2349–2353
157. Zhou Z, Lin S, Yue T, Lee T-C (2014) Adsorption of food dyes from aqueous solution by glutaraldehyde cross-linked magnetic chitosan nanoparticles. J Food Eng 126:133–141
158. Klamerth N, Rizzo L, Malato S, Maldonado MI, Agüera A, Fernández-Alba AR (2010) Degradation of fifteen emerging contaminants at μgL^{-1} initial concentrations by mild solar photo-Fenton in MWTP effluents. Water Res 44:545–554
159. Rodríguez-Chueca J, Polo-López MI, Mosteo R, Ormad MP, Fernández-Ibáñez P (2014) Disinfection of real and simulated urban wastewater effluents using a mild solar photo-Fenton. Appl Catal B 150–151:619–629
160. Wang N, Zheng T, Zhang G, Wang P (2016) A review on Fenton-like processes for organic wastewater treatment. J Environ Chem Eng 4:762–787
161. De Luca A, Dantas RF, Esplugas S (2014) Assessment of iron chelates efficiency for photo-Fenton at neutral pH. Water Res 61:232–242
162. Papoutsakis S, Miralles-Cuevas S, Oller I, Garcia Sanchez JL, Pulgarin C, Malato S (2015) Microcontaminant degradation in municipal wastewater treatment plant secondary effluent by EDDS assisted photo-Fenton at near-neutral pH: an experimental design approach. Catal Today 252:61–69
163. Iervolino G, Vaiano V, Sannino D, Rizzo L, Sarno G, Ciambelli P et al (2015) Influence of operating conditions in the photo-fenton removal of tartrazine on structured catalysts. Chem Eng Trans 43:979–984
164. Sohrabi MR, Khavaran A, Shariati S, Shariati S (2017) Removal of carmoisine edible dye by fenton and photo fenton processes using taguchi orthogonal array design. Arab J Chem 10:S3523–S3531
165. Feng J, Hu X, Yue PL (2005) Discoloration and mineralization of Orange II by using a bentonite clay-based Fe nanocomposite film as a heterogeneous photo-Fenton catalyst. Water Res 39:89–96
166. He J, Tao X, Ma W, Zhao J (2002) Heterogeneous photo-Fenton degradation of an azo dye in aqueous H_2O_2/Iron oxide dispersions at neutral pHs. Chem Lett 31:86–87
167. Vourch M, Balannec B, Chaufer B, Dorange G (2008) Treatment of dairy industry wastewater by reverse osmosis for water reuse. Desalination 219:190–202

168. Janczukowicz W, Zieliński M, Dębowski M (2008) Biodegradability evaluation of dairy effluents originated in selected sections of dairy production. Biores Technol 99:4199–4205
169. Murcia JJ, Hernández-Laverde M, Rojas H, Muñoz E, Navío JA, Hidalgo MC (2018) Study of the effectiveness of the flocculation-photocatalysis in the treatment of wastewater coming from dairy industries. J Photochem Photobiol A 358:256–264
170. Lamas Samanamud GR, Loures CCA, Souza AL, Salazar RFS, Oliveira IS, Silva MB et al (2012) Heterogeneous photocatalytic degradation of dairy wastewater using immobilized ZnO. ISRN Chemical Engineering. 2012:1–8
171. Lucchetti R, Siciliano A, Clarizia L, Russo D, Di Somma I, Natale F et al (2017) Sacrificial photocatalysis: removal of nitrate and hydrogen production by nano-copper-loaded P25 titania. A kinetic and ecotoxicological assessment. Environ Sci Pollut Res 24:5898–5907
172. Li Y, Wang L, Cai T, Zhang S, Liu Y, Song Y et al (2017) Glucose-assisted synthesize 1D/2D nearly vertical CdS/MoS_2 heterostructures for efficient photocatalytic hydrogen evolution. Chem Eng J 321:366–374
173. Wang X, Dong H, Hu Z, Qi Z, Li L (2017) Fabrication of a Cu_2O/Au/TiO_2 composite film for efficient photocatalytic hydrogen production from aqueous solution of methanol and glucose. Mater Sci Eng, B 219:10–19
174. Speltini A, Scalabrini A, Maraschi F, Sturini M, Pisanu A, Malavasi L et al (2018) Improved photocatalytic H2 production assisted by aqueous glucose biomass by oxidized g-C3N4. Int J Hydrogen Energy 43:14925–14933
175. Iervolino G, Vaiano V, Sannino D, Rizzo L, Galluzzi A, Polichetti M, et al (2018) Hydrogen production from glucose degradation in water and wastewater treated by Ru-$LaFeO_3$ /Fe_2O_3 magnetic particles photocatalysis and heterogeneous photo-Fenton 43:2184–2196
176. Tijare SN, Bakardjieva S, Subrt J, Joshi MV, Rayalu SS, Hishita S et al (2014) Synthesis and visible light photocatalytic activity of nanocrystalline PrFeO3perovskite for hydrogen generation in ethanol–water system. J Chem Sci 126:517–525
177. Caravaca A, Jones W, Hardacre C, Bowker M (2016) H(2) production by the photocatalytic reforming of cellulose and raw biomass using Ni, Pd, Pt and Au on titania. Proc Math Phys Eng Sci 472:20160054–20160075
178. Vaiano V, Iervolino G, Sarno G, Sannino D, Rizzo L, Murcia Mesa JJ et al (2015) Simultaneous production of CH4 and H2 from photocatalytic reforming of glucose aqueous solution on sulfated Pd-TiO_2 catalysts. Oil Gas Sci Technol 70:891–902
179. Saxena G, Chandra R, Bharagava RN (2017) Environmental Pollution, Toxicity Profile and Treatment Approaches for Tannery Wastewater and Its Chemical Pollutants. Rev Environ Contam Toxicol 240:31–69
180. Dixit S, Yadav A, Dwivedi PD, Das M (2015) Toxic hazards of leather industry and technologies to combat threat: a review. J Clean Prod 87:39–49
181. Antonopoulou M, Chondrodimou I, Bairamis F, Giannakas A, Konstantinou I (2017) Photocatalytic reduction of Cr(VI) by char/TiO2 composite photocatalyst: optimization and modeling using the response surface methodology (RSM). Environ Sci Pollut Res 24:1063–1072
182. Shet A, Shetty KV (2016) Photocatalytic degradation of phenol using Ag core-TiO_2 shell (Ag@ TiO_2) nanoparticles under UV light irradiation. Environ Sci Pollut Res 23:20055–20064
183. Vaiano V, Iervolino G (2018) Facile method to immobilize ZnO particles on glass spheres for the photocatalytic treatment of tannery wastewater. J Colloid Interface Sci 518:192–199
184. Caracciolo D, Vaiano V, Matarangolo M, Sacco O, Sannino D, Gambicorti T et al (2017) Treatment of dyeing and finishing waters using innovative photocatalysts. Chem Eng Trans 60:187–192
185. High-level expert group on key enabling technologies—final report". 2011. Retrieved October 2017:1–56

Affiliations

Giuseppina Iervolino[1] · Ian Zammit[2] · Vincenzo Vaiano[1] · Luigi Rizzo[2]

✉ Luigi Rizzo
l.rizzo@unisa.it

[1] Department of Industrial Engineering, University of Salerno, Via Giovanni Paolo II 132, 84084 Fisciano, SA, Italy

[2] Department of Civil Engineering, University of Salerno, Via Giovanni Paolo II 132, 84084 Fisciano, SA, Italy

Topics in Current Chemistry (2019) 377:22
https://doi.org/10.1007/s41061-019-0247-2

REVIEW

Photocatalytic Reactor Modeling: Application to Advanced Oxidation Processes for Chemical Pollution Abatement

María de los Milagros Ballari[1] · María Lucila Satuf[1] · Orlando M. Alfano[1]

Received: 3 June 2019 / Accepted: 3 August 2019 / Published online: 23 August 2019

Abstract

A methodology for photocatalytic reactor modeling applied to advanced oxidation processes for chemical pollution abatement is presented herein. Three distinct reactor configurations typically employed in the field of air and water purification—wall reactors, slurry reactors, and fixed-bed reactors—are considered to illustrate the suggested approach. Initially, different mechanistically derived kinetic expressions to represent the photocatalytic rate of pollutant degradation are reviewed, indicating the main assumptions made by the authors in the published contributions. These kinetic expressions are needed to solve the mass balances of the reactant species in the photocatalytic reactors. As is well known, at least one of the steps of the reaction mechanism requires evaluation of the rate of electron–hole generation, which depends on the photon absorption rate: a volumetric property for reactions with the catalyst particles in aqueous suspension or a surface property for systems with a fixed catalyst deposited on an inert support. Subsequently, the different techniques for evaluating the optical properties of slurry and immobilized systems, and the numerical methods applied to calculate the photon absorption rate, are described. The experimental and theoretical results of pollutant degradation in each reactor type are then presented and analyzed. Finally, the definition, calculation, and relevance of different efficiency parameters are briefly reviewed. Using these illustrative examples, we emphasize the need for a systematic and rigorous approach for photocatalytic reactor modeling in order to overcome the inherent drawbacks of photocatalysis and to improve the overall efficiency of the process.

Keywords Photocatalysis · Modeling · Photon absorption · Wall reactor · Slurry reactor · Fixed-bed reactor

Chapter 8 was originally published as Ballari, M. M., Satuf, M. L. & Alfano, O. M. Topics in Current Chemistry (2019) 377: 22. https://doi.org/10.1007/s41061-019-0247-2.

✉ Orlando M. Alfano
alfano@intec.unl.edu.ar

[1] Instituto de Desarrollo Tecnológico para la Industria Química, INTEC (Universidad Nacional del Litoral and CONICET), Ruta Nacional Nº 168, 3000 Santa Fe, Argentina

1 Introduction

The modeling of conventional chemical reactors generally requires consideration of the momentum, thermal energy, and multicomponent mass conservation equations. In the particular case of photoreactors, the radiant energy distribution within the reaction space must be incorporated. Figure 1 schematically illustrates the methodology proposed in this work for modeling of the radiation field in heterogeneous reactors and, from this information, for the evaluation of the photon absorption rate inside the photocatalytic reactor.

The mass conservation equations for the main pollutant and for the most important intermediate species should be considered. Since most photocatalytic reactions are carried out at a fixed temperature, generally close to room temperature, it is not necessary to take into account the thermal energy equation. To solve the mass balances, information about the reaction rate of each of the species involved is required. In turn, reaction rate expressions can be obtained from kinetic schemes of the photocatalytic process.

Normally, a kinetic scheme comprises several elementary steps, the majority of which are thermal (or dark), but there is always one irradiated step (or activation step) which involves the absorption of radiation by the photocatalyst to generate electron–hole pairs. To evaluate the reaction rate of the activation step, or the so-called reaction rate of electron–hole generation, it is essential to know the rate of photon absorption, which can be considered as (i) a volumetric rate (for reactions

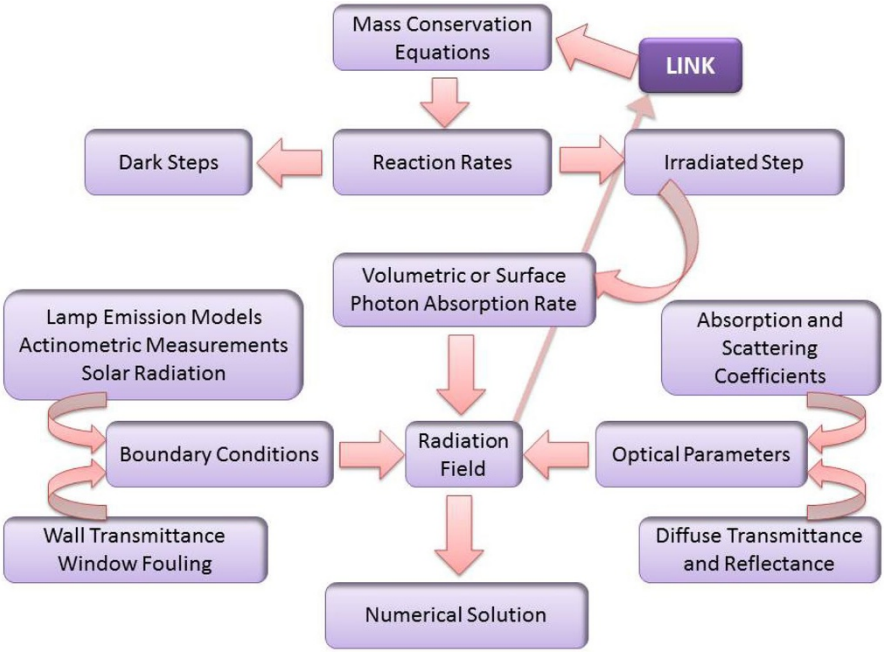

Fig. 1 Evaluation of volumetric or surface photon absorption rate in photocatalytic reactors. Adapted with permission from [1]. Copyright 2009 Elsevier

with the catalyst particles in aqueous suspension) or (ii) a surface rate (for systems with a fixed catalyst deposited on an inert support).

At this point, in order to evaluate the rate of photon absorption, it is necessary to compute the radiation field inside the photocatalytic reactor. To this end, the following information should be provided: the incident radiation at the reactor walls (boundary conditions of the problem) and the optical parameters of the heterogeneous system. The calculation of the boundary conditions of the radiation problem usually requires information that may be obtained from UV–visible lamp emission models (with or without reflecting surfaces), actinometric and radiometric measurements, or measurements (or predictions) of solar radiation. To complete the evaluation of the boundary conditions, it is essential to know the transmittance of the reactor window and, especially in slurry systems, the possible fouling of the walls of the reactor window. On the other hand, the evaluation of the optical parameters of the system consists in determining the absorption and scattering coefficients of suspended catalysts, or the diffuse transmittance and reflectance properties of immobilized catalyst films. With all this information, it will be necessary to implement a numerical method to calculate the volumetric or surface rate of photon absorption.

As shown in Fig. 1, in particular cases of photocatalytic processes, it is necessary to establish a "link" between the radiation field and the mass conservation equations. For example, (i) a reagent or reaction product absorbs radiation and modifies the photon absorption distribution inside the reactor; or, less frequently, (ii) the catalyst undergoes physical changes (e.g. aggregation) over the reaction time that modify its radiation absorption properties. In these cases, the mass balances are coupled with the radiation field, and therefore, the mathematical problem "mass balances-radiation field" must be solved in an integrated way. However, in most photocatalytic systems, including the examples presented in this review, the radiation field is independent of the mass balance equations.

In Sect. 2 of the present work, different kinetic expressions employed to study the photocatalytic oxidation of pollutants in liquid and gaseous phases are summarized. Subsequently, the photocatalytic degradation of chemical pollutants in three different reactor configurations is presented: wall reactors (Sect. 3), slurry reactors (Sect. 4), and fixed-bed reactors (Sect. 5). For each reactor type, the following topics are discussed: the evaluation and resulting profiles of the photon absorption rates, the mass balance equations for the pollutants, and the experimental and theoretical results of pollutant degradation in the reactors. Finally, Sect. 6 presents the definitions of the most frequently employed efficiency parameters, along with examples that illustrate the utility of these parameters to compare results among different photocatalytic reactors.

2 Kinetics of Photocatalytic Oxidation

The purpose of this section is to summarize the principal kinetic expressions reported in the scientific literature for photocatalytic reactions applied to environmental remediation. We will refer only to expressions derived from photocatalytic oxidation mechanisms. Nevertheless, the final form of these mechanistically based

equations can, in certain cases, matches with commonly used empirical reaction rate expressions.

Photocatalytic oxidation reactions start with the activation of the catalyst (a solid semiconductor) by absorption of radiation of a certain wavelength and energy. When the semiconductor energy band gap is exceeded, electron–hole pairs are generated in the solid particles of the catalyst and migrate to the surface, where (i) adsorbed water or hydroxyl ions can trap holes, generating hydroxyl radicals; (ii) adsorbed molecular oxygen can trap electrons, producing the superoxide radical anion; or (iii) the photogenerated electron–hole pairs can recombine, releasing heat.

The spectral surface rate of electron–hole generation ($r_{g,\lambda}$) is proportional to the rate of photon absorption and can be expressed as follows [2]:

$$r_{g,\lambda} = \boldsymbol{\Phi}_{\lambda} e_{\lambda}^{a,s}, \tag{1}$$

where $e_{\lambda}^{a,s}$ represents the spectral local surface rate of photon absorption (LSRPA), and $\boldsymbol{\Phi}_{\lambda}$ is the constant of proportionality defined as the primary quantum yield at wavelength λ.

For polychromatic systems, the rate of electron–hole generation can be expressed as:

$$r_g = \int_{\lambda} \boldsymbol{\Phi}_{\lambda} e_{\lambda}^{a,s} d\lambda = \overline{\boldsymbol{\Phi}}_{\lambda} \int_{\lambda} e_{\lambda}^{a,s} d\lambda, \tag{2}$$

where $\overline{\boldsymbol{\Phi}}_{\lambda}$ is the primary quantum yield averaged over the useful range of wavelengths.

Also, for pseudo-homogeneous systems such as nanoparticle slurries, the initiation rate can be expressed as a function of the local volumetric rate of photon absorption (LVRPA, e_{λ}^{a}) according to [3]:

$$r_g = \frac{\int_{\lambda} \boldsymbol{\Phi}_{\lambda} e_{\lambda}^{a} d\lambda}{a_V} = \frac{\overline{\boldsymbol{\Phi}}_{\lambda}}{a_V} \int_{\lambda} e_{\lambda}^{a} d\lambda, \tag{3}$$

where a_V is the total active catalytic surface per unit volume of the pseudo-homogeneous system. In the case of nanoparticle slurries, a_V is calculated as the product of the photocatalyst load (C_{cat}) and the specific surface area (S_g).

In mechanistically kinetic studies, the reaction rates of the pollutants and of the possible stable intermediates are postulated considering the mass action law for the elemental reactions of the photocatalytic mechanism. Additionally, the micro steady-state hypothesis is normally adopted for short-lived or unstable species. This assumption allows one to obtain kinetic expressions independent of the unknown concentrations of these unstable species [4]. The resulting equations explicitly include the effect of photon absorption on the reaction rate through the LSRPA or LVRPA. There are other commonly advanced hypotheses that differ between liquid- or gas-phase reactions. Consequently, kinetics in both reacting media will be addressed separately in this review.

2.1 Photocatalytic Kinetics in Liquid Phase

In liquid-phase reactions, pollutant oxidation can occur indirectly, through hydroxyl radical attack, or through direct oxidation by photogenerated holes. The following hypotheses are frequently considered in kinetic studies: (i) oxygen concentration is constant, (ii) water or hydroxyl ion concentrations are constant, (iii) reactions occur among adsorbed species, (iv) liquid–solid adsorption equilibrium is achieved, and (v) there is no adsorption competition between water and other species [5].

The most commonly derived reaction rate equations considering hydroxyl radical attack are shown in Table 1. As demonstrated in Muñoz-Batista et al. [4], Eq. (4) corresponds to the most comprehensive expression of the reaction rate of a model pollutant X. This equation employs the Langmuir isotherm to relate bulk and adsorbed concentrations of reactants at the catalytic surface, and a competitive adsorption mechanism among X and the reaction intermediates Y_i. In these expressions, the kinetic parameters α_i group elemental reaction rate constants and adsorption equilibrium constants K_i. The mathematical expression of Eq. (4) is also obtained when considering linear adsorption of reactants, but the parameters α_i comprise different constants.

Under particular operating conditions (high or low irradiation levels, low contaminant concentration, etc.), Equation (4) can be simplified. The most frequent limiting cases and the resulting kinetic expressions are also presented in Table 1.

Table 2, on the other hand, reports commonly used reaction rate equations when pollutant oxidation is carried out by the direct hole attack. Equation (10) represents the most complete mathematical expression. Simplifications reported in the literature under specific conditions, along with the corresponding equations, are also depicted in Table 2. It is interesting to note that the same mathematical expression

Table 1 Common photocatalytic kinetic expressions in liquid-phase photocatalytic reactions involving hydroxyl radical attack

Case	Photocatalytic reaction rate	Equations	References
Complete expression/linear adsorption equilibrium	$r_X = \frac{\alpha_1 C_X \left(1-\sqrt{1+\alpha_2 \int_\lambda e_\lambda^{a,s} d\lambda}\right)}{1+\alpha_3 C_X + \sum_i \alpha_i C_{Y_i}}$	(4)	[6–10]
Low contaminant concentration	$r_X = \alpha_1 C_X \left(1-\sqrt{1+\alpha_2 \int_\lambda e_\lambda^{a,s} d\lambda}\right)$	(5)	[6, 8, 10]
High irradiation level	$r_X = -\frac{\alpha_1 C_X \sqrt{\int_\lambda e_\lambda^{a,s} d\lambda}}{1+\alpha_2 C_X + \sum_i \alpha_i C_{Y_i}}$	(6)	[10, 11]
High irradiation level and low contaminant concentration	$r_X = -\alpha C_X \sqrt{\int_\lambda e_\lambda^{a,s} d\lambda}$	(7)	[3, 5]
Low irradiation level	$r_X = -\frac{\alpha_1 C_X \int_\lambda e_\lambda^{a,s} d\lambda}{1+\alpha_2 C_X + \sum_i \alpha_i C_{Y_i}}$	(8)	[9]
Low irradiation level and low concentration	$r_X = -\alpha C_X \int_\lambda e_\lambda^{a,s} d\lambda$	(9)	[3]

Table 2 Common photocatalytic kinetic expressions in liquid-phase photocatalytic reactions involving direct hole attack

Case	Photocatalytic reaction rate	Equations	References
Complete expression	$r_X = \frac{\alpha_1 C_X}{1+K_X C_X}\left(1-\sqrt{1+\frac{\alpha_2 \int_\lambda e_\lambda^{a,s} d\lambda (1+K_X C_X)}{C_X}}\right)$	(10)	[12–14]
Linear adsorption isotherms/ low contaminant concentration	$r_X = \alpha_1 C_X\left(1-\sqrt{1+\frac{\alpha_2 \int_\lambda e_\lambda^{a,s} d\lambda}{C_X}}\right)$	(11)	[12–14] With $\alpha_2 = \frac{2}{\alpha_1}$ or $\overline{\Phi}_\lambda = 1$: [15–17]
Linear adsorption isotherms/ low contaminant concentration and high irradiation level	$r_X = -\alpha\sqrt{\int_\lambda e_\lambda^{a,s} d\lambda C_X}$	(12)	[14]
Linear adsorption isotherms/ low contaminant concentration and low irradiation level	$r_X = -\alpha \int_\lambda e_\lambda^{a,s} d\lambda$	(13)	[14] For intermediate generation rate: [18]

of Eq. (11) results from the assumption of low contaminant concentration or, alternatively, of linear adsorption at the catalyst surface.

2.2 Photocatalytic Kinetics in Gas Phase

The most frequently reported kinetic expressions for photocatalytic reactions in gas phase, summarized in Table 3, consider hydroxyl radical attack as the main mechanism for the degradation of pollutants. Hypotheses similar to those for the liquid phase are assumed, with two exceptions: (i) water vapor is a variable of the reacting system, and (ii) adsorption competition among water and other species for the actives sites of the catalyst must be considered.

3 Wall Reactors

In this configuration, the photocatalyst is immobilized on the reactor walls, represented by flat or curved extended surfaces of an inert support in contact with the contaminated phase to be treated. This type of photoreactor is frequently employed for kinetic studies in gas and liquid phases [4, 27, 28].

3.1 Evaluation of Photon Absorption

A medium is considered as participating in radiative transfer if it absorbs, emits, or scatters a ray as it travels through the medium. In this case, the radiative transfer equation (RTE) governs the distribution of the radiation intensity. In photocatalytic

Table 3 Common photocatalytic kinetic expressions in gas-phase photocatalytic reactions involving hydroxyl radical attack

Case	Photocatalytic reaction rate	Equations	References
Complete expression	$r_X = \frac{\alpha_1 C_X C_{H_2O}\left(1-\sqrt{1+\frac{\alpha_2 \int_\lambda e_\lambda^{a,s} d\lambda \left(1+K_X C_X+\sum_i K_{Y_i} C_{Y_i}+K_{H_2O} C_{H_2O}\right)}{C_{H_2O}}}\right)}{\left(1+\alpha_3 C_X+\sum_i \alpha_i C_{Y_i}+K_{H_2O} C_{H_2O}\right)\left(1+K_X C_X+\sum_i K_{Y_i} C_{Y_i}+K_{H_2O} C_{H_2O}\right)}$	(14)	[19]
Low contaminant concentration	$r_X = \frac{\alpha_1 C_X C_{H_2O}\left(1-\sqrt{1+\frac{\alpha_2 \int_\lambda e_\lambda^{a,s} d\lambda \left(1+K_{H_2O} C_{H_2O}\right)}{C_{H_2O}}}\right)}{\left(1+K_{H_2O} C_{H_2O}\right)^2}$	(15)	[2, 19, 20]
Low irradiation level and low contaminant concentration	$r_X = -\frac{\alpha C_X \int_\lambda e_\lambda^{a,s} d\lambda}{1+K_{H_2O} C_{H_2O}}$	(16)	[2, 20]
Linear adsorption isotherms	$r_X = \frac{\alpha_1 C_X C_{H_2O}\left(1-\sqrt{1+\frac{\alpha_2 \int_\lambda e_\lambda^{a,s} d\lambda}{C_{H_2O}}}\right)}{1+\alpha_3 C_X+\sum_i \alpha_i C_{Y_i}}$	(17)	[21] without radical termination reaction
Hole trapping by OH^-	$r_X = \frac{\alpha_1 C_X\left(1-\sqrt{1+\alpha_2 \int_\lambda e_\lambda^{a,s} d\lambda}\right)}{1+K_X C_X+K_{H_2O} C_{H_2O}}$	(18)	[22]
Hole trapping by OH^- and low irradiation level	$r_X = -\frac{\alpha C_X \int_\lambda e_\lambda^{a,s} d\lambda}{1+K_X C_X+K_{H_2O} C_{H_2O}}$	(19)	[22–24]
$C_{e^-} = C_{h^+}$, fast recombination rate and low contaminant concentration	$r_X = -\frac{\alpha_1 C_X C_{H_2O} \sqrt{\int_\lambda e_\lambda^{a,s} d\lambda}}{\left(1+\alpha_2 C_X+K_{H_2O} C_{H_2O}\right)\left(1+K_{H_2O} C_{H_2O}\right)}$	(20)	[25, 26]

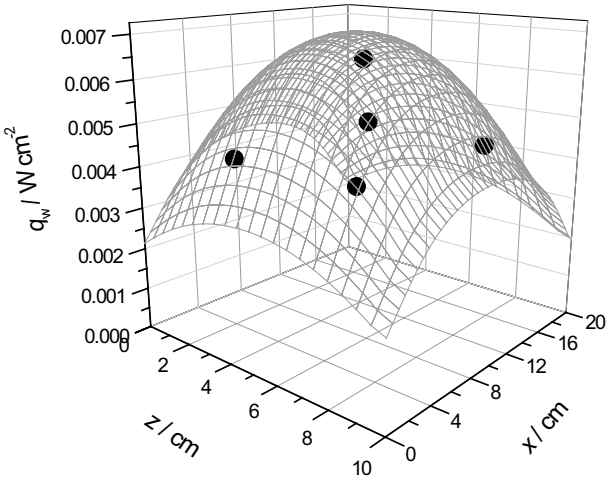

Fig. 2 Experimental validation with radiometer measurements of the incident net radiation flux at the flat-plate reactor window predicted by the surface emission lamp model. Reprinted with permission from [19]. Copyright 2016 Wiley–VCH

wall reactors, the fluid phase (gas or liquid) is generally a non-participating medium. Then there is no need to solve the RTE, since the radiation intensity along the ray path does not change [29]. Nevertheless, the incident radiation flux on the photocatalytic wall must be evaluated as a boundary condition in order to calculate the LSRPA by the photocatalyst.

3.1.1 Radiation Boundary Conditions

The incident net radiation flux on the photocatalytic wall is defined by:

$$q_\lambda(\underline{x},t) = \underline{n}\cdot\underline{q}_\lambda(\underline{x},t) = \int_\Omega I_\lambda(\underline{x},\underline{\Omega},t)\,\underline{\Omega}\cdot\underline{n}\,d\Omega \tag{21}$$

where q_λ is the spectral net radiation flux, $\underline{q}_\lambda$ the spectral radiation flux vector, $\underline{n}$ the outwardly directed unit vector normal to the photocatalytic surface, and I_λ the spectral radiation intensity in the direction of the unit vector $\underline{\Omega}$ corresponding to the solid angle Ω.

Radiation boundary conditions can be evaluated through the resolution of lamp emission or solar radiation models, or by means of experimental measurements. The most frequently applied lamp emission models in photocatalytic reactors are the rigorous voluminal and surface lamp emission models [29] and the simplified linear source with spherical emission model [30–32]. The experimental determination of the incident radiation flux includes radiometer measurements (of the total or spectral radiation flux) or actinometric reactions in liquid or gas phase [33–35]. Figure 2 shows the experimental validation through radiometer measurements of the total incident radiation flux on a flat-plate photocatalytic reactor window predicted

by the surface emission lamp model [19]. Also, multiphysics or computational fluid dynamics (CFD) software, such as COMSOL Multiphysics® or ANSYS Fluent, is used to simulate the radiation field in the reacting system. The ray optics module of COMSOL Multiphysics® treats the radiation field as rays that reflect and refract at surfaces [36]. ANSYS Fluent, on the other hand, can apply the discrete ordinary method (DOM) to solve the radiation field in photoreactors. In the case of a non-participating domain, such as non-absorbing gases or liquids, it allows one to calculate the incident radiation flux on the catalytic wall [37].

3.1.2 Optical Properties

To evaluate the LSRPA on the photocatalytic walls, the optical properties of the wall are also necessary. Measurements and further calculations are frequently involved in determining the absorbed radiation fraction by the photocatalyst-immobilized film. Experimental determinations include the measurement of the diffuse transmittance (T) and reflectance (R) of the immobilized system (photocatalytic film + support) and the inert support alone in a spectroradiometer equipped with an integrating sphere reflectance attachment [38, 39]. Then, applying the ray-tracing method, the optical properties (reflectance and transmittance) of the photocatalytic film can be calculated via the following expressions for a two-layer system (photocatalytic film + support) [27, 38, 40]:

$$R_f = \frac{R_{fs}T_s^2 - T_{fs}^2 R_s}{T_s^2 - R_s^2 T_{fs}^2}, \tag{22}$$

$$T_f = \frac{T_{fs}}{T_s}\left(1 - R_f R_s\right), \tag{23}$$

where the subscript f stands for photocatalytic film, s represents support, and fs corresponds to the film + support.

On the other hand, for a three-layer system when the photocatalyst is immobilized on both sides of the inert support, the following expressions can be derived by applying a net radiation flux balance [19, 39, 41]:

$$R_f = \frac{R_{fsf}T_f - T_{fsf}R_s}{T_{fsf}T_s^2 - T_{fsf}R_s^2 + T_s}, \tag{24}$$

$$T_f = \sqrt{\frac{\left(R_{fsf} - R_f\right)\left[1 - R_f\left(R_s + \frac{T_s^2 R_f}{1 - R_s R_f}\right)\right]}{R_s + \frac{T_s^2 R_f}{1 - R_s R_f}}}. \tag{25}$$

Finally, the fraction of absorbed radiation in the photocatalytic film can be calculated considering that radiation is either absorbed, reflected, or transmitted in the immobilized film [42]:

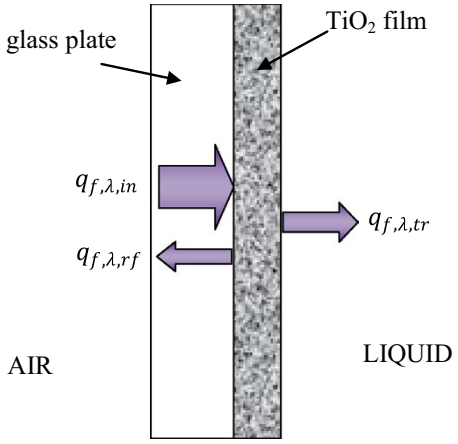

Fig. 3 Schematic representation of the incident, transmitted, and reflected radiation fluxes at the photocatalytic film. Reprinted with permission from [27]. Copyright 2016 Elsevier

$$A_f = 1 - T_f - R_f. \tag{26}$$

3.1.3 Local Surface Rate of Photon Absorption (LSRPA)

Applying a local radiative energy balance in an immobilized layer of photocatalyst, the spectral LSRPA can be calculated according to [27, 40]:

$$e^{a,s}_{\lambda}(\underline{x},t) = q_{\lambda,in}(\underline{x},t) - q_{\lambda,tr}(\underline{x},t) - q_{\lambda,rf}(\underline{x},t) \tag{27}$$

where $q_{\lambda,in}$, $q_{\lambda,tr}$, and $q_{\lambda,rf}$ are the incident, transmitted, and reflected spectral radiative fluxes, respectively, at the photocatalytic film (Fig. 3).

In the case of multilayer photocatalytic films and supports, the net radiation flux balance must be performed in each layer. The resulting radiation fluxes leaving the n^{th} layer can then be written as [19, 41, 42]:

$$q^{+}_{n} = R_n q^{-}_{n} + T_n q^{+}_{n-1}, \tag{28}$$

$$q^{-}_{n-1} = T_n q^{-}_{n} + R_n q^{+}_{n-1}, \tag{29}$$

where q^{+}_{n} and q^{-}_{n} are the forward and backward radiation fluxes, respectively, and T_n and R_n are the diffuse transmittance and reflectance, respectively, of the nth layer. Figure 4 shows a schematic representation of a three-layer system irradiated on both sides and the fluxes involved.

The net incident radiation flux at a single photocatalytic film in which direct and indirect fluxes are contributing can be obtained considering radiation transmission and reflection effects on the involved surfaces [19, 26, 43]:

$$q_{in} = q_{dir} + q_{ind} = q_w T_w \times \left(1 + \frac{R_s T_f - R_s^2 R_f T_f + T_s T_f + T_s^2 R_f T_f}{1 - 2R_s R_f + R_s^2 R_f^2 - T_s^2 R_f^2}\right). \tag{30}$$

Total LSRPA can then be calculated with the net incident radiation flux at the photocatalytic film and with the fraction of absorbed radiation in the whole range of useful wavelengths:

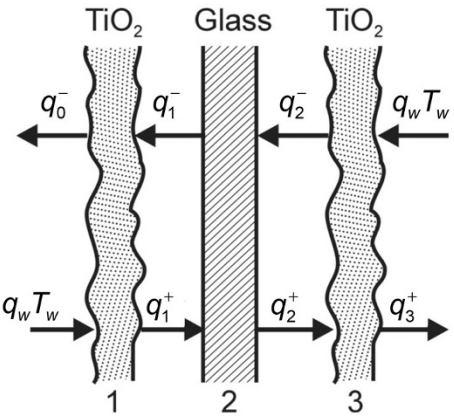

Fig. 4 Schematic representation of a multilayer photocatalytic wall and the reflected and transmitted radiation fluxes. Reprinted with permission from [19]. Copyright 2016 Wiley–VCH

$$e^{a,s}(\underline{x}) = \sum_{\lambda} q_{\lambda,in}(\underline{x}) A_{\lambda,f} \tag{31}$$

Figure 5 shows the LSRPA profiles on flat photocatalytic plates made with different CeO_2–TiO_2 ratios, illuminated on both sides with visible light.

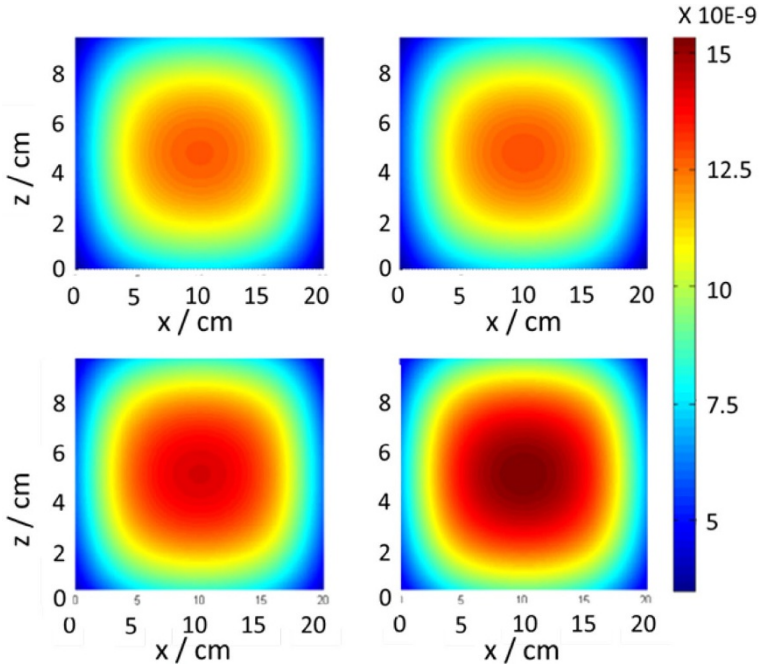

Fig. 5 Local surface rate of photon absorption (Einstein cm^{-2} s^{-1}) under visible irradiation on flat photocatalytic plates. Upper row: Ti and 0.025CeTi. Lower row: 0.05CeTi and 0.25CeTi. Reprinted with permission from [43]. Copyright 2014 Elsevier

3.2 Pollutant Degradation Results

For isothermal systems, the modeling of photocatalytic wall reactors includes the simultaneous resolution of the momentum, radiation transfer, and mass balance equations with heterogeneous reactions. The motion equation for Newtonian non-compressible fluids with constant properties and laminar flow becomes the Navier–Stokes equation. Mass balance equations also include the continuity and species conservation equations [28].

These equations can be solved numerically applying commercial computational fluid dynamics (CFD) software. CFD has been used to solve different configurations and designs of wall reactors, including continuous flat-plate photoreactors [30, 31, 37, 44, 45], annular photoreactors [44, 46, 47], corrugated-plate photoreactor [23, 24, 48], continuous multitubular wall photoreactors [36], cylindrical and rectangular photoreactors with the photocatalytic wall placed in the bottom [49], and submerged photocatalyst-coated plates in tank reactor [50].

As previously mentioned, the set of differential equations solved by CFD modeling at steady state are as follows:

$$\text{Continuity equation: } \underline{\nabla} \cdot \left(\rho \underline{v}\right) = 0, \tag{32}$$

$$\text{Momentum equation: } \underline{\nabla} \cdot \left(\rho \underline{v}\underline{v}\right) = -\underline{\nabla} P + \underline{\nabla} \cdot \left(\underline{\underline{\tau}}\right) + \rho \underline{g}, \tag{33}$$

$$\text{Species } i \text{ conservation equation: } \underline{\nabla} \cdot \left(\rho \underline{v} C_i\right) = \underline{\nabla} \cdot \underline{J_i} + R_i, \tag{34}$$

where ρ is the fluid density, $\underline{v}$ is the velocity vector, P is the pressure, $\underline{\underline{\tau}}$ is the viscous stress tensor, $\underline{g}$ is the gravitational acceleration, C_i is the molar concentration of species i, $\underline{J_i}$ is the diffusion flux vector for i, and R_i is the homogeneous reaction rate of species i. For heterogeneous photocatalytic systems, the homogenous reaction rate is normally null.

The boundary condition at the photocatalytic wall for the species conservation equation can be written as:

$$\underline{n} \cdot \underline{J_i}\Big|_{A_{cat}} = \underline{n} \cdot \left(-D_{i-f} \underline{\nabla} C_i\right)\Big|_{A_{cat}} = r_i \tag{35}$$

Here, r_i is the heterogeneous photocatalytic reaction rate of the main (X) or secondary (Y_i) pollutant, and $D_{i\text{-}f}$ is the molecular diffusivity of compound i in the fluid (liquid or gas). For the remainder of non-active walls, the mass flux equals zero.

Passalía et al. [23, 24, 48], working with a continuous corrugated-plate photocatalytic reactor to treat air contaminated with formaldehyde, applied CFD modeling using ANSYS Fluent commercial software. However, the radiation field was solved externally using a surface lamp emission model and applying a radiation flux balance in the catalytic wall and a view factor of the corrugated plate. The resulting LSRPA profile is shown in Fig. 6a. The kinetic expression employed, previously derived from a flat-plate photoreactor [22], has the form of Eq. (19) in Table 3. It should be noted that this mechanistically kinetic approach considers that water vapor acts as a competitor

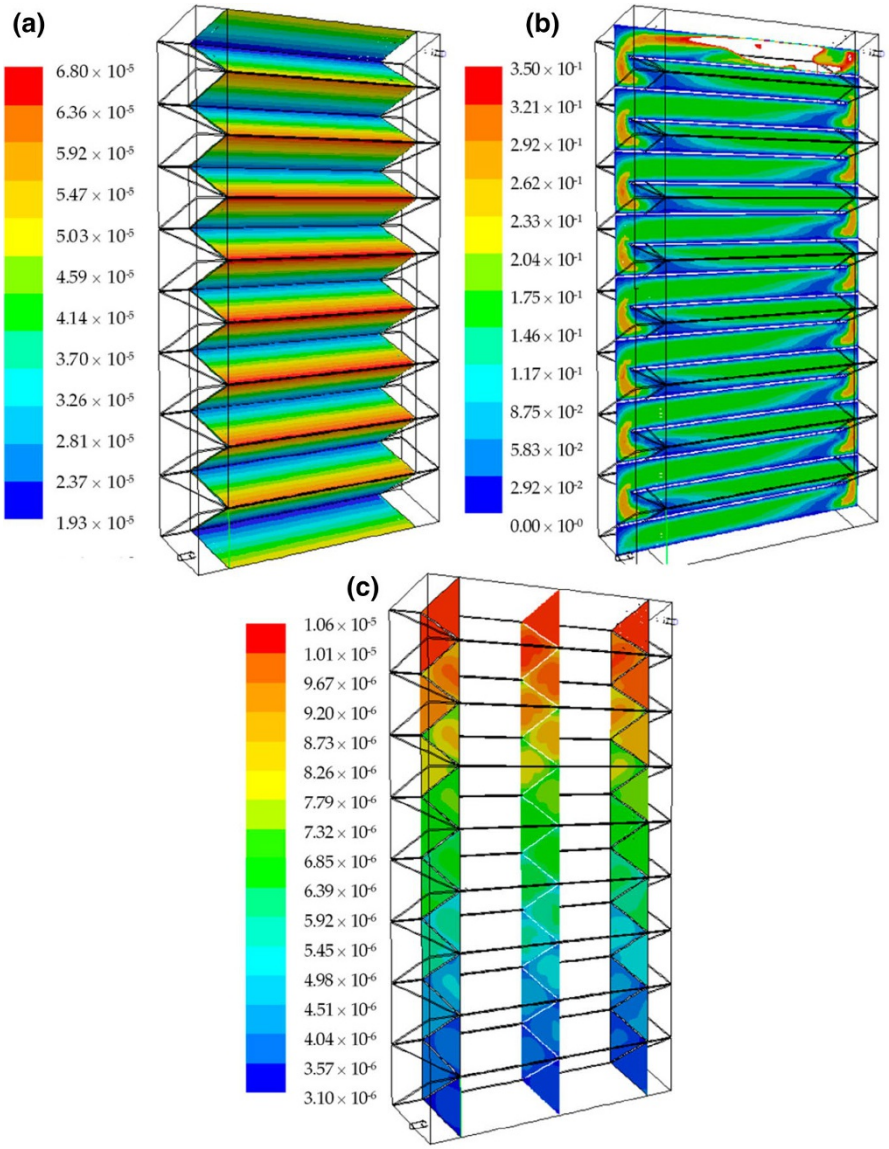

Fig. 6 **a** LSRPA on the corrugated plate (Einstein m^{-2} s^{-1}); **b** contours of velocity (m s^{-1}) in the central plane of the reactor; **c** contours of molar formaldehyde fractions [48]

for the active sites during the adsorption process, but holes are trapped by hydroxyl ions instead of water. The motion equation and formaldehyde conservation equation were solved with ANSYS Fluent. The resulting velocity profile and the formaldehyde concentration gradient in the corrugated-plate photoreactor are presented in Fig. 6b, c, respectively. Very good prediction of the experimental formaldehyde conversion was found with this modeling method.

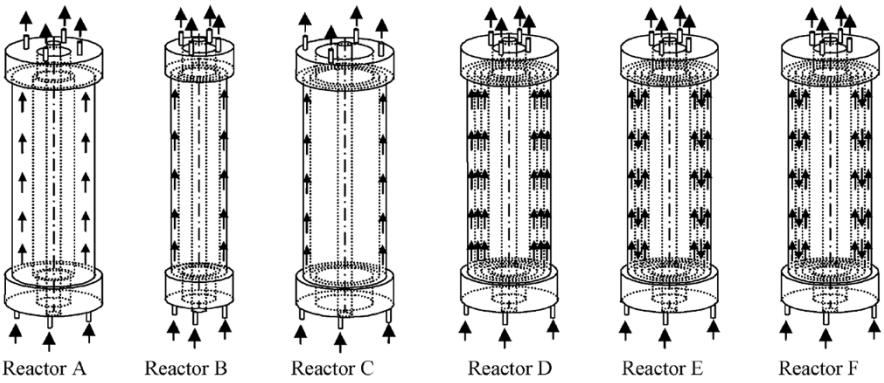

Fig. 7 Photocatalytic annular reactors: **A** single-annular reactor with high residence time; **B**, **C** single-annular reactor with low residence time; **D** multi-annular parallel flow reactor; **E** multi-annular series flow reactor (each annular channel wall coated with TiO_2 film of uniform thickness); **F** multi-annular series flow reactor (surface rate of photon absorption uniformly distributed on the active surfaces). Reprinted with permission from [53]. Copyright 2007 Elsevier

In cases of simpler geometries such as continuous annular [46, 51–56] or flat-plate [2, 19, 21, 26, 32, 57] wall reactors, Eqs. (32)–(34) can be simplified and solved analytically or with numerical methods other than CFD. Imoberdorf et al. [51–53] modeled different configurations of single- or multi-annular photocatalytic wall reactors (Fig. 7). A steady-state two-dimensional axial convection and radial diffusion mass balance for the main pollutant *X* (perchlorethylene, PCE) was proposed for each annular channel *j*:

$$v_{z,j}(r)\frac{\partial C_X(z,r)}{\partial z} = D_{X-f}\frac{\partial}{\partial r}\left(r\frac{\partial C_X(z,r)}{\partial r}\right) \quad 0 < z < Z_R; \quad \chi_j R_j < r < R_j, \quad (36)$$

with the following boundary conditions corresponding to the inner ($r = \chi_j R_j$) or outer ($r = R_j$) photocatalytic wall of the annular channel:

$$D_{X-f}\left.\frac{\partial C_X(z,r)}{\partial r}\right|_{r=\chi_j R_j} = -r_X\left(\chi_j R_j, z\right) \quad 0 < z < Z_R, \quad (37)$$

$$D_{X-f}\left.\frac{\partial C_X(z,r)}{\partial r}\right|_{r=R_j} = r_X\left(R_j, z\right) \quad 0 < z < Z_R, \quad (38)$$

and the following inlet condition for a single-annular or parallel flow multi-annular configurations:

$$C_X(z,r)\big|_{z=0} = C_X^{\text{in}} \quad \chi_j R_j < r < R_j. \quad (39)$$

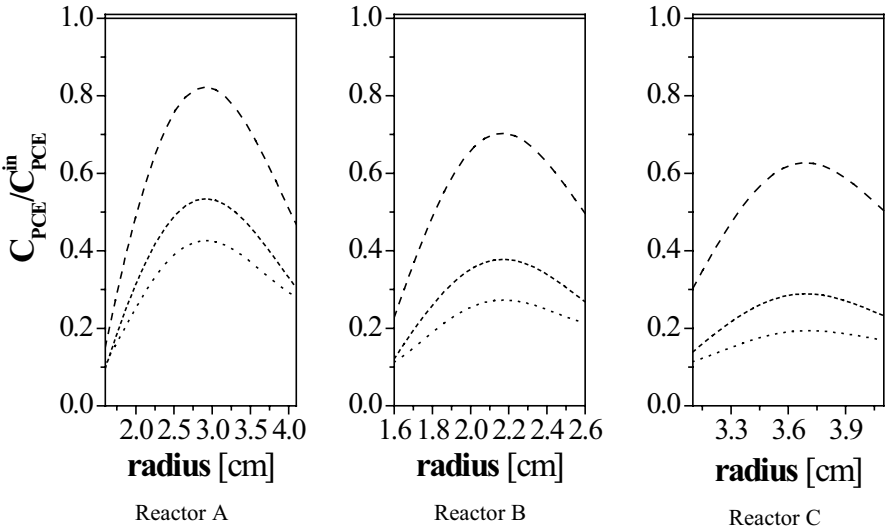

Fig. 8 Predicted dimensionless PCE concentration radial gradients. (—) $z=0$; (– – –) $z=1/3\ Z_R$; (- - -) $z=2/3\ Z_R$; (· · ·) $z=Z_R$. Reprinted with permission from [53]. Copyright 2007 Elsevier

In the case of a series flow pattern configuration, the average outlet concentration of the previous annular channel is the inlet condition for the next channel.

Equation (36) was numerically solved applying the finite difference method, whereas the gas velocity profile was solved analytically. The LSRPA on the reactor walls was calculated from a surface lamp emission model, considering a radiation transmission model on the photocatalytic film and support [2]. The heterogeneous surface reaction rate of perchlorethylene (PCE) had been previously determined in a laboratory-scale, flat-plate photoreactor, and corresponds to Eq. (16) of Table 3. Figure 8 shows PCE radial concentration profiles in the single-annular reactors *A*, *B*, and *C* at different axial positions. The evident concentration radial gradients indicate the existence of important diffusive resistance under the operating conditions in this study. The reported methodology has allowed us to determine that the optimal photoreactor configuration in terms of pollutant conversion is the multi-annular series flow reactor.

For continuous wall photoreactors, the plug flow hypothesis is commonly applied [19, 21, 26, 32, 46, 56, 58]. Then, the species *i* conservation equation becomes:

$$\langle v_z \rangle \frac{\partial C_i}{\partial z} = a_v r_i, \tag{40}$$

where a_v is the ratio of catalytic area to reactor volume.

Figure 9 shows the predictions of acetaldehyde and formaldehyde outlet concentrations versus air flow rate employing the plug flow model in a continuous flat-plate wall photoreactor, applying a heterogeneous reaction rate corresponding

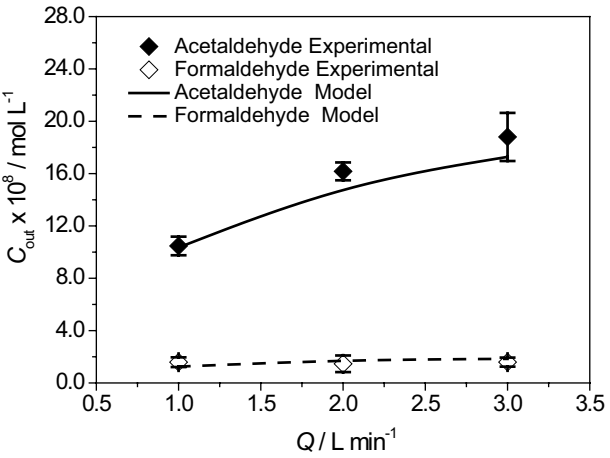

Fig. 9 Simulated and experimental outlet concentrations of acetaldehyde and formaldehyde, varying the flow rate in a flat-plate photocatalytic wall reactor. Reprinted with permission from [19]. Copyright 2016 Wiley–VCH

to Eq. (15). Good correlation is observed between the experimental data and model predictions [19].

An important issue in wall photoreactors is the rate of mass transfer of the pollutant from the fluid bulk to the photocatalyst interphase and within the photocatalytic film. To determine whether the reaction is kinetically controlled, the external and internal mass transfer resistance in the photocatalytic wall should be calculated and compared with the observed reaction rate. In gas-phase reactions, the mass transfer rate is often higher than the reaction rate, and the reacting system is not limited by diffusion [19, 26, 56]. On the other hand, for liquid-phase wall reactors, the pollutant diffusion, especially within the photocatalytic film, is slower and must be considered in the photoreactor model [27, 59, 60].

4 Slurry Reactors

In this section, various applications of different slurry photocatalytic reactors are described. These reactors have been used to obtain the intrinsic kinetics of the photocatalytic decomposition of toxic organic compounds in aqueous solution, using suspended titanium dioxide particles and polychromatic UV–visible radiation.

4.1 Evaluation of Photon Absorption

The LVRPA involved in the reaction rate expressions can be calculated by:

$$e^{a}(\underline{x}) = \int_{\lambda} \kappa_{\lambda} \int_{\Omega=4\pi} I_{\lambda}(\underline{x}, \Omega)\, d\Omega\, d\lambda, \tag{41}$$

where κ_λ is the spectral volumetric absorption coefficient, I_λ the spectral radiation intensity, and Ω the solid angle. For example, in the case where a simple radiation model can be applied, such as a one-dimensional, one-directional radiation model, the LVRPA is calculated as:

$$e^a(x) = 2\pi \int_\lambda \kappa_\lambda \int_{\mu=-1}^{1} I_\lambda(x,\mu)\, \mathrm{d}\mu\, \mathrm{d}\lambda, \tag{42}$$

Here, μ is the direction cosine of the rays.

It should be highlighted that the main complexity in the evaluation of the radiation field within photocatalytic slurry reactors is the simultaneous existence of radiation absorption and scattering generated by the photocatalyst particles in the aqueous suspension. One of the systematic methods that can be used to obtain the spatial and directional distribution of I_λ to replace in Eqs. (41) or (42) is the application of the radiative transfer equation (RTE) to the heterogeneous reactor [29, 61, 62]:

$$\frac{\mathrm{d}I_\lambda(s,\underline{\Omega})}{\mathrm{d}s} + \underbrace{\kappa_\lambda(s)\, I_\lambda(s,\underline{\Omega})}_{\text{Absorption}} + \underbrace{\sigma_\lambda(s)\, I_\lambda(s,\underline{\Omega})}_{\text{Out-Scattering}} = \underbrace{\frac{\sigma_\lambda(s)}{4\pi} \int_{4\pi} p_\lambda(\underline{\Omega}' \to \underline{\Omega})\, I_\lambda(s,\underline{\Omega}')\, \mathrm{d}\Omega'}_{\text{In-Scattering}} \tag{43}$$

where s is a linear coordinate along the direction $\underline{\Omega}$, σ_λ is the spectral volumetric scattering coefficient, and $p_\lambda(\underline{\Omega}' \to \underline{\Omega})$ is the phase function. To solve this equation, the optical parameters of the suspension are necessary: κ_λ, σ_λ, and p_λ. The Henyey–Greenstein (H-G) function ($p_{HG,\lambda}$) has been employed to calculate the phase function [42]:

$$p_{H-G,\lambda}(\mu_0) = \frac{\left(1-g_\lambda^2\right)}{\left(1+g_\lambda^2-2g_\lambda\mu_0\right)^{3/2}} \tag{44}$$

where g_λ is the asymmetry factor (dimensionless) and μ_0 represents the cosine of the angle between the direction of the incident and scattered rays.

4.1.1 Optical Properties

To evaluate the optical properties of the catalyst suspension, the following spectral measurements should be performed: (i) absorbance spectrophotometric measurements of TiO_2 suspensions under specially designed conditions to minimize the collection of scattered rays by the detector, and (ii) diffuse reflectance (R_λ) and transmittance (T_λ) of TiO_2 suspensions in a spectroradiometer equipped with an integrating sphere attachment. The integrating sphere configurations for these measurements are schematically shown in Fig. 10.

From the absorbance measurements (step i), the extinction coefficient β_λ ($\beta_\lambda = \kappa_\lambda + \sigma_\lambda$) can be calculated as $\beta_\lambda = 2.303\, Abs_\lambda/L$, where Abs_λ is the absorbance and L the cell path length. After the experimental diffuse measurements (step ii),

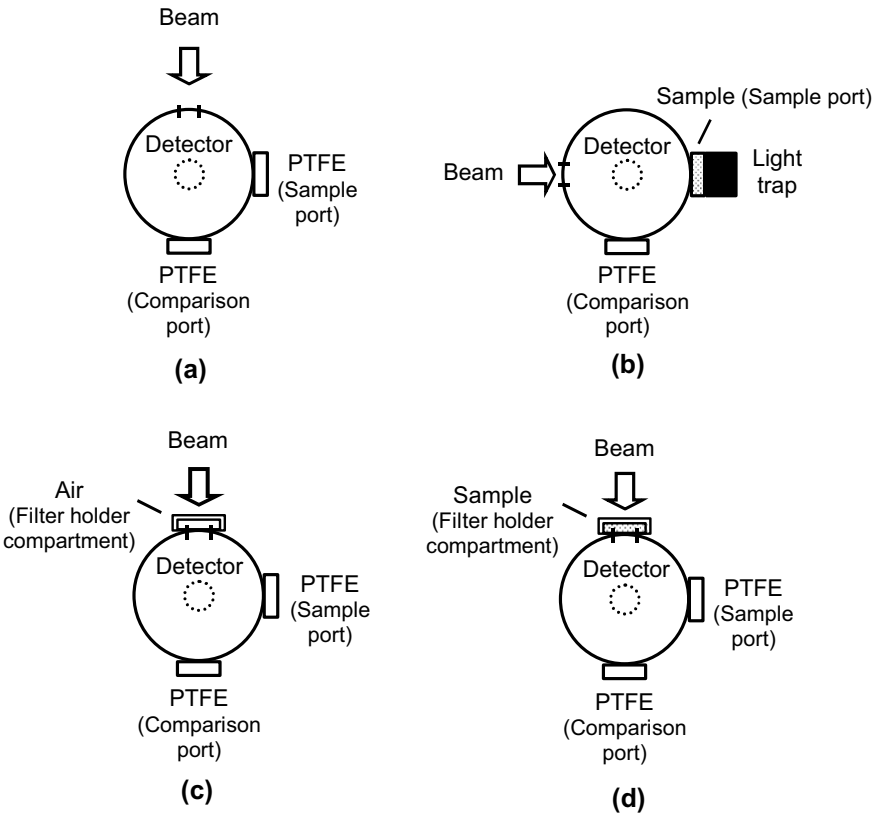

Fig. 10 Integrating sphere configuration for reflectance and transmittance measurements. Reprinted with permission from [63]. Copyright 2005 American Chemical Society

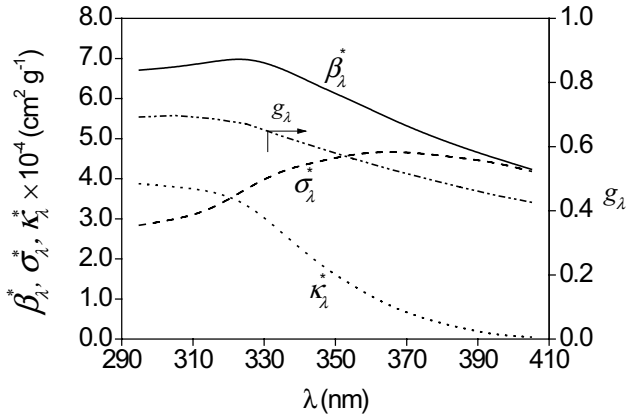

Fig. 11 Optical properties vs. wavelength for the Evonik Aeroxide P 25 TiO_2 catalyst. β_λ^*: solid line; σ_λ^*: dashed line; κ_λ^*: dotted line; g_λ: dashed and dotted line. Reprinted with permission from [63]. Copyright 2005 American Chemical Society

the RTE can be numerically solved in the spectrophotometer sample cell by applying a nonlinear optimization program to adjust the RTE predictions to experimental data. From the parameters estimation made with the optimization program, one can obtain the scattering coefficient σ_λ and the asymmetry factor g_λ of the phase function (Eq. 44). Figure 11 shows the specific optical properties (optical properties per catalyst mass concentration) as a function of wavelength for the Evonik Aeroxide P 25 TiO_2 catalyst. A similar method was applied by Marugán et al. [64] and Tolosana-Moranchel et al. [65] to estimate the optical properties of different titanium dioxide photocatalysts in aqueous suspension. Details on the spectrophotometric measurements and evaluation of the optical properties can be found elsewhere [63].

4.1.2 Local Volumetric Rate of Photon Absorption (LVRPA)

Rigorous and simplified numerical methods have been proposed to solve the RTE in systems with absorption and scattering (Eqs. 41 and 42), and are summarized in the classic books by Ozisik [61], Duderstadt and Martin [66], Modest [67], and Howell et al. [68], among others. The numerical methods most frequently used to calculate the LVRPA in slurry reactors are the discrete ordinate method, the finite volume method, and Monte Carlo simulation. Other approaches of greater or lesser complexity have also been used for the estimation of the radiant field and the design of photocatalytic reactors—for example, the two-flux models for zero [69] and greater than zero [70] reflectance, the six-flux model [71–73], and the probabilistic approach for dense particulates [74].

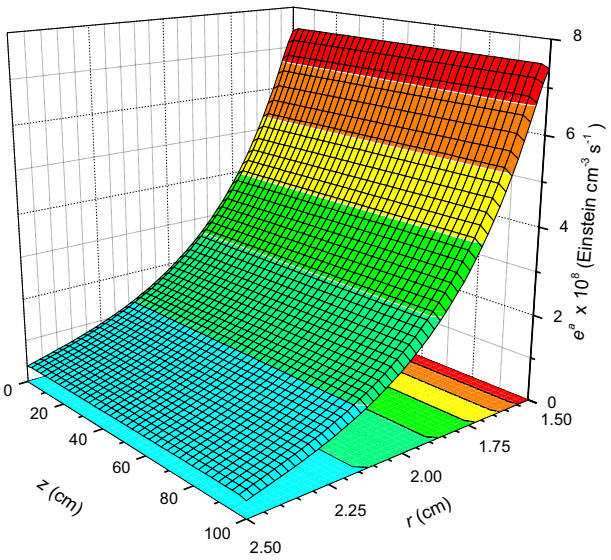

Fig. 12 Spatial distribution of the LVRPA in a bench-scale annular photocatalytic reactor. Reprinted with permission from [79]. Copyright 2013 Elsevier

Briefly, the discrete ordinate method consists in the discretization of the RTE and the transformation of the integro-differential equation in a system of algebraic equations that can be solved numerically. It has been applied in systems with different geometries, such as rectangular (with one and two dimensions) or cylindrical (with two dimensions), and in radiation fields with various degrees of anisotropy [66]. For example, to calculate the e^a (x, z) in a flat-plate, bench-scale solar simulator for 4-chlorophenol photocatalytic degradation, Satuf et al. [75] applied the discrete ordinate method to solve the RTE in a two-dimensional, two-directional rectangular coordinate system. On the other hand, to evaluate the $e^a(r,z)$ in annular slurry photocatalytic reactors, Romero et al. [76–78] and Marugán et al. [79] (Fig. 12) utilized the discrete ordinate method to solve the RTE in a two-dimensional, two-directional cylindrical coordinate system.

When applying the finite volume method [67, 68], the computational domain is divided into a number of control volumes, and the solid angle is discretized into a number of finite solid angles. The RTE is then integrated over all control volumes and angles, and finally, the boundary conditions are used to provide the linear algebraic equations necessary to solve the system with an iterative method. Interesting applications of this technique to calculate the radiation field in photocatalytic slurry reactors have been published by Camera Roda and Santarelli [80], Pareek al. [81], Duran et al. [82], and Huang et al. [83].

The Monte Carlo method, in fact, is not based on the discretization of the RTE, but consists in performing a simulation of the radiation transfer process inside the computer. Basically, this technique uses randomly generated numbers (R_i) to determine the trajectories and fates of the photons entering through the reactor window or, in some problems, those emitted by the radiation source as well. Then, by computing the locations where the photons are absorbed, it is possible to calculate the spatial distribution of the photon absorption rate [84–88].

To calculate the LVRPA in a slurry reactor irradiated through one side, Manassero et al. [8] performed a Monte Carlo simulation considering a one-dimensional, one-directional radiation system. Briefly, the following events were considered in the photon tracking in the reactor: (1) calculation of the photon direction θ at the inner side of the reactor window from the radiation emitted from the lamp: $\sin\theta = 2R_1 - 1$; (2) determination of the length l of the photon flight in the reacting medium without interactions and, consequently, the new location of the photon after traveling that distance: $l = -\frac{1}{\beta_\lambda}\ln(1 - R_2)$; (3) decisions about the fate of the photon: (3a) if the new position of the photon lies outside the reactor, the photon is lost and the process is re-initiated; (3b) if the photon remains inside the reactor after traveling a distance l, a photon–catalyst particle interaction takes place, and two possibilities may occur: (4a) the photon is absorbed according to the value of the albedo ($\omega_\lambda = \frac{\sigma_\lambda}{\beta_\lambda}$): $1 - \omega_\lambda \geq R_3$; (4b) the photon is scattered and a new direction is determined by adopting, for example, the Henyey–Greenstein phase function (Eq. 44), where $cos\theta = \frac{1}{2g_\lambda}\left[1 + g_\lambda^2 - \left(\frac{1-g_\lambda^2}{1+g_\lambda(2R_4-1)}\right)^2\right]$ [87, 88]; (5) if the photon is absorbed, it is stored in the corresponding spatial cell and the trajectory ends. The LVRPA in each cell is

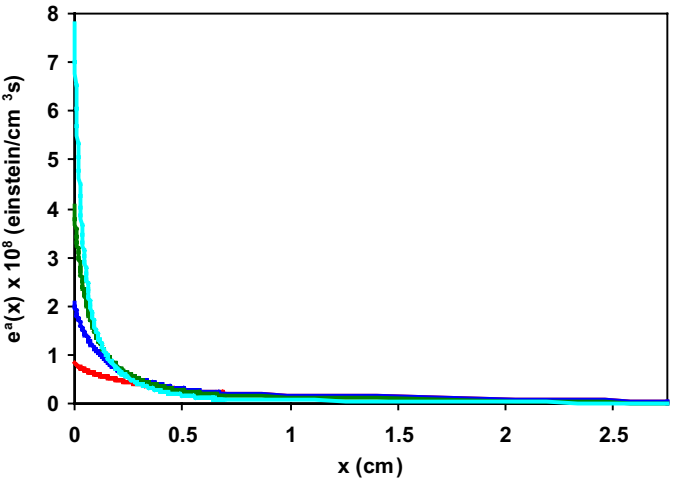

Fig. 13 LVRPA profiles for different catalyst concentrations: 0.1 g L^{-1} (-------); 0.25 g L^{-1} (-------); 0.5 g L^{-1} (-------); 1.0 g L^{-1} (-------). Reprinted with permission from [8]. Copyright 2015 Springer Nature

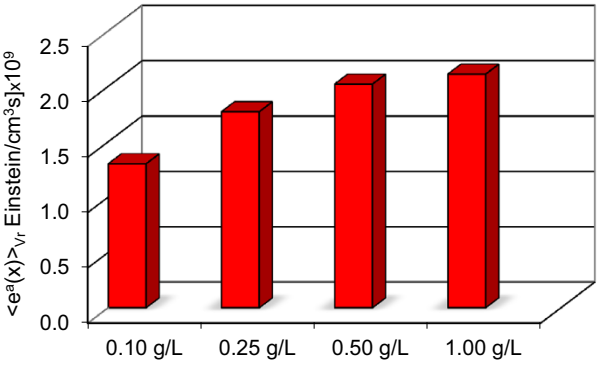

Fig. 14 Volume-averaged LVRPA as a function of photocatalyst concentration

given by $e^a(x) = \sum_\lambda \frac{q_{\lambda,in} n_{\mathrm{ph}\lambda,abs}(x)}{n_{ph,T}\Delta x}$, where $q_{\lambda,in}$ is the incident radiation flux of wavelength λ, $n_{\mathrm{ph}\lambda,abs}(x)$ represents the number of photons of wavelength λ absorbed in a cell of position x, $n_{ph,T}$ is the total number of photons considered in the simulation, and Δx is the length of the cell. Figure 13 shows simulated LVRPA profiles for different photocatalyst concentrations in the slurry reactor. For high catalyst loads, highly nonuniform profiles are found, with very high LVRPA values near the irradiated window ($x=0$). On the contrary, for low catalyst loads, more uniform profiles with low LVRPA values are observed.

Once the $e^a(x)$ profile has been obtained, the average LVRPA in the reactor volume can be calculated as $\langle e^a(x)\rangle_{V_R} = \frac{1}{L_R}\int_{x=0}^{x=L_R} e^a(x)\mathrm{d}x$ (expression valid for one-dimensional radiation models). The values of $\langle e^a(x)\rangle_{V_R}$ enable one to analyze the effect of the catalyst concentration on the total radiation absorption and, consequently, to obtain an optimal catalyst concentration from the perspective of radiation absorption. Figure 14 shows the computed values of the average LVRPA for Aeroxide TiO_2 P 25 as a function of catalyst concentration.

As shown in the figure, at a TiO_2 concentration of 0.5 g L^{-1}, radiation absorption in the reactor reaches some form of saturation, and subsequent increases in catalyst concentration do not produce a significant increase in total radiation absorption.

4.2 Pollutant Degradation Results

This section provides an illustrative example of the kinetic study of the photocatalytic degradation of a pharmaceutical product, clofibric acid (CA) [8]. The formation and subsequent degradation of the primary organic intermediates of the reaction, 4-chlorophenol (4-CP) and benzoquinone (BQ), was also analyzed in the study. The photocatalytic reaction was carried out in a cylindrical glass reactor with two flat windows built with borosilicate ground glass. The experimental system was composed of a halogenated mercury lamp at the focal axis of a parabolic reflector as a source of radiation, a storage tank equipped with a water-circulating jacket to ensure isothermal conditions, and a peristaltic pump to operate the system in batch recirculation and good mixing.

According to the reaction pathway for the CA degradation [89], the following was proposed: (i) formation of the reaction intermediates 4-CP and BQ from CA, (ii) formation of more BQ from 4-CP, and (iii) degradation of 4-CP and BQ to form organic compounds of low molecular weight and, eventually, CO_2, H_2O and HCl. Hence, the mass balances and initial conditions for CA, 4-CP, and BQ in this well-mixed reactor are:

$$\varepsilon_L \left.\frac{\mathrm{d}C_{CA}(t)}{\mathrm{d}t}\right|_{Tk} = -\frac{V_R}{V_T}a_v\left\{\left\langle r_{CA,1}(x,t)\right\rangle_{A_R} + \left\langle r_{CA,2}(x,t)\right\rangle_{A_R}\right\} \quad C_{CA}(t=0) = C_{CA,0}, \tag{45}$$

$$\varepsilon_L \left.\frac{dC_{4-CP}(t)}{dt}\right|_{Tk} = \frac{V_R}{V_T}a_v\left\{\left\langle r_{CA,1}(x,t)\right\rangle_{A_R} - \left\langle r_{4-CP,1}(x,t)\right\rangle_{A_R} - \left\langle r_{4-CP,2}(x,t)\right\rangle_{A_R}\right\}$$
$$C_{4-CP}(t=0) = 0 \tag{46}$$

$$\varepsilon_L \left.\frac{\mathrm{d}C_{BQ}(t)}{\mathrm{d}t}\right|_{Tk} = \frac{V_R}{V_T}a_v\left\{\left\langle r_{CA,2}(x,t)\right\rangle_{A_R} + \left\langle r_{4-CP,2}(x,t)\right\rangle_{A_R} - \left\langle r_{BQ}(x,t)\right\rangle_{A_R}\right\} \quad C_{BQ}(t=0) = 0. \tag{47}$$

From the reaction scheme for the CA photocatalytic degradation, the following reaction rate expressions can be obtained, which are in accordance with Eq. (4) of Table 1:

Table 4 Estimated kinetic parameters. Reprinted with permission from [8]. Copyright 2015 Springer Nature

Parameter	Value
α_1 (s cm^2 Einstein^{-1})	6.07×10^{11}
$\alpha_{2,1}$ (cm s^{-1})	5.83×10^{-6}
$\alpha_{2,2}$ (cm s^{-1})	6.10×10^{-7}
$\alpha_{4,1}$ (cm s^{-1})	1.41×10^{-6}
$\alpha_{4,2}$ (cm s^{-1})	7.97×10^{-6}
α_5 (cm s^{-1})	4.77×10^{-4}

$$r_{CA,1}(x,t)=\frac{\alpha_{2,1}\,C_{CA}(t)\;\mathfrak{F}\left[\alpha_1,e^a(x)\right]}{1+\alpha_3C_{CA}(t)+\alpha_1^{'}C_{4-CP}(t)+\alpha_2^{'}C_{BQ}(t)}$$
$$r_{CA,2}(x,t)=\frac{\alpha_{2,2}C_{CA}(t)\;\mathfrak{F}\left[\alpha_1,e^a(x)\right]}{1+\alpha_3C_{CA}(t)+\alpha_1^{'}C_{4-CP}(t)+\alpha_2^{'}C_{BQ}(t)} \tag{48}$$

$$r_{4-CP,1}(x,t)=\frac{\alpha_{4,1}C_{4-CP}(t)\;\mathfrak{F}\left[\alpha_1,e^a(x)\right]}{1+\alpha_3C_{CA}(t)+\alpha_1^{'}C_{4-CP}(t)+\alpha_2^{'}C_{BQ}(t)}$$
$$r_{4-CP,2}(x,t)=\frac{\alpha_{4,2}C_{4-CP}(t)\;\mathfrak{F}\left[\alpha_1,e^a(x)\right]}{1+\alpha_3C_{CA}(t)+\alpha_1^{'}C_{4-CP}(t)+\alpha_2^{'}C_{BQ}(t)} \tag{49}$$

$$r_{BQ}(x,t)=\frac{\alpha_5C_{BQ}(t)\;\mathfrak{F}\left[\alpha_1,e^a(x)\right]}{1+\alpha_3C_{CA}(t)+\alpha_1^{'}C_{4-CP}(t)+\alpha_2^{'}C_{BQ}(t)} \tag{50}$$

where α_i are intrinsic kinetic parameters of the reaction, and $\mathfrak{F}\left[\alpha_1,e^a(x)\right]$ is defined by:

$$\mathfrak{F}\left[\alpha_1,e^a(x)\right]=\left(-1+\sqrt{1+\frac{\alpha_1}{a_v}e^a(x)}\right). \tag{51}$$

Once the $e^a(x)$ profiles were obtained with the Monte Carlo simulations (Fig. 13), the mass balances were solved (Eqs. 45–47) and the estimation of the kinetic parameters of Eqs. (48)–(51) was performed. A nonlinear parameter estimator (Levenberg–Marquardt algorithm) was applied to minimize the differences between the experimental concentrations and those predicted by the model for the main pollutant and the two intermediate compounds.

Using the estimated kinetic parameters, it was first verified that the terms in the denominator of Eqs. (48)–(50) are negligible compared to 1 (kinetic expressions equivalent to Eq. (5) in Table 1). The values and units of the remaining six kinetic parameters are displayed in Table 4. Figure 15 shows the experimental results and those simulated with the six-parameter model of the three organic compounds CA, 4-CP, and BQ for a mass catalyst concentration of 0.5 g/L. The root-mean-square

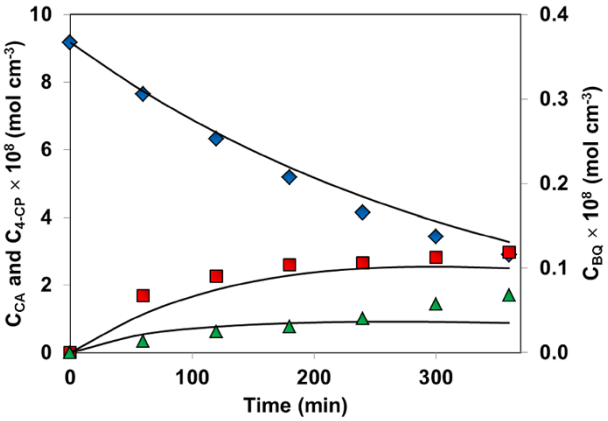

Fig. 15 Experimental and predicted concentrations of CA, 4-CP, and BQ vs. time for 100% irradiation. Experimental data: (◆) CA; (■) 4-CP; (▲) BQ. Model results: solid lines. C_{TiO2}=0.5 g L^{-1}. Reprinted with permission from [8]. Copyright 2015 Springer Nature

error (RMSE) of the predictions was estimated considering the total number of experimental runs, and for the main pollutant, the RMSE was 5.9%. Taking into account all three organic compounds, the RMSE was 16.6%.

On the other hand, if the function $\Im\left[\alpha_1, e^a(x)\right]$ (Eq. 51) is analyzed, two limit dependencies of the reaction rate with respect to the LVRPA can be obtained [3]: (i) for high values of the term $\frac{\alpha_1}{a_v} e^a(x)$, a square root dependence of the reaction rate with LVRPA is found (equivalent to Eq. (7) in Table 1), and (ii) for low values of $\frac{\alpha_1}{a_v} e^a(x)$, a linear dependence of the reaction rate with LVRPA can be demonstrated through a Taylor series expansion of the square root function (equivalent to Eq. (9) in Table 1). Because of the high value of the kinetic parameter α_1 (Table 4), the first approximation is assumed, and the number of kinetic parameters is reduced from six to five. In this case, each kinetic parameter is modified according to the equation: $\alpha_i' = \alpha_i \sqrt{\frac{\alpha_1}{a_v}}$ [90]. The RMSE was calculated with the five-parameter model, and the new RMSE for the main pollutant was 8.1%. Taking into account all three organic compounds with the five-parameter model, the RMSE was 14.4%. These results show that the proposed kinetic model can simulate, with acceptable error percentages, the concentrations of the three organic compounds as a function of time in the slurry photocatalytic reactor.

5 Fixed-Bed Reactors

The main drawback of reactors with immobilized catalyst, such as wall reactors, is the low surface area-to-volume ratio, which can lead to mass transfer limitations and low reaction rates, especially in aqueous-phase reactions. A possible alternative to overcome these disadvantages is the use of fixed-bed reactors, where the catalyst is

supported on an inert material employed to fill the reactor volume. This configuration can reduce diffusion limitations by improving the mixing of reactants. Additionally, it can provide higher photocatalytic surface area and more uniform radiation distribution inside the reactor. Typical catalyst supports reported in the literature include glass beads [91–96], quartz wool [97, 98], foams [99–101], and glass rings [102–105].

5.1 Evaluation of Photon Absorption

In fixed-bed photocatalytic reactors, a thin layer of catalyst is immobilized on the surface of the filling material. Therefore, it is appropriate to refer to the photon absorption rate per unit area of irradiated catalyst-coated surface, and calculate the LSRPA to assess radiation absorption inside the reactors. Because of the inherent differences in the filling (nature of the material, shape, size, packing, surface-to-volume ratio, etc.), it is not possible to develop a radiation model valid for every fixed-bed reactor [97].

Various one-, two-, and three-dimensional models with different degrees of simplification have been reported for the assessment of radiation distribution in this type of reactor. Most of them employed the Monte Carlo method to obtain the numerical solution of the models. Monte Carlo simulations inside fixed-bed reactors basically consider that photons travel with a linear trajectory in the aqueous or gas phase until they reach an element of the filling, or the reactor walls. Those photons that reach the filling can be absorbed by the catalyst film, reflected, or transmitted. The absorbed photons are stored in a spatial cell, the trajectory ends, and a new photon bundle is considered. On the other hand, if the photons are reflected, the new direction is determined by considering a reflection model (the simplest model considers

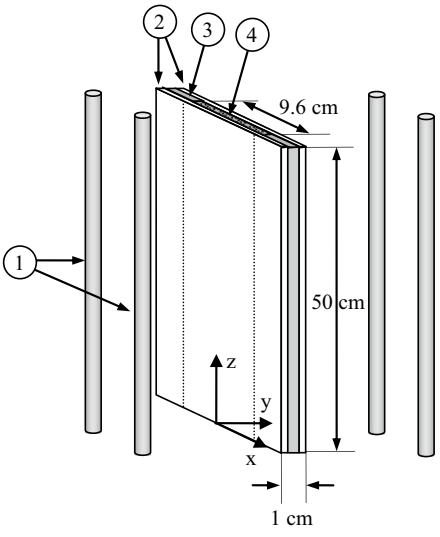

Fig. 16 Geometry of the photocatalytic reactor: (1) UV lamps; (2) borosilicate windows; (3) aluminum rod with rubber seal gaskets; (4) TiO_2-coated quartz wool. Reprinted with permission from [97]. Copyright 2010 John Wiley & Sons

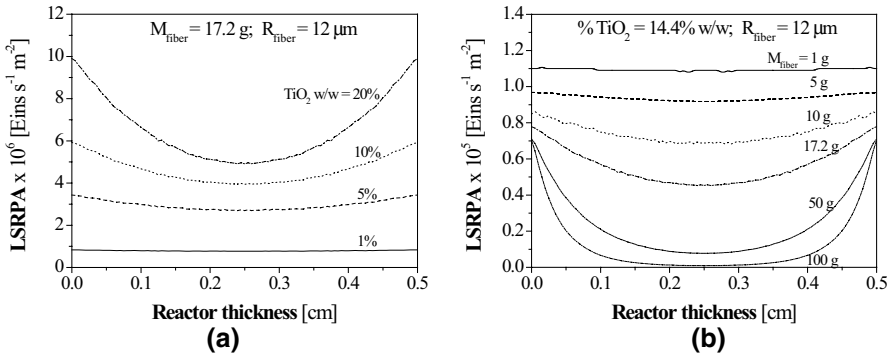

Fig. 17 LSRPA profiles corresponding to variation in the mass of **a** immobilized TiO_2; **b** quartz wool. Reprinted with permission from [97]. Copyright 2010 John Wiley & Sons

specular reflection [91]). Those photons that are transmitted through a filling element may interact with other elements, until they are absorbed or they reach the reactor walls.

To compute the LSRPA, information regarding the radiation flux incident at the reactor windows and the optical properties of the coated filling material is needed. As stated for the other reactor configurations in previous sections, the incident radiation flux can be determined experimentally or through lamp emission (or solar emission) models. The absorption properties of the coated filling material can be assessed experimentally, as described in Sect. 3.1.2 for wall reactors, or by empirical correlations [97]. To compute the reflection of the photons at the coated surface, different models can be adopted, taking into account the characteristics of the materials, especially the surface roughness. Diffuse reflection and specular reflection models have been frequently applied.

Changrani and Raupp [99] used Monte Carlo simulations to solve a three-dimensional radiation model in an annular reactor filled with TiO_2-coated reticulated foam. Two approaches were used to determine the photon flight length inside the reactor: (1) a "spatial" approach that tracks the flight of a photon in a predetermined reticulate structure; (2) a "temporal" approach that generates the random porous structure of the reticulate as the photon flies into it. Although both approaches rendered similar results, the latter was more efficient in terms of computational effort.

In a study reported by Imoberdorf et al. [97], the three-dimensional radiation field of a planar reactor filled with TiO_2-coated quartz wool was modeled using the Monte Carlo method (Fig. 16). The model was experimentally validated, and the effect of different design variables on the radiative energy distribution inside the reactor was analyzed. Figure 17a, b shows the effect of the TiO_2 loading and quartz wool loading on the LSRPA profiles.

Loddo et al. [92] proposed a one-dimensional radiation field in an annular reactor with packed TiO_2-coated beads. Monte Carlo simulations were carried out to obtain the radiation distribution inside the reactor. More recently, Manassero et al. [105] employed the Monte Carlo method to solve a one-dimensional radiation model in a fixed-bed reactor filled with TiO_2-coated rings. The reactor was

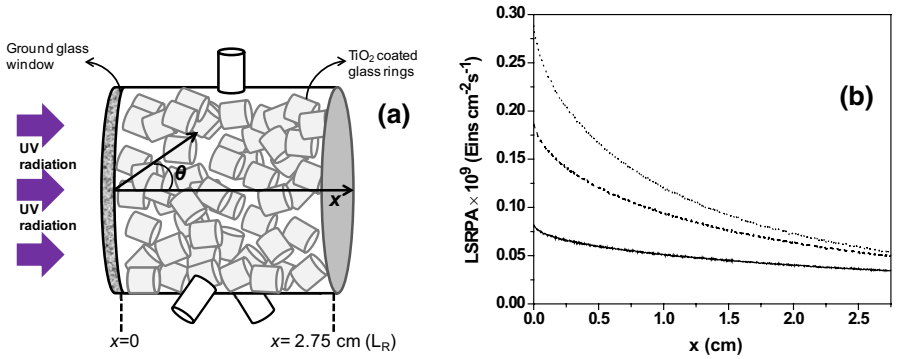

Fig. 18 **a** Schematic representation of the fixed-bed reactor with glass rings; **b** LSRPA profiles in the reactor corresponding to rings with different numbers of TiO_2 coatings: 1 coating (—), 3 coatings (- - -), and 5 coatings (· · ·). Reprinted with permission from [105]. Copyright 2017 Springer Nature

cylindrical, irradiated from one side through a circular flat window with a UV lamp, as schematically shown in Fig. 18a. The profiles of the absorbed radiation in the fixed-bed reactor for different numbers of TiO_2 coatings over the glass rings are depicted in Fig. 18b. The LSRPA increases with the number of TiO_2 coatings, being more significant near the reactor window ($x = 0$).

Additionally, various authors have proposed pseudo-homogeneous models to evaluate the photon distribution inside fixed-bed reactors with different filling materials, in which the RTE [102] or the Helmholtz equation [94] were solved numerically.

5.2 Pollutant Degradation Results

As stated in Sect. 1, in order to simulate the degradation of chemical compounds in photocatalytic reactors, fluid dynamics and reaction kinetics must be combined with the balance of radiant energy in the conservation equation of the species considered. Mass transfer limitations should always be evaluated. If diffusive resistance is significant, mass transfer coefficients must be included in the corresponding equations. Finally, mass balance equations are solved numerically, generally by the finite difference method.

A variety of fluid dynamic models and reaction rate expressions have been reported, depending on the reactor configuration, operation, and type of filling material. Some examples are given in this section.

Two distinct approaches can be adopted to set mass balance equations in fixed-bed reactors: pseudo-homogeneous (where the reaction rate is considered to take place in the whole reaction volume) or heterogeneous (considering the reaction rate as a boundary condition of the mass balance equation).

Changrani and Raupp [100] presented a two-dimensional heterogeneous convection-reaction model for a gas–solid annular photocatalytic reactor. The catalyst was supported on a reticulated foam structure. Mass balances for individual species were

coupled through the reaction rate expression that appeared in the boundary condition at the fluid–solid interface. The heterogeneous reaction rate was modeled using semiempirical Langmuir–Hinshelwood–Hougen–Watson (LHHW) kinetics. Alexiadis et al. [102] modeled an annular fixed-bed reactor with an axial cylindrical UV lamp. The photocatalyst (TiO_2) was supported on quartz rings. The hydrodynamic model assumes convection in the axial direction with radial dispersion. The reaction is considered to take place only on the external surface of the catalyst, and external mass transfer limitations are taken into account. A complex kinetic expression based on a detailed reaction mechanism was employed. Vella et al. [98] assumed a differential reactor operation and kinetic control regime to simulate the degradation of formic acid in a TiO_2-quartz wool-packed bed reactor with recycle. The reaction rate equation was derived from a plausible mechanistic scheme, arriving at a kinetic expression with the form of Eq. (4) in Table 1, in which hydroxyl radical attack was considered to be the main degradation route. Cloteaux et al. [104] employed a plug flow model with axial dispersion, a Langmuir–Hinshelwood kinetic expression, and an external mass transfer coefficient to model the degradation of formaldehyde in a fixed-bed reactor with TiO_2-coated Raschig rings. Vaiano et al. [94] modeled a flat-plate continuous reactor with N-doped TiO_2 immobilized on glass spheres. They developed a reactor model considering plug flow behavior inside the packed bed, without considering external mass transfer phenomena. A Langmuir–Hinshelwood type of kinetic equation was used to model the degradation of methylene blue. Claes et al. [96] assumed apparent first-order kinetics and ideal plug flow reactor model to estimate the kinetic constant for the degradation of methylene blue in a rectangular reactor filled with TiO_2-coated glass beads.

Manassero et al. [105] simulated the degradation of the water pollutant clofibric acid (CA) in a packed-bed batch reactor with recycle. The reactor was filled with TiO_2-coated rings. Reaction rate expressions representing the degradation of CA and the main reaction intermediates were mechanistically derived, and took the form of Eq. (5) in Table 1. Simulated and experimental concentrations of CA and 4-CP using glass rings with different numbers of TiO_2 coatings are shown in Fig. 19.

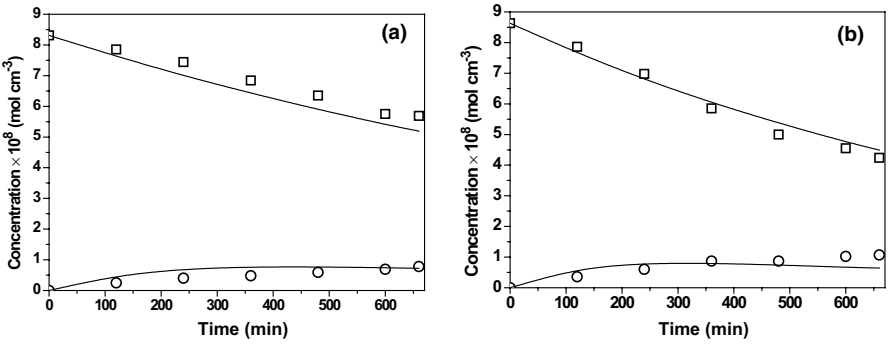

Fig. 19 Photocatalytic degradation of CA using glass rings with different numbers of TiO_2 coatings. Symbols: experimental concentrations (□ = CA; ○ = 4-CP); solid lines: model simulations. **a** 1 coating, **b** 5 coatings. Reprinted with permission from [105]. Copyright 2017 Springer Nature

6 Photocatalytic Efficiency

6.1 Definitions

Reporting photocatalytic conversion or reaction rate data without a reference on energetic efficiency does not allow for objective comparison among different experiments. Efficiency parameters are essential for determining reactor performance and comparing different operating conditions or reactor configurations [62]. In this sense, the global efficiency parameter η_T can be defined, for electrical-energy-driven systems, as the ratio of the number of pollutant molecules decomposed to the electrical power (P) required to operate the radiation source:

$$\eta_T = \frac{\text{observed reaction rate}}{P}. \tag{52}$$

One interesting approach considers η_T as the product of individual efficiencies, each amenable to quantitative measurement, analysis, and optimization [106, 107]:

$$\eta_T = \eta_{ele}\eta_{inc}\eta_{abs}\eta_{rxn}, \tag{53}$$

where η_{ele}, the **electrical efficiency**, refers to the capacity of the radiation source to transform electrical energy into radiant energy (photons); η_{inc}, the **incidence efficiency**, is the ratio between the photons that arrive at the reactor window to the photons supplied by the radiation source; η_{abs}, the **radiation absorption efficiency**, is defined as the ratio of the number of absorbed photons to the total number of incident photons. This parameter strongly depends on the optical properties of the catalyst. Finally, η_{rxn} is the **reaction efficiency**, also called quantum efficiency. It relates the moles of pollutant degraded per mol of photons absorbed by the catalyst. For solar-energy-driven systems, the global efficiency reduces to:

$$\eta_T = \eta_{inc}\eta_{abs}\eta_{rxn}. \tag{54}$$

It is important to note that both η_{inc} and η_{abs} are parameters related to the characteristics of the reactor and photocatalyst, and depend neither on the reaction taking place nor on the chosen operating conditions. On the contrary, the value of η_{rxn} depends on both the specific reaction taking place and the photocatalyst used, and it is strongly affected by the reactor operating conditions [108].

One of the most frequently reported parameters in the scientific literature is the **photonic efficiency** η_{ph}, which relates the moles of reactant molecules degraded per mol of incident photons. η_{ph} can be expressed in terms of the previously defined efficiencies as [108, 109]:

$$\eta_{ph} = \eta_{abs}\eta_{rxn} \tag{55}$$

The electrical energy per order (EE/O) is another parameter used to evaluate the efficiency of water or air treatment processes, and is especially useful for comparing the costs of different systems for industrial applications. The EE/O is the electrical energy in kilowatt-hours required to degrade a contaminant by one order of magnitude in a unit volume of contaminated water or air [110].

Self-defined photoreactor performance parameters have also been reported in the scientific literature. Serrano and de Lasa [111] proposed the photocatalytic thermodynamic efficiency factor (PTFE) based on thermodynamic considerations. The PTFE is the ratio of the energy used for the formation of hydroxyl radicals to the energy absorbed by the catalyst [62, 112]. Li et al. [113] compared the performance of suspended and immobilized systems based on a ratio between initial reaction rates. More recently, Leblebici et al. [114] compared 12 photocatalytic reactor designs with a new benchmark measure, the photocatalytic space–time yield.

6.2 Photonic and Quantum Efficiency for Comparison Purposes

η_{ph}, which relates the photocatalytic reaction rate with the rate of incident radiation, can be expressed according to:

$$\eta_{ph} = \frac{\text{observed reaction rate}}{\text{rate of incident radiation}}. \tag{56}$$

For suspended systems, η_{ph} can be written as:

$$\eta_{ph}^{susp} = \frac{\left\langle r_X^v\left(\underline{x}, t_0\right)\right\rangle_{V_R} V_R}{\left\langle q_w\left(\underline{x}\right)\right\rangle_{A_w} A_w} \tag{57}$$

where $\left\langle r_X^v\left(\underline{x}, t_0\right)\right\rangle_{V_R}$ is the initial volumetric reaction rate of pollutant X degradation averaged over the reactor volume V_R, and $\left\langle q_w\left(\underline{x}\right)\right\rangle_{A_w}$ represents the incident radiation flux averaged over the reactor window area, A_w. Similarly, for immobilized systems, the photonic efficiency can be calculated as:

$$\eta_{ph}^{immob} = \frac{\left\langle r_X\left(\underline{x}, t_0\right)\right\rangle_{A_{cat}} A_{cat}}{\left\langle q_w\left(\underline{x}\right)\right\rangle_{A_w} A_w}, \tag{58}$$

where $\left\langle r_X\left(\underline{x}, t_0\right)\right\rangle_{A_{cat}}$ is the initial surface reaction rate averaged over the catalytic area A_{cat}.

On the other hand, the quantum efficiency parameter relates the photocatalytic reaction rate with the radiation absorption rate:

$$\eta_{rxn} = \frac{\text{observed reaction rate}}{\text{rate of photon absorption}}. \tag{59}$$

In slurry reactors, where radiation absorption occurs in the whole reactor volume, η_{rxn} can be expressed as:

$$\eta_{rxn}^{susp} = \frac{\left\langle r_X^v\left(\underline{x}, t_0\right)\right\rangle_{V_R}}{\left\langle e^a\left(\underline{x}\right)\right\rangle_{V_R}} \tag{60}$$

where $\left\langle e^a\left(\underline{x}\right)\right\rangle_{V_R}$ represents the LVRPA averaged over the reactor volume V_R.

Table 5 Efficiency for Aeroxide P 25 and Kronos vlp 7000 TiO_2 in the degradation of BPA in a slurry reactor under UV–vis radiation

Catalyst	η_{abs} (%)	η_{rxn} (%)	η_{ph} (%)
Aeroxide TiO_2 P 25	67.9	0.20	0.14
Kronos vlp 7000 TiO_2	84.7	0.17	0.15

In reactors with the catalyst immobilized over a surface, η_{rxn} takes the following form:

$$\eta_{rxn}^{immob} = \frac{\left\langle r_X\left(\underline{x}, t_0\right)\right\rangle_{Acat}}{\left\langle e^{a,s}\left(\underline{x}\right)\right\rangle_{Acat}} \tag{61}$$

In this case, $\left\langle e^{a,s}\left(\underline{x}\right)\right\rangle_{Acat}$ represents the LSRPA averaged over A_{cat}.

In photocatalytic studies, the photonic efficiency is more frequently reported than the reaction efficiency, probably because it is much simpler to calculate, but its usefulness is under discussion [109]. The incident radiation flux can be evaluated straightforwardly. On the contrary, calculation of the fraction of energy effectively absorbed by the catalyst involves the measurement of the optical properties of the absorbing material and the resolution of radiation models, taking into account the phenomena of absorption, reflection, and scattering of radiation by the catalyst. Considering that only the absorbed photons are employed in photocatalytic reactions, the reaction efficiency is more appropriate for evaluating the performance of photocatalytic systems. Therefore, η_{ph} can only be considered as the lower limit of η_{rxn} [115].

Efficiency parameters that consider the fraction of absorbed energy (η_{abs} and η_{rxn}) are particularly important for comparing catalytic materials with different absorption properties, as in the case of visible light active catalysts. To illustrate this topic, Table 5 shows the values of efficiency parameters reported in [116] for the degradation of bisphenol A (BPA) in a slurry reactor under UV–visible radiation (350–550 nm). The comparison is made between two commercial catalysts, Aeroxide TiO_2 P 25 and Kronos vlp 7000 carbon-doped TiO_2, which exhibits absorption in the visible region.

The values of η_{ph} for the two catalysts are very similar, 0.14% and 0.15% for Aeroxide P 25 and Kronos vlp 7000, respectively. Nevertheless, radiation absorption is significantly higher for Kronos. Therefore, Kronos renders a lower value for η_{rxn} of 0.17%, versus 0.20% for Aeroxide P 25. This analysis reveals

Table 6 Efficiency comparison between FFR and FBR. Reprinted with permission from [118]. Copyright 2017 Elsevier

Reactor	Reaction rate $\times 10^9$ (mol s^{-1})	Photon absorption rate $\times 10^8$ (Einstein s^{-1})	η_{ph} (%)	η_{rxn} (%)
FFR	1.9	9.4	0.64	2.02
FBR	1.6	5.4	0.54	2.96

that Kronos has good absorption properties, but the absorbed radiation is not efficiently employed to convert the molecules of BPA. Aeroxide P 25 absorbs less radiation, but this energy is more efficiently used to degrade the pollutant. The comparison among these figures reveals that the challenge lies not only in improving the light absorption of the doped catalyst, but also in developing a material that can more efficiently use the harvested energy. It should be stressed that the performance of a photocatalyst for the degradation of a particular compound cannot be extrapolated to substrates of a different chemical structure [117], and that the former analysis is valid under the operating conditions of the study.

Another example that illustrates the convenience of calculating efficiency parameters to compare reactors with different configurations is presented in Table 6 (data extracted from [118]). A fixed-film reactor (FFR) (or wall reactor) with TiO_2 immobilized onto the reactor window is compared with a fixed-bed reactor (FBR) filled with TiO_2-coated glass rings. The degradation of the model pollutant clofibric acid in water was evaluated under artificial UV radiation. The same experimental setup was employed in both systems.

Under the same incident radiation, the FBR renders a reaction rate value about 15% lower than the FFR. Consequently, η_{ph} is also 15% lower for the FBR. Nevertheless, the value of the photon absorption rate in the FBR is much lower (almost 50%) than the value obtained in the FFR. Therefore, the quantum efficiency of the FBR is 1.5 times higher. This analysis indicates that the absorbed radiation is lower in the FBR but it is more efficiently employed for the degradation reaction. Hence, a possible strategy for increasing the reaction rate in the FBR would be to increase the number of TiO_2 coatings over the glass rings, and thus improve radiation absorption in this type of reactor.

7 Conclusions

This review presents a methodology for the modeling of photocatalytic reactors for chemical pollution abatement in water and air. The photocatalytic degradation of model pollutants in three of the most widely used reactor configurations has been analyzed: wall reactors with the catalyst immobilized onto the reactor window, slurry reactors with suspended catalyst particles in aqueous suspension, and fixed-bed reactors filled with catalyst-coated filling material.

The evaluation of the local absorption rate of photons inside the reactors is fundamental for estimating the reaction rate of the electron–hole generation and obtaining the intrinsic kinetics of the photocatalytic process. Additionally, the analysis of the absorbed radiation is essential to understanding the phenomena occurring in photocatalytic reactors and for making improvements in the reactors design, the absorption properties of catalytic materials, and the operating conditions of the processes.

From the results reported, it can be concluded that the proposed methodology has proven to be adequate to simulate the performance of photocatalytic reactors of different types, shapes, sizes, and configurations.

Acknowledgements The authors are grateful to Universidad Nacional del Litoral (UNL, Project PIC50420150100009LI), Consejo Nacional de Investigaciones Científicas y Técnicas (CONICET, Project PIP-2015 0100093), and Agencia Nacional de Promoción Científica y Tecnológica (ANPCyT, Project PICT-2015-2651, Project PICT 2014-1020) for the financial support. They also thank Claudia M. Romani for her technical assistance.

References

1. Alfano OM, Cassano AE (2009) In De Lasa H, Serrano-Rosales B (eds) Advances in chemical engineering, vol. 36: Photocatalytic Technologies, pp 229–287, Elsevier, New York
2. Imoberdorf GE, Irazoqui HA, Cassano AE, Alfano OM (2005) Photocatalytic degradation of tetrachloroethylene in gas phase on TiO_2 films: a kinetic study. Ind Eng Chem Res 44:6075–6085
3. Alfano OM, Cabrera MI, Cassano AE (1997) Photocatalytic reactions involving hydroxyl radical attack I. Reaction kinetics formulation with explicit photon absorption effects. J Catal 172:370–379
4. Muñoz-Batista MJ, Ballari MM, Kubacka A, Alfano OM, Fernández-García M (2019) Braiding kinetics and spectroscopy in photo-catalysis: the spectro-kinetic approach. Chem Soc Rev 48:637–682
5. Turchi CS, Ollis DF (1990) Photocatalytic degradation of organic water contamination: mechanisms involving hydroxyl radical attack. J Catal 122:178–192
6. Satuf ML, Brandi RJ, Cassano AE, Alfano OM (2008) Photocatalytic degradation of 4-chlorophenol: a kinetic study. Appl Catal B Environ 82:37–49
7. Marugán J, van Grieken R, Cassano AE, Alfano OM (2008) Intrinsic kinetic modeling with explicit radiation absorption effects of the photocatalytic oxidation of cyanide with TiO_2 and silica-supported TiO_2 suspensions. Appl Catal B Environ 85:48–60
8. Manassero A, Satuf ML, Alfano OM (2015) Kinetic modeling of the photocatalytic degradation of clofibric acid in a slurry reactor. Environ Sci Pollut Res 22:926–937
9. Tolosana-Moranchel A, Casas JA, Carbajo J, Faraldos M, Bahamonde A (2017) Influence of TiO_2 optical parameters in a slurry photocatalytic reactor: kinetic modelling. Appl Catal B Environ 200:164–173
10. Mueses MA, Machuca-Martinez F, Li Puma G (2013) Effective quantum yield and reaction rate model for evaluation of photocatalytic degradation of water contaminants in heterogeneous pilot-scale solar photoreactors. Chem Eng J 215–216:937–947
11. Brandi RJ, Rintoul G, Alfano OM, Cassano AE (2002) Photocatalytic reactors. Reaction kinetics in a flat plate solar simulator. Catal Today 76:161–175
12. Zalazar CS, Romero RL, Martín CA, Cassano AE (2005) Photocatalytic intrinsic reaction kinetics I: mineralization of dichloroacetic acid. Chem Eng Sci 60:5240–5254
13. Zalazar CS, Romero RL, Martín CA, Cassano AE (2005) Photocatalytic intrinsic reaction kinetics. II: effects of oxygen concentration on the kinetics of the photocatalytic degradation of dichloroacetic acid. Chem Eng Sci 60:4311–4322
14. Ballari MM, Alfano OM, Cassano AE (2009) Photocatalytic degradation of dichloroacetic acid. A kinetic study with a mechanistically based reaction model. Ind Eng Chem Res 48:1847–1858
15. Minero C, Vione D (2006) A quantitative evaluation of the photocatalytic performance of TiO_2 slurries. Appl Catal B Environ 67:257–269
16. Camera-Roda G, Augugliaro V, Cardillo AG, Loddo V, Palmisano L, Parrino F, Santarelli F (2015) A reaction engineering approach to kinetic analysis of photocatalytic reactions in slurry system. Catal Today 259:87–96
17. Camera-Roda G, Loddo V, Palmisano L, Parrino F (2017) Guidelines for the assessment of the rate law of slurry photocatalytic reactions. Catal Today 281:221–230
18. Casado C, Marugán J, Timmers R, Muñoz M, van Grieken R (2017) Comprehensive multiphysics modeling of photocatalytic processes by computational fluid dynamics based on intrinsic kinetic parameters determined in a differential photoreactor. Chem Eng J 310:368–380

19. Salvadores F, Minen RI, Carballada J, Alfano OM, Ballari MM (2016) Kinetic study of acetaldehyde degradation in gas phase applying visible light photocatalysis. Chem Eng Technol 39:166–174
20. Li Puma G, Salvadó-Estivill I, Obee TN, Hay SO (2009) Kinetics rate model of the photocatalytic oxidation of trichloroethylene in air over TiO_2 thin films. Sep Purif Technol 67:226–232
21. Yu QL, Ballari MM, Brouwers HJH (2010) Indoor air purification using heterogeneous photocatalytic oxidation part II: theoretical study. Appl Catal B Environ 99:58–65
22. Passalía C, Martínez Retamar ME, Alfano OM, Brandi RJ (2010) Photocatalytic degradation of formaldehyde in gas phase on TiO_2 Films: a kinetic study. Int J Chem React Eng 8:1–28
23. Passalía C, Alfano OM, Brandi RJ (2011) Modeling and experimental verification of a corrugated plate photocatalytic reactor using computational fluid dynamics. Ind Eng Chem Res 50:9077–9086
24. Passalía C, Alfano OM, Brandi RJ (2012) A methodology for modeling photocatalytic reactors for indoor pollution control using previously estimated kinetic parameters. J Hazard Mater 211–212:357–365
25. Muñoz-Batista MJ, Kubacka A, Gómez-Cerezo MN, Tudela D, Fernández-García M (2013) Sunlight-driven toluene photo-elimination using CeO_2–TiO_2 composite systems: a kinetic study. Appl Catal B Environ 140–141:626–635
26. Muñoz-Batista MJ, Ballari MM, Cassano AE, Alfano OM, Kubacka A, Fernández-García M (2015) Ceria promotion of acetaldehyde photo-oxidation in a TiO_2-based catalyst: a spectroscopic and kinetic study. Catal Sci Technol 5:1521–1531
27. Manassero A, Zacarías SM, Satuf ML, Alfano OM (2016) Intrinsic kinetics of clofibric acid photocatalytic degradation in a fixed-film reactor. Chem Eng J 283:1384–1391
28. Boyjoo Y, Sun H, Liu J, Pareek VK, Wang S (2017) A review on photocatalysis for air treatment: from catalyst development to reactor design. Chem Eng J 310:537–559
29. Cassano AE, Martín CA, Brandi RJ, Alfano OM (1995) Photoreactor analysis and design: fundamentals and applications. Ind Eng Chem Res 34:2155–2201
30. Salvadó-Estivill I, Brucato A, Li Puma G (2007) Two-dimensional modeling of a flat-plate photocatalytic reactor for oxidation of indoor air pollutants. Ind Eng Chem Res 46:7489–7496
31. Salvadó-Estivill I, Hargreaves DM, Li Puma G (2007) Evaluation of the intrinsic photocatalytic oxidation kinetics of indoor air pollutants. Environ Sci Technol 41:2028–2035
32. Assadi AA, Palauc J, Bouzaza A, Wolbert D (2013) Modeling of a continuous photocatalytic reactor for isovaleraldehyde oxidation: effect of different operating parameters and chemical degradation pathway. Chem Eng Res Des 91:1307–1316
33. Kuhn HJ, Braslavsky SE, Schmidt R (2004) Chemical actinometry (IUPAC technical report). Pure Appl Chem 76(12):2105–2146
34. Murov SL, Carmichael I, Hug GL (1993) Handbook of photochemistry, 2nd edn. Marcel Dekker, New York
35. Zalazar CS, Labas MD, Martín CA, Brandi RJ, Alfano OM, Cassano AE (2005) The extended use of actinometry in the interpretation of photochemical reaction engineering data. Chem Eng J 109:67–81
36. Roegiers J, van Walsem J, Denys S (2018) CFD- and radiation field modeling of a gas phase photocatalytic multi-tube reactor. Chem Eng J 338:287–299
37. Muñoz V, Casado C, Suárez S, Sánchez B, Marugán J (2019) Photocatalytic NOx removal: rigorous kinetic modelling and ISO standard reactor simulation. Catal Today 326:82–93
38. Zacarías SM, Satuf ML, Vaccari MC, Alfano OM (2012) Efficiency evaluation of different TiO_2 coatings on the photocatalytic inactivation of airborne bacterial spores. Ind Eng Chem Res 51:13599–13608
39. Ballari MM, Carballada J, Minen R, Salvadores F, Brouwers HJH, Alfano OM, Cassano AE (2016) Visible light TiO_2 photocatalysts assessment for air decontamination. Process Saf Environ 101:124–133
40. Briggiler Marcó M, Quiberoni AL, Negro AC, Reinheimer JA, Alfano OM (2011) Evaluation of the photocatalytic inactivation efficiency of dairy bacteriophages. Chem Eng J 172:987–993
41. Edwards DK (1977) Solar absorption by each element in an absorber-coverglass array. Sol Energy 19:401–402
42. Siegel R, Howell J (2002) Thermal radiation heat transfer, 4th edn. Taylor and Francis, New York
43. Muñoz-Batista MJ, Ballari MM, Kubacka AM, Cassano AE, Alfano OM, Fernández-García M (2014) Acetaldehyde degradation under UV and visible irradiation using CeO_2–TiO_2 composite systems: evaluation of the photocatalytic efficiencies. Chem Eng J 255:297–306

44. Mohseni M, Taghipour F (2004) Experimental and CFD analysis of photocatalytic gas phase vinyl chloride (VC) oxidation. Chem Eng Sci 59:1601–1609
45. Wang Z, Liu J, Dai Y, Dong W, Zhang S, Chen J (2012) CFD modeling of a UV-LED photocatalytic odor abatement process in a continuous reactor. J Hazard Mater 215–216:25–31
46. Queffeulou A, Geron L, Archambeau C, Le Gall H, Marquaire PM, Zahraa O (2010) Kinetic study of Acetaldehyde photocatalytic oxidation with a thin film of TiO_2 coated on stainless steel and CFD modeling approach. Ind Eng Chem Res 49:6890–6897
47. Jovic F, Kosar V, Tomasic V, Gomzi Z (2012) Non-ideal flow in an annular photocatalytic reactor. Chem Eng Res Des 90:1297–1306
48. Passalía C, Alfano OM, Brandi RJ (2017) Integral design methodology of photocatalytic reactors for air pollution remediation. Molecules 22:945–961
49. Einaga H, Tokura J, Teraoka Y, Ito K (2015) Kinetic analysis of TiO_2-catalyzed heterogeneous photocatalytic oxidation of ethylene using computational fluid dynamics. Chem Eng J 263:325–335
50. Trujillo FJ, Safinski T, Adesina AA (2009) Solid–liquid mass transfer analysis in a multi-phase tank reactor containing submerged coated inclined-plates: a computational fluid dynamics approach. Chem Eng Sci 42:1143–1153
51. Imoberdorf GE, Cassano AE, Alfano OM, Irazoqui HA (2006) Modeling of a multiannular photocatalytic reactor for perchloroethylene degradation in air. AIChE J 52(5):1814–1823
52. Imoberdorf GE, Irazoqui HA, Alfano OM, Cassano AE (2007) Scaling-up from first principles of a photocatalytic reactor for air pollution remediation. Chem Eng Sci 62:793–804
53. Imoberdorf GE, Cassano AE, Irazoqui HA, Alfano OM (2007) Optimal design and modeling of annular photocatalytic wall reactors. Catal Today 129:118–126
54. Tomasic V, Jovic F, Gomzi Z (2008) Photocatalytic oxidation of toluene in the gas phase: modelling an annular photocatalytic reactor. Catal Today 137:350–356
55. Marecic M, Jovic F, Kosar V, Tomasic V (2011) Modelling of an annular photocatalytic reactor. React Kinet Mech Cat 103:19–29
56. Vincent G, Marquaire PM, Zahraa O (2008) Abatement of volatile organic compounds using an annular photocatalytic reactor: study of gaseous acetone. J Photochem Photobiol A Chem 197:177–189
57. Adjimi S, Roux J-C, Sergent N, Delpech F, Thivel P-X, Pera-Titus M (2014) Photocatalytic oxidation of ethanol using paper-based nano-TiO_2 immobilized on porous silica: a modelling study. Chem Eng J 251:381–391
58. Demeestere K, De Visscher A, Dewulf J, Van Leeuwen M, Van Langenhove H (2004) A new kinetic model for titanium dioxide mediated heterogeneous photocatalytic degradation of trichloroethylene in gas-phase. Appl Catal B Environ 54:261–274
59. Vezzoli M, Martens WN, Bell JM (2011) Investigation of phenol degradation: true reaction kinetics on fixed film titanium dioxide photocatalyst. Appl Catal A Gen 404:155–163
60. Padoin N, Soares C (2017) An explicit correlation for optimal TiO_2 film thickness in immobilized photocatalytic reaction systems. Chem Eng J 310:381–388
61. Ozisik MN (1973) Radiative transfer and interactions with conduction and convection. Wiley, New York
62. de Lasa H, Serrano B, Salaices M (2005) Photocatalytic reaction engineering. Springer, New York
63. Satuf ML, Brandi RJ, Cassano AE, Alfano OM (2005) Experimental method to evaluate the optical properties of aqueous titanium dioxide suspensions. Ind Eng Chem Res 44:6643–6649
64. Marugán J, van Grieken R, Alfano OM, Cassano AE (2006) Optical and physicochemical properties of silica-supported TiO_2 photocatalysts. AIChE J 52:2832–2843
65. Tolosana-Moranchel A, Manassero A, Satuf ML, Alfano OM, Casas JA, Bahamonde A (2019) Influence of TiO_2-rGO optical properties on the photocatalytic activity and efficiency to photograde an emerging pollutant. Appl Catal B Environ 246:1–11
66. Duderstadt JJ, Martin R (1979) Transport theory. Wiley, New York
67. Modest MF (2003) Radiative heat transfer, 2nd edn. Academic Press, New York
68. Howell JR, Siegel R, Pinar Mengüc M (2011) Thermal radiation heat transfer, 5th edn. CRC Press, Boca Raton
69. Brucato A, Rizzuti L (1997) Simplified modeling of radiant fields in heterogeneous photoreactors. 1. Case of zero reflectance. Ind Eng Chem Res 36:4740–4747
70. Brucato A, Rizzuti L (1997) Simplified modeling of radiant fields in heterogeneous photoreactors. 2. Limiting "two-flux" model for the case of reflectance greater than zero. Ind Eng Chem Res 36:4748–4755

71. Brucato A, Cassano AE, Grisafi F, Montante G, Rizzuti L, Vella G (2006) Estimating radiant fields in flat heterogeneous photoreactors by the six-flux model. AIChE J 52:3882–3890
72. Colina-Márquez J, Machuca-Martínez F, Li Puma G (2009) Photocatalytic mineralization of commercial herbicides in a pilot-scale solar CPC reactor: photoreactor modeling and reaction kinetics constants independent of radiation field. Environ Sci Technol 43:8953–8960
73. Otálvaro-Marín HL, Mueses MA, Machuca-Martínez F (2014) Boundary layer of photon absorption applied to heterogeneous photocatalytic solar flat plate reactor design. Int J Photoenergy 1-8
74. Busciglio A, Alfano OM, Scargiali F, Brucato A (2016) A probabilistic approach to radiant field modeling in dense particulate systems. Chem Eng Sci 142:79–88
75. Satuf ML, José S, Paggi JC, Brandi RJ, Cassano AE, Alfano OM (2010) Reactor modeling in heterogeneous photocatalysis: toxicity and biodegradability assessment. Water Sci Technol 61:2491–2499
76. Romero RL, Alfano OM, Cassano AE (1997) Cylindrical photocatalytic reactors. Radiation absorption and scattering effects produced by suspended fine particles in an annular space. Ind Eng Chem Res 36:3094–3109
77. Romero RL, Alfano OM, Cassano AE (2003) Radiation field in an annular, slurry photocatalytic reactor. 2. Model and experiments. Ind Eng Chem Res 42:2479–2488
78. Romero RL, Alfano OM, Cassano AE (2009) Photocatalytic reactor employing titanium dioxide: from a theoretical model to realistic experimental results. Ind Eng Chem Res 48:10456–10466
79. Marugán J, van Grieken R, Pablos C, Satuf ML, Cassano AE, Alfano OM (2013) Modelling of a bench-scale photocatalytic reactor for water disinfection from laboratory-scale kinetic data. Chem Eng J 224:39–45
80. Camera Roda G, Santarelli F (2007) A rational approach to the design of photocatalytic reactors. Ind Eng Chem Res 46:7637–7644
81. Pareek V, Chong S, Tadé M, Adesina AA (2008) Light intensity distribution in heterogenous photocatalytic reactors. Asia Pac J Chem Eng 3:171–201
82. Duran JE, Taghipour F, Mohseni M (2010) Irradiance modeling in annular photoreactors using the finite-volume method. J Photochem Photobiol A 215:81–89
83. Huang Q, Liu T, Yang J, Yao L, Gao L (2011) Evaluation of radiative transfer using the finite volume method in cylindrical photoreactors. Chem Eng Sci 66:3930–3940
84. Spadoni G, Bandini E, Santarelli F (1978) Scattering effects in photosensitized reactions. Chem Eng Sci 33:517–524
85. Pasquali M, Santarelli F, Porter JF, Yue PL (1996) Radiative transfer in photocatalytic systems. AIChE J 42:532–537
86. Yang Q, Ang PL, Ray MB, Pehkonen SO (2005) Light distribution field in catalyst suspensions within an annular photoreactor. Chem Eng Sc 60:5255–5268
87. Moreira J, Serrano B, Ortíz A, de Lasa H (2010) Evaluation of photon absorption in an aqueous TiO_2 slurry reactor using Monte Carlo simulations and macroscopic balance. Ind Eng Chem Res 49:10524–10534
88. Zekri M, Colbeau-Justin C (2013) A mathematical model to describe the photocatalytic reality: what is the probability that a photon does its job? Chem Eng J 225:547–557
89. Doll T, Frimmel F (2004) Kinetic study of photocatalytic degradation of carbamazepine, clofibric acid, iomeprol and iopromide assisted by different TiO_2 materials-determination of intermediates and reaction pathways. Water Res 38:955–964
90. Alfano OM, Satuf ML, Manassero A (2017) Photon transport phenomena: radiation absorption and scattering effects on photoreactors. Chapter 4, pp 97–122, Word Scientific Pub. Europe
91. Imoberdorf GE, Alfano OM, Cassano AE, Irazoqui HA (2007) Monte Carlo model of UV-radiation interaction with TiO_2-coated spheres. AIChE J 53:2688–2703
92. Loddo V, Yurdakal S, Palmisano G, Imoberdorf GE, Irazoqui HA, Alfano OM, Augugliaro V, Berber H, Palmisano L (2007) Selective photocatalytic oxidation of 4-methoxybenzyl alcohol to p-anisaldehyde in organic-free water in a continuous annular fixed bed reactor. Int J Chem Reactor Eng 5:A57
93. Verbruggen SW, Ribbens S, Tytgat T, Hauchecorne B, Smits M, Meynen V, Cool P, Martens JA, Lenaerts S (2011) The benefit of glass bead supports for efficient gas phase photocatalysis: case study of a commercial and a synthesised photocatalyst. Chem Eng J 174:318–325
94. Vaiano V, Sacco O, Pisano D, Sannino D, Ciambelli P (2015) From the design to the development of a continuous fixed bed photoreactor for photocatalytic degradation of organic pollutants in wastewater. Chem Eng Sci 137:152–160

95. Ramos B, Ookawara S, Matsushita Y, Yoshikawa S (2015) Intensification of solar photocatalysis with immobilized TiO_2 by using micro-structured reaction spaces. J Environ Chem Eng 3:681–688
96. Claes T, Dilissen A, Leblebici ME, Van Gerven T (2019) Translucent packed bed structures for high throughput photocatalytic reactors. Chem Eng J 361:725–735
97. Imoberdorf GE, Vella G, Sclafani A, Rizzuti L, Alfano OM, Cassano AE (2010) Radiation model of a TiO_2-coated, quartz wool, packed-bed photocatalytic reactor. AIChE J 56(4):1030–1044
98. Vella G, Imoberdorf GE, Sclafani A, Cassano AE, Alfano OM, Rizzuti L (2010) Modeling of a TiO_2-coated quartz wool packed bed photocatalytic reactor. Appl Catal B Environ 96:399–407
99. Changrani RG, Raupp GB (1999) Monte Carlo simulation of the radiation field in a reticulated foam photocatalytic reactor. AIChE J 45:1085–1094
100. Changrani RG, Raupp GB (2000) Two-dimensional heterogeneous model for a reticulated foam photocatalytic reactor. AIChE J 46:829–842
101. Kouamé AN, Masson R, Robert D, Keller N, Keller V (2013) β-SiC foams as a promising structured photocatalytic support for water and air detoxification. Catal Today 209:13–20
102. Alexiadis A, Baldi G, Mazzarino I (2001) Modelling of a photocatalytic reactor with a fixed bed of supported catalyst. Catal Today 66:467–474
103. Sampaio MJ, Silva CG, Silva AMT, Vilar VJP, Boaventura RAR, Faria JL (2013) Photocatalytic activity of TiO_2-coated glass raschig rings on the degradation of phenolic derivatives under simulated solar light irradiation. Chem Eng J 224:32–38
104. Cloteaux A, Gérardin F, Thomas D, Midoux N, André J-C (2014) Fixed bed photocatalytic reactor for formaldehyde degradation: experimental and modeling study. Chem Eng J 249:121–129
105. Manassero A, Satuf ML, Alfano OM (2017) Photocatalytic degradation of an emerging pollutant by TiO_2-coated glass rings: a kinetic study. Environ Sci Pollut Res 24:6031–6039
106. Cerdá J, Marchetti JL, Cassano AE (1977) Radiation efficiencies in elliptical photoreactors. Lat Am J Heat Mass Transf 1:33–63
107. Passalía C, Alfano OM, Brandi RJ (2013) Optimal design of a corrugated-wall photocatalytic reactor using efficiencies in series and computational fluid dynamics (CFD) modeling. Ind Eng Chem Res 52:6916–6922
108. Imoberdorf GE, Cassano AE, Irazoqui HA, Alfano OM (2007) Simulation of a multi-annular photocatalytic reactor for degradation of perchloroethylene in air: parametric analysis of radiative energy efficiencies. Chem Eng Sci 64:1138–1154
109. Motegh M, Cen J, Appel PW, van Ommen JR, Kreutzer M (2012) Photocatalytic-reactor efficiencies and simplified expressions to assess their relevance in kinetic experiments. Chem Eng J 207–208:607–615
110. Bolton JR, Bircher KG, Tumas W, Tolman CA (2001) Figures-of-merit for the technical development and application of advanced oxidation technologies for both electric- and solar-driven systems (IUPAC technical report). Pure Appl Chem 73(4):627–637
111. Serrano B, de Lasa H (1997) Photocatalytic degradation of water organic pollutants. Kinetic modeling and energy efficiency. Ind Eng Chem Res 36:4705–4711
112. de Lasa H, Serrano B, Moreira J, Valades-Pelayo P (2016) Efficiency factors in photocatalytic reactors: quantum yield and photochemical thermodynamic efficiency factor. Chem Eng Technol 39:51–65
113. Li D, Xiong K, Li W, Yang Z, Liu C, Feng X, Lu X (2010) Comparative study in liquid phase heterogeneous photocatalysis: model for photoreactor scale-up. Ind Eng Chem Res 49:8397–8405
114. Leblebici ME, Stefanidis GD, Van Gerven T (2015) Comparison of photocatalytic space-time yields of 12 reactor designs for wastewater treatment. Chem Eng Process 97:106–111
115. Brandi RJ, Citroni MA, Alfano OM, Cassano AE (2003) Absolute quantum yields in photocatalytic slurry reactors. Chem Eng Sci 58:979–985
116. Manassero A, Satuf ML, Alfano OM (2013) Evaluation of UV and visible light activity of TiO_2 catalysts for water remediation. Chem Eng J 225:378–386
117. Ryu J, Choi W (2008) Substrate-specific photocatalytic activities of TiO_2 and multiactivity test for water treatment application. Environ Sci Technol 42:294–300
118. Manassero A, Satuf ML, Alfano OM (2017) Photocatalytic reactors with suspended and immobilized TiO_2: comparative efficiency evaluation. Chem Eng J 326:29–36